Geofluids

Near Wellbore Fluid Flow

Lead Guest Editor: Bisheng Wu
Guest Editors: Fengshou Zhang, Qianbing Zhang, Andrew Bunger, and Brice Lecampion

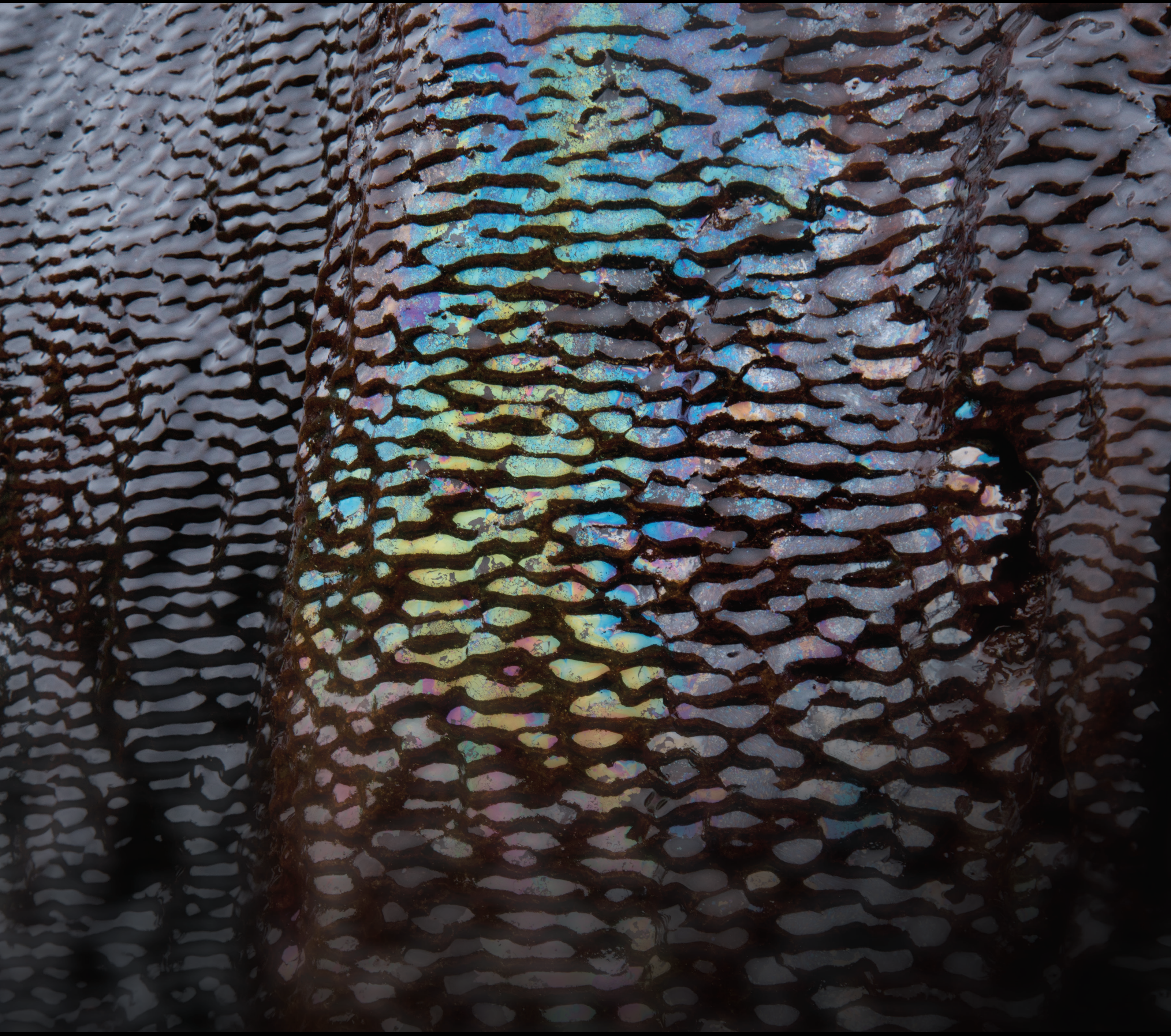

Near Wellbore Fluid Flow

Geofluids

Near Wellbore Fluid Flow

Lead Guest Editor: Bisheng Wu
Guest Editors: Fengshou Zhang, Qianbing Zhang, Andrew Bunger, and Brice Lecampion

Contents

Contents

Hindawi
Geofluids
Volume 2019, Article ID 4923173, 13 pages
https://doi.org/10.1155/2019/4923173

Research Article

The Influence of Injected Fluids on Microscopic Pore Structures in the Intersalt Dolomitic Shale Oil Reservoirs

Tong Zhou,[1] Wei Yan ,[2] Jianzheng Su,[1] Xianglu Tang,[2] Hao Tian,[2] Wenbo Li,[2] Kongyang Wang,[2] Ting Sun ,[2] Ruyue Wang,[1] Rusheng Zhang,[1] and Jun Niu[1]

[1]*Research Institute of Petroleum Exploration and Development of SINOPEC, Beijing 100083, China*
[2]*China University of Petroleum-Beijing, Beijing 102249, China*

Correspondence should be addressed to Wei Yan; yanwei289@126.com

Received 17 October 2018; Revised 12 February 2019; Accepted 29 August 2019; Published 28 November 2019

Guest Editor: Qianbing Zhang

Given their low porosity and permeability, intersalt dolomitic shale oil reservoirs need to be developed via large-scale hydraulic fracturing to achieve economic effects. However, various lithologies and salt materials make these reservoirs vulnerable to salt mineral dissolution and recrystallization and salt plugging during development. This study investigated the variation rules of pore structures, porosity, and permeability of intersalt dolomitic shale oil reservoirs under the influence of hydraulic fracturing fluid. Correspondingly, a series of experiments (i.e., high-temperature and high-pressure soaking experiments, focused ion beam scanning helium ion microscope analyses, and porosity and pulse permeability tests) is performed on the Qian 3^4-10 rhythmic intersalt dolomitic shales. Results show that distilled water dissolves the salt crystals inside the matrix pores to improve the reservoir permeability. However, the distilled water-rock interaction will cause the massive migration of salt minerals. By contrast, the supercritical CO_2 can disperse salt particles, dredge the channels, and enlarge pores by expansion, but it has an overall weak capability of changing the pore structure and matrix permeability. To simulate the supercritical CO_2 composite fracturing, the mixed solution of supercritical CO_2 and distilled water favors the salt dissolution effect in the water-based fracturing fluid and recovery enhancement by CO_2. This solution can remarkably improve the reservoir porosity and permeability and avoid massive salt mineral migration and salt crystallization damage. This study is theoretically and practically important to the effective and enhanced development of intersalt dolomitic shale oil reservoirs.

1. Introduction

In recent years, shale oil has become a key area for unconventional oil and gas exploration and development after shale gas. China's continental basins have developed a number of lacustrine mud shale strata with wide distribution, high abundance of organic matter, large thickness, and huge potential for shale oil resource, and they are considered a strategic option for the sustainable development of old oilfields in the east [1]. Among them, intersalt dolomitic shale oil reservoirs in the Qianjiang Depression of the Jianghan Basin has become an important target for China's shale oil technology breakthrough due to its numerous oil-bearing strata, superior hydrocarbon source conditions, and good oil-bearing properties.

Intersalt dolomitic shale oil reservoirs in the Qianjiang Depression have become so effective that they require volumetric reconstruction through hydraulic fracturing. The production data after hydraulic fracturing show that the initial increase of production is good and that the daily production of a single well can reach 69.2 tons. However, after fracturing, the very high salinity of the fracturing fluid (up to 26×10^4 mg L^{-1}) is ubiquitous, and salt particle crystals can be seen in the flowback fluid. Moreover, the stable production time is short, usually one to four months. After this period, the production drops rapidly. Given the particularity of the intersalt dolomitic shale oil reservoir, the reservoir contains soluble salts, and a thick salt layer develops at the top of the reservoir. After the water-based fracturing fluid enters the reservoir, it dissolves the soluble salt minerals inside the rock, causing the migration and recrystallization of the salt minerals, which forms the “salt blockage” in the formation and wellbore. The seepage capacity near the wellbore gradually decreases, and the production decreases rapidly several months after the fracturing.

CO_2 fracturing is one of the waterless fracturing techniques that has unique production-increasing effects, such as increasing fracture complexity, reducing damage, improving crude oil flow, and increasing formation energy [2–6]. In the early 1980s, CO_2 fracturing has been used in oil/gas field practices and has achieved good production-increasing effects in many wells [2, 7, 8]. For intersalt dolomitic shale oil reservoirs, using CO_2 fracturing can avoid the dissolution and recrystallization of salt minerals caused by water-based fracturing fluids.

In terms of physical properties, CO_2 is easy to transform and can exist in gaseous, liquid, or supercritical fluid forms, which are primarily affected by pressure and temperature. When the temperature and pressure exceed 31.1°C and 7.38 MPa, respectively, CO_2 exists in a supercritical state. In this state, the intermolecular force of CO_2 is small, the surface tension is zero, and the fluidity is so strong that molecules can enter any space larger than the supercritical CO_2 molecule [9]. As CO_2 is easily soluble in formation water and forms carbonic acid, it can dissolve minerals such as feldspar and carbonate in rock under reservoir pressure and temperature. Therefore, the physical properties of the reservoir and the mechanical properties of the rock are changed [8, 10–14]. However, the change processes of microscopic pore structures and the porosity/permeability of shale reservoirs during supercritical CO_2 fracturing remain unknown. In addition, due to the differences in physical properties of shale reservoirs, the influence of supercritical CO_2 on the physical properties of the reservoir is different.

To investigate the influence of water-based fracturing fluid and supercritical CO_2 on the physical properties of an intersalt shale reservoir, a series of high-temperature and high-pressure shale immersion experiments was performed, followed by microscopic pore structure observation and porosity and pulse permeability tests. The pore structure, porosity, and permeability change of intersalt shale under different fluids and the damage law of salt crystallization on physical properties of shale are studied. The results are expected to provide theoretical support for the correct formulation of measures for stable production and increased production in intersalt shale oil reservoirs.

2. Overview of the Region

The Jianghan Basin is an inland salt lake basin. Under the closed, high-salinity, and strong-evaporation environment of the Qianjiang Formation of Paleogene in the Qianjiang Depression, thousands of meters of thick salt-bearing strata are deposited, and hundreds of salt cyclothem (a sedimentary cycle is a rhythm) have developed. Each cyclothem consists of upper and lower salt rocks and a set of carbon-rich laminated argillaceous dolomite, dolomitic mudstone, and calcium-glauber mudstone (or calcium glauber rock filled with cloud mudstone) strata in between. Each salt cyclothem generally has an approximate thickness of 5 to 12 m and can sometimes reach up to 20 m. The formation is composed of hydrocarbon source and reservoir layers, which are blocked by upper and lower salt rock to form an intersalt dolomitic shale oil reservoir.

The intersalt dolomitic shale oil reservoir is a high-quality hydrocarbon source layer integrally, which is composed mainly of argillaceous dolomite facies followed by dolomitic mudstone [15]. Based on fluid compartment theory, the formation water in the intersalt shale reservoir is primary water with no external water interference [16, 17]. At the same time, salt minerals accumulate in the cracks and pore channels for over a long period of time under high-temperature and high-pressure conditions, resulting in no formation water, low reservoir permeability, and good sealing. On-site production data also indicate that wells without water injection measures have no produced water after production.

The object of the study is the intersalt dolomitic shale of Qian 3^4-10 cyclothem in the Qianjiang Depression of the Jianghan Basin. Figure 1 presents the results of mineral composition analysis. The intersalt strata are primarily composed of mud, salt, and carbonate minerals. The upper part of the cyclothem is carbon-rich laminated argillaceous dolomite facies. The dolomite content is 12.8% to 78.2% with an average of 50.7%. The average total content of carbonate minerals in argillaceous dolomite is 65.2%. The middle part is carbon-rich laminated dolomitic or calcareous mudstone facies. The argillaceous mineral content is relatively high, mainly feldspar minerals, which account for approximately 12.5% to 48.7% with an average of 44.5%, followed by carbonate minerals, with an average of 40.2%. The bottom of the cyclothem is mainly composed of glauberite mudstone facies, which consist of argillaceous, salt (mainly sodium chloride and glauberite), and carbonate minerals with indistinguishable contents. In general, the intersalt dolomite shale oil reservoir has a low clay mineral content (mainly chlorite and illite with an average content of 10.3%) that shows characteristics of low clay minerals, low quartz, high sodium feldspar, and high carbon. In addition, the 3^4-10 cyclothem of the intersalt dolomite shale oil reservoir has overall salt-bearing properties. The salt content of the upper and middle argillaceous dolomite and dolomite mudstones is relatively low, ranging from 2.5% to 9.1%. The glauberite mudstone near the bottom of the cyclothem layer has a relatively high salt content of up to 46.6%.

The physical properties of the different lithofacies of Qian 3^4-10 cyclothem in the intersalt dolomite shale reservoir have obvious differences (Table 1). Based on the lithology statistics of several typical wells in the exploration area, the porosity distribution of mud dolomite is mostly between 6% and 15%, and the permeability of around 45% of the sample is below $0.5 \times 10^{-3}\ \mu m^2$. The porosity of dolomite mudstone is less than 25%, with 50% of the samples concentrated in 9% to 12%, and the permeability is basically below $0.5 \times 10^{-3}\ \mu m^2$. The porosity of the glauberite mudstone varies widely (between 0% and 20%), and the permeability is concentrated below $0.5 \times 10^{-3}\ \mu m^2$, as shown in Figure 2. Mercury intrusion experiments show that the upper

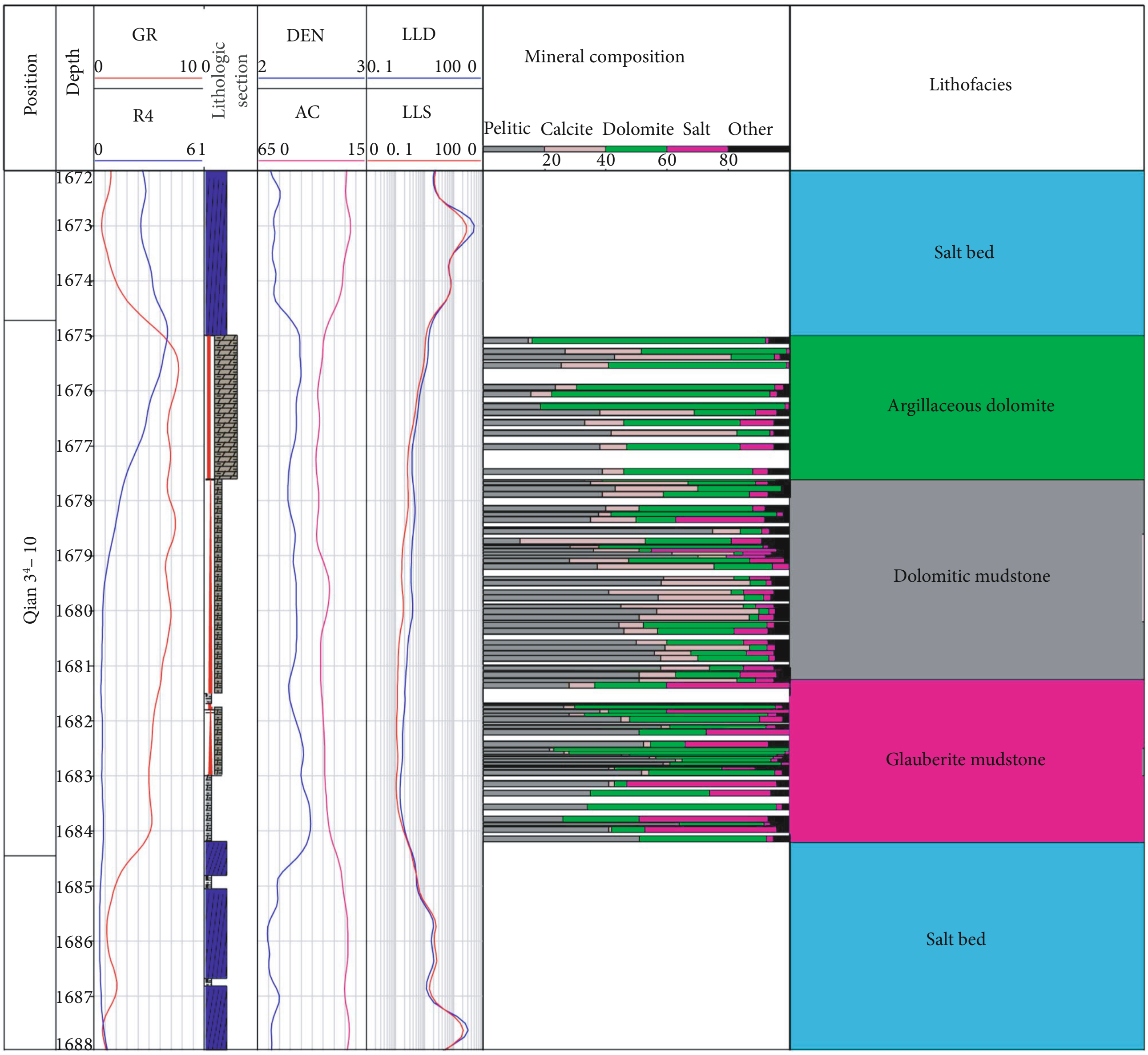

FIGURE 1: Sedimentary facies histogram of Qian 3^4-10 cyclothem in the intersalt dolomite shale reservoir.

TABLE 1: Average pore throat radius of different lithofacies of Qian 3^4-10 cyclothem in the intersalt dolomite shale reservoir.

Lithofacies	Average median pressure (MPa)	Average median pore throat radius (nm)	Average pore throat radius (nm)
Argillaceous dolomite	5.21	87.1	94
Dolomite mudstone	22.9	36.7	37.9
Glauberite mudstone	9.42	71.3	67.2

carbon-rich laminated argillaceous dolomite facies (thickness of approximately 3–4 m) has a high average pore throat radius (>90 nm) and relatively good physical properties. The dolomite mudstone facies in the middle and lower parts of the reservoir have poor physical properties, the median pressure of the mercury injection is high, and the average pore throat radius is less than 40 nm.

3. Microscopic Pore Structure and Salt Characteristics

Scanning electron microscopy observations were performed on the pores using a Zeiss focused ion beam scanning helium ion microscope. The Gatan 691.CS argon ion thinning instrument was used for argon ion polished sampling.

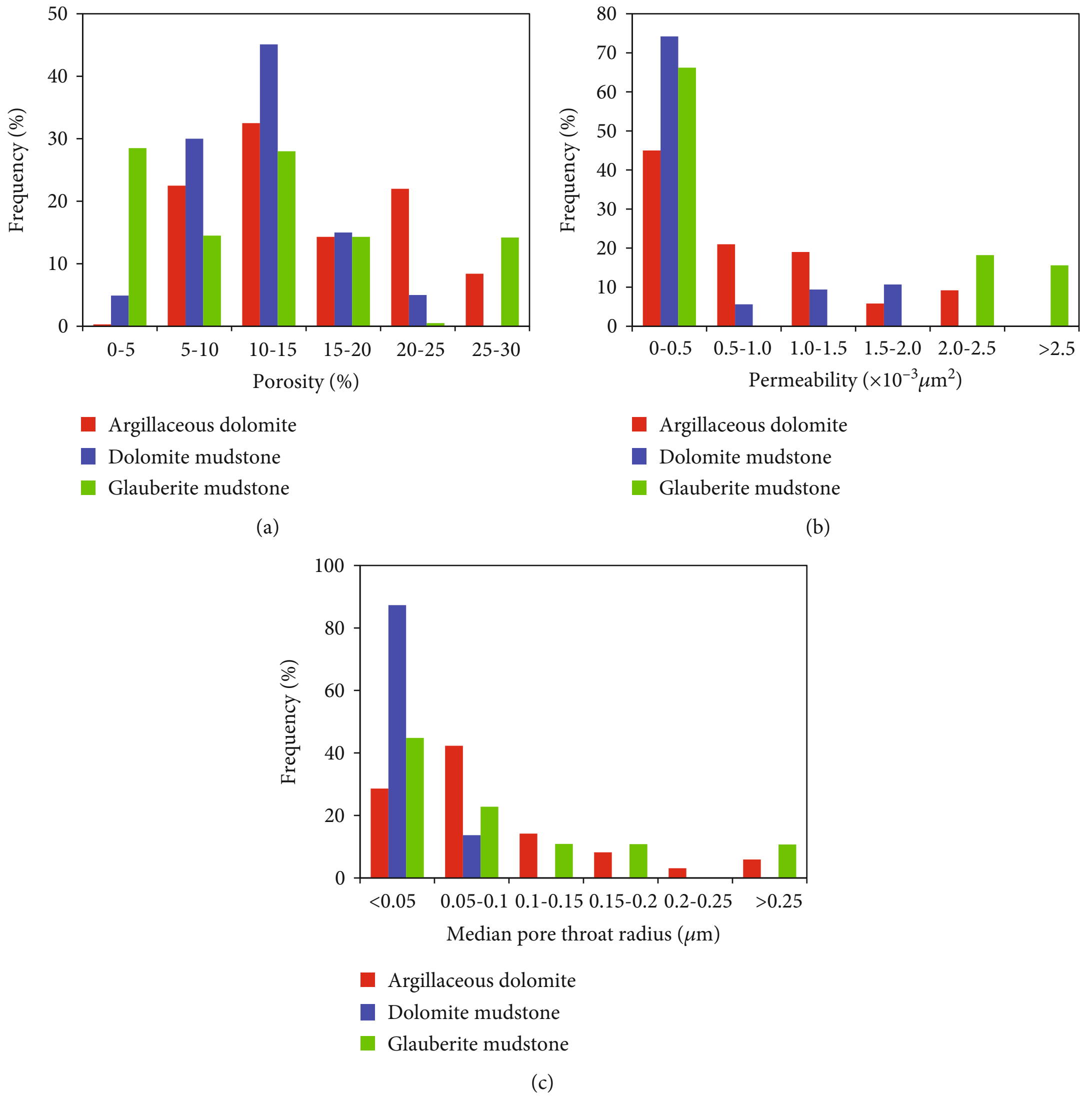

Figure 2: Spectrum statistics results of porosity and permeability of different lithologies.

The main steps include sample pregrinding, high-energy argon ion thinning pretreatment, surface deposition of a conductive film, gold coating treatment, and electron microscope observation. The surface of the argon ion polished sample is smooth, and the backscattered electron imaging used is suitable for observing the microstructure and morphology of the nanopores.

3.1. Microscopic Pore Structure. Dolomites are widely distributed in argillaceous dolomite, often with rhombohedral crystals, and the grains are mostly less than 5 μm in size. It mainly develops dolomite and glauberite intergranular pores. The diameter of the dolomite intergranular pores is generally 0.5–10 μm, which are large intergranular pores supported by dolomite mineral lattice. The average pore diameter is nearly 2 μm, and the surface pore rate can reach 7.8%, as shown in Figure 3(a). The dolomite intergranular pores are one of the important oil storage spaces in the intersalt shale oil reservoir. Dissolution pores are generally distributed with a pore diameter of approximately 0.5–9 μm and a dissolution surface pore rate of around 5%–20%. They develop near the bedding plane and are also the main oil storage space. Most of the dissolution pores are effective pores, but some are filled with a large amount of salt particles, such as rock salt or glauberite, as shown in Figure 3(b). Second, a small number of intragranular pores are developed, including dolomite and quartz intragranular pores. The pore size is generally 5–200 nm with an average of 30 nm, and the surface pore rate can reach up to 4.2%. The dolomitic mud shale also develops intergranular pores of clustered pyrite, bedding joints, and diagenetic shrinkage joints, as shown in Figures 3(c) and 3(d).

The dolomite mudstone mainly develops intergranular pores of clay minerals and dolomite. The pore diameter is generally 0.5–6 μm with an average of around 1 μm, and the surface pore rate can reach up to 6.1%. Rock salt particles are scattered on the pore surface. The rock salt crystals have a good original shape and are tetragonal. The length of the single particles is slightly shorter at around 200 nm. Clay minerals and dolomite intragranular pores are developed. The

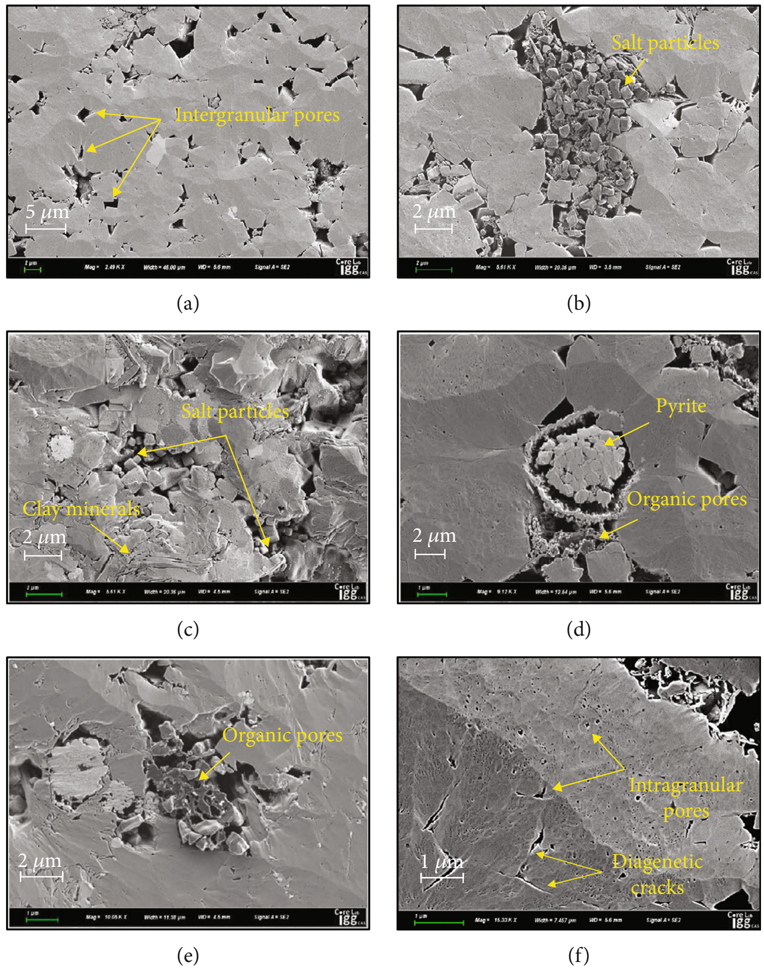

Figure 3: Original pore structure characteristics of intersalt dolomitic shale.

pore size is generally 5–200 nm with an average of around 50 nm, and the surface pore rate can reach up to 3.1%. Compared with argillaceous dolomite, the dolomite mudstone pores are less developed, and the pore size is relatively small, as shown in Figure 3(e).

In addition, a small number of organic pores that developed inside the pyrolysis asphalt are found in the dolomite mudstone. The pore morphology is mostly irregular, bubble-like, and elliptical. The pore size is 5–300 nm, with an average of around 100 nm, and the surface pore rate can reach up to 15%, as shown in Figure 3(f). Secondary mineral particles with complete crystallization are usually developed in the edge or interior of the organic pores, and the pore volume usually accounts for 20%–50% of the total volume of organic particles with good pore connectivity.

3.2. Soluble Salt Minerals. The electron microscopy scanning results showed that the intersalt reservoir has microscopic salinity characteristics. Soluble salt minerals are widely distributed in the pores and cracks. The microscopic morphology of the reservoir salt particles consists of a single salt particle and a collection of salt particles. The intergranular pore size of the salt particles is less than 300 nm. The salt aggregates can completely fill the pores and also block the cracks, resulting in poor pore connectivity of the reservoir and hindering fluid flow in the reservoir.

Moreover, the intersalt cloud shale also has macroscopic salinity characteristics. As can be seen by the naked eyes, the core rock sample is mixed with unequal rock salt and glauberite particles, and some cracks are also filled with salt minerals. The salt characteristics of shale samples are quantitatively described by micro-CT scanning technique. The results show that in the Qian3^4-10 cyclothem, few salt particles are present in the argillaceous dolomite layer and shale in the middle dolomite mudstone layer, mainly distributed between 1.3% and 3.8%, as shown in Figures 4(a) and 4(b). At the same time, the cracks are partially filled with sodium chloride particles and glauberite minerals. The glauberite mudstone near the salt layer has high salt content, and the volume ratio of the sodium chloride and glauberite particles is around 15.7%–21.81%, as shown in Figure 4(c).

Fracturing practice shows that the salinity of the flowback fluid of the shale reservoir is generally high [18, 19]. With the extension of the backflow time, the salinity of the flowback fluid keeps increasing, reaching up to $10 \times 10^4\,\mathrm{mg\,L^{-1}}$, whereas the salinity of the slick water injected during fracturing is very low (approximately $1000\,\mathrm{mg\,L^{-1}}$) [18, 19]. The salt ions in the flowback fluid are mainly derived from the

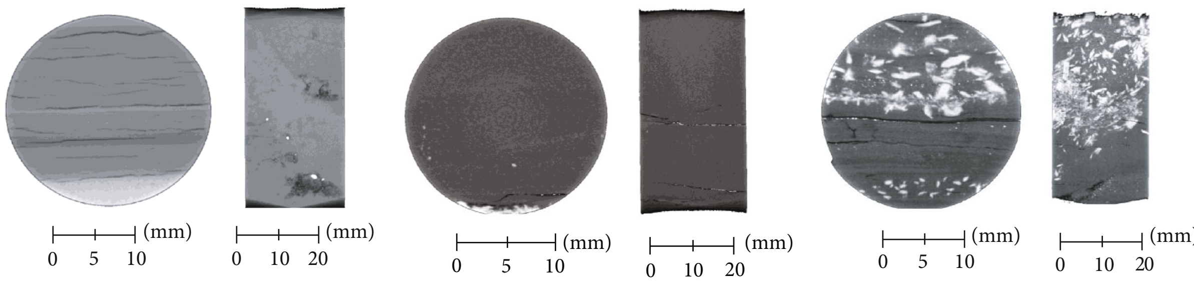

(a) Argillaceous dolomite (b) Dolomite mudstone (c) Glauberite mudstone

Figure 4: Micro-CT scanning results of the core rock (white spots are salt particles).

dissolution of the shale's own minerals and the crystalline salts of the pore walls. When the fracturing fluid with low salinity enters the reservoir, the large difference in salinity between the fracturing fluid and the formation results in a remarkable chemical potential difference between them, which becomes the driving force for the low salinity liquid to enter the shale interior [20–22]. As for the intersalt dolomite shale reservoir, the interior has microscopic and macroscopic salinity properties, and the high-salinity difference will lead to a high chemical potential difference. After the fracturing fluid with low salinity infiltrates into the reservoir, it dissolves the salt minerals inside the reservoir continuously. Superficially, if the matrix and soluble salts in the fractures of the shale reservoir are dissolved, additional circulation channels can be obtained for reservoir oil and gas. This is also one of the main reasons for using low-viscosity slick water fracturing or water injection to increase shale oil production. However, further studies are needed to determine the specific effects of dissolution, migration, and recrystallization of soluble salt minerals on the physical properties of a reservoir.

4. Effects of Different Fluid Types

4.1. Sample Collection and Processing. The core samples are taken from the downhole cores of the Qian3^4-10 cyclothem at varying depths in the Qianjiang Depression, Jianghan Basin. As the intersalt shale is a typical stratified rock mass, the bedding surface is prone to open when exposed to water. However, factors such as the water solubility of salt rock can also contribute to this problem. Therefore, to avoid the opening of the bedding surface and dissolution of soluble minerals within the rock caused by hydraulic cutting, all samples in the experiment undergo anhydrous processing, and the samples are processed into a standard core column with a diameter of 2.54 cm. Then, the side of the core is wrapped and sealed with epoxy resin, and only the two end faces of the core are in contact with the fluid when immersed.

4.2. Methods of Experiment. The shale sample is preplaced in a high-temperature and high-pressure reaction tank with a volume of 157 mL and evacuated. Then, fluid is injected into the reaction tank until the pressure becomes constant at 20 MPa, and the temperature in the incubator is kept constant at 80°C. The experimental immersion fluid includes distilled water, CO_2 (CO_2 is in a supercritical state at 80°C and

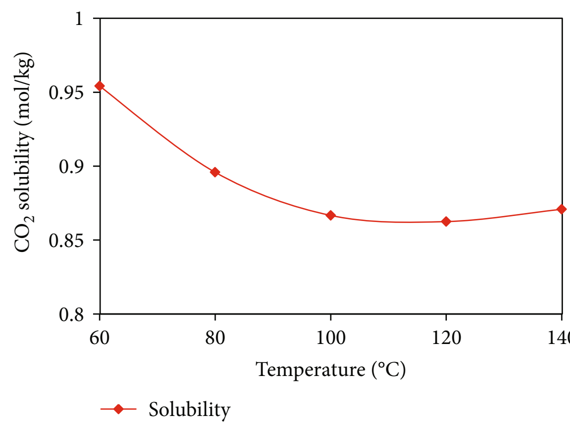

Figure 5: Solubility of CO_2 in water (20 MPa).

20 MPa), and a liquid mixture of CO_2 and distilled water (supercritical CO_2 saturated solution). When the immersion fluid medium is a supercritical CO_2 saturated solution, the immersion step differs from distilled water or pure CO_2. First, 100 mL of distilled water is injected into the reaction tank. The shale sample is placed in an aqueous phase, evacuated, and heated at a constant temperature of 80°C. Thereafter, the high-temperature and high-pressure reaction tank is charged with CO_2 until the fluid pressure in the tank reaches 20 MPa.

After the shale samples are immersed under high-temperature and high-pressure conditions, the porosity and permeability of different shale samples are measured by using helium porosimetry and ultralow permeability meter (pulse attenuation method). Moreover, helium is used as the test gas.

4.3. Solubility of CO_2. When supercritical CO_2 is mixed with water, hydrogen ions are formed through ionization, which makes the solution acidic, as shown in formula (1). Related literatures show that the higher the pressure, the higher the solubility of CO_2, the more hydrogen ions are ionized in the solution, and the lower the pH of the solution [8, 23, 24]. At the same time, the solubility of CO_2 in water at different temperatures under 20 MPa is measured, as shown in Figure 5. As seen in the figure, with the increase in temperature, the solubility of CO_2 in water decreases and tends to be stable when the temperature is greater than 100°C:

$$CO_2 + H_2O \longrightarrow H^+ + HCO_3^- \quad (1)$$

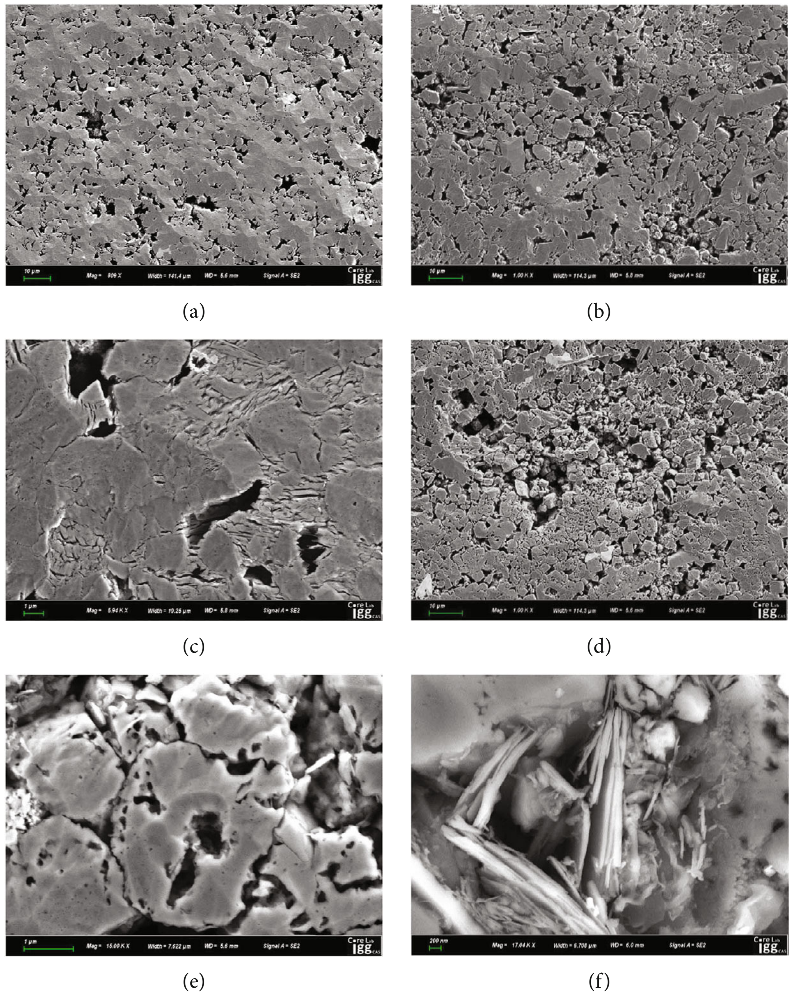

(a) (b) (c) (d) (e) (f)

Figure 6: Microscopic pore structure changes before and after the interaction of different fluids. (a) Pores of muddy dolomite are increased, and salt minerals migrate (supercritical CO_2). (b) Salt minerals are dissolved (distilled water). (c) Clay mineral expansion occurs (distilled water). (d) Pores are dissolved, causing caves (supercritical CO_2 saturated solution). (e) Dolomite particles are dissolved, causing dissolved pores (supercritical CO_2 saturated solution). (f) Clay is released, and particle migration occurs (supercritical CO_2 saturated solution).

For intersalt shale reservoirs, active H^+ and HCO_3^- interact with carbonates, such as calcite and dolomite, to dissolve carbonate rocks:

$$CaCO_3 + H^+ \longrightarrow Ca^{2+} + HCO_3^- \tag{2}$$

$$CaMg(CO_3)_2 + 2H^+ \longrightarrow Ca^{2+} + Mg^{2+} + 2HCO_3^- \tag{3}$$

H^+ and HCO_3^- can also interact with the feldspar minerals inside the reservoir. Aside from causing dissolution and sedimentation of silicate, they can also form kaolinite:

$$2KAlSi_3O_8 + 2H^+ + 9H_2O \longrightarrow 2K^+ + 4H_4SiO_4 + Al_2SiO_5(OH)_4 \tag{4}$$

$$\begin{aligned} NaAlSi_3O_3 + CO_2 + 5.5H_2O \longrightarrow {} & Na^+ + HCO_3^- + 2H_4SiO_4 \\ & + 0.5Al_2SiO_5(OH)_4 \end{aligned} \tag{5}$$

Therefore, the interaction of CO_2-water-reservoir rocks will lead to the dissolution of reservoir rocks and the formation of sediments, which will directly result in the change of pore structure and permeability of reservoirs.

4.4. *Results and Analysis of the Experiment*

4.4.1. Changes in the Microscopic Pore Structure. Under the conditions of 80°C and 20 MPa, the shale samples are immersed in distilled water, supercritical CO_2, and supercritical CO_2 saturated solution. Then, microscopic pore scanning electron microscopy is conducted to compare the microstructure changes in the intersalt cloud shale before and after the fluid action. The results are shown in Figure 6.

For argillaceous dolomite samples, some of the pores are filled with many salt crystals without treatment, as shown in Figure 3(a). The filled salt minerals occupy most of the fluid passages, hindering fluid migration. After immersing in supercritical CO_2, the surface pore rate reaches 9.1%, as shown in Figure 6(a). This result may be due to the expansion

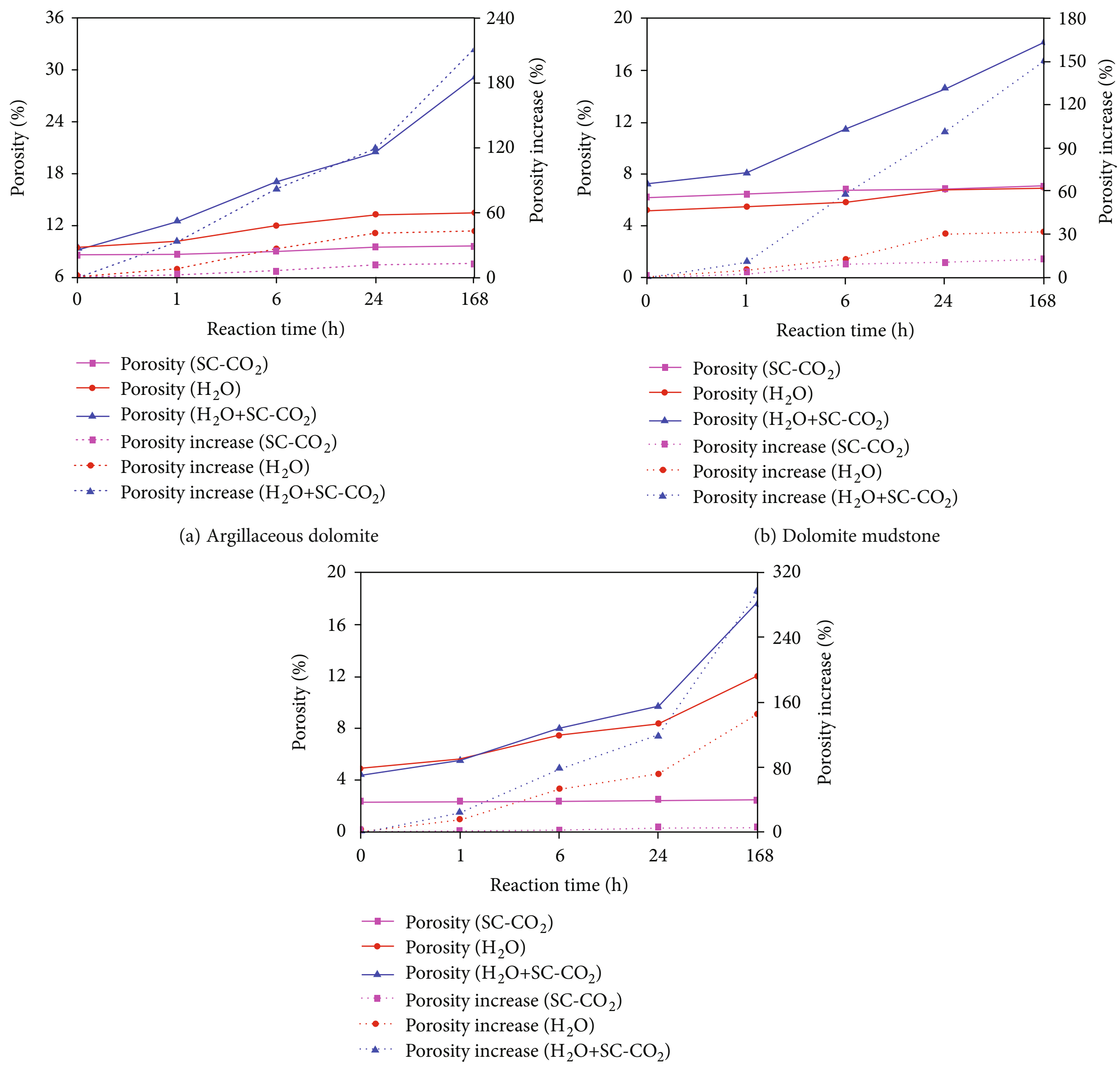

(a) Argillaceous dolomite

(b) Dolomite mudstone

(c) Glauberite mudstone

Figure 7: Change of porosity after immersion in fluid at different times.

of CO_2. On the one hand, the pore throat radius increases and the effective stress decreases due to the volume expansion of CO_2. On the other hand, the CO_2 expansion affects and disperses the collection of salt particles in the pore channels into salt particles, thereby dredging pores and reducing the flow resistance of the reservoir fluid. However, under the reservoir conditions, the salt minerals still remain in the reservoir and occupy the flow channels of the reservoir fluid.

When immersed in distilled water, the salt crystals in the pores dissolve, and the pore channels expand, significantly increasing the surface pore rate (around 40%) and greatly improving pore connectivity, as shown in Figure 6(b). However, distilled water weakens the cohesive force between the rock mineral particles, which loosens the rocks and even produces microcracks. In addition, the clay mineral undergoes hydration expansion under the action of water, as shown in Figure 6(c). However, due to the low clay mineral content of the intersalt shale reservoir, the hydration of clay minerals has minimal effect on the shale skeleton or pore structure.

When the shale sample is immersed in a supercritical CO_2 saturated solution, the saturated solution has the greatest impact on the micropore structure of shale. First, distilled water can dissolve salt, and the pore channels are enlarged when salt crystals dissolve inside the pore channels. In addition, when supercritical CO_2 dissolves in distilled water, it will produce a weak acid that will dissolve the cement and mineral components of the rock particles, thereby greatly increasing the pore radius and even producing the dominant channel of the acid-rock reaction. The surface pore rate can reach up to 23.6%, as shown in Figure 6(d). Second, the weak acid solution will dissolve the skeleton particles, resulting in dissolved pores with a diameter of 50–100 nm inside the

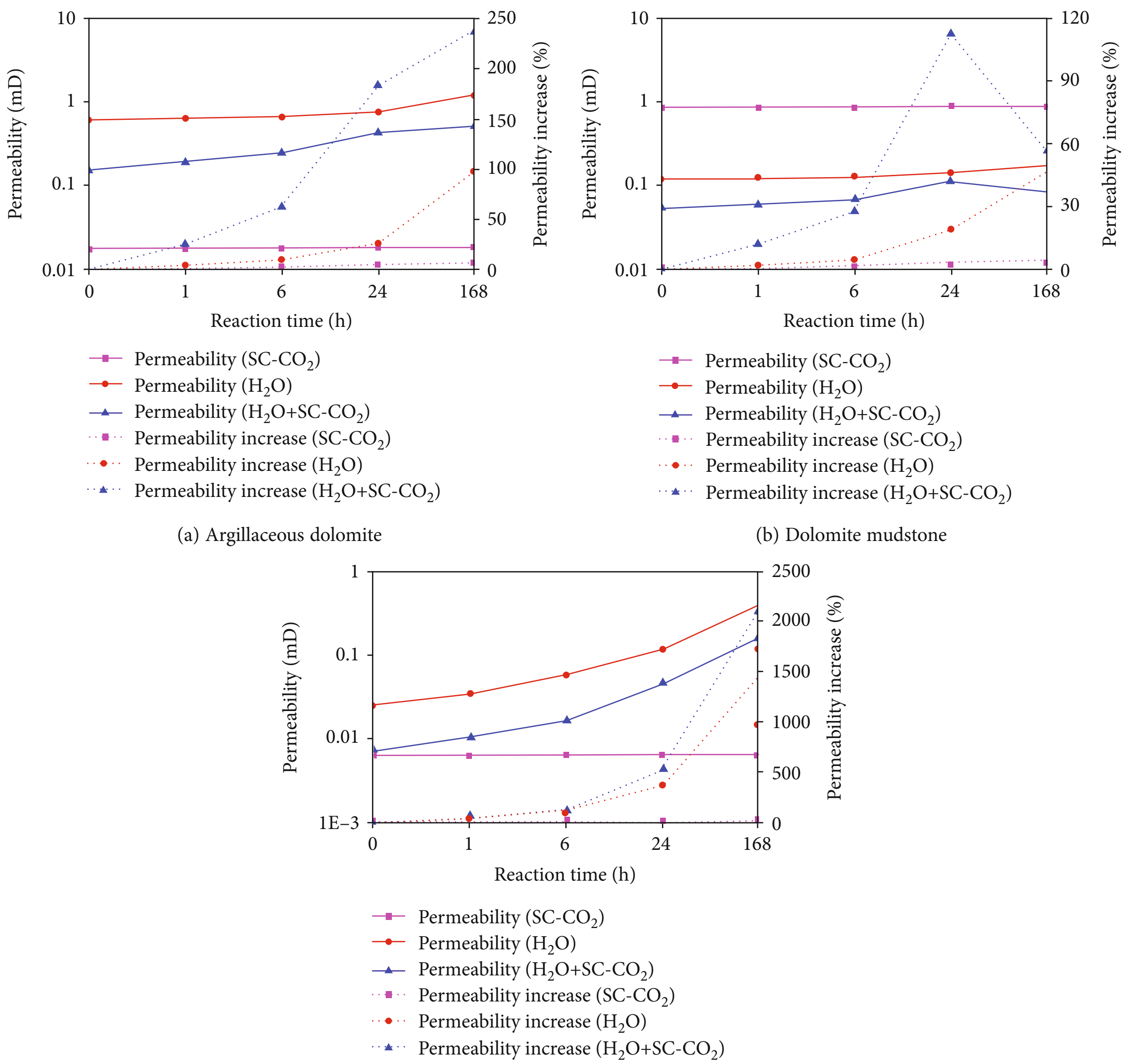

(a) Argillaceous dolomite

(b) Dolomite mudstone

(c) Glauberite mudstone

FIGURE 8: Change of permeability after immersion in fluid at different times.

particles, as shown in Figure 6(e). The saturated solution destroys the stability of the clay minerals and causes the dissolution of the cement of the skeleton particle, leading to the increase of intergranular pores and considerable migration of clay particles, as shown in Figure 6(f).

4.4.2. Change of Porosity. Figure 7 shows the results of porosity change of the shale samples after immersing in supercritical CO_2, distilled water, and supercritical CO_2 saturated solution at 20 MPa and 80°C.

The results of the experiment show that the porosity increased at varying degrees after immersing the samples in different fluids. The supercritical CO_2 saturated solution obtained the largest increase in porosity. The salt solution effect of distilled water combined with the dissolution effect of the weak acid generated by the dissolution of supercritical CO_2 in water will greatly expand the pore and increase the pore volume. The porosity of argillaceous dolomite and glauberite mudstone with high total content of salt minerals and carbonates increased by 210.7% and 296.7%, respectively, after immersion for 168 h. The pore-enlarging effect of distilled water was mainly derived from the dissolution of salt minerals. The effect was most obvious in the glauberite mudstone with high salt content. The porosity of argillaceous dolomite and dolomite mudstone with lower salt mineral content increased by 43% and 31.9%, respectively, after immersion in distilled water for 168 h. By contrast, the pore-enlarging effect of supercritical CO_2 was relatively small, and the porosity of different samples increased by approximately 6.0% to 13.2% after 168 h immersion.

4.4.3. Change of Permeability. After immersion in different fluids, an ultralow permeability meter is used to measure the change in permeability of the shale samples over time. The results are shown in Figure 8.

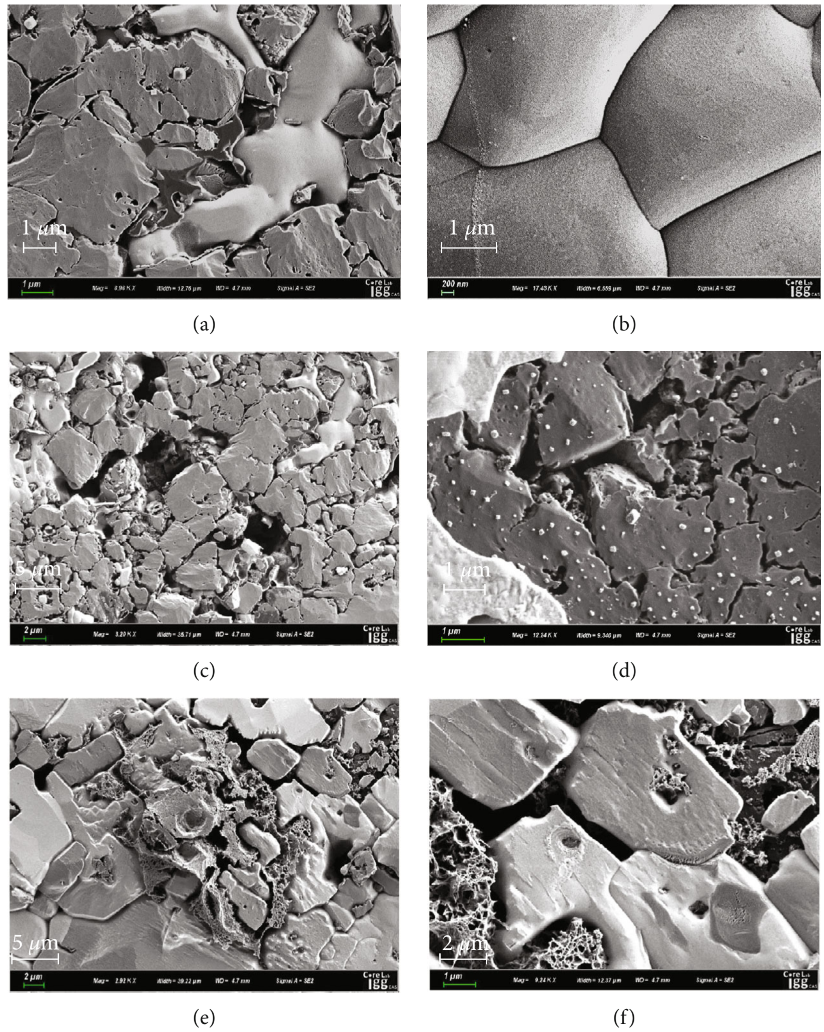

Figure 9: Pore microstructure changes after static evaporation salting out. (a) Clumps of superimposed growth morphology of salt crystals; (b) densely packed salt crystals with no internal permeability; (c) pores partially filled with salt crystals; (d) single-salt-particle dispersion morphology; (e, f) surface-attached layered or flocculent growth morphology of salt crystals.

As can be seen from the figure, the effect of supercritical CO_2 on permeability improvement is not obvious. For the argillaceous dolomite samples with relatively good porosity and permeability, the permeability increases by 13.7% through flushing the salt crystal minerals and dredging the pore channels. For the glauberite mudstone samples, the permeability only changes by 4.2% due to its small internal pores that are mostly blocked by salt minerals. The permeability of distilled water is greatly improved by dissolving the salt minerals in the pores. After immersion for 168 h, the permeabilities of the argillaceous dolomite and dolomite samples increase by 97.6% and 46.2%, respectively. By contrast, the permeability of glauberite mudstone samples with high salt minerals increases by 14.7% after immersion for 168 h. Therefore, the better the initial porosity and permeability conditions, the greater the salt content and the increase in permeability. When the supercritical CO_2 is dissolved in distilled water, the weak acid dissolves and expands the pores, which then improves interporosity connectivity, enlarges the range of water-salt-rock action, and strengthens the salt solution of distilled water. The permeability of the glauberite mudstone minerals increases by 21.1 times after immersion in supercritical CO_2 saturated solution for 168 h.

5. Effects of Recrystallization of Salt Minerals

During the mining process, due to changes of formation temperature and pressure in and near the wellbore, the solubility of the salt minerals changes, causing the precipitation of salt minerals and salt crystallization. Then, salt crystallization will lead to damage near the wellbore reservoir. The static evaporation salting-out method is used to simulate the salt crystallization phenomenon in the formation so as to evaluate the damage degree of salt crystallization on the porosity and permeability of the intersalt shale oil reservoir. The specific steps are as follows: (1) under the conditions of 80°C and 20 MPa, the shale sample is placed in a saturated sodium chloride solution for 24 h using a high-temperature and high-pressure reactor; (2) the shale immersed in the saturated sodium chloride solution is heated in an oven at a constant temperature 60°C and evaporated to constant weight; and (3) the morphology and microscopic

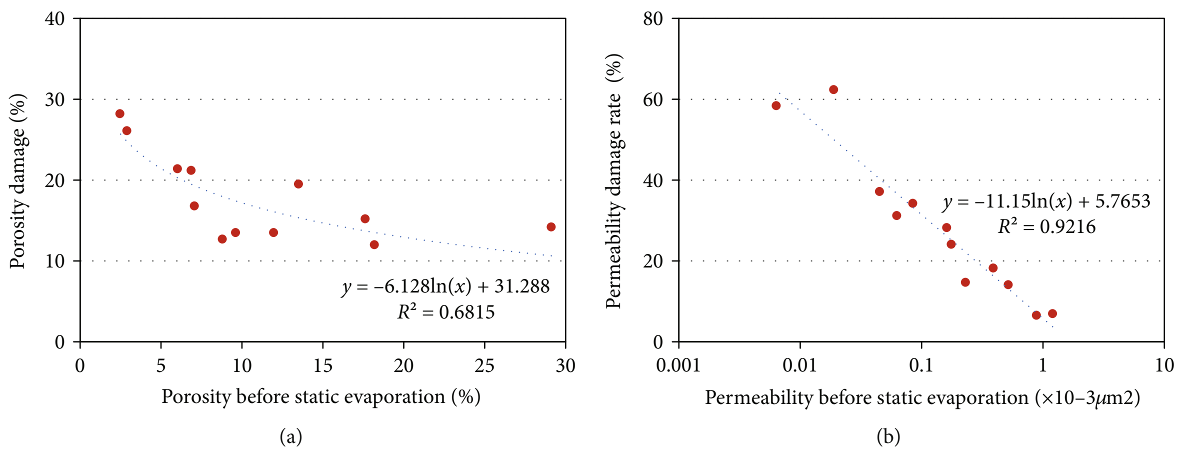

FIGURE 10: Effects of salt precipitation on the porosity and permeability of intersalt dolomitic shale.

distribution of salt crystals are observed under scanning electron microscopy to determine the effect on the porosity and permeability of the intersalt shale.

5.1. Morphology and Microscopic Distribution of Salt Crystal. Scanning electron microscopy observation of salt shale after salt crystallization shows three main forms of salt crystals, including clumps of superimposed growth morphology of intergranular pore/seam filling type, surface-attached layered or flocculent growth morphology, and single-particle dispersion morphology, as shown in Figure 9.

The filling-type agglomerated crystalline salt usually aggregates in the dominant channel with good evaporation environment. These channels generally have large pore size and good connectivity because the fluid saturation in the large pores is usually high and the large pore size also provides a good evaporation environment for the liquid [25–27]. The salt crystals are stably stacked in the large pores and gradually fill the entire pores. However, these filled salt crystals are densely packed and have no internal permeability, as shown in Figure 9(b). Therefore, the filling of the cluster salt crystals may partially cause the dominant pores to fail, as shown in Figure 9(c). At the corners of pores or on the surfaces of rocks, scattered regular single-crystal crystalline salts with a length of tens to hundreds of nanometers are present, as shown in Figures 9(a) and 9(d). Given the small particle size, such salt crystals tend to migrate and block small pores.

When the flow and evaporation environments of the tunnel are relatively poor, irregular flocculated or layered crystals attached to the surface of rock particles are generated due to unstable salt crystal deposition (Figures 9(d)–9(f)). On the one hand, the layered adhesion and flocculation of the salt crystals will make the pore flow channel narrower. On the other hand, the flocculent salt crystals are easy to disperse, accumulate, and block the pore due to the lack of framework support.

5.2. Influence on Porosity and Permeability. The microscopic scanning results show that salt crystallization will occupy a certain reservoir pore space and block the shale pore channels. By measuring the changes of shale porosity and permeability before and after static evaporation salting-out experiments, the salt crystals will lead to the decrease of porosity and permeability of shale. The average porosity and permeability decreased by 17.8% and 37.5%, respectively, as shown in Figure 10. The smaller the porosity and permeability of the shale, the greater the damage of salt crystals to the porosity and permeability. This is due to the small pore throat of rocks with low permeability, most of which contain small pores or micropores. These micropores are easily blocked by fine salt crystals, so the permeability is drastically lowered. For rocks with high permeability, most of the pore channels are relatively large and are not easily blocked by salt crystals. In addition, the dispersed crystalline salt particles are more likely to migrate in cores with better permeability [26–28]. Therefore, the permeability of the shale sample with high permeability will slightly decrease after the salt crystallizes.

6. Discussion

With low water saturation and high salt content in pores, the formation water in the intersalt dolomite shale reservoir mainly exists in the form of salt crystal water. The salt crystals will block the pore channels, reduce the connectivity between pores, and increase flow resistance. Water-based fracturing fluids can greatly increase the porosity and permeability of reservoirs by dissolving the salt minerals in the matrix. The salt minerals are dissolved after contact with water, especially in the glauberite mudstone layer near the salt layer. Then, the rock porosity and permeability will be greatly improved. When the salt minerals are dissolved, they will migrate to the fracture and bottom of the well in the form of high-salinity water. Under the influence of temperature and pressure, high-salinity water recrystallizes and gradually blocks the matrix, cracks, and wellbore. At this point, the water extrusion process can be adopted to restore the production capacity of the reservoir by dissolving the salt minerals. However, the water injected in a later stage continuously acts on the glauberite mudstone layer and strengthens its permeability, thereby providing unfavorable conditions for the dissolution of the salt layer at the top of the reservoir and the migration of many salt minerals.

Supercritical CO_2 fracturing can avoid the problems caused by the dissolution, migration, and recrystallization of salt minerals due to water-based fracturing fluids. At the same time, supercritical CO_2 fracturing increases the complexity of hydraulic fractures and improves the fluidity of the mixed phase. However, the results of microscopic scanning observation and pore infiltration parameter test show that the salt content and pore connectivity of intersalt shale reservoirs are poor. Although supercritical CO_2 can disperse the salt particles, dredge the channels, and enlarge the pores due to expansion, its overall ability to change the structure and permeability of the pores is still weak. Therefore, it cannot meet the requirements of economic development for transformation effect by only using the supercritical CO_2 for the transformation of intersalt shale reservoirs.

At present, the fracturing technology combining CO_2 with water-based fracturing fluid has become an emerging technology for unconventional oil and gas development. For the intersalt shale oil reservoir, the supercritical CO_2 composite fracturing technology can reduce the amount of water-based fracturing fluid and the considerable dissolution and migration of salt minerals. At the same time, after the CO_2-water-shale interaction, the pore circulation channel is enlarged, and porosity and permeability are improved. To a certain extent, the damage of salt crystals to the physical properties of the reservoir near the wellbore is reduced. Therefore, the CO_2 composite fracturing technology combines the salt dissolution effect of water-based fracturing fluid and the unique effect in production increase of CO_2, which may cause effective long-term development of intersalt shale oil reservoirs. However, further research needs to be conducted on how to optimize the amount and proportion of CO_2 and water-based fracturing fluid based on the physical damage law of the reservoir under the interaction of fluid-rock-salt in the intersalt dolomite shale reservoir.

7. Conclusion

(1) The intersalt dolomite shale reservoir has microscopic and macroscopic saliferous characteristics, which lead to poor pore connectivity of the reservoir and hinder the flow of reservoir fluid. Distilled water can enlarge the flow passage by dissolving soluble salt minerals inside the reservoir. However, the dissolution and migration of many salt crystals will cause problems for later production

(2) During the mining process, salt minerals are precipitated, and salt crystals are formed due to changes in formation temperature and pressure in the wellbore and near the well. Salt crystals will occupy a certain pore space and block the pore channel. The smaller the porosity of the shale and the lower the permeability, the greater the damage of salt crystals to the pores

(3) Supercritical CO_2 disperses the salt particles, dredges the channels, and slightly enlarges the pores by expansion, but the overall ability to change the pore structure and connectivity is still weak. By using supercritical CO_2 to transform the intersalt shale reservoir, the problems caused by salt dissolution and recrystallization can be avoided. However, supercritical CO_2 cannot meet the requirement of economic development for the transformation effect

(4) When supercritical CO_2 is dissolved in distilled water, it will produce a weak acid, which erodes the cement and the mineral components of the rock particles, greatly increasing the radius of the channel. At the same time, by reducing the amount of water-based fracturing fluid and increasing the porosity and permeability of the matrix, the cycle of salt plugging caused by the massive migration of salt minerals will be reduced, which is conducive to extending the effective period of increased production

Data Availability

The data used to support this study are included within the article.

Conflicts of Interest

The authors declare that they have no conflicts of interest.

Acknowledgments

This paper was support by the Major National Science and Technology Projects of China (No. 2017ZX05049003-05).

References

[1] Z. Shanwen, "Thinking and practice of tertiary oil and gas exploration of maturing region in eastern China: a case study of Jiyang depression," *Acta Petrolei Sinica*, vol. 33, no. s1, pp. 53–62, 2012.

[2] M. L. Sinal and G. Lancaster, "Liquid CO_2 fracturing: advantages and limitations," *Journal of Canadian Petroleum Technology*, vol. 26, no. 5, pp. 26–30, 1987.

[3] T. Ishida, Q. Chen, Y. Mizuta, and J. C. Roegiers, "Influence of fluid viscosity on the hydraulic fracturing mechanism," *Journal of Energy Resources Technology*, vol. 126, no. 3, pp. 190–200, 2004.

[4] B. C. Nuttall, C. Eble, R. M. Bustin, and J. A. Drahovzal, *Analysis of Devonian black shales in Kentucky for potential CO2 sequestration and enhanced natural gas production*, Kentucky Geological Survey, USA, 2005.

[5] A. Kizaki, H. Tanaka, K. Ohashi, K. Sakaguchi, and K. Matsuki, "Hydraulic fracturing in Inada granite and Ogino tuff with super critical carbon dioxide," in *ISRM Regional Symposium-7th Asian Rock Mechanics Symposium*, International Society for Rock Mechanics and Rock Engineering, 2012.

[6] Z. Bennour, T. Ishida, Y. Nagaya et al., "Crack extension in hydraulic fracturing of shale cores using viscous oil, water, and liquid $_{\text{Carbon Dioxide}}$," *Rock Mechanics and Rock Engineering*, vol. 48, no. 4, pp. 1463–1473, 2015.

[7] A. B. Yost, R. L. Mazza, and J. B. Gehr, "CO2/Sand fracturing in devonian shales," in *SPE Eastern Regional Meeting*, Society of Petroleum Engineers, 1993.

[8] Y. Zou, S. Li, X. Ma, S. Zhang, N. Li, and M. Chen, "Effects of CO_2-brine-rock interaction on porosity/permeability and mechanical properties during supercritical- CO_2 fracturing in shale reservoirs," *Journal of Natural Gas Science and Engineering*, vol. 49, pp. 157–168, 2018.

[9] R. Tudor, C. Vozniak, W. Peters, and M. Banks, "Technical advances in liquid CO_2 fracturing," in *Annual Technical Meeting*, Petroleum Society of Canada, Calgary, Alberta, 1994.

[10] S. Fischer, A. Liebscher, and M. Wandrey, "CO_2-brine-rock interaction – First results of long-term exposure experiments at in situ P-T conditions of the Ketzin CO_2 reservoir," *Chemie der Erde-Geochemistry*, vol. 70, no. S3, pp. 155–164, 2010.

[11] M. Alam, M. Hjuler, H. Christensen, and I. Fabricius, "Petrophysical and rock-mechanics effects of CO_2 injection for enhanced oil recovery: Experimental study on chalk from South Arne field, North Sea," *Journal of Petroleum Science and Engineering*, vol. 122, pp. 468–487, 2014.

[12] Q. Lyu, P. Ranjith, X. Long, and B. Ji, "Experimental investigation of mechanical properties of black shales after CO_2-water-rock interaction," *Materials*, vol. 9, no. 8, p. 663, 2016.

[13] Y. Lu, X. Ao, J. Tang, Y. Jia, X. Zhang, and Y. Chen, "Swelling of shale in supercritical carbon dioxide," *Journal of Natural Gas Science and Engineering*, vol. 30, pp. 268–275, 2016.

[14] H. Yin, J. Zhou, X. Xian et al., "Experimental study of the effects of sub- and super-critical CO_2 saturation on the mechanical characteristics of organic-rich shales," *Energy*, vol. 132, pp. 84–95, 2017.

[15] C. G. Huang, X. L. Ni, and X. M. Ma, "Petroleum and gas enrichment pattern and major controlling factors of stable and high production of tight lacustrine carbonate rock reservoirs: a case of the Yingxi area in Qaidam Basin," *Journal of Northwest University (Natural Science Edition)*, vol. 47, no. 5, pp. 724–738, 2017.

[16] J. M. Hunt, "Generation and Migration of Petroleum from Abnormally Pressured Fluid Compartments (1)," *AAPG Bulletin*, vol. 74, no. 1, pp. 1–12, 1990.

[17] C. G. Huang, J. Y. Yuan, G. R. Tian, L. R. Wu, X. Pan, and Y. Y. Hui, "The geochemical characteristics and formation mechanism of the Eocene lacustrine dolomite reservoirs in the western Qaidam," *Earth Science Frontiers*, vol. 23, no. 3, pp. 230–242, 2016.

[18] F. Wang and Z. Pan, "Numerical simulation of chemical potential dominated fracturing fluid flowback in hydraulically fractured shale gas reservoirs," *Petroleum Exploration and Development*, vol. 43, no. 6, pp. 971–977, 2016.

[19] L. Yang, H. Ge, X. Shi et al., "The effect of microstructure and rock mineralogy on water imbibition characteristics in tight reservoirs," *Journal of Natural Gas Science & Engineering*, vol. 34, pp. 1461–1471, 2016.

[20] H. K. Ge, L. Yang, Y. H. Shen et al., "Experimental investigation of shale imbibition capacity and the factors influencing loss of hydraulic fracturing fluids," *Petroleum Science*, vol. 12, no. 4, pp. 636–650, 2015.

[21] P. Fakcharoenphol, B. Kurtoglu, H. Kazemi, S. Charoenwongsa, and Y. S. Wu, "The effect of osmotic pressure on improve oil recovery from fractured shale formations," in *SPE unconventional resources conference*, Society of Petroleum Engineers, 2014.

[22] T. Zhou, S. Zhang, L. Yang, X. Ma, Y. Zou, and H. Lin, "Experimental investigation on fracture surface strength softening induced by fracturing fluid imbibition and its impacts on flow conductivity in shale reservoirs," *Journal of Natural Gas Science & Engineering*, vol. 36, pp. 893–905, 2016.

[23] R. Shiraki and T. L. Dunn, "Experimental study on water-rock interactions during CO_2 flooding in the Tensleep Formation, Wyoming, USA," *Applied Geochemistry*, vol. 15, no. 3, pp. 265–279, 2000.

[24] Z. H. Duan and R. Sun, "An improved model calculating CO_2 solubility in pure water and aqueous NaCl solutions from 273 to 533 K and from 0 to 2000 bar," *Chemical Geology*, vol. 193, pp. 257–271, 2003.

[25] T. Yong, D. Zhimin, and J. Hongmei, "Reservoir damages caused by formation-water salt precipitation in high-pressure and high-temperature gas reservoirs," *Acta Petrolei Sinica*, vol. 33, no. 5, pp. 859–863, 2012.

[26] C. Guodong, R. Shaoran, L. Zhang et al., "Formation water evaporation induced salt precipitation and its effect on gas production in high temperature natural gas reservoirs," *Petroleum Exploration and Development*, vol. 43, no. 5, pp. 749–757, 2016.

[27] A. H. Alizadeh, M. Akbarabadi, E. Barsotti, M. Piri, N. Fishman, and N. Nagarajan, "Salt Precipitation in Ultra-Tight Hydrocarbon Reservoir Rocks: A Multi-Scale Experimental Study," in *Unconventional Resources Technology Conference, Austin, Texas, 24-26 July 2017*, pp. 2267–2273, Society of Exploration Geophysicists, American Association of Petroleum Geologists, Society of Petroleum Engineers, 2017.

[28] M. Bai, A. Bouhroum, F. Civan, and J. C. Roegiers, "Improved model for solute transport in heterogeneous porous media," *Journal of Petroleum Science & Engineering*, vol. 14, no. 1–2, pp. 65–78, 1995.

Hindawi
Geofluids
Volume 2019, Article ID 6328909, 14 pages
https://doi.org/10.1155/2019/6328909

Research Article

A Research on the Effect of Heterogeneities on Sandstone Matrix Acidizing Performance

Jianye Mou, Lei Wang, Shicheng Zhang, Xinfang Ma, and Boyang Li

State Key Laboratory of Petroleum Resource and Prospecting, China University of Petroleum-Beijing, Karamay Campus, Beijing, China

Correspondence should be addressed to Jianye Mou; moujianye@cup.edu.cn

Received 19 December 2018; Revised 31 March 2019; Accepted 15 May 2019; Published 24 July 2019

Guest Editor: Fengshou Zhang

Matrix acidizing is one of the common methods to enhance production in sandstone reservoirs. Conventional acidizing designs generally neglected the effect of heterogeneities of mineral and flow field distributions both in areal and vertical directions and assumed that the acid front propagates with a piston-like style. However, sandstone formations inevitably have small-scale heterogeneities of minerals and flow properties that may give rise to acid propagation in a manner much different from what is predicted based on homogeneous assumptions. In this paper, we conduct a research to numerically investigate how the heterogeneities affect acidizing performance under in situ conditions. Firstly, a heterogeneity model is built for mineral and porosity distributions by using the semivariogram model of geological statistics, based on which we generate spatially correlated porosity and mineral distributions. Next, a model of radial acid flooding is developed based on mass balance and the chemical reactions between the acids and minerals occurring during the acidizing process. The model is numerically solved to investigate the permeability response, acid distributions, precipitate distributions, and the effect of the heterogeneities on acidizing. The results show that the heterogeneities both in areal and vertical directions have a significant effect on acidizing. The flow field heterogeneities have a more serious impact than the mineral heterogeneities. In a plane, strong porosity heterogeneity can give rise to acid fingering and even channeling, which make the acid penetration distance longer than the homogeneous cases. The secondary precipitate has a significant effect when fast-reacting mineral content is high. Vertically, several-fold permeability contrast creates the acid break through the high-perm zone leaving the low-perm zone understimulated. Both flow field and mineral heterogeneities make it possible to create high-permeability channels during the acidizing process and to obtain a longer acid penetration distance.

1. Introduction

Drilling, completion, or some other well operations inevitably damage formations, which may seriously decrease the well productivity in sandstone reservoirs. Matrix acidizing is a common method to remove the formation damage and recover well productivity. In acidizing, the acid flows into the porous media, reacts with the minerals, and increase formation porosity as well as permeability. Many researchers conducted studies on acid flooding in experiments. One of the unignorable risks in acidizing in sandstone is the secondary precipitate. Crowe [1], Almond et al. [2], and Underdown et al. [3] investigated the conditions that produce precipitate. They found that silica gel is produced at a slow rate due to the slow reaction at room temperature. When the temperature is higher than 55°C, the fast reaction will generate a lot of precipitate and damage the formation seriously.

Due to the small size of the core sample and the complexity of parallel core flooding, field-scale simulation and design necessitates numerical modeling. Sandstone acidizing models include the capillary model, the microscopic model, the kinetic model, the lumped parameter model, the distributed parameter model, the one-acid two-mineral model, the two-acid three-mineral model, and the generalized geochemistry model [4–10], most of which made the assumption of homogenous formation. The two-acid three-mineral model

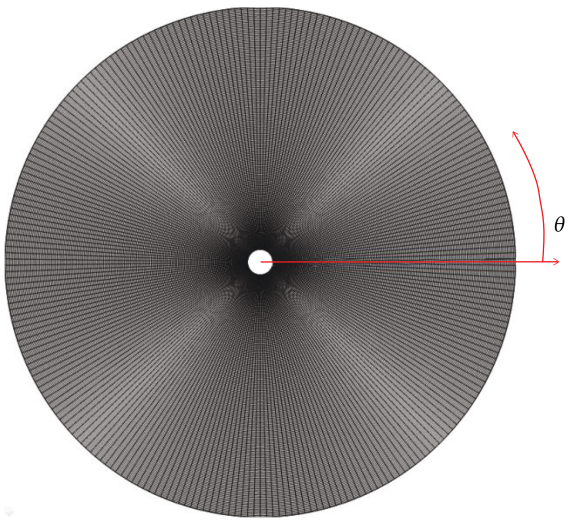

Figure 1: Schematic of computational domain.

developed by Bryant [4] takes into account the effect of precipitates and H_2SiF_6 and can simulate well the physical phenomenon of acidizing. At present, the most sophisticated model [9] is the generalized geochemistry model. The model accounts for the reaction of multiple kinds of minerals and the acid and can analyze the effect of mineral content, reactant, product, and reaction kinetics. They found that dissolution and precipitation do not occur simultaneously. Li et al. [11] built a linear acid flooding model to simulate linear core flooding at an experimental scale with the consideration of the heterogeneities of minerals and flow fields. Li et al. [12] built a radial acidizing model and considered the effect of the temperature field on the reaction, but they did not consider the effect of the heterogeneities. Leong et al. [13, 14] did a modeling of the acidizing of HBF_4 in linear cores with COMSOL.

In this paper, we modeled radial acid flooding based on a two-acid, three-mineral model and considered the heterogeneities of minerals and flow fields in both planar direction and vertical directions. Based on the model, we did extensive numerical simulations to analyze the effect of heterogeneities on acidizing performance. Also considered are multilayer flooding and secondary precipitates.

2. Mathematical Model

In the two-acid three-mineral model, the two acids mean HF and H_2SiF_6, and the three minerals mean fast-reacting mineral (mineral 1), slow-reacting mineral (mineral 2), and silica gel (mineral 3). The chemical reactions are as follows:

$$\begin{aligned}
\theta 1\, \mathrm{HF} + \text{mineral } 1 &\longrightarrow \theta 5\, \mathrm{H_2SiF_6} + \text{Al fluorides} \\
\theta 2\, \mathrm{HF} + \text{mineral } 2 &\longrightarrow \theta 6\, \mathrm{H_2SiF_6} + \text{Al fluorides} \\
\theta 3\, \mathrm{HF} + \text{mineral } 3 &\longrightarrow \theta 7\, \mathrm{H_2SiF_6} + \text{Al fluorides} \\
\theta 4\, \mathrm{H_2SiF_6} + \text{mineral } 1 &\longrightarrow \theta 8\, \text{mineral } 3 + \text{Al fluorides}
\end{aligned} \tag{1}$$

2.1. Governing Equations. Based on material balance, Darcy's law, and acid-rock reaction kinetics, we establish our governing equations as equations 2–7 with the following assumptions: (1) single-phase flow, (2) Darcy flow, (3) incompressible fluid and rock, and (4) neglecting gravity effect. A 2D model is developed as shown in Figure 1 with the wellbore at the center of the domain.

(1) Cylindrical coordinate system is used for the radial flooding

(2) Flow equations

$$\bar{\mathbf{u}} = (u_r, u_\theta) = -\frac{K}{\mu_a}\left(\frac{1}{r}\frac{\partial p}{\partial \theta}, \frac{\partial p}{\partial \theta}\right), \tag{2}$$

$$\frac{1}{r}\frac{\partial (r u_r)}{\partial r} + \frac{1}{r}\frac{\partial u_\theta}{\partial \theta} + \frac{\partial \phi}{\partial t} = 0. \tag{3}$$

(3) Hydrofluoric acid concentration distribution equation

$$\frac{\partial (C_1 \varnothing)}{\partial t} + \bar{\nabla} \cdot (\bar{\mathbf{u}} C_1) = -\sum_{j=1}^{N_m} E_{f,1,j} C_1^\alpha S_j^* V_j (1-\varnothing). \tag{4}$$

(4) Fluosilicic acid concentration distribution equation

$$\frac{\partial (C_2 \varnothing)}{\partial t} + \bar{\nabla} \cdot (\bar{\mathbf{u}} C_2) = -\sum_{j=1}^{N_m} E_{f,2,j} C_2^\alpha S_j^* V_j (1-\varnothing). \tag{5}$$

(5) Mineral content equation

$$\frac{\partial \left((1-\varnothing) V_j\right)}{\partial t} = -\sum_{i=1}^{N_{a,j}} \frac{MW_i S_j^* V_j (1-\varnothing) \beta_{i,j} E_{f,i,j} C_i^\alpha}{\rho_j}. \tag{6}$$

(6) Porosity variation equation

$$\frac{\partial \varnothing}{\partial t} = -\sum_{j=1}^{N_m} \sum_{i=1}^{N_{a,j}} \frac{MW_i S_j^* V_j \beta_{i,j} E_{f,i,j} C_i}{\rho_j}, \tag{7}$$

where $\varnothing$ is the porosity; C_1 is the hydrofluoric acid concentration; C_2 is fluosilicic acid concentration; $\bar{\mathbf{u}}$ is the velocity vector (u_r is the velocity in the radial direction, and u_θ is the velocity in the circumferential direction); V_j is the mineral volume fraction; j is the fast-reacting mineral, slow-reacting mineral, and silica gel; MW_i is the mole weight of acid, S_j^* is the specific surface area of minerals, i is the hydrofluoric acid or fluosilicic acid; $E_{f,i,j}$ is the reaction rate constant; α is the reaction order; ρ is the density of minerals; and $\beta_{i,j}$ is the gravimetric dissolving power.

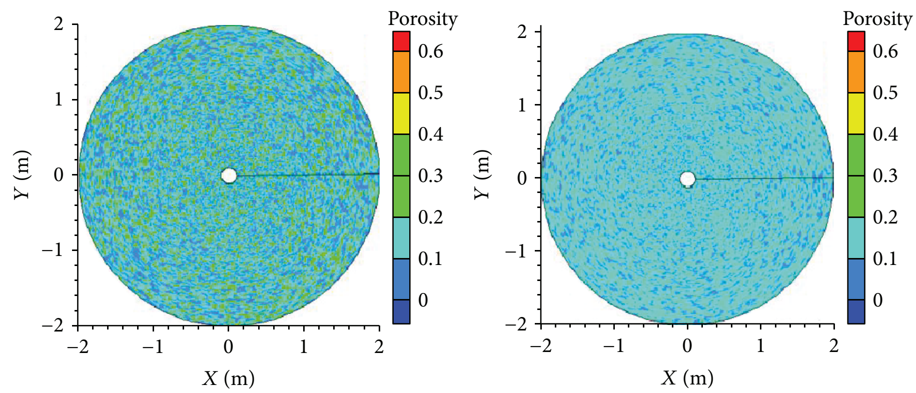

FIGURE 2: Random porosity distribution.

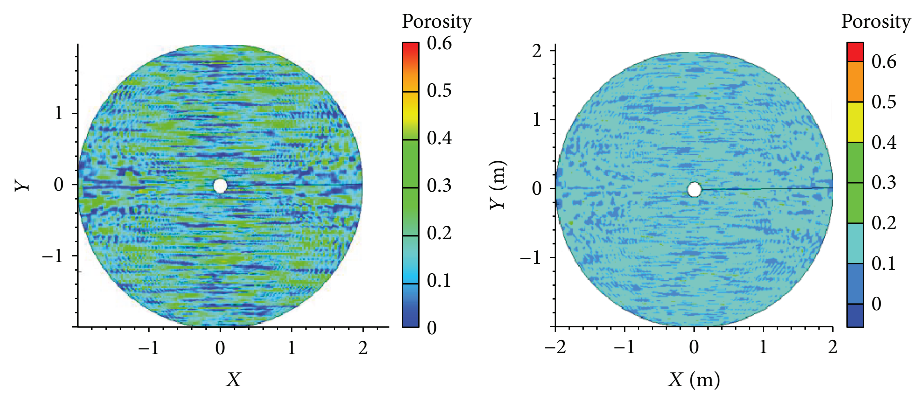

FIGURE 3: Spatially correlated porosity distribution ($l_x = 0.08, l_y = 0.0001$).

2.2. Boundary and Initial Conditions. The initial conditions are as follows:

$$\begin{aligned} p(r,\theta,t=0) &= p_r, \\ C_1(r,\theta,t=0) &= 0, \\ C_2(r,\theta,t=0) &= 0, \\ V_1(r,\theta,t=0) &= V_1^0, \\ V_2(r,\theta,t=0) &= V_2^0, \\ V_3(r,\theta,t=0) &= V_3^0, \\ \varnothing(r,\theta,t=0) &= \varnothing_{r,\theta}^0, \end{aligned} \tag{8}$$

where V_1^0, V_2^0, and V_3^0 are initial mineral 1, mineral 2, and mineral 3 distribution, respectively. $\varnothing_{r,\theta}^0$ is initial porosity distribution. p_r is reservoir pressure.

The boundary conditions are as follows:

$$\begin{aligned} \int_0^{2\pi} Q_\theta d\theta &= Q_{inj}, \\ p(r_e,\theta) &= p_e, \\ C_1(r_w,\theta) &= C_1^0, \\ C_2(r_w,\theta) &= C_2^0, \end{aligned} \tag{9}$$

where Q_{inj} is pump rate. C_1^0 and C_2^0 are the injection concentrations of acids 1 and 2, respectively. p_e is the pressure of the outer boundary.

3. Porosity and Mineral Distributions

3.1. Porosity Distribution. Change of porosity directly affects the permeability of the sandstone formation, thus affecting the distribution and reaction rate of acid fluid. Therefore, it is very important to generate the porosity distribution of a real formation for the accuracy of the whole model. In terms of geostatistics, porosity distribution shows characteristics of directionality [15–17]; that is, they are spatially correlated instead of completely random. A semivariogram model [8, 18], which is an important tool in geostatistics to describe spatially correlated distributions, is used to generate porosity distribution. We use the geostatistical software GSLIB [19], which incorporates a semivariogram model for spatial correlation, to generate spatially correlated numbers, with which we generate porosity distribution as

$$\phi = \begin{pmatrix} 1, & \phi \geq 1 \\ \phi_0 + \phi_0 c_v \widehat{G}(l_x, l_y), & 0.01 < \phi < 1 \\ 0.01, & \phi \leq 0.01 \end{pmatrix}, \tag{10}$$

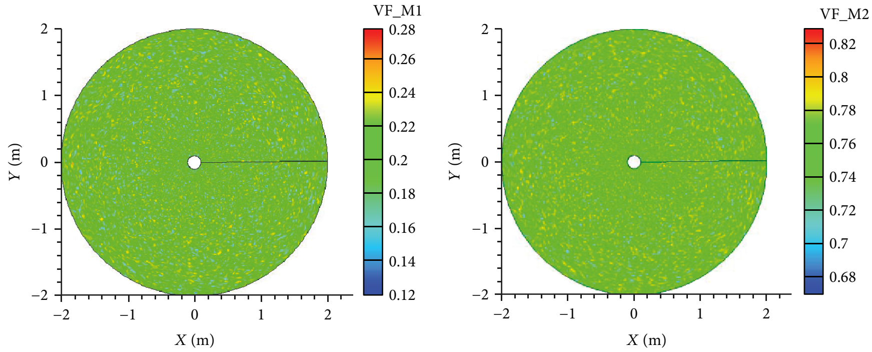

Figure 4: Distribution of the volume fraction (V_j) of fast-reacting and slow-reacting minerals.

Table 1: Model parameters.

Parameters	Value	Parameters	Value
Concentration of hydrochloric acid (wt%)	12	Injection rate (m^3/min/m)	0.1
Concentration of hydrofluoric acid (wt%)	3	Temperature (°C)	80
Density of silica gel (kg/m^3)	740	Radius of wellbore (m)	0.1
Density of fast-reacting mineral (kg/m^3)	2600	Radius of calculation domain (m)	2
Density of slow-reacting mineral (kg/m^3)	2650	Viscosity of acid fluid ($mPa \cdot s$)	1
Molecular weight of M3 (kg/kmole)	96	Acid density (kg/m^3)	1075
Molecular weight of M2 (kg/kmole)	60	M1-specific area (m^3/m^2)	3235000
Molecular weight of M2 (kg/kmole)	262	M2-specific area (m^3/m^2)	52000
Dissolving power of HF to M1	0.486	Silica gel specific area (m^3/m^2)	3300000
Dissolving power of HF to M2	0.5	Dissolving power of H_2SiF_6 to M1	2.47
Dissolving power of HF to M3	0.8	Dissolving power of HCl to carbonate	1.37
Coefficient of reaction equations ($\theta 1 - \theta 8$)		27, 6, 6, 1, 3, 1, 1, 2.5	

Table 2: Formation parameters.

Parameters	Homogeneous	Heterogeneous
Average porosity (%)	15	15
Average permeability (md)	50	50
Average fraction of fast-reacting mineral (%)	20	20
Average fraction of slow-reacting mineral (%)	75	75
Carbonate fraction (%)	5	5
Dimensionless porosity correlation length (x, y)		0.08, 0.0001
Porosity coefficient of variation	0	1

where $\widehat{G}(l_x, l_y)$ is the spatially correlated number output from GSLIB and l_x and l_y represent the dimensionless correlation lengths of x direction and y direction, respectively. c_v is the coefficient of variation of porosity. Bigger c_v means strong inhomogeneity; otherwise, it means slight inhomogeneity. ϕ_0 is the average porosity.

Figures 2 and 3 show the porosity distributions for two layers with $\phi = 0.15$. The figures indicate that porosity distributions vary a lot with different geostatistic parameters so as to affect flow fields significantly.

3.2. Pore-Permeability Correlation. Acid-rock reaction increases porosity, resulting in a change of permeability, which in turn affects acid flow. We use the following model to describe the relationships [20] between permeability and local porosity.

$$\frac{k}{k_0} = \frac{\phi}{\phi_0}\left(\frac{\phi(1-\phi_0)}{\phi_0(1-\phi)}\right)^{2\beta}, \tag{11}$$

where β is a constant which is dependent on the structure of the medium.

3.3. Mineral Distribution. Using the same method for porosity distribution, we generate the spatial association distribution function which is defined as follows:

$$M1 = \begin{pmatrix} 1, & M1 \geq 1 \\ \overline{M1} + \overline{M1} c_v \widehat{G}\left(l_x, l_y, l_z\right), & 0 < M1 < 1 \\ 0, & M1 \leq 0 \end{pmatrix},$$
$$M2 = \begin{pmatrix} 1, & M2 \geq 1 \\ \overline{M2} + \overline{M2} c_v \widehat{G}\left(l_x, l_y, l_z\right), & 0 < M2 < 1 \\ 0, & M2 \leq 0 \end{pmatrix}, \tag{12}$$

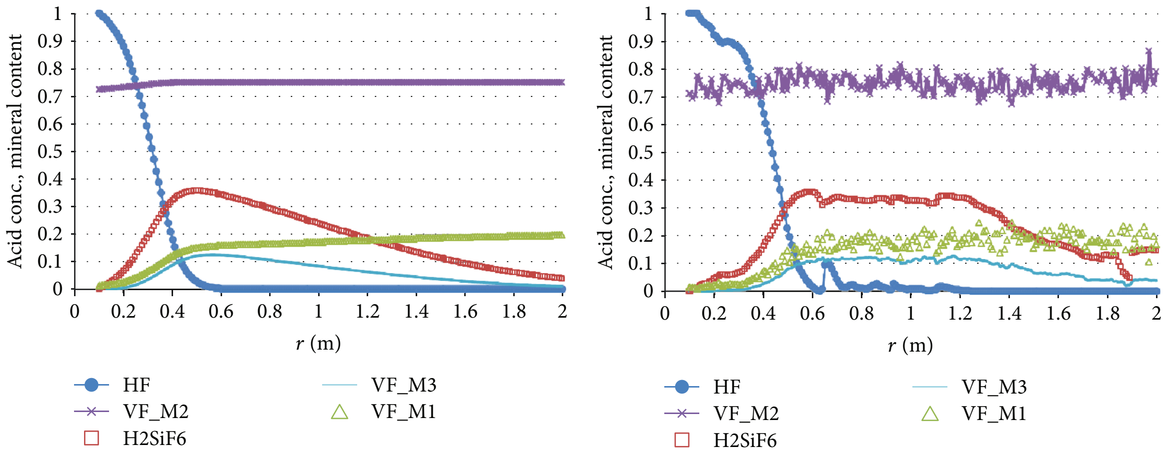

(a) Homogeneous case

(b) Heterogeneous case

Figure 5: Mineral and acid concentration distribution in radial direction.

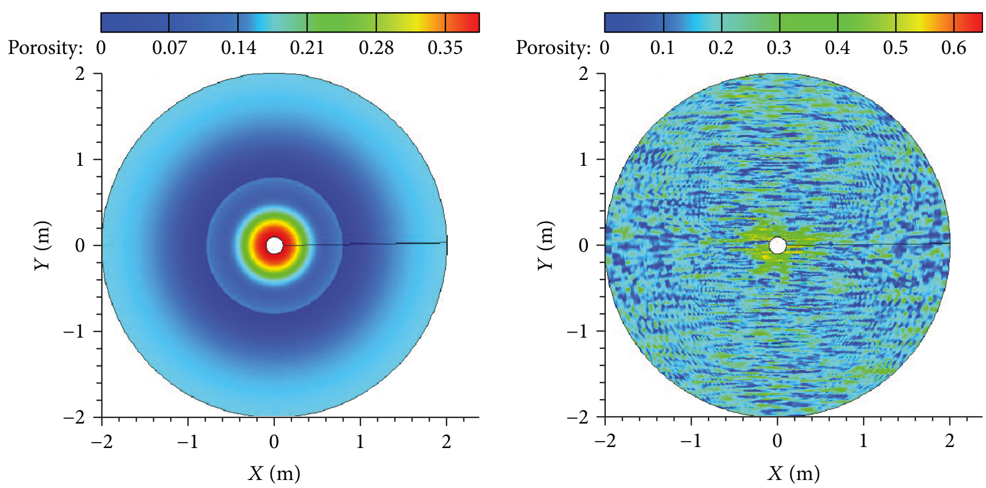

Figure 6: Porosity distribution after acidizing for homogeneous and heterogeneous initial distributions.

where $\overline{M1}$ and $\overline{M2}$ are the average volume fractions of the fast-reacting mineral and slow-reacting mineral, respectively. Figure 4 is an example of the distributions of the volume fraction (V_j) of fast- and slow-reacting minerals.

4. Numerical Solution

The equations are discretized with the finite volume method and solved sequentially. Firstly we generate initial porosity and mineral distributions. Then, we solve equations (2) and (3) to obtain the pressure and velocity fields. Next, we solve equations (4) and (5) to get the acid concentration distribution. Finally, we update the mineral content and porosity distributions based the acid-rock reaction (equations (6) and (7)).

5. Result and Discussion

In this section, extensive numerical simulations are conducted to analyze acid distribution patterns as well as the effect of heterogeneities on acidizing performance with the parameters in Table 1. And acid-rock reaction parameters are determined through references [21–23].

5.1. Comparison of Homogenous and Heterogeneous Cases. The parameters used in the simulation are listed in Table 2. Other parameters are kept the same for the two cases.

Figure 5 shows acid concentration and mineral content distribution in the radial direction. Since they are different in different directions for the heterogeneous cases, only 0 degree (relative to the black line in Figure 5, for example) is chosen for displaying. VF_M1, VF_M2, and VF_M3 stand for fast-reacting mineral, slow-reacting mineral, and silica gel precipitate content. Compared to the homogeneous case, the curves of the heterogeneous case fluctuate apparently, the acid front is longer, and precipitation is deeper. Since the fast-reacting mineral has a much higher reaction rate than the slow-reacting mineral, most the fast-reacting mineral is spent, but a small amount the slow-reacting mineral is dissolved in the live acid zone.

Figures 6–10 show acid and mineral concentration distribution after 90-minute acid injection. The homogeneous case

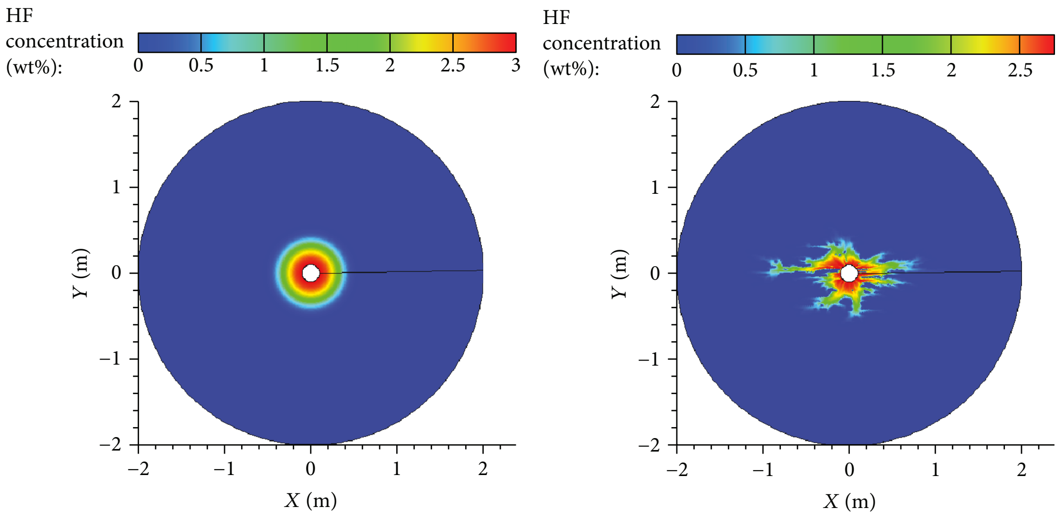

Figure 7: HF distribution after acidizing for homogeneous and heterogeneous initial distributions.

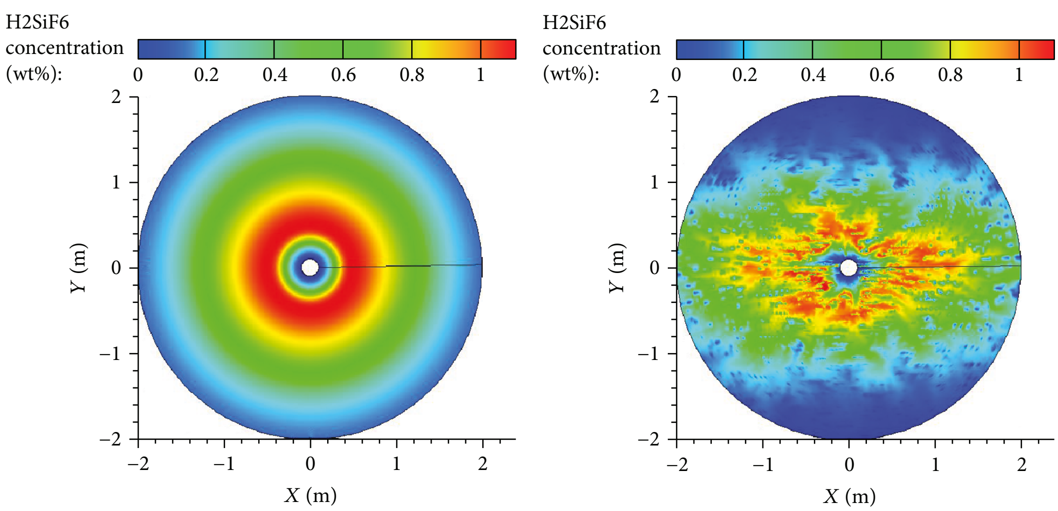

Figure 8: H_2SiF_6 distribution after acidizing for homogeneous and heterogeneous initial distributions.

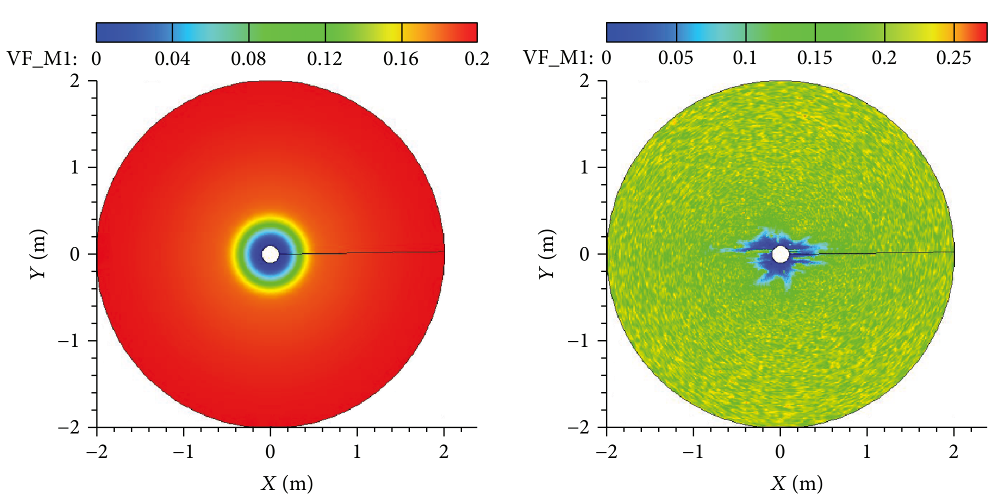

Figure 9: Fast-reacting mineral distribution after acidizing for homogeneous and heterogeneous initial distributions.

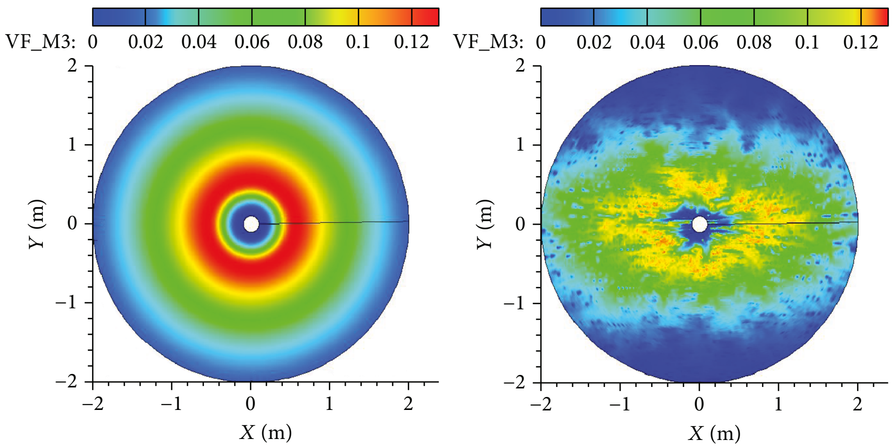

FIGURE 10: Silica precipitation distribution after acidizing for homogeneous and heterogeneous initial distributions.

gives a regular shape of distribution. Meanwhile, the heterogeneous case gives rise to an irregular distribution shape. The porosity distribution is strongly correlated in the horizontal direction. The horizontal direction is the leading flow direction, so acid penetrates deeper in this direction. The acid fingers through the high-perm zone, leaving the acid front to propagate nonuniformly. Some low-perm zones are bypassed by the acid. For the homogeneous case, from the wellbore to the outer zone, there exist zones of high perm, low perm, and original formation perm. Near the wellbore zone, the permeability is enhanced due to rock dissolution by the acid. In the live acid zone, most of the fast-reacting mineral is dissolved. The low-perm zone is cause by the secondary precipitate of spent acid. Silica gel precipitation due the reaction between H_2SiF_6 and the fast-reacting mineral is inevitable [24], which is unfavorable for sandstone acidizing. For the heterogeneous case, the reduced perm zone is not distinctly apparently. The precipitate does exist, but the drastic porosity variation from one place to another makes it hard to identify. The significant difference of the penetration distance between the homogeneous and heterogeneous cases shows just how important it is to consider heterogeneity in field treatments. The acid penetration distance is much longer than the one predicted by the homogenous model, especially when there exists major flow channels.

5.2. Effect of Vertical Heterogeneity. A well often consists of multilayers with much different properties. For this kind of well, an important aspect in acidizing is acid placement. Here, the difference of the properties of the layers is called vertical heterogeneity. Vertical heterogeneity considers the difference of permeability and the mineral mainly in this simulation.

5.3. Effect of Vertical Permeability Heterogeneity. The vertical permeability difference of layers can be characterized by the permeability ratio, which is defined as the ratio of the average permeability of layer A to layer B as follows:

$$\alpha_\beta = \frac{k_{avgA}}{k_{avgB}}, \tag{13}$$

TABLE 3: Parameters for layers A and B.

Parameters	Layer A	Layer A	Layer A	Layer B
Average porosity (%)	18	15	12	10
Average permeability (md)	100	50	20	10
Average fraction of fast-reacting mineral (%)	20			
Average fraction of slow-reacting mineral (%)	75			
Carbonate fraction (%)	5			
Dimensionless porosity correlation length (x, y)	0.08, 0.0001			
Porosity coefficient of variation	1			

where α_β is the permeability ratio and k_{avgA} and k_{avgB} represent the average permeabilities of layer A and layer B, respectively. We did simulations for $\alpha_\beta = 2$, 5, and 10, respectively. Parameters are listed in Table 3. Except for the different porosity and permeability distribution values, other parameters are kept the same. Results after 90-minute acid injection are shown as follows.

As shown in Figure 11, vertical permeability heterogeneity has a notable effect on the acid distribution of the vertical profile. The higher the permeability ratio, the more seriously acid intake differs. When $\propto_\beta = 10$, the acid entering into the low-perm zone is negligible compared to that entering into the high-perm zone. Except for the permeability difference which causes the discrepancy of acid intake, the permeability increase due to rock dissolution also magnifies the difference. The high-permeability zone takes more acid and raises permeability faster, so it accepts more and more acid. This demonstrates the necessity of acid diversion in acidizing multilayer formations.

Figure 12 shows fast-reacting mineral dissolution in two layers. In line with the acid distribution, the dissolution is greater in the higher perm layer, and the dissolutions in the lower perm layer decreases with the increase of the permeability ratio. Figure 13 shows the distribution of precipitation. In the higher perm layer, the precipitate spreads wider because

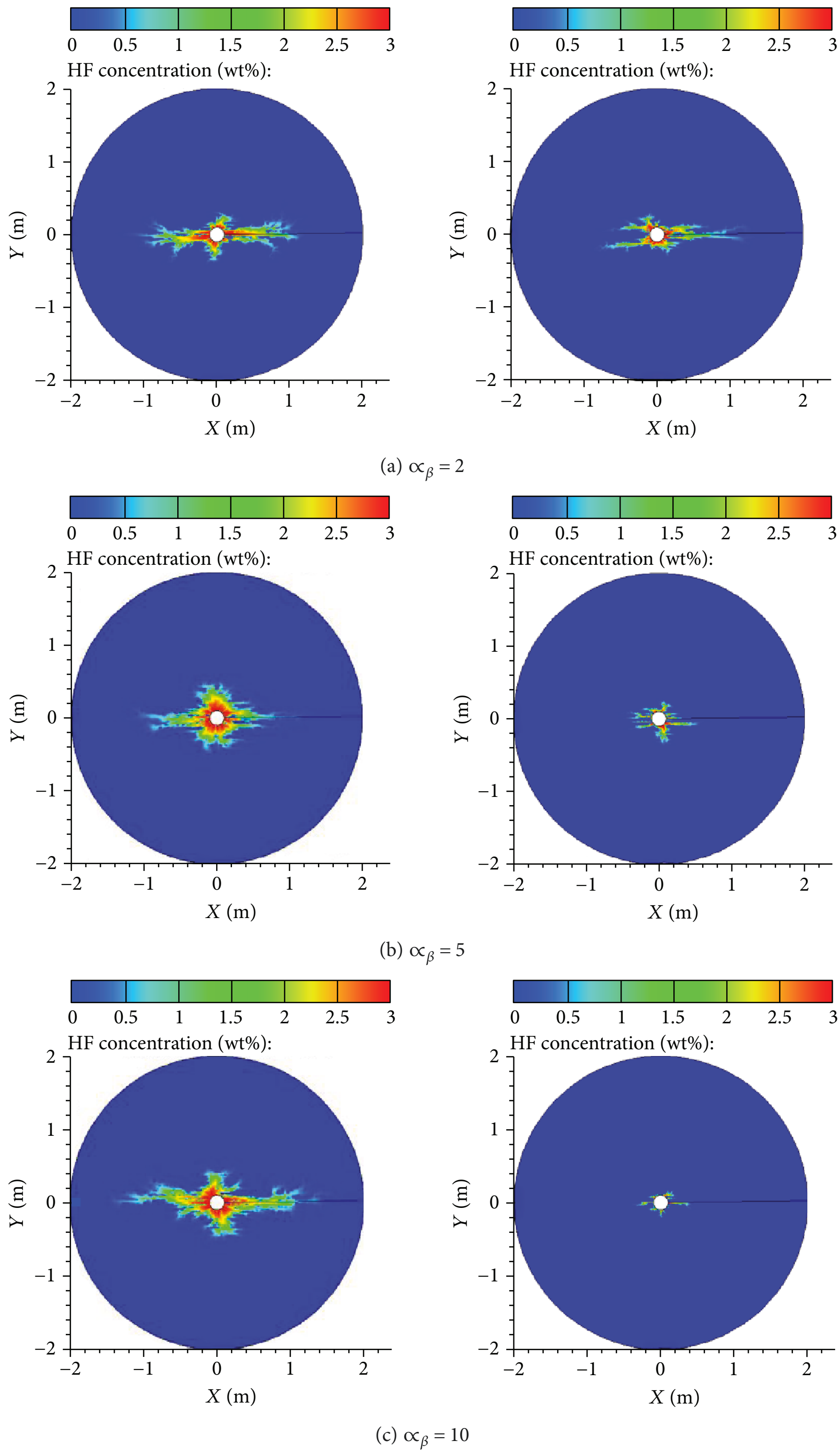

FIGURE 11: HF distribution in two layers.

of more spent acid generated by the acid entering into the layer. Precipitate will decrease the permeability; more precipitate in the higher perm layer will counteract the permeability increase caused by rock dissolution, but due to areal heterogeneity, the acid can channel through the lowered perm zone.

5.4. Effect of Vertical Mineral Content Heterogeneity. When analyzing the effect of mineral content in the two layers, other parameters are kept the same. The fast-reacting mineral of 0.1 and 0.2 and the slow-reacting mineral of 0.85 and 0.75 are set for layers A and B, respectively.

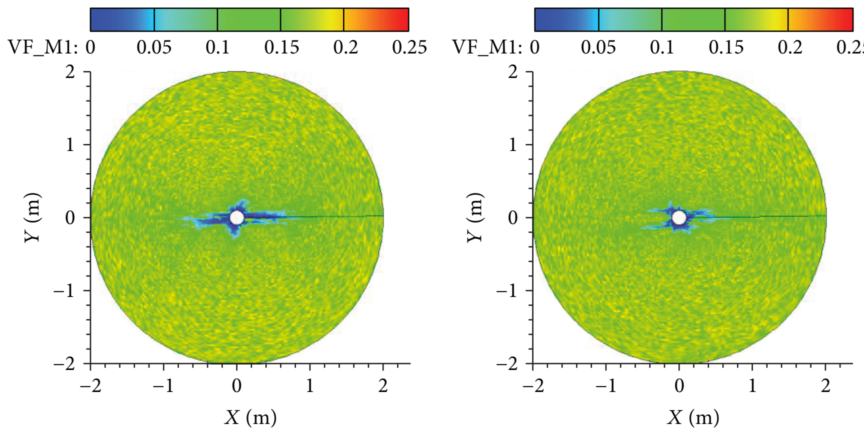

(a) $\propto_\beta = 2$

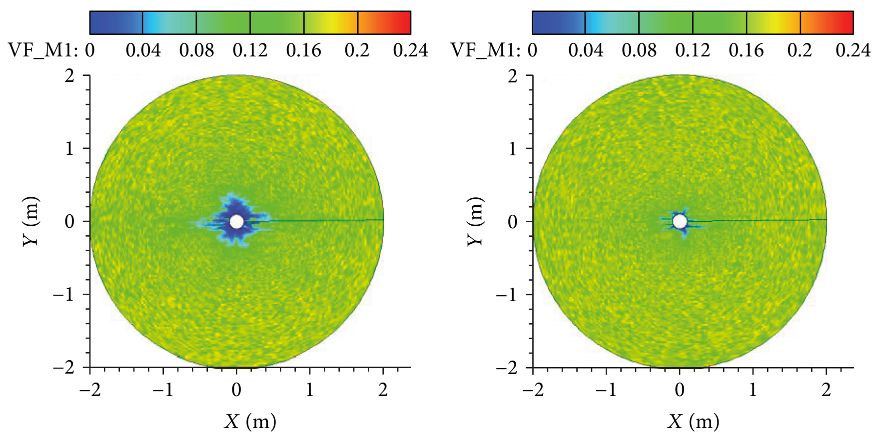

(b) $\propto_\beta = 5$

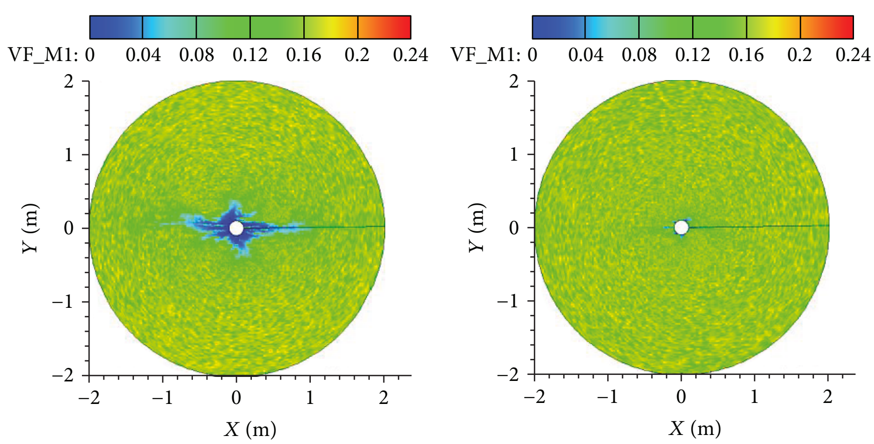

(c) $\propto_\beta = 10$

Figure 12: Fast-reacting mineral distribution in two layers.

Figures 14–16 show the results after acidizing for 90 minutes. Since the two layers have identical initial porosity and permeability distribution, the dissolution geometry is similar, but the extent of layer A is notably larger than layer B. Layer B has a much higher fast-reacting content than layer A. Due to the relative fast reaction rate of the fast-reacting mineral, most of the fast-reacting mineral is dissolved in the area covered by the live acid. The acid front propagates much slower in layer B. Figure 17 shows the pump rate allocation with time for the two layers. The initial rate is the same. As acidizing proceeds, the rate of layer A increases and the rate of layer B decreases, since the total rate is fixed. There are two reasons for this phenomenon. The first is that the acid front moves faster in layer A than layer B. The second is more serious precipitation in layer B due to the higher content of the fast-reacting mineral. Even though the vertical heterogeneity of the mineral content is obvious, its effect is less remarkable than the effect of permeability.

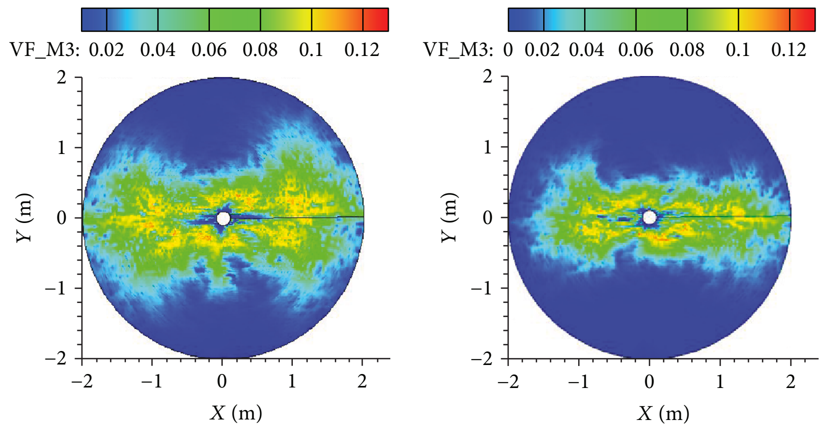

(a) $\propto_\beta = 2$

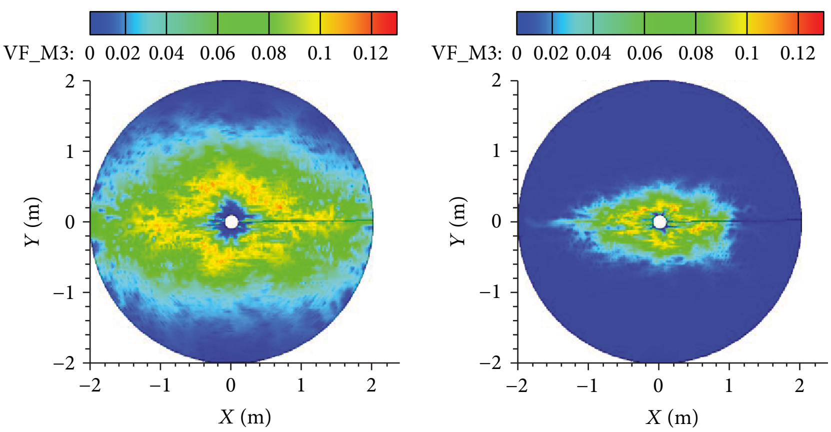

(b) $\propto_\beta = 5$

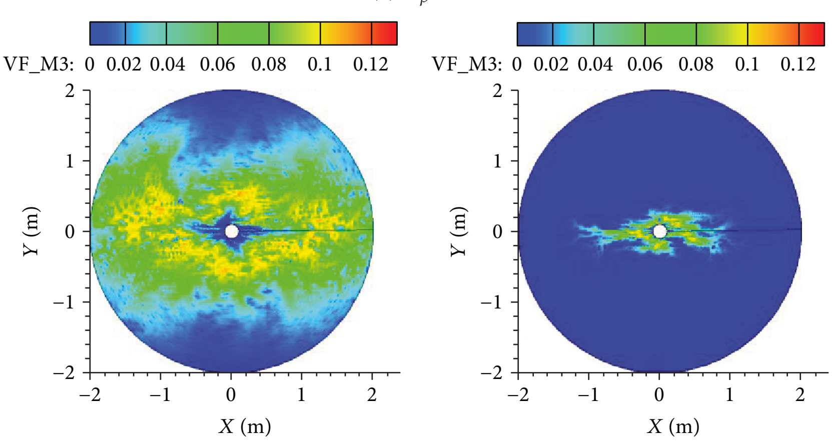

(c) $\propto_\beta = 10$

Figure 13: Silica precipitation distribution in two layers.

5.5. Effect of Areal Heterogeneity. Areal heterogeneity can be expressed by the coefficient of variation of porosity (c_v). The higher the c_v, the more serious the heterogeneity is. $c_v = 0$ means homogeneous case. Figures 18–20 show the results for $c_v = 0.1, 0.3, 1$. The dimensionless correlation lengths are 0.08 and 0.0001 in the x and y directions. $c_v = 0.1$ means very weak heterogeneity. The porosity distribution is very close to the homogeneous case. $c_v = 1$ means very strong heterogeneity, which generates some leading flow paths similar to the channels in the reservoir. The more serious the heterogeneity, the more irregular the geometry of acid coverage is. The case of $c_v = 1$ makes the acid finger through some high-perm paths, making the acid penetration distance much longer than the other two cases. Another areal heterogeneity is natural fractures. For example, there is a fracture connecting to the wellbore as shown in Figure 21. The acid mainly flows through the fracture to reach a deeper distance. These indicate that in strong heterogeneous reservoirs, the acid

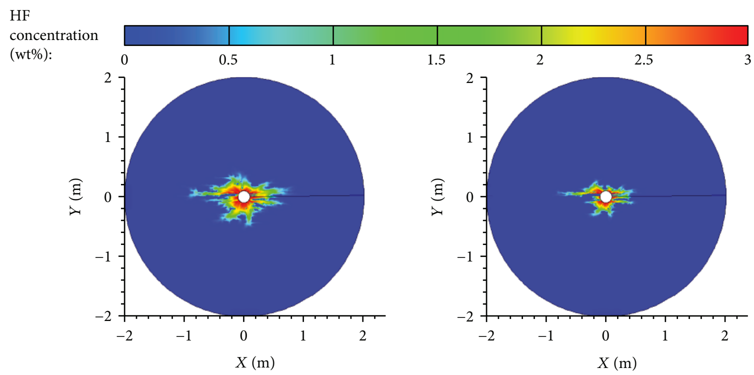

Figure 14: HF distribution in two layers.

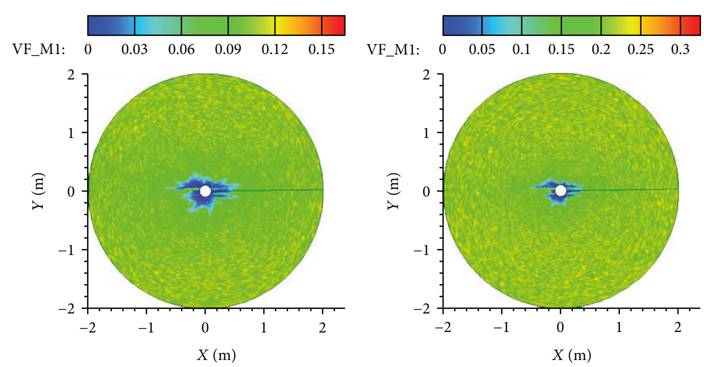

Figure 15: Fast-reacting mineral distribution in two layers.

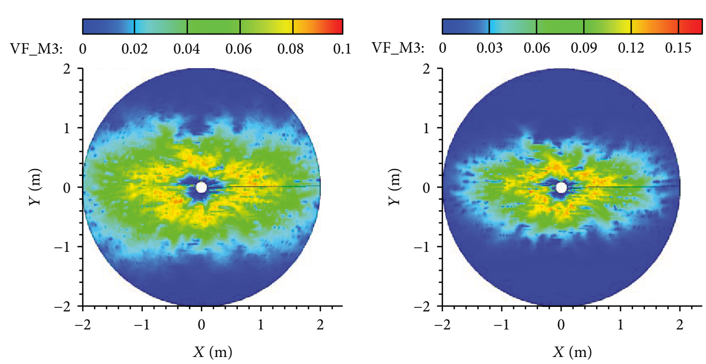

Figure 16: Silica precipitation distribution in two layers.

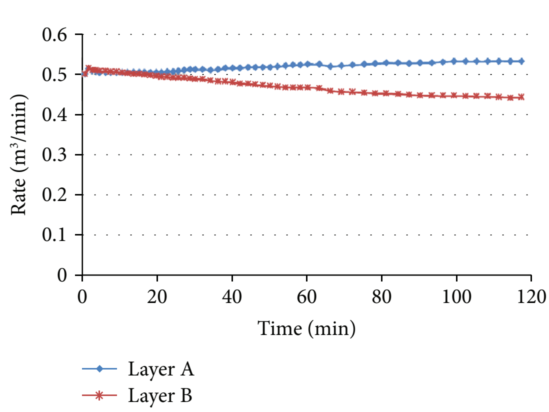

Figure 17: Rate allocation in two layers.

penetration distance may be much deeper than the one predicted by the conventional homogeneous model.

6. Conclusion

In this paper, we built a sandstone matrix acidizing model accounting for areal and vertical heterogeneities and the effect of secondary precipitates. Based on the model, extensive numerical simulation was conducted to investigate the effect of heterogeneity on acidizing performance. The study reached the following conclusions:

(1) The heterogeneities both in areal and vertical directions have a significant effect on acidizing

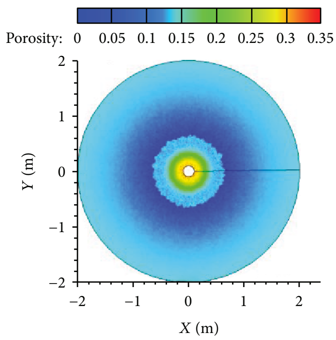

FIGURE 18: Porosity distribution after acidizing in two layers.

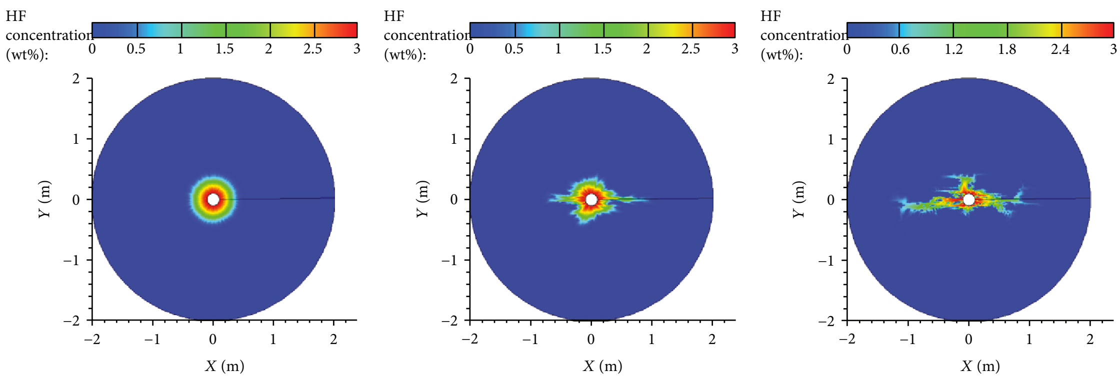

FIGURE 19: HF distribution after acidizing in two layers.

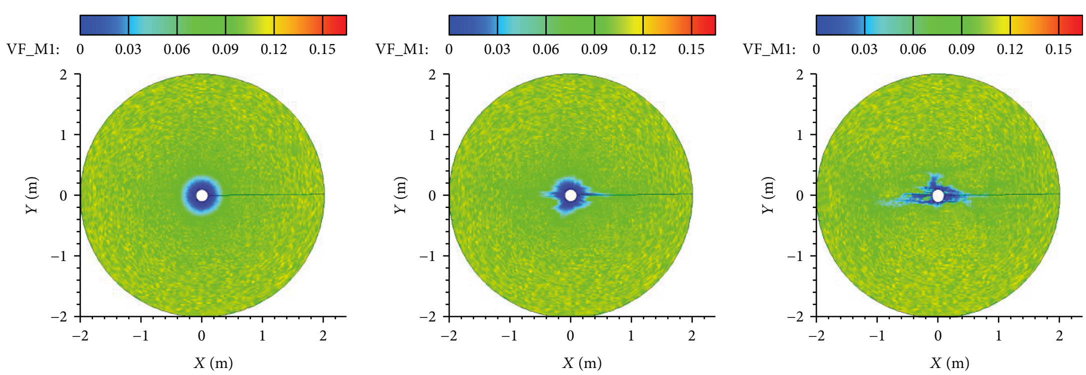

FIGURE 20: Fast-reacting mineral distribution after acidizing in two layers.

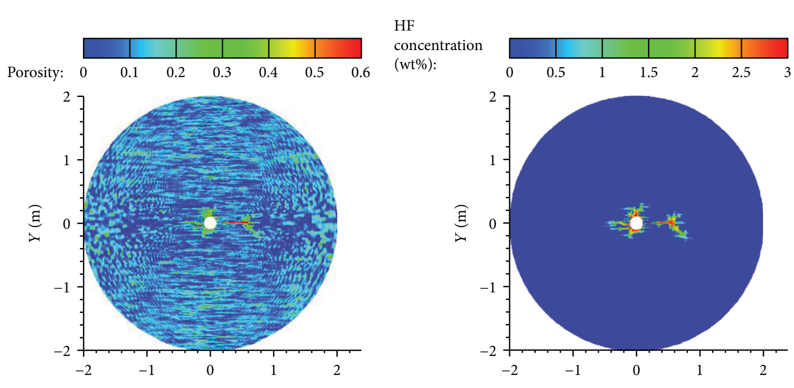

FIGURE 21: Porosity and acid concentration distribution when a fracture connects to the wellbore.

performance. The areal heterogeneity influences the acid dissolution pattern and live acid penetration distance. Heterogeneous cases give longer live acid penetration distance than the homogeneous cases. The vertical heterogeneities determine the vertical acid intake profile

(2) Both flow field and mineral heterogeneities make it possible to create high-permeability channels in acidizing and to obtain longer acid penetration distance. The heterogeneity of a flow field has a more serious effect on the acid dissolution pattern than the mineral heterogeneities

(3) Serious vertical heterogeneities make an unfavorable acid intake profile, with the high-permeability zone taking excessive acid and the low-permeability zone taking insufficient acid. In multilayer formations, heterogeneity creates acid fingering instead of a piston-like pattern, which indicates the necessity of an acid diversion

(4) The secondary precipitate has a significant effect on acidizing performance when fast-reacting mineral content is high

Nomenclature

C_1: Hydrofluoric acid concentration
C_2: Fluosilicic acid concentration
C_1^0: Injection concentration of acid 1
C_2^0: Injection concentration of acid 2
c_v: Coefficient of variation of porosity
$E_{f,i,j}$: Reaction rate constant
$\widehat{G}(l_x, l_y)$: Spatially correlated number output from GSLIB
k_{avgA}: Average permeability of Layer A
k_{avgB}: Average permeability of Layer A
l_x, l_y: Dimensionless correlation lengths of x direction and y direction, respectively
MW_i: Mole weight of acid
$\bar{M}1$, $\bar{M}2$: Average volume fractions of fast-reacting mineral and slow-reacting mineral, respectively
Q_{inj}: Pump rate
p_r: Reservoir pressure
p_e: Pressure at outer boundary
S_j^*: Specific surface area of minerals
$\bar{\mathbf{u}}$: Velocity vector
u_r: Velocity in the radial direction
u_θ: Velocity in the circumferential direction
V_j: Mineral volume fraction
V_1^0, V_2^0, V_3^0: Initial distribution of the volume fractions of mineral 1, mineral 2, and mineral 3, respectively
α: Reaction order
α_β: Permeability ratio
$\beta_{i,j}$: Gravimetric dissolving power
β: Constant dependent on the structure of the medium
$\varnothing$: Porosity
$\varnothing_{r,\theta}^0$: Initial porosity distribution
ϕ_0: Average porosity
ρ: Density.

Data Availability

The numerical simulation data used to support the findings of this study are available from the corresponding author upon request.

Conflicts of Interest

The authors declare that they have no conflicts of interest.

Acknowledgments

The authors gratefully acknowledge the support of the National Science and Technology Major Project of a Research on Controlling Factors of Target-Oriented Acid Fracturing and Experimental Study on Diversion, SINOPEC Northwest Oilfield Branch (2016ZX05014-005-012).

References

[1] C. W. Crowe, “Precipitation of hydrated silica from spent hydrofluoric acid: how much of a problem is it? (includes associated papers 16441 and 16444),” *Journal of Petroleum Technology*, vol. 38, no. 11, pp. 1234–1240, 1986.

[2] S. W. Almond, J. L. Brady, and D. R. Underdown, “Return fluid analysis from the Sadlerochit Formation, Prudhoe Bay, Alaska: A Laboratory study-part II,” in *International Arctic Technology Conference, SPE 18223*, Anchorage, Alaska, May 1991.

[3] D. R. Underdown, J. J. Hickey, and S. K. Kalra, “Acidization of analcime-cemented sandstone, Gulf of Mexico,” in *Annual Technical Conference and Exhibition, SPE 20624*, New Orleans, LA, USA, September 1990.

[4] S. L. Bryant, “An improved model of mud acid/sandstone chemistry,” in *Annual Technical Conference and Exhibition, SPE 22855*, Dallas, TX, USA, October 1991.

[5] R. Gdanski, “Fractional pore volume acidizing flow experiments,” in *European Formation Damage Conference, SPE 30100*, The Hague, Netherlands, May 1995.

[6] R. D. Gdanski, “Kinetics of the primary reaction of HF on alumino-silicateS,” *SPE Production & Facilities*, vol. 15, no. 4, pp. 279–287, 2000.

[7] Y. Hekim, H. S. Fogler, and C. C. Mccune, “Radial movement of permeability fronts and multiple reaction zones in porous media: Soc Pet Engr J, V22, N1, Feb 1982, P99-107,” *International Journal of Rock Mechanics and Mining Sciences & Geomechanics Abstracts*, vol. 19, no. 6, pp. 130–130, 1982.

[8] J. E. McElhiney, A. L. Schalge, R. S. McKnight, and J. R. Robinson, “Coreflood acidization: model, measurement, and methodology,” in *Oilfield and Geothermal Chemistry Symposium, SPE 7891*, Houston, TX, USA, January 1979.

[9] S. D. Sevougian, L. W. Lake, and R. S. Schechter, “A new geochemical simulator to design more effective sandstone acidizing treatments,” *SPE Production & Facilities*, vol. 10, no. 1, pp. 13–19, 1995.

[10] B. F. Wang, “Study of sandstone acidification design model,” *Henan Petroleum*, vol. 2, pp. 28–31, 1999.

[11] C. Li, T. Xie, M. Pournik, D. Zhu, and A. D. Hill, "Fine-scale simulation of sandstone acidizing," *Journal of Energy Resources Technology*, vol. 127, no. 3, pp. 225–232, 2005.

[12] S. Y. Li, Z. M. Li, and B. F. Li, "Acid/sandstone reaction modeling for sandstone-matrix acidizing," *Journal of China University of Mining & Technology*, vol. 41, no. 2, pp. 236–241, 2012.

[13] V. H. Leong, H. B. Mahmud, M. C. Law, H. C. Y. Foo, and I. S. Tan, "A numerical modelling and simulation of core-scale sandstone acidizing process: a study on the effect of temperature," *Journal of Petroleum Exploration and Production Technology*, vol. 9, no. 1, pp. 483–516, 2018.

[14] V. H. Leong, H. B. Mahmud, M. C. Law, H. C. Y. Foo, and I. S. Tan, "A comparison and assessment of the modelling and simulation of the sandstone matrix acidizing process: a critical methodology study," *Journal of Natural Gas Science and Engineering*, vol. 57, pp. 52–67, 2018.

[15] K. R. Kunze and C. M. Shaughnessy, "Acidizing sandstone formations with fluoboric acid," *SPE Journal*, vol. 23, no. 1, pp. 65–72, 1983.

[16] M. U. Shafiq, H. K. B. Mahmud, and M. Arif, "Mineralogy and pore topology analysis during matrix acidizing of tight sandstone and dolomite formations using chelating agents," *Journal of Petroleum Science and Engineering*, vol. 167, pp. 869–876, 2018.

[17] R. L. Thomas and C. W. Crowe, "Matrix treatment employs new acid system for stimulation and control of fines migration in sandstone formations," *Journal of Petroleum Technology*, vol. 33, no. 8, pp. 1491–1500, 1981.

[18] H. H. Hardy and R. A. Beier, "Integration of large- and small-scale data using Fourier transforms," in *ECMOR IV - 4th European Conference on the Mathematics of Oil Recovery*, Roros, Norway, 1994.

[19] C. V. Deutsch and A. G. Journel, "GSLIB: Geostatistical Software Library and User's Guide," Oxford University Press, New York, Oxford, 2nd Edition edition, 1998.

[20] M. K. R. Panga, M. Ziauddin, and V. Balakotaiah, "Two-scale continuum model for simulation of wormholes in carbonate acidization," *AICHE Journal*, vol. 51, no. 12, pp. 3231–3248, 2005.

[21] H. R. Gates and J. H. Lybarger, "SGMA performance, design. Conclusion. Proper reservoir choice, fluid design keys to SGMA success," *Oil & Gas Journal*, vol. 76, no. 43, 1978.

[22] N. Kume, R. V. Melsen, L. Erhahon, and A. F. Abiodun, "New HF acid system improves sandstone matrix acidizing success ratio by 400% over conventional mud acid system in Niger Delta Basin," in *Annual Technical Conference and Exhibition, SPE-56527*, pp. 185–199, Houston, TX, USA, October 1999.

[23] A. N. Martin and K. L. Smith, "New HF acid system produces significant benefits in Nigerian sandstones," in *Annual Technical Conference and Exhibition, SPE-38595*, San Antonio, TX, USA, October 1997.

[24] H. Xue L. Zhao et al., "Acidification simulation for inhomogeneous pore type sandstone oil reservoir," *Oil Drilling & Production Technology*, vol. 37, no. 4, pp. 100–104, 2015.

Hindawi
Geofluids
Volume 2019, Article ID 7405702, 12 pages
https://doi.org/10.1155/2019/7405702

Research Article

Study on the Effect of the Oil-Water Ratio on the Rheological Properties of Hydroxyethyl Cellulose (HEC)

Xiaoming Su, Zhanghua Lian, and Yuan Yuan

State Key Laboratory of Oil and Gas Reservoir Geology and Exploitation, Southwest Petroleum University, Chengdu, China

Correspondence should be addressed to Xiaoming Su; sxm310426@126.com

Received 18 November 2018; Revised 22 February 2019; Accepted 1 April 2019; Published 22 July 2019

Guest Editor: Bisheng Wu

Hydroxyethyl cellulose (HEC) is widely used in water-base drilling fluid as tackifier because of its good fluidity, stability, prop-carrying capacity, and good reservoir protection, while it has insufficient rheological property under higher temperature. In order to make use of its advantages and improve thermal stability, an innovative method that HEC was dissolved in the emulsion was proposed. Research indicated that compared with traditional water solution, the oil-water emulsion as solution could effectively improve the rheological properties and thermal stability. The oil-water ratio has an obvious effect on rheological properties. Firstly, with the decrease in the oil-water ratio, the apparent viscosity and shear stress were decreased; secondly, under constant oil-water ratio or temperature, the larger the shear rate, the lower the apparent viscosity, and the greater the shear strength; lastly under extremely low shear rate, HEC emulsion's viscosity peaked at more than 50000 mPa·s, which can effectively solve the problem of sand carrying difficulty and being easy to form sand bed in horizontal well and high angle hole. In addition, the emulsifying stability was degradative with the increase in the oil-water ratio. The degradation was not obvious when the oil-water ratio was less than 30 : 70. On the contrary, the performance deteriorated drastically when the oil-water ratio was greater than 30 : 70. The separator liquid was more than 2 cm and was even about 1/3 when the oil-water was 50 : 50. On the basis of analysis of the experimental results, we can see that oil-water emulsion could effectively improve the rheological stability and thermal stability of HEC and the optimal oil-water ratio was 30 : 70. This study provided a new thought for application of HEC or other polymers in drilling fluid.

1. Introduction

Drilling fluid known as the "engineering blood" plays an indispensable role in cooling the bit, lubricating the tool, breaking the rock and carrying the debris to the wellhead, balancing the formation pressure, protecting the borehole, transferring the water power, and forming a mud cake on the borehole wall which protect reservoirs and reduce the damage caused by drilling engineering [1–6]. Smooth and efficient drilling operation highly depends on drilling fluid systems with required rheological, fluid filtration, and high-temperature properties in a low-cost and ecologically friendly manner. Generally, two types of drilling fluids including water-based drilling fluids, oil-based drilling fluids, and synthetic-based drilling fluids are used in various drilling conditions. Due to lower environmental impact and lower cost, water-based drilling fluids are extensively used [7]. However, in circumstances such as reactive shales, directional drilling, and high-temperature and high-pressure (HTHP) formations, operators may have to consider oil-based drilling fluids. Compared with water-based drilling fluids, oil-based drilling fluids show better wellbore geomechanical stability, thermal stability, lower friction and drag, and increased drilling efficiency [8–12].

One of the most severe of drilling fluid is the rheological property, which affects removal of cuttings, holding cuttings, and weight material in suspension when not circulating and under a higher temperature [5, 6]. However, oil-based drilling fluid improves the carrying capacity through adding organic clay. There is no doubt that the tackifying effect is poorer than that of the traditional tackifier. Most of all, the addition of organic clay raises solid content in drilling fluid, which is negative for reservoir protection and easily causes reservoir damage [13–15]. So we need to find a new way to decrease the solid content in drilling fluid on the basis of satisfying holding cuttings and suspension demand.

HEC is a tasteless and nontoxic fiber where hydrogen of the hydroxyl group of cellulose is replaced by ethylol as shown in Figure 1 [16]. It has good performances, such as good tackifying performance, suspension, bonding, adhesion, moisture-retaining property, insensitivity to salt, and reservoir protection, and is widely used in water-based drilling fluid as a water-soluble polymer, but its temperature resistance is poorer [17–20]. However, it is rarely used in oil-based drilling fluid. In order to take full advantage of both good tackifying performance, suspension, bonding, adhesion, moisture-retaining property, and reservoir protection of HEC as well as low friction, high rate of penetration, shale inhibition, wellbore stability, high lubricity, salt resistance, and thermal stability of oil-based drilling fluid, we try to dissolve HEC into oil-water emulsion to decrease the solid content of drilling and improve the temperature resistance of HEC to meet deep-well drilling, which puts forward new ideas for the application of HEC in drilling completion fluid and could make use of polymerides.

2. Experiment

2.1. Experimental Apparatus. Experimental installations used were an M3600 automatic rheometer (from Grace Instrument Inc.), a senior speed stepless speed mixer (from Qingdao Tongchun), and a heating device (from Qingdao Tongchun).

2.2. Experimental Reagent and Condition. Experimental reagents include HEC, NaOH, Na_2CO_3, ZR-01, and $0^{\#}$ oil. HEC is a kind of tackifier; it has a density of 0.75 g/cm^3 and the molar degree of substitution is 18~2.0.

Basic formula is $0^{\#}$ oil + 0.2%NaOH + 0.25%Na_2CO_3 + 3.0%emulsifier ZR − 01 + 0.6%HEC. The experimental condition is shown in Table 1.

2.3. Experimental Procedure. The value of the oil-water ratio was usually 90 : 10-20 : 80, considering the environmental pollution and the cost of drilling fluid; the value of oil-water is 50 : 50, 40 : 60, 30 : 70, 20 : 80, 10 : 90, and 0 : 100 (oil-free, respectively). The experimental procedures were as follows.

(I) A certain amount of HEC was slowly added to the diesel emulsion with a different oil-water ratio and stirred at 10000 r/min high speed for 60 min to prepare HEC emulsion

(II) The rheological parameters of the HEC emulsion solution were measured at a constant shear rate (1021.8 S^{-1}, 510.9 S^{-1}, 340.6 S^{-1}, 170.3 S^{-1}, 10.2 S^{-1}, and 5.1 S^{-1}) to evaluate the effect of the oil-water ratio on rheological property at certain temperatures (30°C, 60°C, 80°C, 90°C, and 100°C).

(III) The rheological parameters of the HEC emulsion solution have oil-water ratios of, respectively, 50 : 50, 40 : 60, 30 : 70, 20 : 80, 10 : 90, and 0 : 100 (oil-free) which were measured under constant temperature (30°C, 90°C).

(IV) At a certain temperature (30°C, 90°C), the rheological parameters of HEC emulsion were measured to evaluate the effect of the oil-water ratio on static suspension capacity at a lower shear rate

(V) Let the HEC emulsion stand for 48 hours at room temperature in a colorimetric tube, and then observe the change and difference between the upper and lower sections in the colorimetric tube to evaluate the emulsion stability

(VI) A hot rolling experiment was adopted to evaluate the effect of the oil-water ratio on emulsion stability at different temperatures

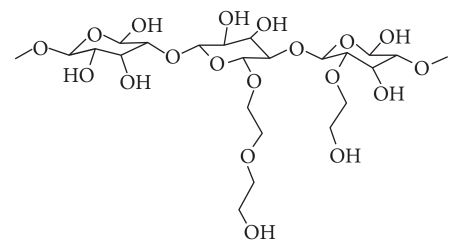

Figure 1: Diagram of the HEC molecular structure.

3. Results and Analysis

Polymer hydroxyethyl cellulose is widely used in the petroleum industry, especially in drilling, completion, workover, and fracturing processes. As drilling completion fluid additives, HEC can effectively reduce the hydrodynamic friction, decrease the starting torque, and protect the production layer. Moreover, the application of HEC is more prominent in hard rock. In this study, the rheological properties of the HEC solution were measured used a viscometer, M3600, at a constant shear rate, constant temperature, constant oil-water ratio, and low shear rate to evaluate the effect of the oil-water ratio on the rheological ability of HEC emulsion. Besides, emulsion stability of HEC emulsion with a different oil-water ratio were measured using two methods, hot rolling and standing and the layering process, to evaluate the effect of the oil-water ratio on emulsion stability of HEC emulsion.

3.1. Constant Shear Rate. The rheological parameters of different oil-water ratio emulsions (50 : 50, 40 : 60, 30 : 70, 20 : 80, 10 : 90, and 0 : 100 (oil-free)) were measured at a constant shear rate (1021.8 S^{-1}, 510.9 S^{-1}, 340.6 S^{-1}, 170.3 S^{-1}, 10.2 S^{-1}, and 5.1 S^{-1}). The results are shown in Figures 2 and 3.

The results shown in Figure 2 revealed that the viscosity of HEC emulsion was continuously reduced with the decrease in the oil-water ratio at six kinds of different constant shear rates. When the oil-water ratio was more than 30 : 70, the viscosity dropped obviously with the decrease in the oil-water ratio, and when it was less than 30 : 70, the

Table 1: The experimental conditions.

Items	Function	Remarks
Oil-water emulsion	Base	The oil-water rate is 50 : 50, 40 : 60, 30 : 70, 20 : 80, 10 : 90, 0 : 100 (oil free), 0# oil
ZR-01	Emulsifier	3.0%
HEC (hydroxyethyl cellulose)	Viscosifier	0.6%
NaOH	pH control	0.2%
Na_2CO_3	Additive	0.25%
Heating device	Thermal evaluation	The temperature is 30, 60, 80, 90, 100°C
M3600 (automatic rheometer)	Rheological evaluation	1021.8 S^{-1}, 510.9 S^{-1}, 340.6 S^{-1}, 170.3 S^{-1}, 10.2 S^{-1}, and 5.1 S^{-1} and 60°C and 90°C
Senior speed stepless mixer	Stirrer	Mixing time is 60 min, and the speed must be more than 10000 r/min
Colorimetric tube	Emulsion stability analysis	The oil-water rate is 50 : 50, 40 : 60, 30 : 70, 20 : 80, and 10 : 90, at room temperature

reduction was lesser. When the oil-water ratio was reduced from 50 : 50 to 30 : 70, the viscosity of HEC emulsion solution decreased dramatically, reducing the rate of up to 87.6%, at 30°C and 5.1 s^{-1}. Comparing the HEC emulsion solution of the oil-water ratio of 50 : 50 with that of 0 : 100, it was found that when the water was reduced by double, the viscosity was increased 72 times at the temperature of 30°C, which expressed that oil-water emulsion is better than aqueous as solution for HEC. At a high shear rate of 1021.8 S^{-1} and experimental temperature of 30°C, we can see that the viscosity difference between 50 : 50 and 30 : 70 was more obvious, and the value was 100 mPa·s. At the same changes in the oil-water ratio, the viscosity was reduced with the increase in temperature in the same shear rate. Although the viscosity of HEC emulsion (50 : 50) decreased to 61.5 mPa·s at a shear rate of 1021.8 S^{-1}, the solution still had a certain viscoelasticity when the temperature was increased from 30°C to 100°C. In contrast, under the same condition, the viscosity of the HEC emulsion solution (30 : 70) decreased to 11 mPa·s, leading to loss in viscoelasticity, and the solution with the oil-water rate of less than 10 : 90 almost lost its viscoelasticity. According to Figure 2, we can see that compared with the viscosity of HEC brine solution, oil-water emulsion could obviously enhance the tackifier performance and improve the rheological property of HEC.

The experimental results of shear stress are listed in Figure 3. It can be seen that shear stress was decreased continuously with the reduction in the oil-water ratio of HEC emulsion. When the value is over 20 : 80, shear stress decreased nonlinearly; when it was less than 20 : 80, the trend was approximately linear, but the degree of diminution was less several times than the former. Meanwhile, compared with the change in viscosity along with the oil-water ratio, the shear stress has a steady decline with the increase in temperature, which was similar to the trend of viscosity decline. Under the constant shear rate 1021.8 S^{-1}, the HEC emulsion (50 : 50) displayed stronger shear stress, whose characteristics were bad for drilling. Under the same condition, the HEC emulsion (20 : 80) displayed low shear stress and the value is only half of 50 : 50 at 30°C.

We can see from Figures 2 and 3 that with the decrease in the oil-water ratio, HEC's viscosity and shear stress both were decreased. With the increase in temperature, HEC's viscosity and shear stress also were decreased continuously, which keeps good consistency in the process of the rise in temperature. This phenomenon conformed to Arrhenius' equation,

$$\ln \eta = \ln A + \frac{\Delta E}{RT}, \tag{1}$$

where ΔE is the activation energy, η is the viscosity, R is the universal gas constant, and T is temperature. Arrhenius' equation indicated that the fluid viscosity was decreased with the increase in temperature, which has good consistency with experimental results (Figure 2).

The results from experiments and Arrhenius' equation were in good agreement with each other, and it was consistent with the law of fluid flow. The experimental results showed that the HEC solution used diesel oil emulsion as solvent which is a good pseudoplastic fluid, which can be used to prepare an ideal drilling and completion fluid system.

3.2. Constant Temperature (30°C, 90°C). In the test of HEC emulsion rheological stability, we set up 30°C and 90°C as the experimental temperature. The rheological experimental results with different oil-water ratios of 50 : 50, 40 : 60, 30 : 70, 20 : 80, 10 : 90, and 0 : 100 (oil-free) HEC oil-water emulsion are shown in Figures 4 and 5.

It can be drawn from Figures 4 and 5 that the apparent viscosity and shear stress had an obvious decrease with the decrease in the oil-water ratio at constant temperatures 30°C and 90°C. We can see that the viscosity increased linearly with the decrease in shear rate and the increase in amplitude was smaller when the shear rate was greater than 170.3 S^{-1}, and it has increased sharply when the shear was lower than 170.3 S^{-1}, whose changes kept a good consistency with the temperature 90°C. And, whether it is at higher temperature (90°C) or lower temperature (30°C), the HEC emulsion solution had a better rheological property and the apparent viscosity was always greater than the HEC brine solution. Besides, we can see that emulsion can improve the high-temperature resistance of the HEC

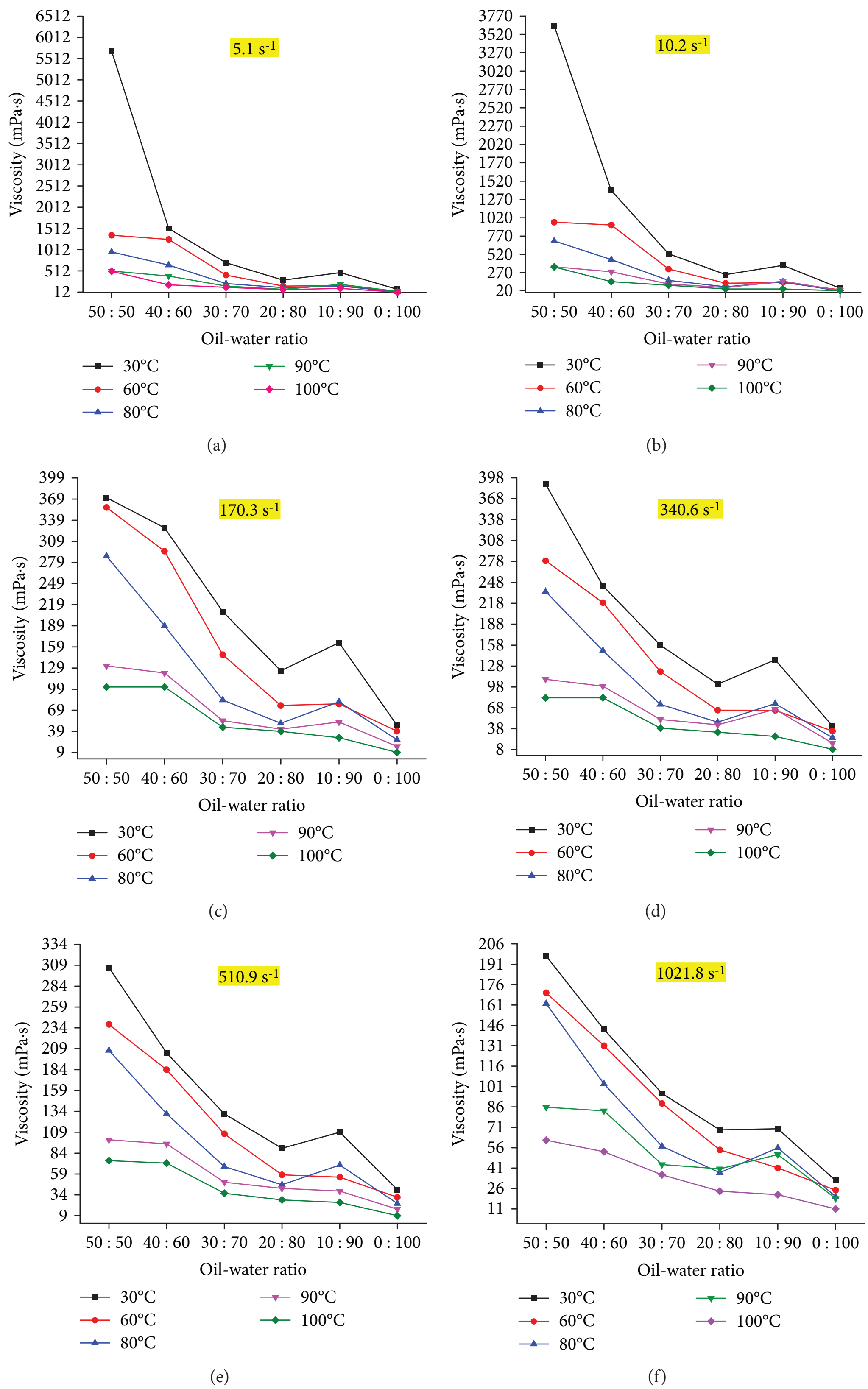

Figure 2: The relationship between the oil-water ratio and viscosity under different shear rates.

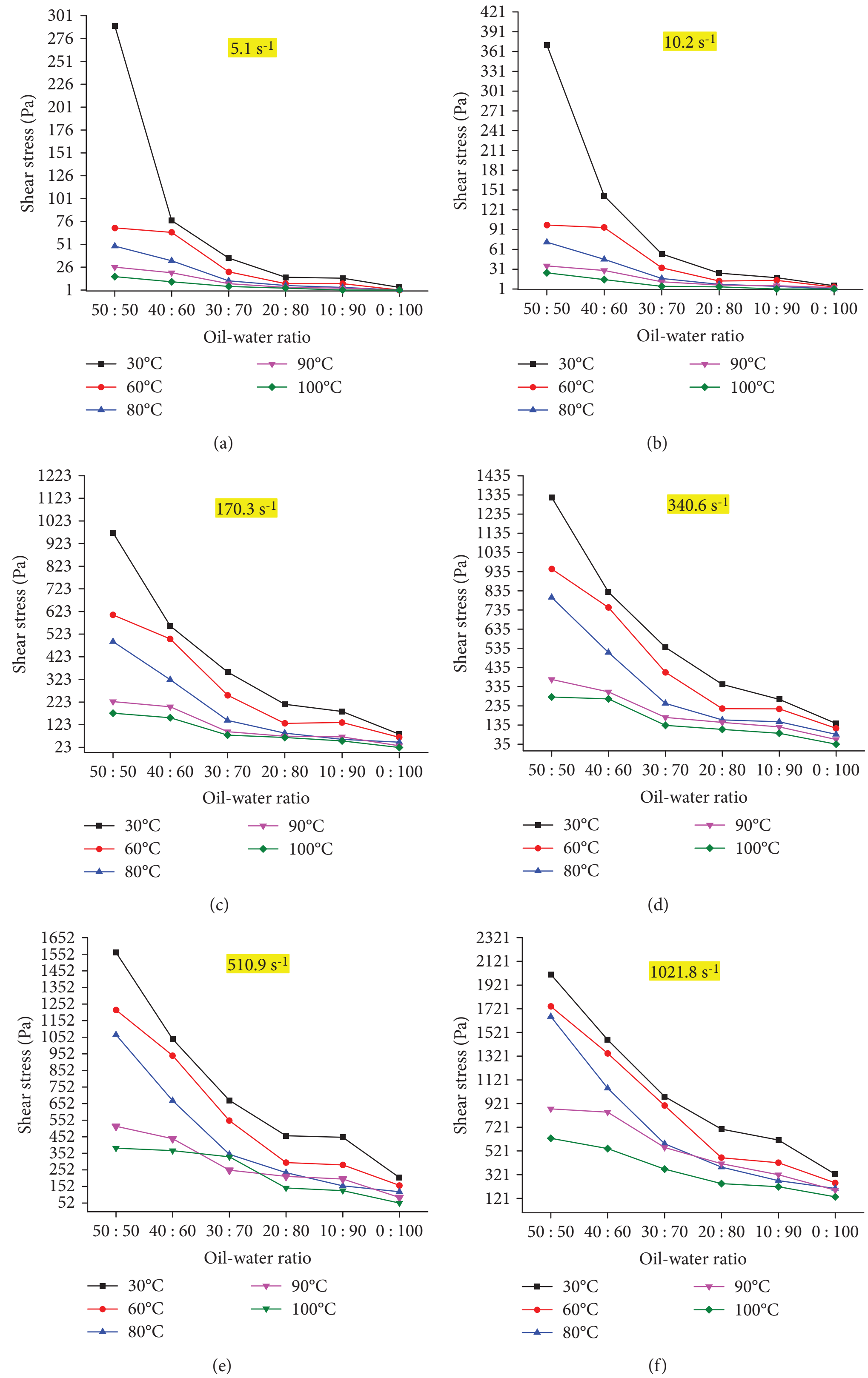

Figure 3: The relationship between the oil-water ratio and shear stress at different shear rates.

solution. The apparent viscosity of the HEC brine solution reduced from 71 mPa·s to 16 mPa·s, reduced by 77.46%, at a higher shear rate. However, the HEC emulsion remained about the same. However, under the same conditions, the tendency of shear stress did not keep a good consistency. With the increase in shear rate, the shear stress revealed

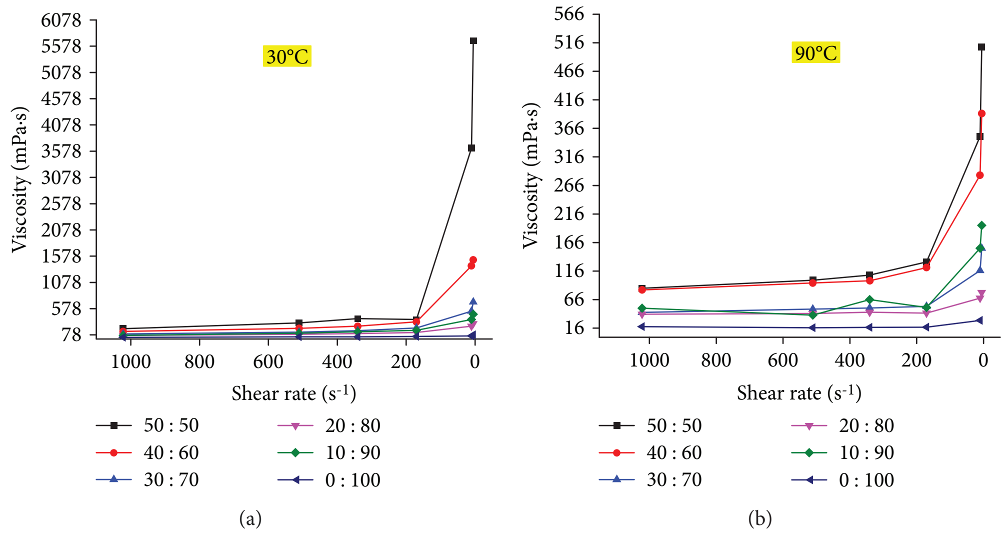

FIGURE 4: The relationship between apparent viscosity and shear rate at different temperatures.

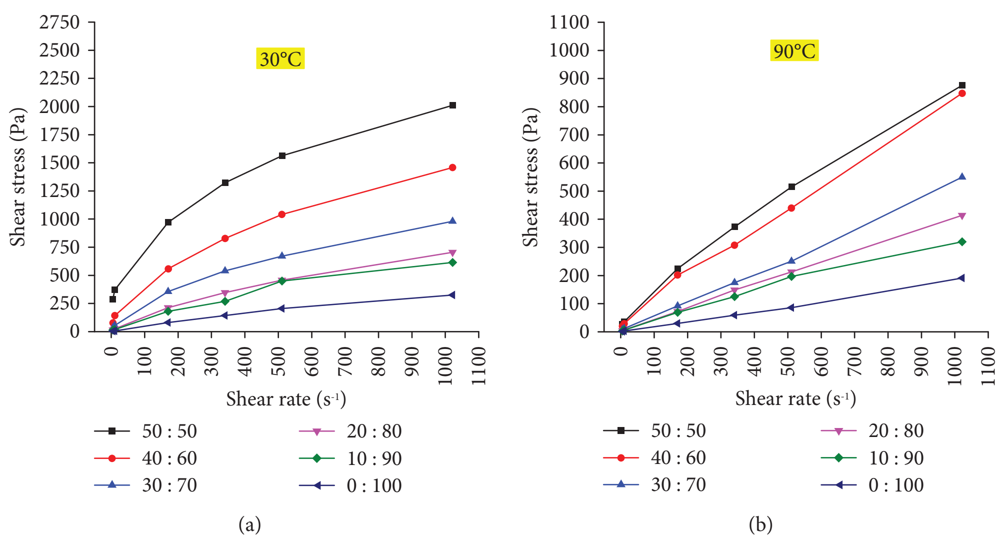

FIGURE 5: The relationship between shear strength and shear rate at different temperatures.

an uptrend at 30°C. When the shear rate was lower than 170.3 S^{-1}, the shear stress increased sharply; when the shear rate was greater than 170.3 S^{-1}, the increase tended to be flat. At the temperature of 90°C, the linear relationship between shear stress and shear rate was shown, but overall shear stress was much smaller than that at 30°C. On the whole, the HEC emulsion solution expressed better rheological properties, which is good for drilling suspended sand and reducing drilling drag.

3.3. Constant Oil-Water Ratio. Under the constant oil-water ratio 50 : 50, 40 : 60, 30 : 70, 20 : 80, 10 : 90, 0 : 100 (oil-free) conditions, the rheological parameters of HEC emulsion were measured at different temperatures; the experimental results are shown in Figures 6 and 7.

The relationships between apparent viscosity and shear rate with different oil-water ratios are shown in Figure 6. The results shown in Figure 6 displayed that the apparent viscosity decreased with the increase in shear rate. As was shown in Figure 6, the apparent viscosity of HEC diesel oil emulsion was affected by the shear rate. At the temperature of 30°C and shear rate of 5.1 S^{-1}, the viscosity increased from 78.4 mPa·s to 5686 mPa·s, nearly 71.5 times, with the oil-water from 0 : 100 to 50 : 50. In contrast, with the equivalent change in the ratio, the viscosity increased from 12.3 mPa·s to 61.5 mPa·s, increased by 4 times at the temperature of 100°C and shear rate of 5.1 S^{-1}. This trend of viscosity decrease is due to thermal motion of the molecule. Under the high temperature, the acceleration of the relative motion of intermolecular in liquids wrecks formation of floc and cuts

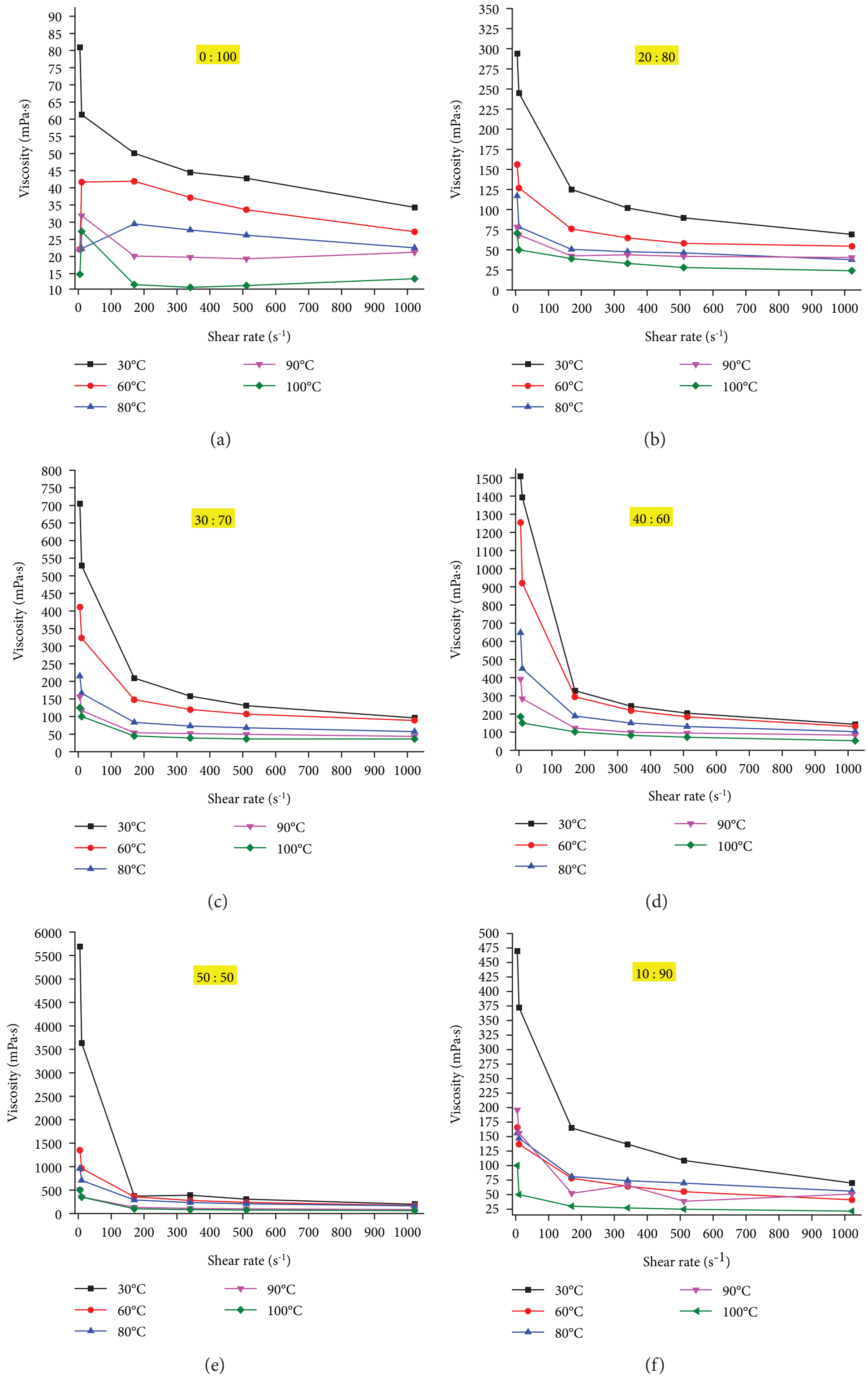

Figure 6: The relationship between apparent viscosity and shear rate of HEC emulsion solution having different oil-water ratios.

down the flocculating effect resulting in viscosity reduction. At the temperature of 100°C, lower oil-water HEC emulsion almost lost its viscoelasticity and could not meet the requirements of the suspension. Conversely, higher oil-water HEC emulsion still could hold a certain viscosity which was greater than mPa·s and could transport cuttings in the process of drilling and completion of horizontal well in order to effectively prevent the formation of the

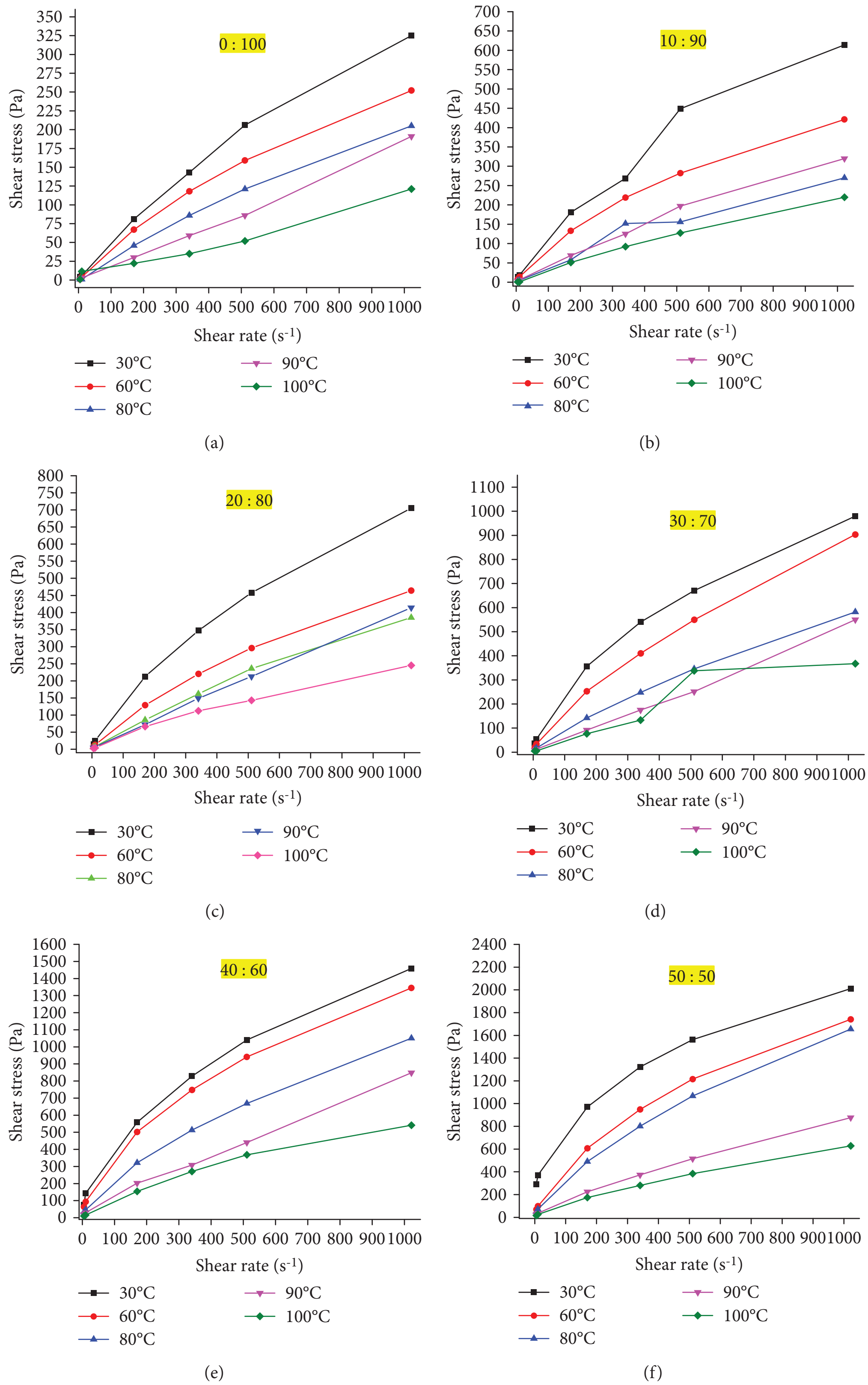

Figure 7: Relationships between the shear stress of different oil-water ratios of HEC and shear rate.

cutting bed, which expressed that higher oil-water emulsion could improve the thermal ability under the same dosage of HEC.

The relationships between shear stress and shear rate of HEC emulsion solution are shown in Figure 7, whose oil-water ratios were 0 : 100 (oil-free), 10 : 90, 20 : 80, 30 : 70,

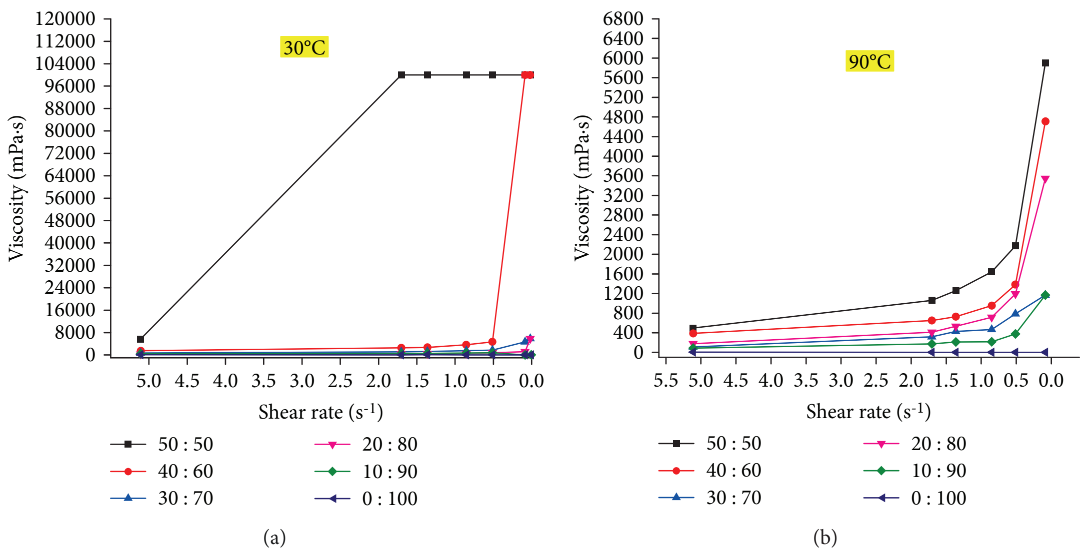

Figure 8: The relationship between shear rate and viscosity at different temperatures.

40 : 60, and 50 : 50, respectively. As shown in Figure 7, it could be found that with the increase in shear rate, the shear stress tended to increase. With the increase in the oil-water ratio, the change in shear stress also increased and both changes showed good consistency. When the oil-water ratio was less than 20 : 80, the shear strength increased linearly with the increase in shear rate, which is due to the fact that the low number of free and independent droplets could cause less friction between droplets and internal friction decrease, showing the characteristics of near Newton fluid. However, when the oil-water ratio was greater than 20 : 80, the increase in shear stress is divided into two phases. In the first phase, the shear stress increased obviously with the increase in shear rate when the shear rate was less than 170.3 S^{-1}. In the second phase, the change was smoother when the shear rate was greater than 170.3 S^{-1}, which indicated that oil can play the role of lubrication.

As was shown in Figure 7, it was suggested that when the oil-water ratio was greater than 20 : 80, viscosity coefficient n was less than 1. According to the power law model, the greater the oil-water ratio was, the smaller the n was, and the greater the consistency index K of emulsion was, and the experimental result has good consistency with it. Meanwhile, the decrease in n was likely to improve the ratio of yield stress to plastic, which could turn gradually the turbulence of the annulus space into a flat plate laminar flow. This flow pattern can effectively avoid the erosion of drilling and completion fluid for the sidewall, which was conducive to the protection of borehole stability. Under the constant oil-water condition, the higher the temperature was, the smaller the K was, the greater the n was, and the stronger the non-Newtonian characteristic was, and the variation trend is close to the power function, which expressed that the system has a better rheological property and could be used in drilling fluid by combining with other additives.

3.4. Low Shear Rate. In the drilling process, high elastic area could be formed in the vicinity of the borehole wall if the drilling fluid system has a high viscosity at low shear rate. This characteristic of high viscosity at low shear rate is good for sand-carrying and could effectively prevent the formation of sand bed [21]. Through analyzing the rheological property under lower shear stress, we could determine whether the system is fit for drilling. The experimental results are shown in Figures 8 and 9.

The relationship between the apparent viscosity, shear stress, and shear rate is shown in Figures 8 and 9. The viscosity increased, and the shear stress decreased with the decrease in shear rate, which indicated that more stable mesh structures were formed at a low shear rate, resulting in the increase in viscosity. At the temperature of 30°C, the shear rate of less than 1.7 S^{-1}, the viscosity of the HEC emulsion with oil-water ratio of 50 : 50 was up to 99999 mPa·s, which has good capacity of sand-carrying and could effectively overcome the problem of sand carrying difficulty for horizontal or deviated well easing to form sand bed. While the viscosity of the HEC solution using brine (0 : 100) as solvent was extremely low, only through putting more HEC to increase the viscosity solves the problem of carrying cuttings, in which there was no doubt that the above method adds the drilling cost and anti-temperature effect of the HEC solution which was not better than HEC emulsion. As was shown in Figures 8 and 9, with the increase in the oil-water ratio, viscosity and shear stress kept a good consistency in the decrease. The oil-water ratio could be further improved to achieve a better performance of temperature resistance, tackifying, and lubricity, which expressed that the HEC emulsion had a better suspension property and thermal stability than aqueous solution and could be used in drilling fluid by combining with other additives to improve the drilling efficiency and reduce the drilling cost.

3.5. Emulsion Stability. Sedimentation is one of the most conventional and intuitionistic experiments analyzing emulsion stability. In the paper, it was adopted to analyze the emulsion stability of HEC emulsion. The experimental steps were as

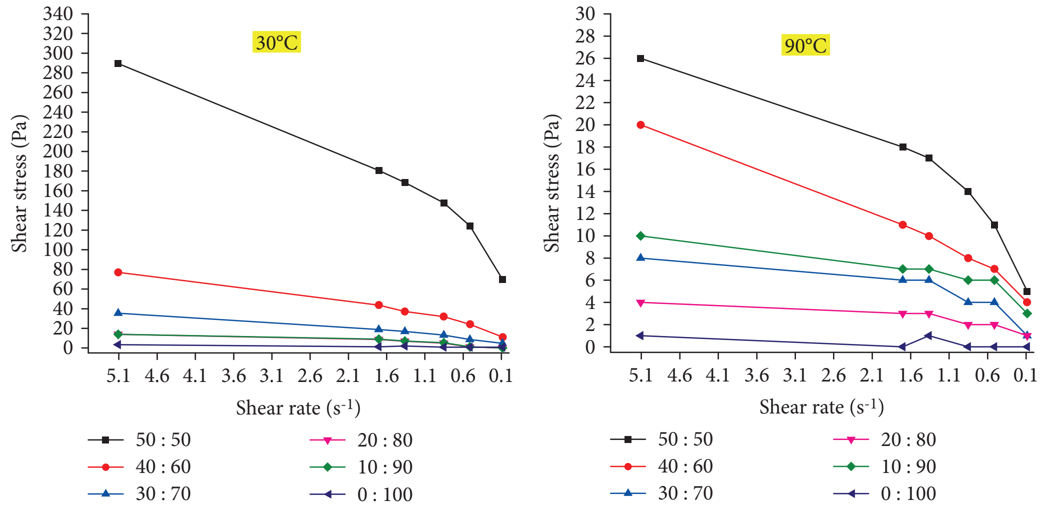

(a) (b)

FIGURE 9: The relationship between shear rate and shear stress at different temperatures.

TABLE 2: The evaluation of sedimentation stability.

Oil-water ratio		10 : 90	20 : 80	30 : 70	40 : 60	50 : 50
Time (h)	0	48	48	48	48	48
Phenomenon						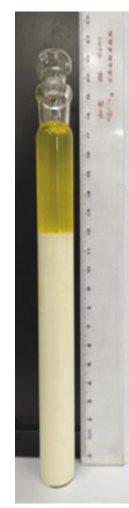
Notes	All are milky white before sedimentation					

follows: let HEC emulsion stir and stand for 48 hours in a colorimetric tube, and then observe the change and difference between the upper and lower sections in the colorimetric tube. The results are shown in Table 2.

Table 2 shows that the bigger the oil-water ratio, the more upper separator liquid there is; there was a small amount of change between 20 : 80 and 30 : 70, and it was still in a reasonable range. However, the separator liquid was more than 2 cm when the oil-water ratio was more than 30 : 70 and it was even about 1/3 when the oil-water was 50 : 50, which meant that the emulsion stability was worse when the oil-water ratio was more than 30 : 70. Besides, we analyzed the stability by temperature resistance experiment and the results are shown in Figure 10. It can be seen that the surface morphology of HEC emulsion after hot rolling lasting 16 h at 100°C changed from ivory to yellow (all are milky white before hot rolling) with the increase in the oil-water ratio.

This phenomenon shown in Figure 10 could be illustrated that a higher temperature had an effect on the emulsifier and led HEC emulsion with a higher oil-water ratio to be unstable. Further, oil and water were separated, with oil floating on the surface, and the solution surface appeared with the same color as that of diesel.

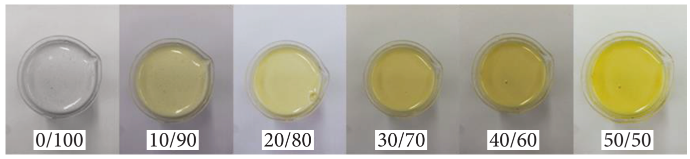

Figure 10: The state of HEC emulsion solution after hot rolling at 100°C after 16 h.

By comparing the results shown above, there was good coherence and it was concluded that the emulsion solution of the too high oil-water ratio was not suitable for the tackifier of HEC because of its poor thermal stability and emulsion stability and the oil-water ratio 30 : 70 emulsion was the optimal solution, which expressed excellent thermal stability and emulsion stability.

4. Conclusion

Based on the experimental results, in Sections 3.1, 3.2, 3.3, and 3.4, the following conclusions can be made:

(1) Diesel oil emulsion can be used in the polymer drilling fluid system. Under the same dosage of the HEC, diesel oil emulsion, as a solvent, can significantly improve the rheological stability of polymer HEC at room temperature and higher temperature and can enhance the lubrication and viscoelasticity of polymer drilling fluid, which is good for improving the drilling speed and reducing the reservoir damage and drilling cost

(2) When the ratio was more than 20 : 80, the HEC emulsion has a better rheological property and thermal stability, but when the ratio was more than 40 : 60, it expressed oil-water separation as shown in Figure 10 and Table 2, the oil floating on the surface, and the solution appeared with the same color as that of diesel. So, the emulsion solution with an oil-water ratio of 30 : 70 was an ideal increasing solvent for HEC

(3) The dosage and variety of other additives need to ascertain for the HEC emulsion drilling fluid, such as emulsifier and filtrate reducer if we want to get a system on it. Besides, the microcosmic displacement mechanism between HEC and oil-water is a complex and meaningful topic and needs to be studied independently to learn more about the emulsion stability of HEC emulsion

Data Availability

The data used to support the findings of this study are available from the corresponding author upon request. The email is sxm310426@126.com.

Conflicts of Interest

The authors declare that they have no conflicts of interest.

References

[1] J. Abdo and M. D. Haneef, “Nano-enhanced drilling fluids: pioneering approach to overcome uncompromising drilling problems,” *Journal of Energy Resources Technology*, vol. 134, no. 1, article 014501, 2012.

[2] N. V. Boyou, I. Ismail, W. R. Wan Sulaiman et al., “Experimental investigation of hole cleaning in directional drilling by using nano-enhanced water-based drilling fluids,” *Journal of Petroleum Science and Engineering*, vol. 176, pp. 220–231, 2019.

[3] J. H. Cai, H. Liu, Y. Chen, and C. B. Xiao, “Study on degradable drilling fluid system for coalbed methane horizontal drilling,” *Journal of China Coal Society*, vol. 36, no. 10, pp. 1683–1688, 2011.

[4] M. M. Dardir, S. Ibrahime, M. Soliman, S. D. Desouky, and A. A. Hafiz, “Preparation and evaluation of some esteramides as synthetic based drilling fluids,” *Egyptian Journal of Petroleum*, vol. 23, no. 1, pp. 35–43, 2014.

[5] A. M. Salem Ragab and A. Noah, “Reduction of formation damage and fluid loss using nano-sized silica drilling fluids,” *Petroleum Technology Development Journal*, vol. 2, pp. 75–88, 2014.

[6] C.-H. Choi, U. Ulmanella, J. Kim, C.-H. Ho, and C.-H. Kim, “Effective slip and friction reduction in nanograted superhydrophobic microchannels,” *Physics of Fluids*, vol. 18, no. 8, article 087105, 2006.

[7] M. Sadeghalvaad and S. Sabbaghi, “The effect of the TiO 2 /polyacrylamide nanocomposite on water-based drilling fluid properties,” *Powder Technology*, vol. 272, pp. 113–119, 2015.

[8] M. Azam, A. Yassin, and A. Kamis, “Palm oil derivative as a based fluid in formulating oil based drilling mud,” in *SPE Latin America Petroleum Engineering Conference*, Rio de Janeiro, Brazil, October 1990.

[9] D. L. Carbajal, C. N. Burress, W. Shumway, and Y. Zhang, “Combining proven anti-sag technologies for HPHT north sea applications: clay-free oil-based fluid and synthetic, submicron weight material,” in *SPE/IADC Drilling Conference and Exhibition*, Amsterdam, The Netherlands, March 2009.

[10] F. T. G. Dias, R. R. Souza, and E. F. Lucas, “Influence of modified starches composition on their performance as fluid loss additives in invert-emulsion drilling fluids,” *Fuel*, vol. 140, pp. 711–716, 2015.

[11] J. Hermoso, F. Martinez-Boza, and C. Gallegos, “Influence of viscosity modifier nature and concentration on the viscous flow behaviour of oil-based drilling fluids at high pressure,” *Applied Clay Science*, vol. 87, no. 1, pp. 14–21, 2014.

[12] J. Hermoso, F. Martinez-Boza, and C. Gallegos, “Influence of aqueous phase volume fraction, organoclay concentration and pressure on invert-emulsion oil muds rheology,” *Journal of Industrial and Engineering Chemistry*, vol. 22, pp. 341–349, 2015.

[13] F. Civan, *Reservoir Formation Damage*, Gulf Professional Publishing, 2007.

[14] L. F. Lopes, B. O. Silveira, and R. B. Moreno, "Loss circulation and formation damage control on overbalanced drilling with different formulations of water based drill-in fluids on sandstone reservoir," in *ASME 2012 31st International Conference on Ocean, Offshore and Arctic Engineering*, pp. 859–869, Rio de Janeiro, Brazil, July 2012.

[15] X. Zhao, Z. Qiu, B. Sun, S. Liu, X. Xing, and M. Wang, "Formation damage mechanisms associated with drilling and completion fluids for deepwater reservoirs," *Journal of Petroleum Science and Engineering*, vol. 173, pp. 112–121, 2019.

[16] S. Ding, H. Liu, L. Bai, W. Yang, and W. Hao, "Thixotropy and anti-thixotropy of hydroxyethyl cellulose aqueous solutions," *Materials Review*, vol. 2013, no. 20, p. 23, 2013.

[17] B. Nystroem and B. Lindman, "Dynamic and viscoelastic properties during the thermal gelation process of a nonionic cellulose ether dissolved in water in the presence of ionic surfactants," *Macromolecules*, vol. 28, no. 4, pp. 967–974, 1995.

[18] D. Mech and J. S. Sangwai, "Effect of molecular weight of polyethylene glycol (PEG), a hydrate inhibitive water-based drilling fluid additive, on the formation and dissociation kinetics of methane hydrate," *Journal of Natural Gas Science and Engineering*, vol. 35, pp. 1441–1452, 2016.

[19] N. A. al Sandouk-Lincke, J. Schwarzbauer, V. Antic et al., "Off-line–pyrolysis–gas chromatography–mass spectrometry analyses of drilling fluids and drill cuttings – identification of potential environmental marker substances," *Organic Geochemistry*, vol. 88, pp. 17–28, 2015.

[20] X. Villegas-Pañeda, S. Pérez-Casas, E. Hernández-Baltazar, and A. E. Chávez-Castellanos, "Study of interactions between octyl-β-D-glucopyranoside and the hydroxyethyl-cellulose biopolymer in aqueous solution," *Journal of Chemical Thermodynamics*, vol. 79, pp. 69–75, 2014.

[21] W. Jian, Z. Rong, and N. Mingshun, "Research and application of HRD weak gel drilling fluid," *Natural Gas Exploration & Development*, no. 4, pp. 52–55, 2008.

Hindawi
Geofluids
Volume 2019, Article ID 2672695, 15 pages
https://doi.org/10.1155/2019/2672695

Research Article

Damage Mechanism of Oil-Based Drilling Fluid Flow in Seepage Channels for Fractured Tight Sandstone Gas Reservoirs

Peng Xu [1,2] **and Mingbiao Xu** [1,3]

[1] College of Petroleum Engineering, Yangtze University, Wuhan 430100, China
[2] State Key Laboratory of Oil and Gas Reservoir Geology and Exploitation, Southwest Petroleum University, Chengdu 610500, China
[3] Hubei Cooperative Innovation Center of Unconventional Oil and Gas, Yangtze University, Wuhan 430100, China

Correspondence should be addressed to Mingbiao Xu; cjdxxmb@126.com

Received 27 November 2018; Revised 12 April 2019; Accepted 27 May 2019; Published 26 June 2019

Guest Editor: Bisheng Wu

Oil-based drilling fluids (OBDFs) have a strong wellbore stabilization effect, but little attention has been paid to the formation damage caused by oil-based drilling fluids based on traditional knowledge, which is a problem that must be solved prior to the application of oil-based drilling fluid. For ultradeep fractured tight sandstone gas reservoirs, the reservoir damage caused by oil-based drilling fluids is worthy of additional research. In this paper, the potential damage factors of oil-based drilling fluids and fractured tight sandstone formations are analyzed theoretically and experimentally. The damage mechanism of oil-based drilling fluids for fractured tight sandstone gas reservoirs is analyzed based on the characteristics of multiphase fluids in seepage channels, the physical and chemical changes of rocks, and the rheological stability of oil-based drilling fluids. Based on the damage mechanism of oil-based drilling fluids, the key problems that must be solved during the damage control of oil-based drilling fluids are analyzed, a detailed description of formation damage characteristics is made, and how to accurately and rapidly form plugging zones is addressed. This research on damage control can provide a reference for solving the damage problems caused by oil-based drilling fluids in fractured tight sandstone gas reservoirs.

1. Introduction

Fractured tight sandstone formations have special engineering geological characteristics and are vulnerable to damage caused by the invasion of foreign fluids during drilling and completion. OBDF is more stable than water-based drilling fluids (WBDFs), and OBDF has been widely used in fractured tight sandstone formation drilling as the cost of OBDF has approached that of WBDF in recent years [1]. Traditionally, OBDF has protected reservoirs more effectively than WBDF [2], because the continuous phase of OBDF is its oil phase and its filtration capacity is low, which reduces the hydration of clay minerals and the invasion of filtrate into the formation. However, many years of applied practice show that OBDF can also cause formation damage and this damage is more serious than WBDF in some cases [3, 4].

Presently, the research on formation damage caused by OBDF has mainly focused on solid phase invasions, wettability changes, and oil traps and there are relatively few studies on why OBDF causes these damages. Cui et al. [4] studied the damage of solid phase invasions to reservoirs, while Korsakova et al. [5] studied the phase distribution and salt exchanges in boreholes during drilling fluid invasion in oil and gas reservoirs. Rong and others [6] used new methods to study the wettability reversal caused by OBDF, Skalli and others [7] studied the wettability effect of surfactants on surface and core in OBDF, and Yan and Sharma [8] studied the wettability change caused by OBDF. Murickan et al. [9] used a relative permeability curve to study trap damages caused by OBDF and WBDF.

To address the lack of damage research for OBDF and why these damages occur, multiple components of OBDF must be further researched, including multiphase fluid states in reservoirs, OBDF properties, and properties of fractured tight sandstone in OBDF environments [10–12].

For the multiphase fluid state of a formation caused by an OBDF intrusion, most studies focus on the oil-water emulsion, but the oil-water emulsion is only in a state of existence [13]. The existing OBDF research is mostly based on the pure oil phase or oil-water two phase type (water-in-oil drilling fluid). In addition to the oil-water two-phase type, oil-oil two-phase, oil-gas two-phase, and oil-gas-water three-phase types are also widespread in the uses of OBDF in China, but these situations are not considered in drilling operations, which directly leads to excessive complex problems in drilling, more serious damage to reservoirs, and even more serious damage to WBDF [14, 15].

The properties of OBDF mainly focus on the aspects of high-temperature stability and suspension stability, which have not been thoroughly solved, thus resulting in a certain difference between reservoir protection technological capabilities and WBDF [16, 17]. The stability problems caused by OBDF emulsification are rarely considered, the changes of wettability and capillary force caused by bubbling in OBDF are only mentioned in a few studies, the chemical changes caused by OBDFs entering reservoirs are rarely considered [18, 19], and the formation of OBDF mud cake and particle size control have been mostly ignored.

The change in properties of fractured tight sandstone in an OBDF environment is one of the key factors causing damage to reservoirs. At present, there are many misunderstandings regarding the use of OBDF. In many cases, OBDF usage does not take into account the actual situation of the formation [20–23]. The use of OBDFs is generally believed to not be complicated when WBDF cannot be drilled smoothly. From the existing research, there is a large misunderstanding of this view. OBDF may not be as suitable as WBDF in some cases. In addition, studies on the characteristics of seepage channels such as fractures and matrix pores in OBDF environments are rare [24–27]. Some common sense errors have been caused by the improper treatment of WBDF environments.

Currently, the research on the formation damage control of OBDFs is mainly based on WBDFs. The theoretical and technical research on formation damage is limited to the scope of water-based fluids. In most cases, WBDF theories and methods rarely take into account the causes of different types or degrees of damage caused by different fluids, although they objectively form a thorough understanding of the reservoir protection effects of OBDF. However, a small amount of OBDF formation damage research has mainly focused on porous formations and few studies have researched fractured reservoirs with ultralow permeability.

The damage causes of OBDF to the fractured tight sandstone reservoir in the Keshen Block of Tarim Oilfield, China, are studied through three aspects: the multiphase fluid characteristics of the seepage channel, the changes in the petrophysical and chemical properties, and the rheological stability of OBDF. OBDF has become widely used in complex formations such as fractured tight sandstone due to the reduced costs of comprehensive uses of OBDFs and mature postprocessing technology. Therefore, based on the study of the formation damage of OBDF, correcting the prejudice of low damage of OBDF over a long period of time is one of the important measures used to effectively improve the efficiency of oil and gas exploitation and to realize the efficient development of oil and gas fields.

2. Experiment Section

2.1. Experimental Materials

2.1.1. Experimental Cores. Taken from the Keshen Block of Tarim Oilfield, China, the size of the core foundation is approximately 25 mm in diameter and 50 mm in length. Core types include matrix cores and fractured cores.

2.1.2. Oil-Based Drilling Fluid. OBDF is mainly made up of drilling fluid additives for field drilling in the Keshen Block. The formula is Diesel + 1.0% organic soil + 1.5% primary emulsifier + 2.1% auxiliary emulsifier + 20% $CaCl_2$ brine (80/20) + 2.5% loss agent + 2.5% lime + 0.5% wetting agent + a weighting agent.

2.2. Experimental Methods

(1) Drilling Fluid Performance Testing. A six-speed rotating viscometer is used to measure the readings at different rotating speeds (600/300/200/100/6/3), and the apparent viscosity, plastic viscosity, and dynamic shear force are calculated according to the standard. API filtration is measured by a medium pressure filtration instrument. The high-temperature and high-pressure filtration instrument is used to measure the high-temperature and high-pressure filtration volume. The demulsification voltage (electric stability) is measured by an electric stabilizer. The experimental reference standard is the National Drilling Fluid Testing Standard "GB/T 29170-2012 Oil and Gas Industry Drilling Fluid Laboratory Testing."

(2) Core Damage Evaluation Experiment. Referring to the standard of the China Petroleum and Natural Gas Industry "SYT 6540-2002 Drilling Fluid Completion Fluid Damage Layer Indoor Evaluation Method," and using the experimental device of core damage evaluation, the device can simultaneously carry out two parallel sample tests to improve the experimental accuracy. This experiment adopts the displacement method: forward direction-reverse direction-forward direction, and the flow of fluid from formation to the wellbore is in the forward direction. The evaluation method for the damage degree is to compare the permeabilities of the formation before and after damage and then calculate the permeability damage rate.

(3) Evaluating the Relationship between Viscosities at Different Temperatures and Shear Rates. A Grace 3600 grade-free heating viscometer was used for this test. The shear rates (S^{-1}) are 1021.38, 510.69, 340.46, 170.23, 10.214, 5.107, 1.702, and 0.851.

TABLE 1: Basic performance of OBDF (1.86 g/cm^3).

Experimental condition	Apparent viscosity (mPa·s)	Plastic viscosity (mPa·s)	Yield point (Pa)	Filter loss$_{API}$ (mL)	Filter loss$_{HTHP\text{-}API}$ (mL)	Emulsion stability (V)
Before aging	93.0	86.0	7.0	0.6	1.6	984
After aging	67.5	60.0	7.5	0	1.6	959

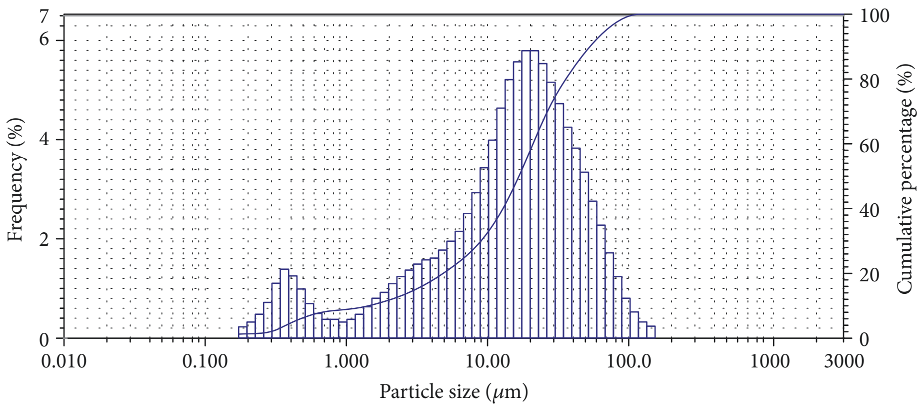

FIGURE 1: Solid particle distribution of oil-based drilling fluid.

(4) Scanning Electron Microscopy. A Quanta 450 environmental scanning electron microscopy was used for testing.

(5) Clay Mineral Composition Analysis. An X'Pert MPD PRO X-ray diffractometer was used.

3. OBDF and Potential Damage Formation

3.1. OBDF. In drilling engineering, the excellent inhibition performance of OBDF is an important reason for its large-scale use. OBDF takes oil in a continuous phase, which can effectively avoid conventional sensitivity damage, especially water sensitivity damage; low filtration and a relatively strong plugging mechanism greatly improve the reservoir protection; at the same time, OBDF can also effectively reduce scaling and corrosion damage, and the oil phase can effectively reduce friction resistance and reduce engineering accidents.

In most cases, OBDF consists of base oil, organic soil, an emulsifier, a filtrate reducer, a wetting agent, a weighting agent, calcium oxide, and some oleophilic colloids and inorganic ions. In addition to some common additives such as filtrate reducers and weighting materials, the differences in the continuous phase media directly determine the huge differences in their properties compared with WBDF. At the same time, the rheological properties of OBDF are different from those of WBDF because of the noncommon additives such as emulsifiers and wetting agents. Therefore, in most cases, the use and treatment of OBDFs are quite different from WBDFs.

For fractured tight sandstone gas reservoirs in ultradeep wells, OBDF is widely used in the Keshen Block and UDM-2 OBDF uses advanced technology. Taking OBDF with a density of 1.86 g/cm^3, the basic performance of the drilling fluid is shown in Table 1 and the experimental aging conditions are 150°C and 16 h. Solid particle distribution of the oil-based drilling fluid is shown in Figure 1.

TABLE 2: Pore size distribution in the Keshen Block.

Particle size distribution (μm)	Sample (%) #1	#2	#3	#4
0-0.017	0.00	0.00	0.00	0.00
0.0170-0.0283	5.60	13.39	21.19	67.24
0.0283-0.0471	41.69	61.86	53.29	22.18
0.0471-0.0785	24.34	20.09	21.97	0.00
0.0785-0.1307	19.04	1.43	0.00	6.04
0.1307-0.2176	8.02	3.23	2.86	4.34
0.2176-0.3625	1.32	0.00	0.49	0.00
0.3625-1.6700	0.00	0.00	0.20	0.20

3.2. Potential Damage Formation. Fractured tight sandstone gas reservoirs are characterized by low porosity, low permeability, fracture development, local ultralow water saturation, high capillary pressure, abnormal formation pressure, and high damage potential [28, 29]. The Keshen Block in Tarim Oilfield has all these characteristics and is a typical fractured tight sandstone gas reservoir. The core permeability of the Keshen Block reservoir is mainly distributed between 0.0020 and 0.0680 × 10^{-3} μm^2. The average core permeability is only 0.0234 × 10^{-3} μm^2, which denotes an ultralow permeability reservoir. The porosity of the reservoir core is mainly distributed between 3.09% and 10.89%, and the average core porosity is only 5.77%, which denotes a low porosity reservoir. The reservoir physical property analysis shows that the reservoir core porosity in the Dabei block is low, and the average porosity is 5.77%. The reservoir pores are fine (Table 2). Reservoir particles show mainly surface-surface

Table 3: XRD analysis of clay mineral content in the Keshen Block.

Core number	Absolute content of clay minerals (%)	Relative content of clay minerals (%)				Interlayer ratio (%S)
		Illite	Illite/montmorillonite	Kaolinite	Chlorite	
ks2-2-8-61	4.9	52.6	8.3	0.0	39.1	15.0
ks2-2-8-67	2.3	53.4	6.6	0.0	40.0	15.0
ks2-2-8-72	6.2	66.0	8.7	0.0	25.3	15.0
ks2-2-8-84	3.0	58.2	3.1	0.0	38.7	10.0
ks2-2-14-131	3.3	57.0	14.3	0.0	28.7	15.0
ks8-114	6.0	66.4	11.7	0.0	21.8	15.0
ks207-90	6.0	53.3	14.4	0.0	32.3	15.0
ks208-104	8.5	53.9	18.3	0.0	27.9	15.0

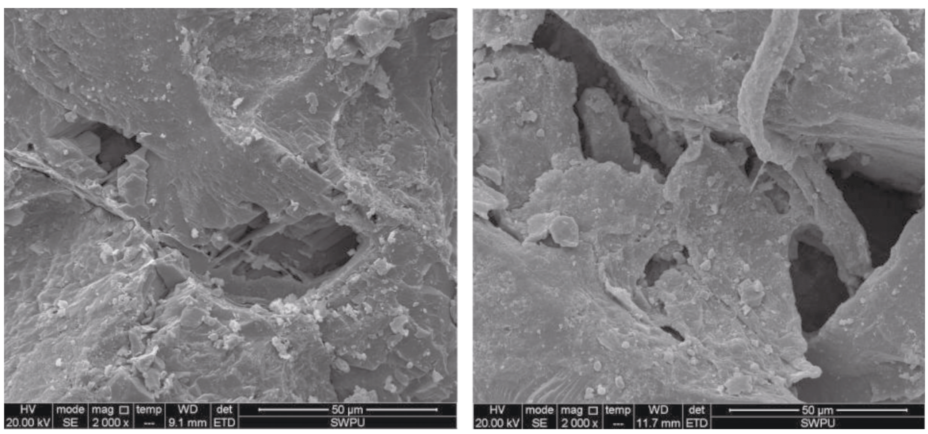

Figure 2: Rock surface morphology without damage.

contacts or line-surface contacts. The contacts between the particles are close, and the porosity is concentrated from 0.80% to 2.70%, with a part less than 0.10%. The rock pores are not uniform. Most areas have no pores and are locally concentrated. The average clay mineral content in the reservoir cores is 5.03%, the illite content is more than 50% (Table 3), and potential formation damage exists. Scanning electron microscopy (SEM) data show that the pore throat of the reservoir is not clear at low multiples (Figure 2), which reflects the characteristics of poor pore development and a poor connectivity of the reservoir in the study area.

The fissure linear density of 3 wells in the Keshen 1-Keshen 2 gas reservoir was calculated. The Keshen 201 well has the most developed fractures. There are 584 interpreted fractures in the 306 m Paleogene and Cretaceous formations, and the fracture density is 1.91 per m. The Keshen 2 well has 116 interpreted fractures in 141.5 m formations, and the fracture density is 0.82 per meter. The least developed fractures are in the Keshen 202 well with 95 interpreted fractures in a 300 m formation and 0.32 fracture densities per meter. According to the reservoir fracture analysis in the Keshen Block, the main seepage channel type of the reservoir in the block is fractures, followed by larger pores. Reservoir fractures are thoroughly developed, with fracture widths of less than 1-2 mm or even 0.5 mm in some cases, most of which are distributed below 0.1 mm (Figures 3 and 4). By analyzing the cores taken from the target formation, obvious fractures can be found in some cores. The reservoir is characterized by low porosity, ultralow permeability, and compact sandstone. At the same time, the reservoir can generate industrial oil and gas flow. The fractures and microfractures are the main seepage channels of the reservoir.

The pressure coefficients of the target formation in the study block are mostly between 1.75 and 2.20, and the formation's static pressure is high. The formation temperature is mostly distributed between 130°C and 160°C, meaning that it is a high-temperature formation.

3.3. Potential Damage Factors of OBDF. In most cases, the main potential damage types from WBDF include rock sensitivity damage and a high filtration rate, but OBDF greatly weakens or even eliminates these damages, resulting in a traditional recognition that OBDF can thoroughly protect reservoirs. However, with the combined compositions and mechanisms of OBDF and WBDF, OBDF also experiences serious reservoir damage. Taking UDM-2 OBDF as an example, dynamic damage experiments of the fractured rock cores are conducted and the results (Table 4 and Figure 5) show that OBDF has more serious damage [30]. Therefore, the potential damage factors of OBDFs must be studied.

According to the lithological and physical characteristics of the reservoir, the study object is a low-porosity/ultralow-permeability reservoir. From the pore throat characteristics and fracture characteristics, the pore throat of the reservoir

Figure 3: Schematic diagram of cores of the research block.

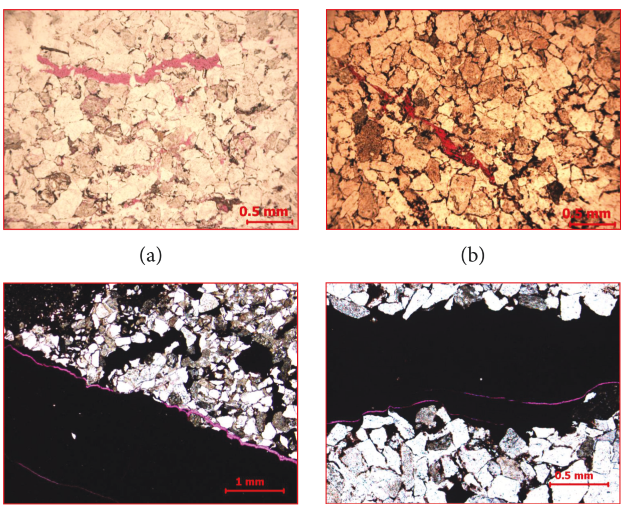

(a) (b) (c) (d)

Figure 4: Thin section analysis of the Keshen Block. (a) Semifilled tectonic fracture (Keshen 207 well: 6998.09 m). (b) Semifilled tectonic fracture (Keshen 207 well: 6998.56 m). (c) Microfracture (0.01-0.05 mm) (Keshen 202 well: 6797.55 m). (d) Microfracture (0.01 mm) (Keshen 202 well: 6797.82 m).

matrix is small, fractures and microfractures are developed, and the pore throat with a relatively high permeability and fractures/microfractures is the main reservoir seepage channel, which is the research focus of damage control technology. The high formation pressure coefficient objectively requires a high suspension stability of the drilling fluid, especially for OBDF; when the high density suspension stability is relatively poor, any safe usage of OBDF is difficult. The formation temperature is high, which requires a high-temperature stability for the drilling fluid; the requirements of high-temperature stability and suspension of the drilling fluid are thus objectively improved, but recreating these conditions for OBDF is difficult. Formation water has a high salinity, so the use of low-salinity drilling fluids must be controlled.

Based on the analysis of the properties of OBDF and the characteristics of fractured tight sandstone gas reservoirs, OBDF is mainly affected by three aspects: its own natural conditions, the interaction between OBDF and rocks, and the nature of OBDF at the contact surface [31]. The most obvious change in the properties of OBDF is its rheological change; rock actions are mainly divided into physical and chemical actions and the coupling effect; the properties of OBDF at the contact surface are mainly a series of fluid characteristic changes after the OBDF contact with rocks and formation fluids.

Based on the analysis of the properties of OBDF and the characteristics of fractured tight sandstone gas reservoirs, OBDF is mainly affected by three aspects: the nature of OBDF themselves, the interaction between OBDF and rocks, and the nature of OBDF at the contact surface [31]. The most obvious change in the properties of OBDF is the rheological change of OBDF; rock actions are mainly divided into physical and chemical actions and the coupling effect; the properties of OBDF at the contact surface are mainly a series of fluid characteristic changes after OBDF contact with rocks and formation fluids.

4. Multiphase Fluid Characteristics of Seepage Channels

The multiphase fluid characteristics in OBDF are mainly embodied in the flow characteristics of different types of fluids with a mixed flow [32]. The fluid includes the OBDF and fluid in the formation. OBDF mainly consists of oil and brine, and the formation fluid mainly includes formation water, crude oil, and gas.

Before OBDF intrudes into the reservoir, oil, gas, and water in the pore throat and microfractures are in a relative equilibrium state and there is generally no interference effect between them. However, when OBDF intrudes into the reservoir, the oil and water phases mix with the fluid in the formation to form a multiphase distribution state of oil, gas, and water (Figure 6). Seepage characteristics will change dramatically with the multiphase flow. Different mixing states may reach different forms that will be directly or indirectly adsorbed or attached to the inside of the seepage channel or

Table 4: Experimental results of dynamic damage (kerosene displacement).

Core	Number	Permeability before damage ($10^{-3}\ \mu m^2$)	Permeability after damage ($10^{-3}\ \mu m^2$)	Fluid loss (mL)	Permeability recovery rate (%)
Natural fractured core	3	2.3988	0.6875	0.4	28.66
	4	3.0395	0.9854	0.4	32.42
Artificial fractured core	6	8.4752	4.5238	0.9	53.38
	7	10.4584	3.6846	0.7	35.23

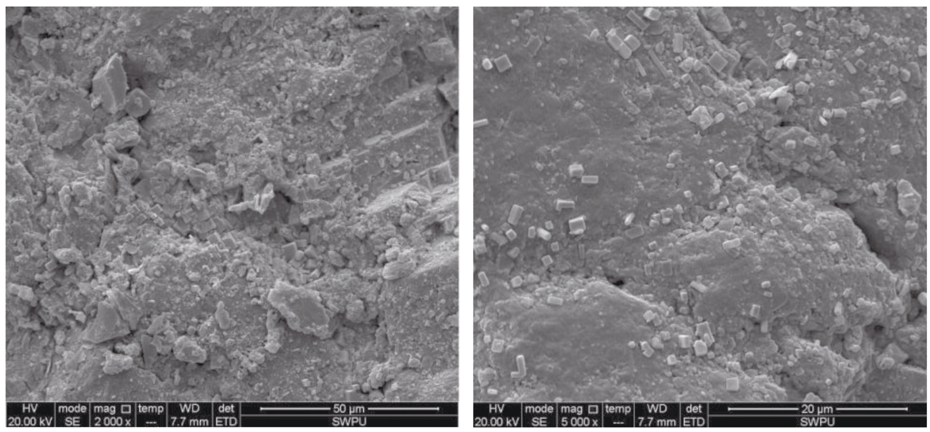

Figure 5: Rock surface morphology after the dynamic damage test.

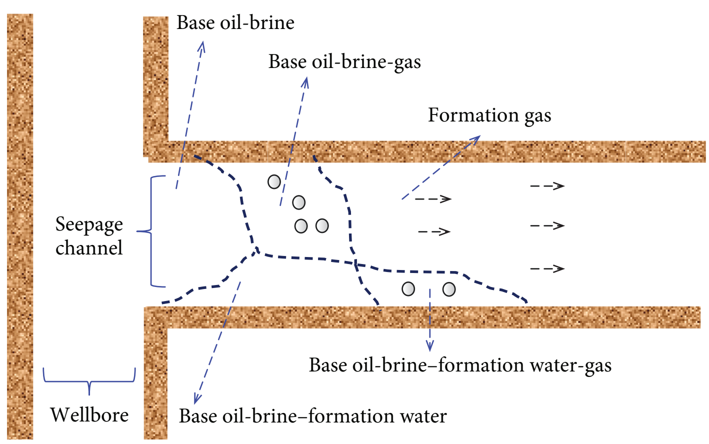

Figure 6: Distribution of oil-gas-water after OBDF invasion (the dotted lines are fracture walls from different zones, and the text indicates the liquid mixing state in different zones; this zoning is an idealized figure for more clearly described multiphase fluids, and the actual fluids are more complex).

they may form a multiphase seepage zone; all of these forms will cause reservoir damage.

The existing space corresponding to the existence of the multiphase fluid is also related to the magnitude of the effect of the multiphase fluid. Most existing studies have found that the main seepage channel of the fractured gas reservoir itself is a fracture itself, while the matrix pore throat showed a relatively small role in the storage and seepage. However, according to the research and engineering practices of the Sichuan Basin in China, the matrix porosity also plays an important role. For fractured tight sandstone gas reservoirs, the existing research and corresponding reservoir protection measures are mainly aimed at fractures. In most cases, the influence of the matrix pore damage is ignored. Taking the fractured tight sandstone gas reservoir of the Keshen Block in China Tarim Oilfield as an example, the fracture is the main seepage channel that can be observed and the matrix pore permeability is less than $0.03 \times 10^{-3}\ \mu m^2$, although the partial permeability is approximately $1.0 \times 10^{-3}\ \mu m^2$. Many studies have shown that a larger pore throat and some ultrafine pore throats connect fractures to ensure continuity in the seepage channel. Therefore, the characteristics of multiphase fluids in pores and fractures must be evaluated.

Most of the existing studies posit that the main seepage channel of fractured gas reservoirs is a fracture, and matrix pores play a relatively small role in storage and seepage.

Table 5: Rheological test of oil base drilling fluid in its original state.

Shear rate (S^{-1})	Viscosity (mPa·s) 40°C	50°C	60°C	70°C	80°C	90°C
1021.38	38.87	36.72	32.51	28.88	25.75	23.20
510.69	47.97	45.43	39.16	33.88	30.55	27.41
340.46	60.80	57.57	50.23	43.18	37.89	31.13
170.23	82.24	77.54	67.56	57.57	51.70	41.71
10.214	597.23	538.49	509.12	421.00	381.84	323.09
5.107	1507.76	1076.97	979.07	861.58	783.25	685.35
1.702	3289.66	2995.94	2643.48	2408.50	2173.53	1879.81
0.851	6344.35	5991.88	5051.98	4464.54	4112.08	3642.12

However, according to research and engineering practices in Sichuan Basin, China, matrix pores also play an important role. For fractured tight sandstone gas reservoirs, existing research and corresponding reservoir protection measures mainly focus on fractures and in most cases neglect the impact of matrix pore damage. Taking the fractured tight sandstone gas reservoir in the Keshen Block of Tarim Oilfield as an example, the fracture is the main observable seepage channel. The matrix pore permeability is less than $0.03 \times 10^{-3}\ \mu m^2$, but there are large pore throats with partial permeability of approximately $1.0 \times 10^{-3}\ \mu m^2$. Research shows that larger pore throats and some ultrafine pore throats play a role in communicating fractures and ensuring the continuity of seepage channels. Therefore, the characteristics of multiphase fluids in pores and fractures must be evaluated.

According to the possible forms of fluid occurring after OBDF intrusion, different mixing states are classified and the possible physical and chemical changes for each form are studied. On this basis, the change trend of the seepage channel size caused by different mixing states is predicted and the possible damage caused by the fluid is judged. OBDF has several characteristics including that the oil phase is a continuous phase, the water phase is a dispersed phase that is relatively small, and the fluid distribution is divided into the following types: base oil-brine, base oil-formation water, base oil-formation gas, base oil-brine-formation gas, base oil-crude oil, base oil-brine-formation water, base oil-brine-formation oil, base oil-brine-formation oil-formation gas, and base oil-brine-formation water-formation oil-formation gas. For other forms of distribution, due to the relatively small amounts of brine and crude oil, they may be referred to in the above listing without further consideration.

4.1. Base Oil-Brine. The distribution state of the base oil-brine form is the flow of the OBDF itself in the fractures and is the most common flow state in the seepage channel. When the OBDF flow is in the original state, the flow in the fractured sandstone reservoir may divide into a fractured flow and porous flow; these two flow types are influenced by the OBDF properties, and Table 5 shows the rheological test results of OBDF in the original state that was used in the oilfield.

The fracture flow is mainly the flow of OBDF within the fractures. The flow pattern shows the characteristics of plastic/pseudoplastic fluids. The main reason for this plastic/pseudoplastic flow pattern is the interactions between the oil phase, organic soil phase, granular material, and other additives. Organic soil is a modified bentonite. When it enters the OBDF, the internal interval of the organic soil enlarges, forming a thinner sheet structure and connecting with each other and forming a spatial network structure and exhibiting plastic fluid characteristics.

Flows in fractures are often subject to large flow pressure differences, which reduces the flocculation state of organic soil and particles in OBDF. With this kind of flow, the OBDF flows faster and the fluid contact space is mainly the wall of the seepage channel. The main reason for reducing the size of the seepage channel is the adsorption and adhesion of the wall based on the wettability of the fluid surface. Without considering the attachment of the oil-loving particles, the adsorption capacity of the base oil-brine two-phase fluid on the fracture surface is very limited, and there is not much of an OBDF effect.

For porous structures, the pore throat of the fractured tight sandstone gas reservoir is small and the capillary force is the main reason [33, 34]. OBDF flow comes from fluid dynamics and capillary force inhalation, showing a gradual decline in flow efficiency, and stops flowing after forming a certain length of a liquid retention zone.

4.2. Base Oil-Brine-Formation Gas. The base oil-brine-formation gas form is the distribution of oil-gas-water formed by gas invasion after OBDF intrudes into the reservoir, and it is also a universal state of a fractured tight sandstone gas reservoir. In essence, this three-phase state presents the flow pattern of the OBDF after being invaded by the gas; there is a difference between the fracture and the pore flow for the reservoir, and there is a certain difference of the mechanism between this pattern and the original OBDF flow. After the gas invasion, OBDF will be filled by bubbles of different sizes. An oil-gas interface and a small amount of gas-water interface state will be formed in the OBDF. The oil-water interface can be weakened to a certain extent. OBDF will change in rheological stability to a certain extent and will also affect suspension efficiency. The weakening of the interface will be strengthened with the increase of gas intrusion, which may eventually aggravate the damage.

In this area, the OBDF flow rate will decrease, forming a certain length of a three-phase mixing zone; the distribution

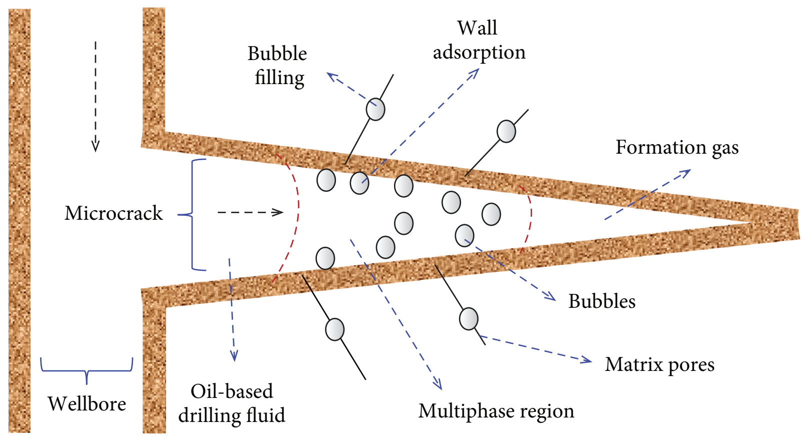

Figure 7: Three-phase seepage of oil-gas-water.

Table 6: Relationship between shear rate and shear stress of OBDF (50°C).

Shear rate (S^{-1})	Shear stress (Pa)					
	80/20	70/30	60/40	50/50	40/60	30/70
1021.38	7.83	14.03	17.94	102.60	151.20	328.50
510.69	4.84	8.79	12.21	70.40	100.80	253.60
340.46	4.09	6.70	9.94	55.40	79.20	191.40
170.23	2.76	4.72	7.45	40.50	58.40	153.30
10.214	1.15	2.11	3.51	21.30	29.30	74.70
5.107	1.15	2.09	3.38	20.50	28.00	69.50
1.702	1.06	1.75	2.80	16.60	22.10	57.60
0.851	0.96	1.61	2.30	12.20	16.40	39.80

of bubbles will increase along with the wellbore in the formation direction, and the three-phase fluid will adsorb on the fracture wall to varying degrees, but this adsorption is not stable. With the continuous invasion of OBDF, the gas phase will be reduced, as shown in Figure 7. For the porous region, the three-phase flow enters the pore via the hydrodynamic force and capillary force. Because of its high deformability and different size distributions, bubbles fill and plug the pore, which to some extent reduces the invasion of the other two phases and indirectly reduces the damage caused by the oil-water phases [35]. The filling effect of the bubbles in the pore also exists in the microfractures.

4.3. Base Oil-Brine-Formation Water. Generally, for fractured tight sandstone gas reservoirs, the water saturation of the formation is relatively small, but during the OBDF invasion, this formation water enters into the OBDF, which will have a greater impact on the performance of OBDF in the microregion. Generally, brine and formation water differ greatly in basic properties such as salinity and pH and cannot be directly mixed into one phase. Base oil-brine-formation water exists in a pseudothree-phase state. Taking OBDF as an example, a formation water intrusion was simulated and its rheological properties and flow patterns were evaluated for different oil-water ratios at 50°C (Table 6).

The evaluation shows that the change in the oil-water ratio will greatly change the flow state of OBDF. When formation water enters the OBDF, it will break the oil-water two-phase equilibrium of OBDF, change the nature of the oil-water interface, and even destabilize the emulsion when the water intrusion becomes too large.

In the area where the OBDF contacts the formation, a transition zone will be formed. Fractures and porous reservoirs in this area will be greatly affected, and serious damage may occur. For fractured reservoirs, when the formation water content is low, the damage mainly comes from wall adsorption; when the formation water content is large, the oil-water interface of OBDF is destroyed, the wettability of the wall shows diversity, and the mixed adhesion of the water phase and oil phase on the fracture wall is the main state, which will also cause regional damage.

For the pore structure, the water phase is the main filling phase in the pore, and the OBDF will continue to displace after invasion. From the microscopic phenomena of OBDF flowing in the pore, this displacement is not serious but is more likely to change the wall's wettability. With the capillary force, the original hydrophilic wetting wall does not necessarily show a wettability change, so the capillary force acting on OBDF in the pore should be considered instead.

4.4. Base Oil-Brine-Formation Water-Formation Gas. For fractured tight sandstone gas reservoirs, this oil-gas-water distribution state of the base oil-brine-formation water-gas form should be common. The multiphase existing area

Table 7: Stress sensitivity of fractured tight sandstone gas reservoir in the study area.

Core	Core number	Permeability (10^{-3} μm^2) 2.5 MPa	20 MPa	2.5 MPa	Damage rate of permeability (%)
Matrix core	111	0.0249	0.0096	0.0115	25.84
	129	0.0106	0.0036	0.0083	21.80
Fracture core	115	27.4762	1.4855	3.6195	86.83
	119	12.3547	0.5964	1.1564	90.64

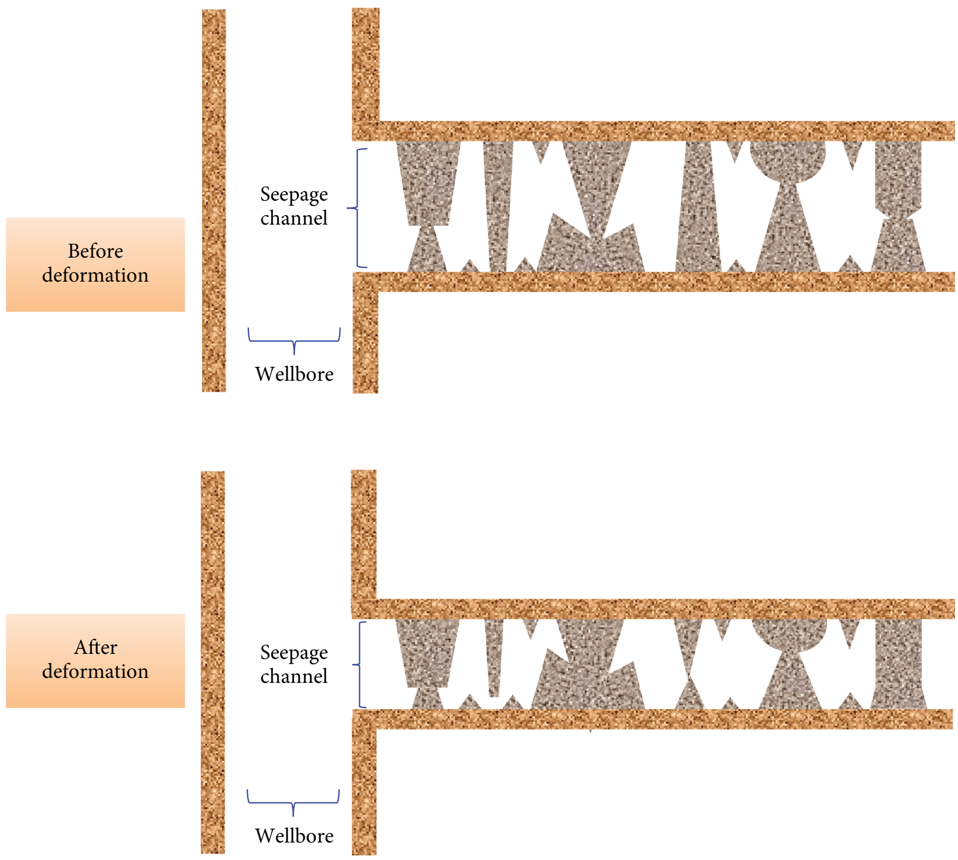

Figure 8: Comparison of the changes of asperities before and after stress.

formed by OBDF entering the reservoir is unclear, as shown in Figure 5. The oil-water distribution state of the base oil-brine-formation water-gas form is also the most common multiphase existing state. In this state, from the fluid level, the change characteristics of the fracture wall and pore structure use the mixture of the first three states and there are many situations in which this may occur.

For the base oil-brine-formation water-gas distribution area, the formation water and oil-based drilling will fill some bubbles in the contact area between the OBDF and formation water. When the formation water saturation is high, the OBDF will move forward after contacting with the formation water. Based on the hydrophilic and wetting properties of the surfaces of most minerals, the mixed fluid will aggravate the attachment on the fracture wall and this kind of attachment is more likely to release bubbles after the OBDF intrudes in large quantities, which are not easy to wash away.

For the porous structure, the capillary force still plays a dominant role. Increased water content will increase the absorption power of the water-wet rock, resulting in a more serious capillary force. For formations with a low water saturation, the mechanism is similar to the high saturation mechanism. Bubbles also play a role in blocking microfractures and pores.

4.5. Base Oil-Brine-Formation Oil and Other Derived States. Base oil-brine-formation oil and other derivative states are not listed in Figure 6. This is because for fractured tight sandstone gas reservoirs, the formation's oil content is miniscule, while the OBDF itself takes the oil phase as a continuous phase, and thus the small amount of formation oil with different properties will not change greatly after invasion. Formation oil itself contains more asphaltene, gum, and lipophilic particles, but when it enters OBDF, it fuses with the

Table 8: Evaluation of water-phase alkali sensitivity.

Core number	Permeability at different pH values (10^{-3} μm^2) 7.0	9.0	11.0	13.0	Permeability recovery rate (%)	Damage degree
125	44.03	30.31	13.87	8.92	20.25	Serious
133	65.30	51.31	31.29	6.85	10.49	Serious

asphaltene, gum, and lipophilic particles existing in OBDF to form a new OBDF. This kind of OBDF has very little difference from the original fluid with regard to the surface properties for fractures and pore throats.

5. Effect of Rock Physics and Chemical Changes

The change in rock strength here mainly refers to the change of mechanical characteristics of rocks on the wall of the seepage passage after OBDF intrusion, and it is also the mechanical expression of the coupling effect of fluids, rock physics, and chemistry.

5.1. Physical Effect. In the drilling operations of deep and ultradeep wells, the overbalanced drilling method is often used. The fluid column pressure applied to the formation by drilling fluid is greater than the formation pressure. This pressure difference is the main cause of drilling fluid intrusion into the reservoir, and it also affects the mechanical properties of surrounding rock to a certain extent.

For the fractured tight sandstone gas reservoirs, the matrix rock itself is more compact and the degree of mechanical impact will be relatively small; however, because of the objective existence of fractures, the pressure applied by OBDF will act on the fractures and the pressure fluctuations acted on the fractures in the formation will have a greater change. Taking the fractured tight sandstone gas reservoir in the Keshen Block as an example, the stress sensitivity with the variable pressure in the standard experimental procedure (standards of the petroleum and natural gas industry of China: SY/T 5358-2010 formation damage evaluation by the flow test) was evaluated (Table 7). The sensitivity of the fracture to the external pressure is stronger than the matrix sensitivity where the dry core is not doped with other factors.

The main reason for such a great change in the gas seepage ability in fractures is that the wall properties of fractures are greatly changed. For the seepage channel, the fractures on the wall are rough and inhomogeneous, showing different sizes of asperities, and the distribution of the asperities vary widely in the two fracture walls. When subjected to external force, the asperities that originally support each other appear to have an elastic deformation by squeezing. When the stress exceeds a certain degree, the asperities will cause plastic deformation, which is the main reason that the permeability decreased rapidly at the initial state and changed slowly during late period; the change in asperities is irreversible to a large extent.

When OBDF exists, the particulate material deposits on the wall of the fractures, which does not react chemically with the rock. The particulate matter in the OBDF mainly includes weighting agents, cuttings, organic soils and some reservoir protection materials. This particulate matter adsorbs and adheres between the asperity bodies to form a layer of granule cover. This has a large impact on the mechanical properties of the rock when subjected to external forces. When the asperity is deformed by force, it is prone to collapse and form a new asperity structure (Figure 8).

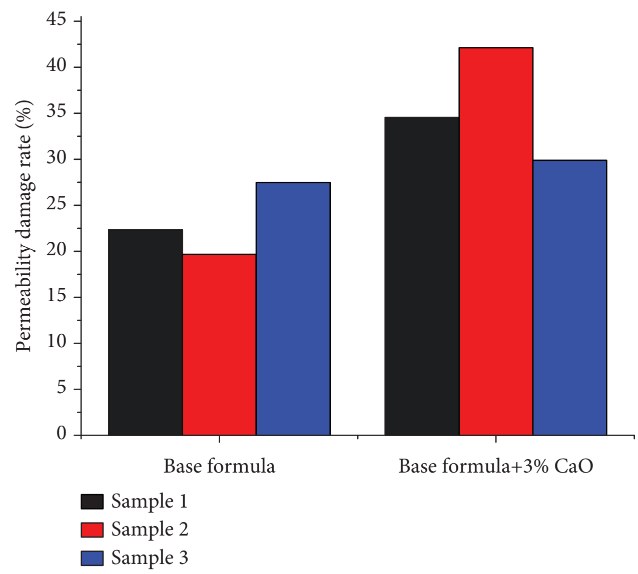

Figure 9: Evaluation of alkaline sensitivity of OBDF.

In some cases, after the OBDF invasion, in addition to the force that is directly applied to the borehole by OBDF, the physical effects also include the filling effect of solid particles in the zone between asperities that indirectly affect the fracture strength. However, parts of solid particles still attach onto the asperities of the fracture surface when the pressure difference drops; the seepage channels become small, which will cause a large change in the permeability. In this case, explaining the effect of physical action on the seepage capacity is inappropriate. Therefore, there is a need for a comprehensive evaluation of the capacity's mechanical effects with fluid participation.

After the invasion of OBDF, the capillary force in the microfractures and capillaries will cause the oil phase to enter, and this existence is not easily removed. For fractured tight sandstone gas reservoirs, the initial water saturation is lower than the irreducible water saturation in most conditions. When the OBDF intrudes, it will cause greater oil trap damage, which is affected by the changes of the invasion amount, formation pressure and saturation.

5.2. Chemical Effect. The chemical action of the rock strength change mainly comes from the action of OBDF on the well perimeter and the wall of the seepage passage. Unlike WBDFs, the chemical action of OBDF on rocks mainly concentrates on alkalinity, and the wettability of rock surface may also have a weak impact [36]. When the oil-water ratio is small, a large amount of the water phase can also cause other forms of damage.

The chemical effect of rock strength change is mainly due to the effect of OBDF on the wellbore and the wall of the seepage channel. Different from water based drilling

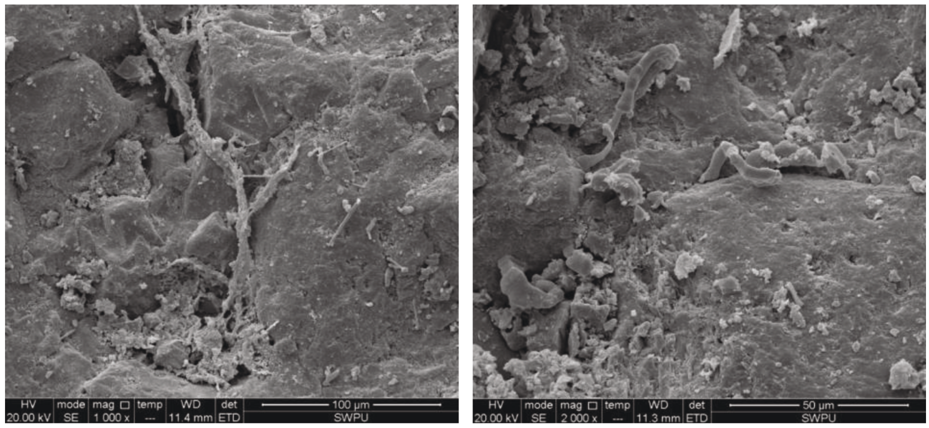

Figure 10: Adsorption of macromolecule treating agents after soaking in OBDF.

fluids, the chemical effects of OBDF on rock are mainly concentrated in alkaline action, and wettability of rock surface may also has a weak impact [36]. At the low oil-water ratio, a large number of water phase will also cause other forms of damage.

The alkaline effect of the OBDF mainly presents as the liquid with a high pH value having an alkali effect on the rock, causing structural changes to the alkali-sensitive minerals in the rock. With the erosion of OBDF, the alkaline minerals fall off, migrate, precipitate or form new colloidal substances that affect the seepage capacity of the seepage channel. Taking the Keshen Block as an example, a water-phase alkali sensitivity evaluation was carried out and the experimental method is based on the standard of oil and gas industry of China "SY/T 5358-2010: formation damage evaluation by flow test," and the results is shown in Table 8.

Since the pH value in the OBDF is mainly the pH value of the water phase, the alkaline treatment agent mainly faces the dispersed water phase in OBDF, while maintaining the stability of the water phase requires the action of emulsifiers. Based on this situation, the basic effects of OBDF can only be evaluated based on the following formula: base oil + 1.5% primary emulsifier + 2.1% auxiliary emulsifier + 20% $CaCl_2$ brine. This is also the reason for the separated water-base sensitivity evaluation. A 3% CaO alkaline treatment agent was added to the base formula to evaluate the damage to the cores by the base formula before and after adding the calcium oxide. The result is shown in Figure 9.

The experimental results show that with the changing formation water pH, the alkali sensitivity damage is serious in the Kenshen Block. The experiment shows that the alkaline single effect severely damages the reservoir and the damage exists objectively in both the water base drilling fluid and the oil base drilling fluid. The alkaline treatment agent in OBDF caused a certain extent of damage, but the damage degree was not serious when compared with the alkaline single effect. The main reason for the decrease in the alkali-sensitive effect of OBDF is that the emulsion itself is attached to the surface of the rock. At the same time, the water phase of the OBDF itself is the dispersed phase and the content is low, which indirectly causes the alkali sensitivity damage degree to be low.

A previous study has shown that the elastic deformation of rock soaked in alkaline liquid is decreased and plastic deformation occurs earlier after soaking in alkaline liquid [37]. This is due to the high pH fluid immersion; the asperities of the fracture wall surface and other structures will be destroyed, and the pore structures of wall interior are damaged. These results show that the rock support capacity decreased, and large changes appeared in the seepage ability.

However, as mentioned previously, particles will deposit, accumulate, and adsorb between the asperity spaces on the wall of the fractures and indirectly affect the mechanical properties of the rock. The processes of accumulation and adhesion are physical changes, but when the wettability of the rock wall changes, the particles that have the same wettability as the wall will accumulate and adsorb more easily on the wall. OBDF contains a wetting agent that can change the wettability of the seepage channel wall from hydrophilic to lipophilic. Then, the rock can adsorb the accumulation of the lipophilic substance in the OBDF on the surface, which influences the strength change of the rock to a certain extent. The adsorption of the treatment agent on the rock also includes the polymer or macromolecule treatment agents in the OBDF [37] (Figure 10), which adsorbs and retains at the pore or fracture wall and blocks the seepage channel with its macromolecular size, resulting in reservoir damage.

When the oil-water ratio is relatively low, the water molecules combine to form larger water particles and the oil-water interface weakens. When the water phase is adsorbed on the wall of the seepage channel and if the change of the wettability of the wall is not stable, the water will come into contact with the rock directly and enter into the reservoir to form water phase damage. Taking the tight sandstone gas reservoir in the Keshen Block as an example, rocks will generate strong water sensitivity, salt sensitivity, and alkali sensitivity damage, which will change the rock properties to a certain extent; the damage was affected by the water content of OBDF.

The change in rock strength is caused by the change in the effective stress of the rock. This change is composed of two parts: body deformation and structural deformation. The body deformation of the rock is caused by the deformation of rock skeleton particles, and the structural deformation is caused by the change of the arrangement mode of skeleton particles. For the fractured tight sandstone gas reservoir example, the reservoir change is mainly a body deformation, which is reversible, and the stress sensitivity of the matrix can explain certain problems (Table 4). For fractures under stress, the asperities produce body deformation, the destroyed fracture surface will produce a new asperity structure, the arrangement mode of asperity particles changes, the rock pore and skeleton volumes are changed, and the stress sensitivity is increased.

For fractured tight sandstone gas reservoirs, the changes in rock strength reflect the change characteristics of fractures, while our previous study focused more on the effect of strength changes on fractures in a closed state. In drilling engineering, the expansion of fractures is the most important factor affecting the flow of OBDF in fractured reservoirs. The main cause of fracture propagation comes from the drilling pressure difference between the wellbore and the formation through OBDF. The fracture tip in the formation is easy to form splitting with differential pressure, which is close to the principle of hydraulic splitting. However, the splitting effect of OBDF is affected by different factors, including the characteristics of the rock itself, the interfacial tension properties of OBDF, the geometric characteristics of fractures, and the drilling pressure. Concurrently, the pressure fluctuation caused during the drilling process will also affect the expansion of the fractures. Taking the tight sandstone gas reservoir in the Keshen Block as an example, in our previous study, the density and opening degree of fractures in several wells of the block are analyzed and summarized. The distribution of the fracture width of the reservoir is wide, and the fracture width changes with the drilling fluid invasion. The large fracture width also causes the loss of drilling fluid and other damages.

6. Rheological Stability of OBDF

Rheology is the basic performance of the drilling fluid, which reflects its flow and deformation properties. The commonly used parameters include apparent viscosity, plastic viscosity, shear force, and so on. OBDF is more susceptible to effects from external factors than WBDF, including temperature, pressure, oil content, particle size, particle concentration, and oil-water interface energy. For practical engineering, rheological properties, suspension problems, and the high-temperature stability of OBDF are the main technical bottlenecks that limit the application of OBDF. To solve these problems including suspension, the rheological performance must be adjusted. If the OBDF is relatively stable at a certain range, many OBDF problems can be solved.

According to the deformation properties, most of the oil-based drilling fluid is plastic or pseudoplastic fluid and the rheological model can also be referred to as a Bingham model or power law model. The OBDF flow is more inclined to be a pseudoplastic fluid in theory, which should be verified in future experiments.

OBDF has obvious rheological instability, while the WBDF instability is relatively small, which is mainly due to the difference between the oil and water properties. Generally, even at a very small temperature range, the viscosity of

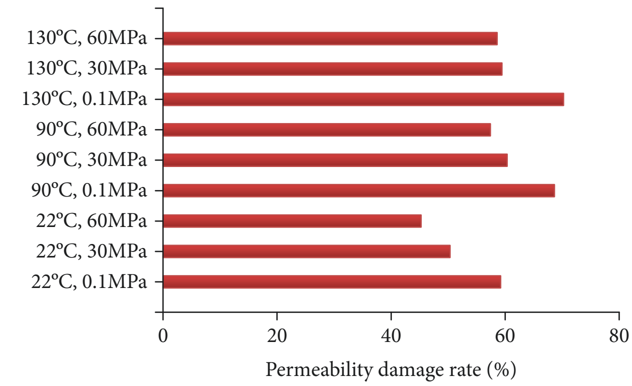

Figure 11: Evaluation of damage experiment at high-temperature and high-pressure conditions.

the oil phase decreases rapidly with the increase of temperature, while the formation temperature is more than 100°C. In the continuous phase, the oil phase is a carrier for a series of treatment agents such as weighting materials and organic soils. The high temperature and high pressure quickly weaken the rheological properties (Figure 11), resulting in an insufficient OBDF amount for suspending excessive particulate matter. After entering the reservoir, the OBDF will settle quickly and cause a series of damages.

Controlling the water phase activity is beneficial to borehole stability. Therefore, the commonly used OBDF is usually in a water-in-oil emulsion and the oil phase and the oil-water interface contents are formed by corresponding treatment agents that can easily influence the stability of OBDF. When the amount of water is large or the water intrusion amount is large, the oil-water interface will decrease, which leads to instability in the OBDF and even in the oil-water separation. In this case, when the OBDF enters the reservoir, the actions of the solid phase and the liquid phase will cause serious damage to the reservoir.

In summary, the stability of rheological properties determines the stability of the OBDF and determines whether the OBDF can play a role in the rapid sealing of a reservoir with particles. The study of the rheological properties of OBDF requires further research through OBDF applications.

7. Research Direction of OBDF Damage Control

7.1. The Key Problem of Damage Control. From the point of view of the formation mechanism of OBDF damage, OBDF causes damage to fractured tight sandstone gas reservoirs due to its rheological properties, changes in rock properties, and multiphase flow characteristics. However, based on the formation mechanism, the damage control process must provide an accurate description of the damage characteristics of OBDF to the fractured tight sandstone gas reservoir and how to achieve an accurate plugging of the reservoir [10, 38–40].

Based on this study's research, the potential damage factors involved are classified into four main types: fluid compatibility type, particle combination type, wall morphology change type, and reservoir property type. These types also include a variety of subdivided damage factors, which are specifically classified as follows:

(1) *Fluid Compatibility*. Fluid compatibility mainly refers to the compatibility between the OBDF and rock or fluid; the OBDF damage caused by compatibility mainly includes (1) OBDF and rock are not compatible: alkaline damage and wettability change, and (2) OBDF and fluid are not compatible: emulsion plugging.

(2) *Particle Combination Damage*. Particles include solid phase and nonsolid phase types. Solid phase particles include weighting materials, cuttings, organic soil, reservoir protection materials, and so on [41]. Nonsolid particles include asphaltene, polymer treatment agents, and other nonsolid particles. The main damages include the following: particle migration, solid particle plugging, and chemical adsorption.

(3) *Formation Properties*. The damage to formation properties is mainly the damage caused by the properties of the fractured tight sandstone gas reservoir, which mainly includes oil phase trapping, pressure and temperature characteristics, wetting changes, oil phase adsorption, stress sensitivity and particle sedimentation, gas or water intrusions, and so on.

7.2. Research Direction of Damage Control. The main purpose of reservoir protection theory and technology is to protect a reservoir from damage or be subjected to less damage from drilling fluids. The methods to achieve this goal are mainly derived from two aspects: reducing invasion and fast plugging. However, from the technical and engineering points of view, both are aimed at reducing invasion as the ultimate goal and rapid plugging is the action needed to reduce invasion. The current OBDF damage control system is faced with technical problems, including several aspects: the downhole properties of OBDF are different, the geological characteristics of fractured gas reservoirs are complex, and few new technologies and new materials that are suitable for the damage control of OBDF exist.

Thus, the main goal should be to reduce the fluid invasion into the reservoir. The fluid invasion includes two sources: from solid particles and from the liquid phase. Although both types cause a great deal of damage, there are obvious differences between the microscopic damage mechanism and the methods of removing damage. From this viewpoint, the type and size distribution of solid particles and fluid types should be the important factors that affect the reservoir protection. Rapid plugging is used to overbalance drilling or microbalanced drilling; new technology and new materials are needed to more effectively execute rapid plugging.

Determining how to achieve damage control for OBDF, simply speaking, mainly includes fracture analysis, OBDF performance regulation and maintenance, optimizations of engineering operations, and introductions of new materials and ideas. In combining the formation mechanism and potential damage factors of OBDF, based on the characteristics of fractured tight sandstone gas reservoirs, the technology selection, material selection, system construction, and so on should be considered to form a fast and efficient damage control scheme for OBDF.

8. Conclusions

(1) Both OBDF and WBDF have formation damage, but there are many differences between them, which include emulsion plugging, wettability change, oil phase trapping, oil phase sensitivity, and so on. When OBDF enters into a formation, the change of OBDF properties, multiphase characteristics of seepage channels, and the physical and chemical properties of the rocks are the main reasons for the OBDF damage to the fractured tight sandstone gas reservoir

(2) Base oil-brine and base oil-brine-formation gas are the main fluid distributions in seepage channels, while other forms of distribution are of little importance due to the relatively small amounts of brine and crude oil present. However, many other forms emerge in a certain area, the distribution will also cause serious damage. Compared with the water base drilling fluid, the effects of physical and chemical change are relatively low, but the increase in fracture lubricity, emulsification effect, and oil adsorption can also cause reservoir damage that is distinct from damaged caused by water-based drilling fluid. The special rheological properties of OBDF can lead to suspension stability and emulsion stability in high-temperature and high-pressure conditions, resulting in great differences of wellbore fluid properties that bring a series of damages

(3) The key problems for damage control of OBDF are an accurate description of the damage characteristics of OBDF on fractured tight sandstone gas reservoirs and achieving an accurate plugging of the reservoir; the main control idea is to reduce the invasion of OBDF, and new materials and technologies are needed to achieve rapid plugging

Data Availability

The data of the study have been attached to the article and supplementary material; all data included in this study are available upon request by contact with the corresponding author.

Conflicts of Interest

The authors declare that they have no conflicts of interest.

Acknowledgments

This work was supported by National Natural Science Foundation of China (Grant No. 51804044), Open Fund of State Key Laboratory of Oil and Gas Reservoir Geology and Exploitation (Southwest Petroleum University) (Grant No. PLN201715), and National Science and Technology Major Project of China (No. 2016ZX05060-015).

References

[1] H. B. Liu, Y. F. Meng, G. Li, and L. Q. Xu, "Impact of drilling fluid system on stability of shale formation and borehole," *Oxidation Communications*, vol. 38, no. 4A, pp. 2273–2278, 2015.

[2] M. I. Abdou, *Formation Damage Caused by Oil-Well Drilling Fluids*, Lulu Press, Inc., 2014.

[3] S. Shivhare and E. Kuru, "A study of the pore-blocking ability and formation damage characteristics of oil-based colloidal gas aphron drilling fluids," *Journal of Petroleum Science & Engineering*, vol. 122, pp. 257–265, 2014.

[4] Y. Cui, S. Guan, L. Li, F. Shu, and X. Xiang, "Evaluation Research on Reservoir Damage of Oil-Based Drilling Fluid," *Drilling Fluid & Completion Fluid*, vol. 29, no. 3, 2012.

[5] N. K. Korsakova and V. I. Pen'kovskii, "Phase distribution and intrapore salt exchange during drilling mud invasion of an oil- and gas-bearing formation," *Fluid Dynamics*, vol. 44, no. 2, pp. 270–277, 2009.

[6] K. Rong, K. E. Xiangui, and X. U. Shengjiang, "New evaluation method for wettability reversion caused by oil-based drilling fluid," *Drilling Fluid & Completion Fluid*, vol. 31, no. 1, 201454-56+99.

[7] L. Skalli, J. S. Buckley, Y. Zhang, and N. R. Morrow, "Surface and core wetting effects of surfactants in oil-based drilling fluids," *Journal of Petroleum Science & Engineering*, vol. 52, no. 1-4, pp. 253–260, 2006.

[8] J. Yan and M. M. Sharma, "Wettability alteration and restoration for cores contaminated with oil-based muds," *Journal of Petroleum Science & Engineering*, vol. 2, no. 1, pp. 63–76, 1989.

[9] G. Murickan, H. Bahrami, R. Rezaee, A. Saeedi, and T. Mitchel, "Using relative permeability curves to evaluate phase trapping damage caused by water- and oil-based drilling fluids in tight-gas reservoirs," *The APPEA Journal*, vol. 52, no. 1, p. 595, 2012.

[10] M. Lei, W.'a. Huang, N. Li et al., "The damage mechanism of oil-based drilling fluid for tight sandstone gas reservoir and its optimization," *Journal of Petroleum Science & Engineering*, vol. 158, pp. 616–625, 2017.

[11] X. Huang, K. Lv, J. Sun et al., "Enhancement of thermal stability of drilling fluid using laponite nanoparticles under extreme temperature conditions," *Materials Letters*, vol. 248, pp. 146–149, 2019.

[12] F. Civan, *Reservoir Formation Damage*, Gulf Professional Pu, 2015.

[13] S. Salehi and R. Nygaard, "Full fluid–solid cohesive finite-element model to simulate near wellbore fractures," *Journal of Energy Resources Technology*, vol. 137, no. 1, article 012903, 2015.

[14] L. I. Yiming, H. E. Minxia, W. Xia, and L. I. Xiangfang, "Study on swelling and migration laws of dissolved gas during gas kick of oil-based drilling fluid in horizontal well," *Journal of Safety Science & Technology*, vol. 12, pp. 44–49, 2016.

[15] M. B. Carrier and G. H. Meeten, *Electrical Treatment for Oil Based Drilling or Completion Fluids*, U.S. Patent, 2011.

[16] H. Bahrami, R. Rezaee, A. Saeedi, and G. Murikhan, "Phase trapping damage in use of water-based and oil-based drilling fluids in tight gas reservoirs," *SPE Asia Pacific Oil and Gas Conference and Exhibition*, 2012, Perth, Australia, 22-24 October, 2012.

[17] M. Meng, Z. Zamanipour, S. Miska, M. Yu, and E. M. Ozbayoglu, "Dynamic wellbore stability analysis under tripping operations," *Rock Mechanics and Rock Engineering*, 2019.

[18] C. P. Ezeakacha, S. Salehi, and A. Hayatdavoudi, "Experimental study of drilling fluid's filtration and mud cake evolution in sandstone formations," *Journal of Energy Resources Technology*, vol. 139, no. 2, article 022912, 2017.

[19] M. Meng, Z. Qiu, R. Zhong, Z. Liu, Y. Liu, and P. Chen, "Adsorption characteristics of supercritical CO_2/CH_4 on different types of coal and a machine learning approach," *Chemical Engineering Journal*, vol. 368, no. 2019, pp. 847–864, 2019.

[20] O. Mahmoud, H. A. Nasr-El-Din, Z. Vryzas, and V. C. Kelessidis, "Nanoparticle-Based Drilling Fluids for Minimizing Formation Damage in HP/HT Applications," *SPE International Conference and Exhibition on Formation Damage Control*, 2016, Lafayette, Louisiana, USA, 24-26 February, 2016.

[21] M. Meng, S. Baldino, S. Z. Miska, and N. Takach, "Wellbore stability in naturally fractured formations featuring dual-porosity/single-permeability and finite radial fluid discharge," *Journal of Petroleum Science and Engineering*, vol. 174, pp. 790–803, 2019.

[22] S.-y. Zhao, J.-n. Yan, Y. Shu, and H.-x. Zhang, "Rheological properties of oil-based drilling fluids at high temperature and high pressure," *Journal of Central South University of Technology*, vol. 15, no. S1, pp. 457–461, 2008.

[23] J. N. Yan, J. L. Monezes, and M. M. Sharma, "Wettability alteration caused by oil-based muds and mud components," *SPE Drilling & Completion*, vol. 8, no. 1, pp. 35–44, 1993.

[24] M. Tsar, H. Bahrami, R. Rezaee et al., "Effect of drilling fluid (water-based vs oil-based) on phase trap damage in tight sand gas reservoirs," *SPE Europec/EAGE Annual Conference*, 2012, Copenhagen, Denmark, 4-7 June, 2012.

[25] J. Erzinger, T. Wiersberg, and M. Zimmer, "Real-time mud gas logging and sampling during drilling," *Geofluids*, vol. 6, no. 3, pp. 225–233, 2006.

[26] H. Wu, P. Chen, X. Fan et al., "Research on Rapid Identification and Evaluation Technology for Gas Formation during Underbalanced Drilling," *Geofluids*, vol. 2017, no. 11, Article ID 2742637, 8 pages, 2017.

[27] M. Meng, Z. Zamanipour, S. Miska, M. Yu, and E. M. Ozbayoglu, "Dynamic stress distribution around the wellbore influenced by surge/swab pressure," *Journal of Petroleum Science and Engineering*, vol. 172, pp. 1077–1091, 2019.

[28] A. Amann-Hildenbrand, J. P. Dietrichs, and B. M. Krooss, "Effective gas permeability of tight gas sandstones as a function of capillary pressure – a non-steady-state approach," *Geofluids*, vol. 16, no. 3, 383 pages, 2016.

[29] B. W. D. Yardley and J. T. Graham, "The origins of salinity in metamorphic fluids," *Geofluids*, vol. 2, no. 4, p. 256, 2002.

[30] M. A. Dick, T. J. Heinz, C. F. Svoboda, and M. Aston, "Optimizing the selection of bridging particles for reservoir drilling fluids," *SPE International Symposium on Formation Damage Control*, 2000, Lafayette, Louisiana, 23-24 February, 2000.

[31] R. R. Fernandes, D. E. V. Andrade, A. T. Franco, and C. O. R. Negrão, "Influence of pre-shearing on rheometric measurements of an oil-based drilling fluid," *Rheologica Acta*, vol. 56, no. 9, pp. 743–752, 2017.

[32] B. Yin, G. Liu, and X. Li, "Multiphase transient flow model in wellbore annuli during gas kick in deepwater drilling based on oil-based mud," *Applied Mathematical Modelling*, vol. 51, pp. 159–198, 2017.

[33] K. Abaa, M. Thaddeus Ityokumbul, and M. Adewumi, "Effect of Acoustic Stimulation on Aqueous Phase Trapping in Low-Permeability Sandstones," *Journal of Energy Resources Technology*, vol. 139, no. 6, article 062905, 2017.

[34] M. Sedaghatzadeh, K. Shahbazi, M. H. Ghazanfari, and G. Zargar, "The impact of nanoparticles geometry and particle size on formation damage induced by drilling nano-fluid during dynamic filtration," *Journal of Nano Research*, vol. 43, pp. 81–97, 2016.

[35] F. Growcock, A. Khan, and G. Simon, "Application of water-based and oil-based aphrons in drilling fluids," *International Symposium on Oilfield Chemistry*, 2003, Houston, Texas, 5-7 February, 2003.

[36] Y. Kang, B. Yang, L. You, Q. Chen, and Y. Yu, "Damage evaluation of oil-based drill-in fluids to shale reservoirs," *Natural Gas Industry*, vol. 33, no. 12, pp. 99–104, 2013.

[37] A. Saasen, S. Ding, P. A. Amundsen, and K. Tellefsen, "The Shielding Effect of Drilling Fluids on Measurement While Drilling Tool Downhole Compasses—The Effect of Drilling Fluid Composition, Contaminants, and Rheology," *Journal of Energy Resources Technology*, vol. 138, no. 5, article 052907, 2016.

[38] P. Xu, Z. Tao, X. Liu, Z. Yan, and M. Xu, "Damage-control technology of oil-based drilling fluid for Kuqa piedmont structure," *Geosystem Engineering*, vol. 21, no. 1, pp. 1–11, 2017.

[39] J. Zhu, L. You, J. Li et al., "Damage evaluation on oil-based drill-in fluids for ultra-deep fractured tight sandstone gas reservoirs," *Natural Gas Industry B*, vol. 4, no. 4, pp. 249–255, 2017.

[40] P. Xu, M. Xu, Z. Tao, Z. Wang, and T. Huang, "Rheological properties and damage-control mechanism of oil-based drilling fluid with different types of weighting agents," *Royal Society Open Science*, vol. 5, no. 7, article 180358, 2018.

[41] B. S. Ba geri, M. Mahmoud, S. H. al-Mutairi, and A. Abdulraheem, "Effect of sand content on the filter cake properties and removal during drilling maximum reservoir contact wells in sandstone reservoir," *Journal of Energy Resources Technology*, vol. 138, no. 3, article 32901, 2016.

Hindawi
Geofluids
Volume 2019, Article ID 3456307, 10 pages
https://doi.org/10.1155/2019/3456307

Research Article

Study on Preliminarily Estimating Performance of Elementary Deep Underground Engineering Structures in Future Large-Scale Heat Mining Projects

Min Tang, Hong Li, and Chun'an Tang

Deep Underground Engineering Research Centre, Dalian University of Technology, Dalian 116024, China

Correspondence should be addressed to Chun'an Tang; tca@mail.neu.edu.cn

Received 24 January 2019; Revised 17 May 2019; Accepted 27 May 2019; Published 13 June 2019

Guest Editor: Bisheng Wu

Geothermal energy will become an important part of energy in the future because of its advantages in source stability, sustainability, and potential high utilization ratio. In particular, the development and utilization of deep geothermal energy from HDR have gradually attracted people's attention. Aiming at solution to the bottleneck of EGS-D, a new EGS-E based on excavation technology is proposed. In this paper, a concise and direct method for estimating the early performance of this disruptive and innovative geothermal development scheme is established as a viable alternative to supercomputing for the subsequent quantitative research of the corresponding relationship between a typical deep engineering structure and its heat extraction efficiency. Firstly, the effects of the fixed temperature at a tunnel wall, the radius of a tunnel, and the rock type on the annual heat extraction rate of the tunnel are studied based on the analytical solution of a one-dimensional radial plane problem of the transient heat conduction through high-temperature surrounding rock to the tunnel wall covering 30 years. Then, three different estimation methods of EGS-E efficiency with comb-shaped and chessboard-shaped underground tunnels, respectively, are studied, and the research ideas for the estimation of the EGS-E system with more complicated cobweb-shaped tunnels are pointed out.

1. Introduction

Geothermal energy will become an important part of energy in the future because of its advantages of source stability, sustainability, and potential high utilization ratio. Geothermal energy stored at depths of less than 10 kilometers underground was estimated to be 170 million times the amount of heat released from all coals stored in the earth, based on a study by Pollack and Chapman in 1977. However, the scale of geothermal energy with temperature lower than 150°C at depths shallower than 3 kilometers underground is usually too small to maintain the demand for long-term stable electricity production. This portion of low-temperature hydrothermal resource only accounts for 10% of total geothermal energy stored in the earth [1]. And the official data released by the Ministry of Land and Resources of China shows that the total hot dry rock (HDR) geothermal resources at depths from 3 to 10 kilometers in the mainland are equivalent to 860 trillion tons of coal, which is 260000 times the current annual energy consumption amount in China [2]. Therefore, a broader scheme of the enhanced geothermal system (EGS) which aims at exploiting geothermal energy from HDR at the depths of 3 to 10 kilometers has gradually attracted people's attention.

The current popular heat extraction method from HDR has been developed as EGS based on drilling technology (EGS-D). A high-permeability fracture system (artificial thermal storage) is established by reservoir stimulation technology such as hydraulic fracturing through an injection well. Injected cold water (or other fluids) is heated by the fracture heat exchange structure, and then, the hot water or steam generated by the production well is pumped out to the ground for power generation. The injection well, production well, and underground thermal reservoir form a closed loop system of high-temperature thermal fluids [3]. The keys to the development of HDR include (1) localization of the resource target area. It should be based on the terrestrial heat flow value and combined with the characteristics of the geological structure. Seismic exploration technology, electrical method, and electromagnetic method as well as gravity and magnetic method could be used to carry out detailed exploration in the selected research area [4–6]. (2) Improvement of the reservoir: deep drilling technology under high temperature and pressure conditions is relatively mature. The depths of oil exploration drilling and comprehensive scientific research drilling have exceeded 7000 meters. At present, hydraulic fracturing [7], chemical stimulation [8], and thermal stimulation [9], as well as the combination of these technologies, are commonly used in creating a heat reservoir in EGS. And the fracture monitoring technologies used frequently now include microseismic monitoring, acoustic emission, downhole imaging, and various tracers [10, 11]. (3) Research on THMC (Thermal-Hydraulic-Mechanical-Chemical) multifield coupling of EGS: some scholars have successfully studied the coupling problem of each process. However, the construction of the thermal reservoir model still needs to be developed, which will continue to be the focus of EGS numerical simulation research [12–14]. And in recent years, scholars and relevant institutions have put forward new alternative systems, such as EGS using supercritical carbon dioxide as circulating fluid [15]and EGS for producing supercritical water vapor [16] as well as Radiator-EGS that consists of a family of vertically interconnected vanes produced through sequential horizontal drilling and frac-induced rubblization [17].

There were several typical EGS-D development cases in the world such as the Fenton Hill, Hijiori, Ogachi, Cooper Basin, and Soultz. However, none of them has achieved large-scale commercial electricity generation owing to the disadvantages of small scale, low efficiency, geographical restriction, and so on [18]. The biggest challenge it faces is how to economically construct an artificial heat repository. In the HDR development report written by researchers in MIT, it was also pointed out that the key to cost-efficient development of EGS in the next 20 years is to obtain economical and effective multireservoir construction technology to ensure enough heat content (volume > 1 km^3) for long-term geothermal development [19].

Past experience in geothermal reservoir construction had shown that the development of an artificial reservoir was mainly caused by shear failure [20] of existing joints, which is different from tensile cracking caused by conventional hydraulic fracturing in oil and gas reservoirs. The shear failure part in the stimulation only occurs where fluid pressure becomes lower than the in situ minimum principal stress of the target reservoir. With the current technology, it is difficult to predict the distribution of the stress field around a well before being drilled, especially the distribution of stress field far from a wellbore. And directions of the in situ principal stresses may change with depth, which as well affects predicting the direction of fracture extension [21, 22]. It is usually difficult to predict the direction of fracture extension in the absence of accurate downhole data measurement. Even if related data had been available, fractures may not develop along the predicted direction. Therefore, it is difficult to achieve the interconnection between wells by hydraulic fracturing. Theoretically, it is better to first have the heat storage developed then find a way (e.g., microseismic monitoring technology and acoustic emission technology) to implement directional drilling secondly [23–25]. However, artificial fracture (caused by perforation as well as fracturing stimulation) only plays a dominant role surrounding the wellbore. The growth and expansion of heat storage during fracturing are mainly controlled by the existing natural fracture system (or joint distribution). The development of heat storage during hydraulic fracturing mainly comes from the activation of existing natural fractures which were controlled by the in situ stress field [26, 27]. Thus, EGS-D has a limitation in geographical selection. Even if the process of heat storage stimulation and directional drilling goes smooth, the cracks formed by hydraulic fracturing are often closed under the action of high in situ stress at depth. This makes the cracks disconnected, thus unable to form a sufficient volume of heat storage [28].

In addition, there are many reasons causing the short-circuit effect of fluid flows, which also makes the failure of thermal recovery unavoidable. These include the following: (1) The use of proppant near the wellbore requires a higher injection pressure and flow rate, and excessive injection pressure will cause continuous fracture growth, resulting in increased water loss and/or fluid short circuit. (2) Repeated high-pressure stimulation of existing fractures may lead to more direct connection which results in fluid flow short circuit between injection and production wells. (3) If natural fractures are connected to wells, hydraulic fracturing may increase connectivity and lead to short circuit, especially when the well spacing is small. (4) Any operation of pressurizing reservoirs is irreversible and not always beneficial to developing heat storage. Long-term high-pressure water injection will cause irreversible damage to rocks, resulting in fluid short circuit and excessive water loss into farther regions. (5) Deeper and shallower reservoirs may be communicated through fracture growth in a water injection test or the wellbores penetrating two reservoirs, which will affect the construction of multiple reservoirs [29–33].

In a word, from the development status of traditional EGS-D, it can be seen that innovative breakthroughs are urgently needed in the research of the deep geothermal exploitation scheme.

2. Materials and Methods

2.1. Enhanced Geothermal System Based on Excavation Technology (EGS-E). Aiming at the disadvantages of EGS-D, such as difficulty on building large-scale stable heat storage, small water flow rate, and easy cause of contamination, a new EGS based on excavation technology (EGS-E) was recently proposed to provide a new scheme for the exploitation of deep HDR heat [34].

As shown in Figure 1, it includes (1) large heat flow formed through the excavation of a super large shaft, (2) heat source with large volume and high permeability due to crack and fragmentation formation through drilling and blasting which are implemented inside the tunnels, and (3) heat

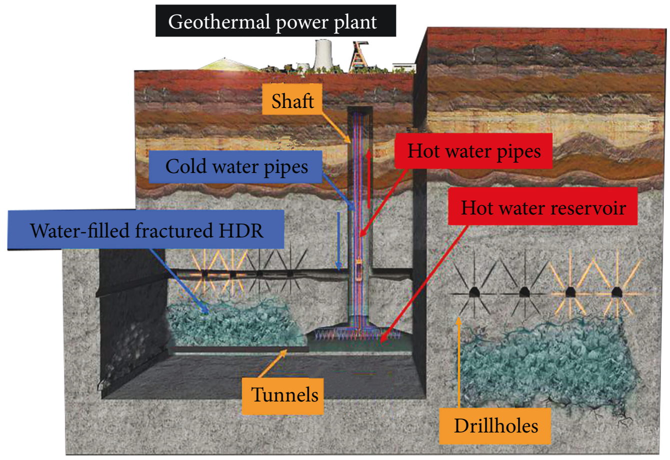

FIGURE 1: Schematic illustration of the EGS-E concept.

storage with a large capacity and high conductivity formed through the caving method based upon the excavation of an underground hot water reservoir and tunnels radially stretched out. In EGS-E, the horizontal tunnels with 360-degree distribution at different depths of the shaft can be excavated through mining excavation technology, and multiple stable large-scale heat storages can be constructed by the caving method from the tunnels. Compared with EGS-D, it can tremendously extend the scale of stable heat storage, expand the area of heat exchange, and upgrade the magnitude of geothermal transport to achieve large-scale geothermal development.

At present, the Mponeng Gold Mine in South Africa has mastered the excavation technology at a depth of 4350 meters [35]. As for the high temperature in the process of excavation, it is urgently needed to develop ice-cooled radiation cooling technology and local refrigeration cooling technology, new-type heat-resistant materials (e.g., thermal insulate lining sandwiched membrane), intelligent machinery, remote control robots, and so forth [36]. A R&D organization in South Africa has recently developed a concept robot for drilling holes. The Kiruna Iron Mine in northern Sweden which is the largest underground mine in the world has basically realized "unattended intelligent mining." These technological breakthroughs are bringing "unmanned mining" closer and closer to us, making EGS-E more and more feasible. It is true that the large-scale production in EGS-E also needs to reduce costs in order to compete with other basic power generation technologies [37]. While attaining a large amount of hot water (or another suitable fluid or fluids for better heat storage, exchange, and transport, e.g., supercritical CO_2), EGS-E can be combined with deep mining to reduce the engineering cost of EGS-E and provide an active cooling scheme for the high-temperature environment of deep mining so as to achieve a win-win situation of resources and energy development. It can also be combined with underground quarrying. Underground granite without weathering not only is ideal high-quality stone but also can be developed into building material to compensate for excavation costs. In the meantime, it can protect the ground surface environment. Moreover, the construction of an underground geothermal power plant can also be considered, which can reduce the loss of heat during transportation and save the fee for long distance transportation of fluid.

However, it is difficult to realize the numerical simulation of a super large scale of the heat mining system in EGS-E without powerful supercomputing. Therefore, preliminary methods to concisely estimate the early performance of EGS-E concept models are proposed in this paper, and their application scope and error evaluation are also studied, which will provide a viable alternative to supercomputing for the subsequent quantitative research of the corresponding relationship between a typical deep engineering structure and its heat extraction efficiency. In the actual EGS-E model, there are many forced heat convection zones consisting of fracture flow and rock mass around tunnels. After heat transfer between fracture flow and HDR, all hot water is collected to the hot water pool at the bottom of the shaft through the forced convection scheme with circulating pipelines installed on the tunnel walls to realize the optimal control of heat transfer structures. Because the main purpose of this paper is to study the effect of estimation for heat extraction efficiency of EGS-E with different tunnel layouts and the transient simulation to large-scale heat convection of fracture flow in EGS-E requires supercomputing, the mechanism of heat transfer is simplified into the large-scale transient heat conduction to the tunnel wall with an equivalent homogenized thermal conductivity at this stage. The equivalent thermal conductivity here is considered to include the homogenized contribution of heat convection in fracture flow and heat conduction in rock. With this simplification, factors influencing heat extraction of tunnel walls are studied first.

2.2. Factors Influencing Heat Extraction of Tunnel Walls in EGS-E. Referring to previous studies [38, 39], the heat conducted in the radial direction of surrounding rock is much larger than that in the axial direction; thus, the latter can be ignored for analytical solution. An axially symmetrical plane problem that the transient heat conduction from high-temperature surrounding rock to a circular tunnel for 30 years is solved in this section to study the factors influencing heat extraction of tunnel walls in EGS-E.

As shown in Figure 2, considering that the cross sections of the tunnel and rock are both circular. The radii from the inside to the outside are R_1 and R_2, respectively. Based on the previous study [40] and according to the existing international criteria for the development and utilization of HDR [41], R_1 is 3 m and R_2 is 100 m; thus, it can be considered that the outer boundary is far enough from the tunnel and its temperature is not affected by heat conduction within 30 years, namely, the outer boundary can be regarded as thermal insulation. It is assumed that the temperature of tunnel wall T_1 is 150°C constantly with continuous heat exchange between cold water and the tunnel wall. And the initial temperature of surrounding rock T_2 is 250°C. The change of temperature field distribution in surrounding rock of the tunnel is studied. And the annual heat extraction efficiency of the tunnel wall for 30 years can be obtained through data processing with MATLAB.

The corresponding analytical solution to the one-dimensional transient heat conduction problem shown in Figure 2 is to solve the one-dimensional homogeneous heat conduction differential equation in cylindrical coordinates, which is expressed as follows [42]:

$$\frac{\partial^2 T}{\partial r^2} + \frac{1}{r}\frac{\partial T}{\partial r} = \frac{1}{\alpha}\frac{\partial T}{\partial t}, \quad R_1 \le r \le R_2, \tag{1}$$

where α is the thermal diffusivity of surrounding rock and $\alpha = \lambda / c\rho$. λ, c, and ρ are the thermal conductivity, heat capacity, and density of surrounding rocks, respectively.

The temperature of inner boundary T_1 is assumed to be 150°C constantly, which is the first type of boundary condition. The outer boundary is regarded as thermal insulation, namely, the heat flux is 0, which is the second type of boundary condition. Initial temperature of surrounding rock T_2 is 250°C. Following analytical solution of the surrounding rock, temperature distribution is obtained through the separation variable method and the orthogonal expansion method [43]:

$$\begin{aligned} T(r,t) &= T_1 + (T_2 - T_1)\sum_{m=1}^{\infty}\frac{1}{N(\beta_m)}e^{-\alpha\beta_m^2 t}R_0(\beta_m, r) \\ &\quad \cdot \int_{R_1}^{R_2} r' R_0\left(\beta_m, r'\right) dr', \\ \frac{1}{N(\beta_m)} &= \frac{\pi^2}{2}\frac{\beta_m^2 J_0^2(R_1\beta_m)}{J_0^2(R_1\beta_m) - J_1^2(R_2\beta_m)}, \\ R_0(\beta_m, r) &= -J_0(B_m r)Y_1(R_2\beta_m) + J_1(R_2\beta_m)Y_0(\beta_m r), \end{aligned} \tag{2}$$

where J_0 and J_1 are the first kind of zero-order and first-order Bessel functions and Y_0 and Y_1 are the second kind

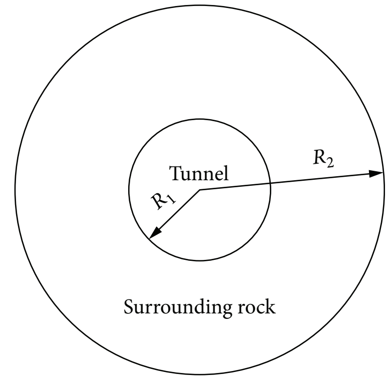

Figure 2: An axially symmetrical plane problem of the transient heat conduction from high-temperature surrounding rock to a circular tunnel.

of zero-order and first-order Bessel functions. All the eigenvalues β_m above need to be accumulated, and the values of β_m are the positive roots of the following equation [44]:

$$-J_0(R_1\beta_m)Y_1(R_2\beta_m) + J_1(R_2\beta_m)Y_0(R_1\beta_m) = 0. \tag{3}$$

Then, the average temperature $\bar{T}$ of the model at $t = 1$a, 2a, $\cdots$, 30a is obtained after processing the temperature of surrounding rock at every point and every moment with MATLAB. And the annual temperature decline $\Delta\bar{T}$ of the model is obtained through subtraction of $\bar{T}$ year by year within 30 years. According to the formula $Q = c \cdot m \cdot \Delta\bar{T}$, the analytical solution of the annual heat extraction rate of the one-meter-long tunnel wall varying with time can be obtained.

At a certain initial temperature of surrounding rock, the heat extraction efficiency of the tunnel wall varies with the wall temperature, radius of the tunnel, and thermodynamic parameters of rock. Therefore, on the basis of the above formulas, the effects of three factors on the annual heat extraction rate of the tunnel wall are studied, respectively. The corresponding changeable calculation conditions are shown in Table 1, and the results are shown in Figures 3–5.

From Figures 3 to 5, it can be seen directly that at a certain initial temperature of surrounding rock, the annual heat extraction rate of the tunnel wall increases with the lower constant temperature of the tunnel wall, the larger radius of the tunnel, or the higher thermal diffusivity of surrounding rock.

2.3. Estimation of EGS-E Performance with Different Tunnel Layouts. It is difficult to realize the numerical simulation of the super-large-scale heat mining system in EGS-E without powerful supercomputing. Does superposition of performance from each individual component give out an acceptable estimate on that of the structure made of them in the early heat mining production? Therefore, on the basis of previous studies, estimation methods of EGS-E efficiency with comb-shaped underground tunnels and chessboard-shaped underground tunnels, respectively, are proposed in this paper. And their application scope and error evaluation are also studied, which will provide the basis for subsequent

Table 1: Different wall temperatures, radii of the tunnel, and rock types.

T_1 (°C)	70	90	110	130	150
R_1 (m)	1.0	1.5	2.0	2.5	3.0
Rock type (α (m^2/d))	Granite (0.1134)	Gneiss (0.0992)	Limestone (0.0827)	Basalt (0.0742)	Dry shale (0.0650)

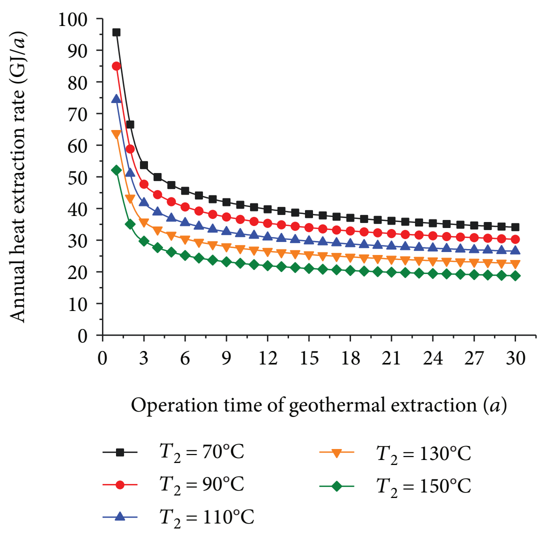

Figure 3: Analytical solution of the annual heat extraction rate varying with time for the one-meter-long tunnel under different wall temperatures when the rock type is granite, and T_1 is 250°C, α is 0.1134 m^2/d, and R_1 is 3 m.

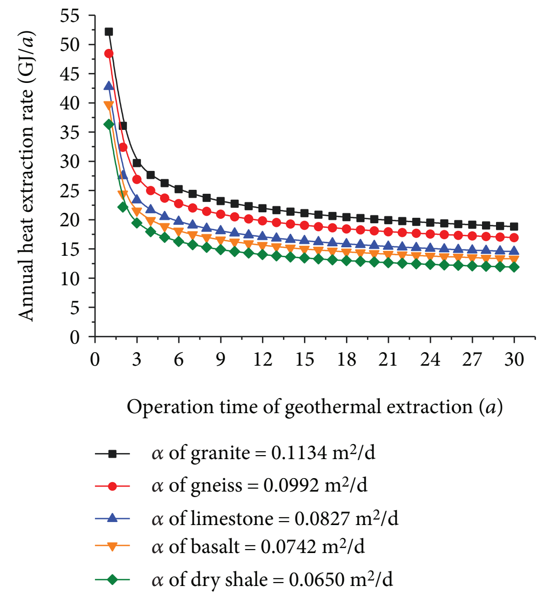

Figure 5: Analytical solution of the annual heat extraction rate varying with time for the one-meter-long tunnel under different rock types when T_1 is 250°C, R_1 is 3 m, and T_2 is 150°C.

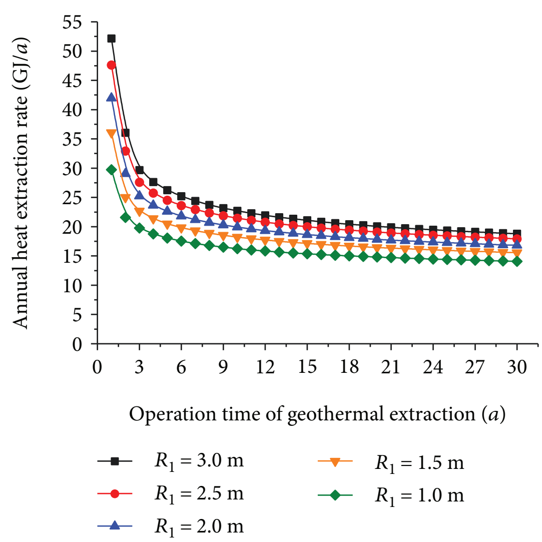

Figure 4: Analytical solution of the annual heat extraction rate varying with time for the one-meter-long tunnel under different radii of the tunnel when the rock type is granite, and T_1 is 250°C, α is 0.1134 m^2/d, and T_2 is 150°C.

research. According to the existing technical conditions, the international criteria for the development and utilization of HDR include that the volume of heat storage should be generally larger than 1 km^3 so as to have development value. Thus, the size of surrounding rock in the numerical model of this section is 1000 m ∗ 1000 m ∗ 1000 m, and the models with chessboard-shaped and comb-shaped underground tunnels together with their finite element meshes are shown in Figures 6 and 7, respectively. The ranges of chessboard-shaped tunnels and comb-shaped tunnels are 1000 m ∗ 1000 m and 1000 m ∗ 200 m, respectively. The cross section of the tunnel is still circular, and the radius of the tunnel is 3 m. The initial temperature of surrounding rock is 250°C. It is assumed that the temperature of the tunnel wall is 150°C constantly with continuous heat exchange between cold water and the tunnel wall. The surrounding boundary is set as thermal insulation, and the type of surrounding rock is granite. The equivalent thermal conductivity should be set as 175 W/(m·K) according to half of the available thermal energy of the cubic geothermal field to be mined in 30 years with chessboard-shaped tunnels (namely, the average temperature of the cubic geothermal field is reduced from 250°C to 200°C), which is reasonable and achievable under the condition of forced convection. Other thermodynamic parameters required for simulation are shown in Table 2, which are derived from the built-in material library of COMSOL Multiphysics.

The core idea of the estimation is to turn the simulation of a large-scale structure into the superposition of

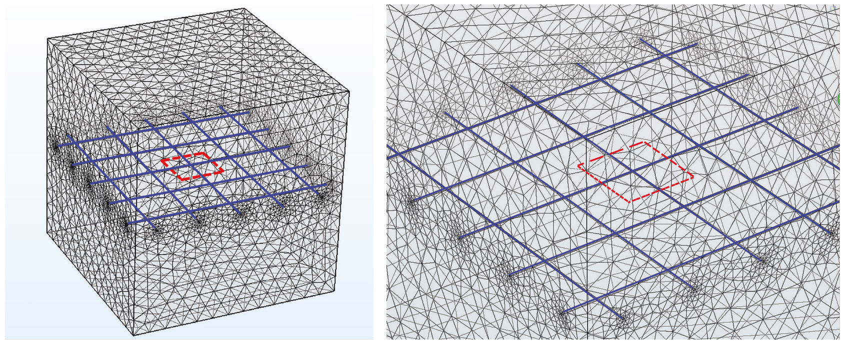

Figure 6: Numerical discretization of the simplified chessboard-shaped tunnel model of EGS-E and its local enlarged graph.

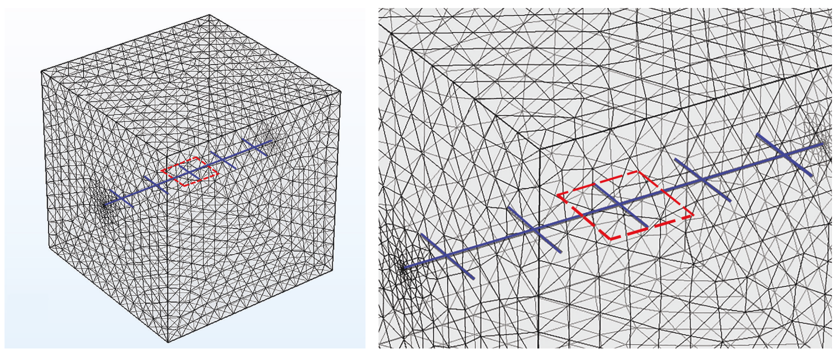

Figure 7: Numerical discretization of the simplified comb-shaped tunnel model of EGS-E and its local enlarged graph.

Table 2: Required thermodynamic parameters for simulation.

Rock type	Heat capacity (J/(kg·K))	Density (kg/m^3)	Equivalent thermal conductivity (W/(m·K))
Granite	850	2600	175

performance from each individual component. As for the simplified chessboard-shaped tunnel model and comb-shaped tunnel model of EGS-E shown in Figures 6 and 7, they can both be decomposed into several cross tunnels. Based on the following three models shown in Figures 8(a), 8(b), and 8(c), respectively, different superposition methods for estimation of EGS-E efficiency with chessboard-shaped and comb-shaped underground tunnels are studied.

As shown in Figure 8(a), the range of surrounding rock in the model is 1000 m $*$ 1000 m $*$ 1000 m. The range of cross tunnels is 200 m $*$ 200 m, which is the same as the cross tunnels marked by the red dotted frame in Figures 6 and 7. Namely, the range of chessboard-shaped tunnels in Figure 6 is equivalent to 25 cross tunnels whose range is 200 m $*$ 200 m, and the range of comb-shaped tunnels in Figure 7 is equivalent to 5 cross tunnels. These models have boundary effect in simulation calculation, but the tunnels are far from reaching the edge of the geothermal field in the actual situation. Therefore, considering the heat extraction efficiency of the whole chessboard-shaped or comb-shaped tunnels is as several times as that of their central cross tunnels to reduce the influence of the model boundary on estimation. The initial conditions, boundary conditions, and parameter settings required for calculation are the same as those of the models in Figures 6 and 7. The heat extraction rates of cross tunnel walls for those three models in Figure 8 at any time within 30 years are obtained and compared with those of chessboard-shaped and comb-shaped tunnels to study the application scope and error evaluation of three different models in Figure 8.

Figure 8(b) shows another estimation scheme. The range of surrounding rock in the model is 1000 m $*$ 1000 m $*$ 1000 m. The range of cross tunnels is 1000 m $*$ 1000 m. The initial conditions, boundary conditions, and parameter settings required for calculation are the same as those of the models in Figures 6 and 7, but only the heat extraction rate of cross tunnels marked by the red dotted frame in Figure 8(b) is taken for comparison. And the range of this part is also 200 m $*$ 200 m.

In the estimation scheme shown in Figure 8(c), the range of surrounding rock is 200 m $*$ 200 m $*$ 1000 m, and the range of cross tunnels is 200 m $*$ 200 m. The initial conditions, boundary conditions, and parameter settings required for calculation are the same as those of the models in Figures 6 and 7. The heat extraction rate of the cross tunnel walls at any time within 30 years is obtained and compared with those of central cross tunnels marked in Figures 6 and 7.

The heat extraction rates of cross tunnels with a range of 200 m $*$ 200 m at any time within 30 years based on the above three estimation schemes are compared with those of

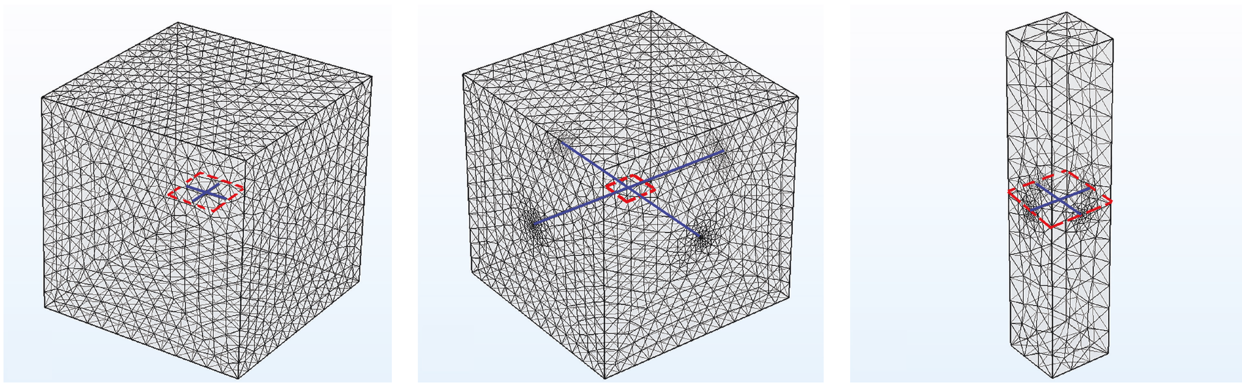

Figure 8: Three superposition models for estimation of EGS-E efficiency. (a) The ranges of tunnels and surrounding rock are 200 m ∗ 200 m and 1000 m ∗ 1000 m ∗ 1000 m, respectively. (b) The ranges of tunnels and surrounding rock are 1000 m ∗ 1000 m and 1000 m ∗ 1000 m ∗ 1000 m, respectively. (c) The ranges of tunnels and surrounding rock are 200 m ∗ 200 m and 200 m ∗ 200 m ∗ 1000 m, respectively.

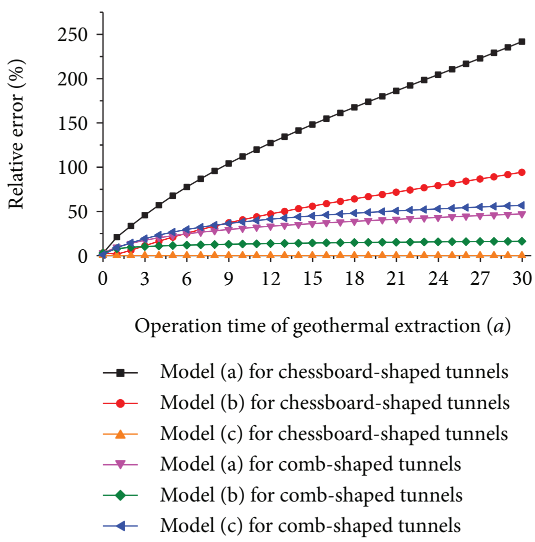

Figure 9: Relative error in the heat extraction rate estimated by different superposition methods varying with time for EGS-E with different tunnel layouts.

central cross tunnels with the same range marked in chessboard-shaped and comb-shaped models, respectively, as shown in Figure 9. It can be seen directly from the figure that the relative error of scheme (c) for chessboard-shaped tunnels is the smallest in superposition estimate of the heat extraction rate covering 30 years. This is because of the fact that for the chessboard-shaped tunnel model in Figure 6, its tunnel part and rock part can be exactly divided into 25 models as shown in Figure 8(c) with the same layout and size. However, there is still a tiny relative error that is less than 1% within 30 years. This is because the thermal field part distributed evenly to the central cross tunnels will begin to be affected by heat extraction of other surrounding tunnels at a certain point within 30 years with the equivalent thermal conductivity, and this part of heat loss cannot be completely compensated for by that itself "plunders" from other thermal field parts around it due to the boundary effect in simulation.

For comb-shaped tunnels, the relative error is the smallest when choosing scheme (b), which falls in less than 20% in 30 years. Analysis can also be given from the perspective of average division of the total thermal field volume to the total tunnel length. Scheme (b) is relatively the best for efficiency estimation of comb-shaped tunnels because its total length of tunnels and range of thermal field are the same with those of the model shown in Figure 7. However, except for the central cross tunnels marked by the red dotted frame in Figure 8(b), the layout of other tunnels is quite different from that of comb-shaped tunnels, so the interaction of central cross tunnels with surrounding tunnels in heat extraction is quite different, which is the main source of its relative error of less than 20%.

And for both chessboard-shaped and comb-shaped tunnels, the largest relative error of the above three estimation schemes during the first year is only about 20%. This conclusion is also of practical significance to estimate the early performance of EGS-E.

Generally speaking, as explained above, it is advisable to replace it with the superposition estimation schemes studied in this paper to some extent when there is no powerful supercomputing to realize the numerical simulation of the super-large-scale heat mining system in EGS-E. And the analysis of relative error can also provide inspiration for further improvement of the estimation scheme.

3. Discussion

(1) The paper [40] has inspired another type of underground tunnel layout (cobweb), which is also convenient for the outward stretching of the underground tunnel structure, thus further increasing the volume of heat storage, as shown in Figure 10. Similarly, the heat extraction efficiency of cobweb-shaped tunnels can also be estimated. The difference lies in the need for numerical simulation of heat transfer of several central cross tunnels with different sizes (as marked by the red dotted frame in Figure 10) and several single cylindrical tunnels with different lengths (namely, the intervals between different cross tunnels). Then,

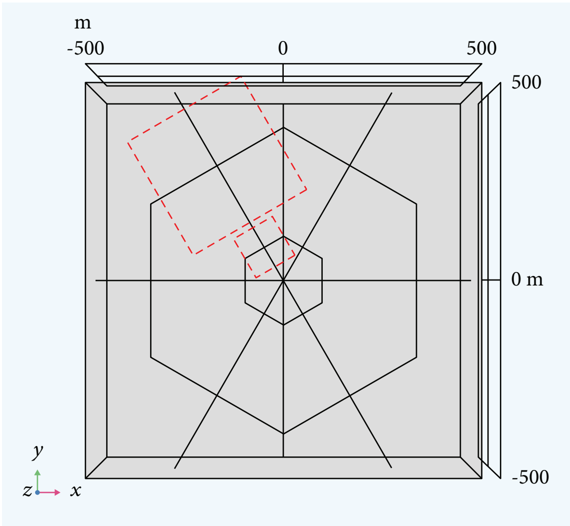

Figure 10: Simplified cobweb-shaped tunnel model of EGS-E.

the estimation results of overall heat extraction efficiency of the model with cobweb-shaped tunnels can be accumulated

(2) The main purpose of this paper is to study the effect of estimation for heat extraction efficiency of EGS-E with different tunnel layouts, and the transient simulation to large-scale heat convection of fracture flow in EGS-E requires supercomputing; thus, the mechanism of heat transfer is simplified into the large-scale transient heat conduction to the tunnel wall with an equivalent homogenized thermal conductivity for the time being

The accuracy of the 3-D model simulation is verified by the following two aspects: (i) The results of simulations for models with different discretizations are nearly the same. (ii) Relative error in the heat extraction rate estimated by the superposition method shown in Figure 8(c) for EGS-E with chessboard-shaped tunnels is less than 1% within 30 years.

This simplification should also consider and involve necessary limitations. That is, the modelling is mainly based on great simplification of a comprehensive homogenized thermal conductivity which already contains effects of the heat convection mechanism through fracture networks within surrounding rock. This simplification would surely depend on the sufficiency of enhanced fracturing, either by alike caving method based on blasting and natural collapse or by hydraulic fracturing stimulation through drilling boreholes. And the sufficiency will be dependent on the total contact area of fracture walls which are interfaces between rock and flows, total length and spacing of fracture and rock lumpiness, etc.

In addition, the influence factors for heat convection in each individual fracture include not only the rock properties and contact area but also the fluid properties (thermal conductivity, viscosity, heat capacity and density, etc.) and the heat transfer surface properties (shape, size and roughness, etc.). It is also closely related to the phase transition. Bidirectional coupling between temperature field and flow field is an important factor that must be considered as well.

In general, compared with heat conduction, the heat convection in fracture flow is a much more complicated process that affected on many factors, and it is necessary to conduct related research according to the classification of influence factors. Subsequently, as a complementary part, a representative local detailed numerical model should be studied based on the heat transfer between fracture flow and HDR, namely, selecting a small fractured area for numerical simulation of bidirectional coupling between the temperature field and flow field to comprehensively study the factors such as flow rate, flow flux, and heat extraction efficiency assuming that the heat storage is designed to consist of several relatively small fractured areas in parallel.

4. Conclusions

Geothermal energy will become an important energy component in the future because of its advantages of stability, sustainability, and efficient utilization. In particular, the development and utilization of deep geothermal energy from HDR have gradually attracted people's attention. Aiming at mitigating the bottleneck of EGS-D, a new EGS-E based on excavation technology was proposed. In this paper, a simple and direct method for estimating the early performance of the large-scale deep geothermal heat mining is studied and established for its applicability in the subversive and innovative scheme, i.e., EGS-E large-scale heat mining, in the near future. A preliminary exploration is made to quantitatively study the corresponding relationship between the deep engineering structure and its heat extraction efficiency. The relevant researches and conclusions are as follows:

(1) The major characteristics (large heat flow, heat source with large volume and high permeability, and heat storage with large capacity and high conductivity) and advantages of EGS-E are introduced. The breakthroughs and prospects about key technologies involved in the construction and operation of the EGS-E system are expounded as well. Moreover, the innovative schemes to reduce the costs of EGS-E are also put forward

(2) The effects of the tunnel wall temperature, tunnel radius, and rock type on the annual heat extraction rate are studied based on the analytical solution of a one-dimensional radial plane problem of the transient heat conduction through high-temperature surrounding rock to the tunnel wall covering 30 years. The results show that at a certain initial field temperature, the annual heat extraction rate from the tunnel wall increases with the lower inner boundary fixed temperature, the longer radius of the tunnel, or the greater thermal diffusivity of surrounding rock

(3) Through undertaking numerical simulations with COMSOL Multiphysics, three different estimation

methods of EGS-E efficiency with comb-shaped and chessboard-shaped underground tunnels, respectively, are proposed, and the research ideas for the estimation of the EGS-E system with more complicated cobweb-shaped tunnels are pointed out. Relative optimum estimation schemes for comb-shaped and chessboard-shaped underground tunnels are obtained, respectively. The relative error of scheme (c) is the smallest for the superposition estimation of the heat extraction rate in 30 years for chessboard-shaped tunnels, which has been less than 1% within 30 years. For comb-shaped tunnels, the relative error is the smallest when choosing scheme (b), which has been less than 20% in 30 years. And for chessboard-shaped and comb-shaped tunnels, the largest relative error of these three estimation schemes in the first year is only about 20%. Thus, generally speaking, it is advisable to take advantage of convenience and effectiveness of the superposition estimation schemes studied in this paper to some extent when there is no powerful supercomputing to realize the numerical simulation of the super-large-scale heat mining system in EGS-E

Data Availability

The values of the calculation parameters needed for numerical simulation solution and analytical solution used to support the findings of this study are included within the article.

Conflicts of Interest

The authors declare that there is no conflict of interest regarding the publication of this paper.

References

[1] J. Guo, J. Chen, W. Cao, and F. Jiang, "Research review on enhanced geothermal system," *Power Construction*, vol. 35, no. 4, pp. 10–24, 2014.

[2] L. Wang, *Geothermal Resources of China Are Equivalent to 860 Trillion Tons of Coal and Can Be Consumed for 260,000 Years*, Xinhuanet[DB/OL], 2012, http://money.163.com/12/1004/16/8D01SPR300253B0H.html.

[3] A. Gérard, A. Genter, T. Kohl, P. Lutz, P. Rose, and F. Rummel, "The deep EGS (Enhanced Geothermal System) project at Soultz-sous-Forêts (Alsace, France)," *Geothermics*, vol. 35, no. 5-6, pp. 473–483, 2006.

[4] G. Foulger, "Geothermal exploration and reservoir monitoring using earthquakes and the passive seismic method," *Geothermics*, vol. 11, no. 4, pp. 259–268, 1982.

[5] G. Volpi, A. Manzella, and A. Fiordelisi, "Investigation of geothermal structures by magnetotellurics (MT): an example from the Mt. Amiata area, Italy," *Geothermics*, vol. 32, no. 2, pp. 131–145, 2003.

[6] V. K. Karastathis, J. Papoulia, B. di Fiore et al., "Deep structure investigations of the geothermal field of the North Euboean Gulf, Greece, using 3-D local earthquake tomography and Curie Point Depth analysis," *Journal of Volcanology and Geothermal Research*, vol. 206, no. 3-4, pp. 106–120, 2011.

[7] G. Zimmermann and A. Reinicke, "Hydraulic stimulation of a deep sandstone reservoir to develop an enhanced geothermal system: laboratory and field experiments," *Geothermics*, vol. 39, no. 1, pp. 70–77, 2010.

[8] S. Portier, F. D. Vuataz, P. Nami, B. Sanjuan, and A. Gérard, "Chemical stimulation techniques for geothermal wells: experiments on the three-well EGS system at Soultz-sous-Forêts, France," *Geothermics*, vol. 38, no. 4, pp. 349–359, 2009.

[9] J. Bradford, M. Ohren, W. L. Osborn, J. McLennan, J. Moore, and R. Podgorney, "Thermal stimulation and injectivity testing at Raft River, ID EGS site," in *Proceedings of 39th Workshop on Geothermal Reservoir Engineering*, Stanford, CA, USA, February 2014.

[10] B. Sanjuan, J.-L. Pinault, P. Rose et al., "Tracer testing of the geothermal heat exchanger at Soultz-sous-Forêts (France) between 2000 and 2005," *Geothermics*, vol. 35, no. 5-6, pp. 622–653, 2006.

[11] E. C. Pope, D. K. Bird, and S. Arnorsson, "Stable isotopes of hydrothermal minerals as tracers for geothermal fluids in Iceland," *Geothermics*, vol. 49, pp. 99–110, 2014.

[12] J. Rutqvist, Y. S. Wu, C. F. Tsang, and G. Bodvarsson, "A modeling approach for analysis of coupled multiphase fluid flow, heat transfer, and deformation in fractured porous rock," *International Journal of Rock Mechanics and Mining Sciences*, vol. 39, no. 4, pp. 429–442, 2002.

[13] G. Izadi and D. Elsworth, "The influence of thermal-hydraulic-mechanical- and chemical effects on the evolution of permeability, seismicity and heat production in geothermal reservoirs," *Geothermics*, vol. 53, pp. 385–395, 2015.

[14] J. Taron and D. Elsworth, "Thermal-hydrologic-mechanical-chemical processes in the evolution of engineered geothermal reservoirs," *International Journal of Rock Mechanics and Mining Sciences*, vol. 46, no. 5, pp. 855–864, 2009.

[15] K. Pruess, "Enhanced geothermal systems (EGS) using CO_2 as working fluid- a novel approach for generating renewable energy with simultaneous sequestration of carbon," *Geothermics*, vol. 35, no. 4, pp. 351–367, 2006.

[16] G. Ó. Friðleifsson, W. A. Elders, and A. Albertsson, "The concept of the Iceland deep drilling project," *Geothermics*, vol. 49, pp. 2–8, 2014.

[17] P. Geiser, B. Marsh, and M. Hilpert, "The Radiator-EGS system: a fresh solution to geothermal heat extraction," in *Proceedings, 40th Workshop on Geothermal Reservoir Engineering Stanford University*, Stanford, CA, USA, 2015.

[18] Z. Liao, T. Wan, and Z. Zhang, "Enhanced geothermal system: great potential and difficult development," *Earth Science Frontiers*, vol. 22, no. 1, pp. 335–344, 2015.

[19] J. W. Tester, B. J. Anderson, A. S. Batchelor et al., *The Future of Geothermal Energy-Impact of Enhanced Geothermal Systems (EGS) on the United States in the 21st Century*, Massachusetts Institute of Technology, Boston, 2006.

[20] R. J. Pine and A. S. Batchelor, "Downward migration of shearing in jointed rock during hydraulic injections," *International Journal of Rock Mechanics and Mining Sciences & Geomechanics Abstracts*, vol. 21, no. 5, pp. 249–263, 1984.

[21] J. T. Whetten, B. R. Dennis, D. S. Dreesen et al., "The U.S. hot dry rock project," *Geothermics*, vol. 16, no. 4, pp. 331–339, 1987.

[22] H. Kaieda, H. Ito, K. Kiho, K. Suzuki, H. Suenaga, and K. Shin, "Review of the Ogachi HDR project in Japan," in *Proceedings*

of *World Geothermal Congress 2005*, Antalya, Turkey, April 2005.

[23] J. W. Tester and J. N. Albright, *Hot Dry Rock Energy Extraction Field Test: 75 Days of Operation of a Prototype Reservoir at Fenton Hill, Segment 2 of Phase I*, Los Alamos Scientific Laboratory, Stanford, NM, USA, 1979.

[24] K. Shin, H. Ito, and Y. Oikawa, "Stress State at the Ogachi Site," in *Proceedings of World Geothermal Congress 2000*, Kyushu-Tohoku, Japan, June 2000.

[25] Y. Li, S. Sun, and C. Tang, "Analytical prediction of the shear behaviour of rock joints with quantified waviness and unevenness through wavelet analysis," *Rock Mechanics and Rock Engineering*, pp. 1–13, 2019.

[26] A. S. Batchelor, R. Baria, and K. Hearn, "Monitoring the effects of hydraulic stimulation by microseismic event location: a case study," in *Proceedings of SPE Annual Technical Conference and Exhibition*, San Francisco, CA, USA, October 1983.

[27] N. Tenma, T. Yamaguchi, and G. Zyvoloski, "The Hijiori hot dry rock test site, Japan: evaluation and optimization of heat extraction from a two-layered reservoir," *Geothermics*, vol. 37, no. 1, pp. 19–52, 2008.

[28] D. Wyborn, "Update of development of the geothermal field in the granite at Innamincka, South Australia," in *Proceedings of World Geothermal Congress 2010*, Bali, Indonesia, April 2010.

[29] O. Kolditz and C. Clauser, "Numerical simulation of flow and heat transfer in fractured crystalline rocks: application to the hot dry rock site in Rosemanowes (U.K.)," *Geothermics*, vol. 27, no. 1, pp. 1–23, 1998.

[30] H. G. Richards, D. Savage, and J. N. Andrews, "Granite-water reactions in an experimental Hot Dry Rock geothermal reservoir, Rosemanowes test site, Cornwall, U K," *Applied Geochemistry*, vol. 7, no. 3, pp. 193–222, 1992.

[31] A. Genter, K. Evans, N. Cuenot, D. Fritsch, and B. Sanjuan, "Contribution of the exploration of deep crystalline fractured reservoir of Soultz to the knowledge of enhanced geothermal systems (EGS)," *Comptes Rendus Geoscience*, vol. 342, no. 7-8, pp. 502–516, 2010.

[32] R. Baria, S. Michelet, J. Baumgaertner et al., "Microseismic monitoring of the world's largest potential HDR reservoir," in *Proceedings of 29th Workshop on Geothermal Reservoir Engineering*, Stanford, CA, USA, January 2004.

[33] S. Yamaguchi, S. Akibayashi, S. Rokugawa, Y. Fujinaga, N. Tenma, and Y. Sato, "The numerical modeling study of the Hijiori HDR test site," in *Proceedings of World Geothermal Congress 2000*, Kyushu-Tohoku, Japan, June 2000.

[34] C. Tang, J. Zhao, and S. Wang, "Conceptual model of enhanced geothermal system based on excavation technology (EGS-E)," in *Proceedings of Chinese Society for Rock Mechanics and Engineering Symposium*, Beijing, 2018.

[35] Q. Zhang, "Thoughts on application of deep well mining technology," *Gold*, vol. 37, no. 6, pp. 46–48, 2016.

[36] F. Yue, X. Hu, and J. Zhang, "Underground cooling technologies for deep mining in South Africa's gold mines," *Gold*, vol. 34, no. 9, pp. 33–37, 2013.

[37] T. Xu, Y. Yuan, Z. Jiang, Z. Hou, and B. Feng, "Hot dry rock and enhanced geothermal engineering: international experience and China prospect," *Journal of Jilin University (Earth Science Edition)*, vol. 46, no. 4, pp. 1139–1152, 2016.

[38] X. Zhou, Y. Zeng, Z. Yang, and X. Zhou, "Numerical solution of the heat transfer between tunnels and rocks in high-temperature geothermal region," *Journal of Railway Science and Engineering*, vol. 12, no. 6, pp. 1406–1411, 2015.

[39] C. Xia, G. Zhang, and S. Xiao, "Analytical solution to temperature fields of tunnel in cold region considering lining and insulation layer," *Chinese Journal of Rock Mechanics and Engineering*, vol. 29, no. 9, pp. 1767–1773, 2010.

[40] M. Tang, H. Li, and C. Tang, "Study on deep underground geometrical model for enhanced geothermal system based on excavation," in *ISRM International Symposium - 10th Asian Rock Mechanics Symposium*, Singapore, October-November 2018.

[41] X. Gong, "Deep geothermal development requires science to speak," *China Science Daily[DB/OL]*, 2016, http://news.sciencenet.cn/htmlnews/2016/8/353773.shtm.

[42] S. Yang and W. Tao, *Heat Transfer*, Higher Education Press, Beijing, 1998.

[43] M. N. Ozisik, *Translated by Changming Yu. Heat Conduction*, Higher Education Press, Beijing, 1983.

[44] Y. Zhang, S. He, and J. Li, "Analytical solution for temperature field of circular tunnel with insulation in cold region," *Journal of Glaciology and Geocryology*, vol. 31, no. 1, pp. 113–118, 2009.

Hindawi
Geofluids
Volume 2019, Article ID 1853274, 21 pages
https://doi.org/10.1155/2019/1853274

Research Article

Numerical Simulation of the Influence of Geological CO_2 Storage on the Hydrodynamic Field of a Reservoir

Zhaoxu Mi,[1] Fugang Wang,[1] Zhijie Yang,[1] Xufeng Li,[2] Yujie Diao,[2] Xin Ma,[2] and Hailong Tian[1]

[1] *Key Laboratory of Groundwater Resources and Environment, Ministry of Education, Jilin University, Changchun 130012, China*
[2] *Key Laboratory of Carbon Dioxide Geological Storage, Center for Hydrogeology and Environmental Geology Survey, China Geological Survey, Baoding, Hebei 071051, China*

Correspondence should be addressed to Fugang Wang; wangfugang@jlu.edu.cn

Received 20 July 2018; Revised 18 March 2019; Accepted 7 May 2019; Published 2 June 2019

Guest Editor: Bisheng Wu

CO_2 geological storage in deep saline aquifers is an effective way to reduce CO_2 emissions. The injection of CO_2 inevitably causes a significant pressure increase in reservoirs. When there exist faults which cut through a deep reservoir and shallow aquifer system, there is a risk of the shallow aquifer being impacted by the changes in reservoir hydrodynamic fields. In this paper, a radial model and a 3D model are established by TOUGH2-ECO2N for the reservoir system in the CO_2 geological storage demonstration site in the Junggar Basin to analyze the impact of the CO_2 injection on the deep reservoir pressure field and the possible influence on the surrounding shallow groundwater sources. According to the results, the influence of CO_2 injection on the reservoir pressure field in different periods and different numbers of well is analyzed. The result shows that the number of injection wells has a significant impact on the reservoir pressure field changes. The greater the number of injection wells is, the greater the pressure field changes. However, after the cessation of CO_2 injection, the number of injection wells has little impact on the reservoir pressure recovery time. Under the geological conditions of the site and the constant injection pressure, although the CO_2 injection has a significant influence on the pressure field in the deep reservoir, the impact on the shallow groundwater source area is minimal and can be neglected and the existing shallow groundwater sources are safe in the given project scenarios.

1. Introduction

Global warming presents a serious threat to the living environment of humans. Reducing the emissions of carbon dioxide (CO_2) is a common challenge for countries worldwide [1]. The geological storage of CO_2 has attracted the attention of governments and scientists around the world as a direct and effective emission reduction method recognized by the international community [2–5]. Once the CO_2 has been transported, it is stored in porous geological formations that are typically located several kilometers below the Earth's surface, and under the pressure and temperature conditions of such reservoirs, CO_2 exists in a dense phase. Suitable storage sites include former gas and oil fields, deep saline formations, or nearly depleted oil fields where the injected carbon dioxide may increase the amount of oil recovered. The storage mechanism includes structural storage, residual storage, dissolution storage, and mineral storage. The geological storage of CO_2 is a complex process and is therefore affected by many factors, such as the reservoir conditions, rock heterogeneity, faults, minerals, relative permeability hysteresis, and dip angle of the reservoir[6–9]. Because deep saline aquifers can be found in widespread areas, these aquifers are considered to have enormous potential for CO_2 storage [1]. Therefore, deep saline aquifers have received much attention as places to store CO_2.

For the large-scale injection of CO_2, the increase in pressure is a major factor affecting the storage capacity and storage safety [10–12]. Two important potential risks associated with the pressure increase have attracted the attention of many scholars. The first risk involves geomechanical effects, such as caprock fracturing, fault resurrection, and induced earthquakes. The second risk involves environmental impacts, such as the impacts on shallow aquifers and

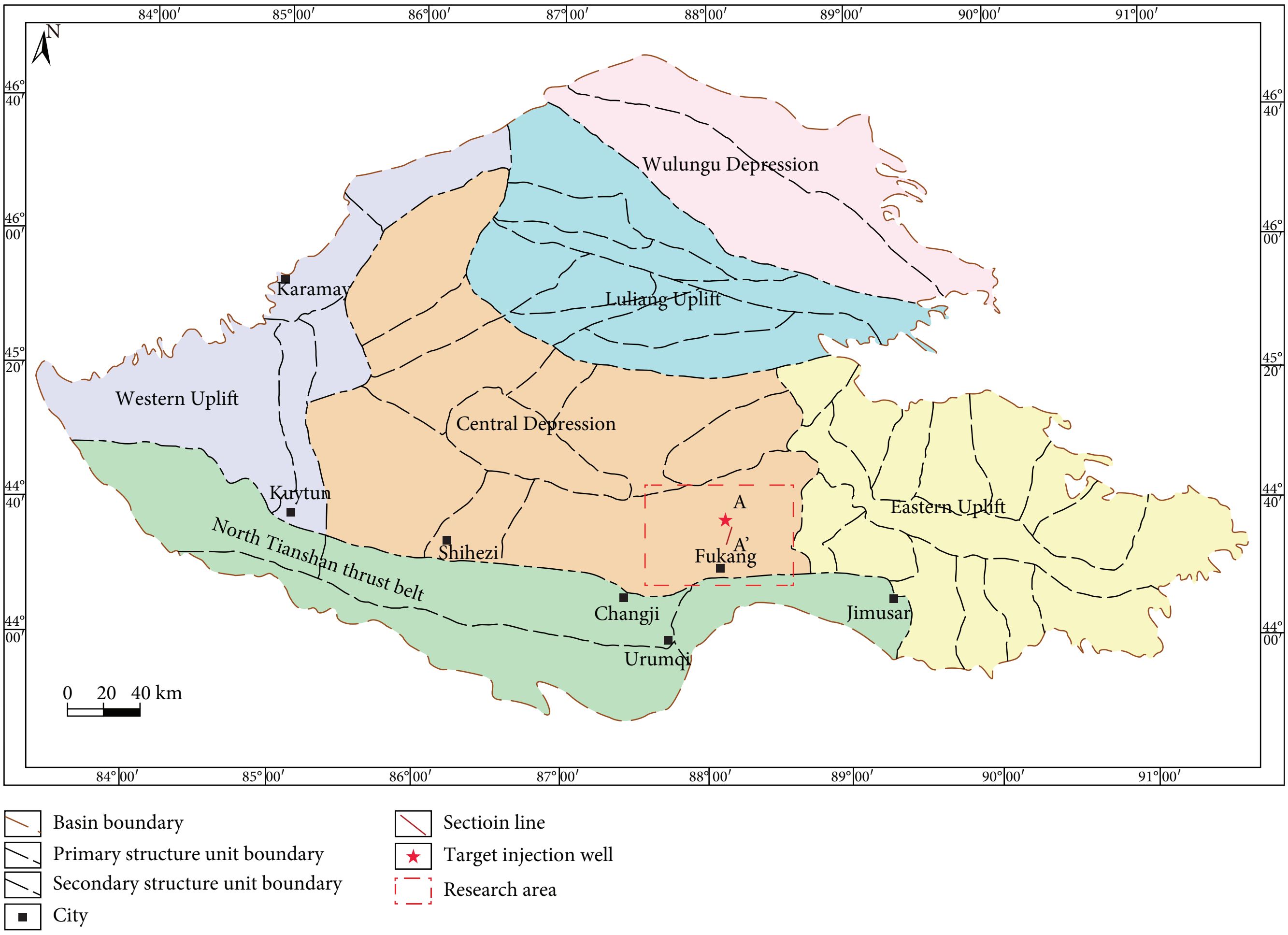

Figure 1: Division of the tectonic units in the Junggar Basin [22, 23].

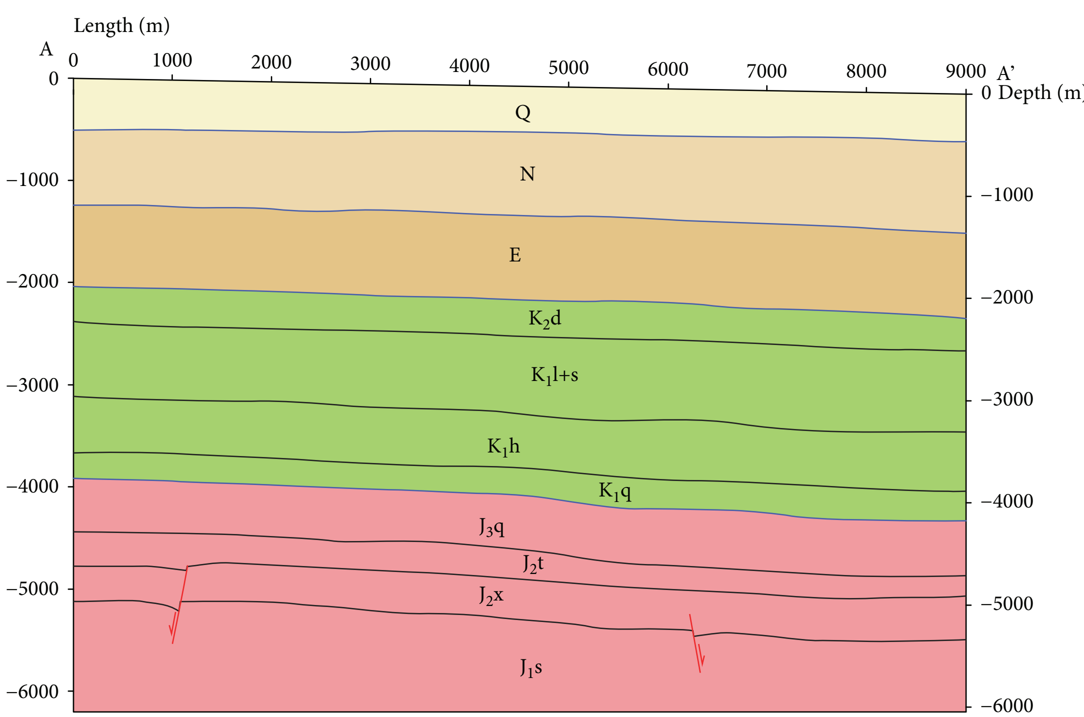

Figure 2: Geological profile near the target injection well (see the location of the profile in Figure 1).

Era	System	Series	Formation	Thickness (m)	Column	Lithological description
Cenozoic	Quaternary	—	(Q)	350		Gray, light-yellow, earthy-yellow quartz sand, with minor clay
	Neogene	—	(N)	1055		Grayish-yellow mudstone and siltstone
	Paleocene	—	(E)	525		Brown-red, taupe argillite and siltstone
Mesozoic	Cretaceous	Upper	Donggou (K_2d)	356		Brown-red, mauve mudstone with siltstone
		Lower	Lianmuqin + Shengjinkou (K_1l+s)	729		Brown-red, mauve mudstone, and gray muddy siltstone
			Hutubi (K_1h)	573		Brown mudstone, sandy mudstone, and gray siltstone
			Qingshuihe (K_1q)	288		Brown mudstone and gray fine sandstone
	Jurassic	Upper	Qigu (J_3q)	418		Maroon mudstone and siltstone
		Middle	Toutunhe (J_2t)	296		Gray mudstone and gray siltstone
			Xishanyao (J_2x)	377		Dark-gray mudstone with grey siltstone and black coal seam
		Lower	Sangonghe (J_1s)	438		Dark-gray sandy mudstone, and gray pebbly sandstone

Figure 3: Lithological column of the target injection well.

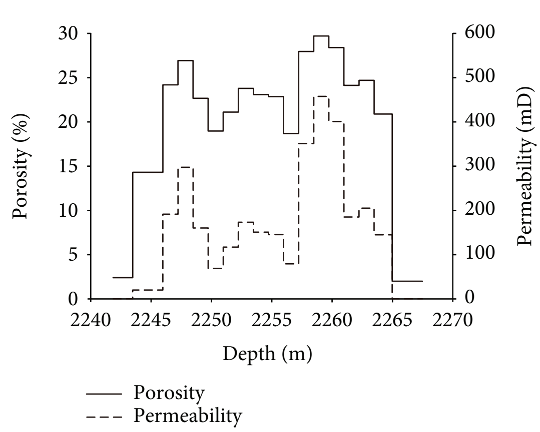

Figure 4: Porosity and permeability of the reservoir strata.

existing underground development activities resulting from the pressure-induced leakage of CO_2 and salt water [13–15].

Nicot [16] studied large CO_2 injections into aquifers along the coast of the Gulf of Mexico. They found that an amount equivalent to 50 million tons of CO_2 per year for 50 years resulted in an average water table rise of 1 m. In a study on CO_2 injection in the Illinois Basin, Birkholzer and Zhou [17] demonstrated that multiple-site storage in the Mount Simon Sandstone would result in a large continuous overpressurized region. With respect to far-field impacts, pressure changes may propagate as far as 200 km from the core injection area hosting the 20 storage sites. Zhao et al. [18] simulated the use of 20 wells in the Songliao Basin to continuously inject CO_2 at different rates. After 50 years, the formation pressure increased by 8.62 MPa. Yamamoto et al. [19] simulated the impact of industrial-scale perfusion of CO_2 in Tokyo Bay, Japan, on pressure increase and

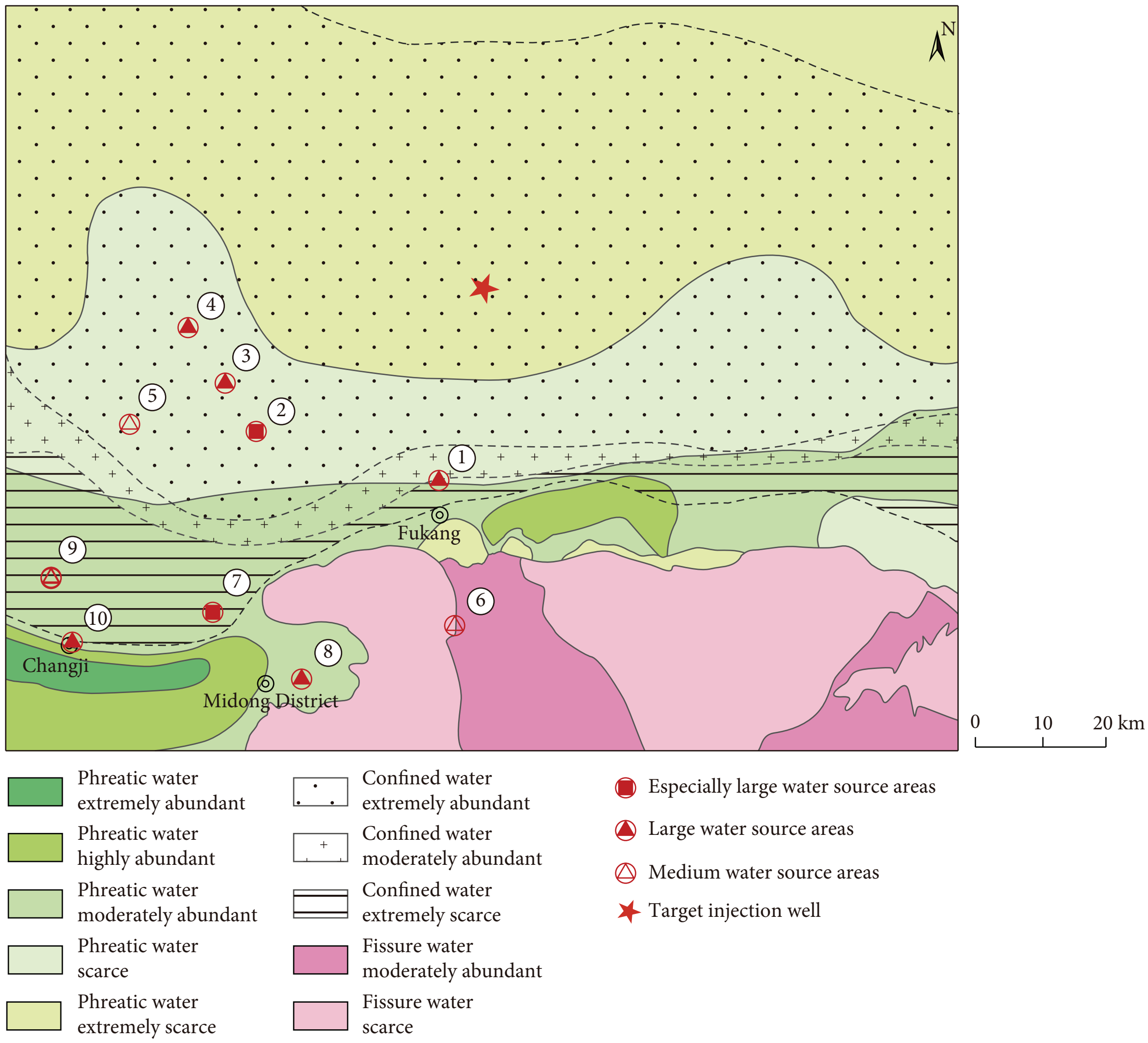

Figure 5: Hydrogeological conditions and distribution of groundwater sources in the study area.

groundwater relocation using 10 injection wells and the injection of 100 million tons per year for 100 years, which caused CO_2 plumes to spread for several kilometers. Birkholzer et al. [17, 20] argued that numerical simulations of large industrial-scale carbon capture and storage (CCS) projects show that pressure changes caused by CO_2 injection may spread far within a CO_2 reservoir and may even affect the entire reservoir and basin.

The availability of water resources seriously affects the economic development and ecological environment in the southern part of the Junggar Basin. The implementation of the CCS demonstration project located to the north of Fukang will affect the water quality and hydrodynamic field of the groundwater. In this paper, the influence of CO_2 injection on the reservoir pressure field is systematically explored through numerical simulation by TOUGH2-ECO2N to analyze the impact of the CO_2 injection on the deep reservoir pressure field and the possible influence on the surrounding shallow groundwater sources. The impact of large-scale CO_2 injection on groundwater development and the shallow surrounding water sources was analyzed under conditions of different numbers of injection wells. This study provides a basis for the CO_2 geological storage project and safety of groundwater sources in the Junggar Basin.

2. Geological Characteristics of the Study Area

The Junggar Basin is located in the northern Xinjiang Uygur Autonomous Region in China. This basin is the second largest inland basin in China, with a total area of approximately 135000 km^2. According to the late Paleozoic tectonic characteristics, the Junggar Basin is divided into six first-order tectonic units, namely, the Wulungu Depression, Luliang Uplift, Western Uplift, Central Depression, Eastern Uplift, and North Tian Shan thrust belt, and 44 secondary tectonic units. The division of tectonic units in the Junggar Basin is shown in Figure 1. The Junggar Basin is an important energy base in China and is rich in coal, oil, natural gas, and other resources. The northern slope of the Tian Shan Mountains in the southern part of the basin is one of the most developed regions in Xinjiang, China. The basin is one of the key areas for the development of western China.

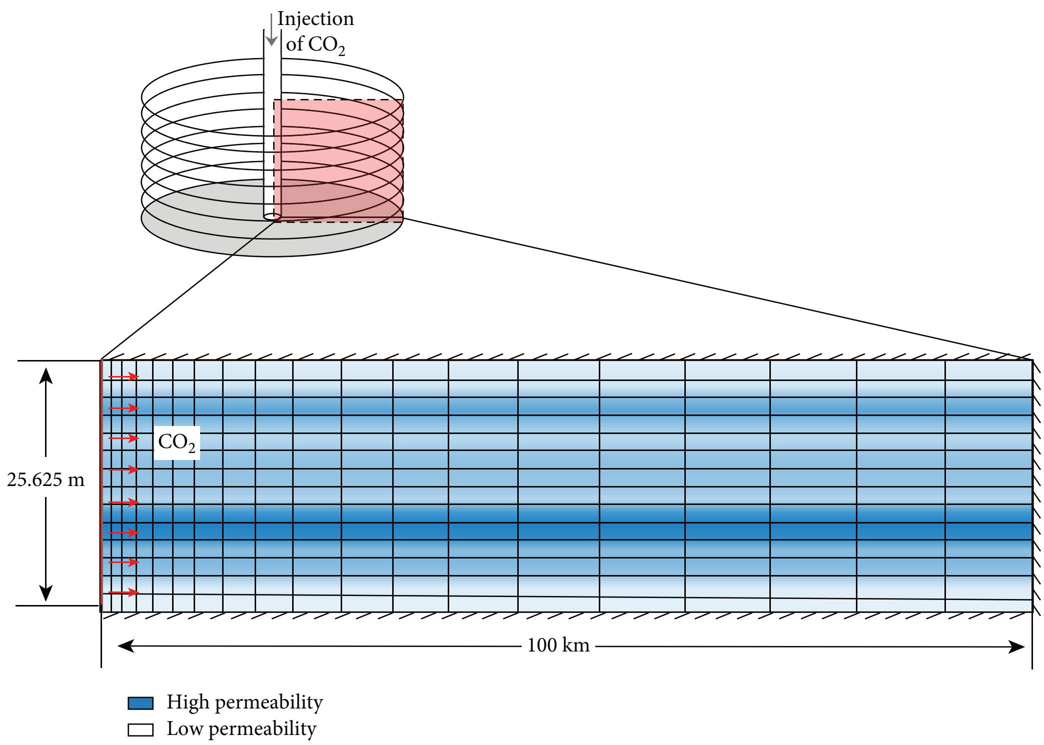

FIGURE 6: Schematic diagram of the radial model for CO_2 injection.

83% of the heavy industry and 62% of the light industry of Xinjiang are concentrated in this region. A large number of coal-fired power plants, steel mills, and coal-based chemical industries are located in Xinjiang and are the major sources of CO_2 emissions [21].

The study area is the CO_2-enhanced saline water recovery demonstration site in the eastern part of the Junggar Basin, located on the northern side of the Tian Shan Mountains and approximately 30 km from Fukang, as shown in Figure 1. The geological structure is located in the northeastern Fukang Depression. The sedimentary strata, similar to those throughout the entire basin, experienced various tectonic events from the late Paleozoic to the Quaternary related to the Hercynian, Indosinian, Yanshanian, and Himalayan orogenies. The geological section of the study area near the injection well is shown in Figure 2, and a stratigraphic column of the target injection well is shown in Figure 3. The target layer in this study is the Cretaceous Donggou Formation (K_2d).

According to the porosity and permeability test data from the target injection well, the relatively high-porosity and high-permeability Donggou Formation was selected as the target reservoir in this study. Above and below the target reservoir, there are formations with low porosity and permeability values to act as the caprocks. The burial depth range of the target strata is determined based on the data from the target well at the demonstration site, which is shown in Figure 4.

The groundwater sources in the study area are located at the southern edge of the Junggar Basin and the northern foot of the Tian Shan Mountains. With economic development, the demand for water resources is increasing. The development and utilization of groundwater have greatly increased. In the south and west of the study area, there are several large water sources. Water source #1 in the south of the study area is the closest one to the injection well, with a distance of approximately 25 km. The distances between the injection well and sources #2, #3, and #4 to the southwest are all approximately 35 km. The groundwater sources extract water from the Quaternary pore aquifer system and shallow bedrock-confined aquifers [24] (Figure 5). With the increase in the amount of groundwater development, the groundwater environment is constantly deteriorating. This situation has led to a series of ecological and environmental problems, such as groundwater overexploitation, vegetation degradation, water quality deterioration, and desertification. The exploitation and protection of groundwater are of great significance to the lives and economic development of the local people. With the implementation of the CO_2 geological storage project located to the northeast of the groundwater source area, CO_2 will migrate to the surrounding area from the injection wells. Although the existing groundwater sources are about 30 km away from the injection well and the vertical distance between the water source-extracted aquifer and the deep reservoir is about 1600 m, there still is the possibility that the groundwater sources are impacted by the injection project for their location near the Tian Shan piedmont fault zone. According to the early geological survey, the scale of the faults is large. The possible impact of the deep reservoir on the shallow aquifer system is from the large faults which might cut through different strata. When the pressure field of the deep reservoir has a significant change, it might affect the shallow groundwater source

(a) (b)

(c)

Figure 7: Rock samples from the Donggou Formation for parameter testing.

Table 1: Parameters of rock used in the model.

Parameter	Value
Rock density	2600 kg/m^3
Thermal conductivity	2.51 W/m·°C
Rock grain specific heat	920 J/kg·°C
Aquifer initial pressure	22.50 MPa
Aquifer initial temperature	63.0°C
Total dissolved solids (TDS)	43223.05 mg/L

safety by the possible connection via the faults. There is a risk of CO_2 entering the groundwater sources and contaminating the groundwater. Once CO_2 enters the water sources, serious consequences may occur, such as the acidification of the groundwater and the release of heavy metal elements into the aquifer. Additionally, the impact of large-

Table 2: Definitions for parameters.

Parameter	Definition	Value
k_{rl}	Liquid relative permeability	Equation (1)
S_l	Liquid saturation	—
S_{lr}	Residual liquid saturation	0.30
m	Empirical coefficient	0.457
S_{ls}	Maximum liquid saturation	0.90
k_{rg}	Gas relative permeability	Equation (3)
S_{gr}	Residual gas saturation	0.05
P_{cap}	Capillary pressure	Equation (5)
P_0	Breakthrough pressure	19.61 kPa
λ	Empirical coefficient	0.457

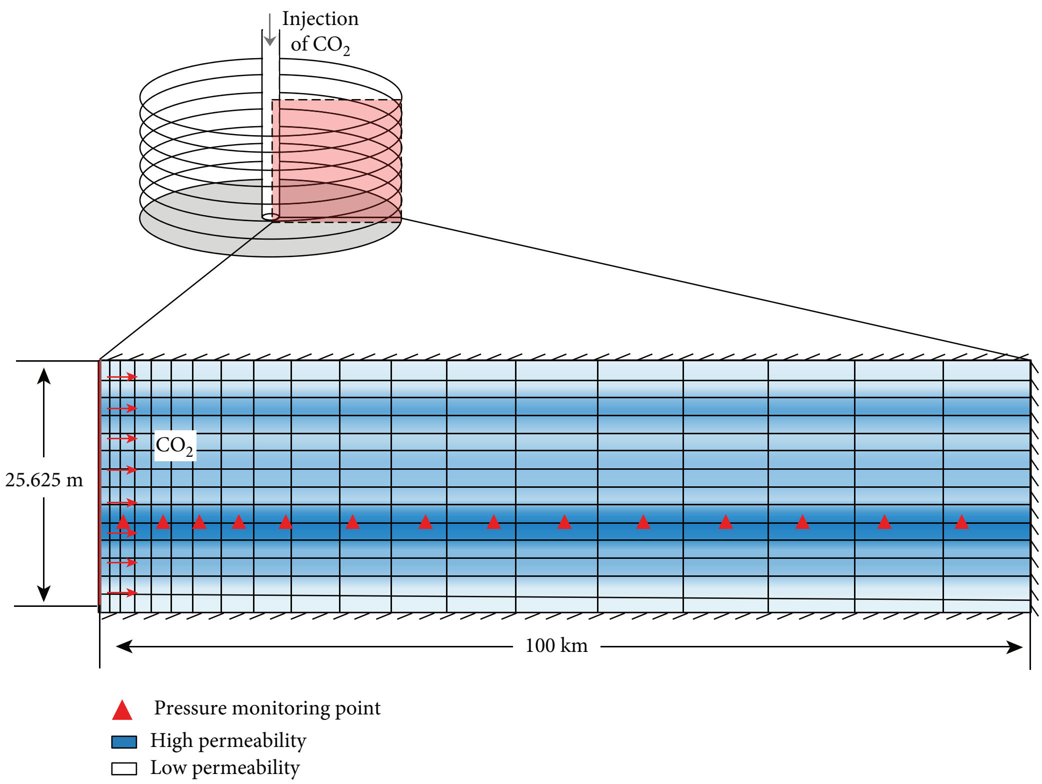

Figure 8: Positions of the pressure monitoring points in the radial model.

scale CO_2 injection on the reservoir pressure field may also lead to changes in the hydrodynamic field of the aquifer associated to the water sources, which could cause groundwater safety problems.

The target reservoir in the Donggou Formation is distributed across the entire study area. The formation is gently undulating and has an inclination of approximately 0° to 3°. The formation is shallower in the northeast and deeper in the southwest. This formation unconformably overlies the Cretaceous Lianmuqin and Shengjinkou Formations. This formation was deposited in a river delta sedimentary environment. The lithology is interbedded sandstone and mudstone. This study selected one of the perforation sections of the Donggou Formation reservoir with a burial depth of 2241.855-2267.48 m. The thickness of this section is 25.625 m. According to the actual measured value in the target injection well, the temperature at the bottom of the reservoir is 63.0°C and the initial pressure is 22.50 MPa.

3. Numerical Simulation Study

In CO_2 geological storage projects, the injection of CO_2 into deep saline aquifers causes the pressure in the reservoir to rise [16, 18, 20, 25]. In the numerical simulation study of geological fluid diffusion in complex geological structures, a complex 3D geological model is generally established to more scientifically represent practical problems. However, as the scale of the 3D simulation model increases, the computing time increases significantly. Therefore, in the actual simulation, the scientific and reasonable selection of the model scale is an important issue. In the case of CO_2 injection, the basin boundary is characterized as infinite relative to the CO_2 injection. In the actual construction of numerical models, it is unrealistic to set infinite boundary conditions for numerical models from the viewpoint of computing time and modeling methods. Therefore, considering actual geological conditions, it is very important to determine a reasonable model scale for simulation accuracy and computational efficiency.

When CO_2 is injected into the reservoir, the pressure field will transmit mainly in the reservoir. According to the geological conditions in the study area, there is a fault zone near the existing shallow groundwater sources on the south of the target injection well. In order to explore the influence range of CO_2 injection on the reservoir pressure field in the horizontal direction and analyze the possible pressure increase in the deep reservoir in the distance of the area where the fault zone exists, a radial model with a radius of 100 km was set up. The purpose of using 100 km as the model radius is to ensure the fault zone is within the simulated area.

3.1. Exploration of the Boundary of Models. In this study, based on the geological conditions of the target reservoirs at the demonstration site, the extent and intensity of the influence of CO_2 injection on the reservoir pressure field are explored through a radial flow model. This exploration lays the foundation for the model scale and boundary setting in the construction of 3D models.

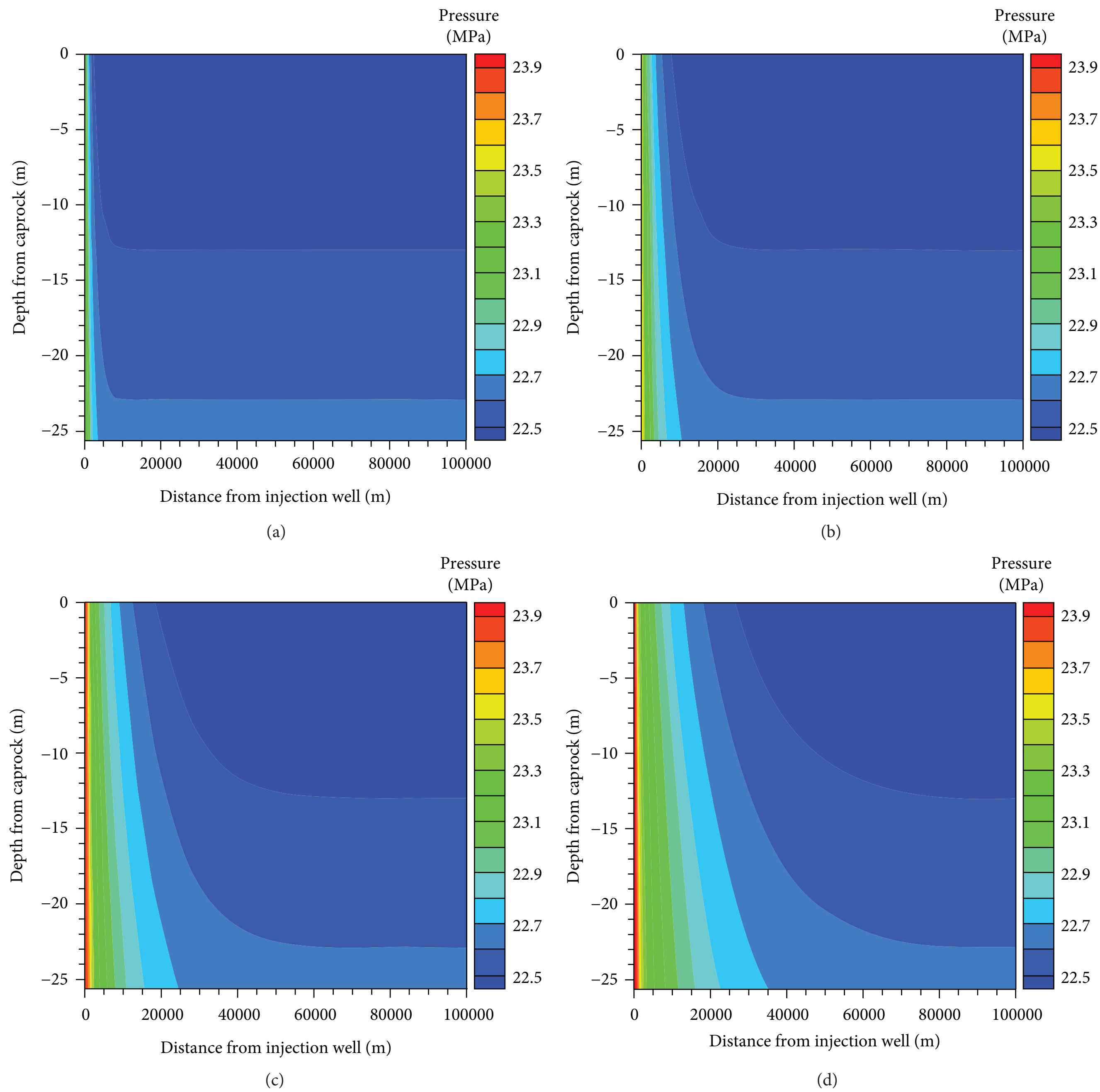

FIGURE 9: Evolution of the reservoir pressure field during injection in the radial model.

The simulations were carried out using the TOUGH2-MP/ECO2N code, the parallel version of TOUGH2 with the fluid property module ECO2N, which describes the nonisothermal flow of multiphase and multicomponent fluids in porous or faulted geologic media. ECO2N is a fluid property module for the TOUGH2 simulator (version 2.0) that was designed for applications for geologic sequestration of CO_2 in saline aquifers [26]. This module includes a comprehensive description of the thermodynamics and thermophysical properties of H_2O–NaCl–CO_2 mixtures and reproduces fluid properties largely within the experimental error for the temperature, pressure, and salinity conditions of interest ($10^\circ C \leq T \leq 110^\circ C$, $P \leq 60$ MPa; and salinity up to full halite saturation).

3.1.1. Design of the Radial Model for Exploring Model Boundaries. To explore the range of the influence of CO_2 injection on the reservoir pressure field, a radial model of the deep saline aquifer is established according to the geological conditions of the target reservoir. The radial length of the model is 100 km, which is divided into 84 grids by means of unequal splitting. The vertical thickness of the reservoir is 25.625 m, which is divided into 18 layers according to porosity and permeability conditions. The radial model is shown in Figure 6.

Because of the very low porosity and low permeability of the formations at the top and bottom of this target reservoir, both the top boundary and bottom boundary of the model are set as impermeable barriers. To explore the influence of CO_2 injection on the reservoir pressure field in the process of CO_2 geological storage, the lateral boundary of the model is also set as a barrier.

The injection well penetrates the entire reservoir. Considering reservoir safety and injection efficiency, the pressure in the injection well is 1.3 times the original pressure in the reservoir. The injection time is set to 10 years according to the plan of the demonstration project. The total simulation time is 100 years based on previous research.

3.1.2. Model Parameters. According to the geological conditions of the site, the formation is generalized into horizontally isotropic sandstone formations. The reservoir was treated as a porous medium. Each grid block is specified with the following parameters: absolute permeability, porosity, rock density, thermal conductivity, and specific heat capacity, as well as the relative permeability and capillary pressure relationships [27]. The reservoir is a saline aquifer, and the concentration of total dissolved solids (TDS) in the groundwater is 43223.05 mg/L based on the analysis results of the actual reservoir groundwater. The initial temperature and the initial pressure of the reservoir are determined based on the actual measured value in the injection well. The rock density, thermal conductivity, and rock grain-specific heat are determined according to the rock test results from the target reservoir (Figure 7) and empirical parameters. The detailed parameters of the model are summarized in Table 1.

Relative permeability and capillary pressure are important physical parameters in the multiphase fluid seepage process. The definitions and values of the parameters are listed in Table 2.

The relative permeability of the liquid phase is calculated using the van Genuchten-Mualem relationship [28]:

$$k_{rl} = \sqrt{S^*}\left(1 - \left(1 - \left(S^*\right)^{1/m}\right)^{m}\right)^{2}, \tag{1}$$

$$S^* = \frac{S_l - S_{lr}}{S_{ls} - S_{lr}}. \tag{2}$$

To calculate the relative permeability for gas, the Corey function is used [29]:

$$k_{rg} = {}^{2}\left(1 - S\wedge^{2}\right), \tag{3}$$

$$\hat{S} = \frac{S_l - S_{lr}}{1 - S_{lr} - S_{gr}}. \tag{4}$$

The capillary pressure is calculated using the van Genuchten function:

$$P_{\text{cap}} = -P_0\left(\left[S^*\right]^{-1/m} - 1\right)^{1-m} \tag{5}$$

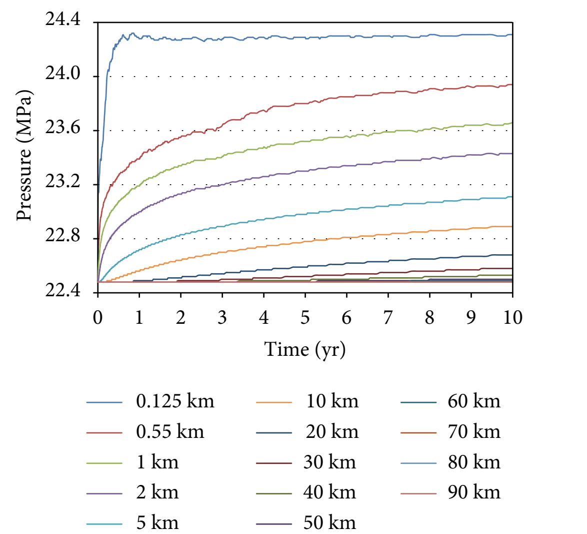

Figure 10: Pressure changes at pressure monitoring points during injection.

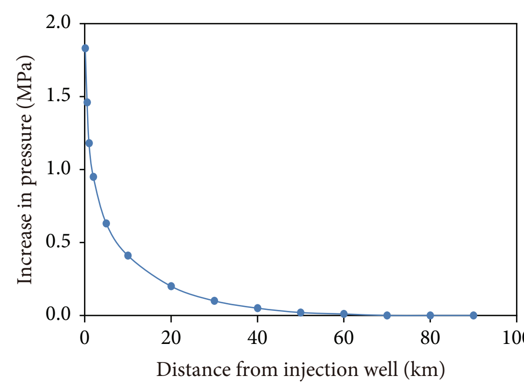

Figure 11: Pressure increases at the monitoring points during injection in the 10th year.

3.1.3. Pressure Monitoring Points in the Reservoir. To monitor the influence of CO_2 injection on the reservoir pressure field and provide a basis for setting the 3D model, the pressure monitoring points are placed at positions 0.125 km, 0.55 km, 1 km, 2 km, 5 km, 10 km, 20 km, 30 km, 40 km, 50 km, 60 km, 70 km, 80 km, and 90 km from the injection well, as shown in Figure 8. High-porosity and high-permeability formations are conducive to pressure field diffusion and CO_2 diffusion. To fully monitor the influence on the pressure field, the monitoring points are set at locations within the reservoir with high-porosity and high-permeability conditions, that is, at $Z = -18$ m below the reservoir caprock.

3.1.4. Evolution of the Pressure Field in the Reservoir. According to the evolution of the pressure field during the CO_2 injection process (Figure 9), the reservoir pressure continuously increases during CO_2 injection. The high-pressure zone is rapidly transferred from the injection well to surrounding areas within the reservoir. The range of influence continuously expands.

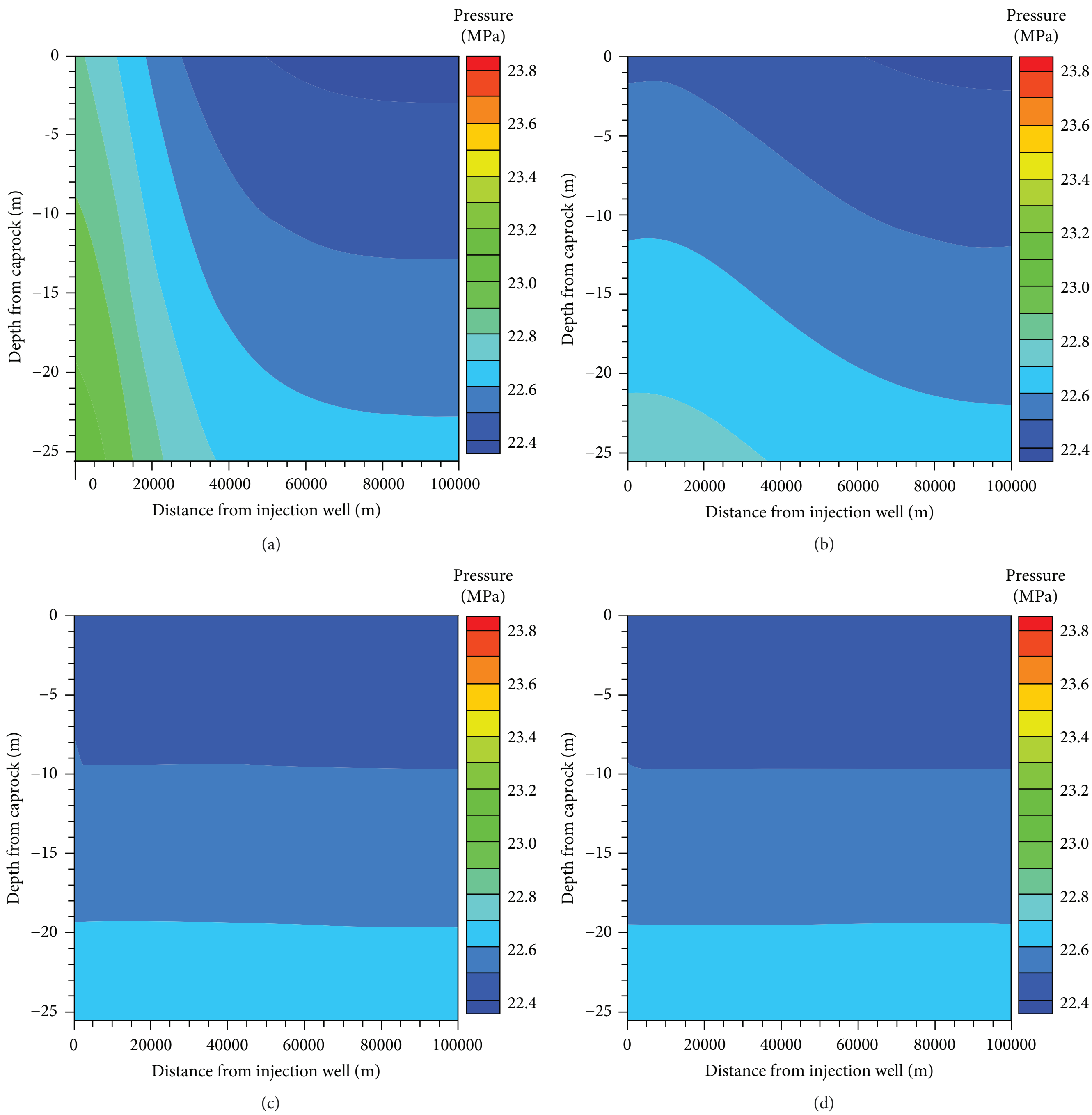

Figure 12: Evolution of the reservoir pressure field after the cessation of CO_2 injection.

The pressure changes at each pressure monitoring point (Figure 10) show that the closer the monitoring point is to the injection well, the more the pressure increases. At the same time, as the injection process progresses, the pressure at each monitoring point gradually stabilizes. The closer the monitoring point is to the injection well, the shorter the stabilization time is. At the pressure monitoring point 125 m from the injection well, after one year of injection, the pressure at this point no longer changes, stabilizing at approximately 24.30 MPa, and the reservoir pressure increase is 1.83 MPa. At the pressure monitoring point 1 km from the injection well, the reservoir pressure basically stabilizes after 9 years of injection and the reservoir pressure increase is 1.18 MPa. Compared to the pressure at the 125 m monitoring point, the pressure at the 1 km monitoring point takes longer to stabilize and the pressure increase is significantly less at the 1 km monitoring point than that at the 125 m monitoring point.

Comparing the pressure at the end of injection in the 10th year at different monitoring points with the initial pressure before the injection, the increases in pressure at different monitoring points can be obtained, as shown in Figure 11.

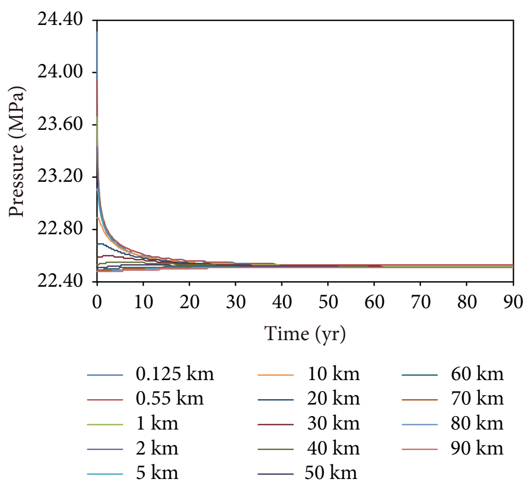

Figure 13: Pressure changes at pressure monitoring points after the cessation of CO_2 injection.

According to the pressure changes, as the distance between the monitoring point and the injection well increases, the pressure change rapidly decreases. Moreover, as the distance from the injection well increases, the pressure change rapidly decreases. At a distance of 0.125 km from the injection well, the pressure increase is as high as 1.83 MPa, while at a distance of 30 km from the injection well, the pressure increase is only 0.1 MPa. In formations more than 50 km from the injection well, there is virtually no change in formation pressure.

According to the change in the reservoir pressure field after the cessation of CO_2 injection (Figure 12), the accumulated pressure gradually dissipates after the CO_2 injection stops. After a certain period of time, the reservoir pressure gradually returns to the initial pressure.

After the CO_2 injection stops, the pressure at each pressure monitoring point changes, as shown in Figure 13. As seen in the figure, for 10 years after the cessation of CO_2 injection, the reservoir pressure decreases. After 30 years following the cessation of CO_2 injection, the formation pressure gradually returns to the initial formation pressure of approximately 22.50 MPa.

3.1.5. Diffusion and Distribution of CO_2 in the Reservoir. The CO_2 diffusion and distribution patterns during the injection process (Figure 14) reveal that after CO_2 is injected into the reservoir, lateral and vertical diffusion occurs under the combined action of gravity and buoyancy. When the injection stops, the maximum lateral diffusion distance of CO_2 is 1099 m.

The CO_2 distribution after the cessation of CO_2 injection is shown in Figure 15. CO_2 continues to undergo lateral and vertical diffusion under the combined effects of gravity and buoyancy. However, the pressure in the reservoir rapidly decreases. The pressure field in the reservoir gradually returns to its original state. The pressure difference at different positions driving CO_2 diffusion is also rapidly reduced. Therefore, the CO_2 diffusion rate declines significantly. After the injection stops, the CO_2 distribution does not change significantly. After 90 years following the cessation of the injection, the maximum CO_2 diffusion distance is 1329 m.

3.2. 3D Numerical Model of the Influence of CO_2 Injection on the Reservoir Pressure Field

3.2.1. Design of Models. Because the radial flow model simulation cannot simulate the evolution of the pressure field under the conditions of multiple injection wells, a 3D model for CO_2 injection into the Donggou Formation reservoir is constructed. The simulations were also carried out using the TOUGH2-MP/ECO2N code.

Although the influence distance of the injection reaches 50 km in the radial model, the pressure change is small. Even at a distance of 30 km from the injection well, the pressure change is only 0.1 MPa. Moreover, considering the distance between the injection well and the water source, the distance from the injection well to the model boundary is set to 30 km in the 3D model. The numerical model is set to 30 km in the X direction, 64 km in the Y direction, and 25.625 m in vertical thickness.

In the 1-well injection model (Figure 16), there are 27 layers in the X direction, 69 layers in the Y direction, and 18 layers in the vertical direction. In the injection model with two wells (Figure 17), there are 27 layers in the X direction, 70 layers in the Y direction, and 18 layers in the vertical direction. In the injection model with three wells (Figure 18), there are 27 layers in the X direction, 71 layers in the Y direction, and 18 layers in the vertical direction.

The top and bottom plates of the model are both water-resistant boundaries. The side boundaries on one side of the well are zero-flow boundaries. The three side boundaries without wells are constant-pressure boundaries. Combining the CO_2 diffusion distance and distribution in the CO_2 injection simulation of the target reservoir in the Donggou Formation, the injection well spacing is set to 2 km in the 2-well and 3-well models.

The porosity, permeability, temperature, and pressure of each reservoir in the model are the actual measured values from the target injection well and are the same as those used in the radial model. The values of the rock density, thermal conductivity, specific heat capacity, relative permeability, and capillary pressure in the model are also the same as those used in the radial model.

Each injection well penetrates the entire reservoir. The constant injection pressure mode is used, and the pressure in the injection well is 1.3 times the original pressure in the reservoir. The injection time is 10 years, and the total simulation time is 100 years.

3.2.2. Pressure Monitoring Points in the Reservoir. To monitor the influence of CO_2 injection on the reservoir pressure field, the pressure monitoring points are set at positions 0.6 km, 1.25 km, 3 km, 5.5 km, 11 km, 20 km, and 25 km from the injection well, as shown in Figure 19 in the 1-well model. High-porosity and high-permeability formations are conducive to pressure field diffusion and CO_2 diffusion. To fully monitor the influence on the pressure field, the monitoring points are set at locations within the reservoir with the

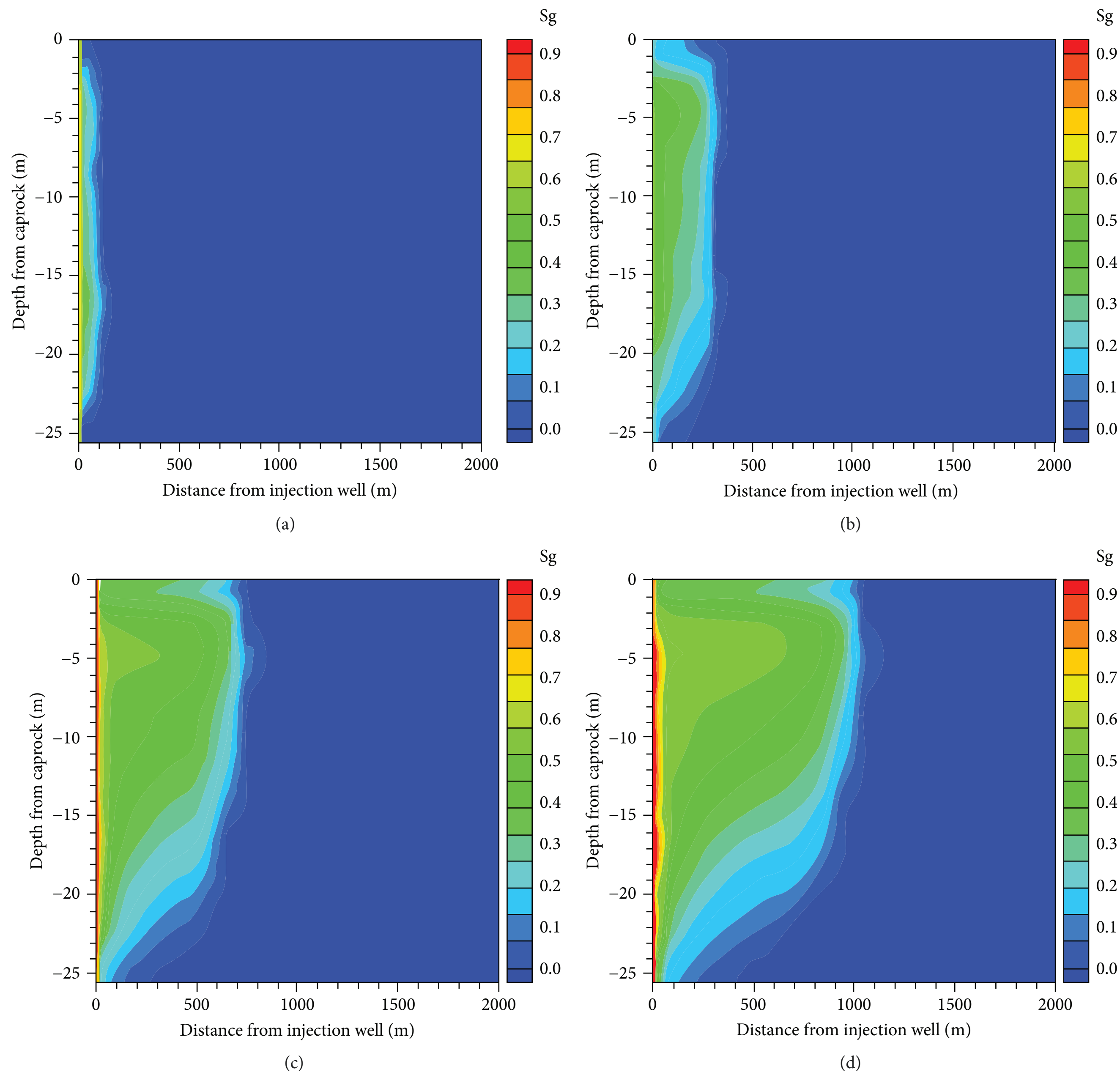

Figure 14: Spatial distributions of supercritical CO_2 during injection (Sg: gas saturation of CO_2).

highest porosity and permeability conditions, that is, at $Z = -18$ m below the reservoir caprock.

In the 1-well model, the pressure monitoring points are shown in Figure 19. In the 2-well model, the pressure monitoring points are divided into two rows, which extend away from vertical well 1 and from a point between the two wells. The monitoring points constitute two pressure monitoring lines, which are shown in Figure 20. In the 3-well model, the pressure monitoring points are also divided into two rows, which extend away from vertical wells 1 and 2 and form two pressure monitoring lines. The locations are shown in Figure 21.

3.2.3. Evolution of the Pressure Field during CO_2 Injection. The pressure changes in the reservoir are caused by the CO_2 injection. The injection rate of every model and the total injection amount for each injection model are shown in Figures 22 and 23. The total CO_2 injection rates were stable at 5.8, 9.6, and 12.4 kg/s to the single well, double wells, and three wells, respectively. During the 10-year injection period, the total injection amounts were 1.81, 3.05, and 3.98 million tons, respectively.

According to the simulation results, the pressure changes at the pressure monitoring points in the models with 1, 2, and 3 wells are shown in Figures 24–26. As with the radial model, there is a positive correlation between the pressure increment and the distance from the monitoring points to the injection well. At the same time, as the injection process progresses, the pressure at each monitoring point gradually stabilizes. At monitoring points

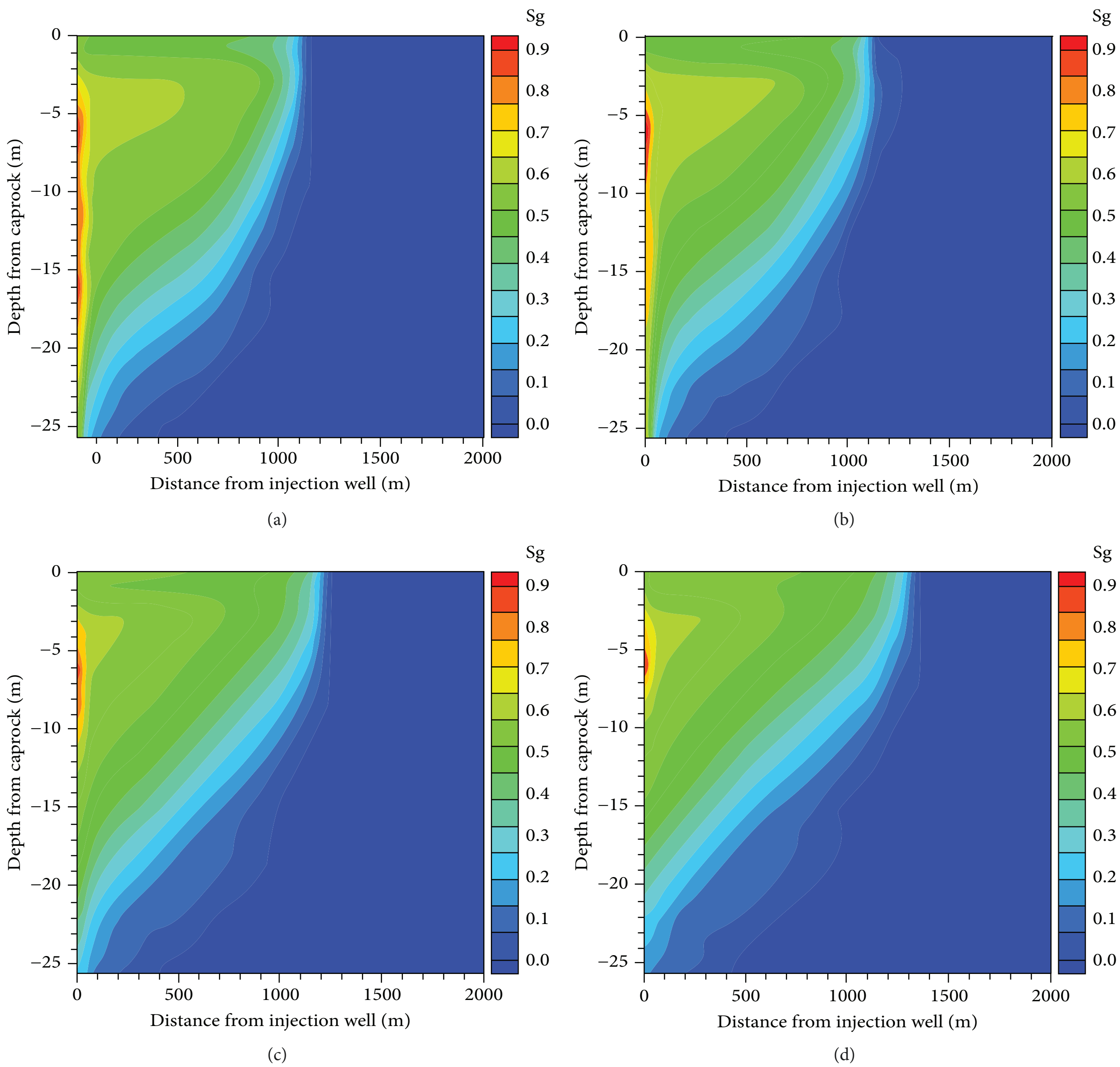

FIGURE 15: Spatial distributions of supercritical CO_2 after injection cessation (Sg: gas saturation of CO_2).

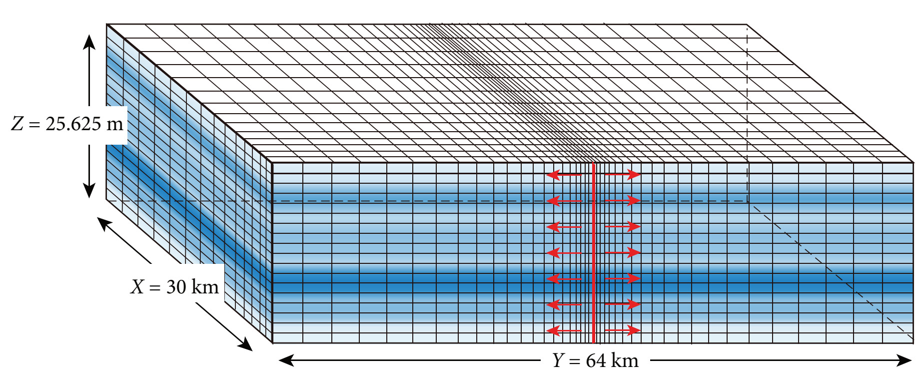

FIGURE 16: 3D model of one injection well.

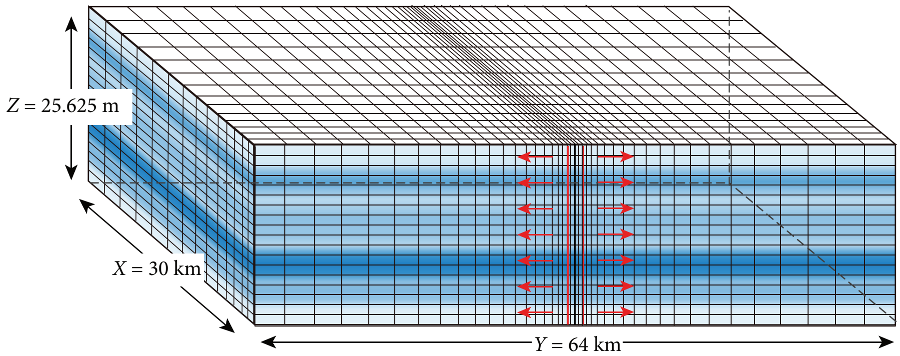

FIGURE 17: 3D model of 2 injection wells.

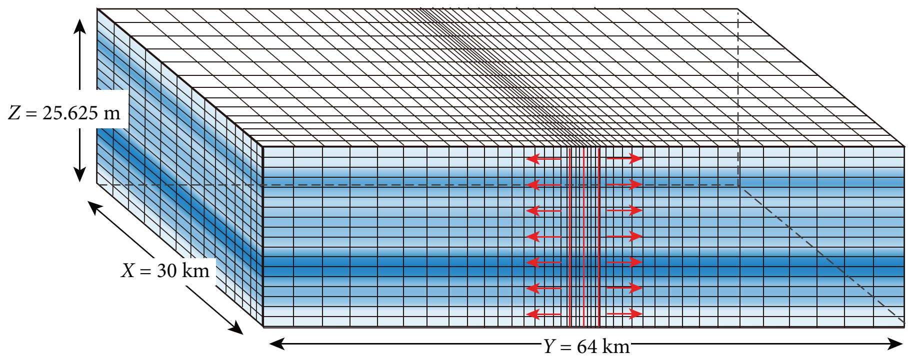

FIGURE 18: 3D model of 3 injection wells.

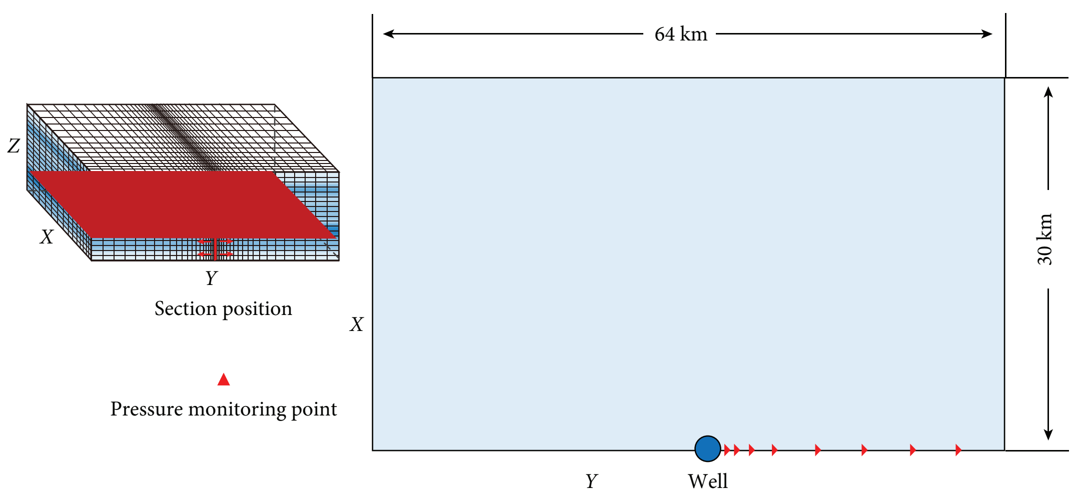

FIGURE 19: Locations of the pressure monitoring points in the 1-well model.

that are closer to the injection well, the pressure basically stabilizes over a shorter time.

To analyze the influence of CO_2 injection on the reservoir pressure field under the conditions of different numbers of injection wells, the effects of the number of injection wells on the pressure change are compared. In the 2-well and 3-well models, the degree of pressure change along the pressure monitoring line exhibits relatively large changes. The pressure changes at different distances from the injection well(s) for different numbers of injection wells are shown in Figure 27. The void space is constant for a fixed-volume reservoir. During the injection process, more injection wells can fill the pore space near the injection well at a faster rate and cause the pressure to increase faster than the circumstance with the lesser number of injection wells. And this makes the fluid move outward faster in the reservoir. Thus, more injection wells in operation simultaneously can produce more pressure buildup at the same time and the same location in the reservoir than a single-well injection.

Taking the change in the pressure field for the 1-well model as an example, the distribution of pressure changes at the pressure monitoring points demonstrates that the

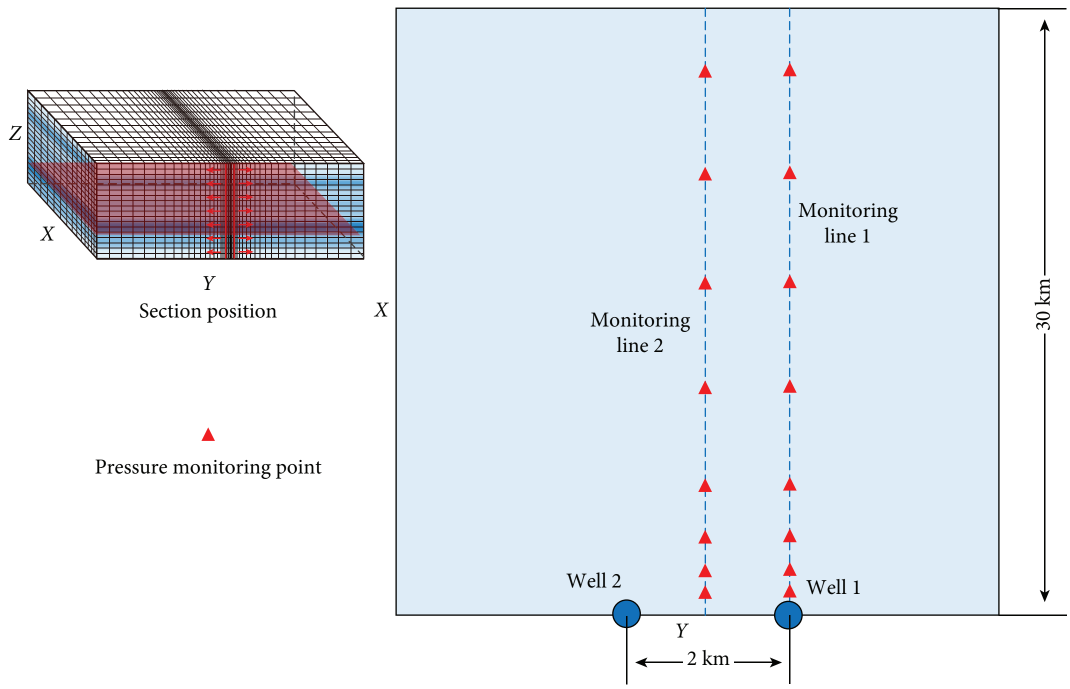

Figure 20: Positions of the pressure monitoring points in the 2-well model.

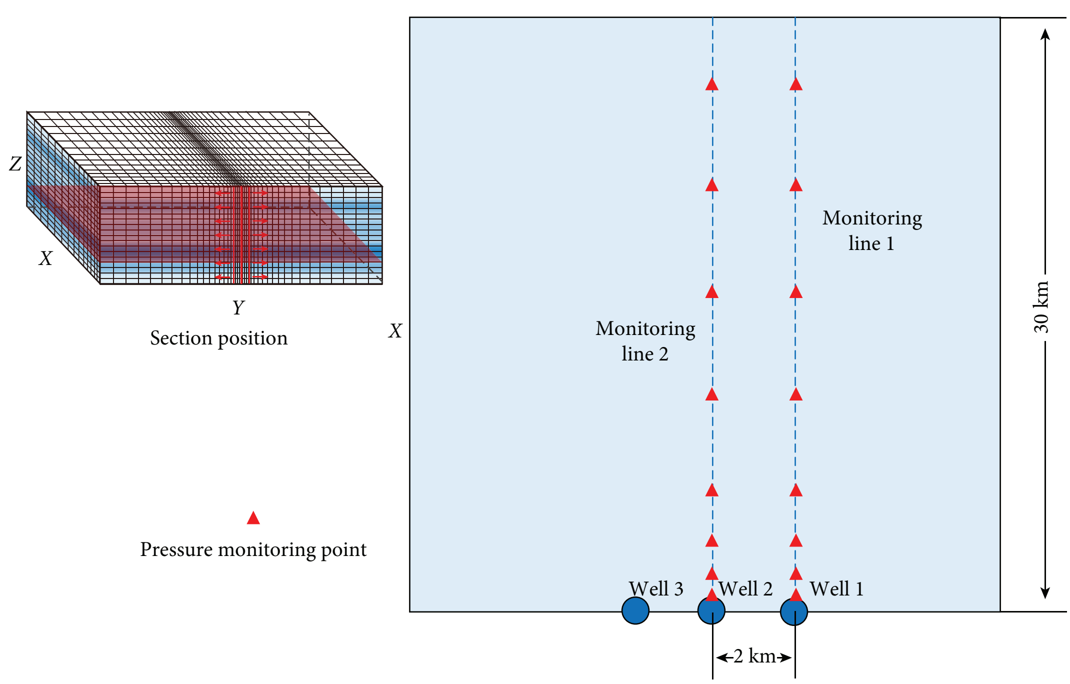

Figure 21: Positions of the pressure monitoring points in the 3-well model.

closer the monitoring point is to the injection well, the greater the pressure increase is. As the distance between the pressure monitoring point and the injection well increases, the pressure change rapidly decreases. At a distance of 0.6 km from the injection well, the pressure increase is as high as 1.1 MPa. However, at 25 km from the injection well, the pressure increase is only 0.03 MPa.

A comparison of the reservoir pressure changes for models with different numbers of injection wells shows that the number of injection wells has a significant effect on reservoir pressure changes. At a distance of 0.6 km from the injection well, the pressure increase in the 1-well model is 1.10 MPa. The pressure increments of the monitoring points at the same distance in the 2-well model and the 3-well model are 1.58 MPa and 2.11 MPa, which are 1.43 and 1.92 times the pressure increment in the 1-well model, respectively. At monitoring points at different distances from the injection well, the magnitude of the pressure change under Mitsui

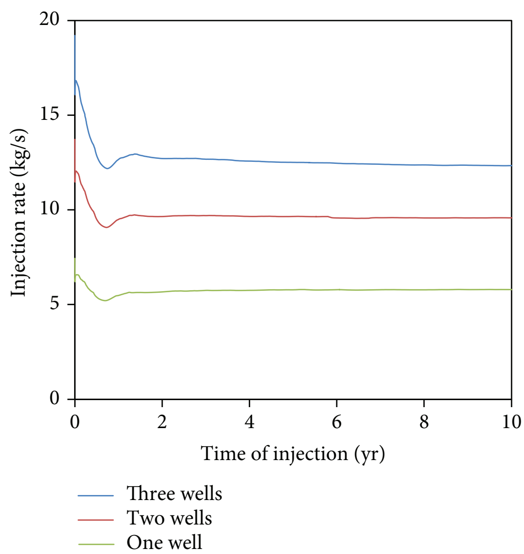

FIGURE 22: Injection rate of every model.

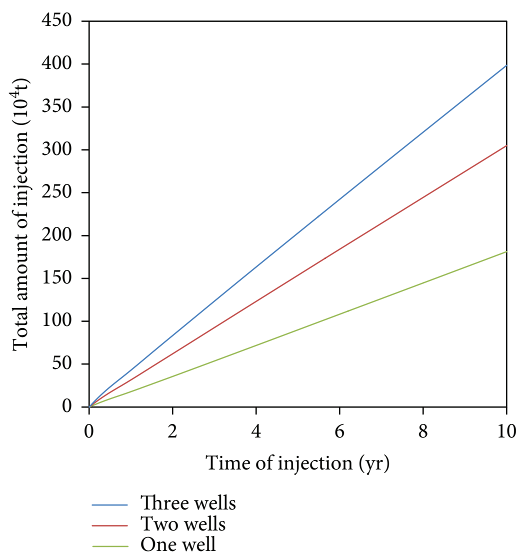

FIGURE 23: Total amount of CO_2 injected.

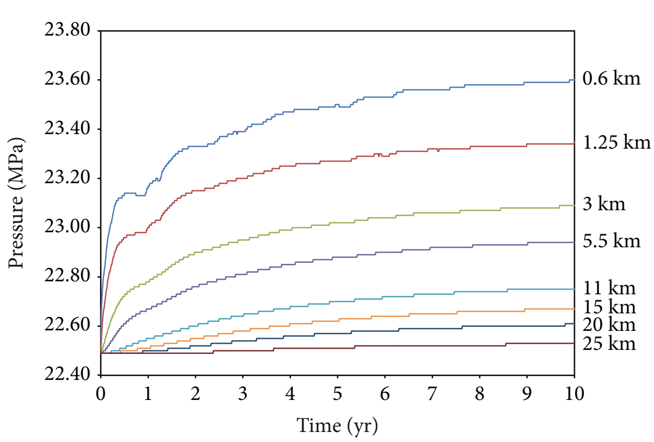

FIGURE 24: Pressure changes at the pressure monitoring points during injection in the 1-well model.

conditions can be two to three times more than that of the 1-well model. The more the injection wells, the more significant the impact on the reservoir pressure field is and the greater the pressure change is.

In the study of Zhao et al. [25], the authors injected CO_2 at a fixed rate method. Therefore, the reservoir pressure changes in this study are smaller than those of Zhao et al. The maximum pressure buildup in the formation ranges from 8.6 MPa to 9.3 MPa. However, the influence of CO_2 injection on the pressure field is not much different. Due to the longer simulation time studied by Zhao et al., the CO_2 diffusion distance in the reservoir is significantly larger than that in this study. The maximum-extent distance of the CO_2 plume from different injection wells is more than 4 km, which is mainly determined by the permeability and structure of the formation.

3.2.4. Evolution of the Pressure Field after Stopping CO_2 Injection. In the 1-well injection model, the changes in pressure at each pressure monitoring point after CO_2 injection cessation are shown in Figure 28. The pressure accumulated in the reservoir gradually dissipates after CO_2 injection cessation. After a certain period of time, the reservoir pressure field slowly returns to the initial pressure field state.

According to the pressure changes under the conditions of the 1-well model (Figure 28), 2-well model (Figure 29), and 3-well model (Figure 30), the reservoir pressure decreases rapidly after CO_2 injection ceases. By 10-15 years after the cessation of the injection process, the reservoir pressures in the different injection well models are restored to the initial reservoir pressure.

When the pressure change of the reservoir is less than 0.05 MPa (2‰ of the initial reservoir pressure), it is considered to return to the initial pressure state. Under such conditions, the time required for the pressure at monitoring points at different distances from the injection well to return to the initial pressure is shown in Table 3.

During the period after the injection ceases, regardless of the number of wells, the nearer area to the injection well, the longer time the needed to recover to the initial reservoir pressure and the shorter the recovery time needed for the far area. For example, to the single-well mode, the pressure recovery time at 0.6 km is 8.1 years and the pressure recovery time at 20 km is 5.4 years. This is mainly because there is more pressure accumulation in the near area to the injection well, and the pressure dissipation process is longer than that in the far area where the pressure accumulation is small.

At the same distance from the injection well, the time of pressure recovery is positively correlated with the number of injection wells. However, the difference in recovery time is not particularly obvious. For example, at a distance of 1.25 km from the injection well, reservoir pressure recovery time is 8.1 years (one injection well), 9.2 years (two injection wells), and 10.4 years (three injection wells), with a maximum difference of 2.3 years (Table 3).

After the 10 years of injection was ceased, the reservoir pressure basically returned to its initial pressure state. The CO_2 loses its drive force in the reservoir, and the storage mechanism gradually shifts to other mechanisms such as dissolved storage and mineral storage.

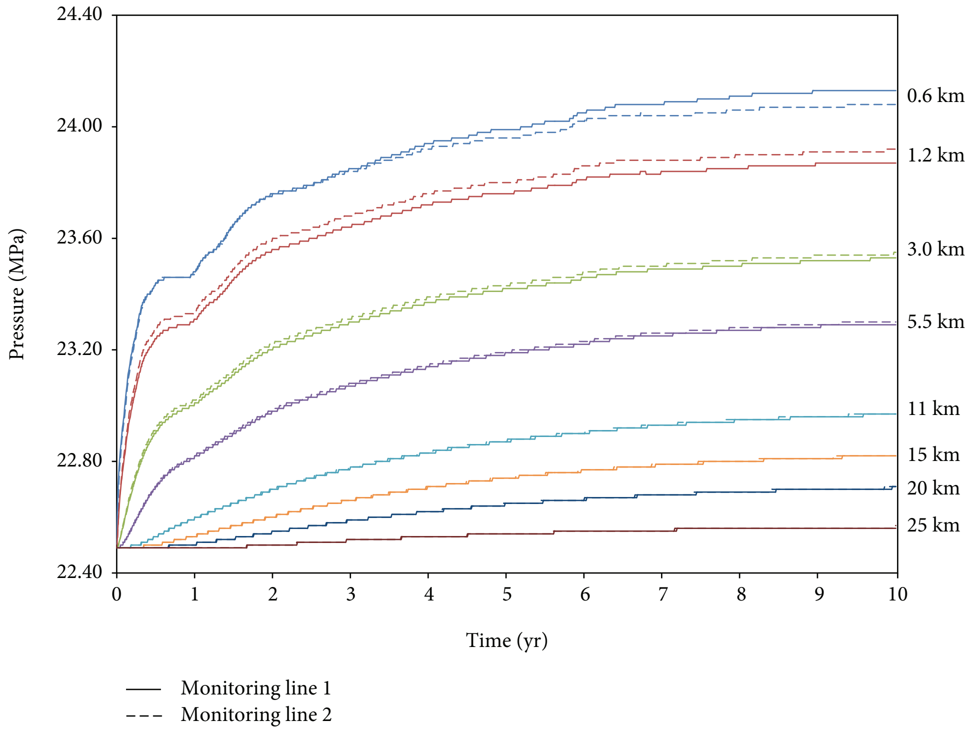

Figure 25: Pressure changes at the pressure monitoring points during injection in the 2-well model.

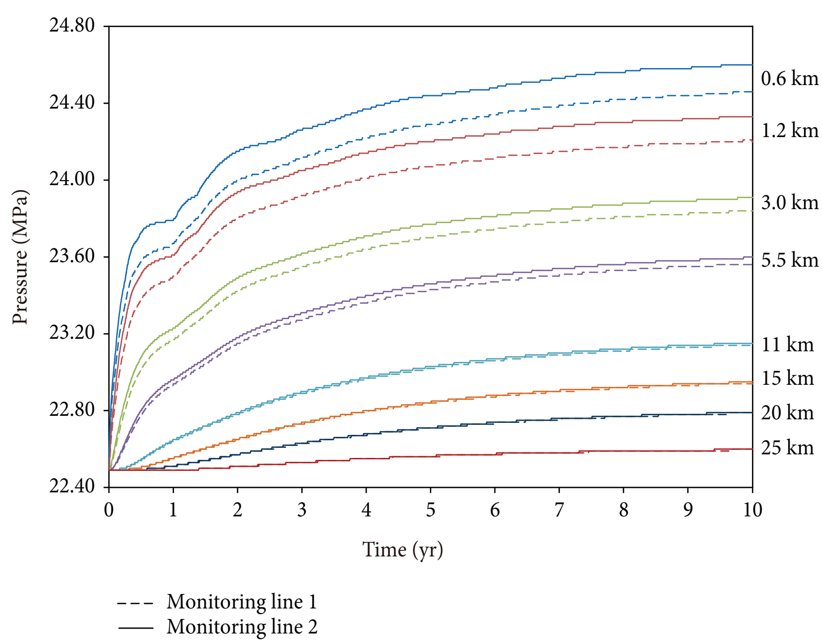

Figure 26: Pressure changes at the pressure monitoring points during injection in the 3-well model.

3.3. The Impact of CO_2 Injection on the Safety of Groundwater. In the radial model, after CO_2 is injected into the reservoir, gravity and buoyancy forces cause lateral and vertical CO_2 diffusion. However, under the injection pressure equivalent to 1.3 times the reservoir pressure, the maximum lateral diffusion distance of CO_2 is 1329 m after a simulation time of 100 years. Due to the small CO_2 diffusion distance, CO_2 cannot migrate to the groundwater source area near the study area, which is 25-40 km from the injection well. Therefore, CO_2 diffusion in the target reservoir will not affect the water quality of the water source.

The large-scale injection of CO_2, especially via multiple injection wells, has a larger effect on the pressure field in the reservoir than on the CO_2 diffusion distance. However, the effect of CO_2 injection on the pressure field is most evident in the regions close to the injection well. As the distance from

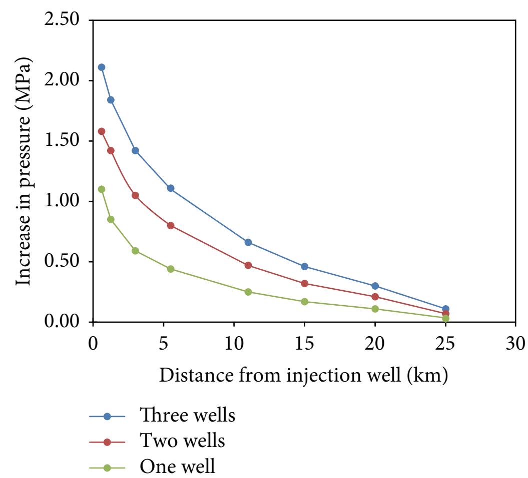

FIGURE 27: Pressure changes at the pressure monitoring points in models with different numbers of wells in the 10th year.

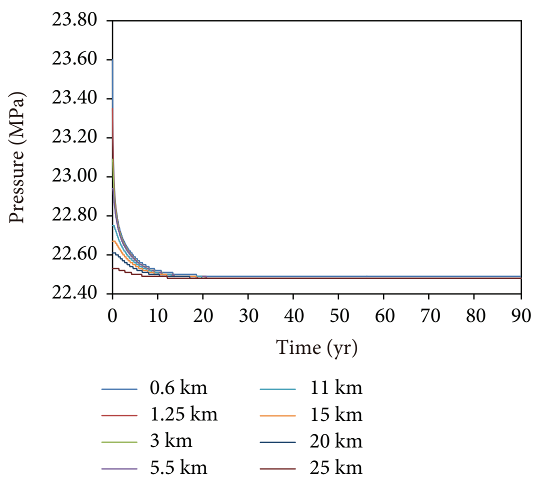

FIGURE 28: Pressure changes at the pressure monitoring points after cessation of CO_2 injection in the 1-well model.

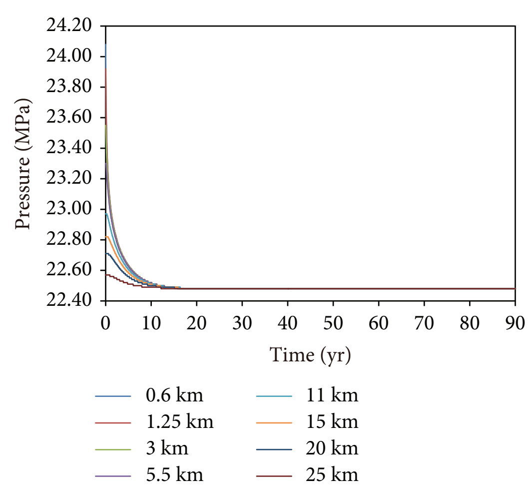

FIGURE 29: Pressure changes at the pressure monitoring points after cessation of CO_2 injection in the 2-well model.

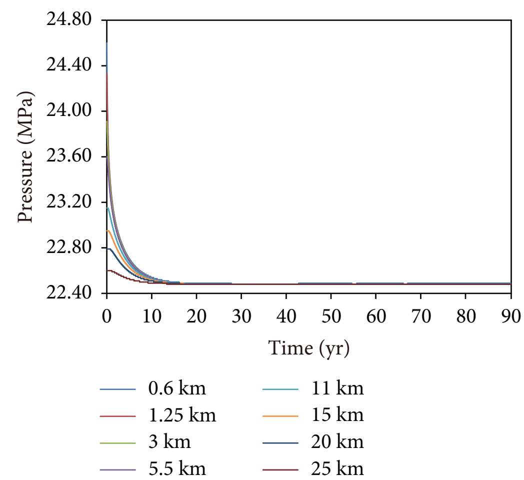

FIGURE 30: Pressure changes at the pressure monitoring points after cessation of CO_2 injection in the 3-well model.

TABLE 3: The time it takes for the pressure at monitoring points at different distances from the injection well to return to the initial pressure (time: yr).

Distance from injection well (km)	0.6	1.25	3	5.5	11	15	20	25
One-injection well model	8.1	8.1	8.1	8.1	7.5	6.6	5.4	1.3
Two-injection well model	9.2	9.2	9.3	9.2	8.7	8.0	7.0	3.9
Three-injection well model	10.4	10.4	10.5	10.4	10.0	9.3	8.3	5.1

the injection well increases, the pressure change in the reservoir decreases rapidly. In the 1-well injection conditions of the radial model, the pressure increase in the reservoir is only 0.1 MPa at 30 km from the injection well. In the 3D model with different numbers of injection wells, under 1-well, 2-well, and 3-well conditions, the pressure increases at a distance of 25 km from the injection well are only 0.03 MPa, 0.07 MPa, and 0.11 MPa, respectively. Under the 3-well conditions, when the injection time is 10 years, the injection has the greatest influence on the reservoir pressure field. The influence distance on the pressure field and the pressure increase in the reservoir at this time are shown in Figure 31.

The groundwater sources in the study area are 25-40 km from the target injection well, and CO_2 injection has a very low impact on the pressure field in the reservoir of the water source area. In addition, the exploitation of groundwater sources occurs mainly in the Quaternary unconfined aquifer and shallow confined aquifer and there are multiple sets of reservoir-caprock combinations between the CO_2 injection level and the exploited water resources. The mining horizon of the water source is approximately 1600 m apart from the CO_2 reservoir. Therefore, it would be difficult for the pressure propagation after CO_2 injection to affect the groundwater dynamic field in the shallow confined aquifers and aquifers. The threat to the water supply safety and water quality safety of water sources can be ignored.

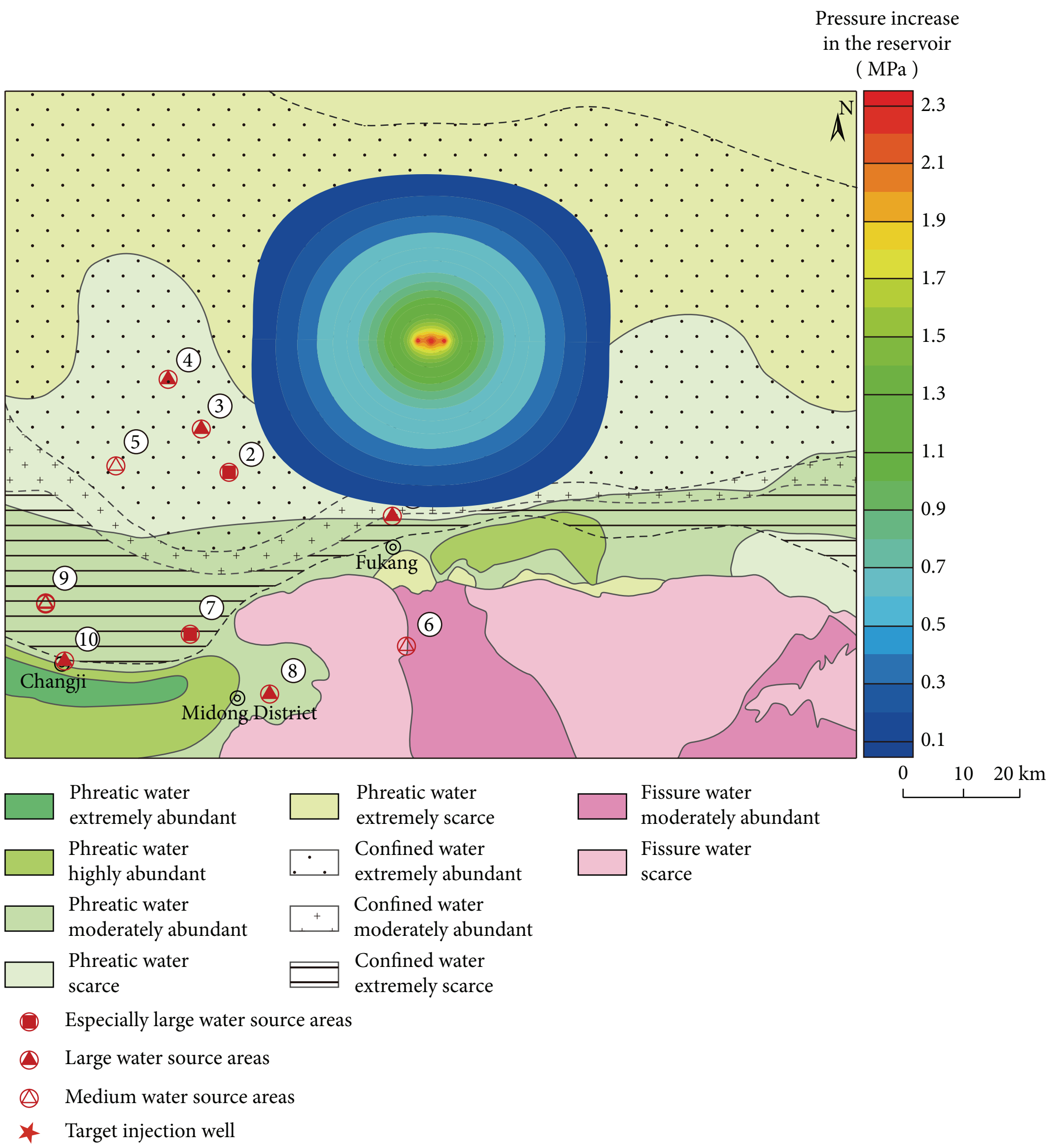

FIGURE 31: Pressure increase in the CO_2 reservoir when injection ceases in the 10th year in the 3-well model.

4. Conclusions and Suggestions

This paper studied the demonstration site for CO_2-enhanced water recovery technology in the Junggar Basin and selected the Cretaceous Donggou Formation as the target reservoir. The CO_2 diffusion and reservoir pressure field changes caused by CO_2 injection via different numbers of injection wells were analyzed by numerical simulation. The following conclusions were obtained:

(1) The influence distance of CO_2 injection on the target reservoir pressure field in the 1-well model was explored through a radial model. Under an injection pressure of 1.3 times the reservoir pressure, the pressure change at a distance of 30 km from the injection well was 0.1 MPa within the 10-year injection period and the reservoir pressure at 50 km was not changed. This result provided a scientific basis for the 3D model scaling and the setting of boundary conditions

(2) The 3D model was used to explore the pressure field evolution of the reservoir. The results showed that during the injection period, the pressure field continuously expanded. The closer the distance to the injection well, the higher the variability of pressure was. As the distance increased, the pressure change decreased rapidly. After the injection ceased, the reservoir pressure completely recovered to the initial reservoir pressure after 15 years

(3) At the same injection pressure, the number of injection wells had a significant effect on the evolution of reservoir pressure. As the number of injection wells increased, the pressure increase at the monitoring points at the same distance from the injection well increased significantly. At monitoring points at

different distances from the injection well, the amount of pressure change under Mitsui conditions was two to three times more than that of a 1-well situation. When the injection of CO_2 ceased, the reservoir pressure returned to its initial pressure level after 10-15 years. The recovery time was not significantly related to the number of injection wells

(4) According to the results of the numerical simulation, due to the small CO_2 diffusion distance, the large-scale injection of CO_2 will not affect the groundwater quality in the water source area. The extent of the pressure field change caused by CO_2 injection is much greater than the extent of CO_2 diffusion. However, the reservoir pressure field near the water source changes very little. The impact of CO_2 injection on the shallow groundwater dynamics on the southern side of the Tian Shan Mountains can therefore be ignored. The scaled injection of CO_2 in the study area will not have a significant impact on the development and utilization of groundwater from nearby water sources

The current simulation results are only based on the 10-year fixed pressure injection. If the project's operating period is extended, the impact of CO_2 injection on the hydrodynamic field will increase. Under the joint of geological structures such as faults, the characteristics of groundwater hydrochemistry and the hydrodynamic field in the shallow surrounding area might be changed, which may affect the safety of the water supply.

Data Availability

The data used to support the findings of this study are available from the corresponding author upon request.

Conflicts of Interest

The authors declare that there is no conflict of interest regarding the publication of this paper.

Acknowledgments

This work was supported by a China National Science and Technology Major Project (grant no. 2016ZX05016-005), a Geological Survey Project (grant no. 121201012000150010), and a Graduate Innovation Fund of Jilin University (grant no. 101832018C056). The paper was also supported by the Key Laboratory of Groundwater Resources and Environment (Jilin University), Ministry of Education, China, and by the Jilin Provincial Key Laboratory of Water Resources and Environment, Jilin University.

References

[1] D. Y. C. Leung, G. Caramanna, and M. M. Maroto-Valer, "An overview of current status of carbon dioxide capture and storage technologies," *Renewable and Sustainable Energy Reviews*, vol. 39, pp. 426–443, 2014.

[2] S. Bachu, "CO_2 storage in geological media: role, means, status and barriers to deployment," *Progress in Energy and Combustion Science*, vol. 34, no. 2, pp. 254–273, 2008.

[3] H.-H. Qiu and L.-G. Liu, "A study on the evolution of carbon capture and storage technology based on knowledge mapping," *Energies*, vol. 11, no. 5, p. 1103, 2018.

[4] E. A. Al-Khdheeawi, S. Vialle, A. Barifcani, M. Sarmadivaleh, and S. Iglauer, "Enhancement of CO_2 trapping efficiency in heterogeneous reservoirs by water-alternating gas injection," *Greenhouse Gases: Science and Technology*, vol. 8, no. 5, pp. 920–931, 2018.

[5] M. Z. Hasanvand, M. A. Ahmadi, S. R. Shadizadeh, R. Behbahani, and F. Feyzi, "Geological storage of carbon dioxide by injection of carbonated water in an Iranian oil reservoir: a case study," *Journal of Petroleum Science and Engineering*, vol. 111, pp. 170–177, 2013.

[6] F. Wang, J. Jing, T. Xu, Y. Yang, and G. Jin, "Impacts of stratum dip angle on CO_2 geological storage amount and security," *Greenhouse Gases: Science and Technology*, vol. 6, no. 5, pp. 682–694, 2016.

[7] S. Krevor, C. Reynolds, A. Al-Menhali, and B. Niu, "The impact of reservoir conditions and rock heterogeneity on CO_2-brine multiphase flow in permeable sandstone," *Petrophysics*, vol. 57, pp. 12–18, 2016.

[8] R. Juanes, E. J. Spiteri, F. M. Orr Jr, and M. J. Blunt, "Impact of relative permeability hysteresis on geological CO_2 storage," *Water Resources Research*, vol. 42, no. 12, 2006.

[9] N. Zhao, T. Xu, K. Wang, H. Tian, and F. Wang, "Experimental study of physical-chemical properties modification of coal after CO2 sequestration in deep unmineable coal seams," *Greenhouse Gases: Science and Technology*, vol. 8, no. 3, pp. 510–528, 2018.

[10] Q. Zhou, J. T. Birkholzer, C.-F. Tsang, and J. Rutqvist, "A method for quick assessment of CO_2 storage capacity in closed and semi-closed saline formations," *International Journal of Greenhouse Gas Control*, vol. 2, no. 4, pp. 626–639, 2008.

[11] E. A. Al-Khdheeawi, S. Vialle, A. Barifcani, M. Sarmadivaleh, and S. Iglauer, "The effect of $WACO_2$ ratio on CO_2 geo-sequestration efficiency in homogeneous reservoirs," *Energy Procedia*, vol. 154, pp. 100–105, 2018.

[12] E. A. Al-Khdheeawi, S. Vialle, A. Barifcani, M. Sarmadivaleh, Y. Zhang, and S. Iglauer, "Impact of salinity on CO_2 containment security in highly heterogeneous reservoirs," *Greenhouse Gases: Science and Technology*, vol. 8, no. 1, pp. 93–105, 2018.

[13] D. Liu, R. Agarwal, and Y. Li, "Numerical simulation and optimization of CO_2-enhanced water recovery by employing a genetic algorithm," *Journal of Cleaner Production*, vol. 133, pp. 994–1007, 2016.

[14] T. Kabera and Y. L. Li, "Injecting CO_2 and pumping out saline formation water simultaneously to control pressure build-up while storing CO_2 in deep saline aquifers," *Defect and Diffusion Forum*, vol. 332, pp. 63–75, 2012.

[15] M. A. Ahmadi, B. Pouladi, and T. Barghi, "Numerical modeling of CO_2 injection scenarios in petroleum reservoirs: application to CO_2 sequestration and EOR," *Journal of Natural Gas Science and Engineering*, vol. 30, pp. 38–49, 2016.

[16] J.-P. Nicot, "Evaluation of large-scale CO_2 storage on freshwater sections of aquifers: an example from the Texas Gulf Coast Basin," *International Journal of Greenhouse Gas Control*, vol. 2, no. 4, pp. 582–593, 2008.

[17] J. T. Birkholzer and Q. Zhou, “Basin-scale hydrogeologic impacts of CO_2 storage: capacity and regulatory implications,” *International Journal of Greenhouse Gas Control*, vol. 3, no. 6, pp. 745–756, 2009.

[18] R.-R. ZHAO, Q.-H. MENG, and J.-M. CHENG, “Fluid migration modeling of CO_2 injection in deep saline aquifers-a case study of the Sanzhao Depression, Songliao Basin,” *Rock and Soil Mechanics*, vol. 4, p. 44, 2012.

[19] H. Yamamoto, K. Zhang, K. Karasaki, A. Marui, H. Uehara, and N. Nishikawa, “Numerical investigation concerning the impact of CO_2 geologic storage on regional groundwater flow,” *International Journal of Greenhouse Gas Control*, vol. 3, no. 5, pp. 586–599, 2009.

[20] J. T. Birkholzer, C. M. Oldenburg, and Q. Zhou, “CO_2 migration and pressure evolution in deep saline aquifers,” *International Journal of Greenhouse Gas Control*, vol. 40, pp. 203–220, 2015.

[21] Y. Duan, N. Li, H. Mu, and S. Gui, “Research on CO_2 emission reduction mechanism of China’s iron and steel industry under various emission reduction policies,” *Energies*, vol. 10, no. 12, p. 2026, 2017.

[22] D. Li, D. He, M. Santosh, D. Ma, and J. Tang, “Tectonic framework of the northern Junggar Basin part I: the eastern Luliang Uplift and its link with the East Junggar terrane,” *Gondwana Research*, vol. 27, no. 3, pp. 1089–1109, 2015.

[23] H. Yang, L. Chen, and Y. Kong, “A novel classification of structural units in Junggar Basin,” *Xinjiang Petroleum Geology*, vol. 25, pp. 686–688, 2004.

[24] B.-Q. Zhu, Y. Gao, and X.-J. Meng, “Natural water quality and its suitability in the northern Tianshan catchments (Central Asia),” *Hydrology*, vol. 6, no. 1, pp. 32–42, 2018.

[25] R. Zhao, J. Cheng, K. Zhang, N. Liu, and F. Xu, “Numerical investigation of basin-scale storage of CO_2 in saline aquifers of Songliao Basin, China,” *Greenhouse Gases: Science and Technology*, vol. 5, no. 2, pp. 180–197, 2015.

[26] K. Pruess and N. Spycher, “ECO2N–a fluid property module for the TOUGH2 code for studies of CO_2 storage in saline aquifers,” *Energy Conversion and Management*, vol. 48, no. 6, pp. 1761–1767, 2007.

[27] Z. Yang, T. Xu, F. Wang, Y. Yang, X. Li, and N. Zhao, “Impact of inner reservoir faults on migration and storage of injected CO_2,” *International Journal of Greenhouse Gas Control*, vol. 72, pp. 14–25, 2018.

[28] M. T. Van Genuchten, “A closed-form equation for predicting the hydraulic conductivity of unsaturated soils 1,” *Soil Science Society of America Journal*, vol. 44, no. 5, pp. 892–898, 1980.

[29] A. T. Corey, “The interrelation between gas and oil relative permeabilities,” *Producers Monthly*, vol. 19, pp. 38–41, 1954.

Hindawi
Geofluids
Volume 2019, Article ID 5061216, 11 pages
https://doi.org/10.1155/2019/5061216

Research Article

Effects of Fine-Grained Particles' Migration and Clogging in Porous Media on Gas Production from Hydrate-Bearing Sediments

Jongwon Jung[1], **Hongsig Kang**[1], **Shuang Cindy Cao**[2], **Riyadh I. Al-Raoush**[3], **Khalid Alshibli**[4], and **Joo Yong Lee**[5]

[1]*School of Civil Engineering, Chungbuk National University, Cheongju-si, Chungbuk 28644, Republic of Korea*
[2]*Department of Civil and Environmental Engineering, Louisiana State University, Baton Rouge, LA 70803, USA*
[3]*Department of Civil & Architectural Engineering, Qatar University, P.O. Box 2713, Doha, Qatar*
[4]*Department of Civil and Environmental Engineering, The University of Tennessee, Knoxville, TN 37996, USA*
[5]*Petroleum and Marine Research Division, Korea Institute of Geoscience and Mineral Resources, Daejeon, Republic of Korea*

Correspondence should be addressed to Joo Yong Lee; jyl@kigam.re.kr

Received 7 January 2019; Accepted 16 April 2019; Published 23 May 2019

Guest Editor: Andrew Bunger

The migration of fine particles in porous media has been studied for different applications, including gas production from hydrate-bearing sediments. The clogging behavior of fine particles is affected by fine particle-pore throat size ratio, fine particle concentration, ionic concentration of fluids, and single/multiphase fluid flow. While previous studies presented valuable results, the data are not enough to cover a broad range of particle types and sizes and pore throat size in natural hydrate-bearing sediments. This paper presents a novel micromodel to investigate the effects of fine particle-pore throat size ratio, fine concentration, ionic concentration of fluid, and single/multiphase fluid flow on clogging or bridging in porous media. The results show that (1) the concentration of fine particles required to form clogging and/or bridging in pores decreased with the decrease in fine particle-pore throat size ratio, (2) the effects of ionic concentration of fluid on clogging behaviors depend on the types of fine particles, and (3) fine particles prefer to accumulate along the deionized water- (DW-) CO_2 interface and migrate together, which in turn easily causes clogging in pores. As a result, multiphase fluid flow during gas production from hydrate-bearing sediments could easily develop clogging in pore throats, where the relative permeability of DW-CO_2 in porous media decreases. Accordingly, the relatively permeability of porous media should be evaluated by considering the clogging behavior of fines.

1. Introduction

The migration of fine particles in porous media has been studied for different applications such as oil extraction [1, 2], pore clogging by fines [3–5], sand production in oil reservoirs [6], fracturing in sediments during production of shale oil and gas [7], and gas production from hydrate-bearing sediments [8, 9]. The migration of fine particles has been studied in laboratory experiments using two-dimensional (2D) microfluidic pore models at the microscale [10, 11] and three-dimensional (3D) porous sediment models at the macroscale [12–16] to better understand the migration behavior of fine particles and its impacts on bridging and/or clogging in porous media [8–11, 17–23]. Previous studies have identified four distinct mechanisms that are influenced by two critical size ratios: the ratio of fine particle diameter to pore throat width (d/o) and the ratio of fine particle diameter to host particle diameter (d/D) (Figure 1, [14]). They are piping and no interaction ($d/o < 0.01$ or $d/D < 0.067$), multiparticle blocking or bridging ($0.01 < d/o < 0.6$ or $0.067 < d/D < 0.2$), and blocking/no invasion ($d/o > 0.6$ or $d/D > 0.2$) (Figure 1). Also, previous

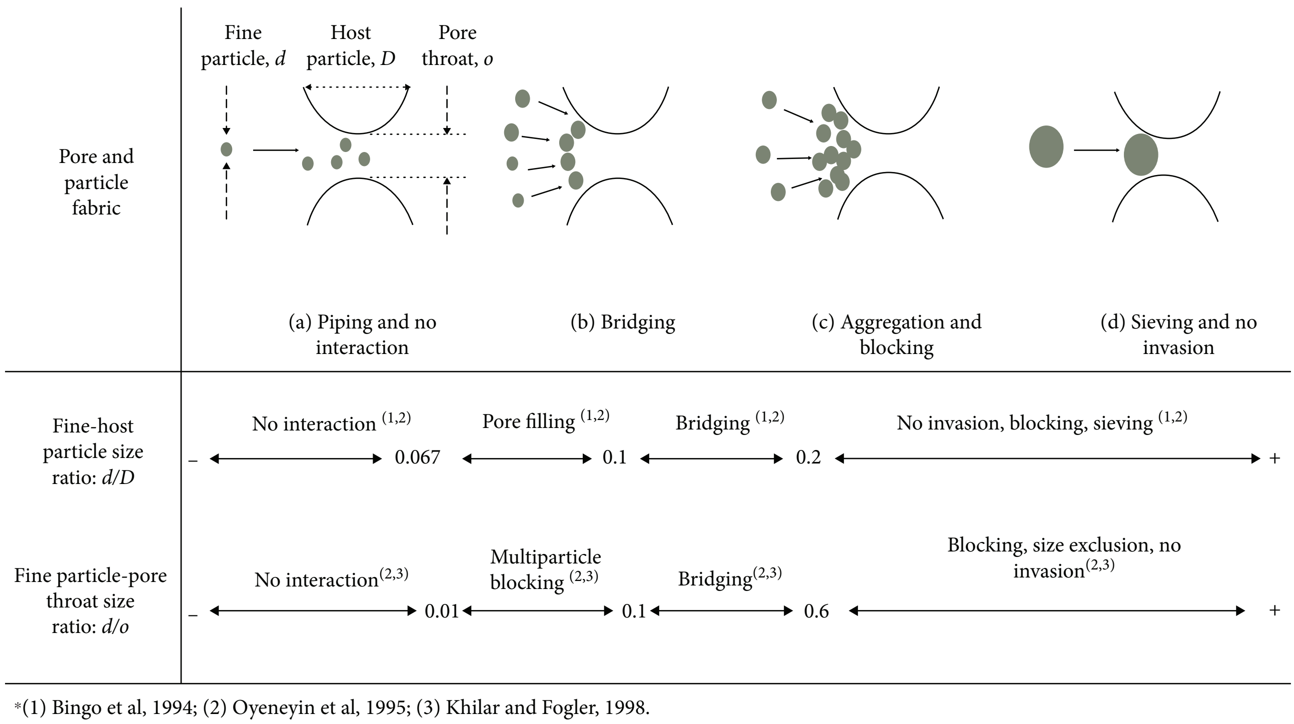

Figure 1: Main mechanisms for fines migrating and clogging at pore throats, classified based on critical size ratios (d/D, d/o), where D is the host particle diameter, d is the diameter of fine particle, and o is the pore throat width [8].

studies have reported that clogging occurs more easily at higher concentration of fine particles [10, 24, 25] and at the lower flow rate because a higher flow rate prevents fine particles to form bridging or/and clogging due to disruptions by pressure distribution or flow reversals [2, 12].

In addition to the effect of fine particles size relative to the pore throat size, parameters such as fine concentration, flow rate, pore-fluid chemistry influence, and fine migration/clogging behavior [8, 26]. Fine particles have unbalanced surface charge densities and specific surface areas. Their electrical surface charge distribution and fine particle shapes result in three electrical interactions such as electrostatic Coulombic forces, the Sogami-Ise model, and Van der Waals attraction and double layer repulsion that is described by the Derjaguin-Landau-Verwey-Overbeek (DLVO) theory, which influence the aggregation of fine particles. Thus, the ionic concentration of the fluid affects particle interactions and causes the aggregation due to the above three electrical interactions, which links to the ratios of fine particle size and the pore throat size [8].

A multiphase fluid flow is defined as a simultaneous flow of two or more fluids with different phases (i.e., gas or liquid). Previous studies have shown that multiphase fluid flow has more impact on fine particle accumulation along the fluid-fluid interface resulting in fine clogging/bridging in porous media [2, 8, 9, 26, 27]. Therefore, for a given ratio of fine particle size to the pore throat size, fine clogging/bridging in porous media during a multiphase fluids flow requires less fine concentration as compared to a single-phase flow [8, 26].

In natural conditions, multiphase flow occurs during methane extraction from gas hydrate. Also, porewater freshening occurs during gas hydrate dissociation caused by release of freshwater coming from hydrates. Both a multiphase fluid flow and a porewater freshening influence on fine particle migration and clogging behaviors with the size ratio of fine particles and pore throats. There are limited experimental studies on fine particle migration and clogging during methane extraction from hydrate [8]. [8] experiments were conducted for pore throat sizes between 20 μm and 100 μm.

The objectives of this study are (1) to investigate the impact of fine migration and potential clogging behaviors of fine particles during gas hydrate dissociation in a wide range of pore throat sizes using a 2D micromodel system and (2) to present a "clogging map" to be used to understand the clogging potential of natural hydrate-bearing sediments during gas production with basic information such as mineralogy and grain size distribution. A wide range of fines sizes between 20 μm and 200 μm and particle concentrations between 0.1% and 20% were used in the study.

2. Experimental Study

2.1. Materials. Six fine particles that are widely common in natural gas hydrate-bearing sediments were selected for this study, namely, silica, silt, mica, calcium carbonate (primarily calcite, $CaCO_3$), diatom, kaolin (primarily kaolinite), and bentonite (primarily montmorillonite) [28–30]. Table 1 lists the median particle size of each fine particle. In this paper, the concentrations of fine particles are calculated as the weights of fine particles and fluid (in weight/weight percent (w/w%)), which has a wide range between 0.1% and 20% (i.e., 0.1%, 0.2%, 0.5%, 1%, 2%, 5%, 10%, 13%, 15%, 17%,

Table 1: Median particle sizes of the fines used in this study.

Fine-grained particles	Median particle size (d_{50}) (μm)
Silica silt	10.5[a]
Mica	17[a]
$CaCO_3$	8[a]
Diatoms	10[a]
Kaolinite	4
Bentonite	<2[b]

[a]Data from manufacturer. [b]Approximated value from literature (Arnott, 1965).

and 20%). Deionized water (DW) and 2M sodium chloride (NaCl) solution were used as pore fluid to study the effects of ionic concentration on fine migration and clogging.

2.2. Micromodels. The micromodels used in this study were fabricated using polymeric materials known as polydimethylsiloxane (PDMS, [4]). The micromodels were made of a homogeneous 2D pore network pattern as depicted in Figure 2 and were bonded to a PDMS-coated glass slide. The micromodel measures 20 mm × 10 mm. The circular solid diameter (D) represents the host particle size in sediments. Pore throat widths, o, have a wide range of 20, 40, 60, 100, 150, 180, and 200 μm, which were determined by pore throat sizes in natural sediments. The pore height is 100 μm, which does not influence the fluid flow and particle migration.

2.3. Experimental Setup. Figure 2 shows a schematic of the experimental setup. The micromodel is placed horizontally on an Olympus IX51-LWD 4X/0.1 microscope. Inlet and outlet ports of the micromodel are connected to a Teledyne ISCO pump and to a syringe pump (NE-1010; Kats Scientific), respectively. The syringe pump (NE-1010; Kats Scientific) injects DW mixed with fines into the micromodel. And then, while the syringe pump (NE-1010; Kats Scientific) controls the imbibition of DW from the micromodel, the Teledyne ISCO pump injects CO_2 gas (99.99%, Airgas) into the micromodel. The system was maintained at 10 ± 1 kPa by a pressure regulator and the pressure pump at room temperature ($25 \pm 1^{\circ}$C). A filter was placed between the micromodel and the pressure regulator to prevent fine migration into the pressure regulator. The microscope has monitored the channels of micromodels during tests, and the camera captured both images and video (Figure 2).

2.4. Experimental Procedure. After thorough cleaning of the experimental system including micromodel channels, tubings, and its components using absolute ethanol (ACS reagent grade; Mallinckrodt Baker), DW was injected to rinse the system. Then, an experimental setup was dried at room temperature ($25 \pm 1^{\circ}$C) for 72 hr and was assembled (Figure 2). The micromodel was saturated by DW containing fine particles at different concentrations (0.1%, 0.5%, 1%, 2%, 5%, 10%, 13%, 15%, 18%, and 20% by weight) using the syringe pump. Then, the pressure was increased up to 10 ± 1 kPa using a pressure regulator and the ISCO pump. Both pressure (10 ± 1 kPa) and temperature ($25 \pm 1^{\circ}$C) were kept constant during all tests. The syringe pump withdrew DW with fine particles from the micromodel at a constant flow rate of 50 μl/min. The microscope and the camera monitor fine migration and DW flow through the micromodel, and images were saved for further analysis.

2.4.1. Single-Phase Flow. The micromodel with a 200 μm pore throat width was first used. The fine concentration was gradually increased until clogging was observed in the micromodel. At the state of clogging, the fine concentration was labelled as the critical fine concentration for a given pore throat size. Next, the micromodel with a smaller pore throat size (e.g., 180 μm) was used for a given fine concentration, and another critical fine concentration was identified at a given pore throat size. A series of experiments were conducted to determine the critical fine concentration at a given pore throat size.

2.4.2. Multiphase Fluid Flow. The micromodel was saturated with DW mixed with fine particles. A combination of pore throat size and fine concentration was selected such that the pore throats in the micromodel were not clogged after the injection of 100 pore volume of DW containing fines. CO_2 was then injected into the micromodel while DW-fine particles were withdrawn using the syringe pump. Both pressure (10 ± 1 kPa) and temperature ($25 \pm 1^{\circ}$C) were kept constant during experiments. The experiments were repeated for different combinations of pore throat size and fine concentration where clogging was not induced during a single-phase flow.

3. Results and Discussion

3.1. Effects of Particle Concentration and Particle Pore Throat Size Ratio on Clogging Behavior in a Single-Phase Flow

3.1.1. Particle Concentration. Figure 3 displays a few snapshots of DW injection with kaolinite into the micromodel at various particle concentrations from 0.1% to 1%. The flow rate (50 μl/min) and pore throat size (150 μm) were kept constant for all experiments. Results show that clogging occurs at 0.5% and 1% kaolinite particle concentration at a given experimental condition. It implies that the 0.5% kaolinite is the minimum concentration that causes clogging at pore throats, which can be called as the critical clogging concentration in this study. Note that the critical clogging concentration is defined as the ratio of fine particle mass to liquid mass that induces clogging. For example, 0.5% kaolinite is the critical clogging concentration at a given condition (e.g., flow rate is 50 μl/min, pore throat size is 150 μm, and fluid type is DW). In general, the critical clogging concentration decreases as the particle-pore throat size ratio increases (Figure 4), which is consistent with previous studies [8, 10, 25, 26].

3.1.2. Particle Pore Throat Size Ratio. Figure 5 shows three images of DW injections with kaolinite into the micromodels with various pore throat sizes from 40 to 100 μm. The flow rate (50 μl/min) and kaolinite concentration (0.5%) were constant for all experiments. Neither bridging nor clogging

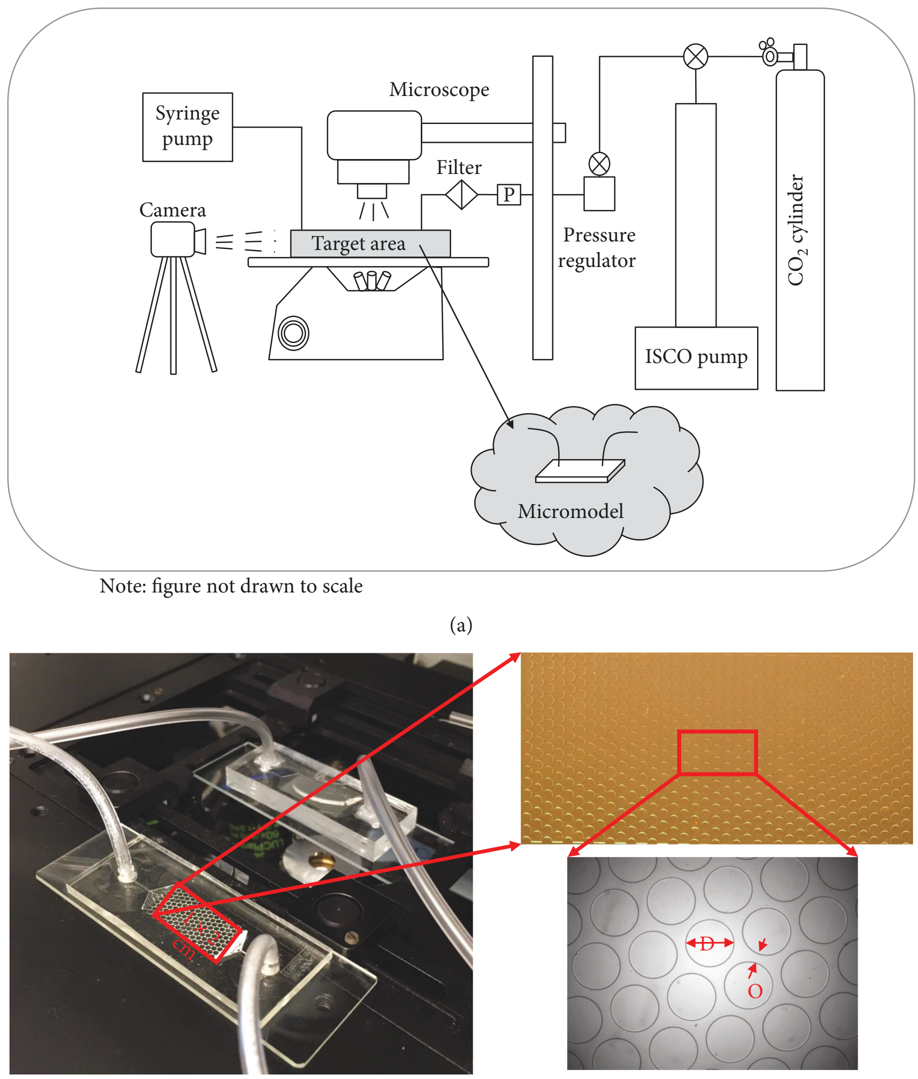

Figure 2: Experimental setup [8, 26].

was observed in the microfluidic pore models at the given pore throat sizes of 60 μm and 100 μm (flow rate = 50 μl/min, kaolinite concentration = 0.5%). However, clogging occurs at a pore throat size of 40 μm at the same flow rate and kaolinite concentration. It implies that clogging easily occurs as pore throat size decreases.

3.2. Effects of Ionic Concentration on Clogging Behavior of Fines in a Single-Phase Flow. Figure 6 shows a few images of pore fluid-specific clogging tendencies and behaviors of diatom, $CaCO_3$, and kaolinite between DW and 2M-brine. Clogging behavior depends on the type of injected fluid (i.e., DW or 2M-brine) due to the ionic concentration of fluids. For instance, kaolinite particles in 2M-brine (0.2% kaolinite concentration) are uniformly dispersed in the 60 μm pore throat micromodel, and no clogging is observed in Figure 6(f). In contrast, with the identical geometry and kaolinite concentration, kaolinite particles in DW are locally concentrated at some pore throats that are identified as clogged (red circles in Figure 6(c)). This result provides clear evidence that kaolinite particles clog more easily in DW than in 2M brine. However, for both diatom and $CaCO_3$ particles, results show the similar clogging tendencies of them in both DW and 2M-brine (Figures 6(a), 6(b), 6(c), and 6(d)). The number of clogging in pores is different between DW and 2M-brine; however, both particles clog in both DW and 2M-brine at the same conditions (i.e., particle size, pore size, and concentration).

Figure 4 shows critical clogging concentrations of all types of fine particles (i.e., silica silt, mica, $CaCO_3$, diatoms, kaolinite, and bentonite) between DW and 2M-brine. A detailed discussion of results follows.

3.2.1. Kaolinite. While fine particle pore throat size ratios were from 0.04 to 0.2 in the previous study [8], a broader range of size ratios is investigated in this study from 0.02 to 0.2. Thus, new data in the range of size ratio from 0.02 to 0.04 was added onto the “clogging map” including only

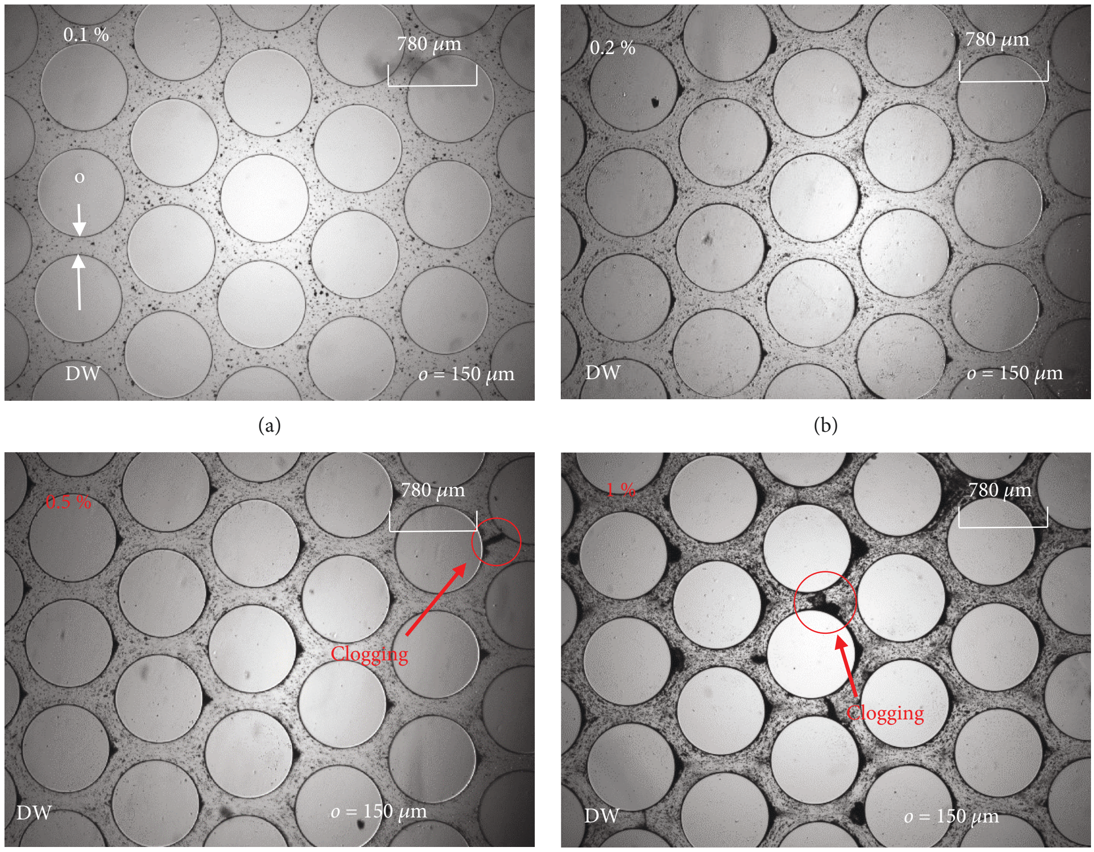

(a) (b) (c) (d)

Figure 3: Particle concentration effects on clogging behaviors in pore throats during DW flow with diatom.

data from 0.04 to 0.2 (Figure 4). In contrast, the critical clogging concentration of kaolinite in 2M-brine is higher than in DI water when the fine pore throat size ratio is less than 0.04. The results demonstrate that kaolinite forms aggregation more easily in DW than in 2M-brine, which can be explained by Coulombic forces between platy particles that cause compact, face-to-face aggregation of kaolinite particles in 2M-brine. However, kaolinite platy particles form bulky, edge-to-face aggregation in DW, which cause the kaolinite to form a bridge or clogging in pore throats.

However, the critical clogging concentration of kaolinite is similar between 2M-brines and DW when the fine pore throat size ratio is higher than 0.04, which shows the same trends in a previous study [8]. A higher fine pore throat size means a larger fine particle size. Thus, it implies that the large particle size governs the clogging in pores.

3.2.2. Silica Silt. While the size ratios of fine particle-pore throat were from 0.105 to 0.525 in the previous study [8], a broader range of size ratio is investigated in this study from 0.0525 to 0.525. Experimental results in the range of size ratio from 0.0525 to 0.105 are added to the "clogging map" with the critical particle concentration. Figure 4 presents that the critical clogging concentration of silica silt in DW is higher than in 2M brine in all range of size ratios, which shows trends reported by [8]. The silica silt forms aggregations more easily in 2M-brine than in DW. Silica silt has a more negative charge distribution on the surface, which causes silica particles not to aggregate in freshwater. However, the positive ions in 2M-brine decrease the interparticle repulsive force, which influences on the easier clogging of silica silt in 2M-brines than in DW. The net attractive interaction in 2M-brines is described by the Sogami-Ise model [31]. It implies that silica silt decreases their potential for forming bridges and blocks at the pore throat by freshwater during gas production from hydrate-bearing sediments.

3.2.3. Bentonite. The size ratios of fine particle pore throat were from 0.02 to 0.1 in the previous study [8], and the broader range of the size ratio is reported in this paper from 0.01 to 0.1. Note that the range of size ratios from 0.01 to 0.02 is added to Figure 4. Experimental results in the range of size ratio from 0.01 to 0.02 are added to the "clogging map" with the critical particle concentration of bentonite particles. Figure 4 shows that the critical clogging concentration of bentonite in DW is much higher than in 2M-brine in all range of size ratios, which shows the same trends reported by [8]. Bentonite aggregates more easily in 2M-brine than in DW, which can be explained by double layer thickness of bentonite particles since bentonite particles have a high surface charge concentration and surrounded by a relatively thick double layer of freshwater [32], which is explained by a combination of Van der Waals attraction and double layer

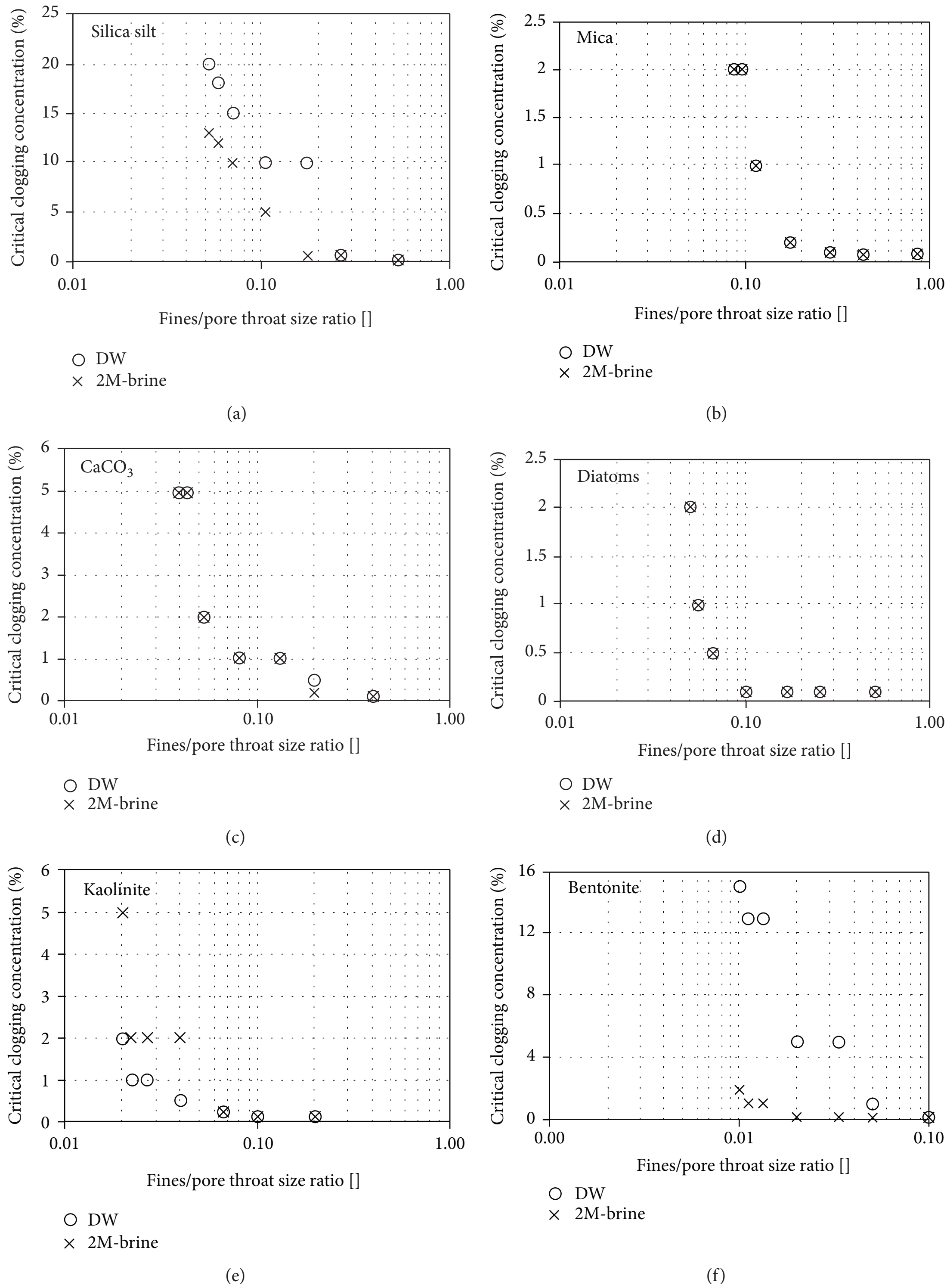

Figure 4: The effects of ionic concentration of fluids (DW or 2M-brine) on clogging behaviors in pore throats.

repulsion described by the DLVO theory. However, the double layer thickness decreases with the increased ionic concentration in water, which cause bentonite particles to form bridges and blocks at pore throats. It implies that bentonite particles decrease their potential for forming bridges and blocks at the pore throat by freshwater during gas production from hydrate-bearing sediments.

3.2.4. Mica, $CaCO_3$, and Diatoms. Mica, $CaCO_3$, and diatoms show the same critical particle concentrations between DW and 2M-brine in each size ratio of the fine particle pore throat. Mica, $CaCO_3$, and diatom have a relatively large particle size (Table 1), which governs the interparticle interactions rather than electrical forces. Thus, clogging of relatively large particles such as mica, $CaCO_3$,

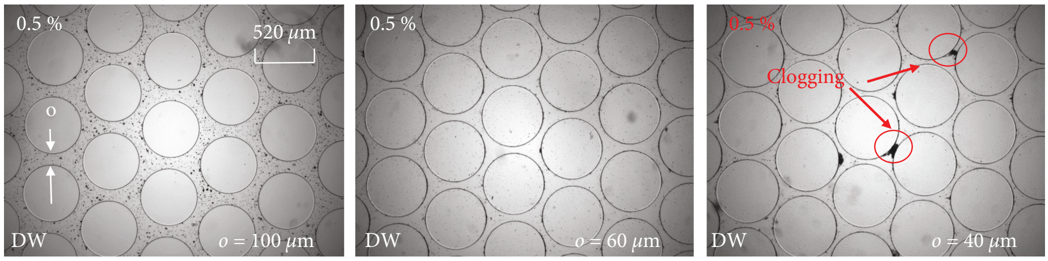

Figure 5: Pore throat size effects on clogging behaviors during DW flow with kaolinite.

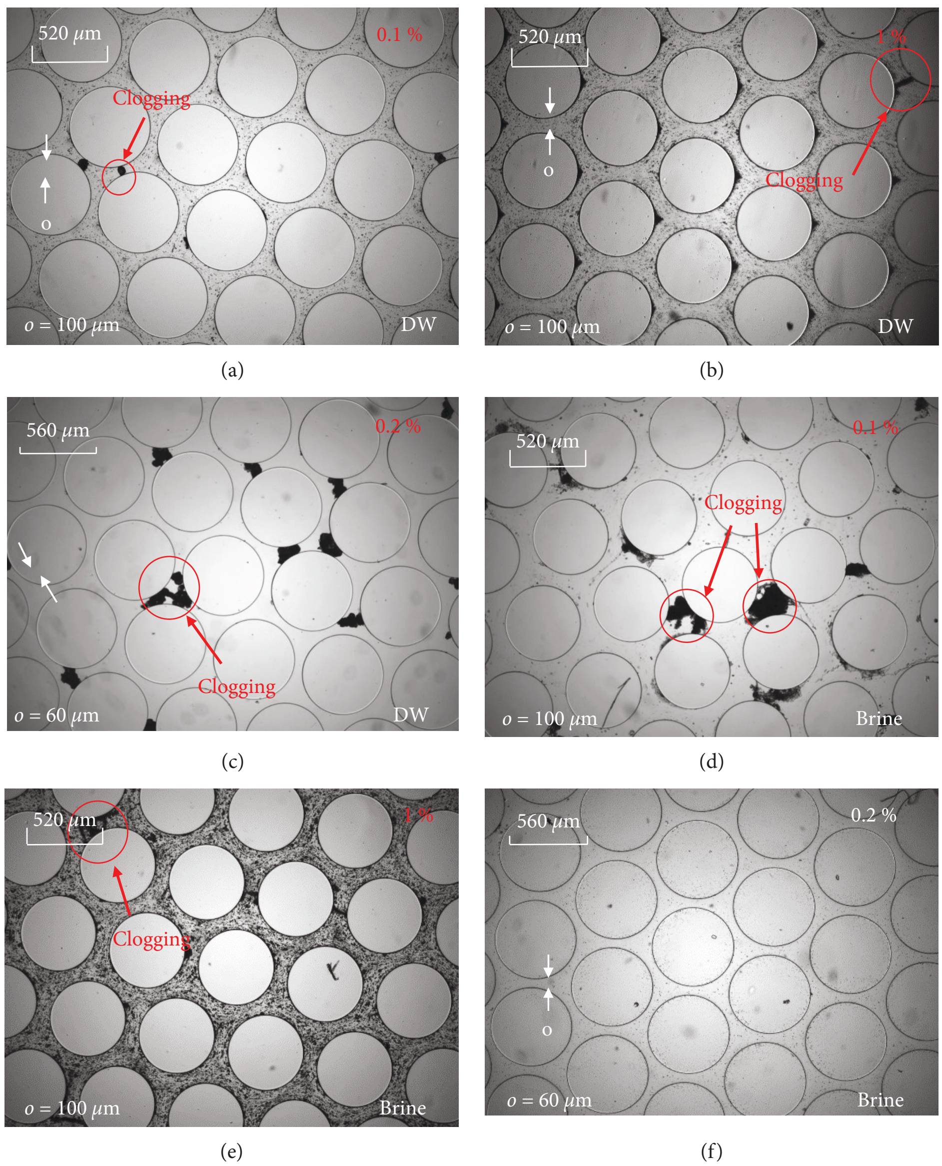

Figure 6: The effects of ionic concentration of fluid on clogging behaviors in pore throats. (a) DW with diatom, (b) DW with $CaCO_3$, (c) DW with kaolinite, (d) 2M-brine with diatom, (e) 2M-brine with $CaCO_3$, and (f) 2M-brine with kaolinite.

and diatom is controlled by their particle shape. The results provided clear evidence that freshwater during hydrate dissociation does not influence aggregation of mica, $CaCO_3$, and diatom particles.

3.3. Effects of Multiphase Fluid Flow on Fine Migration and Clogging Behavior. After the DW percolated the micromodel, CO_2 gas was injected to simulate multiphase fluid flow during gas production from hydrate-bearing sediment. Gas

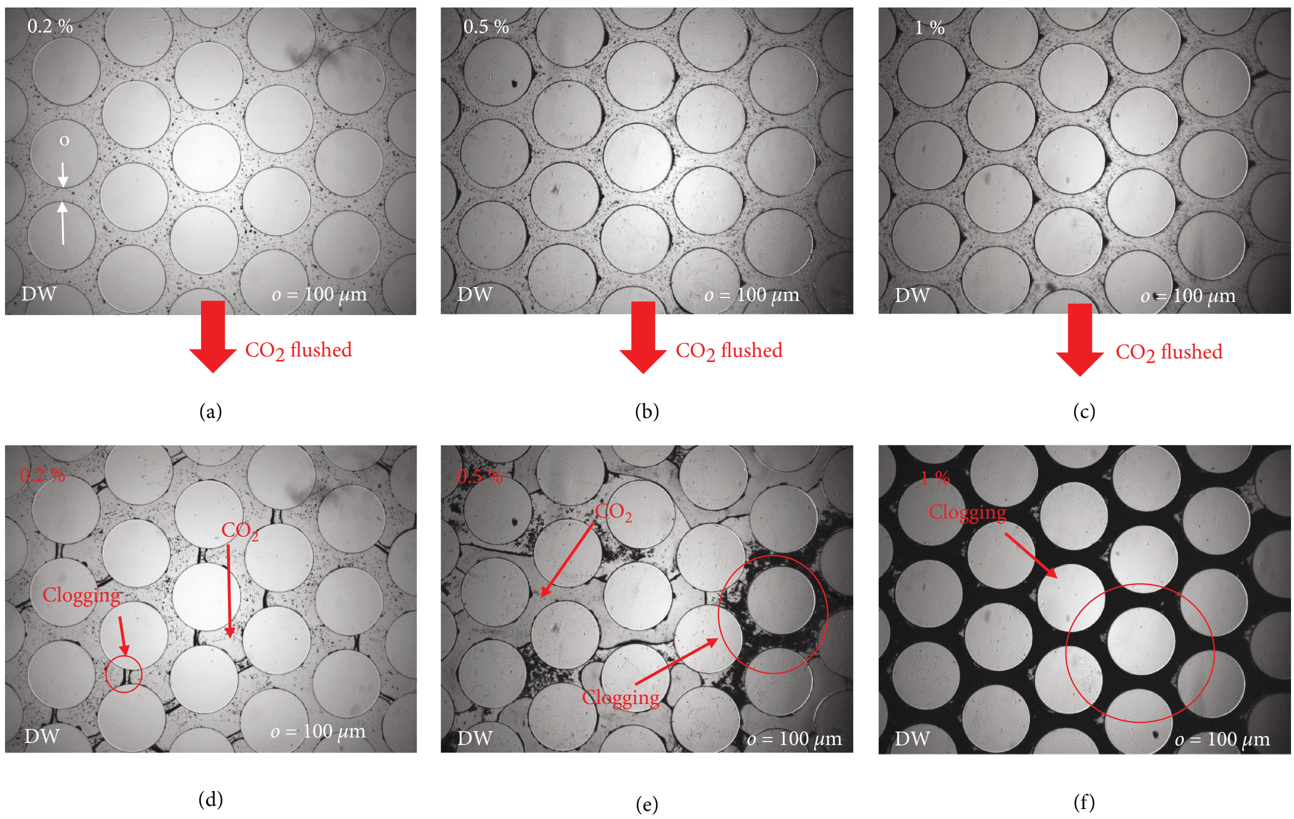

Figure 7: The effects of multiphase fluid flow on clogging behaviors in pore throats during DW or 2M-brine flow with kaolinite: (a) DW with 0.2% kaolinite, (b) DW with 0.5% kaolinite, (c) DW with 1% kaolinite, (d) DW-CO_2 with 0.2% kaolinite, (e) DW-CO_2 with 0.5% kaolinite, and (f) DW-CO_2 with 1% kaolinite.

hydrate dissociation releases freshwater that decreases the ionic concentration in liquid during gas production. Therefore, only DW was used in multiphase fluid flow. Figure 7 shows a few images between single-phase flow and multiphase fluid flow. When DW with kaolinite at a given concentration from 0.2% to 1% was injected into the micromodel ($o = 100\,\mu$m), no clogging was observed in Figures 7(a), 7(b), and 7(c). Then, CO_2 gas was injected into the micromodel with identical geometry and kaolinite concentration to explore the effects of multiphase fluid flow on migration and clogging behaviors of kaolinite particles (Figures 7(d), 7(e), and 7(f)). As CO_2 gas was injected into the micromodel, it displaced DW which was already filling the pore space. CO_2 gas-DW interfaces in the micromodel accumulated kaolinite particles as indicated by the dark leading edge in the micromodel, and kaolinite particles were migrating ahead of the CO_2 gas front. Thus, the clogging occurred in pore throats as CO_2 gas was injected. This result implies that kaolinite particles clog more easily in a multiphase fluid flow than in a single-phase flow.

Clogging of fine particles in multiphase fluid flow could locally increase the pressure in the pores during hydrate dissociation due to the decreased relative permeability, which could push the host particles in sediments and change the pore geometry [9]. While the results in this study do not show such a migration of host particles due to the fixed host particle in the micromodel, clogging observed during multiphase fluid flow could cause a fracture in natural sediment during gas production from hydrate-bearing sediments. The locally increased fine particle concentration along the interface and clogging can explain the fracture in the previous study by [9].

Figure 8 shows critical clogging concentrations of all types of fine particles (i.e., silica silt, mica, $CaCO_3$, diatoms, kaolinite, and bentonite) between DW (single-phase flow) and DW-CO_2 (multiphase fluids flow). Results show that (1) the critical clogging concentration is higher in DW than in DW-CO_2 in all types of particles and all range of fine pore size ratios, and (2) when the particle size is relatively larger (i.e., fine-pore throat size ratio > 0.1), the critical clogging concentration is similar between DW and DW-CO_2 because the particle size mainly governs the interparticle interactions.

4. Conclusions

Fine behavior in porous media broadly classified by four regions, namely, piping (no interaction), bridging, aggregation (blocking), and sieving (no invasion). Such classification is affected by fine particle-pore throat size ratio, fine particle concentration, ionic concentration of fluids, and multiphase fluid flow. Published data shows that neither clogging nor bridging was observed at a lower fine particle pore throat size

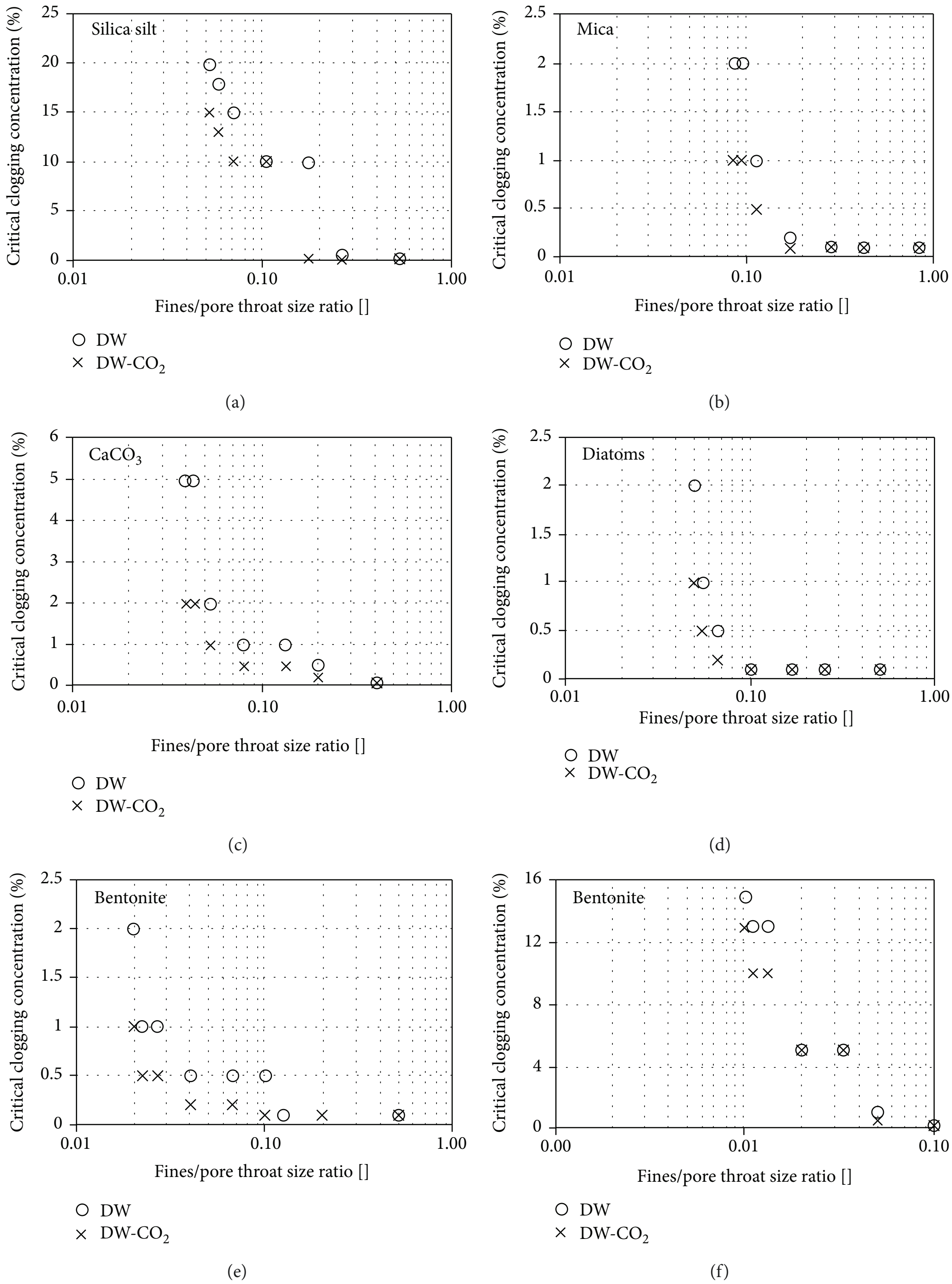

Figure 8: The effects of multiphase fluid flow on clogging behaviors in pore throats.

ratio. However, recent studies show that clogging occurs even at a lower fine particle pore throat size ratio with a multiphase fluid flow and the change in ionic concentration of liquid. Previous studies did not present enough measurements to cover a broad range of particle types and sizes and pore throat size in natural hydrate-bearing sediments. This paper presents the results of a novel micromodel that was developed to investigate the impact of fine particle pore throat size ratio, fine concentration, ionic concentration of fluid, and multiphase fluid flow on clogging or bridging in porous media.

Single-phase flow experiments were conducted with more percentages of fine particle concentration and fine particle pore throat size ratio than what was published in previous studies. The results show that the concentration of fine particles required to form clogging and/or bridging in pores decreased with the decrease in fine particle pore throat size ratio.

The impact of ionic concentration of fluid on clogging behavior depends on the types of fine particles. Kaolinite easily clogged the pore throat in DW than in 2M-brine, which could be explained by Coulombic forces between platy particles that cause compact, face-to-face clusters of kaolinite particles in 2M-brine. On the contrary, silica silt clogged the pore space in 2M-brine easier than in DW, which is attributed to the negative charge distribution of silica silt on the surface. The positive ions in 2M-brine decrease the interparticle repulsive force between the silica particles and cause aggregations followed by clogging at the pore throat in 2M-brines. Clogging develops easily for bentonite in 2M-brine than in DW which can be explained by a relatively thick double layer around the bentonite particles. Others such as mica, $CaCO_3$, and diatoms exhibit the same critical particle concentrations for fines in DW and 2M-brine due to the relatively large particle size, which governs the interparticle interactions rather than electrical forces.

Multiphase fluid flow experiments show that fine particles prefer to accumulate along the DW-CO_2 interface and migrate together, which in turn easily cause clogging in pores. This result implies that multiphase fluid flow during gas production from hydrate-bearing sediments could easily form clogging in pore throats, where the relative permeability of DW/CO_2 in porous media decreases. Also, the fracture could occur due to the increased pressure by the clogging in pores. Thus, the relative permeability of porous media should be evaluated by considering the clogging behavior of fines.

The results imply that the decrease in the salinity and the presence of the gas phase induced from gas hydrate production can damage the formation permeability and thus reduce the productivity. The measure for preventing pore clogging should be developed for sustainable gas production in the presence of fines in the reservoirs.

Data Availability

The data used to support the findings of this study are available from the corresponding author upon request.

Disclosure

The findings achieved herein are solely the responsibility of the authors.

Conflicts of Interest

The authors declare that they have no conflicts of interest.

Acknowledgments

This research was made possible by an NPRP grant # NPRP8-594-2-244 from the Qatar National Research Fund (a member of Qatar Foundation). Also, this research was supported by a grant (2018-MOIS31-009) from the Fundamental Technology Development Program for Extreme Disaster Response funded by the Korean Ministry of the Interior and Safety (MOIS) and by the Basic Science Research Program through the National Research Foundation of Korea (NRF) funded by the Ministry of Education (2017R1D1A3B03 031369). This research was supported by the Ministry of Trade, Industry, and Energy (MOTIE) through the Project "Gas Hydrate Exploration and Production Study (19-1143)" under the management of the Gas Hydrate Research and Development Organization (GHDO) of Korea and the Korea Institute of Geoscience and Mineral Resources (KIGAM).

References

[1] C. Gruesbeck and E. Collins, "Entrainment and deposition of fine particles in porous media," *Society of Petroleum Engineers Journal*, vol. 22, no. 6, pp. 847–856, 1982.

[2] T. W. Muecke, "Formation fines and factors controlling their movement in porous media," *Journal of Petroleum Technology*, vol. 31, no. 2, pp. 144–150, 1979.

[3] G. Kampel, G. H. Goldsztein, and J. C. Santamarina, "Plugging of porous media and filters: maximum clogged porosity," *Applied Physics Letters*, vol. 92, no. 8, article 084101, 2008.

[4] J. C. McDonald and G. M. Whitesides, "Poly(dimethylsiloxane) as a material for fabricating microfluidic devices," *Accounts of Chemical Research*, vol. 35, no. 7, pp. 491–499, 2002.

[5] J. R. Valdes and J. C. Santamarina, "Clogging: bridge formation and vibration-based destabilization," *Canadian Geotechnical Journal*, vol. 45, no. 2, pp. 177–184, 2008.

[6] E. Papamichos, I. Vardoulakis, J. Tronvoll, and A. Skjaerstein, "Volumetric sand production model and experiment," *International Journal for Numerical and Analytical Methods in Geomechanics*, vol. 25, no. 8, pp. 789–808, 2001.

[7] H. Shin and J. C. Santamarina, "Fluid-driven fractures in uncemented sediments: underlying particle-level processes," *Earth and Planetary Science Letters*, vol. 299, no. 1-2, pp. 180–189, 2010.

[8] S. C. Cao, J. Jang, J. Jung, W. F. Waite, T. S. Collett, and P. Kumar, "2D micromodel studies of pore-throat clogging by pure fine-grained sediments and natural sediments from NGHP-02, Offshore India," in *U.S. Geological Survey data release*, Marine and Petroleum Geology, 2018.

[9] J. W. Jung, J. Jang, J. C. Santamarina, C. Tsouris, T. J. Phelps, and C. J. Rawn, "Gas production from hydrate-bearing sediments: the role of fine particles," *Energy & Fuels*, vol. 26, no. 1, pp. 480–487, 2012.

[10] G. C. Agbangla, É. Climent, and P. Bacchin, "Experimental investigation of pore clogging by microparticles: evidence for a critical flux density of particle yielding arches and deposits," *Separation and Purification Technology*, vol. 101, pp. 42–48, 2012.

[11] J. R. Valdes, "Fine migration and formation damage-microscale studies," Civil Engineering, Geoogia Institute of Technology, 2002, Doctor of Philosophy.

[12] Y. Bigno, M. B. Oyeneyin, and J. M. Peden, "Investigation of pore-blocking mechanism in gravel packs in the management and control of fines migration," in *Proceedings of Society of Petroleum Engineers International Symposium on Damage Control*, vol. 9no. 10, pp. 29–40, Lafayette, Louisiana, 1994.

[13] E. Dressaire and A. Sauret, "Clogging of microfluidic systems," *Soft Matter*, vol. 13, no. 1, pp. 37–48, 2017.

[14] K. C. Khilar and H. S. Fogler, "Migrations of fines in porous media," in *Theory and Applications of Transport in Porous Media*, Kluwer Academic Publishers, 1998.

[15] M. B. Oyeneyin, J. M. Peden, A. Hosseini, and G. Ren, "Factors to consider in the effective management and control of fines migration in high permeability sands," in *SPE European Formation Damage Conference*, pp. 15-16, The Hague, 1995.

[16] M. Xiao and N. Shwiyhat, "Experimental investigation of the effects of suffusion on physical and geomechanic characteristics of sandy soils," *Geotechnical Testing Journal*, vol. 35, no. 6, p. 104594, 2012.

[17] L. T. Fan, R. Nassar, S. H. Hwang, and S. T. Chou, "Analysis of deep bed filtration data: modeling as a birth-death process," *AIChE Journal*, vol. 31, no. 11, pp. 1781–1790, 1985.

[18] J. P. Herzig, D. M. Leclerc, and P. L. Goff, "Flow of suspensions through porous media—application to deep filtration," *Industrial & Engineering Chemistry*, vol. 62, no. 5, pp. 8–35, 1970.

[19] A. O. Imdakm and M. Sahimi, "Computer simulation of particle transport processes in flow through porous media," *Chemical Engineering Science*, vol. 46, no. 8, pp. 1977–1993, 1991.

[20] K. C. Khilar and H. S. Fogler, "Colloidally induced fines migration in porous media," *Reviews in Chemical Engineering*, vol. 4, no. 1-2, pp. 213–221, 1987.

[21] R. I. Mackie, R. M. W. Horne, and R. J. Jarvis, "Dynamic modeling of deep-bed filtration," *AIChE Journal*, vol. 33, no. 11, pp. 1761–1775, 1987.

[22] S. D. Rege and H. S. Fogler, "A network model for deep bed filtration of solid particles and emulsion drops," *AIChE Journal*, vol. 34, no. 11, pp. 1761–1772, 1988.

[23] M. M. Sharma and Y. C. Yortsos, "Fines migration in porous media," *AIChE Journal*, vol. 33, no. 10, pp. 1654–1662, 1987.

[24] S. K. Bhuniya, "Flow of suspension through packed beads: studies on the influences of the particle concentration. M. Tech. Thesis," IIT Bombay, 1996.

[25] V. B. Pandya, S. Bhuniya, and K. C. Khilar, "Existence of a critical particle concentration in plugging of a packed bed," *AIChE Journal*, vol. 44, no. 4, pp. 978–981, 1998.

[26] J. W. Jung, S. C. Cao, Y. H. Shin, R. I. Al-Raoush, K. Alshibli, and J. W. Choi, "A microfluidic pore model to study the migration of fine particles in single-phase and multiphase flows in porous media," *Microsystem Technologies*, vol. 24, no. 2, pp. 1071–1080, 2018.

[27] G. Han, T. H. Kwon, J. Y. Lee, and T. J. Kneafsey, "Depressurization-induced fines migration in sediments containing methane hydrate: X-ray computed tomography imaging experiments," *Journal of Geophysical Research: Solid Earth*, vol. 123, no. 4, pp. 2539–2558, 2018.

[28] J. J. Bahk, D. H. Kim, J. H. Chun et al., "Gas hydrate occurrences and their relation to host sediment properties: results from second Ulleung Basin gas hydrate drilling expedition, east sea," *Marine and Petroleum Geology*, vol. 47, pp. 21–29, 2013.

[29] K. Egawa, O. Nishimura, S. Izumi et al., "Bulk sediment mineralogy of gas hydrate reservoir at the East Nankai offshore production test site," *Marine and Petroleum Geology*, vol. 66, pp. 379–387, 2015.

[30] W. J. Winters, R. W. Wilcox-Cline, P. Long et al., "Comparison of the physical and geotechnical properties of gas-hydrate-bearing sediments from offshore India and other gas-hydrate-reservoir systems," *Marine and Petroleum Geology*, vol. 58, pp. 139–167, 2014.

[31] I. Sogami and N. Ise, "On the electrostatic interaction in macroionic solutions," *The Journal of Chemical Physics*, vol. 81, no. 12, pp. 6320–6332, 1984.

[32] G. Sposito, *The Chemistry of Soils*, Oxford University Press, New York, 1989.

Hindawi
Geofluids
Volume 2019, Article ID 1315451, 11 pages
https://doi.org/10.1155/2019/1315451

Research Article

Pore Pressure Disturbance Induced by Multistage Hydraulic Fracturing in Shale Gas: Modelling and Field Application

Yijin Zeng,[1,2] Zizhen Wang ,[3,4] Yanbin Zang ,[1,2] Ruihe Wang ,[3,4] Feifei Wang ,[5] Xinming Niu ,[1,2] and Feng Niu [3,4]

[1]*State Key Laboratory of Shale Oil and Gas Enrichment Mechanisms and Effective Development, Beijing, China*
[2]*Sinopec Research Institute of Petroleum Engineering, Beijing, China*
[3]*Key Laboratory of Unconventional Oil & Gas Development (China University of Petroleum (East China)), Ministry of Education, Qingdao, China*
[4]*School of Petroleum Engineering, China University of Petroleum (East China), Qingdao, China*
[5]*College of Pipeline and Civil Engineering, China University of Petroleum (East China), Qingdao, China*

Correspondence should be addressed to Zizhen Wang; wangzzh@upc.edu.cn

Received 20 January 2019; Revised 20 March 2019; Accepted 26 March 2019; Published 12 May 2019

Guest Editor: Andrew Bunger

Currently, there is no proper method to predict the pore pressure disturbance caused by multistage fracturing in shale gas, which has challenged drilling engineering in practice, especially for the infilling well drilling within/near the fractured zones. A numerical modelling method of pore pressure redistribution around the multistage fractured horizontal wellbore was put forward based on the theory of fluid transportation in porous media. The fracture network of each stage was represented by an elliptical zone with high permeability. Five stages of fracturing were modelled simultaneously to consider the interactions among fractures. The effects of formation permeability, fracturing fluid viscosity, and pressure within the fractures on the pore pressure disturbance were numerically investigated. Modelling results indicated that the pore pressure disturbance zone expands as the permeability and/or the differential pressure increases, while it decreases when the viscosity of the fracturing fluid increases. The pore pressure disturbance level becomes weaker from the fracture tip to the far field along the main-fracture propagation direction. The pore pressure disturbance contours obviously have larger slopes with the variation of permeability than those of the differential pressure. The distances between the pore pressure disturbance contours are smaller at lower permeability and higher viscosity. The modelling results of the updated pore pressure distribution are of great importance for safe drilling. A case study of three wells within one platform showed that the modelling method could provide a reliable estimation of the pore pressure disturbance area caused by multistage fracturing.

1. Introduction

Shale gas becomes more and more important worldwide. The shale gas production reached $7500 \times 10^8\ m^3$ in America in 2016, which made up more than 40% of the total natural gas production of America [1]. The horizontal well factory and multistage hydraulic fracturing are the two most important technologies for shale gas production commercially [2–4].

There is over sixty years of history in the study of fracture propagation in porous media, and many models have been developed, such as the PKN model [5, 6], KGD model [7, 8], and some three-dimensional models [9, 10]. Recently, more complex models for multiple-fracture propagation in horizontal wells have been built, such as the Unconventional Fracture Model (UFM) [11, 12]. In order to obtain complex fracture networks in low permeable shale reservoirs through multistage hydraulic fracturing, many studies have been done to analyze the stress distribution around the fractured horizontal wellbore [13], which is mainly focused on the extent of stress reversal [14] and the effect of stress shadow [15]. Besides the analysis of fracture initiation and propagation, the stress redistribution results are further used to optimize the stage spacing [14, 16, 17] and well space [18]. Such kinds of works have greatly helped to improve the efficiency of stimulation treatments in shale gas formation.

In fact, hydraulic fracturing in the pay zone also has a pressure-elevating effect. The pore pressure will increase during and after the fracturing work. The natural gas within the pay zone of the fracturing well would be driven to the nearby well. When the gas invades the nearby wellbore under drilling, it would lead to a gas kick and overflow. It seems easy to understand the pore pressure elevation caused by hydraulic fracturing, but it is not easy to quantitatively describe these updated pore pressure distributions. Currently, there is no proper method to predict or detect such pore pressure disturbances from the industry, and it has not yet gained enough concerns to warrant a scientific study. [19]. Unfortunately, it has challenged the drilling engineering in practice, especially for the infilling well drilling within/near the fractured zones. The infilling well drilling practice in Fuling, the first and largest commercially developed shale gas field in China, indicated that some well drilling works were obviously influenced by troubles related to the large-scale hydraulic fracturing work [20], such as gas kick, overflow, and drilling fluid being polluted by fracturing fluid from neighbouring wells. The resultant percentage of nonproductive time could reach as high as 21.04~52.82% according to a simple summary of six infilling wells.

Pore pressure distribution around a single fracture could be approximately described as an ellipse (Koning, 1985; [21, 22]). But for the multistaged fracturing in shale gas, pore pressure distribution around several fractures should be evaluated simultaneously considering the interactions among fractures. In this study, firstly, a numerical modelling method of pore pressure distribution around a multistage fractured horizontal wellbore was put forward based on the theory of fluid transportation in porous media. Then, a series of numerical modelling experiments were carried out to investigate the effects of formation permeability, fracturing fluid viscosity, and pressure within the fractures on the pore pressure distribution. Finally, the implication of the safe drilling of an infilling well was further discussed. And a case study of infilling well drilling with the aid of numerical modelling showed that the average ROP reached 11.02 m/h and no drilling troubles or accidents occurred.

2. Methods

2.1. Model Description. The horizontal section for shale gas production is usually around 1000 meters. Multistage fracturing can produce a fracture network including main fractures and different scales of subfractures (Figure 1(a)). The length of the fracture network of each stage can be 200~400 meters according to the interpretation of microseismic monitoring. In order to investigate the pore pressure disturbance at the scale of the horizontal well, the modelled size is $L_x = 1000\,\mathrm{m}$ in length and $L_y = 500\,\mathrm{m}$ in width, representing the half horizontal plane along the horizontal wellbore section (Figure 1(b)). According to the wire-mesh model by Xu et al. [23], the fracture network of each stage can be represented by an elliptical zone. Here, we use an ellipse (semimajor axis $L = 200\,\mathrm{m}$, short axis $d = 2\,\mathrm{m}$) with very high permeability of $k_f = 10^8\,\mathrm{mD}$ to represent the fracture network (as shown in Figure 1(c)) compared to that of the low permeability of the shale formation ($k_m < 1\,\mathrm{mD}$). In this study, we simulate five stages of fracturing. The center points of these five half-ellipses from left to right are (440, 0), (470, 0), (500, 0), (530, 0), and (560, 0). The space between two nearby ellipses is 30 meters equal to the fracturing stage space.

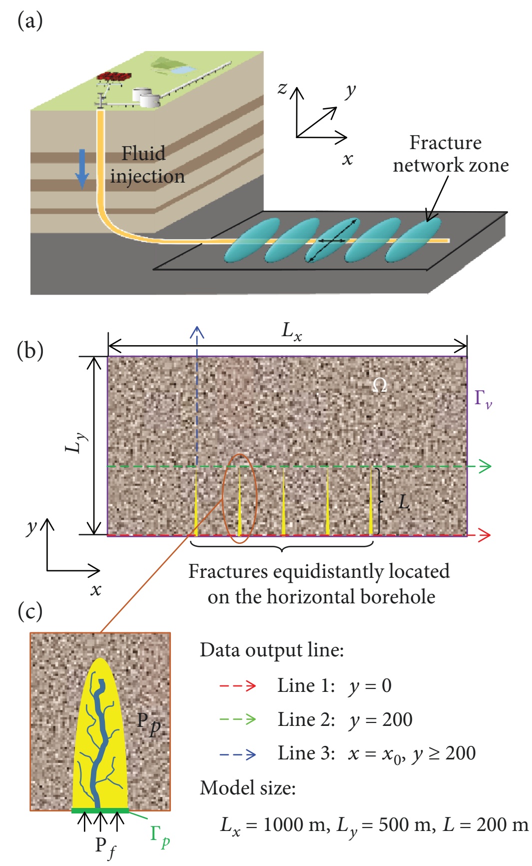

Figure 1: Numerical model of the pore pressure disturbance by hydraulic fracturing. Modelled domain size = 1000 × 500 m. The fracture network of each stage is represented by an elliptical zone (semimajor axis = 200 m, short axis = 2 m) with high permeability.

For the transportation of any single phase (fluid or gas) within the porous formation, it is controlled by the continuity equation [24] according to the law of conservation of mass:

$$\frac{\partial(\rho\phi)}{\partial t} + \nabla\cdot(\rho\mathbf{V}) = 0, \tag{1}$$

where ρ is the density of the fluid, ϕ is the porosity, and $\mathbf{V}$ is the percolation velocity. If the fluid percolation follows Darcy's law, the motion equation should be [25]

$$\mathbf{V} = -\frac{k}{\mu}\nabla P, \tag{2}$$

where μ is the viscosity of the fluid, k is the permeability of the formation, and ∇P is the gradient of pressure.

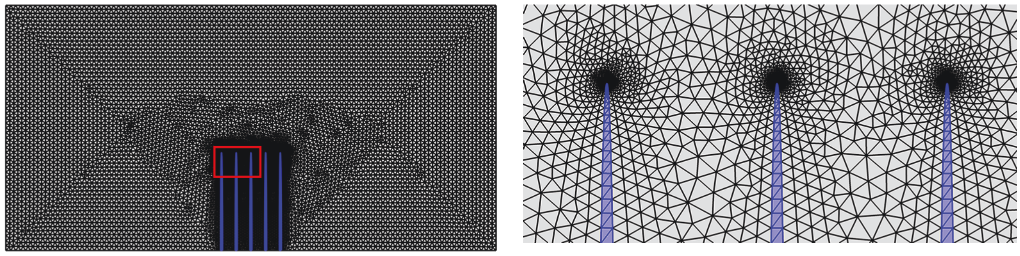

(a) (b)

Figure 2: Meshed model with triangular grids. The grids within the fracture network zone are refined to ensure convergence and accuracy of the numerical modelling.

Combining equations (1) and (2) gets

$$\nabla \cdot \left[\rho \frac{k}{\mu} \nabla P\right] = \frac{\partial(\rho\phi)}{\partial t}. \tag{3}$$

For a horizontal well, the influence of temperature on the density of fluid can be neglected. So the density variation with pressure can be expressed by

$$\rho = \rho_0 \left[1 + \beta_p (P - P_0)\right], \tag{4}$$

where ρ_0 is the density at the reference pressure (P_0) and $\beta_p = (1/\rho)(\partial\rho/\partial P)|_{T=\text{const.}}$ is the compressibility of the fluid. Because the compressibility of the shale rock is much smaller than that of fluid, the decrease of porosity with pressure is very small, so the right side of equation (3) can be further derived as

$$\frac{\partial(\rho\phi)}{\partial t} = \phi \frac{\partial\rho}{\partial t} = \phi\rho_0\beta_p \frac{\partial(P - P_0)}{\partial t}. \tag{5}$$

Therefore, equation (3) can be written as

$$\nabla \cdot \left(\rho \frac{k}{\mu} \nabla P\right) = \rho_0\phi\beta_p \frac{\partial(P - P_0)}{\partial t}. \tag{6}$$

For a certain investigated domain (Ω) as shown in Figure 1(b), the initial pressure (P_0) is equal to the shale gas reservoir pressure which is taken as the reference pressure:

$$P|_{t=0,\Omega} = P_0. \tag{7}$$

For the pressure boundary of Γ_p in Figure 1(c), the hydraulic fracturing pressure (P_f) is applied:

$$P|_{t,\Gamma_p} = P_f. \tag{8}$$

So the differential pressure ($\Delta P = P_f - P_0$) is approximately the power on the fracture surface driving the seepage of fracturing fluid into the shale formation, which basically results in the increase of pore pressure (P) near the fracture.

For other outer boundaries of the model (Figure 1(b)), they are defined to be zero flow because these boundaries are at the far-field condition:

$$\frac{k}{\mu} \nabla P \cdot \vec{n}\Big|_{t,\Gamma_v} = 0. \tag{9}$$

The numerical calculation for the definite problem described by equations (6)–(9) within the domain shown in Figure 1(b) is carried out by FEM software. The multifrontal massively parallel sparse (MUMPS) method is used to solve the equations with speed-up convergence. Triangular grids are used to mesh the model. In order to ensure modelling convergence and acceptable accuracy, the maximum grid size is 1/(2-3) of the elliptical minor axis. Generally, the number of grids in a model is about 10^4~10^5 (as shown in Figure 2). After the pressure field $P(x, y)$ at every time step is calculated, the pressure variation on the output lines (see definitions in Data Processing) can be extracted for detailed analysis.

2.2. Data Processing. The initial reservoir pressure is taken as a reference pressure to define the pore pressure disturbance as $P(x, y, t)/P_0$. Therefore, the pressure disturbance (P/P_0) is dimensionless and represents the pore pressure elevation due to hydraulic fracturing. In order to quantitatively analyze the pore pressure disturbance, three data output lines are set as shown in Figure 1(b).

(1) Data Output Line 1: $y = 0$. This line starts from the origin point of the model and extends to the right boundary of the model along the positive x-axis direction. The pore pressure distribution along this line can reflect the variation of pore pressure near the horizontal wellbore

(2) Data Output Line 2: $y = 200$. This line starts from the point (0, 200) on the left boundary of the model and extends to the right boundary along the positive x-axis direction. The pore pressure distribution along this line can reflect the variation of pore pressure near the fracture tip in the x-axis direction

(3) Data Output Line 3: $x = 440$ and $y \geq 200$. This line starts from the tip (440, 200) of the left fracture and extends to

Table 1: Numerical modelling series and their modelling parameters.

Series index	Variable parameters		Constant parameters
1	Permeability of the shale formation (mD) (k)	$k = [0.2, 0.5, 0.8, 1.0, 2.0]$	$\mu = 1$ mPa·s $\Delta P = 70$ MPa
2	Viscosity of the fracturing fluid (mPa) (μ)	$\mu = [1, 2, 3]$	$k = 0.5$ mD $\Delta P = 70$ MPa
3	Differential pressure (MPa) ($\Delta P = P_f - P_0$)	$\Delta P = [60, 70, 80]$	$\mu = 1$ mPa·s $k = 0.5$ mD

the top boundary along the positive y-axis direction. The pore pressure distribution along this line can reflect the variation of pore pressure in the y-axis direction

For each modelling, the pore pressure distributions along these three lines are extracted, and then the corresponding pore pressure disturbances are calculated for further analysis.

2.3. Design of the Numerical Modelling Experiments. To investigate the effects of different factors of permeability (k), viscosity of the fracturing fluid (μ), and differential pressure (ΔP, via changes in the hydraulic fracturing pressure at a constant initial reservoir pressure) on the pore pressure disturbance induced by fracturing, three series of modelling experiments are designed as detailed in Table 1. For each series, only one of the controlling parameters of permeability, viscosity of the fracturing fluid, or differential pressure is varied while the others are held constant. Therefore, any resultant change in overall pore pressure disturbance should be directly caused by the change of the varied parameter. Other modelling parameters for all these modellings are shown in Table 2 unless otherwise stated.

Table 2: Parameters used in the numerical modelling.

Parameters	Value
Shale gas reservoir pressure (initial pressure) P_0 (MPa)	30
Compressibility of the shale C_m (Pa^{-1})	0.05×10^{-9}
Porosity of the shale formation ϕ	0.05
Effective permeability of the fracture network zone k_f (mD)	10^8
Density of the fracturing fluid ρ (g/cm^3)	1.0
Fracturing pressure duration time for modelling t (s)	18000
Time step for numerical calculation dt (s)	10

3. Results and Discussions

With the range of parameters shown in Tables 1 and 2, the pressure distribution patterns of the modellings are similar. Figure 3 shows the modelling results for one of the realizations of Table 1. The affected zone of pore pressure disturbance increases with the duration of differential pressure. In the following, the pore pressure distributions on the three output lines at different times are analyzed quantitatively for each series of modelling (Table 1).

3.1. The Influence of Permeability. To investigate the influence of permeability on the pore pressure disturbance, a series of modellings (series 1 in Table 1) with different permeabilities varying from 0.2 mD to 2.0 mD are carried out for the constant fracturing pressure and viscosity ($\Delta P = 70$ MPa and $\mu = 1$ mPa·s, respectively). The results are shown in Figure 4.

The results shown in Figure 4 indicate that the pore pressure disturbance zone ($P/P_0 > 1.0$) expands obviously from the fractures in both the x and y directions if the permeability of the shale formation increases. Although the permeability of a shale gas reservoir is usually very low, the pore pressure disturbance due to such large-scale, multistage hydraulic fracturing is significant. According to our modelling at $k = 0.5$ mD, the pore pressure disturbance zone with 5% increase ($P/P_0 = 1.05$) could be reached as far as 40.3 m in the x direction and 48.4 m in the y direction from the fracture.

3.2. The Influence of Viscosity. To understand the influence of viscosity on the pore pressure disturbance, a series of modellings (series 1 in Table 1) with varying viscosities (1 mPa·s, 2 mPa·s, and 3 mPa·s) are carried out when the permeability and the differential pressure are held constant ($k = 0.5$ mD, $\Delta P = 70$ MPa). The results are shown in Figure 5.

The pore pressure disturbance zone decreases when the viscosity of the fracturing fluid increases (Figure 5). This is because the increase of viscosity makes the fluid transportation in the shale much more difficult. Slick water with relatively low viscosity (usually <10 mPa·s) is widely used for the fracturing in shale gas reservoirs. According to our modelling at $\mu = 3$ mPa·s, the pore pressure disturbance zone with 5% increase ($P/P_0 = 1.05$) could be reached at 24.6 m in the x direction and 27.3 m in the y direction from the fracture. These results indicate that the influence of viscosity on the pore pressure disturbance is much less than that of formation permeability.

3.3. The Influence of Differential Pressure. In order to study the influence of differential pressure on the pore pressure disturbance, the formation pressure ($P_0 = 30$ MPa), permeability ($k = 0.5$ mD), and viscosity of the fracturing fluid ($\mu = 1$ mPa·s) are kept constant and the hydraulic fracturing pressure is set to be 90 MPa, 100 MPa, and 110 MPa.

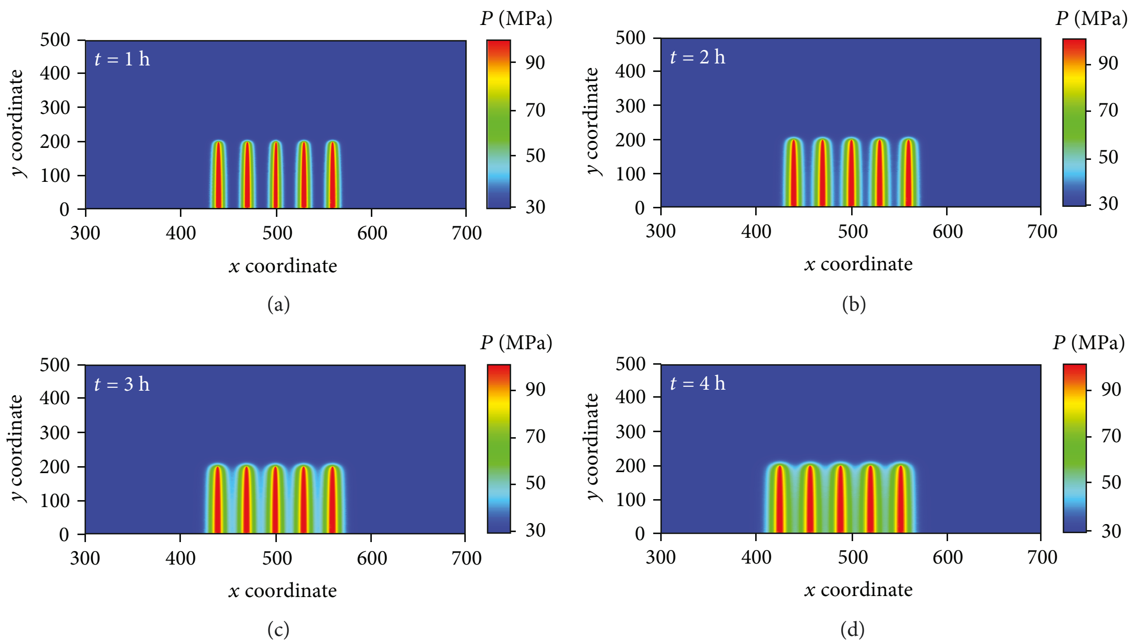

FIGURE 3: The pore pressure distributions at different times from the modelling ($k = 0.2$ mD, $\mu = 1$ mPa·s, $P_0 = 30$ MPa, and $\Delta P = 70$ MPa): (a) $t = 1$ h, (b) $t = 2$ h, (c) $t = 3$ h, and (d) $t = 4$ h.

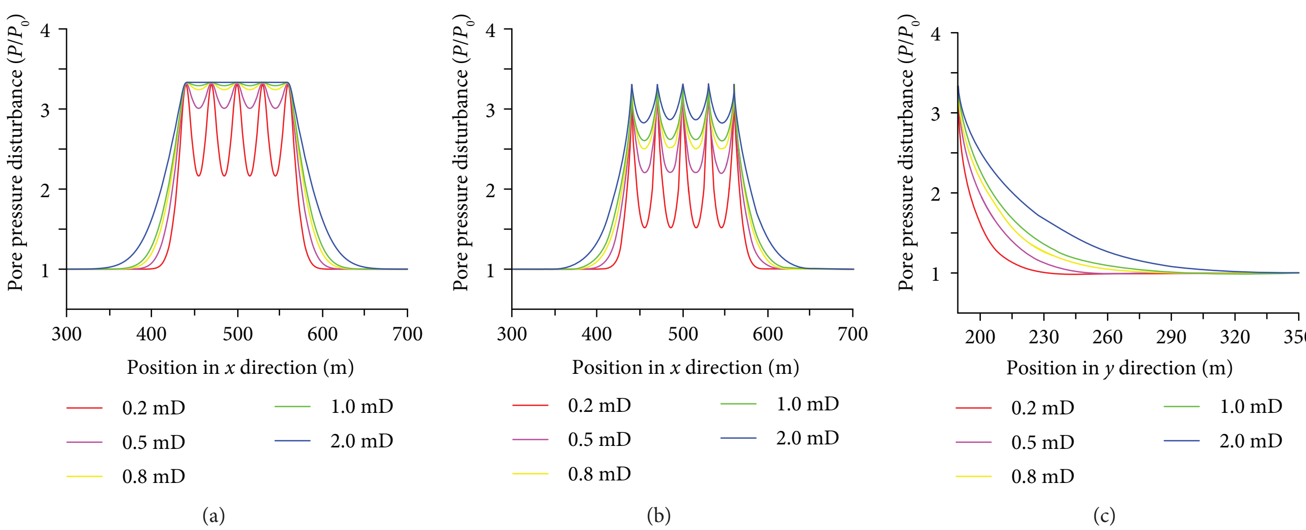

FIGURE 4: Pore pressure disturbance for different permeabilities at $t = 4$ h: (a) for data output line 1, (b) for data output line 2, and (c) for data output line 3.

So the differential pressure varies at 60 MPa, 70 MPa, and 80 MPa, respectively. The modelling results are shown in Figure 6.

As shown in Figure 6, the pore pressure disturbance zone expands as the differential pressure increases. But the increasing rate is relatively low. According to our modelling at $k = 0.5$ mD and $\mu = 1$ mPa·s, when the differential pressure increases from 70 MPa to 80 MPa, the pore pressure disturbance zone with 5% increase ($P/P_0 = 1.05$) only increases 1.19 m and 1.41 m in the x and y directions, respectively. This means, for the pressure level usually applied in the fracturing of shale gas formation, the influence of differential pressure on further expansion of the pore pressure disturbance zone is very small, which can almost be ignored compared to the larger scale of the fracture network zone (semimajor axis $L = 200$ m).

3.4. Implication of the Safe Drilling of the Infilling Well. For the implementation of the "well factory," it is important to design a safe well spacing to avoid well interference during drilling and fracturing, especially for infilling well drilling. Based on the geometric positions of wells and fractures, the

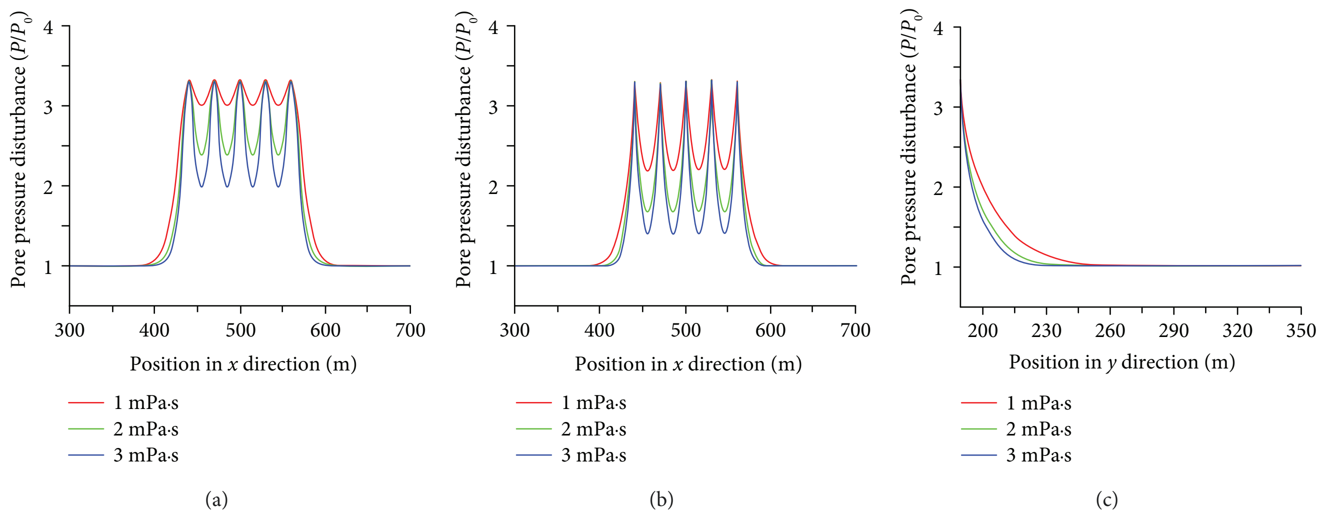

FIGURE 5: Pore pressure disturbance for different viscosities at $t = 4$ h: (a) for data output line 1, (b) for data output line 2, and (c) for data output line 3.

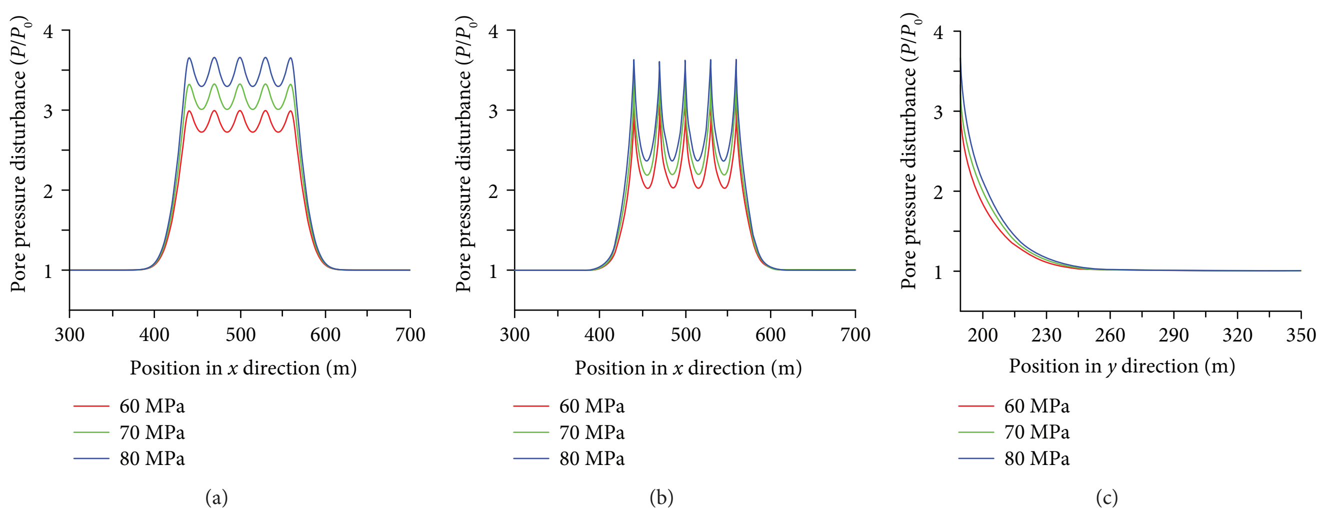

FIGURE 6: Pore pressure disturbance for different fracturing pressures at $t = 4$ h: (a) for data output line 1, (b) for data output line 2, and (c) for data output line 3.

pore pressure disturbance along the main-fracture propagation direction should be carefully considered. Generally, the effective fracture zones are expected to connect to one another between the two closest nearby stimulation stages from the two sides of the two parallel wells [18], based on the view of gas production. However, such a connection between the effective fracture zones should be controlled to a certain extent to avoid troubles and events during infilling well drilling, such as gas kick and lost circulation, which requires a safe well spacing.

For example, there are two parallel horizontal wells (Well A and Well B) within the same plane and both of them have been hydraulically fractured (as shown in Figure 7) at the same condition that the pore pressure disturbance zones are the same. Now an infilling well (Well C) is planned to drill to accelerate shale gas recovery. If the density of the drilling fluid is designed according to the initial reservoir

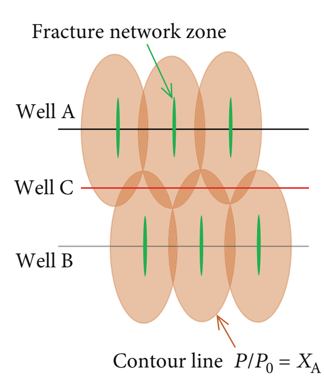

FIGURE 7: Pore pressure disturbance caused by the fracturing of Well A and Well B influences the safe drilling of Well C. Note that the pore pressure disturbance zone overlapped within the contour line $P/P_0 = X_A$ and $P/P_0 > 2X_A$.

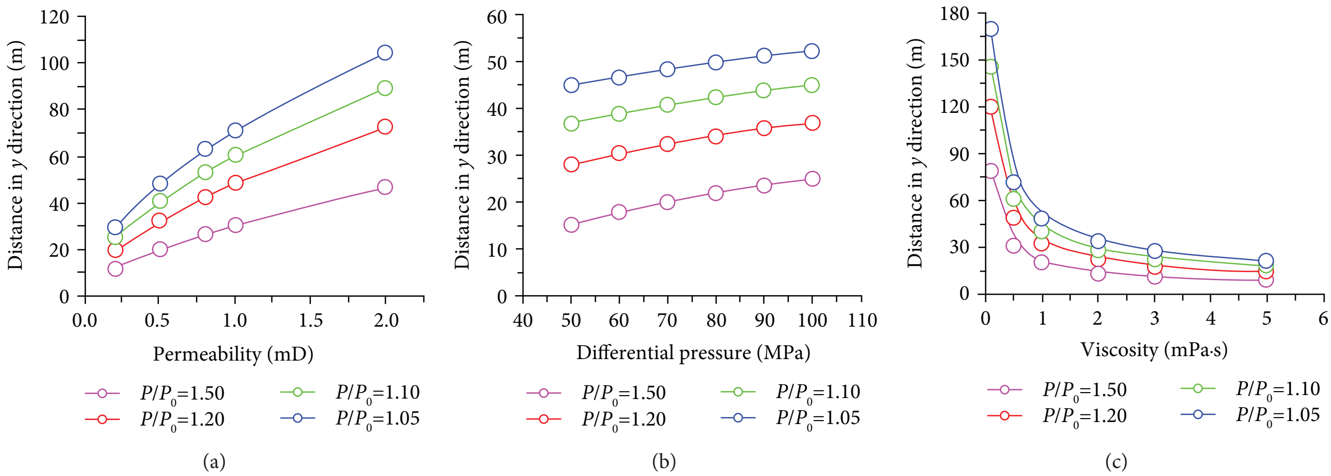

FIGURE 8: Different levels of pore pressure disturbance along the y direction from the fracture tip with the variation of (a) permeability, (b) differential pressure, and (c) viscosity.

pressure and the ability of well control could deal with pressure disturbances lower than X_A, then Well C would probably undergo gas kick in sections where the pore pressure disturbance zones of Well A and Well B overlapped ($P/P_0 > 2X_A$). To drill Well C safely, the density of the drilling fluid should be optimized considering the pore pressure disturbance. Therefore, it is important to understand the pore pressure disturbance along the main-fracture propagation direction.

In order to quantitatively investigate the pore pressure disturbance along the main-fracture propagation direction (y direction in this paper), the modelling results on data output line 3 are further analyzed (Figure 8). As shown in Figure 8, the pore pressure disturbance level becomes weaker from the fracture tip to the far field along the main-fracture propagation direction. The pore pressure disturbance contours obviously have larger slopes with the variation of permeability than those of the differential pressure (Figures 8(a) and 8(b)), which indicates that the distance of the pore pressure disturbance in the y direction is more sensitive to the change of permeability. The pore pressure disturbance contours first decrease quickly at relatively low viscosity and then go down slowly to a plateau with further increase of the viscosity (Figure 8(c)). The distances between the pore pressure disturbance contours are smaller at lower permeability and higher viscosity (Figures 8(a) and 8(c)), which means that the gradient of pore pressure along the y direction is large.

To analyze the sensitivity of pore pressure to different parameters in a universal way, we define two dimensionless parameters along the main-fracture propagation direction:

(1) Dimensionless pressure (P_D):

$$P_D = \frac{\mu}{k}\frac{vR_y}{P_f - P} \tag{10}$$

(2) Dimensionless distance (R_D):

$$R_D = \frac{R_y}{L}, \tag{11}$$

where L is the half-length of the fracture, $R_y = y - L$ is the seepage distance in the y direction from the fracture tip, and v is the seepage velocity.

Our modelling results of series 3 (see detailed parameters in Table 1) show that the P_D~R_D curves for different differential pressures completely overlap with each other. It means the relationship between P_D and R_D at a certain time is independent to the hydraulic fracturing pressure (P_f) and is controlled by the fluid mobility (k/μ). This is because the seepage velocity is proportional to the pressure gradient for Darcy's flow which is consistent with equations (10) and (11). So here we discuss the dimensionless pressure distribution along the data output line 3 at a constant differential pressure ($\Delta P = 70$ MPa, $P_0 = 30$ MPa), and the results are shown in Figure 9. On the whole, the dimensionless pressure decreases quickly as the dimensionless distance increases. The lower the fluid mobility is within the formation, the faster the dimensionless pressure drops, which means a smaller pore pressure disturbance area (Figure 9). For different types of mobility, there is a sharp decrease of the dimensionless pressure near the fracture tip ($R_D < 0.01$). And following the sharp drop, there is a small section with a slower dimensionless pressure drop or even a slightly dimensionless pressure increase due to the fracture interaction. The nearby fracture can contribute to the pore pressure and the seepage velocity, which leads to the abnormal high value of the dimensionless pressure according to equation (10). This effect becomes more obvious as the mobility increases. The pore pressure disturbance contours are also added to Figure 9 for comparison.

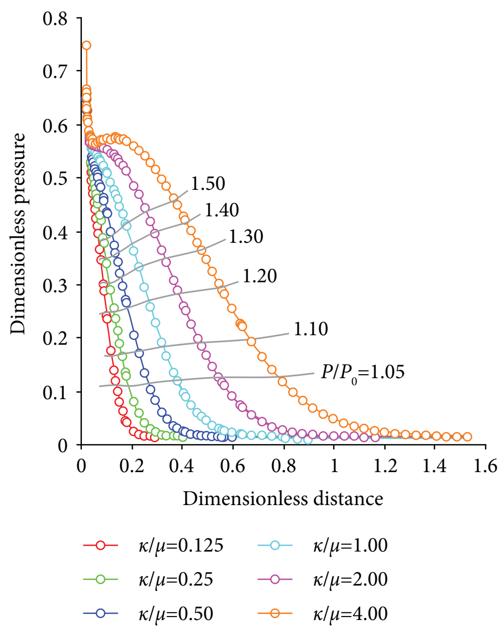

Figure 9: The change of the dimensionless pressure with the dimensionless distance along data output line 3 for different types of fluid mobility. The value of the fluid mobility (k/μ) here is calculated with the unit mD/mPa·s. The circle points are from numerical modellings. The gray curves are pore pressure disturbance contours with the initial reservoir pressure $P_0 = 30$ MPa.

According to the design method of casing program [26], the safety margin of equivalent density for gas kick is 0.05-0.10 g/cm^3. This indicates that it would be safe for the infilling well drilling with similar designs (including drilling fluid density and casing program) of the nearby wells in the areas where the pore pressure disturbance is smaller than 1.05 (i.e., $P/P_0 < 1.05$). If the infilling well needs to penetrate zones with a pore pressure disturbance of $P/P_0 > 1.05$ to meet reservoir engineering or geological design requirements, the casing program or/and the drilling fluid density for the infilling well should be carefully optimized based on the updated pore pressure distribution. At this condition, the numerical modelling of the pore pressure disturbance as mainly discussed in this study could provide helpful and practical results.

4. Field Applications

The spacing of two nearby paralleled horizontal wells is relatively large at the early development stage of the Fuling shale gas field, mainly 600-1300 meters [27, 28]. By contrast, the well spacing within the same drilling unit for shale gas production in America is usually 200-300 m [29]. For such a kind of large well spacing in Fuling, infilling well drilling is a promising way to accelerate recovery. However, the pore pressure of the interested block has been greatly disturbed by numerous multistage hydraulic fracturing, which push the drilling work of infilling wells into great risk.

Well 81-2HF, Well 81-3HF, and Well 81-4HF are horizontal wells within the same well platform no. 81 (Figure 10). These three wells have similar casing program: 473.1 mm × 55~60 m (conductor) + 339.7 mm × 700~720 m (1st spud) + 244.5 mm × 2840~2900 m (2nd spud) + 139.7 mm × 4500~5100 m (3rd spud). Their targets are within the same formation.

Well 81-2HF was drilled to 5005 m (TVD = 3873.81 m) at the third spud using oil-based mud (OBM) with a density of 1.47 g/cm^3 (Figure 10). And it was completed on June 12, 2015. Then, the 1000 m horizontal section was hydraulically fractured with fifteen stages. The fracturing work continued for about ten days and finished on Aug. 9, 2015. Nearly 31200 m^3 of fluid was injected to the formation. The pump pressure was about 50~95 MPa with a pump displacement of 2~15 m^3/min. The tested transient gas production was 5.03×10^4 m^3/d. Then, Well 81-2HF was closed due to an unfinished gas pipeline network.

The pore pressure disturbance caused by the hydraulic fracturing in Well 81-2HF was numerically modelled. Although there was no microseismic detection data to quantitatively describe the fracture half-length of Well 81-2HF, the microseismic data of 104 stages of similar fracturing stimulations from 4 wells in the Fuling Gas Field showed that the average fracture half-length was 189.4 m. Our modelling results based on the fracturing parameters of Well 81-2HF showed that the pore pressure disturbance contour of $P/P_0 = 1.05$ was about 48.73 m from the facture tip along the fracture propagation direction. However, the nearest distance from the target point of Well 81-2HF to that of Well 81-3HF was only 217.4 m at TVD = 2968.96 m. This means Well 81-3HF penetrated the zones with the pore pressure disturbance of $P/P_0 > 1.05$, which has a high probability of undergoing gas kicks.

In fact, the drilling practice of Well 81-3HF verified the above prediction. Well 81-3HF and Well 81-4HF were drilled by the "well factory" mode after Well 81-2HF was fractured. The drilling sequence is shown in Figure 11. The third spud drilling of Well 81-3HF was seriously influenced by the multistage fracturing of Well 81-2HF. When Well 81-3HF was at the third spud, Well 81-2HF was closed with the wellhead pressure as high as 40 MPa. There were gas kicks fifteen times in Well 81-3HF within the depth of 2994~4505 m. Among these fifteen gas kicks, thirteen kicks had to close the well and exhaust the gas by burning. The flames of these burnings reached 2~6 meters, and the average burning time was nearly 70 min. The drilling fluid was weighted seven times, and its density increased from 1.36 g/cm^3 to 1.85 g/cm^3 (Figure 11). The nonproductive time due to these kicks reached 288 hours, and the average ROP of the third spud decreased to 5.17 m/h. As a comparison, there was no gas kick during the third spud drilling of Well 81-2HF with the drilling fluid density of 1.47 g/cm^3 and the average ROP was 6.77 m/h.

Direct evidence of the drilling troubles in Well 81-3HF related to the fracturing of Well 81-2HF was a string sticking at 4129 m on Apr. 21, 2016. It failed to release the sticking by conventional methods. But after the wellhead pressure of

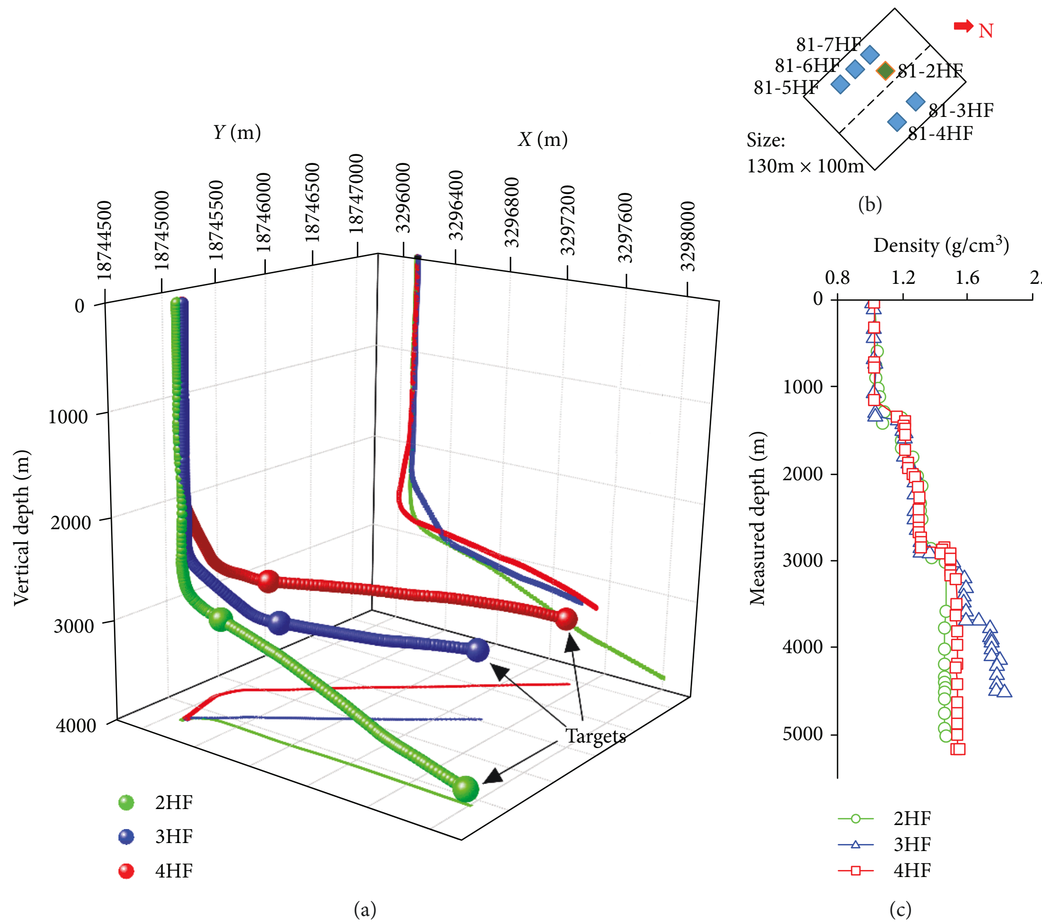

Figure 10: The basic information about the three nearby wells in platform 81: (a) the 3D trajectory and the corresponding horizontal and vertical projections for Well 81-2HF, Well 81-3HF, and Well 81-4HF; (b) the well location layout of platform 81; (c) the drilling fluid density used in these three wells.

Well 81-2HF dropped to 30 MPa at 8:00 am on Apr. 24, the drill string was successfully released (Figure 11). This indicated that the geostress and pore pressure disturbance caused by the hydraulic fracturing were responsible for the sticking.

On the other hand, the nearest distance from the target point of Well 81-2HF to that of Well 81-4HF was about 528.0 m at TVD = 2697.98 m. So according to the modelling results, the trajectory of Well 81-4HF is out of the pore pressure disturbance area of Well 81-2HF. The drilling practice of Well 81-4HF was consistent with this result. There was only one gas kick for the third spud drilling of Well 81-4HF with the drilling fluid density of 1.54 g/cm^3 (Figure 10), and the average ROP was 8.14 m/h.

5. Conclusions

A numerical modelling method of pore pressure redistribution around a multistage fractured horizontal wellbore was put forward based on the theory of fluid transportation in porous media. The fracture network of each stage was represented by an elliptical zone with high permeability. Five stages of fracturing were modelled simultaneously to consider the interactions among fractures.

The effects of formation permeability, fracturing fluid viscosity, and pressure within the fractures on the pore pressure disturbance were numerically investigated. Modelling results indicated that the pore pressure disturbance zone expands as the permeability and/or the differential pressure increases, while it decreases when the viscosity of the fracturing fluid increases. The pore pressure disturbance level becomes weaker from the fracture tip to the far field along the main-fracture propagation direction. The pore pressure disturbance contours obviously have larger slopes with the variation of permeability than those of the differential pressure. The distances between the pore pressure disturbance contours are smaller at lower permeability and higher viscosity.

The modelling results of the updated pore pressure distribution is of great importance for safe drilling. A case study of three wells within one platform showed that the modelling method could provide a reliable prediction of the pore pressure disturbance area caused by multistage fracturing.

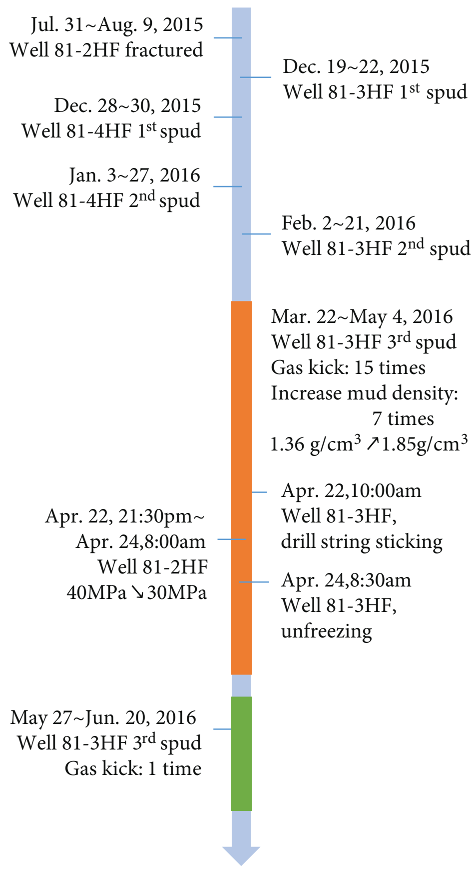

Figure 11: Main related events in the three nearby wells in chronological order.

Data Availability

The data in the tables used to support the findings of this study are included within the article. The data in the figures used to support the findings of this study are available from the corresponding author (wangzzh@upc.edu.cn) upon request.

Conflicts of Interest

The authors declare that there is no conflict of interest regarding the publication of this paper.

Acknowledgments

This study is supported by the State Key Laboratory of Shale Oil and Gas Enrichment Mechanisms and Effective Development, China (No. ZC0607-0016); the National Natural Science Foundation of China (No. 51704309); and the Fundamental Research Funds for the Central Universities, China (18CX07008A).

References

[1] K. L. Krisanne, S. Weissert, J. B. Jackson, and D. Marcotte, "Marcellus shale hydraulic fracturing and optimal well spacing to maximize recovery and control costs," in *SPE Hydraulic Fracturing Technology Conference*, The Woodlands, TX, USA, January 2011.

[2] T. R. Koløy, K. Brække, T. Sørheim, and P. Lonning, "The evolution, optimization and experience of multistage frac completions in a North Sea environment," in *SPE Annual Technical Conference and Exhibition*, Amsterdam, The Netherlands, October 2014.

[3] N. Sorek, J. A. Moreno, R. Rice, G. Luo, and C. Ehlig-Economides, "Optimal hydraulic fracture angle in productivity maximized shale well design," in *SPE Annual Technical Conference and Exhibition*, Amsterdam, The Netherlands, October 2014.

[4] J. Yao, H. Sun, D. Y. Fan, C. C. Wang, and Z. X. Sun, "Numerical simulation of gas transport mechanisms in tight shale gas reservoirs," *Petroleum Science*, vol. 10, no. 4, pp. 528–537, 2013.

[5] R. P. Nordgern, "Propagation of a vertical hydraulic fracture," *Society of Petroleum Engineers Journal*, vol. 12, no. 4, pp. 306–314, 1972.

[6] T. K. Perkins and L. R. Kern, "Widths of hydraulic fractures," *Journal of Petroleum Technology*, vol. 13, no. 9, pp. 937–949, 1961.

[7] J. Geertsma and F. De Klerk, "A rapid method of predicting width and extent of hydraulically induced fractures [J]," *Journal of Petroleum Technology*, vol. 21, no. 12, pp. 1571–1581, 1969.

[8] S. A. Khristianovitch and Y. P. Zheltov, "Formation of vertical fractures by means of highly viscous fluids," in *Proceedings of the 4th World Petroleum Congress*, pp. 579–586, Roma, Italy, 1955.

[9] J. I. Adachi, E. Detournay, and A. P. Peirce, "Analysis of the classical pseudo-3D model for hydraulic fracture with equilibrium height growth across stress barriers," *International Journal of Rock Mechanics and Mining Science*, vol. 47, no. 4, pp. 625–639, 2010.

[10] E. V. Dontsov and A. P. Peirce, "An enhanced pseudo-3D model for hydraulic fracturing accounting for viscous height growth, non-local elasticity, and lateral toughness," *Engineering Fracture Mechanics*, vol. 142, pp. 116–139, 2015.

[11] X. Weng, O. Kresse, C. Cohen, R. Wu, and H. Gu, "Modeling of hydraulic fracture network propagation in a naturally fractured formation," *SPE Production & Operations*, vol. 26, no. 4, pp. 368–380, 2011.

[12] K. Wu, "Simultaneous multi-frac treatments: fully coupled fluid flow and fracture mechanics for horizontal wells," in *SPE Annual Technical Conference and Exhibition*, New Orleans, LA, USA, September 2013.

[13] Y. Cheng, "Mechanical interaction of multiple fractures: exploring impacts of the selection of the spacing/number of perforation clusters on horizontal shale-gas wells," *SPE Journal*, vol. 17, no. 4, pp. 992–1001, 2012.

[14] N. P. Roussel and M. M. Sharma, "Optimizing fracture spacing and sequencing in horizontal-well fracturing," *SPE Production & Operations*, vol. 26, no. 2, pp. 173–184, 2011.

[15] M. K. Fisher, J. R. Heinze, C. D. Harris, B. M. Davidson, C. A. Wright, and K. P. Dunn, "Optimizing horizontal completion techniques in the Barnett Shale using microseismic fracture mapping," in *SPE Annual Technical Conference and Exhibition*, Houston, TX, USA, September 2004.

[16] C. Liu, H. Liu, Y. P. Zhang, D. W. Deng, and H. A. Wu, "Optimal spacing of staged fracturing in horizontal shale-gas

well," *Journal of Petroleum Science and Engineering*, vol. 132, pp. 86–93, 2015.

[17] J. C. Morrill and J. L. Miskimins, "Optimizing hydraulic fracture spacing in unconventional shales," in *SPE Hydraulic Fracturing Technology Conference*, The Woodlands, Texas, USA, February 2012.

[18] X. Shen, W. Standifird, and S. Evans, "Optimizing multistage hydraulic fracturing design base on 3D continuum damage mechanics," in *SPE/IADC Middle East Drilling Technology Conference and Exhibition*, Abu Dhabi, UAE, January 2016.

[19] Z. Wang and R. Wang, "Pore pressure prediction using geophysical methods in carbonate reservoirs: current status, challenges and way ahead," *Journal of Natural Gas Science and Engineering*, vol. 27, Part 2, pp. 986–993, 2015.

[20] Q. Xue, L. Henry, L. Huang et al., "Modeling of torsional oscillation of drillstring dynamics," *Nonlinear Dynamics*, pp. 1–17, 2019.

[21] J. Ge, *Modeling and analysis of reservoir response to stimulation by water injection, [M.S thesis]*, A& M University, College Station, TX, USA, 2009.

[22] N. R. Warpinski and L. W. Teufel, "Influence of geologic discontinuities on hydraulic fracture propagation (includes associated papers 17011 and 17074)," *Journal of Petroleum Technology*, vol. 39, no. 2, pp. 209–220, 1987.

[23] W. Xu, U. Ganguly, and X. Weng, "Wire mesh: a novel shale fracturing simulator," in *International Oil and Gas Conference and Exhibition in China*, Beijing, China, June 2010.

[24] J. Bear, *Dynamics of Fluids in Porous Media*, American Elsevier Publishing Company, New York, NY, USA, 1972.

[25] L. P. Dake, "Fundamentals of reservoir engineering," in *Developments in Petroleum Science*, Elsevier Science, Amsterdam, 8 edition, 1978.

[26] SY/T 5431-2008, *The Design Method of Casing Program*, Standards Press of China, 2008.

[27] B. Lu, "Sinopec engineering technical advances and its developing tendency in shale gas," *Petroleum Drilling Techniques*, vol. 41, pp. 1–10, 2013.

[28] Z. Fanhui, G. Jianchun, L. Heng, and X. Yong, "Experience of efficient fracturing of shale gas in North America and enlightenment to China," *Journal of Southwest Petroleum University (Science & Technology Edition)*, vol. 35, pp. 90–96, 2013.

[29] O. Hummes, P. R. Bond, W. Symons et al., "Using advanced drilling technology to enable well factory concept in the Marcellus shale," in *2012 in IADC/SPE Drilling Conference and Exhibition*, San Diego, CA, USA, March 2012.

Hindawi
Geofluids
Volume 2019, Article ID 5316149, 15 pages
https://doi.org/10.1155/2019/5316149

Research Article

Experimental Study on the Brittle-Ductile Response of a Heterogeneous Soft Coal Rock Mass under Multifactor Coupling

Weijian Yu[1,2] **Genshui Wu**[1] **Baifu An,**[2] **and Ping Wang**[2]

[1]*School of Resource & Environment and Safety Engineering, Hunan University of Science and Technology, Xiangtan, Hunan 411201, China*
[2]*Hunan Key Laboratory of Safe Mining Techniques of Coal Mines, Hunan University of Science and Technology, Xiangtan, Hunan 411201, China*

Correspondence should be addressed to Weijian Yu; ywjlah@163.com and Genshui Wu; wu_genshui@163.com

Received 27 November 2018; Revised 27 February 2019; Accepted 28 March 2019; Published 2 May 2019

Guest Editor: Bisheng Wu

After a gas drainage event causes different degrees of initial porosity in the coal seam, the heterogeneity of the coal mass becomes much more obvious. In this paper, soft coal testing samples with different degrees of heterogeneity were prepared first by a new special experimental research method using hydrogen peroxide in an alkaline medium to generate oxygen. Then, a series of mechanical tests on the soft coal mass samples were carried out under multiple factor coupling conditions of different heterogeneities and confining pressures. The results show that with a low strength, the ductility failure characteristic and a kind of rheology similar to that for soft rock flow were reflected for the soft coal; i.e., the stress-strain curve of the coal mass had no apparent peak strain and residual strength. An interesting phenomenon was found in the test process: there was an upwardly convex critical phase, called the brittle-ductile failure transition critical phase, for the heterogeneous soft coal mass between the initial elastic compression phase and the ductile failure transition phase in the stress-strain curve of the coal mass. An evolution of the brittle-ductile modulus coefficient of the soft coal was developed to analyze the effect of the internal factor (degree of heterogeneity) and external factors (confining pressure) on the transition state of the brittle-ductile failure of soft coal. Further analysis shows that the internal factor (heterogeneity) was also one of the essential factors causing the brittle-ductile transition of soft coal.

1. Introduction

A soft coal mass with a complex composition and a cementation structure is a typical inhomogeneous medium and has more complicated mechanical properties compared with other rock masses [1–7]. In addition, due to the high number of interformational pores, fractures, and microfractures caused by the occurrence of gas, this kind of gas-filled coal mass was found to be damaged to varying degrees [8–11]. In high gas and deep mines, the "three fields of surrounding rock," i.e., the original rock stress field, the mining stress field, and the support stress field, will change after a gas drainage event or roadway excavation, which will result in instability of the surrounding rocks and even lead to some dynamic destructive disasters, such as coal and gas bursts or rock burst, causing an unrecoverable loss of economy and time [12–20]. In particular, under a high-stress environment and a complex disturbance stress field, the high-pressure gas inside the coal mass not only weakens the strength of the coal but also leads to nonlinear characteristics of the coal mass. Therefore, the mechanical properties of a heterogeneous coal rock mass are dynamically changing under the influence of different stress fields and gas pressure fields in the deep underground.

For the heterogeneity of the soft coal mass, most scholars in past research programmes believed that the parameter value of the mesoscopic unit of the coal mass followed the Weibull distribution [21–24] which could be evaluated by using one defined Weibull distribution function. Additionally, numerous results show that the macroscopic mechanical properties of the soft coal mass depend largely on the heterogeneity of the mesoscopic parameters [25, 26], which is the main reason for the macroscopic inhomogeneity and nonlinear characteristics of the coal mass under an external load [27–31]. Feng and Zhao [32] studied the relationship between the macroscopic deformation behaviour of rock and the mechanical properties of the mesoscopic particles and found that regardless of whether its mesoscopic particles are an ideal elastic-plastic material, an extremely brittle material, or a transitional material, the macroscopic deformation behaviour of the rock depends only on its heterogeneity. Furthermore, the more uniform the mesoscopic particle distribution of the rock is, the more obvious the brittle characteristics of the rock. In contrast, the less uniform the mesoscopic particle distribution of the rock is, the more obvious the elastoplastic characteristics of the rock. Yang et al. [33] found that the inhomogeneity caused by material defects played a key role in the distribution of small voids and cracks in the materials, as well as in the mode of crack propagation. Hudyma et al. [34] showed that the relationship between the mechanical characteristics and the porosity of tuff was that with increasing porosity; its compressive strength and elastic modulus were reduced. From the above, heterogeneity is clearly an important index and has been widely used by scholars to evaluate the mechanical parameters of coal and rock masses. Moreover, the damage accumulation of the rock mass depends largely on the homogeneity of the rock, especially the impact fragmentation of brittle heterogeneous solids [35].

Recently, with the increasing depth of mining, the mechanical characteristics of the coal and rock around roadways at high pressure, high gas pressure [36, 37], and high temperature [38, 39] have been systematically researched. Yang et al. [40] obtained the failure mechanisms and stability control technology for a deep roadway with some soft rocks in the Xin'an Coal Mine in Gansu Province, China, and one new useful "bolt-cable-mesh-shotcrete+shell"-combined support was proposed to support the ventilation roadway. Yu et al. [41, 42] proved that the fracture expansion of the coal and rock mass caused its permeability to increase, weakening the surrounding rock strength. Then, they proposed a core support technology with a prestressed truss anchor cable to support the roadway.

The mechanical properties of intact hard rocks with high homogeneity will change under certain conditions. Researchers found that under high temperature, high confining pressure, and other conditions, the rock would transition from brittle failure to ductile failure [43–45]. Generally, the heterogeneity of rocks is a concentrated expression of microcracks and rock defects from a microperspective. From a macro perspective, it is the result of the dynamic development and penetration of macrocracks and pores, as well as the coupling of various other influencing factors such as water and gas. This special property of rock is not an idealized assumption of simple and single conditions but is the result of multidimensional, multifactor, and multilevel coupling. Unfortunately, most of the researches on the special characteristics of the brittle-ductile transition of rock are concentrated on the analysis of mechanical properties of rock by external single factors (e.g., single confining pressure and single temperature), thus neglecting the influence of mutual coupling with internal factors of rock (e.g., heterogeneity, water, gas, and temperature). Therefore, this paper takes the heterogeneous coal seam mining affected by gas or after gas extraction as the engineering background. A series of mechanical tests were carried out on heterogeneous soft coal samples. The influence of the internal factors (heterogeneity) and external factors (confining pressure) on the brittle-ductile failure and mechanical characteristics of the coal mass was analyzed in detail. The brittleness-ductility of the soft coal mass model was established. Then, the change law of the internal structure of the soft coal mass affected by the gas was inferred.

2. Effect of Gas on the Heterogeneity and Mechanics of Soft Coal Mass

Similar to loose soil, the gas-filled coal mass is easily destroyed under a complicated stress condition due to its soft structure, low strength, poor deformation resistance capability, and the fact that the internal area contains many weak surfaces and original damage. After gas drainage in the coal seam, the coal mass becomes loose and soft, showing macroscopic heterogeneity and nonlinear characteristics due to the combined disturbed stress field.

The heterogeneity parameters of the coal medium are reflected by the expansion degree of the specimen (i.e., the initial porosity of the different coal samples), as shown in equation (1):

$$m = n \cdot k + m_0, \tag{1}$$

where m is the heterogeneity parameter of the coal mass, k is the rock material constant, n is the porosity (initial porosity) of the coal mass, and m_0 is the initial heterogeneity parameter of the soft coal mass.

The comprehensive effect of axial compression, confining pressure, and gas pressure on the gas-filled coal mass can be expressed by an abstract macroscopic effective stress, which is an equivalent parameter to describe the deformation process of the coal mass [46]. The effective stress σ' can be determined [47]:

$$\sigma' = \sigma - P_g + (1 - n)P_g, \tag{2}$$

where $n = (m - m_0)/k$, the rock porosity is related to heterogeneity m, P_g is the pore pressure of the gas, and σ is the total stress of heterogeneous coal and rock.

Assuming that the failure of heterogeneous soft coal conforms to the Mohr-Coulomb failure criterion, the effective stress failure criterion can be obtained:

$$\tau' = c + \sigma' \tan \varphi, \tag{3}$$

where c is the cohesive force and φ is the internal friction angle.

By substituting equation (2) into (3), we can obtain

$$\tau' = c + (\sigma - P_g) \tan \varphi + P_g(1 - n) \tan \varphi. \tag{4}$$

Let $(1 - n) \tan \varphi = \tan \varphi'$, where φ' is the effective internal friction angle, and the value is related to the heterogeneity of the coal and rock mass.

$$\tau' = c + (\sigma - P_g) \tan \varphi + P_g \tan \varphi'. \tag{5}$$

Equation (5) shows that the effective shear strength of the heterogeneous coal and rock mass is composed of cohesion, one strength caused by the stress variable $\sigma - P_g$ and another strength caused by the stress variable P_g. The strength caused by the stress variable $\sigma - P_g$ is related to the angle of internal friction, while the shear strength caused by stress variable P_g is related to the effective internal friction angle.

Let $c' = c + P_g \tan \varphi'$, where c' is the effective cohesion. Therefore, equation (5) can be simplified as follows:

$$\tau' = c' + (\sigma - P_g) \tan \varphi. \tag{6}$$

The stresses $\sigma - P_g$ and τ in the plane are determined by the stress circles of the principal stresses $\sigma_1 - P_g$ and $\sigma_3 - P_g$, as follows:

$$\sigma_1 - P_g = \frac{1 + \sin \varphi}{1 - \sin \varphi} (\sigma_3 - P_g) + \frac{2c' \cos \varphi}{1 - \sin \varphi}. \tag{7}$$

According to equation (7), the obtained theoretical curve of heterogeneous coal is shown in Figure 1. The triaxial compressive strength (TCS) of coal is affected by gas pressure and heterogeneity m. Under the action of gas, the TCS of the coal sample decreases linearly with the increase of gas pressure and the coal with higher heterogeneity has lower peak strength.

3. Test Design for a Heterogeneous Soft Coal Specimen

3.1. Process Flow and Preparation Principle. Due to unfavorable construction conditions and test equipment factors, it is difficult to obtain raw coal samples underground. However, corresponding rock samples could simulate the characteristics of raw coal [48–50]. Niu et al. [51, 52] have done a lot of researches on natural and reconstituted anthracite coals, and the results show that the swelling strain of reconstituted coal is similar to the homogeneous isotropic variety. Therefore, this method is used to produce heterogeneous soft coal specimens. The specimens consisted of anthracite coal ash through a 100 mesh screen (the average diameter is 150 μm) as the main aggregate and P32.5 ordinary Portland cement as the main cementitious material, and the degree of heterogeneity was controlled by 30% hydrogen peroxide, which generated oxygen through the disproportionation reaction in the alkaline medium, as shown in the chemical

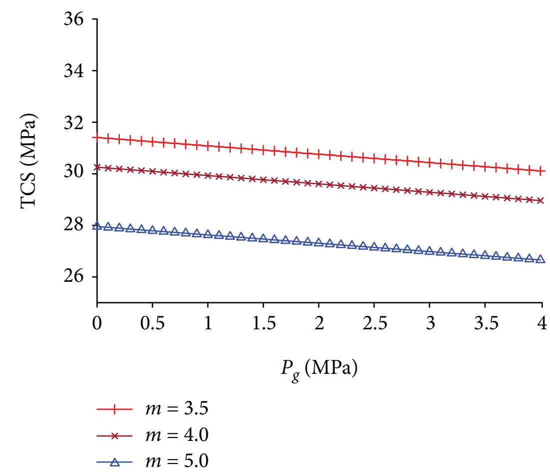

Figure 1: Theoretical curves of peak strength, gas pressure, and heterogeneity of heterogeneous soft coal rock mass ($\sigma_3 = 2$ MPa, internal friction angle = 8°).

reaction equation (8), to create pores and fissures in the specimens. The basic weight ratio of the white cement to anthracite coal ash in the specimen was 7 : 3, and the water to cement ratio was 0.4.

$$2H_2O = 2H_2O + O_2\uparrow \tag{8}$$

Additionally, to reduce the three-dimensional distribution of pores and cracks in the sample, we first used the mixer to mix and tamp the sample fully. Then, the coal samples that were screened twice by comparing the quality and testing the rock wave velocity were selected for the test.

Figure 2 illustrates the process flow for preparing specimens with different heterogeneities. The main flow of the sample preparation is as follows: First, the raw materials (except hydrogen peroxide) were measured at the set ratio and the uniform slurry was stirred at a water temperature of approximately 20°C, with the mixing time controlled within 60~80 s. Then, the designated quantity of hydrogen peroxide was added to the slurry and quickly stirred. The chemical reaction occurred after mixing hydrogen peroxide and other materials. Generally, the basic chemical reaction time and initial setting time of the cement were less than 5 min and 10 min, respectively. In the preparation of samples, H_2O_2 and other aggregates need to be stirred and poured into the mould with other complex procedures. These procedures will take a lot of time, so it is required that adding the H_2O_2 mixture should be completed in a relatively short time (controlled within 30-40 s). Except for the test specimens into which hydrogen peroxide was not added, the other test samples were filled to 70% of the mould volume. To reduce error, it was forbidden to cast multiple sets of specimens at once. After the vibration compaction and initial setting of the test specimens, the expansion process was observed and recorded for 8 hours. After removing the expansion and smoothing the ends, the specimens were demoulded from the containers and maintained for 28 d at room temperature

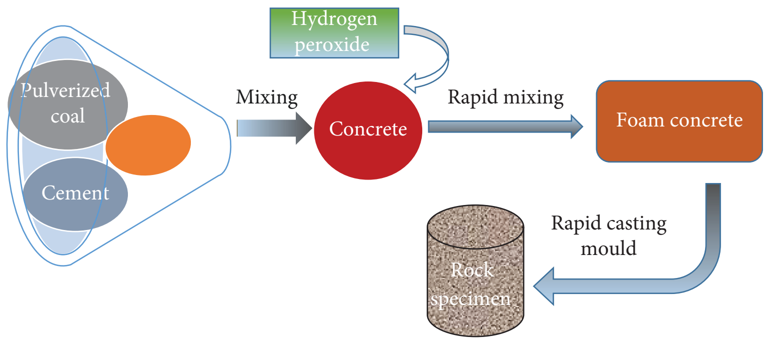

FIGURE 2: Preparation process for a gas-affected heterogeneous soft coal mass specimen.

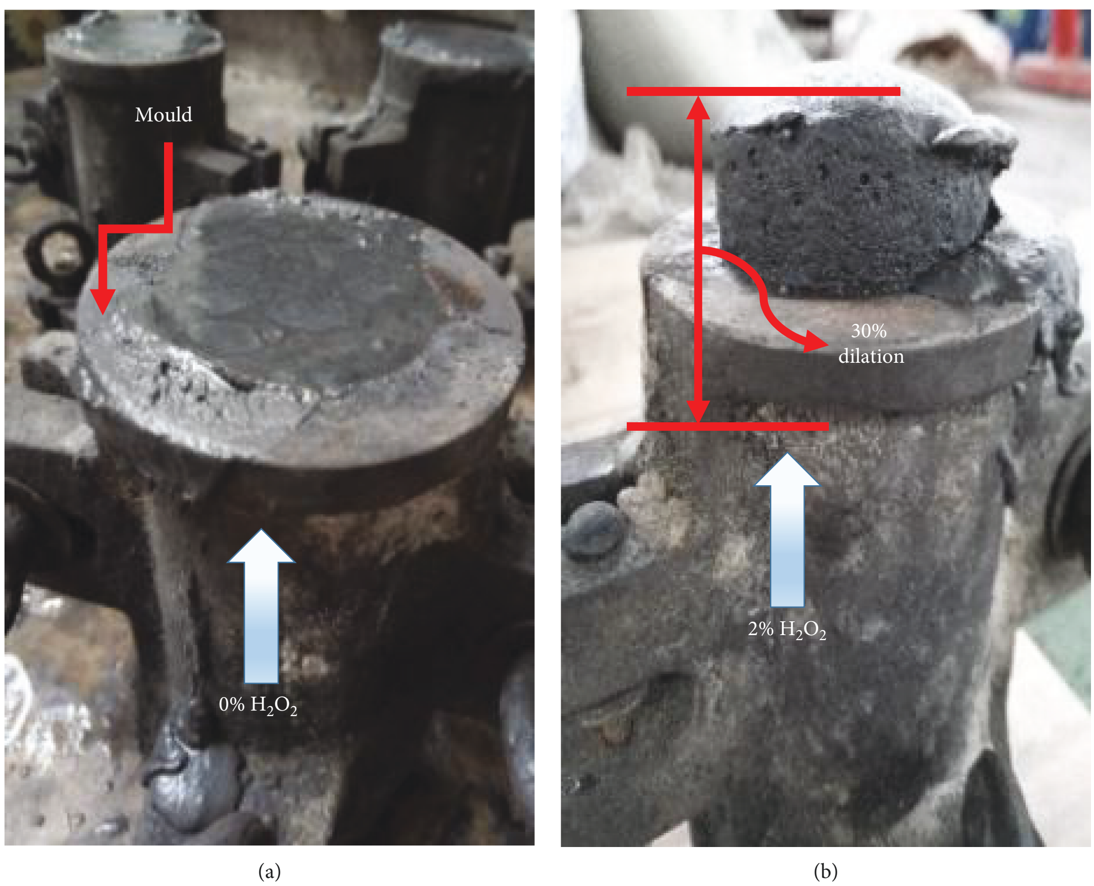

FIGURE 3: Swelling behaviour of rock-like specimens made with different hydrogen peroxide contents: (a) specimen without expansion ($H_2O_2 = 0\%$, $m = 1$); (b) specimen with expansion of 30% ($H_2O_2 = 2\%$, $m = 4$).

according to the International Society for Rock Mechanics (ISRM) standards [53, 54].

The test moulding tool is a customized three-opening mould made of cast iron, as shown in Figure 3, which can create a standard test piece with a height and diameter ratio of 2 : 1 (50 mm × 100 mm). Figure 3(a) indicates that no expansion occurred in the mould without hydrogen peroxide. The hydrogen peroxide is easily dispersed in the concrete, and the gas velocity and mass can be controlled by the temperature, the concentration of the hydrogen peroxide, and the stirring speed. Different test pieces with different degrees of heterogeneity were made by this process. When only 2% of hydrogen peroxide was added, the volume of coal expanded by 30% (Figure 3(b)).

3.2. Test Scheme. The species were all tested in the digital control electrohydraulic servo rock test system developed by the Wuhan Institute of the Chinese Academy of Sciences (RMT-150C). The test equipment is mainly used for mechanical property testing of rock and concrete materials. Fourteen sensors are equipped to record the load, stress, strain, displacement, and other parameters from the axial and

Table 1: Relationship between initial porosity and the heterogeneity parameter of the specimen.

Number	Hydrogen peroxide content (%)	Average dilation volume (%)	Heterogeneity (m)
A	0	0	1.0
B	1	25	3.5
C	2	30	4.0
D	3	40	5.0
E	4	45	5.5
F	5	50	6.0

transverse direction of the specimen during loading. The settings of the axial loading rate and the confining pressure loading rate are 0.20 kN/s and 0.05 MPa/s, respectively, and two levels of confining pressure (2.0 MPa and 4.0 MPa) are set for the triaxial test and the uniaxial compression coupling factor test, respectively, for different heterogeneous and gas content soft coal samples.

A comparison test of 6 groups of samples with hydrogen peroxide content varying from 0% to 5% (with % indicating the mass ratio of the hydrogen peroxide content to the aggregate) was established.

According to equation (1), each initial porosity of the soft coal specimen corresponds to the degree of heterogeneity parameter. In this paper, the k value of soft coal is 10 and the value of m_0 is 1 to reflect the mechanical properties of the heterogeneous soft coal mass. The corresponding relationship is shown in Table 1.

4. Results and Discussion

4.1. External Single Factor (Confining Pressure). Figure 4 shows the stress-strain curves of the specimens with heterogeneous $m = 1$ under triaxial and uniaxial compression tests. Compared with the uniaxial tests, the test curve obtained under the triaxial confining pressure tests has no apparent peak strain and residual strength, presenting a kind of rheology similar to that for the soft rock flow.

4.2. Internal Multifactor Coupling (Confining Pressure, Heterogeneity, and Gas Content). The triaxial compressive stress-strain test results of the soft coal masses with different heterogeneities and gas content under different confining pressure couplings are shown in Figure 5. The test curve is similar to the experimental results of the coal mass with less homogeneity, and there is no obvious peak strain or residual strength. In the process of compression, the effects of the degree of initial porosity (i.e., the heterogeneity parameter m) on the coal mass deterioration are different (Figure 5(a)). The microcracks and pores can produce more massive fissures during the stress loading process, and the specimens will be destroyed when the pores and fissures penetrate to the end (Figure 5(b)).

The failure of the specimen (Figure 5(b)) shows that dilatancy failure is the main damage form for the soft coal mass with a low degree of heterogeneity (m value is within 1~4). With increasing degree of heterogeneity ($m > 5$), the distribution of the internal mineral medium becomes more nonuniform, the overall structure becomes worse, and microcracks and pores gradually develop, while the cohesive force decreases slowly. At this point, dilatancy failure can be clearly observed. As the degree of heterogeneity of the coal mass increases, the damaged form of the specimens will become loose and broken due to dilatancy and expansion (see Figure 5(b)).

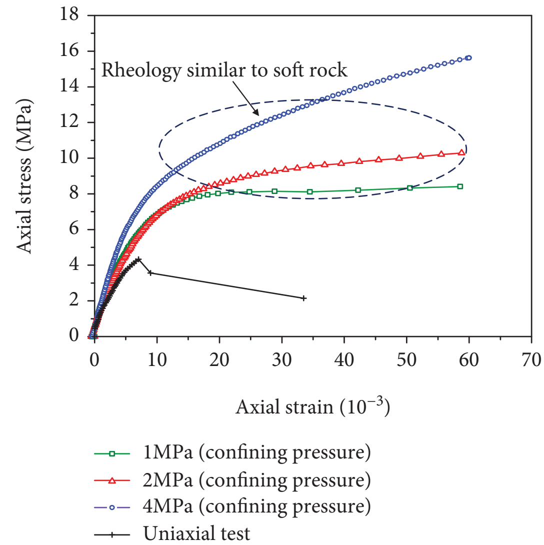

Figure 4: Stress-strain curves of triaxial and uniaxial compression tests for nonexpansive specimens ($m = 1$).

4.3. Brittle-Ductile Failure of Heterogeneous Soft Coal under Multiple Factor Coupling. After further analysis of the stress-strain failure curves of the specimens with different heterogeneities (shown in Figure 5(a)), the compression process can be divided into the compaction stage, the elastic stage, and the strain-hardening stage. As shown in Figure 5, there is an upwardly convex critical phase between the initial linear elastic compaction phase and the ductile failure phase. And we call this as a critical phase which is a brittle-ductile failure transition phase. The key to distinguish this critical phase is the process of the strain curve from the linear elastic phase to the plastic rupture phase, in which the slope of the tangent line at one point of the overstrain curve is larger than that of the tangent line at the latter point of the critical phase. Figure 6 shows the determination of the critical phase. The slope of the tangent line at point H_1 is larger than that at point H_2 (i.e., $\tan\theta_1 > \tan\theta_2$), and hence, the slope can be regarded as the critical phase. Several points fit into the critical phase; therefore, in order to determine the critical inflection point H more accurately in the critical phase, we can select the average value of stress increments in the critical phase as the critical inflection point value H, i.e., the critical inflection point value $H = \Delta\sigma/2$.

The deformation process of the coal mass exhibits an ideal elastic to brittle feature before point H. After this point H, the coal mass undergoes typical strain-hardening plastic flow. If the degree of heterogeneity is higher (i.e., the m value increases from 1 to 6), the critical inflection point stress value

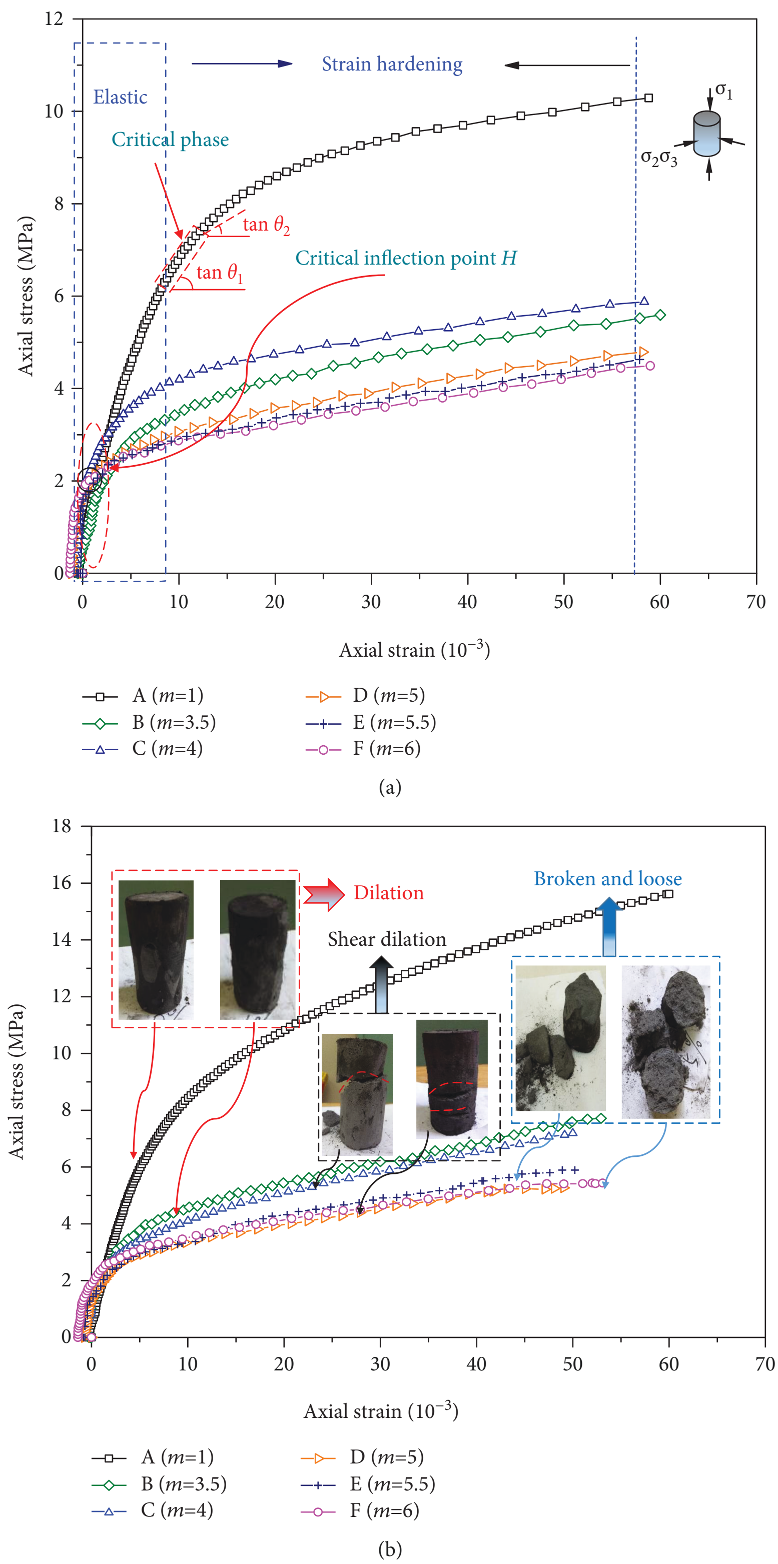

Figure 5: Stress-strain law of the triaxial test under different confining pressures: (a) 2 MPa confining pressure test and (b) 4 MPa confining pressure test results and failure modes of specimens.

H is lower (i.e., the critical inflection point stress value H drops from 7.1 MPa to 2.5 MPa). Besides, the compaction degree of the pore and fracture in the line-elastic phase of the coal sample decreases with the increase of heterogeneity parameter m. In contrast, the strain grows rapidly after this point and the stress is almost unchanged. The critical

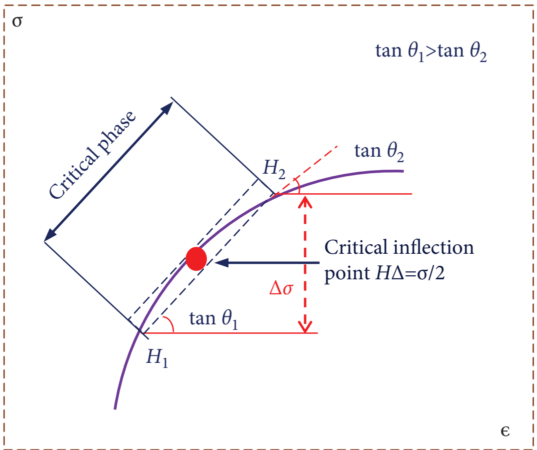

Figure 6: Determination of the critical phase and critical inflection point.

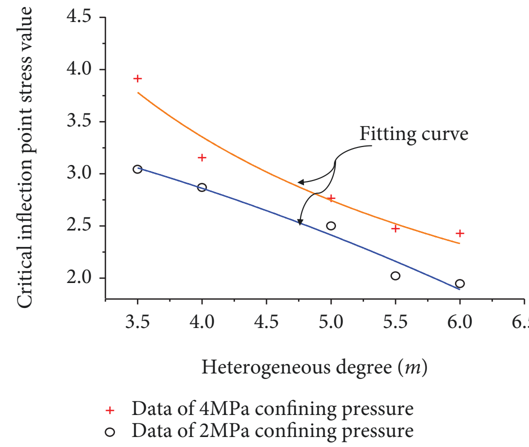

Figure 7: The relationship between the critical inflection point stress value and the degree of heterogeneity of the soft coal mass.

inflection point H is one key factor in predicting whether the specimen undergoes ideal brittle failure or the transformation of failure due to strain hardening.

The brittle-ductile transition failure occurs obviously in the soft coal body under the coupling of multiple factors (e.g., confining pressure and heterogeneity). To further explore whether or not the intrinsic factor (heterogeneity) of the soft coal mass can change the brittle-ductile transition failure of the coal, in this section, the critical inflection point stress value H of the brittle-ductile failure transition of the heterogeneous soft coal mass is analyzed statistically, and the relationship between the critical inflection point stress value and the degree of heterogeneity is obtained, as shown in Figure 7.

The linear regression equation of the test data was obtained by linear function regression, as follows:

(i) Under 2 MPa confining pressure:

$$H = 11.63m^{-0.897}, \quad R^2 = 0.939 \tag{9}$$

(ii) Under 4 MPa confining pressure:

$$H = -0.038m^2 - 0.105m + 3.891, \quad R^2 = 0.937 \tag{10}$$

Considering fixed external factors (confining pressure), equations (9) and (10) further indicate that the coal mass with a higher degree of heterogeneity m has a lower stress value for the brittle-ductile critical inflection point H and that the probability of brittle-ductile transition of coal increases, i.e., an easier transition from dilatancy and expansion to loose and broken rock. In addition, the variation of the confining pressure has some effect on the change of the critical inflection point stress value. The higher the confining pressure is, the larger the value of H. Therefore, a higher confining pressure can increase the integrity of the soft coal mass and enhance its bearing capacity.

5. Brittle-Ductile Failure Transformation of Soft Coal

5.1. Brittle-Ductile Failure. The process from brittle failure to ductile failure of rock is not merely the result of a single factor but more the result of multifactor coupling. In actual complex underground rock engineering, the coupling of high pressure, high temperature, and high pressure gas is often encountered. Therefore, the multifactor coupling is the fundamental reason for the brittle-ductile failure transformation of rock. However, it has great limitations with regard to analyzing the brittle-ductile transition of rocks when compared to only using a single factor, which is an idealized assumption of rock mechanics research. The brittle-ductile failure transition of soft coal refers to the three-dimensional stress relief caused by excavation, gas pressure reduction caused by gas drainage from boreholes, increased heterogeneity of coal mass, or the superposition of various engineering blasting and mining disturbance stresses in deep complex rock engineering. These processes change the external factors (stress environment) and internal factors (heterogeneity) of the coal mass, causing the coal mass to undergo a change from stress concentration to stress relief and then to stress concentration and the corresponding rock to undergo a shift from compaction to loose and then to compaction. Therefore, the change refers to the evolution of the coupling factors between the internal homogeneity and the external stress state of the rock, resulting in different degrees of the brittle-ductile transformation of the coal mass.

The distinction between the brittle and the ductile behaviour depends on whether a macroscopic fracture forms (strain localization occurs) after substantial permanent straining (see Figure 8) [44]. In soft coal, brittle deformation is cataclastic in nature, where deformation involves microcrack formation and frictional sliding along grain boundaries, whereas ductile

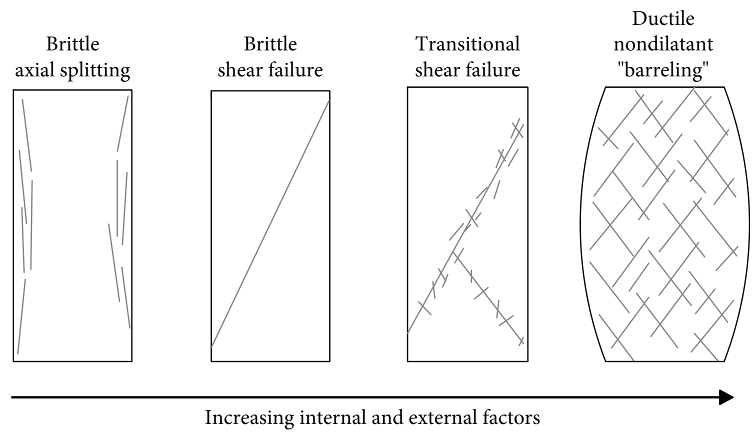

Figure 8: Schematic illustrating changes in failure patterns in relation to internal and external factors and ductility (revised from [44]).

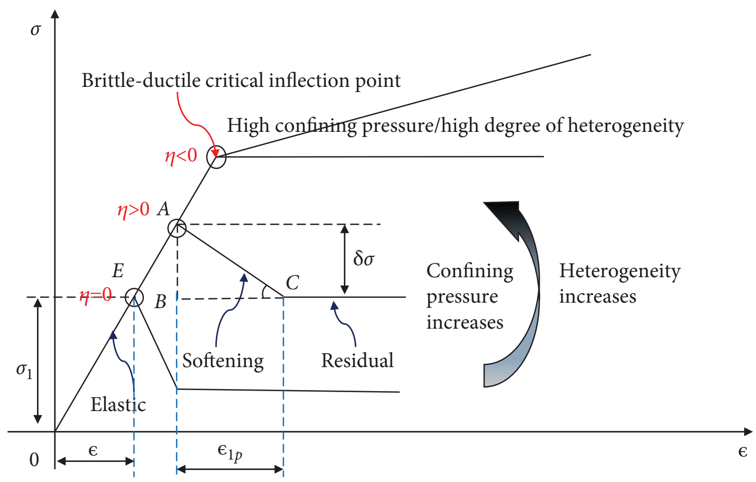

Figure 9: Idealized triaxial stress-strain curve of soft coal mass (revised from [32, 55, 56]).

deformation (different degrees of heterogeneity) transitions to delocalized cataclasis (or "cataclastic flow"). Also, as deformation becomes increasingly ductile, internal factors (pore collapse) begin to play a more significant role than microcracking, leading to an initially compactant stage in porous soft coal deformation.

By simplifying the curves and data in Figures 5 and 7, the stress-strain curve of the idealized soft coal mass is obtained [32, 55, 56], as shown in Figure 9. The influence of the confining pressure and the degree of heterogeneity coupling factors on the failure evolution of the soft coal mass is described by tan∠ACB in the figure. Under the influence of an external factor, i.e., a low confining pressure, the damage form of the coal mass is an ideal elastic-plastic failure. Both the tan∠ACB and the elastic-plastic-ductile transition of the failure state of the coal mass decrease faster due to the increase in the confining pressure. Furthermore, the residual strength of the postpeak coal mass increases, and the ductility is enhanced. The heterogeneity of the soft coal mass also has a significant impact on the transformation between failure modes. The higher the heterogeneity parameters are, the faster the change in the elastic-plastic-ductile failure state of the coal mass (the lower critical inflection point value). According to the results given in Figure 7, the influences of the confining pressure and heterogeneity on the brittle-ductile critical transition state of soft coal are discussed in the next section.

5.2. External Factors (Confining Pressure) on Brittleness-Ductility of Soft Coal Mass. The value of tan∠ACB in Figure 9 can be named the brittle modulus, which is the absolute value of the slope of the stress-strain curve at the softening stage after the peak softening of the coal rock specimen and is obtained by

$$E_b = \frac{\delta\sigma}{\varepsilon_{1p}}, \tag{11}$$

where $\delta\sigma$ is the difference between the peak strength and the residual strength and ε_{1p} is the axial plastic strain during the process of coal mass strength degradation.

Figure 9 shows that with an increase in the confining pressure, the postpeak brittleness and the plasticity of soft coal decrease and the transition to ductile damage gradually evolves. During the increase in confining pressure, a

Table 2: Brittle-ductile modulus for different rocks.

(a)

Tennessee marble (data from [55, 57])						
Confining pressure σ_3 (MPa)	0.00	3.45	6.90	13.80	20.70	34.50
Peak strength σ (MPa)	130	145	160	180	195	245
Residual strength σ_r (MPa)	10	60	80	110	130	230
Brittleness modulus E_b (MPa)	174545	104615	85333	74666	34666	5333
γ	1.000	0.599	0.489	0.428	0.199	0.031

(b)

Gebdykes dolomite (data from [58])					
Confining pressure σ_3 (MPa)	0	5	20	40	90
Peak strength σ (MPa)	60	98	131	150	180
Residual strength σ_r (MPa)	10	42	101	148	200
Brittleness modulus E_b (MPa)	16667	8000	3529	2000	1900
γ	1.000	0.480	0.212	0.120	0.113

(c)

Vosges sandstone (data from [59])					
Confining pressure σ_3 (MPa)	0	10	20	40	60
Peak strength σ (MPa)	31	74	92	108	110
Residual strength σ_r (MPa)	22	38	75	94	107
Brittleness modulus E_b (MPa)	6923	4500	4232	3337	1060
γ	1.000	0.650	0.561	0.482	0.153

(d)

Heterogeneous soft coal rock mass $m = 1$				
Confining pressure σ_3 (MPa)	0	1	2	4
Peak strength σ or critical inflection point value H (MPa)	4.5	6.2	7.1	8.2
Residual strength σ_r or ductility strength (MPa)	2.2	8.3	10.1	15.3
Brittleness modulus E_b (MPa)	575	241	143	70
γ	1.000	0.330	0.248	0.121

dynamically evolving postpeak brittle-ductile modulus factor can be established:

$$\gamma = \frac{E_b}{E_{b0}}, \quad 0 < g < 1, \tag{12}$$

where E_{b0} is the brittle modulus of the soft coal mass under uniaxial loading, $E_{b0} = \sigma_1/\varepsilon$, and E_b is the brittle modulus of the soft coal mass under confining pressure.

The corresponding brittle modulus and brittleness coefficient obtained from the triaxial test data of Tennessee marble [55, 57], Gebdykes dolomite [58], Vosges sandstone [59], and heterogeneous soft coal mass are shown in Table 2, and the relationship between the confining pressure and the brittle-ductile modulus of the rock is shown in Figure 10. The brittle modulus E_b of the rock changes gradually with the confining pressure; i.e., the brittle-ductile modulus coefficient γ of the rock undergoes an evolution process with the change of the confining pressure (the γ value changes from 0 to 1). According to the heterogeneous coal rock mass and multiple experimental [55, 57–59] results, we obtained the variation law of the brittle-ductile transition inflection point stress H of the rock (see Figure 6). Based on this law, in the relation curve of the confining pressure and brittle-ductile modulus, a brittle-ductile modulus transition boundary of rock can be determined. At present, the brittle-ductile modulus γ value is approximately 0.2. According to Figure 10, from the analysis, it can be seen that when the γ value is between 0.2 and 1, the coal and rock mass show ideal brittle failure, and the corresponding brittle modulus coefficient is now called the

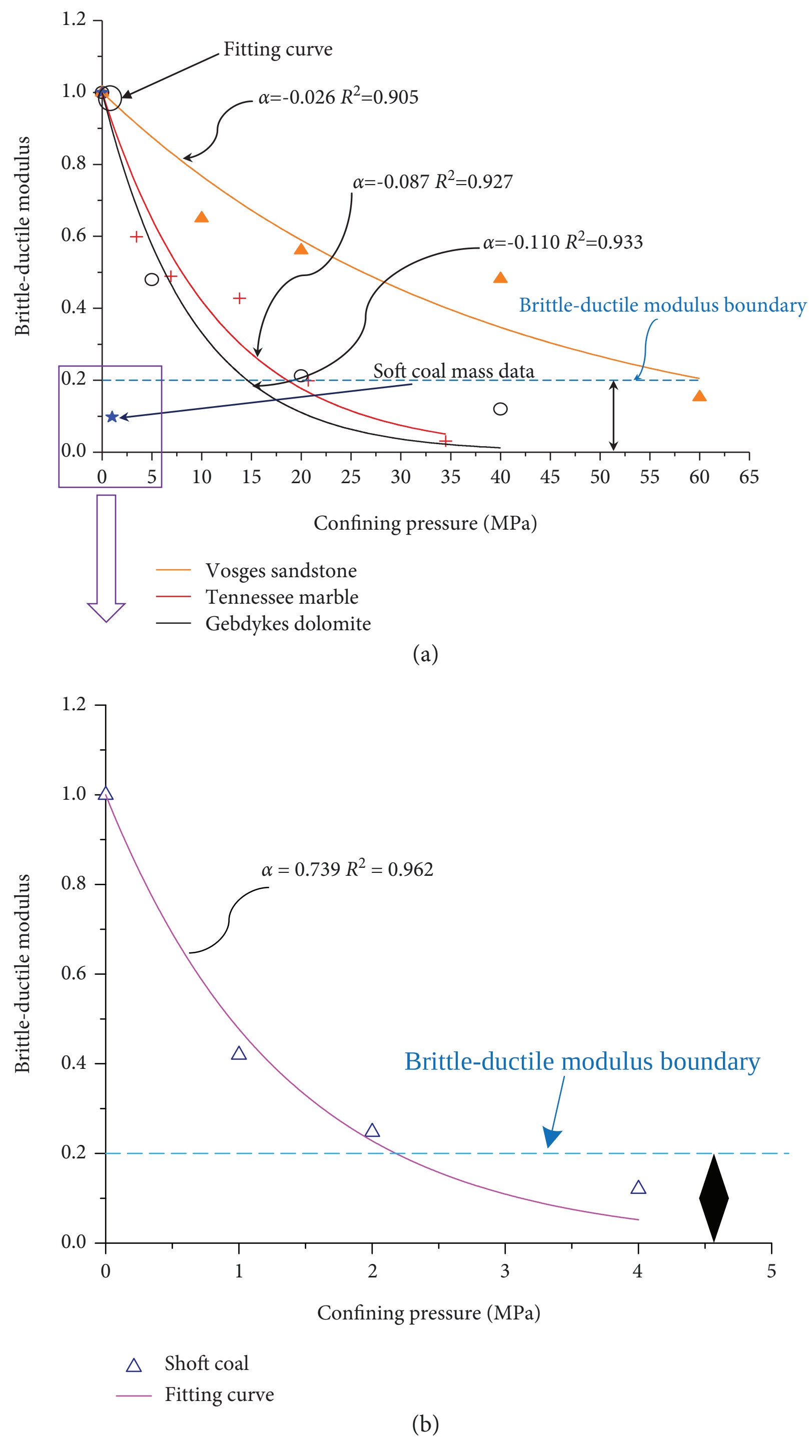

Figure 10: The relationship between confining pressure and rock brittle-ductile modulus: (a) brittle rock; (b) heterogeneous soft coal rock mass.

brittle modulus coefficient (Figure 10(b)). When the confining pressure continues to increase, γ decreases gradually from 0.2 infinitely to 0. Then, the coal mass transitions from brittle to ductile failure, and the mechanical characteristics are similar to those of the soft rock. The corresponding brittle-ductile modulus coefficient is called the ductile modulus coefficient with a small value (i.e., γ is within 0~0.2).

If this kind of soft coal mass is under high pressure, regardless of the damage characteristics or mechanical properties of the coal, ductile failure flow appears under the condition of a small confining pressure. Therefore, according to the test results, the modulus coefficient of heterogeneous soft coal is generally in the range of 0 to 0.2.

By fitting the test data, the relationship between the brittle-ductile modulus coefficient γ and the confining

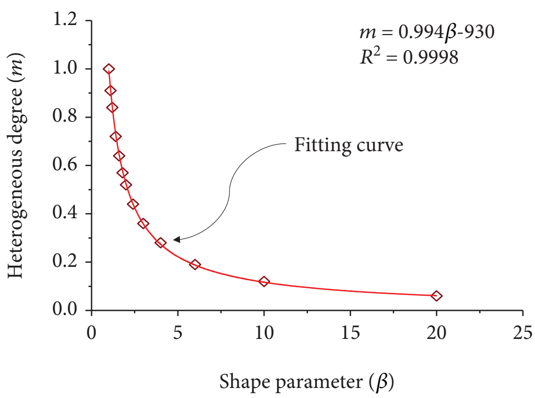

FIGURE 11: The relationship between the shape parameter β and the inhomogeneous parameter m.

pressure almost obeys a negative exponential function. With further increases in the confining pressure, the brittle-ductile modulus coefficient γ decreases to a certain extent, and the following relationship can be obtained [60]:

$$\gamma = \frac{E_b}{E_{b0}} = \exp\left(-a\sigma_3\right), \tag{13}$$

where a is the fitting constant of the experiment and σ_3 is the confining pressure.

5.3. Internal Factor (Heterogeneity Degree Parameter) on the Brittleness-Ductility of Soft Coal Mass. Whether brittle failure or ductile-plastic failure occurs in the coal mass depends on not only the stress environment but also the impact tendency of the coal mass. The impact tendency of the coal mass is also closely related to the heterogeneity parameter m of the coal mass. Hence, the relationship between the brittle-ductile state transitions of soft coal rock is described by introducing the index η of the impact tendency as follows:

$$\eta = \frac{E}{E_b}, \tag{14}$$

where E is the elastic modulus before the peak strength of the coal mass and E_b is the brittle modulus of the coal and rock under a certain confining pressure.

Similarly, as shown in Figure 9, the range of values represents the physical and mechanical properties of the coal mass, with $\eta = \infty$ representing the ideal elastoplastic material, $\eta = 0$ representing the extremely brittle material, $\eta < 0$ representing the strain-hardening material, and $0 < \eta < \infty$ representing the softening material.

The shape parameter β of the Weibull distribution indicates the heterogeneity parameter m of the mesoelement [61]. The relationship between the shape parameter β and the heterogeneous parameter m can be obtained from the fitting curve of the soft coal mass, as shown in Figure 11.

The equation of the shape parameter β and the heterogeneous parameter m can be obtained by fitting the experimental data curve, as follows:

$$m = 0.994\beta^{-0.93}, \tag{15}$$

where β is the shape parameter.

The above relations can be described as follows.

$$\eta = \frac{E}{E_b} = b(\beta - 1)^{-c}, \tag{16}$$

where both b and c are material constants.

Based on the above analysis, with an increase in the shape parameter β (i.e., β is increased from 0 to 20), the heterogeneity parameter m of the coal mass decreases gradually (i.e., the m value is reduced from 1 to infinitely close to 0). A decrease in the heterogeneity parameter m causes the impact tendency index η to decrease gradually (see Figure 11). Meanwhile, if the brittleness of the coal mass increases, the critical softening depth of the surrounding rock will decrease, and the rock will be prone to dynamic phenomena, e.g., coal and gas outburst. According to the change law of the critical brittle-ductile inflection point of soft coal with different heterogeneities (see Figure 7), the higher the heterogeneity parameter m is, the smaller the stress intensity of the brittle-ductile critical inflection point of the coal mass and the more obvious the ductile failure characteristic stage. In contrast, the lower the heterogeneity parameter m of the soft coal rock is, the higher the homogeneity of the coal mass and the more homogeneous the mineral composition structure. Therefore, more ideal brittle fracture characteristics of the coal mass are reflected in the macromechanical characteristics.

Equation (17) can be obtained from equations (13) and (16) as follows:

$$\frac{E}{E_{b0}} = B(\beta - 1)^{-c}, \tag{17}$$

where $B = \exp\left(-a\sigma_3\right) \cdot b$.

The material parameter b in the expression of the impact tendency index η of the soft coal mass is related to the confining pressure. If the confining pressure is not considered, i.e., $\sigma_3 = 0$, equation (17) is consistent with equation (16). At the same time, the brittle-ductile transition relationship of the soft coal and rock is related only to the heterogeneity parameter m. Therefore, even if only considering the heterogeneity of soft coal, it also plays a vital role in the brittle-ductile transition failure of soft coal. If the confining pressure is increased, the coupling effect of the confining pressure and heterogeneity parameter m influences the damage to the coal body. With a change in the confining pressure and the heterogeneity parameter m, both the factors have an influence on the change rate of the shock tendency. Both the heterogeneity m of the coal mass and the confining pressure coupling not only determine the speed of the transition between the brittle and the ductile failure of the coal rock but also affect

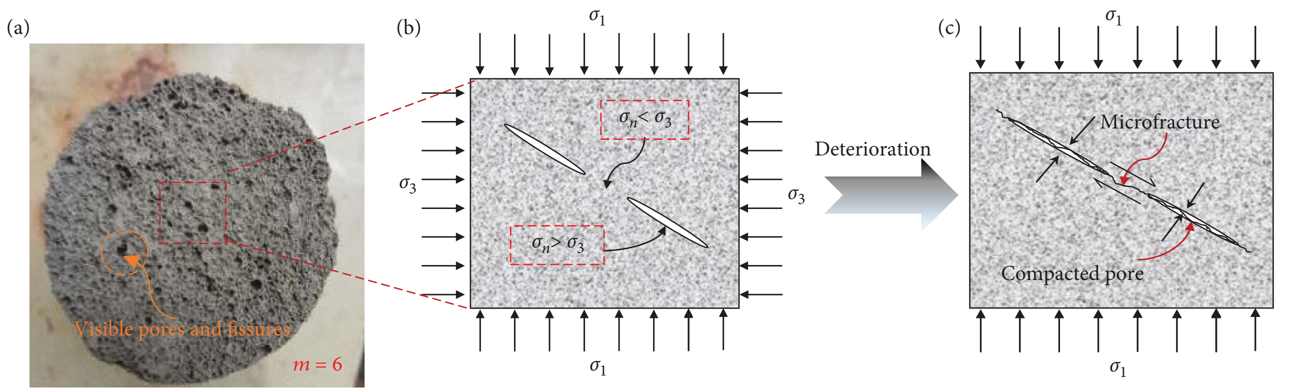

Figure 12: Microfracture propagation in a soft coal mass due to a macrofailure process. (a) Fracture diagram of the coal mass specimen ($m = 6$). (b) Three-dimensional stress stability structure of the coal mass. (c) The microfracture develops into a macroscopic fissure.

the general failure mode of the gas-bearing coal mass and the probability of coal and gas outburst and rock burst tendency in the underground roadway.

Figure 12 illustrates the evolution of microfracture propagation relative to the fracture macroscopic failure process in the coal rock mass with high heterogeneity ($m = 6$). The soft coal mass forms an initial porosity with different degrees after the internal gas drainage. From a mesoscopic point of view, the effective normal stress σ_n is less than the macroconfining pressure σ_3, but the effective normal stress σ_n of the joint is greater than the confining pressure σ_3 of the coal mass (see Figure 12(b)), so the ability of the microfissure to resist macroshear yielding of the coal is limited [62]. When the lateral unloading yield of the coal mass is shifted from the three-direction stress state to the two-direction unbalanced stress concentration, the microcrack tends to open, and the stress development deterioration causes a new coalescence fracture between the original fissures. When the lateral limit is large, the whole surface will produce a smooth shear fracture, but when the lateral limit is small, the surface will produce a rough split crack (see Figure 12(c)).

6. Conclusions

This study attempts a new experimental research idea, based on the heterogeneity characteristics of the soft coal mass, by using hydrogen peroxide (H_2O_2) in an alkaline medium to generate oxygen as the major impact indicators. Different proportioning schemes and different kinds of heterogeneous soft coal mass specimens were made in cast-iron moulds. A series of multifactor coupling mechanical tests were carried out for soft coal masses with different heterogeneities, and the brittle-ductile response of a soft coal rock mass was discussed. The following conclusions can be drawn.

(1) The uniaxial and triaxial compression tests were carried out on heterogeneous soft coal samples. The ductility failure characteristic is reflected; i.e., the test curve has no apparent peak strain and residual strength, which presents a kind of similarity to the rheology of soft rock flow. The coal specimens in the loading process show internal factors (different degrees of heterogeneity m) that vary due to the degradation effect on the coal mass, from coal body crack initiation and propagation, overlapping with the process of heterogeneous coal mass destruction from shear compression to bulging expansion and even fracture failure

(2) In the heterogeneous mechanical test curve of the soft coal specimen, there is an upwardly convex critical phase between the initial linear elastic compaction phase and the ductile failure phase. A key point can be determined at this phase which is called the critical inflection point H of the brittle-ductile failure transition. Before this point, ideal elastoplastic characteristics are expressed. In contrast, after this point or phase, the mechanical properties of the coal masses are transformed into ductile strain hardening

(3) The more the confining pressure and the degree of the heterogeneity parameter m increase, the more obvious the ductile failure of the specimens is. The heterogeneity degree of rock is also the critical factor for the brittle-ductile transition of rocks

(4) With the influence of coal mass excavation or gas drainage, the coal rock mass meso- and macropore and fracture development will expand, weaken the strength of the coal mass, or even cause the deterioration of the internal structure, resulting in the incomplete integrity of the coal mass and, after shear and dilatancy, the evolution from loose to broken rock

Data Availability

The data used to support the findings of this study are available from the corresponding authors upon request.

Conflicts of Interest

The authors declare that they have no conflicts of interest.

Acknowledgments

This study was supported by the National Natural Science Foundation of China (51574122, 51434006, and 51774130). The financial support is greatly appreciated. We also appreciate the reviewers and editors for their careful work and thoughtful suggestions that have helped improve this paper substantially. A special acknowledgment is given to Mr. Qingjun Guan and Miss Meichen Du (Hunan University of Science and Technology), who provided language editing for this paper.

References

[1] S. C. Blair and N. G. W. Cook, "Analysis of compressive fracture in rock using statistical techniques: part I. A non-linear rule-based model," *International Journal of Rock Mechanics and Mining Sciences*, vol. 35, no. 7, pp. 837–848, 1998.

[2] G. Z. Li, C. A. Tang, and L. C. Li, "Three-dimensional micro flow-stress-damage (FSD) model and application in hydraulic fracturing in brittle and heterogeneous rocks," *Key Engineering Materials*, vol. 452-453, pp. 581–584, 2010.

[3] M. Sabri, A. Ghazvinian, and H. R. Nejati, "Effect of particle size heterogeneity on fracture toughness and failure mechanism of rocks," *International Journal of Rock Mechanics and Mining Sciences*, vol. 81, pp. 79–85, 2016.

[4] C. H. Scholz, "Microfracturing and the inelastic deformation of rock in compression," *Journal of Geophysical Research*, vol. 73, no. 4, pp. 1417–1432, 1968.

[5] S. C. Yuan and J. P. Harrison, "A review of the state of the art in modelling progressive mechanical breakdown and associated fluid flow in intact heterogeneous rocks," *International Journal of Rock Mechanics and Mining Sciences*, vol. 43, no. 7, pp. 1001–1022, 2006.

[6] C. H. Zhang, Q. S. Zhao, and Y. J. Yu, "Model of coupled gas flow and deformation process in heterogeneous coal seams and its application," *Journal of Coal Science and Engineering (China)*, vol. 17, no. 1, pp. 76–80, 2011.

[7] W. C. Zhu, J. Liu, T. H. Yang, J. C. Sheng, and D. Elsworth, "Effects of local rock heterogeneities on the hydromechanics of fractured rocks using a digital-image-based technique," *International Journal of Rock Mechanics and Mining Sciences*, vol. 43, no. 8, pp. 1182–1199, 2006.

[8] T. K. Lu, Z. J. Zhao, and H. F. Hu, "Improving the gate road development rate and reducing outburst occurrences using the waterjet technique in high gas content outburst-prone soft coal seam," *International Journal of Rock Mechanics and Mining Sciences*, vol. 48, no. 8, pp. 1271–1282, 2011.

[9] M. Mastalerz, A. Drobniak, D. Strąpoć, W. Solano Acosta, and J. Rupp, "Variations in pore characteristics in high volatile bituminous coals: implications for coal bed gas content," *International Journal of Coal Geology*, vol. 76, no. 3, pp. 205–216, 2008.

[10] G. Wang, W. X. Li, P. F. Wang, X. X. Yang, and S. T. Zhang, "Deformation and gas flow characteristics of coal-like materials under triaxial stress conditions," *International Journal of Rock Mechanics and Mining Sciences*, vol. 91, pp. 72–80, 2017.

[11] S. G. Wang, D. Elsworth, and J. S. Liu, "Permeability evolution in fractured coal: the roles of fracture geometry and water-content," *International Journal of Coal Geology*, vol. 87, no. 1, pp. 13–25, 2011.

[12] R. Q. Huang and X. N. Wang, "Analysis of dynamic disturbance on rock burst," *Bulletin of Engineering Geology and the Environment*, vol. 57, no. 3, pp. 281–284, 1999.

[13] M. Krzesinska, "Ultrasonic studies of outburst-prone coals," *International Journal of Rock Mechanics and Mining Sciences*, vol. 34, no. 1, pp. 167–171, 1997.

[14] J. Shepherd, L. K. Rixon, and L. Griffiths, "Outbursts and geological structures in coal mines: a review," *International Journal of Rock Mechanics and Mining Sciences & Geomechanics Abstracts*, vol. 18, no. 4, pp. 267–283, 1981.

[15] S. P. Singh, "Burst energy release index," *Rock Mechanics and Rock Engineering*, vol. 21, no. 2, pp. 149–155, 1988.

[16] N. Skoczylas, "Laboratory study of the phenomenon of methane and coal outburst," *International Journal of Rock Mechanics and Mining Sciences*, vol. 55, pp. 102–107, 2012.

[17] J. Toraño, S. Torno, E. Alvarez, and P. Riesgo, "Application of outburst risk indices in the underground coal mines by sublevel caving," *International Journal of Rock Mechanics and Mining Sciences*, vol. 50, pp. 94–101, 2012.

[18] Y. Xue, F. Gao, T. Teng, and Y. Xing, "Effect of gas pressure on rock burst proneness indexes and energy dissipation of coal samples," *Geotechnical and Geological Engineering*, vol. 34, no. 6, pp. 1737–1748, 2016.

[19] A. Zhou, K. Wang, L. Li, and C. Wang, "A roadway driving technique for preventing coal and gas outbursts in deep coal mines," *Environmental Earth Sciences*, vol. 76, no. 6, p. 236, 2017.

[20] A. Zubelewicz and Z. Mróz, "Numerical simulation of rock burst processes treated as problems of dynamic instability," *Rock Mechanics and Rock Engineering*, vol. 16, no. 4, pp. 253–274, 1983.

[21] S. C. Li and G. Y. Li, "Effect of heterogeneity on mechanical and acoustic emission characteristics of rock specimen," *Journal of Central South University of Technology*, vol. 17, no. 5, pp. 1119–1124, 2010.

[22] P. Z. Pan, X. T. Feng, and J. A. Hudson, "The influence of the intermediate principal stress on rock failure behaviour: a numerical study," *Engineering Geology*, vol. 124, pp. 109–118, 2012.

[23] J. Song and K. Kim, "Micromechanical modeling of the dynamic fracture process during rock blasting," *International Journal of Rock Mechanics and Mining Sciences & Geomechanics Abstracts*, vol. 33, no. 4, pp. 387–394, 1996.

[24] S. H. Wang, C. I. Lee, P. G. Ranjith, and C. A. Tang, "Modeling the effects of heterogeneity and anisotropy on the excavation damaged/disturbed zone (EDZ)," *Rock Mechanics and Rock Engineering*, vol. 42, no. 2, pp. 229–258, 2009.

[25] P. K. Kaiser and C. A. Tang, "Numerical simulation of damage accumulation and seismic energy release during brittle rock failure—part II: rib pillar collapse," *International Journal of Rock Mechanics and Mining Sciences*, vol. 35, no. 2, pp. 123–134, 1998.

[26] C. A. Tang and P. K. Kaiser, "Numerical simulation of cumulative damage and seismic energy release during brittle rock failure—part I: fundamentals," *International Journal of Rock Mechanics and Mining Sciences*, vol. 35, no. 2, pp. 113–121, 1998.

[27] L. Biolzi, J. F. Labuz, and G. Muciaccia, "A problem of scaling in fracture of damaged rock," *International Journal of Rock*

Mechanics and Mining Sciences, vol. 48, no. 3, pp. 451–457, 2011.

[28] Y. L. Tan, D. M. Huang, and Z. Zhang, "Rock mechanical property influenced by inhomogeneity," *Advances in Materials Science and Engineering*, vol. 2012, Article ID 418729, 9 pages, 2012.

[29] W. J. Yu and F. F. Liu, "Stability of close chambers surrounding rock in deep and comprehensive control technology," *Advances in Civil Engineering*, vol. 2018, Article ID 6275941, 18 pages, 2018.

[30] G. S. Wu, W. J. Yu, Z. Liu, and Z. Tang, "Failure law and mechanism of the rock-loose coal composite specimen under combined loading rate," *Advances in Civil Engineering*, vol. 2018, Article ID 2482903, 10 pages, 2018.

[31] Q. J. Guan, W. Sun, Y. Hu et al., "Simultaneous control of particle size and morphology of α-CaSO4·1/2H_2O with organic additives," *Journal of the American Ceramic Society*, vol. 102, pp. 2440–2450, 2018.

[32] Z. C. Feng and Y. S. Zhao, "Correlativity of rock inhomogeneity and rock burst trend," *Chinese Journal of Rock Mechanics and Engineering*, vol. 11, pp. 1863–1865, 2003.

[33] Y. F. Yang, C. A. Tang, and K. W. Xia, "Study on crack curving and branching mechanism in quasi-brittle materials under dynamic biaxial loading," *International Journal of Fracture*, vol. 177, no. 1, pp. 53–72, 2012.

[34] N. Hudyma, B. B. Avar, and M. Karakouzian, "Compressive strength and failure modes of lithophysae-rich Topopah Spring tuff specimens and analog models containing cavities," *Engineering Geology*, vol. 73, no. 1-2, pp. 179–190, 2004.

[35] G. Ma, Y. D. Zhang, W. Zhou, T. T. Ng, Q. Wang, and X. Chen, "The effect of different fracture mechanisms on impact fragmentation of brittle heterogeneous solid," *International Journal of Impact Engineering*, vol. 113, pp. 132–143, 2018.

[36] B. Liang, M. Zhang, Y. S. Pan, and Y. J. Wang, "The experimental research on the effect of gas on mechanical properties and mechanical response of coal," *Chinese Journal of Geotechnical Engineering*, vol. 17, pp. 12–18, 1995.

[37] G. Z. Yin, M. H. Li, J. G. Wang, J. Xu, and W. P. Li, "Mechanical behavior and permeability evolution of gas infiltrated coals during protective layer mining," *International Journal of Rock Mechanics and Mining Sciences*, vol. 80, pp. 292–301, 2015.

[38] B. Wu, T. Ma, G. Feng, Z. Chen, and X. Zhang, "An approximate solution for predicting the heat extraction and preventing heat loss from a closed-loop geothermal reservoir," *Geofluids*, vol. 2017, Article ID 2041072, 17 pages, 2017.

[39] B. Wu, X. Zhang, R. G. Jeffrey, A. P. Bunger, and C. Huddlestone-Holmes, "Perturbation analysis for predicting the temperatures of water flowing through multiple parallel fractures in a rock mass," *International Journal of Rock Mechanics and Mining Sciences*, vol. 76, pp. 162–173, 2015.

[40] S. Q. Yang, M. Chen, H. W. Jing, K. F. Chen, and B. Meng, "A case study on large deformation failure mechanism of deep soft rock roadway in Xin'an coal mine, China," *Engineering Geology*, vol. 217, pp. 89–101, 2017.

[41] W. J. Yu, W. J. Wang, G. S. Wu, X. Y. Yu, and W. Q. Peng, "Three zones and support technique for large section incline shaft crossing goaf," *Geotechnical and Geological Engineering*, vol. 35, no. 5, pp. 1921–1931, 2017.

[42] W. J. Yu, S. H. Zhai, and Q. Gao, "Stability evaluation indexes of deep stope pillar and roadway surrounding rock," *Disaster Advances*, vol. 5, no. 4, pp. 120–126, 2012.

[43] K. Hu, Q. Z. Zhu, L. Chen, J. F. Shao, and J. Liu, "A micromechanics-based elastoplastic damage model for rocks with a brittle–ductile transition in mechanical response," *Rock Mechanics and Rock Engineering*, vol. 51, no. 6, pp. 1729–1737, 2018.

[44] G. Walton, A. Hedayat, E. Kim, and D. Labrie, "Post-yield strength and dilatancy evolution across the brittle–ductile transition in Indiana limestone," *Rock Mechanics and Rock Engineering*, vol. 50, no. 7, pp. 1691–1710, 2017.

[45] Q. H. Wu, L. Weng, Y. L. Zhao, B. Guo, and T. Luo, "On the tensile mechanical characteristics of fine-grained granite after heating/cooling treatments with different cooling rates," *Engineering Geology*, vol. 253, pp. 94–110, 2019.

[46] G. S. Wu, W. J. Yu, P. Wang, Z. Liu, F. F. Liu, and Z. Huan, "Deformation failure mechanism and experimental study of gas coal rock mass based on percolation mechanism," *Journal of China Coal Society*, vol. 43, no. 3, pp. 724–734, 2018.

[47] Z. Zhou, Y. Y. Lu, Z. L. Ge, F. Yang, and X. W. Zhang, "Theoretical and experimental study on strength characteristics of coal under coupling effect of water and gas," *Journal of China Coal Society*, vol. 39, no. 12, pp. 2419–2424, 2014.

[48] J. Bodziony, J. Krawczyk, and J. Topolnicki, "Determination of the porosity distribution in coal briquettes by measurements of the gas filtration parameters in an outburst pipe," *International Journal of Rock Mechanics and Mining Sciences & Geomechanics Abstracts*, vol. 31, no. 6, pp. 661–669, 1994.

[49] C. B. Jiang, G. Z. Yin, X. Q. Li, and B. Cai, "Experimental study of gas permeability of outburst coal briquettes in complete stress-strain process," *Chinese Journal of Rock Mechanics and Engineering*, vol. 29, pp. 3482–3487, 2010.

[50] N. Skoczylas, B. Dutka, and J. Sobczyk, "Mechanical and gaseous properties of coal briquettes in terms of outburst risk," *Fuel*, vol. 134, pp. 45–52, 2014.

[51] Q. H. Niu, L. W. Cao, S. X. Sang, X. Z. Zhou, Z. Z. Wang, and Z. Y. Wu, "The adsorption-swelling and permeability characteristics of natural and reconstituted anthracite coals," *Energy*, vol. 141, pp. 2206–2217, 2017.

[52] Q. H. Niu, L. W. Cao, S. X. Sang, X. Z. Zhou, and Z. Z. Wang, "Anisotropic adsorption swelling and permeability characteristics with injecting CO_2 in coal," *Energy and Fuels*, vol. 32, no. 2, pp. 1979–1991, 2018.

[53] C. E. Fairhurst and J. A. Hudson, "Draft ISRM suggested method for the complete stress-strain curve for intact rock in uniaxial compression," *International Journal of Rock Mechanics and Mining Sciences & Geomechanics Abstracts*, vol. 36, no. 3, pp. 279–289, 1999.

[54] E. T. Brown, Ed., *Rock Characterization, Testing & Monitoring: ISRM Suggested Methods*, Pergamon Press, Oxford, UK, 1981.

[55] Z. Fang and J. P. Harrison, "A mechanical degradation index for rock," *International Journal of Rock Mechanics and Mining Sciences*, vol. 38, no. 8, pp. 1193–1199, 2001.

[56] C. H. Zhang, Q. S. Zhao, L. G. Wang, N. Zhao, and Y. J. Yu, "Test and numerical modeling on strain softening behavior and permeability evolution of rock under tri-axial compression," *Journal of China Coal Society*, vol. 8, pp. 1774–1782, 2015.

[57] X. Tan, H. Konietzky, and T. Frühwirt, "Laboratory observation and numerical simulation of permeability evolution during progressive failure of brittle rocks," *International Journal of Rock Mechanics and Mining Sciences*, vol. 68, pp. 167–176, 2014.

[58] S. C. Yuan and J. P. Harrison, "An empirical dilatancy index for the dilatant deformation of rock," *International Journal of Rock Mechanics and Mining Sciences*, vol. 41, no. 4, pp. 679–686, 2004.

[59] P. Bésuelle, J. Desrues, and S. Raynaud, "Experimental characterisation of the localisation phenomenon inside a Vosges sandstone in a triaxial cell," *International Journal of Rock Mechanics and Mining Sciences*, vol. 37, no. 8, pp. 1223–1237, 2000.

[60] Z. Z. Zhang, F. Gao, and X. J. Shang, "Rock burst proneness prediction by acoustic emission test during rock deformation," *Journal of Central South University*, vol. 21, no. 1, pp. 373–380, 2014.

[61] R. Luo, Y. W. Zeng, Y. Cao, and L. Li, "Research on influence of inhomogeneity degree on mechanical parameters of inhomogeneous rock," *Rock and Soil Mechanics*, vol. 33, pp. 3788–3794, 2012.

[62] Q. Jiang, X. T. Feng, and G. Q. Chen, "Study on constitutive model of hard rock considering surrounding rock deterioration under high geostresses," *Chinese Journal of Rock Mechanics and Engineering*, vol. 27, pp. 144–152, 2008.

Hindawi
Geofluids
Volume 2019, Article ID 3786293, 8 pages
https://doi.org/10.1155/2019/3786293

Research Article

The Rheology and Performance of Geothermal Spring Water-Based Drilling Fluids

Emine Avci and Bayram Ali Mert

Iskenderun Technical University, Faculty of Engineering and Natural Sciences, Department of Petroleum and Natural Gas Engineering, 31200 Iskenderun, Hatay, Turkey

Correspondence should be addressed to Bayram Ali Mert; bali.mert@iste.edu.tr

Received 30 November 2018; Revised 12 March 2019; Accepted 7 April 2019; Published 2 May 2019

Guest Editor: Bisheng Wu

In this study, the rheological properties and performances of mud prepared with geothermal spring water to be used by geothermal drilling operators were examined at ambient and elevated temperatures. In this context, mud samples were prepared in the compositions detailed in the API specification by using five different geothermal spring water types and a distilled water type. Afterwards, density, apparent viscosity, plastic viscosity, yield point, gel strength, fluid loss, pH, and filter cake thickness of these samples were measured. The drilling muds were analyzed by means of rheological tests in accordance with the standards of the American Petroleum Institute (API). The experimental results have revealed that the mud prepared with geothermal water have lower viscosity and yield point compared to those prepared with freshwater at elevated temperatures. The stability of the muds decreases, especially at temperatures higher than 250°F, and they start to become flocculated. It was concluded that geothermal water-based muds have higher API fluid loss and cake thickness than the freshwater-based one. Therefore, it could be interpreted that the muds prepared with geothermal spring water will exhibit lower flow performance and lower ability of hole cleaning and rate of penetration compared to the freshwater muds. Hence, it is recommended that this kind of water should not be used to prepare drilling mud.

1. Introduction

Drilling fluids are an important circulation component for the drilling process [1]. The drilling fluids are basically divided into three categories according to their continuous phase: water-based muds, oil-based muds, and gas-based muds [2]. A typical water-based mud usually consists of suspension of clay particles in water. Some of the main functions of the muds are transporting of cuttings, lubricating of drill string, preventing an influx of formation fluids, controlling the hydrostatic pressure, and stabilizing the well [3, 4]. The drilling muds must have certain rheological and filtration properties in order to perform these functions [5]. It is relatively difficult to maintain these properties of the mud during geothermal drilling [6, 7]. As it is well-known, geothermal drillings are carried out under hot and naturally fractured and/or vugular formations where they cause a large amount of lost circulation and degradation [8]. The lost circulation is one of the most complicated problems that have existed in drilling engineering and leads to the requirement for a large volume of drilling fluid [9]. Therefore, it is significant for the operators to provide water from the source closest to the well site, both economically and technically. Operators sometimes use a geothermal spring source which is close to the well site to prepare drilling mud. In geothermal systems, geothermal water ascends to the surface by reacting with the subsurface formations causing mineral dissolution, so the variety and concentration of dissolved constituents in the geothermal waters are higher than those of freshwaters. The geothermal water composition is characterized by the macroelements of the reservoir rock and the subsurface environment to which it is exposed most of the time. The most frequently observed ions with high concentrations are Na^+, K^+, Ca^{2+}, Mg^{2+}, HCO_3^-, CO_3^{2-}, SO_4^{2-}, and CO_2. Other micropollutants are heavy metals such as mercury, copper, lead, silver, iron, zinc, arsenic, manganese, chromium, beryllium, selenium, vanadium, cadmium, nickel, strontium, uranium, cobalt, gallium, and antimony. Some other elements of boron and silica could be present in geothermal waters as well [10]. Therefore, these waters are likely to affect the drilling fluid properties such as rheology, fluid loss, shale inhibition, and lubricity.

There are various studies in the literature regarding the change in rheological and filtration properties depending on temperature, pressure, various contaminants and some additives, or the chemistry of the clays used. Some of these studies examined the effect of various additives on rheological properties without changing the fluids used to prepare mud while others have studied the effect of different fluids on rheological properties by keeping the additives constant. For instance, Vipulanandan and Mohammed [11] used nanoclays, Jain et al. [12] used nanocomposites, Kang et al. [13] used nanoparticles, Cai et al. [14] used nanosilicates, Li et al. [15] used cellulose nanocrystals, Navarrete et al. [16] used guar gum, Yan et al. [17] used synthetic polymers, Mahto and Sharma [18] used tamarind gum, Ahmad et al. [19] used acrylamide-based copolymer, and Meng et al. [20] used carbon ash as an additive to examine the effects on drilling mud. As a result, they observed that these additives improved the rheological properties to be present in an effective drilling mud. Luo et al. [4] and Ofei et al. [21] have used ionic liquids as an additive for drilling muds, and they concluded that these liquids reduce fluid loss by improving the rheological properties of drilling muds even at elevated temperatures. Kelessidis et al. [22] and Abu-Jdayil [23] analyzed the rheological properties of drilling muds prepared with salty water. They have stated that viscosity and yield point decreased whereas the filtrate volume increased as the concentration of salt increased. Furthermore, they observed that mud samples present shear thickening behavior with an increase in salt content. Zhao et al. [24] studied the effect of Na, K, Mg, and Ca inorganic salt cations on the rheological properties of the polyacrylamide/xanthan gum solution for drilling mud and concluded that these cations affected rheological properties negatively and reduced the viscosity and cutting capacity significantly at high concentrations. Willson et al. [25], Choi et al. [26], and Mao et al. [27] examined the performance of drilling mud prepared by seawater.

In this study, the rheological and filtration characteristics of drilling muds prepared with geothermal spring water were examined, and their effects on drilling performance were revealed.

2. Materials and Methods

2.1. Materials. Four different geothermal spring water samples obtained from various geothermal areas (*gs*1, *gs*2, *gs*3, and *gs*4), distilled water (*dw*1), Na-bentonite being the most commonly used clay type in drilling mud, XCD (xantham gum) for modifying viscosity, and CMC (carboxymethyl cellulose) for controlling fluid loss were used to prepare the mud samples. The chemical properties of geothermal spring water and distilled water are given in Table 1.

Table 1: Chemical properties of geothermal spring water samples and distilled water sample.

Chemical parameters	Samples				
	*gs*1	*gs*2	*gs*3	*gs*4	dwl
pH	7.41	7.72	8.33	7.64	8.10
Specific conductivity (μS/cm)	6714	3015.5	2028	1805	10.49
K^+ (mg/L)	98.8	26	33.2	34	—
Na^+ (mg/L)	1215	256	423	363	1.42
NH_4 (mg/L)	<0.1	1.28	1.92	1.82	—
Ca^{2+} (mg/L)	97	287	22.4	28.8	0
Mg^{2+} (mg/L)	17.5	34.3	0.72	8.64	0
$As_{(T)}$ (mg/L)	—	<0.05	—	—	0
$B_{(T)}$ (mg/L)	5.6	0.2	15.1	12.3	0
Li^+ (mg/L)	1.5	—	1.05	0.98	—
SiO_2 (mg/L)	81	56	203	187	—
CO_2 (mg/L)	0.5	7.47	—	—	—
HCO_3^- (mg/L)	7.6	245	580	626	—
CO_3^{2-} (mg/L)	<10	<10	90	0.0	—
SO_4^{2-} (mg/L)	432	839	139	141	1
Cl^- (mg/L)	1670	325	216	196	0.34
F^- (mg/L)	—	<0.1	—	—	—
NO_2^- (mg/L)	—	<0.1	<0.05	<0.05	0
NO_3^- (mg/L)	—	12.4	4.1	3.7	—
Salinity (ppt)	—	—	1.0	0.9	—
TDS (mg/L)	—	—	1504	1390	—
$Fe_{(T)}$ (mg/L)	—	—	0.46	0.475	0

The crystallographic properties of the sample used in this study were determined using a Rigaku Miniflex II X-ray diffractometer equipped with Cu α radiation in the 2θ range of 3–90° with a 0.01 step size and 0.5 deg/min, and the patterns were evaluated using a PDXL software program for mineral identification. The pattern given in Figure 1 shows that the bentonite sample was composed of sodium-rich montmorillonite (NaM) mineral together with quartz, clipoptilolite, albite, and illite which were identified as impurities.

The elemental analysis of bentonite sample was performed by X-ray fluorescence (XRF) using a Thermo ARL X-ray spectrometer. From the obtained results, it is found that the Na-bentonite sample is composed mainly of SiO_2 (61.59 wt%), Al_2O_3 (15.88 wt%), and Fe_2O_3 (5.62 wt%), in addition to Na_2O (2.71 wt%), MgO (2.21 wt%), CaO (1.53 wt%), K_2O (1.07 wt%), TiO_2 (0.92 wt%), and L.O.I. (7.82 wt%) trace elements in the bentonite which are P_2O_5, MnO, SrO, NiO, CuO, ZnO, and ZrO_2. These results showed that the Al_2O_3/SiO_2 ratio was about 1/3 to 1/4 as expected for montmorillonite which is the main component of bentonite used in the study.

2.2. Preparation of Drilling Mud Samples. The mud samples were prepared in the compositions detailed in the American Petroleum Institute (API) specification [28]. As shown in Figure 2, 500 mL of geothermal spring water was stirred with 32.14 g of bentonite for 20 minutes to maintain the clay-

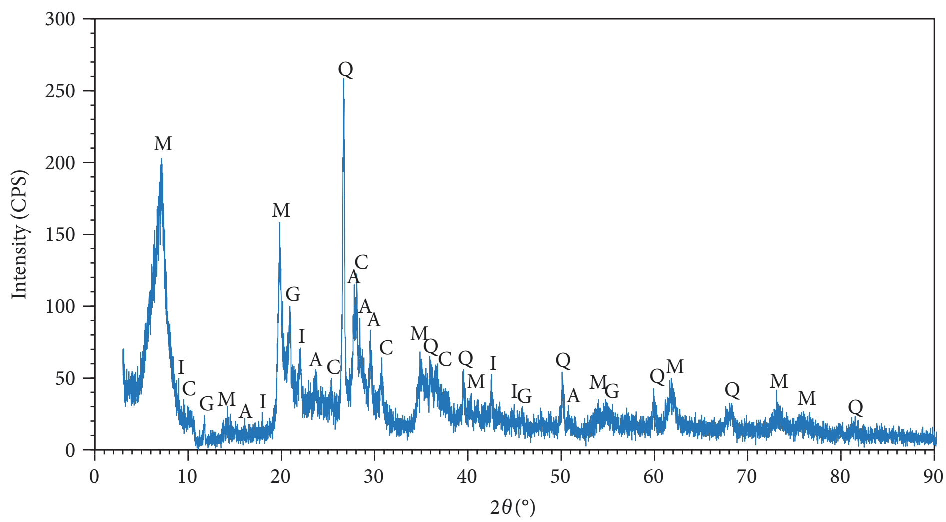

Figure 1: X-ray diffraction (XRD) of Na-bentonite.

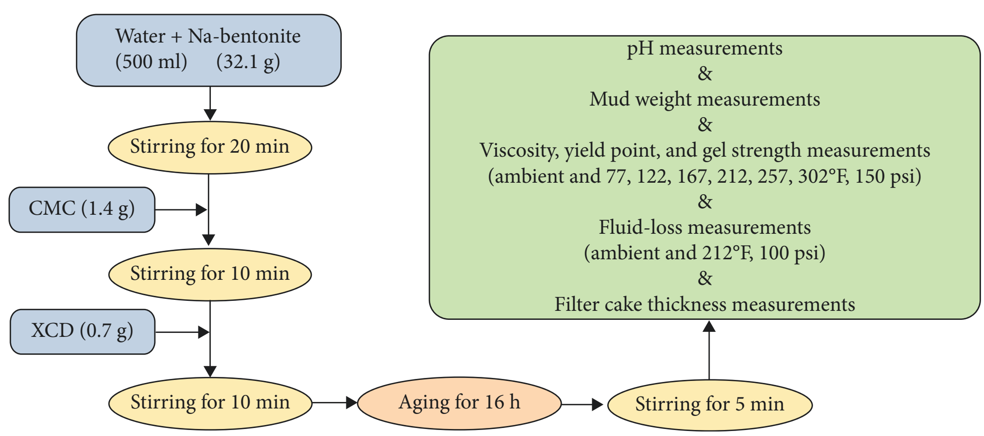

Figure 2: Flowchart of the experimental procedure.

water ratio according to API standards. Then, 1.4 g of CMC and 0.7 g of XCD were added to the solution, respectively. Finally, the solution was stirred for 10 minutes to form a homogeneous mixture. A Hamilton-Beach multiple mixer (model 9B) was used for mixing.

The above process was repeated for each geothermal spring water, and a total of four different mud samples were prepared. These samples were labeled as $S1$, $S2$, $S3$, and $S4$. Moreover, a sample was prepared with 500 mL of distilled water as base fluid in order to examine the effects of the water on the mud by following the steps. This sample was also labeled as $D1$. Prepared samples were remained in static condition at room temperature for 16 hours as specified in the API standard for bentonite clay. The five mud samples labeled $S1$, $S2$, $S3$, $S4$, and $D1$ were subjected to rheological and filtration tests. These tests were mud weight, viscosity, gel strength, fluid loss, and mud cake thickness measurements, respectively.

2.3. Determination of Rheological Properties. In the experimental study, API Standard Procedures were used in order to determine rheological properties [29].

The weight of the considered mud samples was determined by using the conventional OFITE (model 900) mud balance at ambient temperature, while the rheological properties (viscosity, yield point, and gel strength) were measured at both ambient and elevated temperatures by means of a Fann model 35 viscometer and Fann model 50 SL rheometer, respectively. Since the temperatures of geothermal resources ranged between 30°C (86°F) ± 150°C (302°F) [30], viscometer shear stress dial readings were obtained under 77, 122, 167, 212, 257, and 302 (°F) temperatures and 150 psi pressure every five seconds for each standard shear rate (3, 6, 100, 200, 300, and 600 rpm).

The Bingham plastic, power-low, and Herschel-Bulkley models are the fundamental models to describe the behavior of drilling mud [2]. Moreover, Vipulanandan [31] and hyperbolic models [32, 33] have been used for the same purpose recently. However, drilling fluid is generally considered to be classified as Bingham plastic in the drilling industry and the rheological properties of drilling mud are determined based on this model [20, 34].

According to the Bingham plastic model, the apparent viscosity, plastic viscosity, and yield point were calculated using the following equations from 600 and 300 rpm reading:

$$\text{Apparent viscosity (AV)} = \frac{\theta_{600}}{2\,(\text{mPas})}, \tag{1}$$

$$\text{Plastic viscosity} \left(\mu_{\mathrm{p}}\right) = \theta_{600} - \theta_{300}(\text{mPas}), \tag{2}$$

$$\text{Yield point} \left(y_{\mathrm{p}}\right) = 0.5\left(\theta_{300} - \mu_{\mathrm{p}}\right)\ (\text{Pa}). \tag{3}$$

The gel strength of muds was measured with the rotating viscometer. After that, the mud samples were immobilized for 10 seconds and 10 minutes. The maximum deflection value seen at 3 rpm was found as 10-second gel and 10-minute gel, respectively.

Fluid-loss measurements were conducted both at ambient and 212°F temperature conditions. The measurements at ambient temperature were performed using a LPLT (low pressure-low temperature) filter press, and the measurements at 212°F were made using the Fann 500 mL filter press in a pressure of 100 psi.

After the fluid-loss measurements, the mud cake on the No. 50 filtrate paper was left to evaporate water at ambient temperature for 24 hours, then the thickness of the mud cake was measured with a Vernier-type caliper.

3. Results and Discussion

The shear stress values and their relationship with the mud samples prepared with *S*1-4 and *D*1 are given in Figure 3 under both ambient and elevated temperatures (77, 122, 167, 212, 257, and 302 (°F)).

Figures 3(a)–3(f) reveal that the relationship between the shear stress and the shear rate is not linear between 0 and 100 rpm, but linearly increases up to 600 rpm, so the behavior of these samples can be described by the two-parameter Bingham plastic model, which assumes a linear relationship between the shear stress and the shear rate. As a matter of fact, the Bingham plastic model does not accurately predict fluid flow behavior at low shear rates but is useful for continuous monitoring and treating of drilling fluids. Fluids that exhibit Bingham plastic behavior do not flow until the shear stress exceeds a critical value known as the yield point. Once the yield point is reached, changes in shear stress and shear rate are proportional. This constant of proportionality, or the slope of the curve, is termed plastic viscosity. Moreover, it has been highlighted that shear stress values decreased as temperature increased for all the samples due to the thermal degradation of the components of the mud samples. When the rheograms are compared, it is seen that the shear stress values of the *D*1 sample is higher than those of *S*1, *S*2, *S*3, and *S*4 samples in all terms and conditions. For all samples, the shear stress values decreased at 257 and 302 (°F) temperatures and low shear rate (3-6 (rpm)). Normally, it is expected that the shear stress increases with the increase in the shear rate value. Nevertheless, bentonite muds can maintain their stability up to 250°F and show shear thickening behavior at temperatures higher than 250°F. Therefore, gelling and filtration problems will occur at temperatures higher than 250°F in the boreholes where these drilling muds are used. These problems will cause the drilling fluid to flow into formation and reduce the carrying capacity.

Table 2 shows AV, PV, and YP and the ratio of YP to PV of the drilling mud samples depending on the temperature.

As can be seen in Table 2, temperature affects the AV of geothermal and freshwater muds negatively. On the other hand, the AV of freshwater mud is greater than that of geothermal water muds at constant temperature. As AV shows the flowability of the drilling mud and affects the rate of penetration, it could be noted that the muds prepared with geothermal spring water will have lower flow performance.

From Table 2, it is seen that the PV of the muds prepared with geothermal spring water is lower than that of mud prepared with freshwater at all temperatures. This indicates that the spring water causes reduction in bentonite swelling ability compared to distilled water. This difference is the result of the different concentration of dissolved solid in the content of geothermal water and distilled water and leads to a difference in the viscosity of water that is used to prepare mud samples, in which the viscosity of water is one of the factors affecting plastic viscosity. The yield point of the all samples varies considerably with elevated temperature. Furthermore, similar to the viscosity, the highest yield point values are seen for the *D*1 sample at all temperatures. The low YP will cause drilling mud not to meet the task of suspending the cuttings and carrying capacity. In addition, the plastic viscosities of the samples generally decrease up to 167°F temperature. Although an increase is observed in a temperature range from 167°F to 212°F, it decreases consistently at the temperatures higher than 212°F. However, the plastic viscosity of the *S*2 sample decreases continuously at temperatures higher than 167°F. Although fluctuations are observed for the yield points of the samples up to 167°F, the yield points of all samples reduce distinctly at temperatures higher than 167°F. Interestingly, the yield point of the *S*2 sample reached a negative value at 257 and 302 (°F). This could be due to the wall slip phenomena. Wall slip is a common problem during rheology measurements of drilling fluids and is defined as a difference between the velocity of the walls of the measuring geometry and of the adjacent fluid layer [35]. The low shear rate [36] is one of the parameters in which "wall slip" is traditionally associated.

Shear thinning behavior is a desired property as it provides a reduction in the pumping pressure and an improvement in the rate of penetration when the viscosity is low in the pipes and where the drilling mud has a high shear rate. The YP/PV ratio is the measurement of the shear thinning as well [1, 37]. When the ratio gets higher, the shear thinning becomes greater [1, 2]. It is observed that the YP/PV ratio is the highest for the D1 sample in all conditions. Moreover, this ratio should be at least 0.375 Pa/mPas to

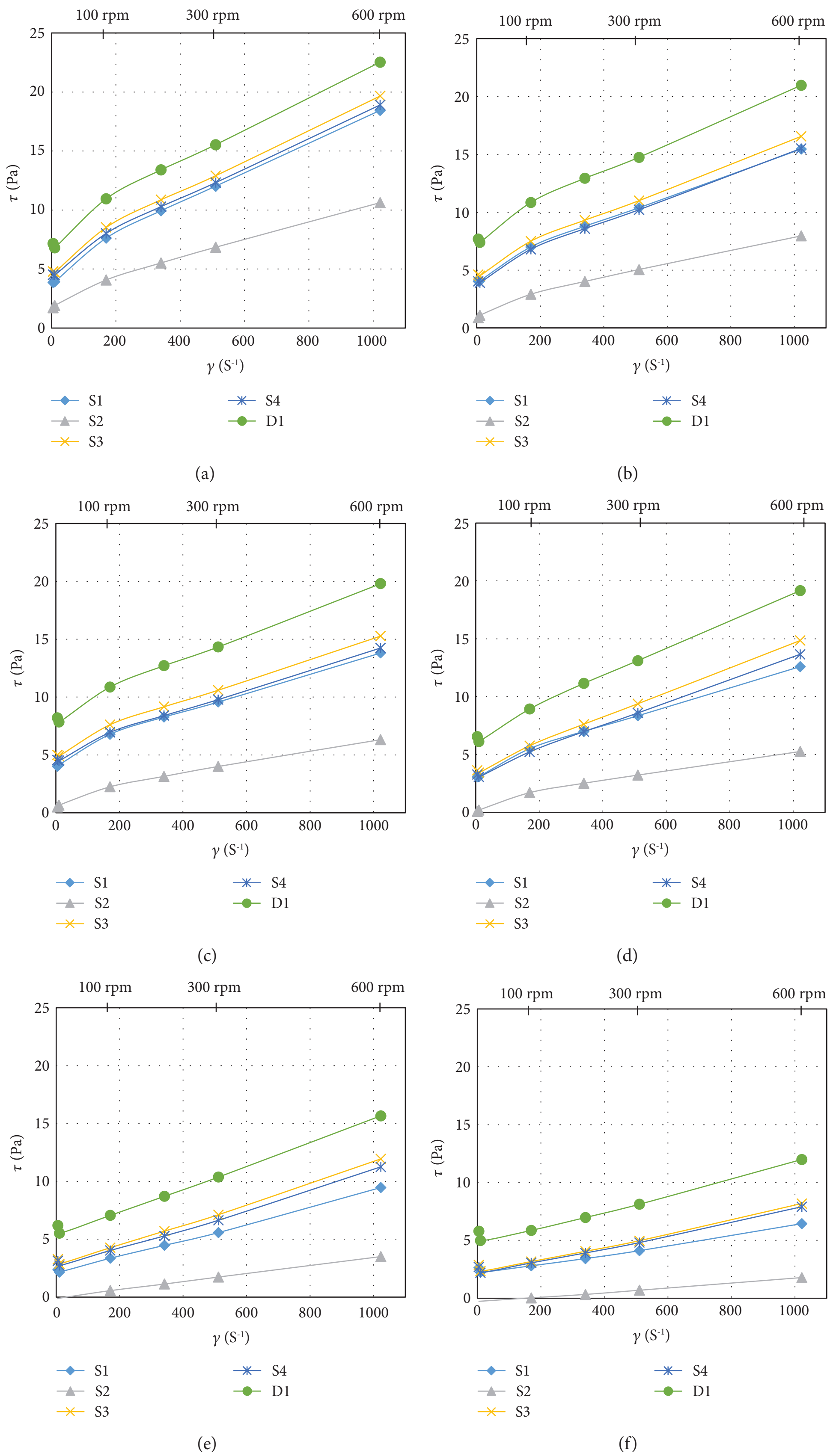

Figure 3: The rheograms of the $S1$, $S2$, $S3$, $S4$, and $D1$ samples at constant temperatures (a) 77°F, (b) 122°F, (c) 167°F, (d) 212°F, (e) 257°F, and (f) 302°F.

Table 2: Rheological properties of drilling mud samples.

Samples	*S*1	*S*2	*S*3	*S*4	*D*1
Apparent viscosity (AV) mPas at 150 psi					
Amb. con	17.305	11.180	19.700	18.900	22.895
77°F	19.265	11.095	20.535	19.747	23.535
122°F	16.154	8.315	17.298	16.209	21.910
167°F	14.422	6.604	15.948	14.874	20.675
212°F	13.153	5.490	15.506	14.267	20.008
257°F	9.881	3.648	12.465	11.748	16.354
302°F	6.735	1.867	8.551	8.260	12.526
Plastic viscosity (PV) mPas at 150 psi					
Amb. con.	9.590	6.920	10.650	10.650	10.650
77°F	13.404	7.887	14.097	13.748	14.602
122°F	10.602	4.489	11.609	11.073	13.004
167°F	8.847	4.838	9.763	9.312	11.411
212°F	8.870	4.253	11.401	10.588	12.625
257°F	8.129	3.690	10.068	9.640	11.060
302°F	4.877	2.282	6.707	6.464	8.079
Yield point (YP) Pa at 150 psi					
Amb. con.	7.884	4.353	9.249	8.431	12.514
77°F	5.985	3.279	6.578	6.130	9.129
122°F	5.673	4.248	5.813	5.247	9.100
167°F	5.697	1.804	6.320	5.683	9.467
212°F	4.376	1.264	4.194	3.758	7.543
257°F	1.789	-0.04	2.449	2.153	5.410
302°F	1.897	-0.41	1.884	1.835	4.543
YP/PV Pa/mPas at 150 psi					
Amb. con.	0.822	0.629	0.868	0.791	1.175
77°F	0.446	0.415	0.466	0.445	0.625
122°F	0.535	0.946	0.500	0.473	0.699
167°F	0.643	0.372	0.647	0.610	0.829
212°F	0.493	0.297	0.367	0.354	0.597
257°F	0.220	−0.01	0.243	0.223	0.489
302°F	0.388	−0.41	0.280	0.283	0.562

achieve sufficient hole cleaning [4, 21]. The YP/PV ratio of the D1 sample is higher than 0.375 Pa/mPas at all temperatures. However, it is noted that the ratio of geothermal water-based mud samples is below this value at temperatures above 212°F. This indicates that freshwater bentonite muds exhibit more shear thinning behavior compared to geothermal water-based bentonite muds. As the ratio decreases depending on temperature, muds prepared using geothermal water will adversely affect the hole cleaning and penetration rate. Therefore, it will directly cause a considerable increase in the cost of drilling.

Density, gel strength, mud cake thickness, pH, and fluid loss tests were also performed. The results are shown in Table 3.

Table 3: The other rheological properties of the drilling mud samples.

	*S*1	*S*2	*S*3	*S*4	*D*1
Density (g/cm^3)	1.031	1.031	1.031	1.031	1.031
Filtration pH at 75°F	6.0	7.0	8.0	8.0	7.0
Filter cake thickness (mm)	0.13	0.15	0.12	0.15	0.11
Gel strength (lb/100 ft^2) 10 s/10 min	7.5/17	4/8	10/27	12/27	16/19
API fluid loss cc at 100 psi and amb. temperature					
30 s	0.5	0.8	0.5	0.3	0.8
1 min	0.8	1.2	1.0	0.5	1.2
3 min	2.1	2.5	1.6	1.5	1.7
5 min	2.6	3.5	2.4	2.3	2.4
7.5 min	3.4	4.4	3.3	3.0	3.2
10 min	4.2	5.3	3.9	3.7	3.7
15 min	5.4	6.6	5.1	4.8	4.8
20 min	6.4	7.7	6.0	5.7	5.1
25 min	7.2	8.7	7.0	6.4	6.5
30 min	8.0	9.7	7.6	7.1	7.05
High-temperature fluid loss. cc at 100 psi and 212°F					
30 s	2.4	1.0	3.0	3.0	3.3
1 min	2.6	1.8	3.2	3.2	4.3
3 min	3.2	2.8	3.8	4.2	5.8
5 min	3.8	3.8	4.8	5.6	6.7
7.5 min	4.9	5.4	5.8	6.6	7.6
10 min	5.6	6.4	6.7	7.2	8.4
15 min	7.2	8.6	8.4	8.8	9.9
20 min	8.8	10.2	10.0	10.4	11.4
25 min	10.3	12.0	11.2	12.0	12.8
30 min	11.4	13.8	13.6	14.0	13.0

Mud density is one of the key parameters for successful drilling and affects the performance of drilling mud. The mud density measurements revealed that the density of each of the samples was 1.031 g/cm^3. It has been noted that the density of the samples taken from different locations would not change the drilling performance in drilling mud suspensions prepared with the same concentration of bentonite and water.

The gel strength is the shear stress measured at low shear rate after the mud was set quiescently for a period of time (10 seconds and 10 minutes in the standard API procedure). The minimum difference between the results of 10 sec and 10 min was measured in the D1 sample as 3.0 lb/100 ft^2. This indicates that the *D*1 sample has a higher cutting carrying capacity and thixotropic properties than the other mud samples. As a matter of fact, when circulation was over, suspended particles were prevented from collapsing into the bottom of the well. The problem of pipe sticking was also prevented due to gel strength. The initial gel strengths of the drilling muds should be high enough to prevent the cuttings in suspension from collapsing. Therefore, it is possible that the muds prepared with geothermal spring water cause high-pressure changes during maneuvering and it is likely to crack the weak formations.

It is observed that the fluid loss of all samples increased in the course of time at ambient and elevated temperatures up to 302°F. When the API and the high-temperature fluid loss values at the end of 30 seconds and 30 minutes of each sample are examined, it is seen that the mud sample retained its stability and the lowest difference is the sample labeled as $D1$. As the increment in the filtration rate of the fluid increases, the filtrate volume flowing into the underground formation may cause contamination of the production zone and/or deterioration of well stability. In all these cases, more filtration control agents will be required, and the cost of fluid will be directly affected.

After the API fluid loss test, the best filter cake measured by caliper of the mud samples is obtained for the $D1$ sample with a value of 0.11 mm. This indicates that the mud prepared by using geothermal water causes a thicker filter cake on wellbore during drilling operations compared to the freshwater muds. When geothermal water is preferred to prepare mud by operators, it will be more likely to encounter problems such as stuck pipe, excessive torque, drag, high swab, and surge pressures compared to freshwater muds.

4. Conclusions

As a result of experiments conducted on five different mud samples in order to compare the drilling performance of the drilling muds prepared with geothermal spring water and freshwater, the following conclusions were found.

(i) Muds prepared with geothermal water have lower viscosities and yield points than those prepared with freshwater at elevated temperatures. The stability of the muds deteriorates, and the muds start to become flocculated especially at temperatures higher than 250°F. Moreover, since the viscosity and yield point of both types of muds are not high enough for drilling mud to perform its functions, this will lead to an increase in the amount of mud filtrate invasion and decrease the carrying capacity of drilling muds

(ii) The shear stress values at constant shear rate and shear thinning behavior of geothermal water-based muds are found to be lower than those of muds prepared with freshwater at both ambient and elevated temperatures. Therefore, these muds will exhibit lower flow performance, lower ability of hole cleaning, and lower rate of penetration compared to freshwater muds

(iii) Geothermal water muds lead to greater filtrate volume than that of freshwater muds at both ambient and elevated temperatures. In other words, it could be noted that there is an increase in the volume of filtrate flowing through the formation during drilling when geothermal water-based muds are used. It could also lead to contamination of the production zone and degradation of well stability. Therefore, it will require a significant amount of fluid loss additive to control the filtration. As a result, this will directly affect the cost of the well

(iv) Muds prepared with geothermal water are found to have a greater cake thickness than are muds prepared with freshwater. Therefore, it may cause the drill string to stick to the wellbore and increase the possibility of other damages inside the well due to higher swab and surge pressures

Briefly, it could be noted that the muds prepared with geothermal spring water will cause lower drilling performance and high cost compared to muds prepared with freshwater. Therefore, it is recommended that geothermal spring water should not be used to prepare drilling mud in terms of effectiveness and cost of drilling.

Data Availability

No data were used to support this study.

Conflicts of Interest

The authors declare that there is no conflict of interest regarding the publication of this paper.

Acknowledgments

The authors would like to thank Dr. Gursat Altun (Istanbul Technical University, Department of Petroleum and Natural Gas Engineering) for his valuable suggestions and for providing laboratory opportunities.

References

[1] A. T. Bourgoyne, M. E. Chenevert, K. K. Millheim, and F. S. Young Jr., *Applied drilling engineering*, vol. 2 of Society of Petroleum Engineers Textbook Series, , Society of Petroleum Engineers, 1991.

[2] R. Caenn, H. C. Darley, and G. R. Gray, *Composition and Properties of Drilling and Completion Fluids*, Gulf Professional Publishing, Amsterdam, 2011.

[3] V. C. Kelessidis, C. Tsamantaki, A. Michalakis et al., "Greek lignites as additives for controlling filtration properties of water–bentonite suspensions at high temperatures," *Fuel*, vol. 86, no. 7-8, pp. 1112–1121, 2007.

[4] Z. Luo, J. Pei, L. Wang, P. Yu, and Z. Chen, "Influence of an ionic liquid on rheological and filtration properties of water-based drilling fluids at high temperatures," *Applied Clay Science*, vol. 136, pp. 96–102, 2017.

[5] M. Amani, M. Al-Jubouri, and A. Shadravan, "Comparative study of using oil-based mud versus water-based mud in HPHT fields," *Advances in Petroleum Exploration and Development*, vol. 4, no. 2, pp. 18–27, 2012.

[6] S. Saito, S. Sakuma, and T. Uchida, "Drilling procedures, techniques and test results for a 3.7 km deep, 500°C exploration well, Kakkonda, Japan," *Geothermics*, vol. 27, no. 5-6, pp. 573–590, 1998.

[7] S. Saito and S. Sakuma, "Frontier geothermal drilling operations succeed at 500°C BHST," *SPE Drilling and Completion*, vol. 15, no. 3, pp. 152–161, 2000.

[8] S. Santoyo-Gutiérrez, A. García, M. Morales, J. Perezyera, and A. Rosas, "Applied technology in the solution of geothermal drilling problems of deep wells in La Primavera caldera (Mexico)," *Journal of Volcanology and Geothermal Research*, vol. 47, no. 1-2, pp. 195–208, 1991.

[9] B. Ma, X. Pu, Z. Zhao, H. Wang, and W. Dong, "Laboratory study on core fracturing simulations for wellbore strengthening," *Geofluids*, vol. 2019, Article ID 7942064, 18 pages, 2019.

[10] V. G. Gude, "Chapter 4 - geothermal source for water desalination—challenges and opportunities," in *Renewable Energy Powered Desalination Handbook*, pp. 141–176, Butterworth-Heinemann, 2018.

[11] C. Vipulanandan and A. Mohammed, "Effect of nanoclay on the electrical resistivity and rheological properties of smart and sensing bentonite drilling muds," *Journal of Petroleum Science and Engineering*, vol. 130, pp. 86–95, 2015.

[12] R. Jain, V. Mahto, and V. P. Sharma, "Evaluation of polyacrylamide-grafted-polyethylene glycol/silica nanocomposite as potential additive in water based drilling mud for reactive shale formation," *Journal of Natural Gas Science and Engineering*, vol. 26, pp. 526–537, 2015.

[13] Y. Kang, J. She, H. Zhang, L. You, and M. Song, "Strengthening shale wellbore with silica nanoparticles drilling fluid," *Petroleum*, vol. 2, no. 2, pp. 189–195, 2016.

[14] J. Cai, M. E. Chenevert, M. M. Sharma, and J. E. Friedheim, "Decreasing water invasion into Atoka shale using nonmodified silica nanoparticles," *SPE Drilling & Completion*, vol. 27, no. 1, pp. 103–112, 2012.

[15] M. C. Li, Q. Wu, K. Song, Y. Qing, and Y. Wu, "Cellulose nanoparticles as modifiers for rheology and fluid loss in bentonite water-based fluids," *ACS Applied Materials & Interfaces*, vol. 7, no. 8, pp. 5006–5016, 2015.

[16] R. C. Navarrete, R. E. Himes, and J. M. Seheult, "Applications of xanthan gum in fluid-loss control and related formation damage," in *SPE Permian Basin Oil and Gas Recovery Conference*, Midland, TX, USA, March 2000.

[17] L. Yan, C. Wang, B. Xu, J. Sun, W. Yue, and Z. Yang, "Preparation of a novel amphiphilic comb-like terpolymer as viscosifying additive in low-solid drilling fluid," *Materials Letters*, vol. 105, pp. 232–235, 2013.

[18] V. Mahto and V. P. Sharma, "Rheological study of a water based oil well drilling fluid," *Journal of Petroleum Science and Engineering*, vol. 45, no. 1-2, pp. 123–128, 2004.

[19] H. M. Ahmad, M. S. Kamal, and M. A. Al-Harthi, "High molecular weight copolymers as rheology modifier and fluid loss additive for water-based drilling fluids," *Journal of Molecular Liquids*, vol. 252, pp. 133–143, 2018.

[20] X. Meng, Y. Zhang, F. Zhou, and P. K. Chu, "Effects of carbon ash on rheological properties of water-based drilling fluids," *Journal of Petroleum Science and Engineering*, vol. 100, pp. 1–8, 2012.

[21] T. N. Ofei, C. B. Bavoh, and A. B. Rashidi, "Insight into ionic liquid as potential drilling mud additive for high temperature wells," *Journal of Molecular Liquids*, vol. 242, pp. 931–939, 2017.

[22] V. C. Kelessidis, C. Tsamantaki, and P. Dalamarinis, "Effect of pH and electrolyte on the rheology of aqueous Wyoming bentonite dispersions," *Applied Clay Science*, vol. 38, no. 1-2, pp. 86–96, 2007.

[23] B. Abu-Jdayil, "Rheology of sodium and calcium bentonite–water dispersions: effect of electrolytes and aging time," *International Journal of Mineral Processing*, vol. 98, no. 3-4, pp. 208–213, 2011.

[24] D. Zhao, H. Liu, W. Guo, L. Qu, and C. Li, "Effect of inorganic cations on the rheological properties of polyacrylamide/xanthan gum solution," *Journal of Natural Gas Science and Engineering*, vol. 31, pp. 283–292, 2016.

[25] S. M. Willson, P. M. Driscoll, A. Judzis et al., "Drilling salt formations offshore with seawater can significantly reduce well costs," *SPE Drilling & Completion*, vol. 19, no. 3, pp. 147–155, 2004.

[26] J. H. Choi, C. S. Yoo, and Y. S. Han, "A study on engineering characteristics of the drilling fluid depending on the mix water," *Journal of the Korean Geosynthetic Society*, vol. 15, no. 4, pp. 43–52, 2016.

[27] H. Mao, Z. Qiu, B. Xie, Z. Wang, Z. Shen, and W. Hou, "Development and application of ultra-high temperature drilling fluids in offshore oilfield around Bohai Sea bay basin, China," in *Offshore Technology Conference Asia*, Lumpur, Malaysia, March 2016.

[28] American Petroleum Institute 13A, *Specification for Drilling-Fluid Materials*, American Petroleum Institute, Production Department, Bellevue, USA, 2010.

[29] American Petroleum Institute RP13B1, *Recommended Practice for Field Testing Water-Based Drilling Fluids*, American Petroleum Institute, Bellevue, USA, 3rd edition, 2004.

[30] K. Wang, B. Yuan, G. Ji, and X. Wu, "A comprehensive review of geothermal energy extraction and utilization in oilfields," *Journal of Petroleum Science and Engineering*, vol. 168, pp. 465–477, 2018.

[31] A. P. Tchameni, L. Zhao, J. X. F. Ribeiro, and T. Ting Li, "Evaluating the thermal effect on the rheological properties of waste vegetable oil biodiesel modified bentonite drilling muds using Vipulanandan model," *High Temperatures High Pressures Journal*, 2018.

[32] C. Vipulanandan and A. S. Mohammed, "Hyperbolic rheological model with shear stress limit for acrylamide polymer modified bentonite drilling muds," *Journal of Petroleum Science and Engineering*, vol. 122, pp. 38–47, 2014.

[33] A. S. Mohammed, "Effect of temperature on the rheological properties with shear stress limit of iron oxide nanoparticle modified bentonite drilling muds," *Egyptian Journal of Petroleum*, vol. 26, no. 3, pp. 791–802, 2017.

[34] R. V. Lauzon and K. I. G. Reid, "New rheological model offers field alternative," *Oil & Gas Journal*, vol. 77, no. 21, pp. 51–57, 1979.

[35] D. Bonn, M. M. Denn, L. Berthier, T. Divoux, and S. Manneville, "Yield stress materials in soft condensed matter," *Reviews of Modern Physics*, vol. 89, no. 3, article 035005, 2017.

[36] H. A. Barnes, "A review of the slip (wall depletion) of polymer solutions, emulsions and particle suspensions in viscometers: its cause, character, and cure," *Journal of Non-Newtonian Fluid Mechanics*, vol. 56, no. 3, pp. 221–251, 1995.

[37] P. Skalle, *Drilling Fluid Engineering*, BookBoon, 2011.

Hindawi
Geofluids
Volume 2019, Article ID 8013851, 9 pages
https://doi.org/10.1155/2019/8013851

Research Article

A Fractal Approach for Predicting Unsaturated Hydraulic Conductivity of Deformable Clay

Gaoliang Tao,[1] Xueliang Zhu,[1] Jianchao Cai,[2] Henglin Xiao,[1] Qingsheng Chen,[1] and Yin Chen[1]

[1]Hubei Provincial Ecological Road Engineering Technology Research Center, Hubei University of Technology, Wuhan 430068, China
[2]Institute of Geophysics and Geomatics, China University of Geosciences, Wuhan 430074, China

Correspondence should be addressed to Jianchao Cai; caijc@cug.edu.cn and Henglin Xiao; xiao-henglin@163.com

Received 18 December 2018; Revised 30 January 2019; Accepted 7 March 2019; Published 2 May 2019

Guest Editor: Fengshou Zhang

The relative hydraulic conductivity is one of the key parameters for unsaturated soils in numerous fields of geotechnical engineering. The quantitative description of its variation law is of significant theoretical and technical values. Parameters in a classical hydraulic conductivity model are generally complex; it is difficult to apply these parameters to predict and estimate the relative hydraulic conductivity under deformation condition. Based on the fractal theory, a simple method is presented in this study for predicting the relative hydraulic conductivity under deformation condition. From the experimental soil-water characteristic curve at a reference state, the fractal dimension and air-entry value are determined at a reference state. By using the prediction model of air-entry value, the air-entry values at the deformed state are then determined. With the two parameters determined, the relative hydraulic conductivity at the deformed state is predicted using the fractal model of relative hydraulic conductivity. The unsaturated hydraulic conductivity of deformable Hunan clay is measured by the instantaneous profile method. Values of relative hydraulic conductivity predicted by the fractal model are compared with those obtained from experimental measurements, which proves the rationality of the proposed prediction method.

1. Introduction

The seepage analysis of unsaturated soils is one of the hot topics in geotechnical and geoenvironmental engineering. There are many phenomena related to seepage problem, such as slope landslide disasters caused by rainfalls, antiseepage of the earth dikes, and transport of pollutants in underground soils. The unsaturated hydraulic conductivity is the most critical parameter in seepage analysis [1], which can be directly measured in laboratory experiments, e.g., steady-state test [2–4], instantaneous profile test, and other tests [5–7]. However, the direct methods are not only complex, time consuming, and labor intensive but also the accuracy and operability of test instrument require improvement. These problems have motivated many researchers to study the prediction method of hydraulic unsaturated conductivity. In addition, the seepage analysis of unsaturated soil under complex conditions relies on the prediction method of hydraulic conductivity [8]. Therefore, it is of great significance to preciously predict and estimate the unsaturated hydraulic conductivity [9, 10].

Mualem and Klute [11] provided a detailed overview of various models for hydraulic conductivity and divided the prediction model of hydraulic conductivity into three species: empirical forms, macroscopic models, and statistical models. The empirical forms and macroscopic models describe the relationship between unsaturated hydraulic conductivity and matric suction (or volumetric water content) through mathematical simple functions [12–16]. The statistical models are indirect methods for predicting unsaturated hydraulic conductivity from the soil-water characteristic curve (SWCC). Fredlund et al. [17] established a method for predicting unsaturated hydraulic conductivity through a complicated calculation procedure. The calculation procedure is done as follows: the SWCC was divided into m stage along the direction of volumetric water content, each stage of hydraulic conductivity was calculated by the matric suction at the middle point of each stage, and the accumulative calculation was carried out for obtaining unsaturated hydraulic conductivity. Based on the previous achievements in seepage analysis field, Agus et al. [18] evaluated and summarized four statistical models, i.e., the CCG model [19], modified CCG model [20], Burdine model [21], and Mualem model [22]. Although these models commendably describe the variation of hydraulic conductivity for different soils, the applicability of these models is still principally limited due to its complexity to some extent [23–26].

On the other hand, some researchers have devoted to improving these classical statistical models for more convenient and simple methods. Since Mandelbrot and Wheeler [27] proposed the concept of fractal geometry, the fractal theory has been widely used in the analysis of physical geometry properties as a mathematical method [28–31]. The fractal theory relates the unsaturated hydraulic conductivity to characterization of soil structure [32, 33], which provides a powerful tool to indirectly predict the hydraulic conductivity. Compared with the method of sectional calculation and integral calculation proposed by Fredlund et al. [17] and Agus et al. [18], the fractal model can simplify the complicated calculation procedure about relative hydraulic conductivity. Tyler and Wheatcraft [34] derived the fractal model of relative hydraulic conductivity based on a fractal model of SWCC. Based on the fractal theory, many researchers have derived new models for estimating the relative hydraulic conductivity, but the influence of deformation on hydraulic conductivity was not considered [35–43].

Many efforts have been done to examine the unsaturated hydraulic conductivity under deformation condition. Lloret and Alonso [44] investigated the effect of the void ratios and saturation separately on the unsaturated hydraulic conductivity and put forward the method of relative unsaturated hydraulic conductivity under deformation condition. Huang et al. [45, 46] proposed and verified an innovative method of hydraulic conductivity of unsaturated soil under deformation condition. Wang et al. [47] researched the variation of unsaturated hydraulic conductivity with volumetric water content and dry density. Assouline [48] proposed a model to predict the influence of soil density on hydraulic conductivity. Hu et al. [49] investigated a model taking into account the variation of pore size distribution, which predicted the relative hydraulic conductivity under deformation condition combined with the Mualem model. Cai et al. [50] presented an indirect prediction approach for the relative hydraulic conductivity taking account of the effect of initial void ratios. Fortunately, based on the fractal theory, Zhou et al. [51] proposed the unsaturated hydraulic conductivity model considering the effect of porosity. In this method, two fractal dimensions were used to describe the fractal characteristics of pore structure. The change law of maximum pore size with porosity was predicted from the existing empirical model; then, the air-entry value can be predicted. Eventually, based on the Mualem model, Zhou et al. [51] derived a fractal model of relative hydraulic conductivity considering the effect of porosity.

Tao and Kong [52] derived a new theoretical model from microscopic pore channels to predict the relative hydraulic conductivity. However, the predicted relative hydraulic conductivity is in a scatter plot, which is uncontinuous and hard to meet the requirement of unsaturated seepage analysis. Moreover, the calculation programs of prediction methods are complex and inconvenient for engineering application. Therefore, it can be seen that a new simple method is further expected to predict the relative hydraulic conductivity under deformation condition. According to the fractal theory, the predicted method of SWCC taking into account the influence of initial void ratio was proposed by Tao et al. [53]. On this basis, a predicted method of relative hydraulic conductivity under deformation condition was presented in this paper combined with the fractal model of relative hydraulic conductivity. This method is able to obtain the continuous curve of relative hydraulic conductivity under different matric suction conditions, which satisfy the theoretical research on seepage analysis. Furthermore, it is simple and convenient for practical engineering application. It is worth noting that the model presented in this paper is different from that proposed by Zhou et al. [51]. In this paper, only one fractal dimension is used to describe the pore distribution characteristics, the air-entry value is directly predicted by the air-entry value model proposed by Tao et al. [53], and a fractal model of relative hydraulic conductivity is derived by using the Tao-Kong model (Tao et al. [54] indicated that the Tao-Kong model yields good predictions against measured data when the fractal dimension is large, while the predictions of the Mualem model agree well with the measured results of the relative hydraulic conductivity when the fractal dimension is relatively small). In contrast with the proposed model in this paper, the computational efforts of Zhou et al. [51] are relatively complex.

In addition, due to the experimental difficulty and long experimental period, little experimental data is reported to verify the existing models considering the effect of different initial void ratios. Thus, it is particularly urgent to supplement relevant experiments. In this paper, the unsaturated hydraulic conductivity of deformable Hunan clay is measured by the instantaneous profile method to verify the proposed model. The instantaneous profile method took more than a year; consequently, the experimental data obtained in this study will be a useful supplement in the hydraulic field for unsaturated soils. The good agreement between the predicted values of the relative hydraulic conductivity and experimental data demonstrates that the proposed model efficiently captures the effects of deformation condition on the hydraulic conductivity.

2. Basic Theory

2.1. Hydraulic Conductivity Model. According to the channels of microscopic pore, a saturated hydraulic conductivity model can be expressed as [52]

$$k_s = \frac{\gamma T_s^{\,2} \cos^2\alpha}{2p_i\eta} \int_{\theta_r}^{\theta_s} \frac{d\theta}{\psi^2(\theta)}, \tag{1}$$

where k_s is the saturated hydraulic conductivity, γ is the bulk density, T_s is the surface tension, α is the contact angle, η is the viscosity, p_i is the ratios of the actual length of the micropore channel in the class i to the soil sample length, θ is the volumetric water content (θ_r and θ_s are the residual volumetric and saturated volumetric water content, respectively), and ψ is the matric suction.

On this basis, the unsaturated hydraulic conductivity k_w can be obtained:

$$k_w = \frac{\gamma T_s^{\ 2} \cos^2\alpha}{2p_i\eta}\int_{\theta_r}^{\theta}\frac{d\theta}{\psi^2(\theta)}. \tag{2}$$

Dividing equation (2) by equation (1), the calculus form of the relative hydraulic conductivity be described as

$$k_r(\theta) = \frac{\int_{\theta_r}^{\theta}\left(d\theta/\left(\psi^2(\theta)\right)\right)}{\int_{\theta_r}^{\theta_s}\left(d\theta/\left(\psi^2(\theta)\right)\right)}, \tag{3}$$

where k_r is the relative hydraulic conductivity, which is defined as the ratio between the unsaturated hydraulic conductivity and its corresponding saturated hydraulic conductivity (k_w/k_s).

2.2. Fractal Form of Hydraulic Conductivity Model. As presented by Tao et al. [53], a SWCC fractal model can be proposed; it is expressed as follows:

$$\begin{cases} w = w_s\left(\dfrac{\psi_a}{\psi}\right)^{3-D}, & \psi \geq \psi_a, \\ w = w_s, \quad \psi < \psi_a, \end{cases} \tag{4}$$

where w is gravimetric water content (w_s is saturated gravimetric water content), D is the fractal dimension, and ψ_a is the air-entry value.

The fractal model of SWCC is derived by the gravimetric water content. According to the relationship between the gravimetric and volumetric water content, it is also applicable to volumetric water content through the conversion equation:

$$\theta = \frac{w \cdot G_s}{1+e}, \tag{5}$$

where e is the initial void ratio and G_s is the relative particle density.

Then, substituting equation (5) into equation (4), the volumetric water content of fractal characteristics can be obtained:

$$\begin{cases} \theta = \theta_s\left(\dfrac{\psi_a}{\psi}\right)^{3-D}, & \psi \geq \psi_a, \\ \theta = \theta_s, \quad \psi < \psi_a. \end{cases} \tag{6}$$

The differential form of equation (6) is expressed as

$$d\theta = (D-3)\theta_s\psi_a^{3-D}\psi^{D-4}d\psi. \tag{7}$$

Equation (7) is differential expression of equation (6) at $\psi \geq \psi_a$; accordingly, the application range of equation (7) is $\psi \geq \psi_a$. Then, substituting equation (7) into equation (3), the following expression is yielded:

$$\begin{aligned} k_r(\theta) &= \frac{\int_{\theta_r}^{\theta}\left(d\theta/\left(\psi^2(\theta)\right)\right)}{\int_{\theta_r}^{\theta_s}\left(d\theta/\left(\psi^2(\theta)\right)\right)} \\ &= \frac{\theta_s(D-3)\psi_a^{3-D}\int_{\psi_d}^{\psi}\psi^{D-6}d\psi}{\theta_s(D-3)\psi_a^{3-D}\int_{\psi_d}^{\psi_a}\psi^{D-6}d\psi} = \frac{\int_{\psi_d}^{\psi}\psi^{D-6}d\psi}{\int_{\psi_d}^{\psi_a}\psi^{D-6}d\psi} \\ &= \frac{\left(\psi^{D-5}-\psi_d^{D-5}\right)}{\left(\psi_a^{D-5}-\psi_d^{D-5}\right)} = \frac{\left(\psi/\psi_a\right)^{D-5}-\left(\psi_d/\psi_a\right)^{D-5}}{1-\left(\psi_d/\psi_a\right)^{D-5}}, \end{aligned} \tag{8}$$

where ψ_d is the matric suction corresponding to residual volumetric water content (θ_r). Since $D < 3$ and $\psi_a \ll \psi_d$, $\left(\psi_d/\psi_a\right)^{D-5}$, is approaching infinitesimal, so Equation (8) is simplified as

$$k_r(\psi) = \left(\frac{\psi_a}{\psi}\right)^{5-D}. \tag{9}$$

It is noted that equation (9) is applicable to the stage when the matric suction is greater than the air-entry value ($\psi \geq \psi_a$), while the k_r value is taken as one when the matric suction is less than the air-entry value ($\psi < \psi_a$). The continuous curve of the relative hydraulic conductivity can be obtained by the fractal form of the hydraulic conductivity model, which is simple and convenient for practical engineering application.

2.3. Estimation of Unsaturated Hydraulic Conductivity. The main purpose of this paper is to predict the relative hydraulic conductivity under deformation condition. It is found from equation (9) that the unsaturated relative hydraulic conductivity is mainly controlled by the fractal dimension and the air-entry value, and it can also be applied to the prediction of relative hydraulic conductivity under deformation condition.

The process of determining the fractal dimension and the air-entry value is described as follows.

By taking the logarithm of both sides of equation (6), there is

$$\ln\theta = (3-D)(-\ln\psi) + \ln\left[\theta_s \cdot \psi_a^{\ (3-D)}\right]. \tag{10}$$

Then, it is easy to obtain

$$\ln\theta \propto (3-D)(-\ln\psi). \tag{11}$$

The fractal dimension is obtained by fitting experimental SWCC to equation (11). According to Tao et al. [55], the matric suction corresponding to the maximum pore size

(r_{max}) is defined as the air-entry value (ψ_a). Meanwhile, the fractal model of pore volume should be satisfied with $r \le r_{max}$. On the basis of the Young-Laplace equation, ψ is inversely proportional to r. So for a better fitting effect, it is better to adopt the experimental data at the stage of $\psi \ge \psi_a$. By plotting the $\ln\theta$ against $-\ln\psi$, the fractal dimension can be calculated by $D = 3 - k$, in which k is the gradient of the graph. Note that the fractal dimension is seen as a constant for the same soil with different initial void ratios [53].

Following Tao et al. [53], the air-entry value at different initial void ratios can be determined as

$$\psi_{ai} = \frac{\psi_{a0}}{(e_i/e_0)^{1/(3-D_0)}}, \tag{12}$$

where ψ_{a0} is the air-entry value of a maximum initial void ratio (e_0), ψ_{ai} is the air-entry value of a random initial void ratio e_i ($e_i < e_0$), and D_0 is the fractal dimension of a maximum initial void ratio (e_0).

It is worth pointing that the maximum initial void ratio (e_0) refers to the reference state of soil sample, while the random initial void ratio e_i ($e_i < e_0$) is corresponding to the deformed state of soil samples. Therefore, the same soil with different initial void ratios is taken as a different type of deformation condition.

By using equation (12), the air-entry value of random initial void ratios (e_i) is determined. After determination of the fractal dimension and air-entry value, the unsaturated relative hydraulic conductivity with different initial void ratios can be predicted from equation (9).

2.4. Hydraulic Experiments of Deformable Hunan Clay. The soil samples in this study are unsaturated clay soils in Hunan Province with a liquid limit of 46.34%, a plastic limit of 27.84%, and a relative particle density of 2.76. For the preparation of the soil sample, firstly, the soil was air-dried naturally until no obvious changes in gravimetric water content were measured, and that soil should be crushed and passed through the 2 mm standard sieve later. Soils were then mixed with a certain water quantity to reach the objective initial gravimetric water content about 19%. Importantly, the mixture should be placed in the hermetic box for at least 48 hours to make sure of the migration of water in soil, and then, the gravimetric water content was measured again.

Two sets of soil samples at five different initial void ratios (1.12, 1.04, 0.97, 0.90, and 0.84) were prepared by hydraulic jack. After vacuum and saturation, one set of samples was used to the SWCC test, and another set of samples was used in the variable water head test for measuring the saturated hydraulic conductivity. In the experimental process, the gravimetric water content was measured. But for calculation and model verification, the gravimetric water content should be converted into the volumetric water content by using equation (5).

2.5. Soil-Water Characteristic Curve Test. The pressure plate instrument produced by the Soil Moisture Company of the USA was selected for the SWCC test. The tests were executed by increasing gradually the matric suction from 0 to 1250 kPa (0, 5, 10, 30, 80, 280, 280, 450, 700, and 1250 kPa) without net stress. When the pore water was allowed to drain from the soil sample in pursuit of equilibrium in each level, the volumetric water content corresponding to specified matric suction was calculated from the amount of drainage in the soil sample. The experimental SWCC at the reference state ($e_0 = 1.12$) of Hunan clay is shown in Figure 1.

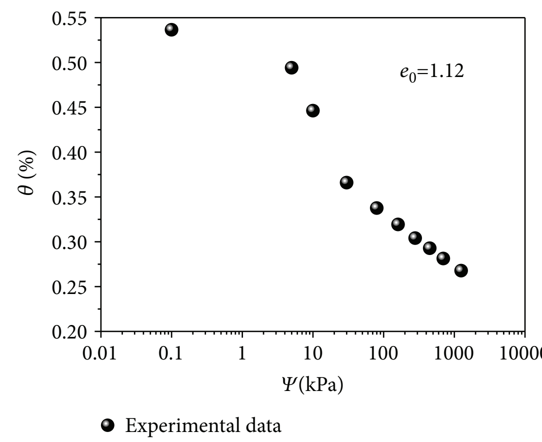

Figure 1: Measured SWCC for Hunan clay ($e_0 = 1.12$).

Figure 2: Saturated permeability test.

2.6. Permeability Test

2.6.1. Saturated Permeability Test. The saturated hydraulic conductivity of Hunan clay with different initial void ratios was measured by the variable water head test; the equipment of testing was TST-55 Permeameter (Figure 2). Then, multiple tests were performed to obtain the average value for high accuracy. The saturated hydraulic conductivity of soil samples with different initial void ratios at 20°C was obtained by temperature modification as shown in Table 1.

2.6.2. Unsaturated Permeability Test. The instantaneous profile method was employed to measure the unsaturated

Table 1: Measured values of saturated hydraulic conductivity of Hunan clay.

e	1.12	1.04	0.97	0.90	0.84
k_s (cm/s)	7.72×10^{-4}	4.15×10^{-4}	2.49×10^{-4}	1.73×10^{-4}	7.63×10^{-5}

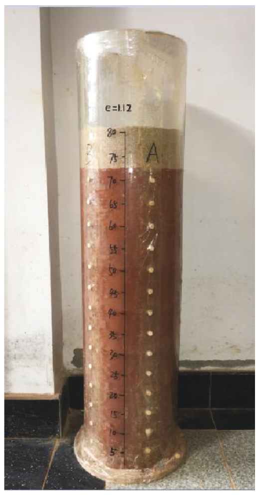

Figure 3: Unsaturated permeability test.

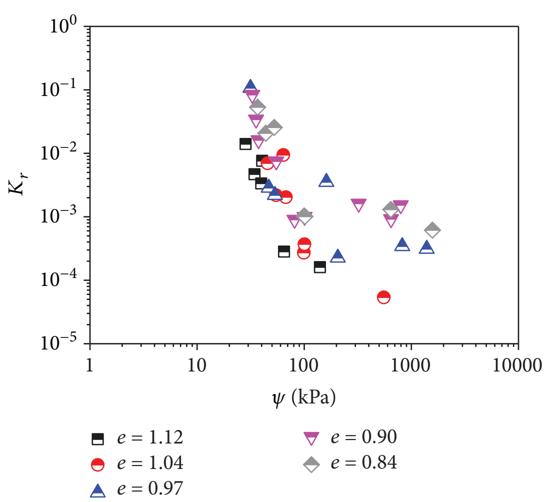

Figure 4: Measurement of the relative hydraulic conductivity of deformable Hunan clay.

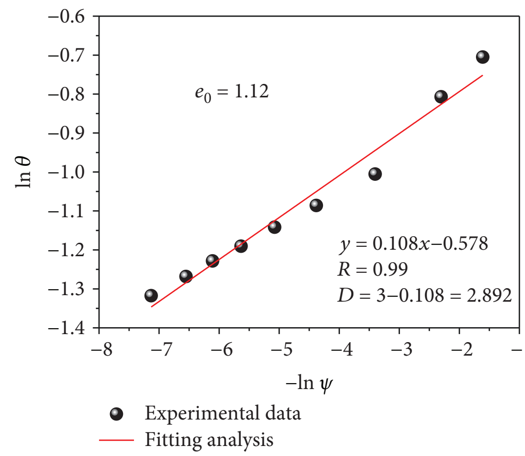

Figure 5: Fractal dimension of Hunan clay.

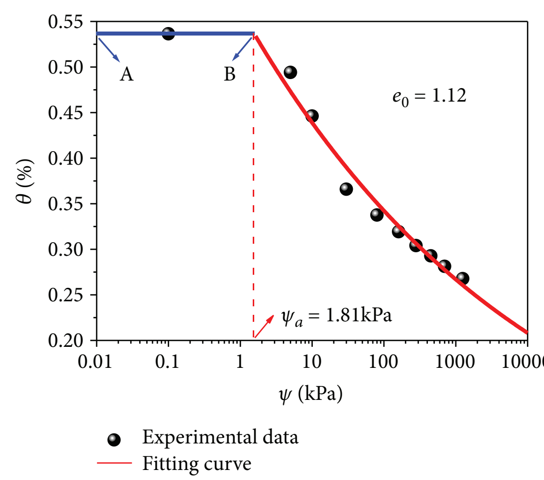

Figure 6: SWCC fitting to get the air-entry value at a reference state ($e_0 = 1.12$).

Table 2: Predicted and experimental result of air-entry value.

Initial void ratios	Air-entry value (kPa) Experimental results	Predicted values
1.12	1.81	1.81
1.04	3.56	3.59
0.97	6.69	9.17
0.90	9.49	13.71
0.84	20.96	25.97

hydraulic conductivity of deformable Hunan clay. The equipment of the instantaneous profile method was a special type of glass cylinder with a height of 1 m and a diameter of 25 cm, which was designed by ourselves. At the side of the glass cylinder, 5 columns of holes were arranged uniformly, and each column of holes was evenly distributed with a vertical interval of 5 cm (Figure 3). But, these holes were sealed when the test was starting. Under the action of gravity and capillary force, the water flow permeated into the bottom of the cylinder, which accelerated the test process. The water flow accorded with the requirement of one-dimensional seepage condition and Darcy's law.

The specific test steps are as follows:

(1) Soil Preparation. The preparation of remolded soil had the steps similar to the SWCC test. For the homogenization

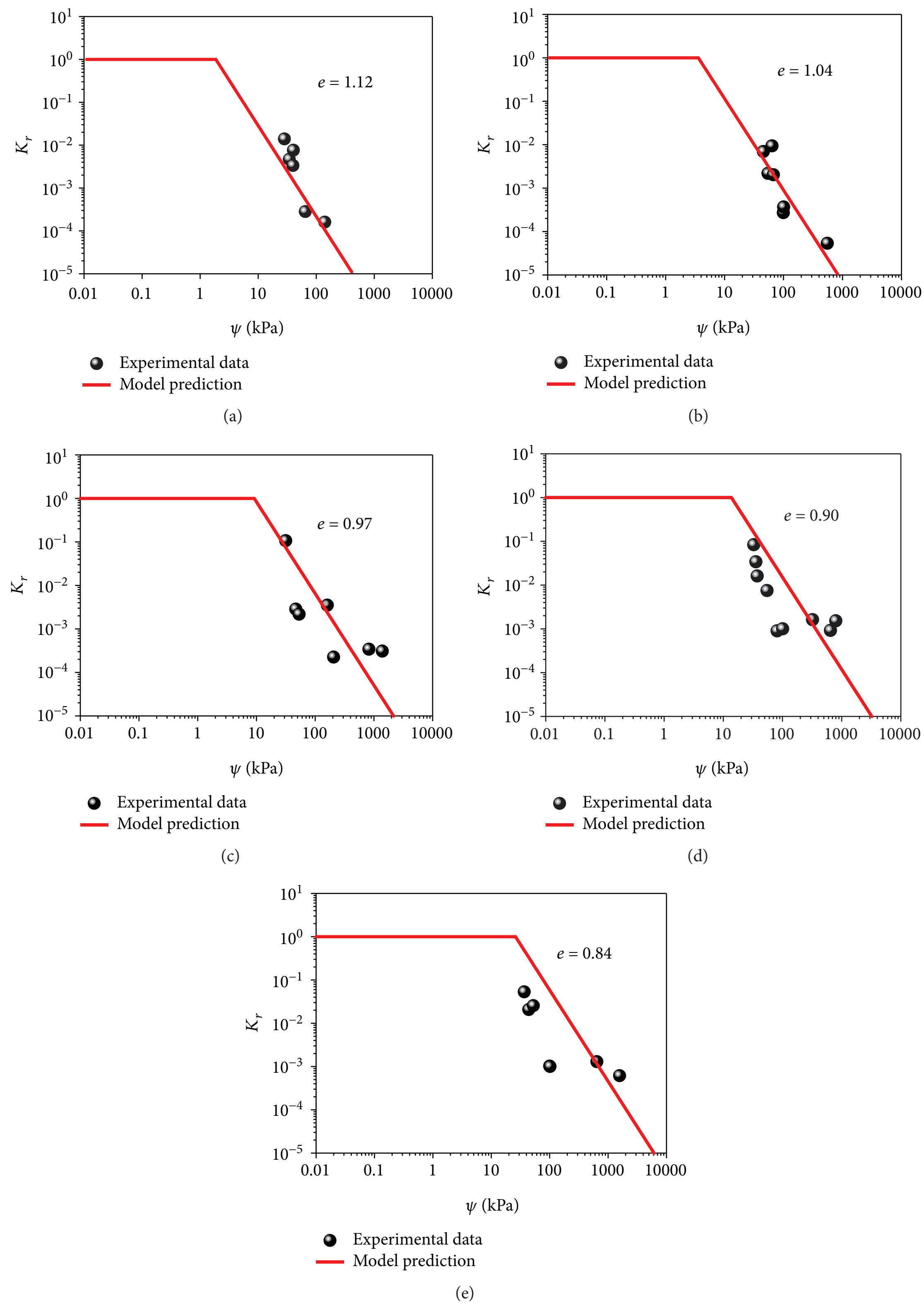

FIGURE 7: Comparison between predicted values and experimental results of the relative hydraulic conductivity of deformable Hunan clay.

of water, the soil sample was stirred evenly by the blender, and then, the soil was sealed for more than 48 hours. After the water migrate uniformly, the gravimetric water content was measured again.

(2) Sample Preparation. The sample was prepared by stratified compaction. To ensure close contact between soil layers, the interface of different layers was scraped. When the sample preparation was finished, an 8 cm thick fine sand

layer was evenly spread on the surface of each sample, which ensured that the water permeated uniformly and prevented the surface layer of each sample from caking during the seepage process.

(3) Water Permeation. The certain amount of water (1500 mL) was continuously added on the top of the sample during the 20 min. Then, it is necessary to immediately seal the top of the cylinder with fresh film to prevent water evaporation.

(4) Measurement of Gravimetric Water Content. Taking a soil sample for instance, when the wetting front infiltrated in the heights of 15 cm~20 cm of the soil sample, the gravimetric water content from top to bottom was beginning to be measured by taking out a certain amount of soil from a column of holes at the same time. By repeating the above work, the gravimetric water content of the other columns was measured at different time intervals, which depends on the falling velocity of wetting front. Finally, the variation of gravimetric water content with heights of soil samples at different times can be obtained.

The soil samples at initial void ratios of 1.12, 1.04, 0.97, 0.90, and 0.84 were tested in turn by using the above method. The unsaturated hydraulic conductivity was calculated using the method presented by Wang et al. [56]. Based on the experimental saturated hydraulic conductivity, the unsaturated hydraulic conductivity is converted to the relative hydraulic conductivity (Figure 4). It is noteworthy that the calculated relative hydraulic conductivity of Hunan clay is based on capillary theory, so the matric suction considered in this paper is mainly influenced by capillary water. However, at the stage of higher matric suction (about greater than 1000 kPa), the matric suction is greatly influenced by film water which is not studied in this paper, so the corresponding data are not analyzed. That is to say, the proposed model is suitable for lower suction (about smaller than 1000 kPa) stage because capillary suction is only considered.

2.7. Model Verification. By fitting equation (11) to the experimental SWCC at a reference state ($e_0 = 1.12$), the fractal dimension (D) was determined to be 2.892 for deformable Hunan clay (Figure 5). While by fitting equation (6) to the experimental SWCC at a reference state ($e_0 = 1.12$), the corresponding air-entry value ψ_{a0} can be determined to be 1.81 (Figure 6). According to equation (6), the volumetric water content is a constant (θ_s) when the range of matric suction is $\psi < \psi_a$ (it can be represented as AB in Figure 6).

On the basis of the fractal dimension and air-entry value at a reference state, the air-entry values of Hunan clay at deformed state were determined using Equation (12), as shown in Table 2. It can be seen that the predicted air-entry values are close to the experimental results at a deformed state.

Based on the fractal dimension and the predicted air-entry values at a deformed state, the relative hydraulic conductivity of Hunan clay at a deformed state can be calculated by using equation (9). In Figure 7, the predicted values are in good agreement with the measured values, which verifies the accuracy of the proposed method.

3. Conclusions

A fractal prediction method was presented to determine the relative hydraulic conductivity under deformation condition in this study. The method was only necessary to obtain the fractal dimension and the air-entry value at a reference state by the SWCC test. The relative hydraulic conductivity at a deformed state was predicted combined with the air-entry value and fractal form of the hydraulic conductivity model. Compared with the tedious calculation work (i.e., integral and sectional calculation) in the existing procedure, the proposed method requires less work to determine the relative hydraulic conductivity under deformation condition. In order to demonstrate the accuracy of the proposed method, the instantaneous profile method of deformable Hunan clay was carried out to obtain the experimental data of the relative hydraulic conductivity with different initial void ratios. By comparing the measured values with the predicted values, the accuracy of the proposed method was validated.

Data Availability

The SWCC and hydraulic conductivity data of Hunan clay used to support the findings of this study are included within the article.

Conflicts of Interest

The authors declare no conflict of interest.

Authors' Contributions

G.T., H.X., and X.Z. conceived and performed the experiments and wrote the manuscript. J.C., Q.C., and Y.C. performed the data analysis and revised the manuscript.

Acknowledgments

The research was funded by the National Key R&D Program of China (No. 2016YFC0502208), National Natural Science Foundation of China (No. 41722403), Outstanding Young and Middle-Aged Scientific and Technological Innovation Team Project of Hubei Provincial Department of Education (T201605), and Research Project of Hubei Provincial Department of Education (No. D20161405), and they are gratefully acknowledged.

References

[1] J. H. Dane and G. C. Topp, *Methods of Soil Analysis: Part 4 Physical Methods*, Soil Science Society of America, 2002.

[2] A. Klute, "Laboratory measurement of hydraulic conductivity of unsaturated soils," in *Methods of Soil Analysis, Monograph 9, Part 1*, pp. 253–261, American Society of Agronomy, 1965.

[3] P. A. Londra, "Simultaneous determination of water retention curve and unsaturated hydraulic conductivity of substrates using a steady-state laboratory method," *HortScience*, vol. 45, no. 7, pp. 1106–1112, 2010.

[4] C. Gallage, J. Kodikara, and T. Uchimura, "Laboratory measurement of hydraulic conductivity functions of two unsaturated sandy soils during drying and wetting processes," *Soils and Foundations*, vol. 53, no. 3, pp. 417–430, 2013.

[5] S. J. Richards and L. V. Weeks, "Capillary conductivity values from moisture yield and tension measurements on soil columns," *Soil Science Society of America Journal*, vol. 17, no. 3, pp. 206–209, 1953.

[6] H. Krisdani, H. Rahardjo, and E.-C. Leong, "Use of instantaneous profile and statistical methods to determine permeability functions of unsaturated soils," *Canadian Geotechnical Journal*, vol. 46, no. 7, pp. 869–874, 2009.

[7] A. K. Leung, J. L. Coo, C. W. W. Ng, and R. Chen, "New transient method for determining soil hydraulic conductivity function," *Canadian Geotechnical Journal*, vol. 53, no. 8, pp. 1332–1345, 2016.

[8] J. Cai, E. Perfect, C.-L. Cheng, and X. Hu, "Generalized modeling of spontaneous imbibition based on Hagen–Poiseuille flow in tortuous capillaries with variably shaped apertures," *Langmuir*, vol. 30, no. 18, pp. 5142–5151, 2014.

[9] Y. Mualem, "Hydraulic conductivity of unsaturated porous media: generalized macroscopic approach," *Water Resources Research*, vol. 14, no. 2, pp. 325–334, 1978.

[10] E. C. Leong and H. Rahardjo, "Permeability functions for unsaturated soils," *Journal of Geotechnical and Geoenvironmental Engineering*, vol. 123, no. 12, pp. 1118–1126, 1997.

[11] Y. Mualem and A. Klute, *Hydraulic Conductivity of Unsaturated Soils: Prediction and Formulas*, American Society of Agronomy, 1986.

[12] S. F. Averjanov, "About permeability of subsurface soils in case of incomplete saturation," *Engineering Collection*, vol. 7, pp. 19–21, 1950.

[13] W. R. Gardner, "Some steady-state solutions of the unsaturated moisture flow equation with application to evaporation from a water table," *Soil Science*, vol. 85, no. 4, pp. 228–232, 1958.

[14] R. H. Brooks and A. T. Corey, "Hydraulic properties of porous media," *Hydrology*, vol. 3, no. 1, pp. 352–366, 1964.

[15] J. M. Davidson, L. R. Stone, D. R. Nielsen, and M. E. Larue, "Field measurement and use of soil-water properties," *Water Resources Research*, vol. 5, no. 6, pp. 1312–1321, 1969.

[16] J. D. Campbell, *Pore pressures and volume changes in unsaturated soils, [Ph.D. thesis]*, University Illinois Urbana Champaign, 1973.

[17] D. G. Fredlund, A. Xing, and S. Huang, "Predicting the permeability function for unsaturated soils using the soil-water characteristic curve," *Canadian Geotechnical Journal*, vol. 31, no. 4, pp. 533–546, 1994.

[18] S. S. Agus, E. C. Leong, and T. Schanz, "Assessment of statistical models for indirect determination of permeability functions from soil–water characteristic curves," *Géotechnique*, vol. 53, no. 2, pp. 279–282, 2003.

[19] E. C. Childs and N. Collis-George, "The permeability of porous materials," *Proceedings of the Royal Society A*, vol. 201, no. 1066, pp. 392–405, 1950.

[20] N. Collis-George, "Calculation of the permeability of porous media from their moisture characteristics," *Transactions, American Geophysical Union*, vol. 34, no. 4, pp. 589–593, 1953.

[21] N. T. Burdine, "Relative permeability calculations from pore size distribution data," *Journal of Petroleum Technology*, vol. 5, no. 3, pp. 71–78, 1953.

[22] Y. Mualem, "A new model for predicting the hydraulic conductivity of unsaturated porous media," *Water Resources Research*, vol. 12, no. 3, pp. 513–522, 1976.

[23] M. T. van Genuchten, "A closed-form equation for predicting the hydraulic conductivity of unsaturated soils," *Soil Science Society of America Journal*, vol. 44, no. 5, pp. 892–898, 1980.

[24] R. J. Kunze, G. Uehara, and K. Graham, "Factors important in the calculation of hydraulic conductivity," *Soil Science Society of America Journal*, vol. 32, no. 6, pp. 760–765, 1968.

[25] S. Oh, Y. Kim, and J.-W. Kim, "A modified van Genuchten-Mualem model of hydraulic conductivity in Korean residual soils," *Water*, vol. 7, no. 10, pp. 5487–5502, 2015.

[26] V. V. Terleev, W. Mirschel, V. L. Badenko, and I. Y. Guseva, "An improved Mualem–Van Genuchten method and its verification using data on Beit Netofa clay," *Eurasian Soil Science*, vol. 50, no. 4, pp. 445–455, 2017.

[27] B. B. Mandelbrot and J. A. Wheeler, "The fractal geometry of nature," *American Journal of Physics*, vol. 51, no. 3, pp. 286-287, 1983.

[28] J. Cai, X. Hu, B. Xiao, Y. Zhou, and W. Wei, "Recent developments on fractal-based approaches to nanofluids and nanoparticle aggregation," *International Journal of Heat and Mass Transfer*, vol. 105, pp. 623–637, 2017.

[29] J. Cai, L. Zhang, Y. Ju, G. Pia, and Z. Zhang, "An introduction to fractal-based approaches in unconventional reservoirs—part I," *Fractals*, vol. 26, no. 2, article 1802001, 2018.

[30] Y. Xu, "Shear strength of granular materials based on fractal fragmentation of particles," *Powder Technology*, vol. 333, pp. 1–8, 2018.

[31] E. Perfect, M. Díaz-Zorita, and J. H. Grove, "A prefractal model for predicting soil fragment mass-size distributions," *Soil and Tillage Research*, vol. 64, no. 1-2, pp. 79–90, 2002.

[32] L. Zhang, X. Zhang, H. Chai, Y. Li, and Y. Zhou, "Pore structure characterization for a continental lacustrine shale parasequence based on fractal theory," *Fractals*, vol. 27, no. 1, article 1940006, 2019.

[33] Y. Xu and Y. Wang, "Size effect on specific energy distribution in particle comminution," *Fractals*, vol. 25, no. 2, article 1750016, 2017.

[34] S. W. Tyler and S. W. Wheatcraft, "Fractal processes in soil water retention," *Water Resources Research*, vol. 26, no. 5, pp. 1047–1054, 1990.

[35] P. Xu, H. Liu, A. P. Sasmito, S. Qiu, and C. Li, "Effective permeability of fractured porous media with fractal dual-porosity model," *Fractals*, vol. 25, no. 4, article 1740014, 2017.

[36] A. Cihan, J. S. Tyner, and E. Perfect, "Predicting relative permeability from water retention: a direct approach based on fractal geometry," *Water Resources Research*, vol. 45, no. 4, 2009.

[37] Y. F. Xu and D.'. A. Sun, "A fractal model for soil pores and its application to determination of water permeability," *Physica A: Statistical Mechanics and its Applications*, vol. 316, no. 1-4, pp. 56–64, 2002.

[38] Y. Xu, "Calculation of unsaturated hydraulic conductivity using a fractal model for the pore-size distribution," *Computers and Geotechnics*, vol. 31, no. 7, pp. 549–557, 2004.

[39] D. S. Sun, P. Liu, X. H. Xia, and J. H. Wang, "Permeability coefficient of unsaturated soils," *Journal of Hydraulic Engineering*, vol. 35, no. 3, pp. 71–75, 2004.

[40] B. Ghanbarian-Alavijeh and A. G. Hunt, "Unsaturated hydraulic conductivity in porous media: percolation theory," *Geoderma*, vol. 187-188, pp. 77–84, 2012.

[41] A. G. Hunt, B. Ghanbarian, and K. C. Saville, "Unsaturated hydraulic conductivity modeling for porous media with two fractal regimes," *Geoderma*, vol. 207-208, pp. 268–278, 2013.

[42] S. D. Bartolo, C. Fallico, G. Severino, and M. Veltri, "Two fractal regimes of the soil hydraulic properties," *Applied Mathematics*, vol. 5, no. 12, pp. 1773–1779, 2014.

[43] M. A. Alfaro Soto, H. K. Chang, and M. T. van Genuchten, "Fractal-based models for the unsaturated soil hydraulic functions," *Geoderma*, vol. 306, pp. 144–151, 2017.

[44] A. Lloret and E. E. Alonso, "Consolidation of unsaturated soils including swelling and collapse behaviour," *Géotechnique*, vol. 30, no. 4, pp. 449–477, 1980.

[45] S. Huang, S. L. Barbour, and D. G. Fredlund, "Development and verification of a coefficient of permeability function for a deformable unsaturated soil," *Canadian Geotechnical Journal*, vol. 35, no. 3, pp. 411–425, 1998.

[46] S. Huang, D. G. Fredlund, and S. L. Barbour, "Measurement of the coefficient of permeability for a deformable unsaturated soil using a triaxial permeameter," *Canadian Geotechnical Journal*, vol. 35, no. 3, pp. 426–432, 1998.

[47] T. H. Wang, J. Lu, and J. F. Zhang, "Experimental study on permeability coefficient of artificially compacted unsaturated loess considering influence of density," *Chinese Journal of Rock Mechanics and Engineering*, vol. 25, no. 11, pp. 2364–2368, 2006.

[48] S. Assouline, "Modeling the relationship between soil bulk density and the hydraulic conductivity function," *Vadose Zone Journal*, vol. 5, no. 2, pp. 697–705, 2006.

[49] R. Hu, Y.-F. Chen, H.-H. Liu, and C.-B. Zhou, "A water retention curve and unsaturated hydraulic conductivity model for deformable soils: consideration of the change in pore-size distribution," *Géotechnique*, vol. 63, no. 16, pp. 1389–1405, 2013.

[50] G. Cai, A. Zhou, and D. Sheng, "Permeability function for unsaturated soils with different initial densities," *Canadian Geotechnical Journal*, vol. 51, no. 12, pp. 1456–1467, 2014.

[51] A. Zhou, Y. Fan, W.-C. Cheng, and J. Zhang, "A fractal model to interpret porosity-dependent hydraulic properties for unsaturated soils," *Advances in Civil Engineering*, vol. 2019, Article ID 3965803, 13 pages, 2019.

[52] G. L. Tao and L. W. Kong, "A model for determining the permeability coefficient of saturated and unsaturated soils based on micro pore channel and its application," *Journal of Hydraulic Engineering*, vol. 48, no. 6, pp. 702–709, 2017.

[53] G. Tao, Y. Chen, L. Kong, H. Xiao, Q. Chen, and Y. Xia, "A simple fractal-based model for soil-water characteristic curves incorporating effects of initial void ratios," *Energies*, vol. 11, no. 6, p. 1419, 2018.

[54] G. L. Tao, X. K. Wu, H. L. Xiao, Q. Chen, and J. Cai, "A unified fractal model for permeability coefficient of unsaturated soil," *Fractals*, vol. 27, no. 1, article 1940012, 2019.

[55] G. L. Tao, L. W. Kong, H. L. Xiao, Q. Ma, and Z. Z. Zhu, "Fractal characteristics and fitting analysis of soil-water characteristic curves," *Rock & Soil Mechanics*, vol. 35, no. 9, pp. 2443–2447, 2014.

[56] H. Wang, T. L. Li, and Y. K. Fu, "Determining permeability function of unsaturated loess by using instantaneous profile method," *Journal of Hydraulic Engineering*, vol. 45, no. 8, pp. 997–1003, 2014.

Hindawi
Geofluids
Volume 2019, Article ID 3161852, 12 pages
https://doi.org/10.1155/2019/3161852

Research Article

Study of the Fracture Law of Overlying Strata under Water Based on the Flow-Stress-Damage Model

Zhijie Wen,[1,2] Suolin Jing,[1] Yujing Jiang,[1] Lei Tian,[1] Jinhao Wen,[3] Zhiguo Cao,[2] Shaoshuai Shi,[4] and Yujun Zuo[5]

[1]*State Key Laboratory of Mining Disaster Prevention and Control Co-Founded by Shandong Province and Ministry of Science and Technology, Shandong University of Science and Technology, Qingdao 266590, China*
[2]*State Key Laboratory of Water Resource Protection and Utilization in Coal Mining, Beijing 100011, China*
[3]*School of Mechanics and Civil Engineering, China University of Mining and Technology (Beijing), Beijing 100083, China*
[4]*Geotechnical and Structural Engineering Research Center of Shandong University, Jinan 250061, China*
[5]*Mining College, Guizhou University, Guiyang 550003, China*

Correspondence should be addressed to Lei Tian; sunwuxiantianlei@163.com and Jinhao Wen; wenjh0532@163.com

Received 27 October 2018; Revised 11 January 2019; Accepted 4 February 2019; Published 2 May 2019

Guest Editor: Bisheng Wu

To accurately detect the development height of the water flowing fractured zone (WFFZ) in the overlying strata of the working face after mining under water and to ensure the safety and reliability of coal mining, the coal seam located under Weishanhu Lake in the Jisan coal mine was used as the experimental system. A similar laboratory simulation and water injection-based fracturing test system were used with the working face before and after mining activity to calculate, quantitatively detect, and qualitatively analyze the development height of the WFFZ in the overlying strata. Meanwhile, a flow-stress-damage model and its criterion of fracture expansion were established based on the Mohr-Coulomb criterion, and the FLAC 3D software was used to simulate the deformation and failure of the overlying strata and the evolution of WFFZ during the mining process. The results showed that the height ranges of the WFFZ beneath Weishanhu Lake of the Jisan coal mine as established by the above three methods are 30-45 m, 30-48 m, and 30-50 m. In the process of mining, the caving zone and fractured zone are, respectively, subjected to tensile failure and shear failure. The development height of the water flowing through the fractured zone in the overlying strata is basically consistent with the range of the "breaking arch." The flow-stress-damage model and its criterion of fracture expansion can be applied to the fracture law of overlying strata under water under similar geological conditions.

1. Introduction

China's coal resources are widely distributed and are rather common under buildings, railways, and water bodies. The mining of coal resources under water is particularly seriously threatened by the overlying aquifer; as such, the mining of coal under water has become a focus of research. The primary hazard is mainly caused by the movement and failure of overlying strata and the development of water flowing fractured zone (WFFZ) during the mining process. The continuous development of the WFFZ will cause it to be linked to the main aquifer, and even the surface water system, of the mining area. Because of this, the surface, underground water system near the mining area, and the surface ecological environment will change. The key to achieving safe, green, and efficient production of coal resources under water is to ensure that the WFFZ is not affected by the main aquifer [1]. Therefore, it is of great practical significance to carefully study the development process of the WFFZ and the movement of overlying strata while mining under water.

Both domestic and international scholars have studied the damage of overlying strata and the accuracy of improving predictions of the height of the WFFZ from different perspectives. These studies have provided technical support for safe mining under water. The height and evolution of the WFFZ are often studied using empirical formulas, physical experiments, numerical simulations, and field tests. The hydraulic fracturing process involves the coupling of fluid

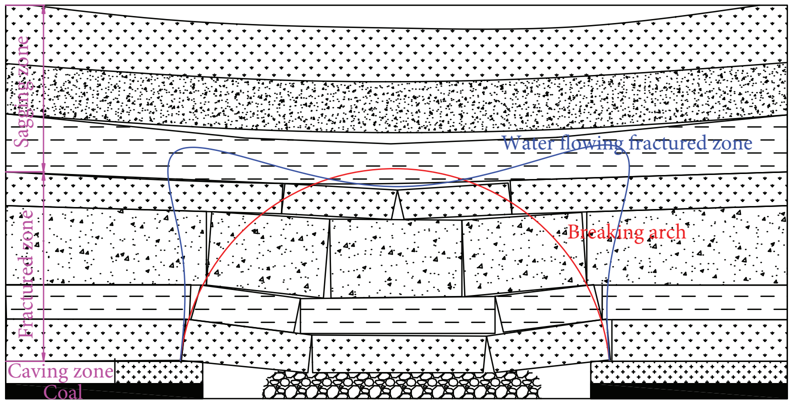

Figure 1: Mechanical structure model of the breaking arch in the stope.

movement, rock deformation, and fracture propagation. Fractures may form whenever stress in any part of the material exceeds its strength, which could be either shear stress, normal stress, or a combination of both [2]. The deformation of flexible strata during complete failure is not brittle; rather, brittle failures occur only as mining is in progress [3]. The mining-induced fracture zone provides pressure-relief passageways for gas that flows from coal seams and the surrounding coal/rock strata as well as spaces for gas storage [4, 5]. The mining-induced fracture zone, together with the caving zone, is defined as the WFFZ. Bai et al. [6] acquired an empirical formula for the height of the WFFZ through field tests in multiple coal mines under the condition of a stable gob. Majdi et al. [7] presented five new simple, yet conclusive, mathematical approaches to estimate the height of the distressed zone. Liu et al. [8] used on-site measurements, mechanical theory calculations, and numerical simulations to analyze the regularity of the height of the WFFZ. As the face continuously advances, the overlying strata collapse, and destruction and dissociation occur on the weak side [9]. Zhang et al. [10] analyzed the regularity of the development of the WFFZ under the influence of different factors in the process of block mining and established a height prediction model of the WFFZ for block mining. Other scholars have calculated the height of the WFFZ in the mining process according to the prediction formula presented in the Regulations of Mine Hydrogeology issued by the Ministry of Coal Industry. The above research has provided a foundation for coal mining under rivers and lakes. However, mining-induced fracturing and the deformation of overlying strata require further exploration from the perspective of mining under surface water and aquifers.

Based on the mining that occurs under Weishanhu Lake in the Jisan coal mine, as well as on the theoretical analysis of mining-induced fractures, deformation laws, and structural mechanics models of overlying strata, this paper provides a simulation-based analysis of the development height of the WFFZ on a working face before and after mining occurs. The established fracture expansion criterion based on the Mohr-Coulomb criterion is imbedded in the FLAC 3D software to simulate and analyze mining-induced fracturing and deformation laws of overlying strata and the regularity of the development of the WFFZ and to verify the engineering according to field-measured data in the mining process.

2. The Breaking Arch Model and Fracture Expansion Criterion

2.1. Mechanical Structure Model of the Breaking Arch. A stope mechanical structure model is established [11–13] as shown in Figure 1.

According to an existing theory, the overlying strata can be divided into three zones in the vertical direction: the caving, the fractured, and the sagging [14]. The breaking arch consists of the caving zone and the fractured zone, and the height of the WFFZ is basically consistent with the range of the breaking arch.

(1) *The Caving Zone*. The caving and final arrangement of blocks in the stope after breaking are irregular. The bulking coefficient is relatively high, generally up to 1.3-1.5. However, after they are recompacted by overlying strata, the bulking coefficient can reach approximately 1.03. This zone is directly above the roof of the mining area, and in many cases, it is caused by immediate roof caving.

(2) *The Fractured Zone*. After the strata are fractured, the area where rock blocks remain arranged in an orderly manner is called the fractured zone, which is located above the caving zone. Since the rock blocks are arranged in an orderly fashion, the bulking coefficient is relatively low.

(3) *The Sagging Zone*. All strata from the top of the fractured zone to the surface are called the sagging zone. The notable characteristic of stratal movement in this zone is that the movement is continuous; it is also integral that the movement of strata from the top of the fractured zone to the surface is stratified and integral. In the vertical section, subsidence values of all upper and lower parts are quite low. If there is a thick and hard key layer, a separation area may emerge in the sagging zone.

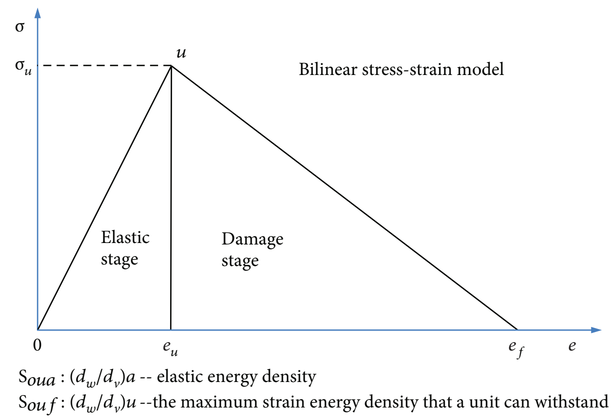

Figure 2: Bilinear stress-strain curve.

The WFFZ is distributed in the shape of a "saddle" [15], including the caving zone and the fractured zone. If the overlying aquifer is located within the WFFZ, it will cause the fracture water to flow from the fractured strata into the gob and working face.

2.2. Fracture Expansion Criterion. Due to the interaction of seepage pressure and coal seam mining under water, the strata will fracture and form a fracture zone that utilizes existing holes in the strata, which causes the strata to shear and slide along the fracture zone, and eventually causes the destruction of the entire structure.

2.2.1. The Range of the Fractured Zone Generated during Mining. The working face mining process is divided into two stages, including (1) the stage of incomplete mining, during which the mining distance of the working face is less than the width of the working face, and (2) the full mining stage, during which the mining distance of the working face is greater than the width of the working face.

The fracture height of the overlying strata in the stope is determined by the width of the working face. When this is fixed, the maximum height of the WFFZ of the overlying strata is definite. When the mining distance of the working face does not reach the width of the working face, the development height of the overlying strata space structure is related to the length of the working face; overall, the height of the overlying strata space structure in the stope develops linearly as the work face is mined. When the mining distance of the working face reaches the width of the working face, the development height of the overlying strata space structure is approximately one-half of the width of the working face [16].

2.2.2. Fracture Expansion Criterion. As a natural material, pores and cracks exist in rock masses and have significant influence on the mechanical properties of the host rock mass. When the rock mass is subjected to external forces, it often breaks down in such defective areas first, followed by instability and failure of the entire rock mass [17]. Fracturing can be classified as three basic types based on how the fractures form under external forces: opening mode (Type I), sliding mode (Type II), and tearing mode (Type III). The splitting that is caused by water pressure is different from other mechanical splitting because any newly generated fracture will be immediately filled with water and that water pressure is applied to the fracture surface. Fractures formed under tension are Type I fractures. According to the Griffith theory [18, 19], the appearance of a fracture will produce a new surface for the solid material, which has the same surface energy as the surface of the liquid, and a part of the energy (U) released by the system will be converted to surface energy. Assume that the surface energy on the surface of the material is γ, namely, surface tension, and the maximum length of the rock is 2α; then, the surface energy is $S = 4\alpha\gamma$. When the fracture is in an equilibrium state $((d/d\alpha)(W - U) = \gamma)$, the left side of the formula is the force that drives fracture expansion, while the right side of the formula is the force with which the material hinders fracture expansion. Griffith believes that if the applied stress exceeds the critical stress value or the input energy exceeds the critical energy, the material will fracture. If the fluid in the fracture is continuously supplemented through permeation, the fracture pressure is maintained so that the external input energy continues to be greater than the critical energy; thus, part of the fracture will continue to expand.

2.2.3. Numerical Simulation Method for Fracture Expansion. From the perspective of energy, the fracturing of rock material mainly occurs when the input energy exceeds the maximum value of the material itself; thus, the material will begin to break down; the more energy the material bears, the higher the degree of damage. In the initial fracture, since the crack tip is not very sharp and the degree of energy accumulation is low, the cracking is slow; however, the crack tip becomes very sharp after cracking, and a large amount of energy will accumulate at the crack tip, resulting in fracturing of the rock. Wang et al. [20] presented the acoustic emission hits can be used to analyze the damage in rock material, but the number of acoustic emission hits cannot be used alone to determine the degree of rock damage directly. Therefore, it is an appropriate method to judge the degree of cracking from the perspective of energy.

As the rock is damaged, the microstructure changes, the material strength and the elastic modulus decrease, and the permeability becomes higher. The damage variable D is defined to estimate the degree of damage. According to the ratio of dissipated energy to the maximum strain energy of rock, the degree of damage to the rock is estimated. The strain energy of the rock is as follows:

$$\frac{dW}{dV} = \int_0^{\varepsilon_{ij}} \sigma_{ij} d\varepsilon_{ij}. \tag{1}$$

For the convenience of simple calculations, we believe that the stress-strain curve for the rock can be simplified into a bilinear stress-strain model that consists of two straight lines (Figure 2). The area surrounded by the stress-strain curve is the energy that the unit body bears. The input energy for the element is partly used to increase the elastic energy of the material and is also partly consumed by other kinds of energy, such as sound waves and crack propagation. Theoretically, this is called the dissipated strain energy density of the element, which is shown as follows:

$$\left(\frac{dw}{dv}\right)_d = \left(\frac{dw}{dv}\right) - \frac{1}{2E_0^*}\left(\sigma_1^2 + \sigma_2^2 + \sigma_3^2 - 2v\left(\sigma_1\sigma_2 + \sigma_2\sigma_3 + \sigma_3\sigma_1\right)\right), \tag{2}$$

where E_0^* is Young's modulus after reduction, which is related to the stress path. When the energy of the element is greater than the critical energy, cracks appear, which are generally oriented perpendicular to σ_3 or the maximum tensile stress.

Based on the built-in Fish function of FLAC 3D, the damage model is built with the energy defined as the determining criterion of fracturing. The simulation progress is shown in Figure 3. At the initial stage, the strain energy density of the element is set to 0 (that is, z_extral = 0), and the strain energy density of the element calculation step I is as follows:

$$\begin{aligned}\left(\frac{\mathrm{d}W}{dV}\right)_i = \left(\frac{\mathrm{d}W}{dV}\right)_{(i-1)} &+ \frac{1}{2}\left(\sigma_x^i + \sigma_x^{i-1}\right)\left(\varepsilon_x^i - \varepsilon_x^{i-1}\right) \\ &+ \frac{1}{2}\left(\sigma_y^i + \sigma_y^{i-1}\right)\left(\varepsilon_y^i - \varepsilon_y^{i-1}\right) \\ &+ \frac{1}{2}\left(\sigma_z^i + \sigma_z^{i-1}\right)\left(\varepsilon_z^i - \varepsilon_z^{i-1}\right) \\ &+ \frac{1}{2}\left(\sigma_{xy}^i + \sigma_{xy}^{i-1}\right)\left(\varepsilon_{xy}^i - \varepsilon_{xy}^{i-1}\right) \\ &+ \frac{1}{2}\left(\sigma_{yz}^i + \sigma_{yz}^{i-1}\right)\left(\varepsilon_{yz}^i - \varepsilon_{yz}^{i-1}\right) \\ &+ \frac{1}{2}\left(\sigma_{yz}^i + \sigma_{yz}^{i-1}\right)\left(\varepsilon_{yz}^i - \varepsilon_{yz}^{i-1}\right).\end{aligned} \tag{3}$$

The strain energy accumulation of the element during the simulation process is recorded. σ_x^i, σ_y^i, σ_z^i, σ_{xy}^i, σ_{yz}^i, and σ_{xz}^i are the element stresses in step I; σ_x^{i-1}, σ_y^{i-1}, σ_z^{i-1}, σ_{xy}^{i-1}, σ_{yz}^{i-1}, and σ_{xz}^{i-1} are the element stresses prior to step I. Stress-strain is indicated in the same way.

If the element energy meets $(dW/dV) \le S_{oua}$, the element will not be damaged.

If the element energy meets $S_{oua} < (dW/dV) < S_{ouf}$, the damage variable D will be defined as the ratio of (dW/dV) to S_{ouf}.

If $S_{ouf} < (dW/dV)$, the element is considered to be completely damaged, and the bearing capacity is lost. To ensure that the element does not produce singular points, the element is given a residual volume modulus E_C^* and a larger permeability η^*.

It is necessary to note that the loss of the bearing capacity of the element does not indicate the host rock sample is destroyed. Under three-directional pressure, the cohesion of the material is lost, but overall damage will not occur; the rock will be destroyed only when the confining pressure is withdrawn. Therefore, it is practical and appropriate to give the damage element a smaller volume variable and higher permeability.

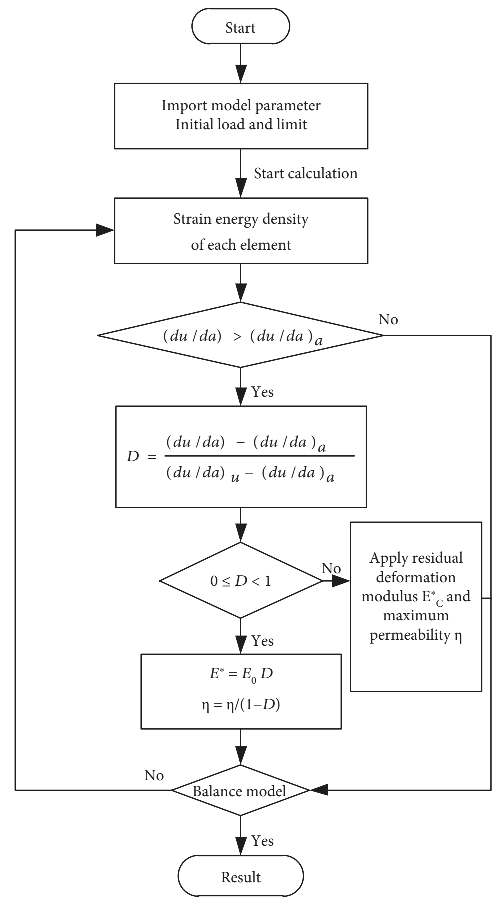

Figure 3: Flow chart of numerical simulation.

Therefore, the FLAC 3D rock mass energy-determining criterion can be used to comprehensively estimate the rock mass damage caused by mining-induced stress and fracture water pressure. Meanwhile, the development of the WFFZ can be simulated well.

3. Methods and Results

3.1. Numerical Simulation of the Development Regularity of the WFFZ

3.1.1. Model Configuration. Based on the 183upper04 working face that is located under Weishanhu Lake of the Jisan coal mine, the FLAC 3D simulation software was used to build a numerical model to study the movement of overlying strata and the development of the WFFZ during mining. According to the test results of rock samples, the strata overlying the coal seam are mainly sandstone, with fine-grained sandstone and medium-grained sandstone in the upper part and thick siltstone and mudstone in the lower part, where fractures are well-developed. Table 1 lists the main lithologies of the 183upper04 working face. The fracture parameters are obtained according to the properties of the rock materials [21].

The length, width, and height of the design model were 800 m, 400 m, and 200 m, respectively, as shown in Figure 4. The boundary conditions of the model mechanics

Table 1: Mechanical parameters of the main strata.

Lithology	Bulk modulus (GPa)	Shear modulus (GPa)	Cohesion (MPa)	Tensile strength (MPa)	Friction (°)
Mudstone	0.6	0.32	0.5	0.6	28
Fine sandstone	1.63	1.2	2.5	1.1	32
Medium sandstone	1.6	1.14	2.2	1.0	31
Siltstone	1.87	1.12	2.0	1.0	30
Coal	0.8	0.14	0.3	0.5	26

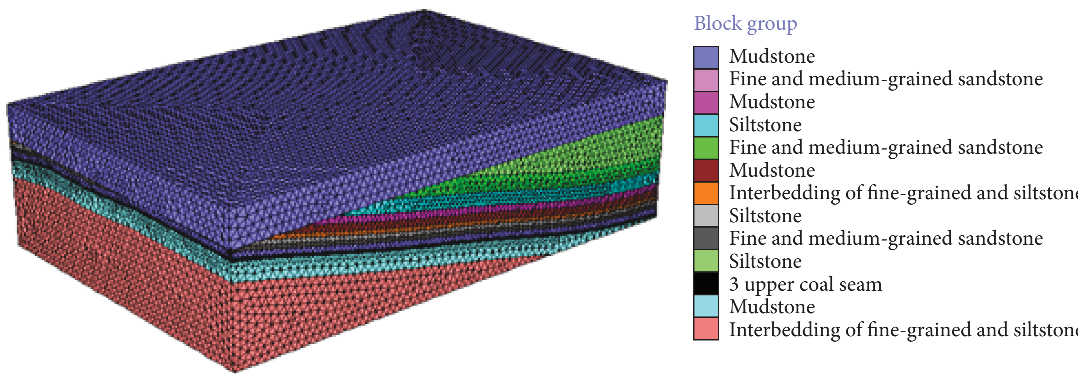

Figure 4: Numerical simulation model.

were as follows: the top boundary of the model was a free boundary; the bottom, front, back, left, and right boundaries of the model were set as stress boundaries.

In the FLAC 3D model, the S-B method was applied to initialize the ground stress by applying the stress boundary; the equivalent load, namely, the gravity stress, was applied at the top of the model. The load σ_z is obtained by the following formula:

$$\sigma_z = \gamma H, \tag{4}$$

where γ indicates the unit weight of overlying strata and H indicates the depth from the top boundary of the model to the surface. The lateral stress generated by gravity stress in the horizontal direction is determined by the following formula:

$$\sigma_x = \sigma_y = \lambda \sigma_z, \tag{5}$$

where λ is the side pressure coefficient, determined by the formula $\lambda = (\mu/(1-\mu))$, where μ is Poisson's ratio.

After modeling, the deformation and failure conditions of overlying strata were simulated, and the height and shape of the caving zone and WFFZ during mining were analyzed. During the simulation, the mining height is 3 m, and the open-off cuts are made from elevations of -715 m, -710 m, and -705 m, with each step of the excavation being 50 m. Then, the development of the WFFZ was analyzed.

3.1.2. Analysis of Simulation Results

(1) The Distribution of the Failure Field at Different Mining Distances. By analyzing the failure field, the distribution of failure areas in overlying strata after mining can be directly observed. Based on Figure 5, which shows the simulation results of the distribution of the plastic zone at different mining distances of the working face, when the mining of the working face reaches 50 m, the plastic zone is concentrated directly above the upper gob, which gradually decreases and mainly belongs to shear failure. The siltstone strata below are dominated by tensile failure. As the mining of the working face reaches 100 m and the gob area increases, the coal seam roof falls and sinks further. Tensile failure occurs mainly in the immediate roof above the gob, and tensile shear failure above the coal pillar indicates that the collapse of the immediate roof occurs directly from this area. Tensile shear failure occurs in the main roof stratum above the immediate roof, and shear failure becomes more obvious upward. The range of the plastic zone increases in the horizontal and vertical directions as the working face is mined further. Finally, the heights of the caving zone and fracture zone are approximately 15 m and 50 m, respectively, which develops into the mudstone with 8.5 m height. As the mining of the working face reaches 150 m or more, the development height of the caving zone and the WFFZ basically remains stable. In summary, the distribution of the plastic zone above the gob and above the coal wall in the front and back of the gob basically corresponds to the development height of the caving zone and the WFFZ. When open-off cuts are made from elevations of -715 m, -710 m, and -705 m, there is little change in geological conditions, and the regularity of the WFFZ is similar.

(2) Distribution of the Failure Field in Different Mining Upper Limits. For open-off cuts made at different elevations, the simulation results of the distribution of the plastic zone in

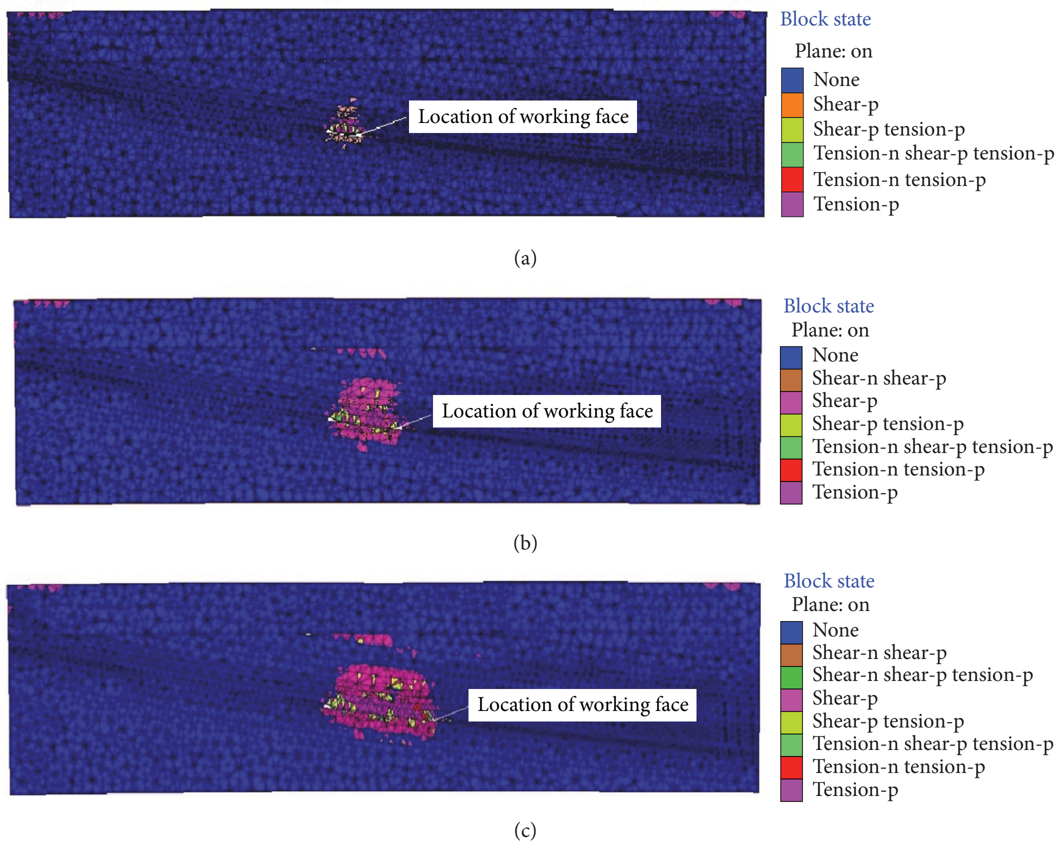

FIGURE 5: Distribution of plastic deformation of the overlying strata at different mining distances: (a) working face mined to 50 m, (b) working face mined to 100 m, and (c) working face mined to 150 m.

overlying strata after excavating 200 m are shown in Figure 6. From the simulation results of different mining upper limits, the displacement vector map and contour of displacement of each mining upper limit are similar in shape with consistent stratal movement. After mining, stress is concentrated at the edge of the gob and shear failure occurs in the rock mass above the coal pillar. According to the distribution of the maximum and minimum principal stresses, the coal seam roof area is a destressed zone, where stress is redistributed after the coal seam is mined. The rock mass is dominated by tensile failure. On the upper gob, tensile failure, tensile shear failure, and shear failure zones develop successively from the bottom to the top. As the mining area increases, the range of the maximum principal stress contour constantly expands, the shape and height constantly change, and the plastic failure zone of the strata continues to develop forward and upward, indicating that the caving zone and the WFFZ are increasing continuously.

Overall, if the mining height is 3 m, the height of the caving zone is approximately 15 m and the height of the WFFZ is approximately 50 m.

We investigate two other methods to calculate, quantitatively detect, and qualitatively analyze the development height of the WFFZ in overlying strata to verify the practicality of the numerical model.

3.2. Physical Experiment on the Development Regularity of the WFFZ

3.2.1. Similar Simulation Test Design. A similar simulation test model was built based on the 3upper coal seam in the Jisan coal mine. During the simulation, the movement, failure, and distribution of stress in the overlying strata were continuously monitored. The mechanical phenomena and rules in site mining were obtained by inversion. Eighty-meter boundaries were left on both sides of the 183upper04 working face at the tail entry and head entry. The physical similarity model is shown in Figure 7. The length, width, and height of the model were 1.8 m × 0.3 m × 0.8 m, the geometric similarity parameter of the model was $\alpha_1 = L_p/L_m = 200$, the unit weight similarity parameter was $\alpha_\gamma = \gamma_{pi}/\gamma_{mi} = 1$, the stress similarity parameter was $\alpha_\sigma = \alpha_1\alpha_\gamma = 200$, and the elastic modulus similarity parameter was $\alpha_E = \alpha_\sigma$. Table 2 lists the main model similar parameters.

3.2.2. Mining and Field Monitoring. The mining height in the model was 1.5 cm, equivalent to 3 m in an actual mining scenario. Forty centimeter-wide boundaries were left on the left and right sides of the model, equivalent to 80 m boundaries in an actual mining scenario. Mining was performed from left to right.

To monitor the settlement of overlying strata, the coordinate grid and the light lens displacement meter were

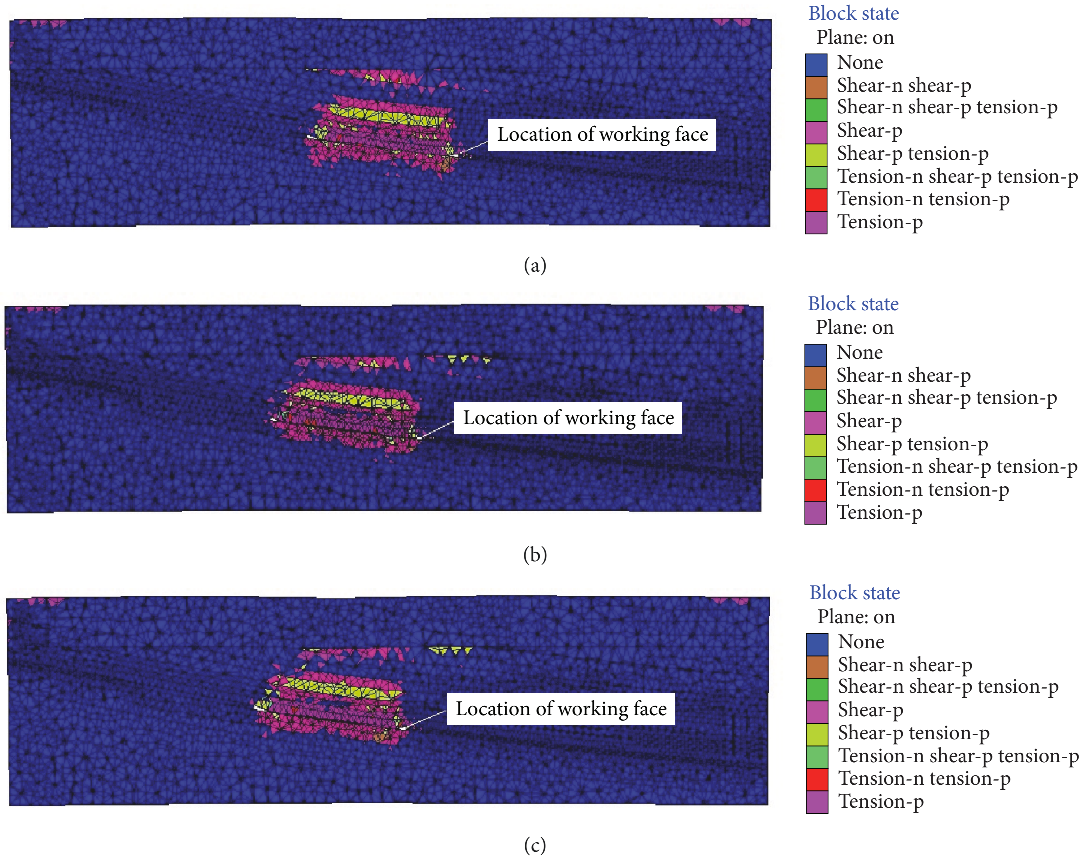

Figure 6: Distribution of plastic deformation in overlying strata at different mining upper limits: (a) mined upper limit of -715 m, (b) mined upper limit of -710 m, and (c) mined upper limit of -705 m.

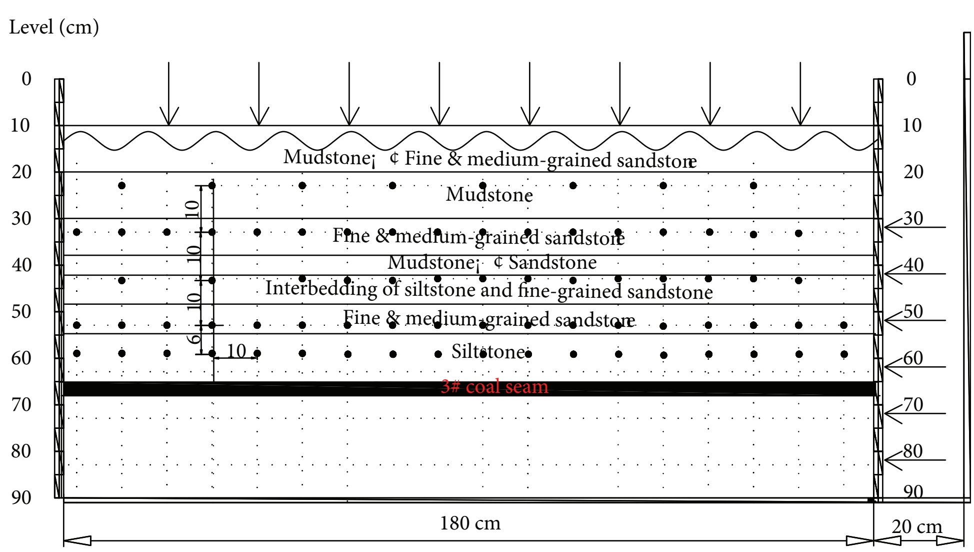

Figure 7: Similar material simulation model.

used for calibration, and the plane displacement monitoring grid was arranged on the front side of the model. The layout of monitoring spots is shown with red dots in Figure 7.

The mining process of the model was monitored, the movement of overlying strata during mining and the parameters in the failure state of the overlying strata were recorded, and the images were processed.

Table 2: Model parameters.

Index	Parameter
Geometric similarity parameter	200 : 1
Thickness of coal seam (m)	0.03
Time similarity parameter	$\sqrt{200}:1$
Unit weight similarity parameter	1 : 1
Stress similarity parameter	200 : 1
Elastic modulus similarity parameter	200 : 1

3.2.3. Experimental Results and Analysis. Excavation is begun from 40 cm on the left boundary in 5 cm increments, which is equivalent to actual excavation increments of 10 m. The height variation and location of the boundary of the WFFZ during the process of model mining are measured and recorded, and the relationship between the development height and the mining distance is also recorded. The physical model is shown in Figure 8.

Each time stratal movement is stabilized after mining, all points of displacement and failure on the model are observed and calculated comprehensively. The analysis of experimental results for the 183upper04 working face is shown in Figure 9.

During mining, the development height of the WFFZ increases with the mining distance, but when the mining distance exceeds a certain value, it no longer develops upward. Figure 10 shows the relationship between the failure height of the overlying strata and the mined distance of the working face.

When the mined distance of the working face is short, the overlying strata can maintain a state of stability without extensive rock collapse; the development height of the WFFZ also remains low, as shown in Figure 9(b). As mining progresses, the development heights of the caving zone and the WFFZ increase rapidly with the first weighing of the working face and the rapid collapse of overlying strata. Afterward, the development height of the caving zone gradually falls and stabilizes, with a maximum height reaching 12 m, as shown in Figure 9(c). As the mining distance increases, the development height of the WFFZ continues to increase steadily, and the fractures rapidly spread upward. When the working face is mined to 150 m, its maximum development height reaches 44.14 m, as shown in Figure 9(e). The ratio of the height of the fractured zone to the mining height is 14.71. Meanwhile, an obvious curved subsidence zone is formed above the WFFZ. Subsequently, with a further increase in the mining length, the development height of the WFFZ gradually decreases and stabilizes between 30 and 45 m.

From Figure 9(e), the development of the WFFZ is distributed in the shape of a "saddle," in which the shape is slightly higher on both sides and lower in the middle. The reduction area appears in the middle of the gob, which corresponds to the results of the theoretical study of the failure of overlying strata. The broken overlying strata in the gob are gradually compacted as the working face advances, the gob boundary is supported by the coal wall, and the degree of reconsolidation of the fractured and caved strata in the middle of the gob is greater than that of the gob boundary.

As Figure 10 shows, the caving zone and the WFFZ follow a pattern of increasing first and then decreasing and stabilizing as the distance of coal mining increases. The height of the caving zone of the model is stable at a range of 8-12 m, and the development height of the WFFZ is 44.14 m. Compared to the strike model, the tilt angle is the main cause of the higher height of the WFFZ.

3.3. Field Measurements of the WFFZ

3.3.1. Application of Water Injection Fracturing Test System. The "underground up-hole observation device" was arranged in a chamber in a certain position around the downhole mining face, and the upward-inclined drill holes were pitted from the chamber to the WFFZ in the strata overlying the gob of the working face. A double-sided water plugging device was used to observe the development height of the WFFZ in the overlying strata before and after mining and to analyze the deformation and failure of the overlying strata, ultimately providing scientific technical parameters for the safety mining under water [22].

The observation method used for borehole injection water leakage in the surface is a traditional and reliable method. However, when mining under large water bodies, the traditional method of observing the height of the WFFZ through ground drilling cannot be performed due to the presence of a water body. In this study, underground water leakage was measured by up-hole injection. That is, at the periphery of the working face, up-holes were drilled upward to the gob; leakage measuring by subsection, sealing, and water injection was performed in the drill holes to determine the height of the WFFZ according to seepage in the drill holes at each depth. According to the existing roadway layout, the height observation station was selected on the side of the stopping line of the working face. In the auxiliary haulage gate of the 183upper04 working face, appropriate observation profiles were selected to arrange premining observation holes and postmining observation holes. The observation results from premining observation hole 1 and postmining observation hole 2 are shown in Figures 11 and 12, respectively. The injection water leakage of observation hole 1 is generally between 0.2 and 0.5 L/min. The drilling is not affected by mining action, and the data mainly fluctuate because the overlying strata of the 3upper coal seam include interbedded siltstone, fine sandstone, medium sandstone, and mudstone, for which the fracture development and water conductivity of each stratum are different, leading to different injection water leakages in each stratum. The entire pore segment shows different injection water leakages, which indicates that the upper strata that were exposed by premining drilling are relatively intact and fractures are not developed. The injection water leakage in observation hole 2 is obviously higher than that in observation hole 1, which indicates that fractures are better developed within the drilling depth of 60 m. As the drilling depth increases, the injection water leakage in the pore segment slowly increases until it is approximately consistent with observation hole 1, indicating that

Figure 8: Simulation experiment model.

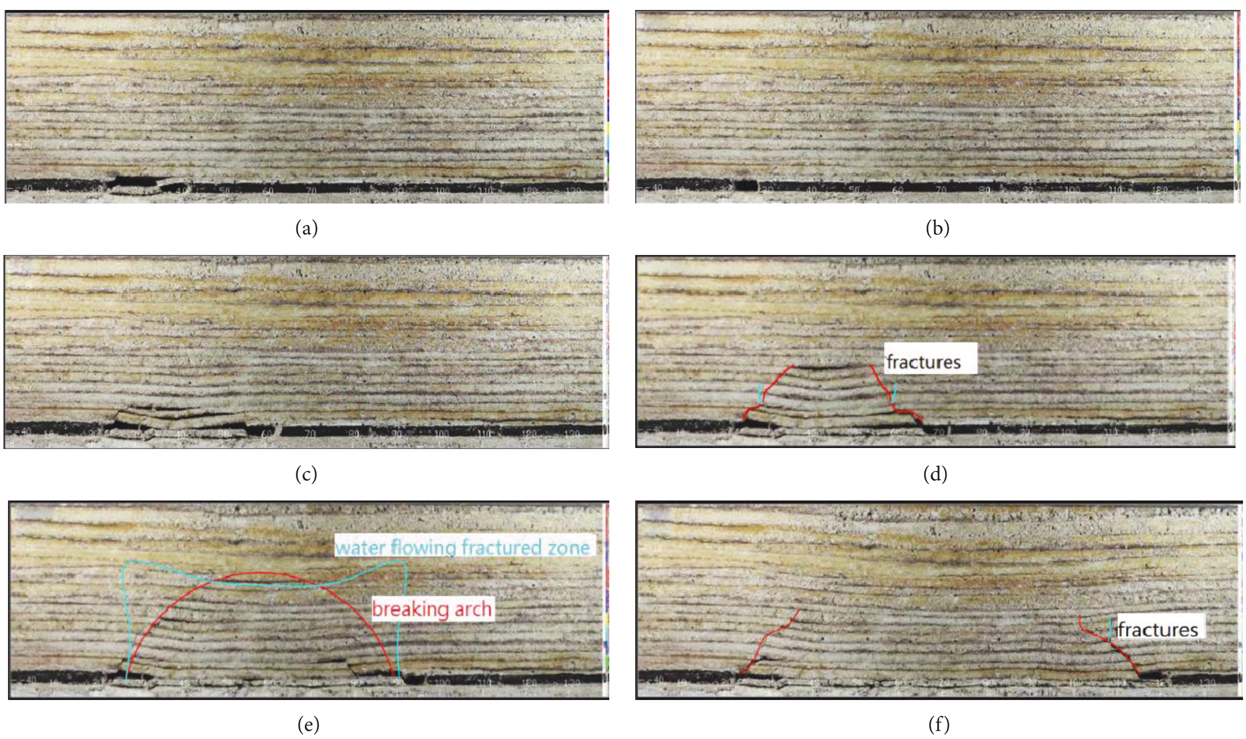

Figure 9: Failure and movement of overlying strata during mining: (a) open-off cut, (b) working face mined to 40 m, (c) working face mined to 80 m, (d) working face mined to 100 m, (e) working face mined to 150 m, and (f) working face mined to 200 m.

the degree of fracture development is reduced. Therefore, from observation hole 2, the upper limit of water conductivity is the depth of the hole at 60 m, and the height of the WFFZ is calculated by the following formula:

$$H_2 = 60 \times \sin 40.5^\circ = 39.97\ \text{m}. \tag{6}$$

Based on the test results of all observation holes, the height of WFFZ in the strata overlying the working face is approximately 40 m.

According to the observation results, the development height of the WFFZ on the first mining face of the 3upper coal seam located under Weishanhu Lake of the Jisan coal mine is saddle-shaped, as shown in Figure 12. The width of the side expansion (or extrusion) of the WFFZ is approximately 10 m. The upper surface of the WFFZ is in the mudstone, which is in the eighth layer overlying the 3upper coal seam with a thickness of 8.5 m. It is believed that its upper surface is the boundary between the 8.5 m thick mudstone and the 1.6 m thick fine and medium-grained sandstone.

The reason for the formation of the saddle-shape and side boundary convex-shape is that the curvature of the overlying strata is the largest at the mining boundary, so the height of the WFFZ at the mining boundary is also the highest. On the outside of the mining boundary, that is, above the coal pillar, the overlying strata are in a state of tensile stress, which easily produces opening fractures. Therefore, the outer convex type is caused on the side boundary of the WFFZ.

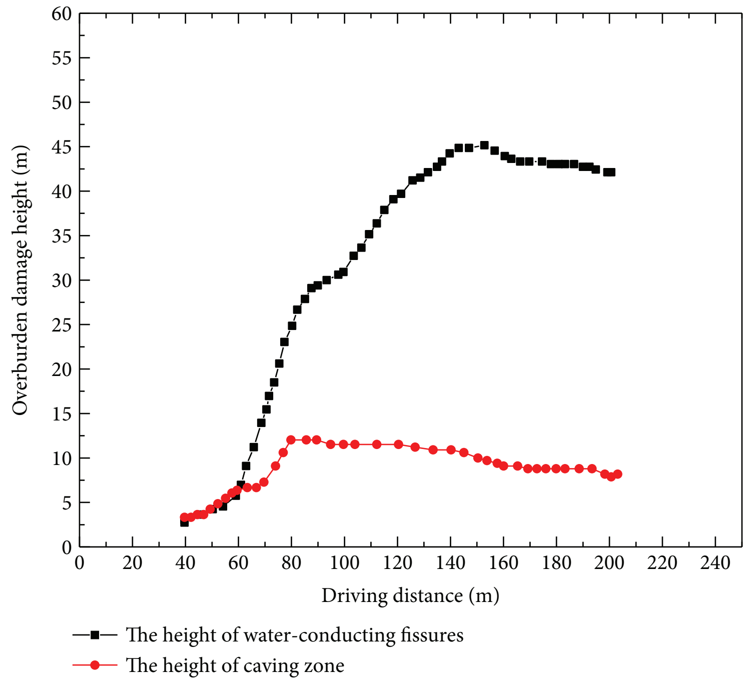

Figure 10: Relationship between overburden damage height and driving distance of the working face.

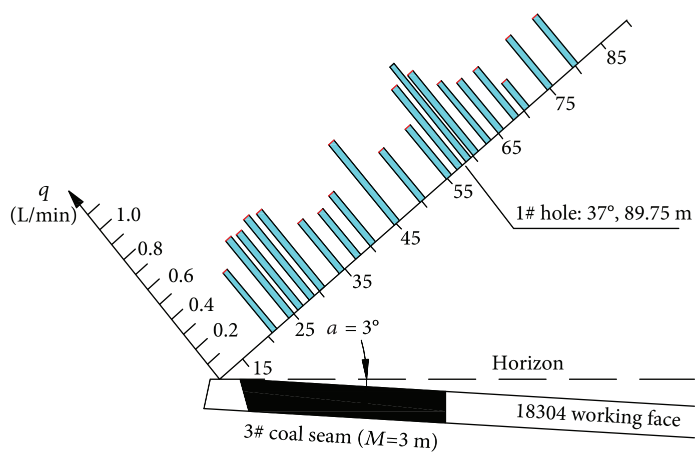

Figure 11: The amount of water leakage of 1# borehole (37°) before mining.

3.3.2. Visual Observation of Boreholes. The fracture development of the 183upper04 working face roof was observed by a YTJ20 borehole television (Figure 13); the observation depth was 13.43 m due to limited equipment conditions. According to the nearest C4-11 bore hole columnar section to the chamber, the borehole camera passes through the 1.75 m thick siltstone of the roof, the 2.95 m thick fine siltstone interbed, and 5.22 m thick claystone in sequence, and the ultimate depth is at 5.22 m in the claystone. Based on the analysis of the borehole video, the height of the caving zone on the 183upper04 working face is greater than or equal to 9.92 m.

The heights of the WFFZ obtained using the above three methods were approximately 50 m, 30-45 m, and 40 m. The respective caving zone heights were approximately 15 m, 8-12 m, and 9.92 m. The results of the physical experiment and field measurements showed that the numerical simulation results are correct. The results verified the practicality of the flow-stress-damage model to study the fracture of overlying strata under water during mining. However, there is an obvious bias in the data obtained from the three methods; the data obtained from the physical experiment and field measurements were slightly lower than those of numerical simulation. The possible reasons mainly include the selected mechanical parameters of the strata, which have a significant influence on the experimental results. Another possible reason is that the caving zone height results are inaccurate because of limited equipment conditions that were presented in the field measurement section.

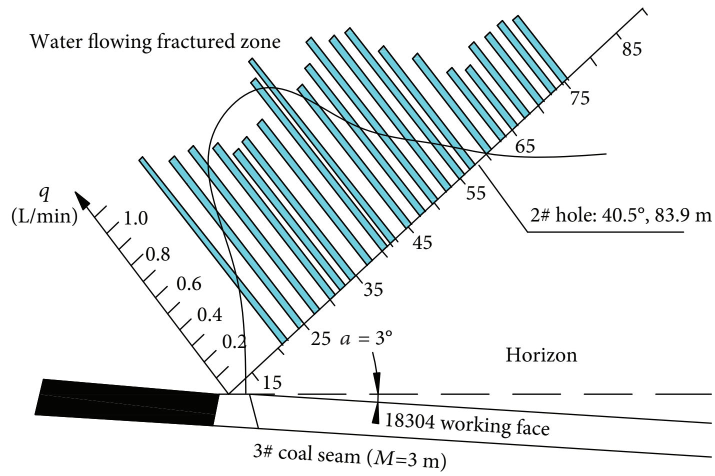

Figure 12: The amount of water leakage of 2# borehole (40.5°) after mining.

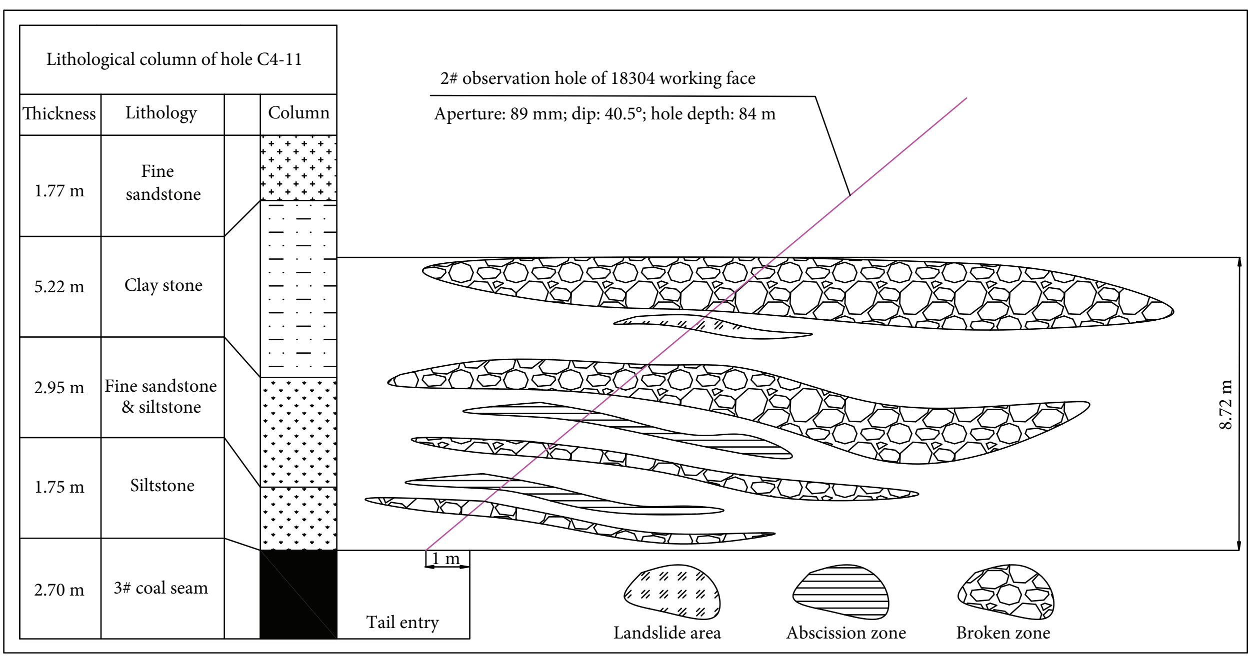

Figure 13: Post-mining distribution of strata failure on the 183upper04 working face.

4. Conclusions

Based on the Griffith theory, energy was used as the fracture expansion criterion. Through the use of the Fish language, the flow-stress-damage model and its criterion were embedded in FLAC 3D software, and a calculation program was applied to simulate the mining process under a water body. The failure of the surrounding rock in the mining process under the water body was analyzed. Combined with the field observation results and laboratory simulation results for the height of the WFFZ, the effectiveness of the determination method was verified and the evolution law of the height of the WFFZ was obtained.

The WFFZ consists of the caving zone and the fracture zone, and its development height is basically the same as that of the “breaking arch.” As the working face is mined, caving occurs in the overlying strata and the degree of fracture development increases, but the height of the WFFZ will not increase if the overlying strata are supported by waste rock, which is formed after caving and expansion of the working face. The height of the WFFZ obtained by numerical simulations was approximately 50 m, the development height obtained by laboratory simulations was in the range of 30 m to 45 m, and the development height obtained by the water injection fracturing test system was approximately 40 m.

The key to safe mining under water is to ensure that the WFFZ does not affect the overlying water. The height of the WFFZ measured in the field was within the safe range, and thus, safe mining under water can be realized. The research results provide theoretical support for coal mining under water in the Jisan coal mine and a reference for determining the height of the WFFZ in similar geological conditions.

Data Availability

The tables, some figures, and data used to support the findings of this study are currently under embargo while the research findings are commercialized. Requests for data six months after the publication of this article will be considered by the corresponding author.

Conflicts of Interest

The authors declare that they have no conflicts of interest.

Acknowledgments

This research was financially supported by the State Key Research Development Program of China (No. 2016YFC0600708), the Open Fund for State Key Laboratory (SHGF-18-13-30), the Tai'shan Scholar Engineering Construction Fund of the Shandong Province of China, the Tai'shan Scholar Talent Team Support Plan for Advanced and Unique Discipline Areas, the Shandong Province Higher Educational Science and Technology Program (No. J15LH04), the Natural Science Foundation of Shandong Province (No. ZR2018 MEE001), the State Key Laboratory of Open Funds (No. MDPC201601), the Source Innovation Programme (No. 18-2-2-68-jch).

References

[1] J. F. Ju, "Progress of water-preserved coal mining under water in China," *Coal Science and Technology*, vol. 46, no. 1, pp. 12–19, 2018.

[2] A. Dahi Taleghani, M. Gonzalez-Chavez, H. Yu, and H. Asala, "Numerical simulation of hydraulic fracture propagation in naturally fractured formations using the cohesive zone model," *Journal of Petroleum Science and Engineering*, vol. 165, pp. 42–57, 2018.

[3] E. Jiránková, "Utilisation of surface subsidence measurements in assessing failures of rigid strata overlying extracted coal seams," *International Journal of Rock Mechanics and Mining Sciences*, vol. 53, pp. 111–119, 2012.

[4] R. R. Jozefowicz, *The Post-Failure Stress-Permeability Behavior of Coal Measure Rocks, [Ph.D. thesis]*, University of Nottingham, 1997.

[5] D. N. Whittles, I. S. Lowndes, S. W. Kingman, C. Yates, and S. Jobling, "The stability of methane capture boreholes around a long wall coal panel," *International Journal of Coal Geology*, vol. 71, no. 2-3, pp. 313–328, 2007.

[6] M. Bai, F. Kendorski, and D. Van Roosendaal, "Chinese and North American high-extraction underground coal mining strata behavior and water protection experience and guidelines," in *Proceedings of the 14th International Conference on Ground Control in Mining*, pp. 209–217, Morgantown, WV, USA, 1995.

[7] A. Majdi, F. P. Hassani, and M. Y. Nasiri, "Prediction of the height of destressed zone above the mined panel roof in longwall coal mining," *International Journal of Coal Geology*, vol. 98, no. 1, pp. 62–72, 2012.

[8] S. Liu, W. Li, and Q. Wang, "Height of the water-flowing fractured zone of the Jurassic coal seam in northwestern China," *Mine Water and the Environment*, vol. 37, no. 2, pp. 312–321, 2018.

[9] C. Özgen Karacan and G. Goodman, "Hydraulic conductivity changes and influencing factors in longwall overburden determined by slug tests in gob gas ventholes," *International Journal of Rock Mechanics and Mining Sciences*, vol. 46, no. 7, pp. 1162–1174, 2009.

[10] Y. Zhang, S. G. Cao, S. Guo, T. Wan, and J. J. Wang, "Study on the height of fractured water-conducting zone under aquifer for short wall blocking mining," *Journal of Mining & Safety Engineering*, vol. 35, no. 1, pp. 7–14, 2010.

[11] V. Palchik, "Formation of fractured zones in overburden due to longwall mining," *Environmental Geology*, vol. 44, no. 1, pp. 28–38, 2003.

[12] Z. Q. Song, Y. J. Jiang, and J. K. Liu, "Theory and model of "practical method of mine pressure control"," *Coal Science & Technology Magazine*, vol. 2017, no. 2, pp. 1–10, 2017.

[13] Z. J. Wen and H. Xia, "The time effect of strata obvious movement," *Science & Technology, Review*, vol. 26, no. 2, pp. 42–45, 2011.

[14] Y. L. Tan, J. G. Ning, S. T. Gu et al., *Mining Pressure and Strata Control*, Coal Industry Press, Beijing, China, 2011.

[15] D. P. Adhikary and H. Guo, "Measurement of longwall mining induced strata permeability," *Geotechnical and Geological Engineering*, vol. 32, no. 3, pp. 617–626, 2014.

[16] Z. J. Wen, *Study on the Key Technologies and Mechanical Model of Job-Side Retaining Entry, [Ph.D. thesis]*, Shandong University of Science and Technology, 2011.

[17] Z. J. Wen, X. Wang, Q. H. Li, G. Lin, S. J. Chen, and Y. J. Jiang, "Simulation analysis on the strength and acoustic emission characteristics of jointed rock mass," *Tehnicki vjesnik - Technical Gazette*, vol. 23, no. 5, pp. 1277–1284, 2016.

[18] L. J. Chen, T. F. Li, G. Wang, X. X. Wu, Y. J. Jiang, and Z. Z. Han, "Study on crack expansion judgment method in overlying strata and its application for coal mining under aquifers," *Journal of China Coal Society*, vol. 39, no. S2, pp. 301–307, 2014.

[19] A. A. Griffith, "The phenomena of rupture and flow in solids," *Philosophical Transactions of the Royal Society A: Mathematical, Physical and Engineering Sciences*, vol. 221, no. 582-593, pp. 163–198, 1921.

[20] X. Wang, Z. J. Wen, Y. J. Jiang, and H. Huang, "Experimental study on mechanical and acoustic emission characteristics of rock-like material under non-uniformly distributed loads," *Rock Mechanics and Rock Engineering*, vol. 51, no. 3, pp. 729–745, 2018.

[21] J. Li, *Evolution Mechanism and Control of Water-Flowing Fracture with Gangue Backfill under Aquifer in Coal Mines, [Ph.D. thesis]*, China University of Mining and Technology, 2013.

[22] G. Baobin, L. Yunpeng, and P. Jiayu, "Detection and analysis of height of water flowing fractured zone in underwater mining," *Chinese Journal of Rock Mechanics and Engineering*, vol. 33, no. 2, pp. 3384–3390, 2014.

Hindawi
Geofluids
Volume 2019, Article ID 2603296, 20 pages
https://doi.org/10.1155/2019/2603296

Research Article

Experimental Study of Fracturing Fluid Retention in Rough Fractures

Yanjun Zhang,[1,2] Hongkui Ge ,[1,2] Guangyu Liu,[3] Yinghao Shen ,[1,2] Hao Chen,[1,2] Jianbo Wang,[1,2] Dunqing Liu,[1,2] and Zehui Huang[1,2]

[1]*State Key Laboratory of Petroleum Resources and Prospecting, China University of Petroleum, Beijing 102249, China*
[2]*Unconventional Natural Gas Institute, China University of Petroleum, Beijing 102249, China*
[3]*PetroChina Jilin Oilfield Company, Songyuan, Jilin 138000, China*

Correspondence should be addressed to Hongkui Ge; gehongkui@163.com

Received 21 November 2018; Revised 17 February 2019; Accepted 12 March 2019; Published 22 April 2019

Guest Editor: Fengshou Zhang

Multistage hydraulic fracturing is a key technology for developing tight reservoirs. Field data indicate that a small fraction of the injected water can be recovered during flowback. Fractures play an important role in the retention of fracturing fluid, but the mechanisms and rules remain uncertain. Therefore, an experimental facility was established for studying the fluid retention in fractures using an improved conductivity apparatus. The fluid trapped in rough fractures was measured, and the dynamic changes of the drainage volume and rate under various apertures were analyzed. The effects of different factors, such as the fracture aperture, surface roughness, tortuosity, and matrix imbibition, on the fluid retention were studied. An empirical formula between the retention rate and fracture aperture was derived on the basis of mass conservation. Results showed that the fluid retention rate slowly decreased with an aperture increase in the fracture, and it would increase with considerable roughness, high tortuosity, and significant matrix imbibition. Meanwhile, drainage volume and rate change dramatically resulted from the gas drive. Secondary fractures and microcracks played an important role in the retention of fracturing fluid. Furthermore, the mechanisms of fracturing fluid retained in the tight reservoir, including viscous trapping and "locking" in fractures, the effect of gravity, surface-bound water film, capillary force retention, and matrix imbibition, were discussed. This study is significant for understanding the flowback rules of fracturing fluid, diagnosing fracture development, and identifying reservoir properties.

1. Introduction

Multistage hydraulic fracturing is a key technique for the effective exploitation of tight reservoirs. In the process of multistage hydraulic fracturing, a large amount of fracturing fluid is injected into the formation. However, field data show that the flowback rate of the fracturing fluid after fracturing is generally no higher than 30% [1]. For conventional reservoir hydraulic fracturing, the flowback rate should be higher to reduce the damage caused by the external fluids to the reservoir [2–4]. Nevertheless, the relationship between the flowback rate and the stimulated effect in tight reservoirs is unclear, and the production from wells with high flowback rates is unnecessarily high. The retained fracturing fluid is closely related to reservoir damage, environmental protection, and oil and gas production [5–8].

During the hydraulic fracturing, a part of retained fracturing fluid is imbibed into the matrix, and another portion is trapped in the fracture. Published studies have suggested that fracturing fluid enters the matrix by capillary force and gradually spreads to the deep matrix, which is influenced by rock composition, mineral content, porosity, permeability, wettability, geochemical characteristics, and liquid properties [9–11]. For example, the spontaneous imbibition of marine and continental shale shows that the imbibition capacity of marine shale is stronger than that of continental shale due to the difference of clay mineral content and wettability [12]. However, some researchers mentioned that only a few fracturing fluids can enter the shale matrix given the change

Table 1: Classification criteria of fractures.

Type	Aperture	Characteristic	Connectivity
Primary fracture	>0.80 mm	Single, large aperture, main flow channel	Excellent conductivity
Secondary fracture	0.25–0.80 mm	Large number, small aperture	Good connectivity with primary fracture
Microcrack	<0.25 mm	Discrete distribution, small scale	Poor connectivity

Table 2: Sample properties.

Basin	Formation	Depositional environment	Porosity (%)	Permeability (mD)
Sichuan Basin	Silurian Formation	Marine deposition	5.56	0.7×10^{-3}

in pressure gradient during fracturing and flowback. The fracturing fluid, which is similar to proppants in the fracture, could support some closure fractures [13]. Some studies have also found that the fracturing fluid cannot flow back in time during the rapid closure of an unpropped fracture [14].

Realizing fracture characteristics is a prerequisite to studying the retention of fracturing fluid in fractures. A single rough fracture is the basic unit that comprises a fracture network. Many studies have been conducted on the description methods of rough fracture surfaces and the fluid flow rules in fractures [15–18]. In the published study, fracture aperture, surface roughness, and tortuosity are important parameters in describing fracture characteristics. However, no uniform standard exists for describing the characteristics of rough fractures. In the publications of numerical simulation, a discrete fracture network model has been established, and fracture length, density, and connectivity have been studied. Enhancing the contact between the matrix and the fracture can improve the capability of the fracturing fluid to enter the matrix [19]. The flowback rate may decrease with a complex fracture network and a large stimulated volume. So far, this phenomenon cannot be explained clearly from the level of mechanisms.

Some works have given their views on the retention mechanism of fracturing fluid by laboratory experiments, numerical simulations, and field data analysis [20–22]. A numerical simulation study shows that matrix imbibition, secondary fracture trapping, and shut-in time significantly affect production due to fluid retention [19]. The fracture closure and gravity in the primary fracture are the main mechanisms of FFR [23]. Experimental results show that the surface tension and wetting in primary fractures influence FFR, while gas displaces liquid during flowback. Meanwhile, the effect of gravity separation in a primary fracture on the fracturing fluid is significant [20]. Until now, there have been few studies on the mechanism of FFR.

The mechanism and rule of retention in rough fractures are unclear, and the relationship between the flowback rate and development of artificial fractures is uncertain. Few experimental methods have been conducted to simulate the fluid retention process. In this study, we built an experimental facility to evaluate fluid retention. The fluid trapped in rough fractures was measured, and dynamic changes in drainage volume and rate under various apertures were analyzed. The effects of different factors, such as the fracture aperture, surface roughness, tortuosity, and fracture surface imbibition, on fluid retention were studied, and the retention rate was calculated on the basis of mass conservation.

2. Classification of Fractures

A complex fracture network that consists of a single rough fracture is formed during multistage hydraulic fracturing. Previous studies related to hydraulic fracturing have divided fractures into primary and secondary fractures [24, 25]. For further study, fractures are divided into three types, namely, primary fractures, secondary fractures, and microcracks according to the customary method and the characteristics of various man-made fractures [26, 27]. The main classification characteristics of fractures are shown in Table 1.

The aperture of the primary fracture is greater than 0.80 mm. The fracture has a large opening, which is the main flow channel of the fluid, and has high conductivity. The aperture of the secondary fracture is between 0.25 and 0.80 mm. The secondary fractures, which are minor channels of the fluid flow that have good connectivity with the primary fracture, are numerous and have small apertures. The aperture of a microcrack is less than 0.25 mm. They distribute in a scattered state and have a small scale, which can enhance rock permeation. The primary fracture, secondary fracture, and microcrack mentioned in this paper are based on the classification criteria of fractures, as listed in Table 1.

3. Experimental Materials and Methods

3.1. Sample Acquisition and Characteristics. The sample was acquired from the shale outcrop (30.00 cm × 30.00 cm × 30.00 cm) of the Silurian Formation, a marine deposit in the Sichuan Basin of Southeastern Chongqing. Sample properties of the standard cores are listed in Table 2. The average porosity, measured by a helium porosity measurement device, is 5.56%. The average permeability, measured by a steady-state method, is 0.0007 mD (SY/T5336-2006). X-ray diffraction analysis results of the shale mineral composition are shown in Table 3. The clay mineral content is 14.5%–40.2%, the quartz content is 38.0%–54%, the feldspar content is 5.6%–12.1%, and the carbonate rock content is 4.2%–16.0%. Scanning electron microscopy images showed

Table 3: Mineral composition.

Mineral type	Clay	Quartz	Feldspar	Carbonate
Mass percentage	14.5%–40.2%	38.0%–54.0%	5.6%–12.1%	4.2%–16.0%

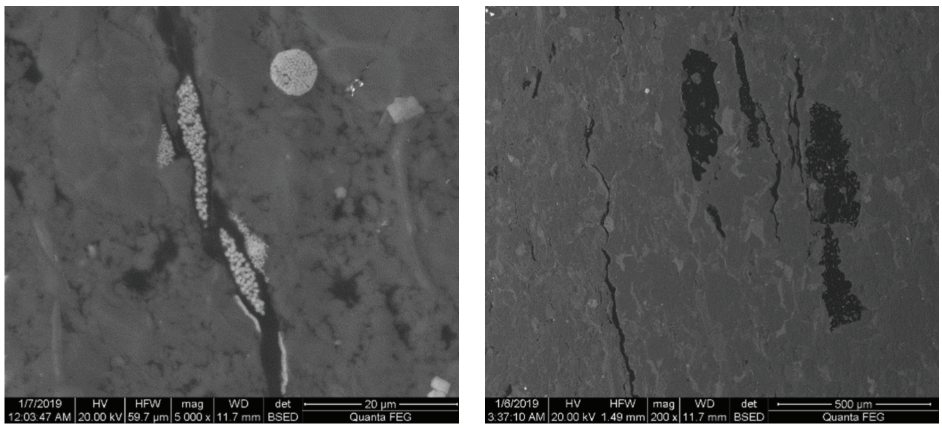

(a) (b)

Figure 1: SEM images: (a) natural fracture filled with pyrite and (b) organic development.

that an organic fracture is developed and filled with pyrite, as shown in Figure 1. The elastic modulus is 20.17 GPa, Poisson's ratio is 0.28, and the density is 2.53 g/cm^3.

For the convenience of research, four sets of rock samples and one group of steel samples were prepared before the experiment, and they were marked CI, CII, CIII, GHI, and GHII. The fractures of CI, CII, CIII, and GHI were formed along the bedding. GHI's fracture surface was polished by a grinder, and the fracture of GHII was formed by two steel plates. They are all shown in Figure 2. The standard cores were drilled in the direction of the vertical bedding for performing a single-sided spontaneous imbibition experiment.

3.2. Measurement of Surface Roughness. ContourGT is a three-dimensional optical microscope, which is used to obtain the roughness and surface topography of the fracture surface. The principle of white light interference was adopted for measuring the optical path difference that reflects the surface physical properties. The measuring resolution is 0.1 nm, the measuring range is 0.1–10 mm, and the closed loop is not stitching, as shown in Figure 3.

The surface topographies of CI, CII, CIII, GHI, and GHII were scanned using Contour-GT. The local typical morphology of the fracture surface was obtained, as shown in Figure 4. We could thus acquire the mean square roughness (R_q), arithmetic mean deviation (R_a), and maximum height drop (R_v).

3.3. Experimental Apparatus and Methods

3.3.1. Experimental Apparatus. Artificial fractures have different apertures, roughness, and surface properties. The fracturing fluid is displaced by the gas during flowback. The flow and retention rule of fracturing fluid in rough fractures must be understood. Therefore, a retention experimental facility was built for studying the effects of fractures between two test samples on fluid retention. The experimental setup includes a modified conductivity apparatus and a spontaneous imbibition device, as shown in Figure 5. The modified conductivity apparatus consists of a conductivity room, a hydraulic pump with automatic pressure control, a laser ranging sensor for measuring the fracture aperture, and a computer with SmartSeries software. The device has a maximum closure pressure of 137 MPa, the conductivity room area is 64.5 cm^2, and the fracture aperture-controlling accuracy is 0.1 mm. The spontaneous imbibition device is composed of an electronic balance, a constant-temperature and humidity box, and a computer with software. The accuracy of the electronic balance is 0.00001 g; it was used to obtain the value of matrix imbibition mass for calculating the retention rate.

3.3.2. Experimental Methods. The surface morphology of the samples was scanned before the experiment for determining surface roughness and three-dimensional topography. The experimental setup established using the conductivity apparatus was used for liquid loading and gas displacing, as shown in Figure 6(a) (the green pipeline is the gas-displacing system and the blue pipeline is the liquid-loading system). Figure 6(b) shows the placement of the specimen inside the testing cell, orientation of the fracture, and fluid flow/drainage direction. Distilled water was used, and its volume flow rate was 5 mL/min. Nitrogen was also used, and its volume flow rate was 10 mL/min. The change in the fracture aperture could be monitored in real time through a displacement sensor. The drainage liquid mass could be collected by the balance at the outlet. The total amount of the injected water mass could be obtained by an integral. The loading mass and retention rate of fluids with different apertures, surface roughness, tortuosity, and matrix imbibition were

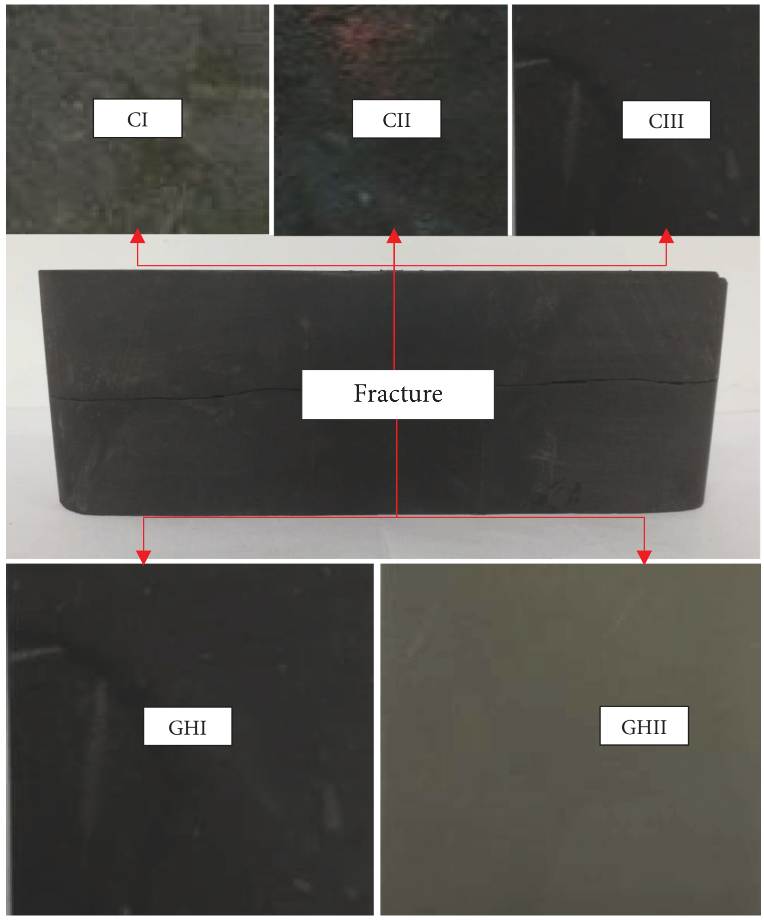

Figure 2: Surface characteristics of samples, four sets of test samples, and one group of steel samples (top view).

obtained. A one-sided spontaneous imbibition experiment of the standard core was conducted to obtain the mass of the spontaneous imbibition matrix.

An experiment on fluid retention was performed in the following procedure. (1) The test sample was loaded into the conductivity room according to the industrial standard SY/T 6302-2009. (2) The device was opened, and the initial fracture aperture was set. (3) The inlet valve was opened for injecting liquid into the crack and closed after the stability of flow at the outlet for 15 min. (4) The gas valve was opened for 30 min for simulating the gas displacement that would occur upon disappearance of the liquid flow at the outlet. (5) The fracture aperture was adjusted before the next cycle, and the experimental data were recorded by the computer in real time. The experimental process ended upon completion of the above steps.

4. Experimental Results

4.1. Characteristics of Drainage Mass and Rate. The experiment was performed using four sets of test samples and one group of steel plates by adjustment of the fracture aperture. The drainage characteristics of CI, CII, and CIII at different fracture apertures were analyzed. In Figure 7(a), the fracture apertures are 1.7, 1.0, 0.5, and 0.1 mm. The experiment was used as a basic experiment without gas drive. The mass of the drainage fluid continuously increases under the different apertures. The drainage mass of the same set of experiments decreases with the reduction in the fracture aperture. In Figures 7(b) and 7(c), the fracture apertures are 1.6, 1.3, and 0.2 mm. The gas drive increases the drainage mass by comparison. In Figures 7(d) and 7(e), the fracture apertures are 2.2, 1.8, 1.6, and 1.3 mm. Figures 7(b) and 7(d) represent the case without gas drive, whereas Figures 7(c) and 7(e) represent the case with gas drive. When the apertures are 2.2 and 1.8 mm, the drainage mass increases and then fluctuates severely due to a gas breakthrough in the fracture. In the initial stage, the drainage mass increases rapidly, and the increase in the drainage mass gradually decreases. The gas drive increases the final mass of the drainage fluid. The drainage mass in the rear of the gas drive begins to fluctuate, which results in a certain increase in the total drainage volume.

In Figure 8(a), the fracture apertures are 1.7, 1.0, 0.5, and 0.1 mm. The rate of the drainage fluid shows a decrease trend with time. A remarkable difference in the initial drainage rate with different apertures is observed, and the difference gradually decreases with time. In Figures 8(b) and 8(c), the fracture apertures are 1.6, 1.3, and 0.2 mm. The gas drive, which was conducted in Figure 8(c) but not in Figure 8(b), clearly increases the drainage rate.

In Figures 8(d) and 8(e), the fracture apertures are 2.2, 1.8, 1.6, and 1.3 mm. The gas drive, which was conducted in

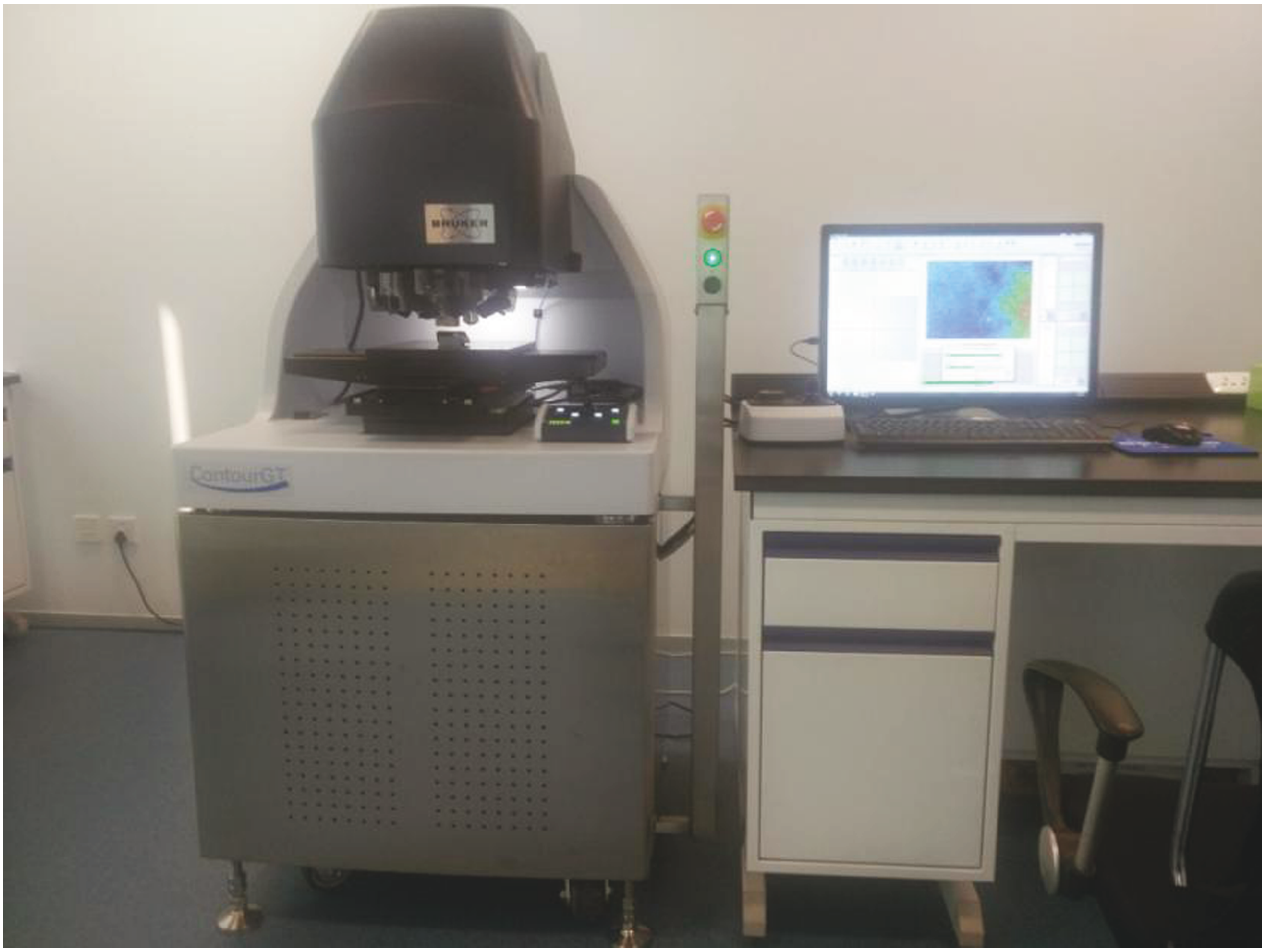

Figure 3: ContourGT.

Figure 8(e) but not in Figure 8(d), increases the rate of the drainage fluid significantly. A comparison of Figures 8(b) and 8(c) with Figures 8(d) and 8(e) shows a noticeable difference in the drainage rate under the condition of gas displacement. The gas drive results in a sudden increase in the drainage mass and rate. This process is considered to simulate the beginning of gas production of hydraulic fracturing flowback. The characteristic of the gas-water ratio during flowback can identify the complexity of reservoir fractures. The stimulated volume was evaluated on the basis of the material balance equation [28].

4.2. Factors Affecting Liquid Retention. A large number of fractures will be generated after a tight reservoir is fractured. The fracture has different apertures, surface roughness, and tortuosity. The high imbibition capacity and adsorbed water film are caused by a large number of micro–nanopores, rich clay content, and a large stimulated area, which are not found in conventional reservoirs. Therefore, the aperture, roughness, tortuosity, and surface imbibition are studied. According to the principle of mass conservation, the amount of injected fracturing fluid in the formation is equal to the sum of the mass of fluid discharged and retained in the fractures. The total amount of liquid injected is calculated according to the injection rate. The drainage mass after gas drive can be read directly from the outlet balance. The retention mass is equal to the difference between the total amount of the injected liquid and the collecting mass of the balance after the gas drive.

4.2.1. Aperture of the Fracture. The fracture aperture is an important parameter describing the fracture feature. It decreases with the increase in the closure stress. The true opening value is obtained by comparing the initial set value with the closure value. Five groups of experiments were carried out, including sixteen different sets of apertures. The aperture is 0.1 mm, 0.2 mm, 0.5 mm, 0.7 mm, 0.8 mm, 1.0 mm, 1.3 mm, 1.6 mm, 1.7 mm, 1.8 mm, and 2.2 mm. The frequency of the fracture aperture is obtained by a statistical analysis, as shown in Figure 9. According to the classification criteria of fractures, 25% of microcracks, 25% of secondary fractures, and 50% of primary fractures are representative.

Figure 10 shows the loading mass (retention mass) of the liquid at different apertures of CI, CII, and CIII. The loading mass decreases with the increase in the aperture of the fracture. CI and CII show that the effect of aperture change on a small scale on the fluid retention is greater than that on a large scale. However, CIII shows no such obvious

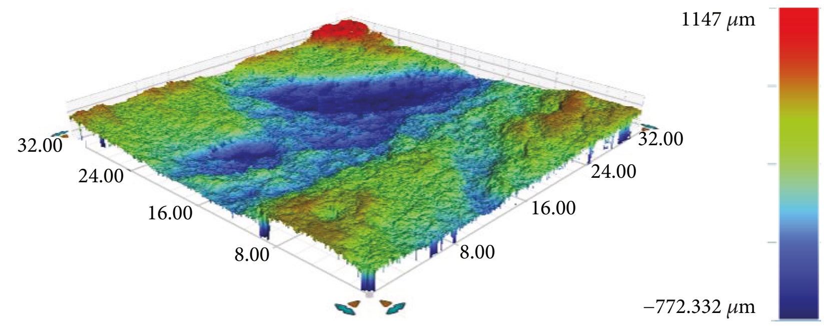

(a)

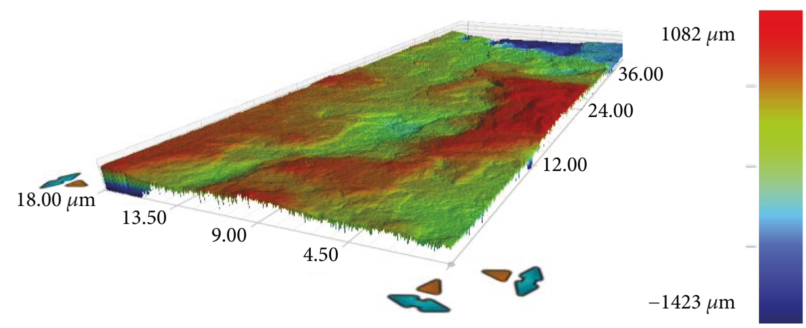

(b)

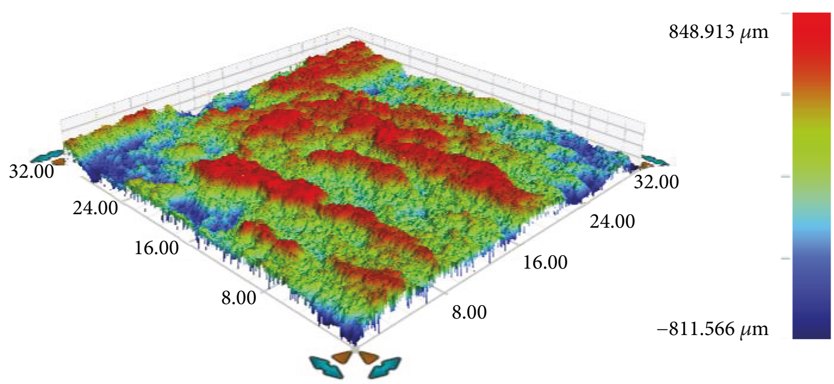

(c)

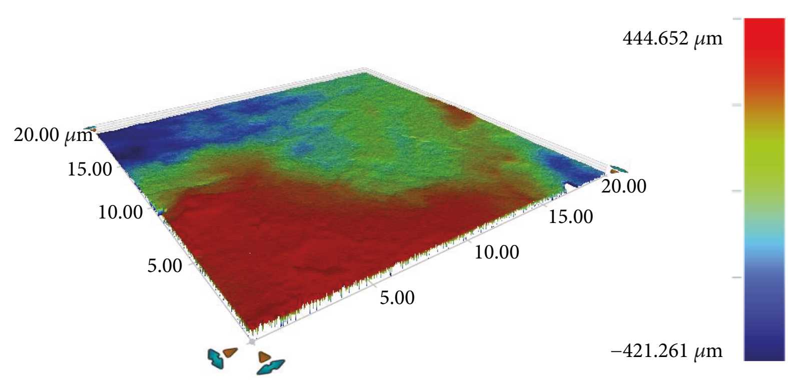

(d)

Figure 4: Continued.

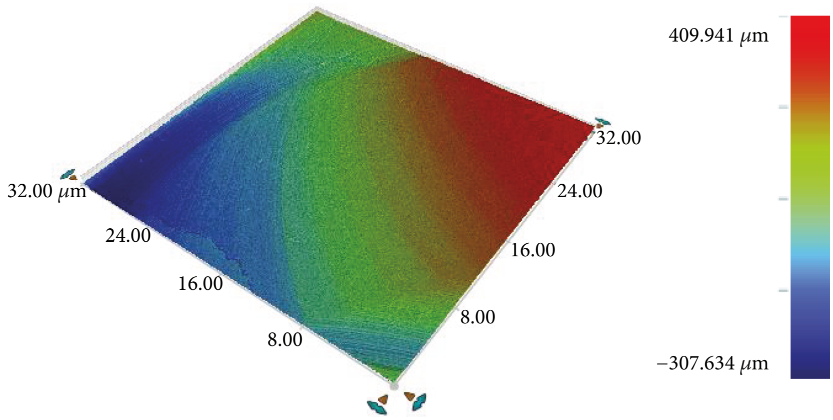

(e)

Figure 4: Typical morphology of the fracture surface: (a) CI, (b) CII, (c) CIII, (d) GHI, and (e) GHII.

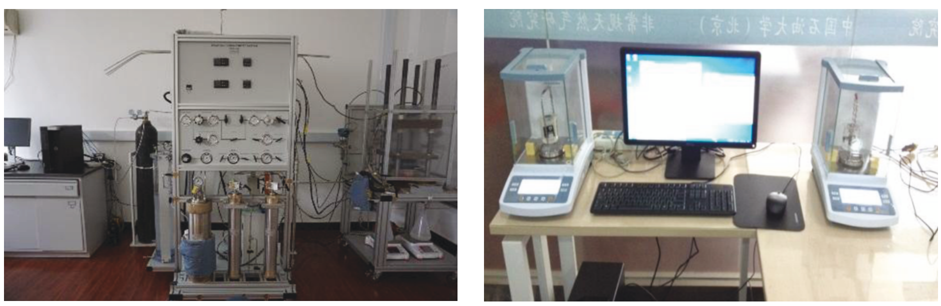

(a) (b)

Figure 5: Experimental apparatus: (a) modified conductivity apparatus and (b) spontaneous imbibition device.

pattern that could be caused by gas displacement. There is some difference between gas displacement and no gas displacement. The discharge of liquid depends mainly on the elasticity of formation and liquid expansion without gas displacement [29]. The gas provides displacement pressure and increases the discharge capacity of the liquid.

4.2.2. Surface Roughness. The relevant typical morphology of the sample fracture surface is extracted, as shown in Table 4. Considering R_q, R_a, and R_v, we can determine the contrast of roughness: $R_{CI} > R_{CII} > R_{CIII} > R_{GHI} > R_{GHII}$. The maximum drops of CI, CII, and CIII are much larger than those of GHI and GHII. The asperity on the fracture surface determines the primary roughness, which is the first contact area with the decrease in the fracture aperture.

Different test samples have different roughness under the same aperture. When the aperture is 0.1 mm and 0.5 mm, the loading mass of CI is higher than that of GHI. When the opening aperture is 0.2 mm, the loading mass of CIII is greater than that of GHI. When the aperture is 1.6 mm, the loading mass of CII is greater than that of CIII. High roughness leads to a large loading mass. The difference is that the loading mass of CII is lower than that of CIII when the aperture is 1.3 mm, although the roughness of CII is higher than that of CIII.

One possible reason is that the aperture exerts a main effect on the liquid retention under large apertures, as shown in Figure 11. The primary roughness dominates the direction of the fluid flow and pressure distribution and is characterized by the maximum peak, height of the maximum peak valley, and maximum height drop. The secondary roughness was characterized by root-mean-square roughness and contour arithmetic mean square deviation, which mainly influences the distribution of the fracturing fluid in the fractures [30]. The surface roughness is an important parameter that affects the fluid flow state, and it also has a significant effect on the retention of the fracturing fluid [31, 32].

4.2.3. Fracture Tortuosity. Fractures were modeled using parallel plates in the study of fluid flow in fractures [33], as shown in Figure 12(a). The real fracture surface is rough, and the fracture formed by the rough surface has a certain tortuosity, as shown in Figure 12(b). Roughness and tortuosity affect the flow state and the regularity of fluid in fractures. The presence of tortuosity increases the flow space and the fracture surface area connected with fluid.

Tortuosity can be characterized by different methods. The simplest method for describing tortuosity is the rate of chord and arc, which is defined as the ratio of the length of the curve to the distance between the endpoints. According to the definition of tortuosity, we can obtain $\tau_{CI} > \tau_{CII} > \tau_{CIII} > \tau_{GHI} \approx \tau_{GHII}$. When the aperture is 0.1 mm, the loading mass of CI is higher than that of GHI. When the aperture is 0.2 mm, the loading mass of CIII is

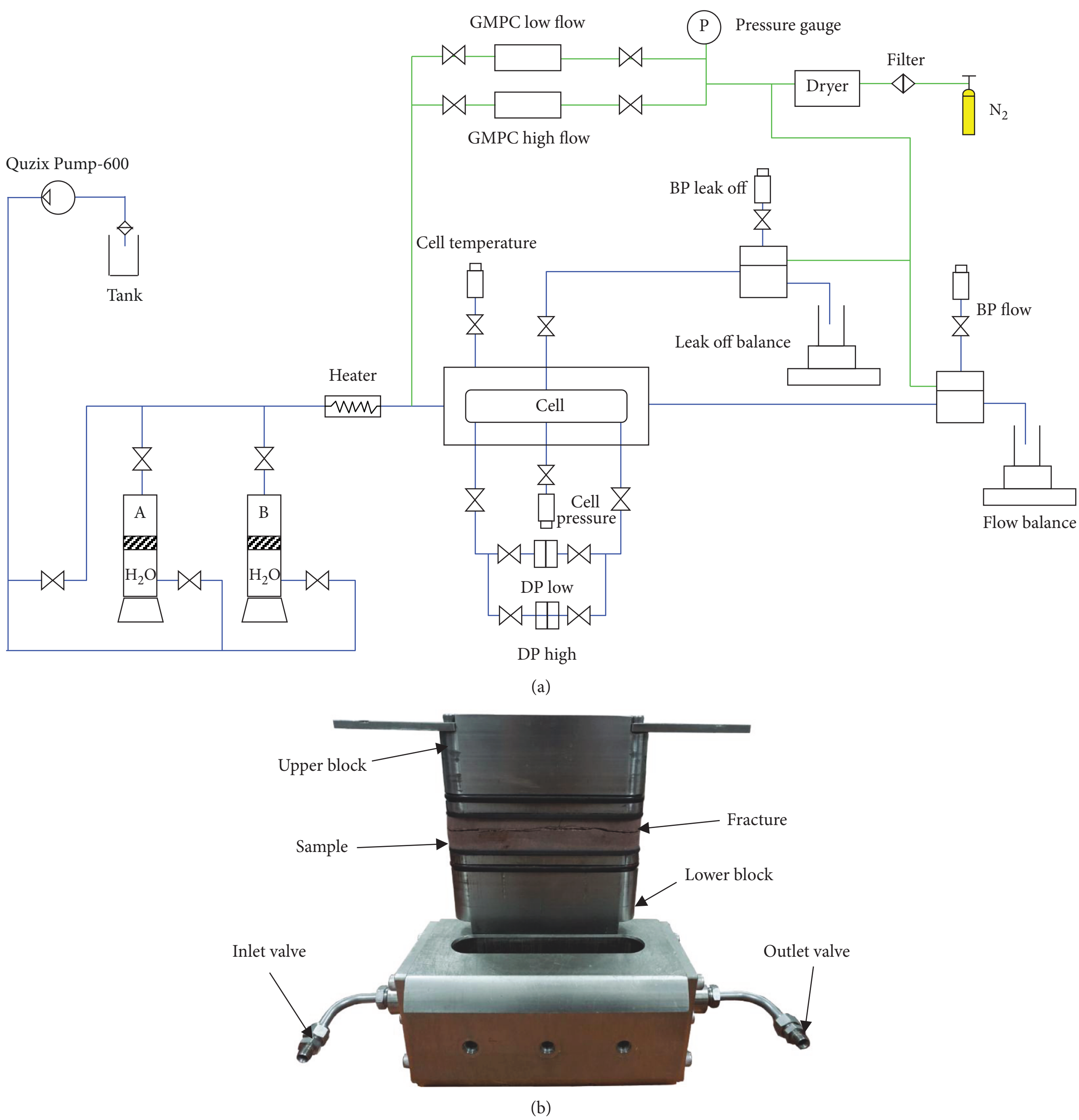

Figure 6: Experimental apparatus pictures. Retention (blue) and gas-displacing (green) systems: (a) sketch map and (b) physical map.

higher than that of GHI. As shown in Figure 13, the loading mass increases with great tortuosity.

4.2.4. Imbibition of the Matrix. The degree of rock dryness affects the matrix imbibition. In the process of reservoir formation, hydrocarbon drainage and vaporization occur in a tight reservoir. The high temperature and pressure conditions underground keep the water evaporating continuously, thereby resulting in the low water saturation of the rock. The fracturing fluid enters the dry reservoir under a "thirsty" state and is thus difficult to expel. A single-sided spontaneous imbibition experiment of four groups (I, II, III, and IV) was performed. The core circumference and top surface were sealed by epoxy resin to appear as a face. The sample immersed in the liquid completely was suspended from the analytical balance with a waterproof line [9]. As shown in Figure 14, we could gain the single surface spontaneous imbibition mass. And then, we calculated the single surface spontaneous imbibition mass per unit area. Finally, we would gain the imbibition mass of test samples. The special properties of the shale lead to high imbibition. However, compared with the FFR in the fracture (for example, Figure 10), the

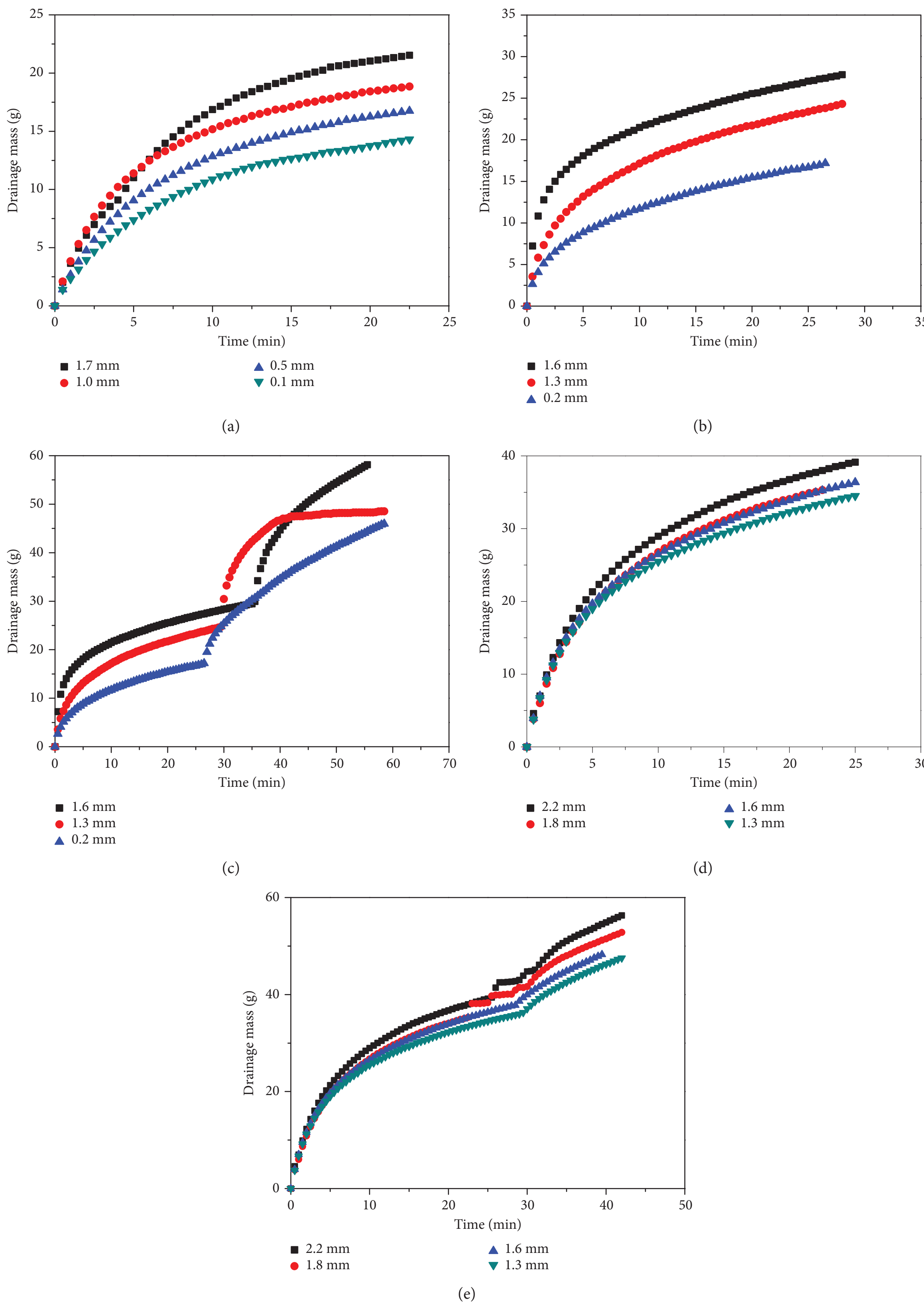

Figure 7: Drainage mass with different fracture apertures: (a) CI (without gas drive), (b) CII (without gas drive), (c) CII (with gas drive), (d) CIII (without gas drive), and (e) CIII (with gas drive).

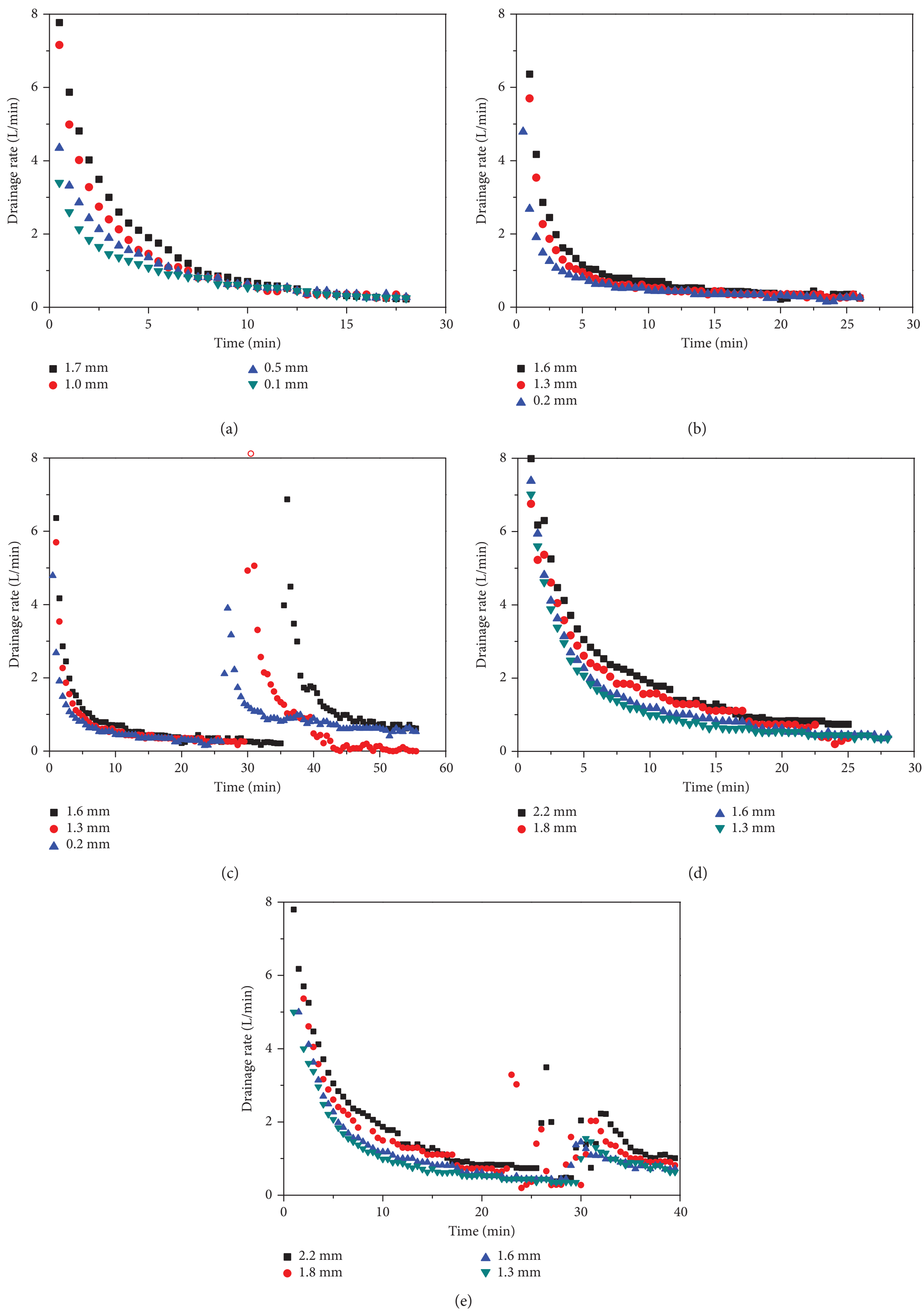

FIGURE 8: Drainage rate with different fracture apertures: (a) CI (without gas drive), (b) CII (without gas drive), (c) CII (with gas drive), (d) CIII (without gas drive), and (e) CIII (with gas drive).

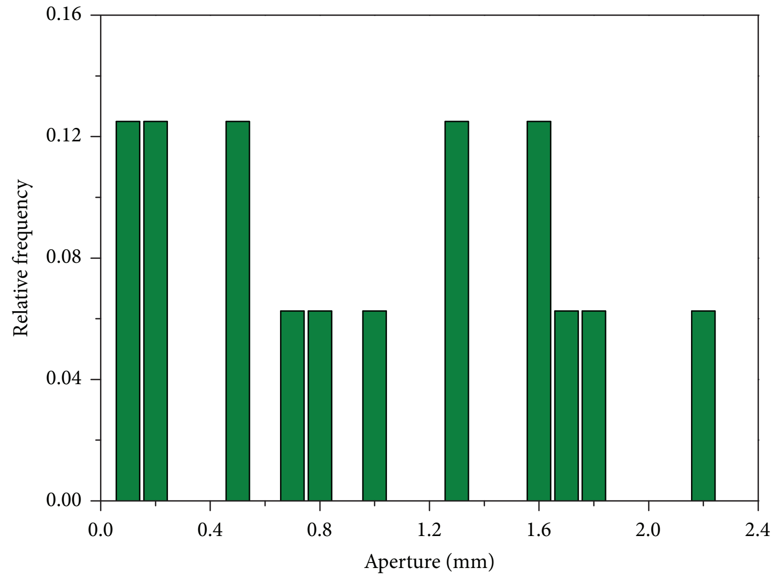

Figure 9: Distribution frequency of the aperture.

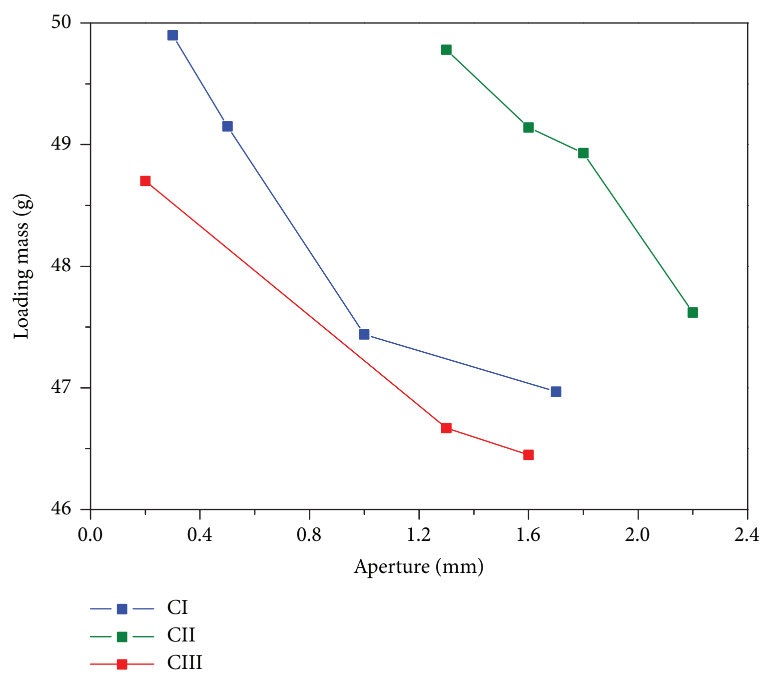

Figure 10: Loading mass at different apertures.

Table 4: Local roughness of test samples.

Test sample name	R_a (μm)	R_q (μm)	R_v (μm)
CI	270.025	330.888	772.332
CII	231.824	286.561	691.251
CIII	97.358	117.974	421.261
GHI	18.589	26.389	146.435
GHII	8.953	7.957	59.837

proportion of spontaneous imbibition near the fracture surface is smaller.

5. Calculation of the Retention Rate

According to mass conservation, the amount of the injected fluid in the formation is equal to the sum of the amount of fluid discharged and liquid retained in the fractures. The amount of liquid retained in the fractures can be decomposed

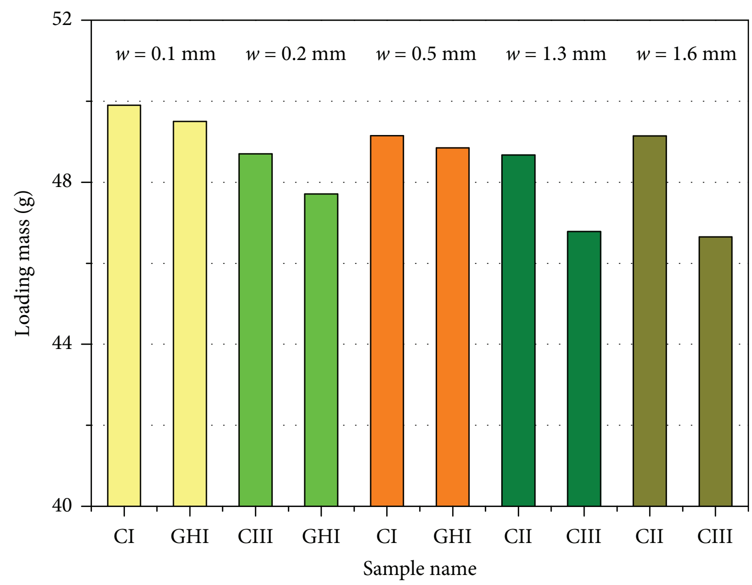

Figure 11: Loading mass at different roughness.

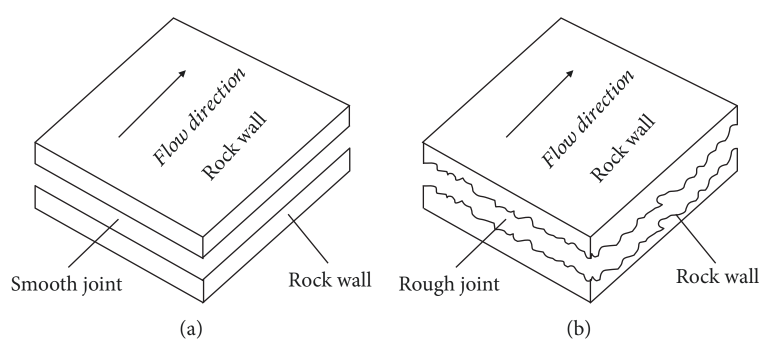

Figure 12: Model of fracture: (a) parallel plate model and (b) rough fracture model.

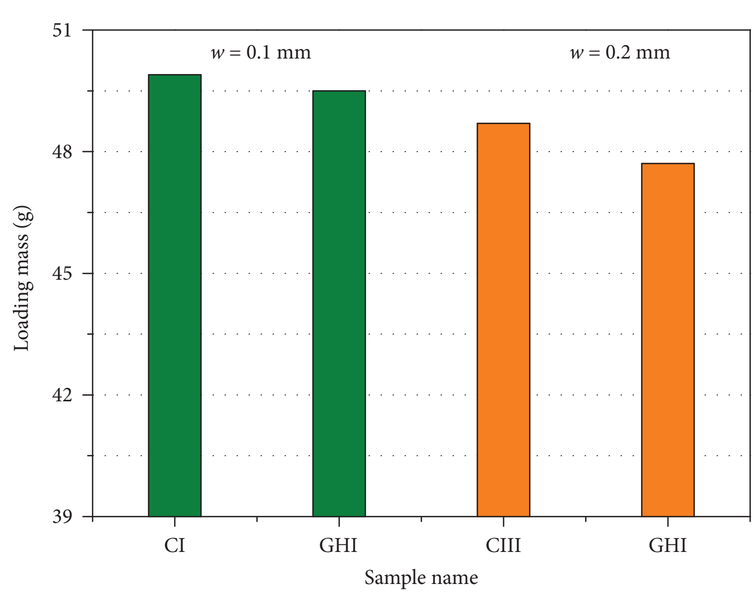

Figure 13: Loading mass at different tortuosity.

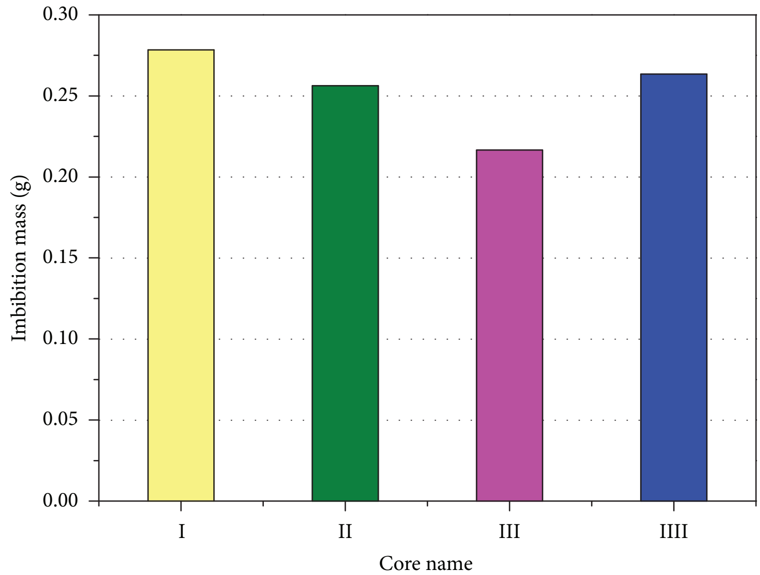

(a)

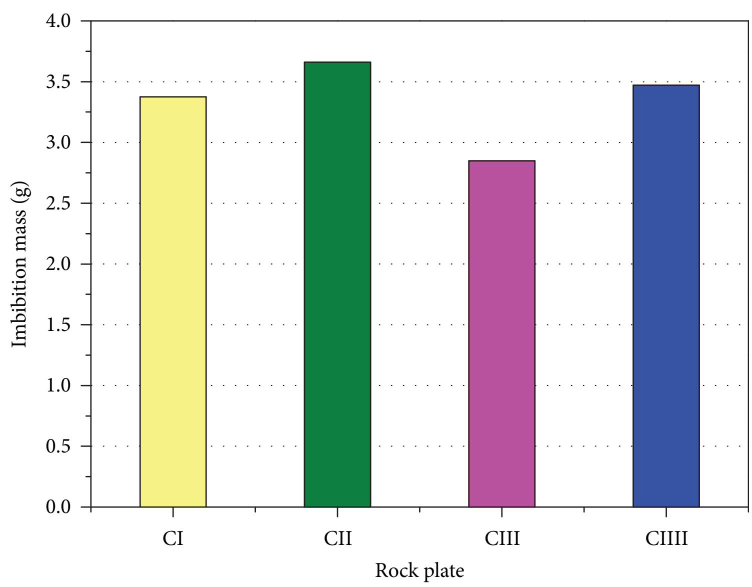

(b)

Figure 14: Single-sided imbibition: (a) standard rock imbibition and (b) test sample imbibition.

into matrix imbibition, surface-bound water film, capillary retention on the surface, viscous retention in the fractures, and the retention due to fracture "locking." They are described by using

$$\sum M = M_f + M_m + M_s + M_c + M_v + M_1, \quad (1)$$

where ΣM is the total injection mass (g), M_f is the drainage mass (g), M_m is the matrix imbibition (g), M_s is the surface-bound water film retention (g), M_c is the capillary retention (g), M_v is the viscous retention (g), and M_l is the fracture "lock" retention (g). In this study, the parameters in equation (1) can be obtained via an experiment of retention and spontaneous imbibition.

$$R = \frac{\sum M - M_f}{\sum M}, \quad (2)$$

where R is the retention rate and is a dimensionless parameter. The total injection ΣM can be obtained by integration of the pump displacement. The matrix mass after the imbibition stability is included in the numerator of (2) considering the time effect of imbibition. The retention rate of the fracturing fluid of the four groups of test

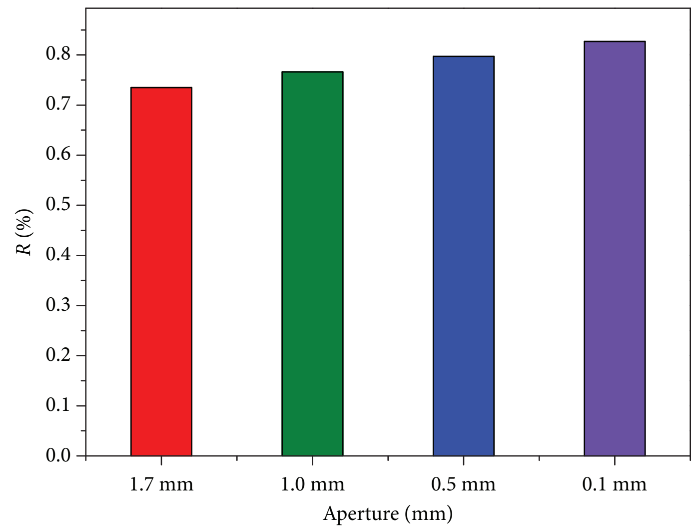

(a)

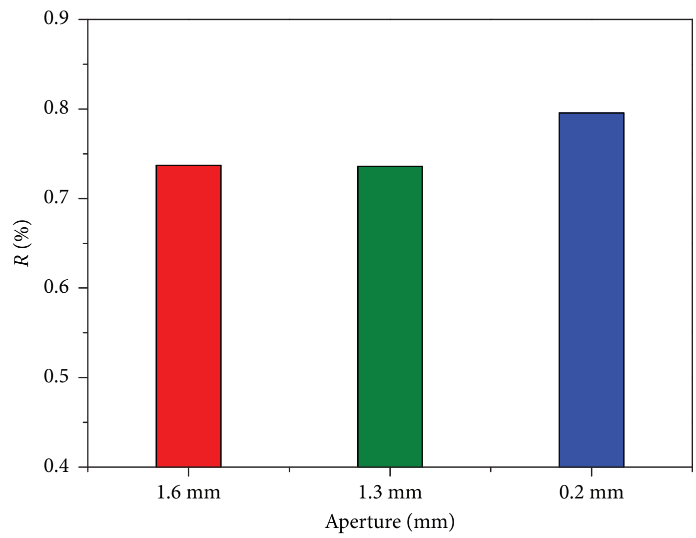

(b)

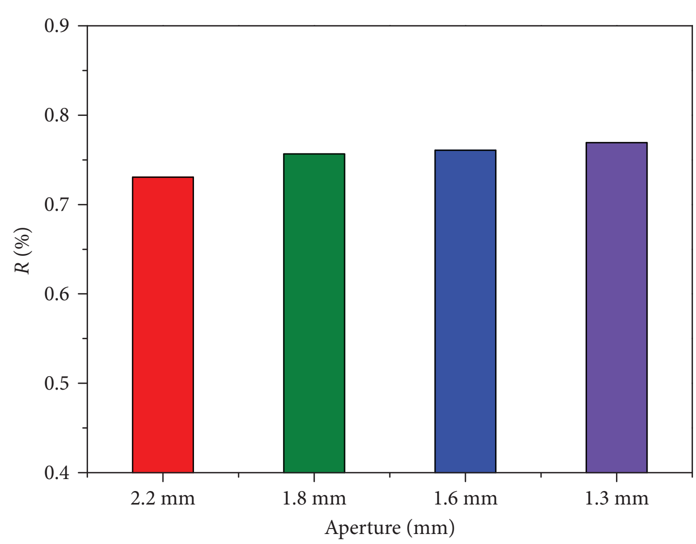

(c)

Figure 15: Continued.

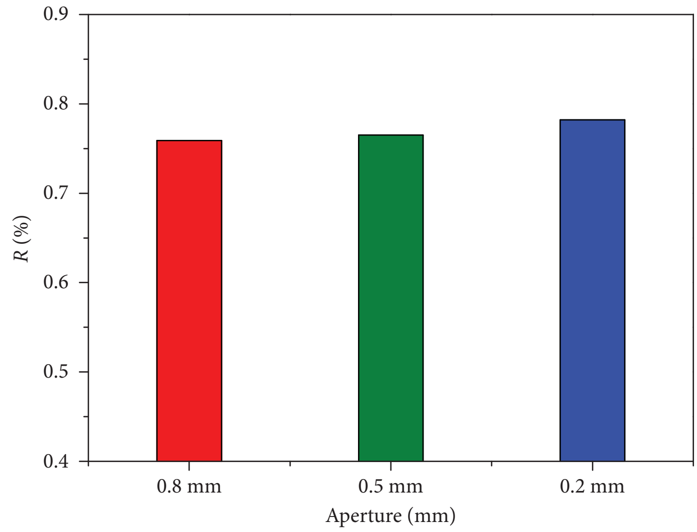

(d)

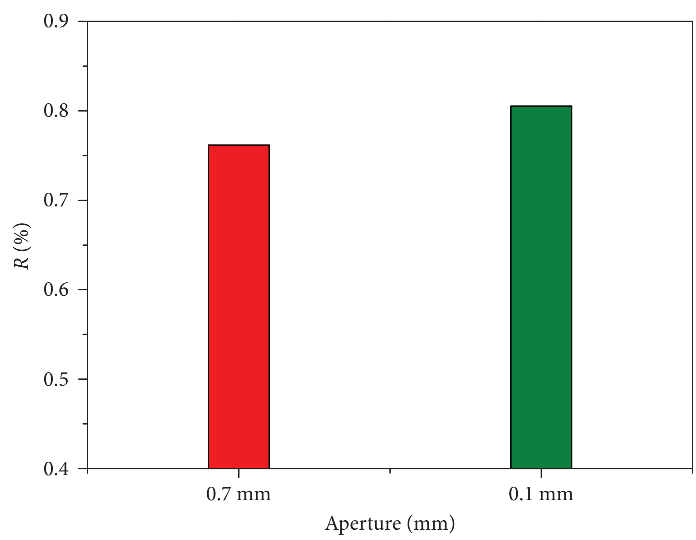

(e)

Figure 15: Retention rate at different apertures: (a) CI, (b) CII, (c) CIII, (d) GHI, and (e) GHII.

samples and a set of steel samples under different fracture apertures was obtained, as shown in Figure 15.

The retention rate decreases with the increase in aperture and maintains at 70%–85%. The retention rate of the primary fracture is between 70% and 77%, the retention rate of the secondary fracture is between 75% and 80%, and the retention rate of the microcrack is between 78% and 85%. A partition evaluation diagram of the FFR rate is shown in Figure 16.

Microcracks, secondary fractures, and primary fractures correspond to three related fracture zones. The retention rates of the microcrack and secondary fracture zones are higher than that of the primary fracture zone. The aperture increases from 0.1 mm to 2.2 mm, and the retention rate decreases from approximately 85% to 70%. The empirical formula $y = -0.024\ln x + 0.7582$ can be obtained by fitting the curve, as shown in Figure 16. The retention rates of the rough fracture are scattered on both sides of fitting line A, and the retention rates of the smooth fracture are scattered on both sides of fitting line C. With a decrease in the aperture of the primary fracture to the secondary fracture, the asperity of the fracture surface can cause local contact and retain the fluid near the contact points.

The samples were split along the bedding, and one of them was subjected to a smooth treatment. The smooth fracture surface may be damaged in the treatment process and reduce the fracturing fluid imbibition. The dry surface and the driving pressure difference are small, and the fitting points are uniformly distributed near fitting line A. Considerable retention rate points of small fractures distribute around fitting line C with great tortuosity and high retention rate. Tortuosity increases the complexity of the channels, thereby requiring high pressure and energy to drain the fluid. The retention rate becomes high with small aperture, large

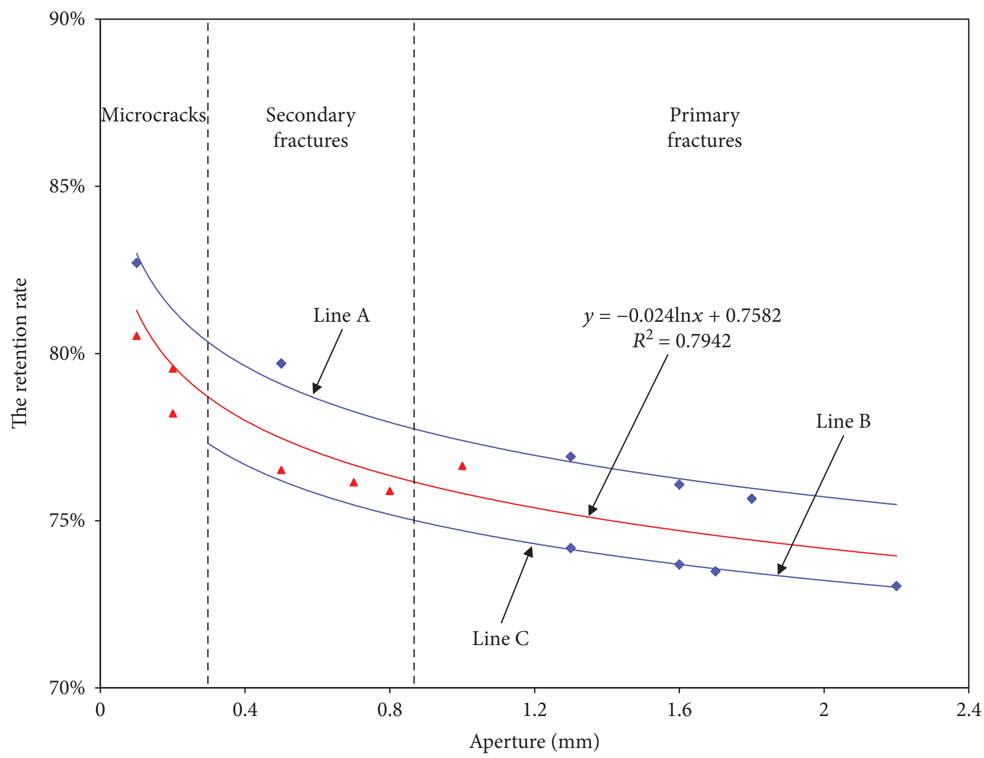

FIGURE 16: Relationship between the aperture and retention rate.

roughness, high tortuosity, and high imbibition of the matrix. Fracturing fluid is mainly trapped in fracture systems, which has different functions at various apertures. Secondary fractures and microcracks play an important role in the retention of fracturing fluid.

6. Discussion

6.1. Mechanisms of FFR. The retention of fracturing fluid in the rough fractures of tight reservoirs is controlled by various mechanisms. The predominant mechanism of FFR varies under different fracture geometry characteristics and reservoir properties. Experiments in this study were conducted to study the retention mechanism, including retention of the surface capillary force, irreducible water film, matrix imbibition, and viscous trapping in the fracture.

Restricted by experimental conditions, mechanisms not studied also include the gravity in the primary fracture and the "locking" in the microcrack [24]. The fluid flowback rate when the gas displacement direction is the same as the direction of gravity is greater than that opposite in the primary fracture [19]. Gravity segregation is an important mechanism that influences the retention in the primary fracture, which is affected by the fracture aperture, fracture height, and liquid viscosity. The retention rate becomes large with high fracture height, rough fracture surface, and high density of the network.

The viscous force and capillary force exert significant influences on the exchange of fluid in fractures and the matrix at low velocity. Viscous retention in the microcrack is caused by the viscous force, and capillary retention on the fracture surface is formed by the capillary force. The viscous retention has a significant effect with small aperture and pressure difference and great viscosity. The capillary retention is influenced by great roughness and water-wet reservoirs. The rock fracture surface will be covered with a layer of water film influenced by the content of clay minerals, formation water, and property of fracturing fluid. The surface-bound water film is another important mechanism of FFR impacted by the dryness and the property of the rock surface. The dry rock surface and strong hydrophilic rock are conducive to fluid retention, as shown in Figure 17.

"Locking" is defined as storage of liquids in rough fractures under the condition of a certain contact area and external pressure. A portion of the secondary fracture is partially supported by a proppant. The fracturing fluid is trapped in the fractures after the closure of fracture, as shown in Figure 18. The "locking" of fractures may be an important mechanism that improves formation energy, which can store high-pressure fracturing fluid. The "locking" is mainly controlled by the aperture, roughness, closure stress, and contact area. High roughness, local "locking," and large area of contact are conducive to the retention of the fracturing fluid.

Spontaneous imbibition is an important mechanism of fluid retention during the flowback affected by the porosity, clay minerals, surfactant, and injection fluid salinity. Micro–nanopores, high clay and ionic content, and wettability of the fluid are conducive to spontaneous imbibition [10, 12]. The retention mechanisms of fracturing fluid are summarized according to the retention type, controlling factor, and favorable condition, as shown in Table 5.

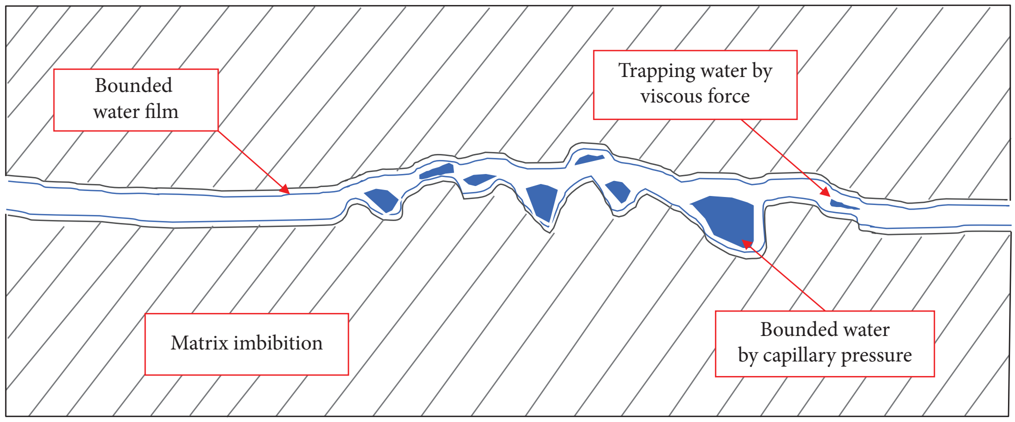

Figure 17: Fracture surface retention and viscous trapping in the fracture.

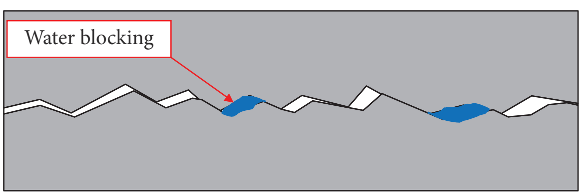

Figure 18: Fracture "locking."

6.2. Retention Rules of Fracturing Fluid. Based on the above research, we could see that the mechanism of fluid retention mainly includes gravity retention in the primary fracture, which is related to the fracture aperture. Surface-bound water film, fracture closure "locking," and viscous trapping dominate in the secondary fracture. Surface capillary retention, surface-bound water film, and matrix pore imbibition are key control factors of fluid retention in the microcracks. Retention is divided into fracture volume-dependent retention and surface-related retention. The fluid retained in fractures may be driven out owing to volume-dependent retention, whereas fluid trapped due to surface-related retention is difficult to drive out. The aperture of the primary fracture is greater than 0.9 mm. When the aperture is sufficiently large, the fluid retention is mainly affected by the fracture aperture and the gas drive pressure. However, roughness and tortuosity have minimal effects. When the aperture reaches the scale range of the secondary fracture (aperture between 0.25 and 0.7 mm), the contact of the microconvex body on the rough fracture surface will reduce the drainage of liquid. The roughness and tortuosity of the fracture play an important role in the retention of the fracturing fluid in a secondary fracture. With a further reduction in the fracture aperture, the scale range of a microcrack (less than 0.2 mm) is gradually reached. The contact area between the two joints increases.

The retention rate of the fracturing fluid in the primary fracture is approximately 30% owing to the surface tension of the proppant, wettability, and gravity [20]. The difference in the retention rate in the primary fracture between this study and previous research is attributed to the following reasons. (1) The fracture area is 64.5 cm^2, and the material is shale outcrop in this study. The fracture area is 625 cm^2, and the material is glass plate in Parmer's study. (2) A proppant was not used in the primary fracture of this study, in which the retention rate of liquid in the primary fracture may be overestimated. However, the subsidence of the proppant in the main fracture is typically considered.

Flowback is required in tight reservoirs during the later stages of fracturing. During the process of flowback, the fracturing fluid and gas are produced at the same time. The experiment simulated two stages of liquid flowback. The first stage relies on the elastic energy of the rock itself to drain the liquid in fractures. In the second stage, the incoming gas provides the power for the drainage of the liquid. The free gas generated during the formation of the fracture network can be produced and consumed continuously when the fracturing fluid is discharged in the initial stage. The gas was injected after a certain period of drainage in this experiment. When the gas-dominant channel was formed in the fracture, the capability of driving fluid dropped dramatically. Once this "breakthrough" occurred during flowback, it could aggravate the retention in fractures. The discharge of liquid is mainly dependent on the elastic energy of formation and liquid expansion without gas providing the energy of displacement.

The nozzle size can be adjusted to control the flowback speed during the period of loading water recovery. "Breakthrough" should be avoided as much as possible owing to the damage to the formation. The drainage rate represents the discharge velocity of the fracturing fluid, and it is high under large apertures in the initial stage. The presence of gas has a significant effect on the drainage rate. Development of the tight reservoir is efficient with high reservoir quality and a complex network.

6.3. Application of FFR. The engineering parameter that corresponds to the retention rate of fracturing fluid is the flowback rate in the field. A low postfracturing flowback rate for efficient and fracture-developed wells in tight reservoirs exist. Fracturing fluid entering the formation gradually diffuses into the deep part of the matrix. Yang et al. found that the capacity for spontaneous imbibition is positively correlated with the content and type of clay mineral. The

Table 5: FFR mechanisms.

Retention mechanism	Controlling factor	Favorable condition
Surface capillary retention	Wettability, surface roughness	Large roughness, hydrophilic rock, low flow rate
Surface-bound water film	Surface dryness, liquid surface properties	Dry surface, strong hydrophilicity
Matrix pore imbibition	Physical properties, liquid type, clay and ion content	Small pores, wetting liquids, high clay/ion content
Fracture closure "locking"	Contact area, fracture aperture, roughness, stress	Large contact area/stress, high roughness, small aperture
Gravity retention	Liquid viscosity, fracture aperture, roughness, fracture height	High viscous force, large aperture
Viscous trapping	Fracture aperture, drive pressure, liquid viscosity	Small aperture and pressure, high viscosity

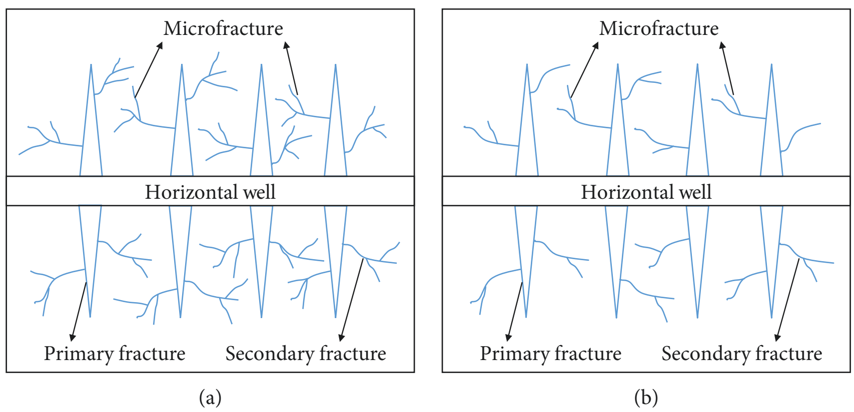

Figure 19: Comparison of fractures: (a) complex fractures and (b) simple fractures (modified from Ghanbari and Dehghanpour [24]).

volume of imbibition is larger than its pore volume [9]. Hu et al.'s research showed that the retention of fracturing fluid in organic pores is directly related to the mineral types. The thermal maturity of an organic matter and the roughness of the pores are closely related to the retention [33]. The reduced flowback rate results from the surface-bound water film, surface retention by capillary force, and matrix imbibition. A high retention rate is related to great matrix imbibition, rich organic matter content, and complex organic pore. The retention rate can reflect the reservoir property.

Multistage hydraulic fracturing usually forms multistage fractures. A large amount of fracturing fluid is injected into the formation to create fractures, accompanied by a large amount of free gas. When the fracture size is less than 0.1 mm (microcrack), the fluid entering the microcrack cannot easily flow back. When the fracture size is between 0.2 and 0.9 mm (secondary fracture), the fluid entering the secondary fracture can flow back partially. When the fracture size is larger than 0.9 mm (hydraulic fracture), the fluid entering the primary fracture is likely to flow back. A high retention rate is related to the high frequency of secondary fractures and microcracks formed in the fracture system and the high roughness and tortuosity. A good fracturing effect is related to good connectivity between the matrix and fracture, as shown in Figure 19. Compared with simple fractures, the complex fractures have more secondary and microfractures, larger stimulated volume, and more matrix imbibition. Therefore, they have a lower flowback rate and a higher initial gas production rate.

7. Conclusions

We can draw the following conclusions from the above results.

(1) Fluid is mainly retained in the fracture system, and secondary fractures and microcracks play a major role in fluid retention. The retention of fracturing fluid decreases with an increase in the fracture aperture. The retention rate of fluid will increase with the small aperture, high roughness, high tortuosity, and high matrix imbibition

(2) Gas drive can cause abrupt changes in the drainage mass and rate. When gas drive is not performed, the drainage rate decreases smoothly and the drainage mass increases steadily. After the gas drive, sufficient gas volume is related to improving drainage rate and mass. As the gas creates a "breakthrough" phenomenon in the fractures, the increase in the drainage mass tends to plateau off

(3) Liquid retention in the primary fracture is mainly affected by the fracture aperture. Liquid retention in the secondary fracture is mainly affected by the surface roughness and tortuosity. The liquid retention in the microfractures is mainly affected by the fracture aperture and surface roughness. The retained fluid related to the volume may be driven out, whereas that related to the surface is difficult to drive out

Nomenclature

R_q: Mean square roughness (μm)
R_a: Arithmetic mean deviation of roughness (μm)
R_v: Maximum height drop of roughness (μm)
ΣM: Total injection mass (g)
M_f: Drainage mass (g)
M_m: Matrix imbibition (g)
M_s: Surface-bound water film retention (g)
M_c: Capillary retention (g)
M_v: Viscous retention (g)
M_l: Fracture "lock" retention (g)
R: Retention rate (%).

Data Availability

The data used to support the findings of this study are available from the corresponding author upon request.

Conflicts of Interest

The authors declare that they have no conflicts of interest.

Acknowledgments

This work was supported by the National Science and Technology Major Project (grant number 2017ZX05039-004), the National 973 Program (grant number 2015CB250903), and the National Natural Science Foundation of China (grant number 51604287). We will also like to thank Bruker in China for measuring the rock surface morphology.

References

[1] G. E. King, "Hydraulic fracturing 101: what every representative, environmentalist, regulator, reporter, investor, university researcher, neighbor and engineer should know about estimating Frac risk and improving Frac performance in unconventional gas and oil wells," in *SPE Hydraulic Fracturing Technology Conference*, p. 80, The Woodlands, TX, USA, 2012.

[2] B. M. Robinson, S. A. Holditch, and W. S. Whitehead, "Minimizing damage to a propped fracture by controlled flowback procedures," *Journal of Petroleum Technology*, vol. 40, no. 6, pp. 753–759, 2013.

[3] D. M. Willberg, N. Steinsberger, R. Hoover, R. J. Card, and J. Queen, "Optimization of fracture cleanup using flowback analysis," in *SPE Rocky Mountain Regional/Low-Permeability Reservoirs Symposium*, p. 13, Denver, CO, USA, 1998.

[4] J. D. Weaver, N. C. Schultheiss, and F. Liang, "Fracturing fluid conductivity damage and recovery efficiency," in *SPE European Formation Damage Conference & Exhibition*, p. 12, Noordwijk, The Netherlands, 2013.

[5] P. Bedrikovetsky, A. S. L. Vaz, C. J. A. Furtado, and A. R. Serra de Souza, "Formation-damage evaluation from nonlinear skin growth during coreflooding," *SPE Reservoir Evaluation & Engineering*, vol. 14, no. 2, pp. 193–203, 2013.

[6] H. Son, H. Kim, G. Lee, J. Kim, and W. Sung, "Enhanced oil recovery using nanoparticle-stabilized oil/water emulsions," *Korean Journal of Chemical Engineering*, vol. 31, no. 2, pp. 338–342, 2014.

[7] L. He, Y. Chen, L. Ren, J. Li, and L. Liu, "Synergistic management of flowback and produced waters during the upstream shale gas operations driven by non-cooperative stakeholders," *Journal of Natural Gas Science and Engineering*, vol. 52, pp. 591–608, 2018.

[8] H. B. Lee, I. W. Yeo, and K. K. Lee, "The modified Reynolds equation for non-wetting fluid flow through a rough-walled rock fracture," *Advances in Water Resources*, vol. 53, no. 1, pp. 242–249, 2013.

[9] L. Yang, H. Ge, Y. Shen et al., "Experimental research on the shale imbibition characteristics and its relationship with microstructure and rock mineralogy," in *SPE Asia Pacific Unconventional Resources Conference and Exhibition*, p. 10, Brisbane, Australia, 2015.

[10] B. Roychaudhuri, T. T. Tsotsis, and K. Jessen, "An experimental investigation of spontaneous imbibition in gas shales," *Journal of Petroleum Science & Engineering*, vol. 111, no. 11, pp. 87–97, 2013.

[11] J. Li, W. Yu, D. Guerra, and K. Wu, "Modeling wettability alteration effect on well performance in Permian basin with complex fracture networks," *Fuel*, vol. 224, pp. 740–751, 2018.

[12] Y. Shen, H. Ge, C. Li et al., "Water imbibition of shale and its potential influence on shale gas recovery—a comparative study of marine and continental shale formations," *Journal of Natural Gas Science and Engineering*, vol. 35, pp. 1121–1128, 2016.

[13] C. A. Ehlig-Economides and M. J. Economides, "Water as proppant," in *SPE Annual Technical Conference and Exhibition*, p. 8, Denver, CO, USA, 2011.

[14] M. Mcclure, "The potential effect of network complexity on recovery of injected fluid following hydraulic fracturing," in *SPE Unconventional Resources Conference*, p. 19, The Woodlands, TX, USA, 2014.

[15] M. Wang, Y. F. Chen, G. W. Ma, J. Q. Zhou, and C. B. Zhou, "Influence of surface roughness on nonlinear flow behaviors in 3D self-affine rough fractures: lattice Boltzmann simulations," *Advances in Water Resources*, vol. 96, pp. 373–388, 2016.

[16] G. Rong, J. Yang, L. Cheng, and C. Zhou, "Laboratory investigation of nonlinear flow characteristics in rough fractures during shear process," *Journal of Hydrology*, vol. 541, pp. 1385–1394, 2016.

[17] T. Babadagli, X. Ren, and K. Develi, "Effects of fractal surface roughness and lithology on single and multiphase flow in a single fracture: an experimental investigation," *International Journal of Multiphase Flow*, vol. 68, pp. 40–58, 2015.

[18] J. Tang, K. Wu, B. Zeng et al., "Investigate effects of weak bedding interfaces on fracture geometry in unconventional reservoirs," *Journal of Petroleum Science and Engineering*, vol. 165, pp. 992–1009, 2018.

[19] M. Wang and J. Y. Leung, "Numerical investigation of fluid-loss mechanisms during hydraulic fracturing flow-back operations in tight reservoirs," *Journal of Petroleum Science & Engineering*, vol. 133, pp. 85–102, 2015.

[20] J. Parmar, H. Dehghanpour, and E. Kuru, "Displacement of water by gas in propped fractures: combined effects of gravity, surface tension, and wettability," *Journal of Unconventional Oil and Gas Resources*, vol. 5, pp. 10–21, 2014.

[21] Y. Shen, H. Ge, M. Meng, Z. Jiang, and X. Yang, "Effect of water imbibition on shale permeability and its influence on gas production," *Energy & Fuels*, vol. 31, no. 5, pp. 4973–4980, 2017.

[22] J. Cai, W. Wei, X. Hu, R. Liu, and J. Wang, “Fractal characterization of dynamic fracture network extension in porous media,” *Fractals*, vol. 25, no. 2, article 1750023, 2017.

[23] Y. Liu, J. Y. Leung, R. Chalaturnyk, and C. J. J. Virues, “Fracturing fluid distribution in shale gas reservoirs due to fracture closure, proppant distribution and gravity segregation,” in *SPE Unconventional Resources Conference*, p. 21, Calgary, Alberta, Canada, 2017.

[24] E. Ghanbari and H. Dehghanpour, “The fate of fracturing water: a field and simulation study,” *Fuel*, vol. 163, pp. 282–294, 2016.

[25] J. Tang and K. Wu, “A 3-D model for simulation of weak interface slippage for fracture height containment in shale reservoirs,” *International Journal of Solids and Structures*, vol. 144-145, pp. 248–264, 2018.

[26] J. Hampton, M. Gutierrez, L. Matzar, D. Hu, and L. Frash, “Acoustic emission characterization of microcracking in laboratory-scale hydraulic fracturing tests,” *Journal of Rock Mechanics and Geotechnical Engineering*, vol. 10, no. 5, pp. 805–817, 2018.

[27] W. Kan, S. Anusarn, and T. Jizhou, “Numerical study of flow rate distribution for simultaneous multiple fracture propagation in horizontal wells,” in *50th U.S. Rock Mechanics/Geomechanics Symposium*, p. 7, Houston, TX, USA, 2016.

[28] Y. Fu, H. Dehghanpour, D. O. Ezulike, and R. S. Jones Jr., “Estimating effective fracture pore volume from flowback data and evaluating its relationship to design parameters of multistage-fracture completion,” *SPE Production & Operations*, vol. 32, no. 4, pp. 423–439, 2017.

[29] M. A. Abbasi, D. O. Ezulike, H. Dehghanpour, and R. V. Hawkes, “A comparative study of flowback rate and pressure transient behavior in multifractured horizontal wells completed in tight gas and oil reservoirs,” *Journal of Natural Gas Science and Engineering*, vol. 17, pp. 82–93, 2014.

[30] J. Q. Zhou, S. H. Hu, S. Fang, Y. F. Chen, and C. B. Zhou, “Nonlinear flow behavior at low Reynolds numbers through rough-walled fractures subjected to normal compressive loading,” *International Journal of Rock Mechanics and Mining Sciences*, vol. 80, pp. 202–218, 2015.

[31] Y. F. Chen, J. Q. Zhou, S. H. Hu, R. Hu, and C. B. Zhou, “Evaluation of Forchheimer equation coefficients for non-Darcy flow in deformable rough-walled fractures,” *Journal of Hydrology*, vol. 529, pp. 993–1006, 2015.

[32] Z. Zhang and J. Nemcik, “Fluid flow regimes and nonlinear flow characteristics in deformable rock fractures,” *Journal of Hydrology*, vol. 477, no. 1, pp. 139–151, 2013.

[33] Y. Hu, D. Devegowda, A. Striolo et al., “The dynamics of hydraulic fracture water confined in nano-pores in shale reservoirs,” *Journal of Unconventional Oil and Gas Resources*, vol. 9, pp. 31–39, 2015.

Hindawi
Geofluids
Volume 2019, Article ID 1956715, 10 pages
https://doi.org/10.1155/2019/1956715

Research Article

Effect of Arenite, Calcareous, Argillaceous, and Ferruginous Sandstone Cuttings on Filter Cake and Drilling Fluid Properties in Horizontal Wells

Badr S. Bageri, Mohammed Benaafi, Mohamed Mahmoud, Shirish Patil, Abdelmjeed Mohamed, and Salaheldin Elkatatny

King Fahd University of Petroleum and Minerals, Dhahran, Saudi Arabia

Correspondence should be addressed to Badr S. Bageri; badr.bageri@kfupm.edu.sa

Received 29 November 2018; Revised 19 February 2019; Accepted 28 February 2019; Published 16 April 2019

Guest Editor: Bisheng Wu

Fine, small-size, drilled cuttings, if not properly separated using mud conditioning equipment at the surface, are circulated with the drilling fluid from the surface to the bottom hole. These drilled cuttings have a significant effect on the drilling fluid properties and filter cake structure. During drilling long lateral sandstone formations, different cuttings with varied properties will be generated due to sandstone formations being heterogeneous and having different mineralogical compositions. Thus, the impact of these cuttings on the drilling fluid and filter cake properties will be different based on their mineralogy. In this paper, the effect of different sandstone formation cuttings, including arenite (quartz rich), calcareous (calcite rich), argillaceous (clay rich), and ferruginous (iron rich) sandstones, on the filter cake and drilling fluid properties was investigated. Cuttings of the mentioned sandstone formations were mixed with the drilling fluid to address the effect of these minerals on the filter cake thickness, porosity, and permeability. In addition, the effect of different sandstone formation cuttings on drilling fluid density and rheology, apparent viscosity (AV), plastic viscosity PV), and yield point (YP) was investigated. High-pressure high-temperature (HPHT) fluid loss test was conducted to form the filter cake. The core sample's petrophysical properties were determined using X-ray fluorescence (XRF) and X-ray diffraction (XRD) techniques and scanning electron microscopy (SEM). The results of this work indicated that all cutting types increased the rheological properties when added to the drilling fluid at the same loadings but the argillaceous sandstone (clay rich) has a dominant effect compared to the other types because the higher clay content enhanced the rheology. From the filter cake point of view, the ferruginous sandstone improved the filter cake sealing properties and reduced its thickness, while the argillaceous cuttings degraded the filter cake porosity and permeability and allowed the finer cuttings to penetrate deeply in the filter medium.

1. Introduction

During the drilling process, an impermeable layer called a filter cake is formed on the face of the drilled formation to minimize the filtration and solid invasion [1, 2]. There are several variables that affect filter cake properties, filtration volume, and invasion depth, such as drilling fluid additives, formation properties, and well conditions (temperature, pressure, and drill pipe rotation). The drilling fluid additives highly affect the filtration properties. Therefore, intensive research has been carried out to improve the characteristics of drilling fluid additives to minimize their adverse effect on drilled formations. Currently, nanomaterials have been introduced in the drilling fluid application for different functions. Silica and ferric oxide nanoparticles were introduced to stabilize the performance of drilling fluid and improve the filter cake properties [3–6]. Nanoclay, cellulose, and polymers were used to improve the rheological properties of drilling fluid [7–9]. On the other hand, the formation permeability and lithology play a great role on the cumulative mud filtrate loss [10, 11]. Thus, the filter cake buildup through either static or dynamic conditions was simulated to understand the filter cake properties [12–15].

Although drilling fluid is carefully designed through several comprehensive API tests [16–21], it is important to control drilling fluid properties during drilling operations to control the wellbore stability and prevent formation damage [22–29]. Many factors affect drilling fluid properties while drilling, including changing the particle size of additives during the fluid circulation, passing through high-temperature formations, and contaminating the drilled formation [28, 30–32]. The key factors that cause major changes in drilling fluid properties are changing the property of drilling fluid additives and/or introducing new solids to the drilling fluid during the drilling operation. Mainly, the source of the noncontrollable solids added to the drilling fluid during the drilling process is the drilled formation particles.

In practice, solid removal equipment is installed at the surface to control the sloid content generated during the drilling process and maintain the drilling fluid properties for efficient drilling operations. Solid removal units consist of shale shakers, sand traps, desanders, desilters, and centrifuges [33, 34]. Many factors affect the overall solid removal efficiency, such as total solid content, particle size, mud properties, and cleaning equipment design. Each piece of equipment is designed to remove solids with a specific particle size range, and combining them together will increase the sloid removal efficiency [35]. Particle size is a challenging factor in the solid removal process and drilling operation, and its effect becomes more serious as the particle size decreases [33]. The desander can remove particle sizes of 40 μm to 45 μm, while the desilter can remove particle sizes of 20 to 25 micron. From a practical point of view, it is not recommended to use desanders and desilters with oil-based drilling fluids because of their very wet solid discharge [33, 34].

For long horizontal sections of the well, it has been reported that the sand content could reach 30% in the filter cake structure while drilling the sandstone is lateral with a 3000 ft. length [23]. The reported results showed that mixing the drilled sand particles with the drilling fluid while drilling had a significant impact on the drilling fluid properties [30, 36]. Furthermore, integrating high sand content with the circulated drilling fluid produced a thicker filter cake, degraded the sealing properties of the filter cake, and allowed the solids to invade into the formation [30, 37, 38]. This will reduce the productivity of the well and will require additional costs in order to stimulate the near-wellbore area. Lots of research was conducted to investigate the impact of drilling fluid properties on the wellbore stability, well integrity, and filter cake formation during the drilling operations [23–28, 36, 39].

The properties of the drilled solids contaminating the drilling fluid depend on the formation characteristics. Although, the properties of the drilled formation are based on the same clay type and amount of other contamination metals, no attention was paid on the effect of different sand types on drilling fluid and filter cake properties. For the sandstone, there are four common types—quartz arenite, ferruginous, calcareous, and argillaceous sandstones. Quartz arenite is a matrix-poor sandstone with more than 90% quartz [40]. Ferruginous sandstone is a sandstone with more than 15 percent of iron oxides (e.g., hematite). The iron oxides occur as pore-filling and grain-coating materials and stained rock with the reddish brown colour [41]. Calcareous sandstone is composed of more than 15 percent of carbonate minerals (e.g., calcite) as cementing materials. Argillaceous sandstone has significant amounts of clay minerals (e.g., kaolinite), which come from the dissolution of unstable detrital minerals such as feldspars.

In the past, a majority of the research focused on the drilled cutting rock type (i.e., sandstone and limestone), while studying the effect of different mineralogy of the same formation was not addressed. In order to address the knowledge gap, it is critically important to understand whether changing the mineralogy of the sandstone formation with a large percentage (about 30 wt.%) of calcite, clay, and iron will have major effect on filter cake porosity, sealing properties (permeability), and drilling fluid properties.

The main objective of this study is to address the effect of drilled cuttings of quartz arenite, calcareous, argillaceous, and ferruginous sandstone formations on filter cake and drilling fluid properties. The drilled cuttings were mixed with the drilling fluid in varying quantities (ranging from 15 to 30 wt.%) to study their impact on filter cake and drilling fluid properties.

2. Materials and Experiments

2.1. Rock Sample. Four types of the sandstone cores with varying mineralogy were used—quartz arenite, calcareous, argillaceous and ferruginous sandstone formations. The selected core samples were crushed to generate the drilled cuttings. From this point forward, we will refer to quartz arenite as sandstone (reference sample) and the others will be referred to as calcareous argillaceous and ferruginous.

The petrophysical properties (porosity and permeability) of the tested core samples were measured in the laboratory. The helium porosimeter was used to measure the porosity and grain density of the core samples. The gas permeabilities of the selected core samples were obtained using Hassler Core Holder Assembly.

The elemental and mineralogical composition of the cuttings were determined using X-ray fluorescence (XRF) and X-ray diffraction (XRD) techniques. The cuttings generated with the different sandstone core samples were mixed with the drilling fluid with two concentrations (15% and 30 wt.%).

2.2. Rock Sample Properties. The XRD and XRF results showed that the first core sample (the reference sample sandstone) consisted mainly of quartz (90 wt.%), whereas the amount of the quartz in the other three samples ranged between 65 and 70%. The remaining 25-30% constitutes other types of rock particles—either calcite (calcareous sandstone), clay (argillaceous sandstone), or iron (ferruginous sandstone). Figure 1 shows the difference in the mineralogy between the sandstone core samples used in the study. The detailed mineralogical composition using XRD and XRF results of the core samples is presented in Figures 2 and 3.

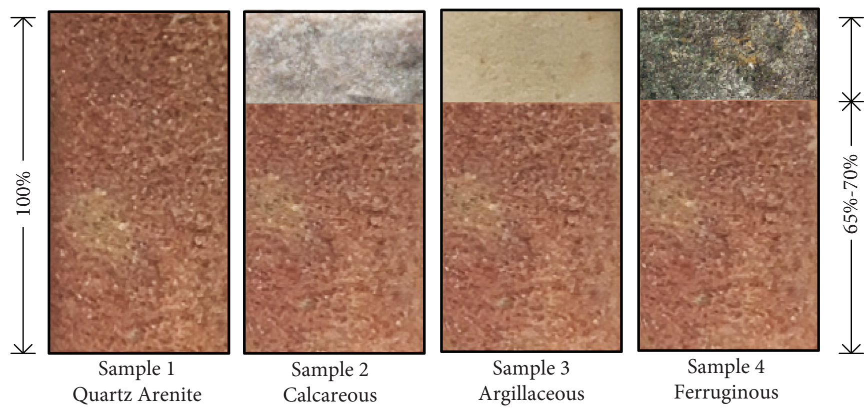

FIGURE 1: Diagram showing the difference in the mineralogy of the sandstone core samples for this work.

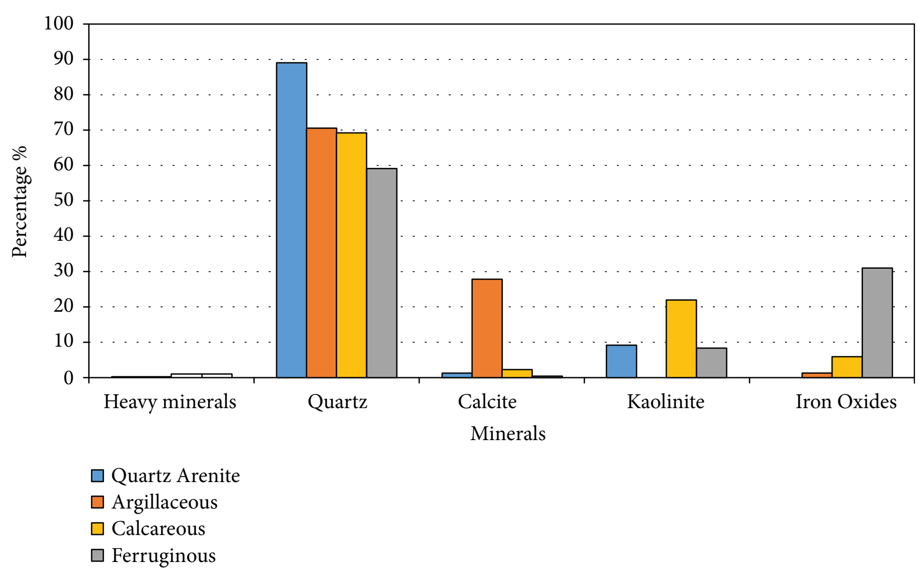

FIGURE 2: XRD results of the drilled cuttings (core samples).

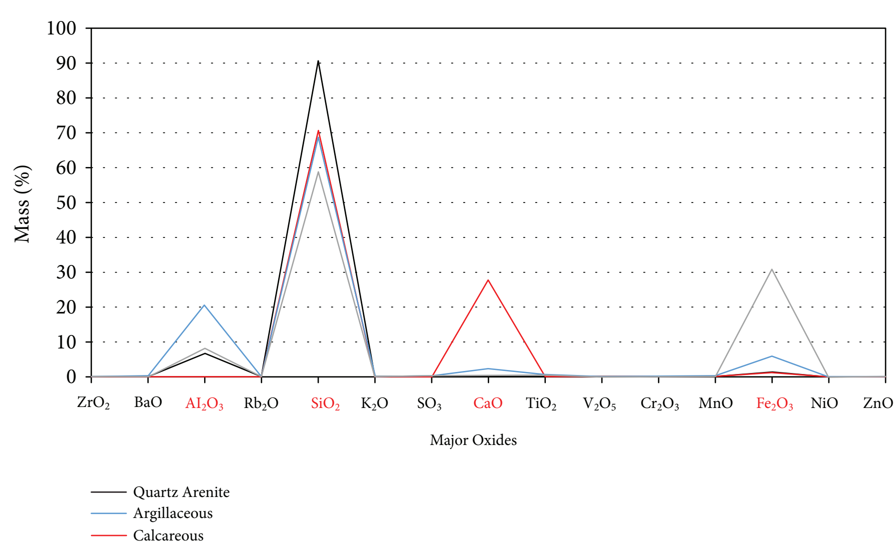

FIGURE 3: XRF results of the drilled cuttings (core samples).

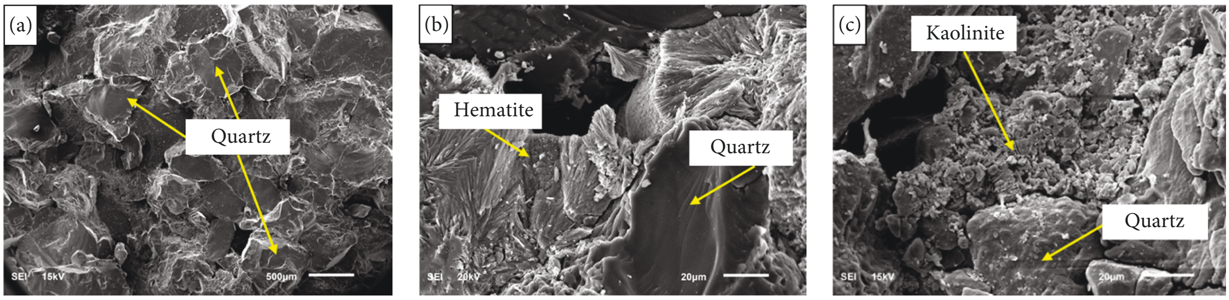

(a) (b) (c)

Figure 4: SEM photomicrographs showing (a) quartz arenite sandstone (quartz-rich sandstone), (b) ferruginous sandstone, (c) argillaceous sandstone.

Furthermore, the argillaceous and ferruginous drilled cutting particle samples were identified using scanning electron microscopy (SEM), as shown in Figure 4.

The porosity of the sandstone and argillaceous core samples (samples 1 and 3) was 28% and 17%, respectively. The other two samples, calcareous and ferruginous, displayed low porosity values of 8.5% and 2.3, respectively. The permeability measurements showed that the calcareous, argillaceous, and ferruginous sandstones displayed low permeability values, 1.3 mD, 0.67 mD, and 0.28 mD, respectively, while the first sample (sandstone) permeability was 329.5 mD.

2.3. Drilling Fluid Properties. The density and rheology of the drilling fluid was measured after adding different cutting types with different percentages (15% and 30%) using mud balance and a Fann viscometer. The cuttings generated from drilling operations vary in size from large, medium, fine, and ultrafine particles. Table 1 shows the particle size of the solids that can be separated with solid removal equipment [33]. This study focuses on the fine particles that cannot be removed with the main solid removal equipment, less than 20 μm. Therefore, the rock samples were crushed to fine powder and then sieved to make sure that only fine particles will be used.

Calcite-weighted water-based drilling fluid was used in this study. The composition of the drilling fluid is listed in Table 2. The primary properties of the base drilling fluid such as density, apparent viscosity (AV), plastic viscosity (PV), and yield point (YP) are shown in Table 3.

2.4. HPHT Fluid Loss Test. The filter cake was formed using HPHT fluid loss test. The static test was conducted at 300 psi differential pressure and 90°F. The filter cake was formed on the face of the ceramic disk. The 50 μm ceramic disk was used as a filter medium. Drilling fluid consisting of a cutting concentration of 30% was used to form the filter cake. The thickness of the ceramic disk was 6.35 mm.

Filter cake porosity ($\varnothing_c$) was determined using the equation presented by Dewan and Chenevert [42]:

$$\varnothing_c = \frac{\alpha}{\alpha + \left(\rho_f / \rho_g\right)}, \tag{1}$$

where ρ_f and ρ_g are the fluid and the grain densities, respectively, and α is measured using the following equation [42]:

$$\alpha = \frac{\text{net wet weight of the filter cake}}{\text{net dry weight of the filter cake}} - 1. \tag{2}$$

The weight of the filter cake over the saturated ceramic disk was recorded. After this step, the disk with the filter cake was placed in the oven for 24 hrs, at 100°C in order to evaporate the water [23]. The dry weight of the filter cake was recorded after this step.

The permeability of the formed filter cake (K_c) was calculated using Khatib [43] correlation for the water-based $CaCO_3$ mud:

$$K_c = 112.7\, e^{-8.8(1-\varnothing_c)}. \tag{3}$$

2.5. Solubility Test. Solubility experiments were conducted to investigate the effect of the drilled cuttings (of different sandstone formations) on the filter cake removal efficiency. One gram of the solids was added to 50 mL of GLDA (20 wt.%) at a pH of 4 [23]. Solids contain 70 wt.% weighting material (calcite) and 30 wt.% drilled cuttings. The experiments were performed at 100°C under static conditions for 24 hours.

3. Results and Discussion

3.1. Effect of Cutting Content on Drilling Fluid Properties. The cuttings generated with the different core samples were mixed with the drilling fluid with concentrations of 15% and 30 wt.%. This range of the cutting content was observed as the maximum amount of sand content that may contaminate the drilling fluid while drilling long horizontal sections [12, 23]. The effect of different sandstone cutting content (quartz arenite, calcareous, argillaceous, and ferruginous) on drilling fluid density was not significant. The drilling fluid density of the base fluid was 10.5 ppg, while the density of the drilling fluid mixed with sandstone cuttings was in the range 10.5 to 11 ppg. This is due to the similarity in the weighting agent density ($CaCO_3$ = 2.71 gm/cc) and the density of the mixed sand contents—quartz arenite (2.64 gm/cc), calcareous (2.69 gm/cc), argillaceous (2.68 gm/cc), and ferruginous (2.84 gm/cc).

Table 1: Solid removal by type of equipment.

Equipment	Particle size (μm)
Shale shaker	>74
Mud cleaner	>74
Desander	>45
Desilter	>20-25
Centrifuge	<8

Table 2: Drilling fluid formulation.

Component	Description	Units	Function
Water	308	cc	Base
Defoamer	0.08	g	Antifoam agent
XC polymer	1.5	g	Viscosifier
Starch	6	g	Loss circulation control
KCl	80	g	Clay stabilizer
KOH	0.3	g	pH adjustment
Sodium sulfide	0.25	g	Oxygen scavenger
$CaCO_3$ (MED)	80	g	Weighting material

Table 3: Drilling fluid properties.

Property	Value	Units
Apparent viscosity (AV)	24.1	cP
Plastic viscosity (PV)	15.1	cP
Yield point (YP)	18	lb/100 ft^2
Gel strength (GS) (10 sec)	13	lb/100 ft^2
Gel strength (GS) (10 min)	14	lb/100 ft^2
Density	10.3	ppg
pH	10.5	—

Increasing the concentration of the cutting content resulted in a noticeable increase in the drilling fluid viscosity. Particularly, as shown in Figure 5, the results demonstrate that the apparent viscosity of the drilling fluid consisting of 15 wt.% of argillaceous was the highest compared to the reference samples (quartz arenite-based drilling fluid) and the other two samples, calcareous- and ferruginous-based drilling fluids. Similar observations for the drilling fluid mixed with argillaceous sandstone cuttings were demonstrated for the other rheological parameters (plastic viscosity, yield point) in Figures 6 and 7. On the other hand, there was a minor variation in the drilling fluid gel strength (10 min and 10 sec) for all drilling fluids, as seen in Figure 8.

Based on the results obtained by this study, the experimental data of AV and PV show linear fitting of the drilling fluid AV and PV across the sand contents of the four different sandstone cuttings as shown in Figures 5 and 6, respectively. This finding is in agreement with the linear relationship reported for invert emulsion drilling fluid viscosity as a function of the sand content [36].

The highly rich clay cutting (argillaceous) drilling fluid showed the highest apparent viscosity compared to other drilling fluids (Figure 5). This can be attributed to the high clay content of the drilled cuttings mixed with the drilling fluid and enhanced drilling fluid rheology. This behavior of the argillaceous cutting confirmed the use of clay particles as viscosifier additives. In the same range, the 30 wt.% cutting content for the other two samples, calcareous and ferruginous, shows higher AV (Figure 5), PV (Figure 6), YP (Figure 7), and GS (Figure 8) values than that of the quartz arenite.

These results demonstrate that the drilled formation mineralogical composition has a strong impact on the drilling fluid rheological properties and this may affect the drilling operations. Drilling and mud engineers on the wellsite have to monitor the drilling fluid properties regularly and adjust these properties due to the contamination of the drilled formation cuttings.

3.2. Effect of Cutting Content on Filter Cake Properties. The filter cake thickness was measured at the end of the fluid loss test. To ensure accuracy, the measurement was conducted through different points [14]. An average of these values was taken as the final value of the filter cake thickness, as presented in Figure 9. The experimental data shows that the thickness of the filter cake for the base mud was around 2.9 mm. The results established that adding the same amounts of drilled cuttings of quartz arenite, calcareous, argillaceous, and ferruginous sandstone formations does not have the same effect on the filter cake thickness. As shown in Figure 9, it is clearly observed that there is a minor increase in the filter cake thickness by adding the quartz arenite. Calcareous sandstone also produced a thicker filter cake, while the ferruginous and argillaceous sandstones formed a very thin filter cake at the same test conditions.

The results of filter cake porosity and permeability are presented in Figure 10. In order to gain a deeper understanding of the effect on filter cake structure, both results for the thickness and permeability were linked together. For the quartz arenite sandstone, the sealing properties of the filter cake were not affected by mixing this type of cutting with the drilling fluid (i.e., mostly the filter cake porosity and permeability have the same values of the base drilling filter cake with a slight increase). Thus, the rate of building the filter cake mostly will be the same. The slight increment in the filter cake thickness formed by arenite sandstone can be attributed to the slight increment in the filter cake permeability of this sample, Figure 10.

On the other hand, the calcite-rich sandstone particles (calcareous) produced a thicker filter cake compared to the other drilling fluids. This can be attributed to the bad bridging of the calcite particles when mixed with the drilling fluid. This is very crucial while drilling calcite-rich sandstone formations, and care should be taken by adjusting the drilling fluid composition to eliminate the formation of a thick mud cake.

For the argillaceous-based drilling fluid, although the filter cake thickness was lower than the thickness of the filter cake formed by the base drilling fluid, the sealing properties of the formed filter cake were poor. The highest filter cake permeability was observed for this type of cutting. Consequently, the fine particles still find a way to invade the filter

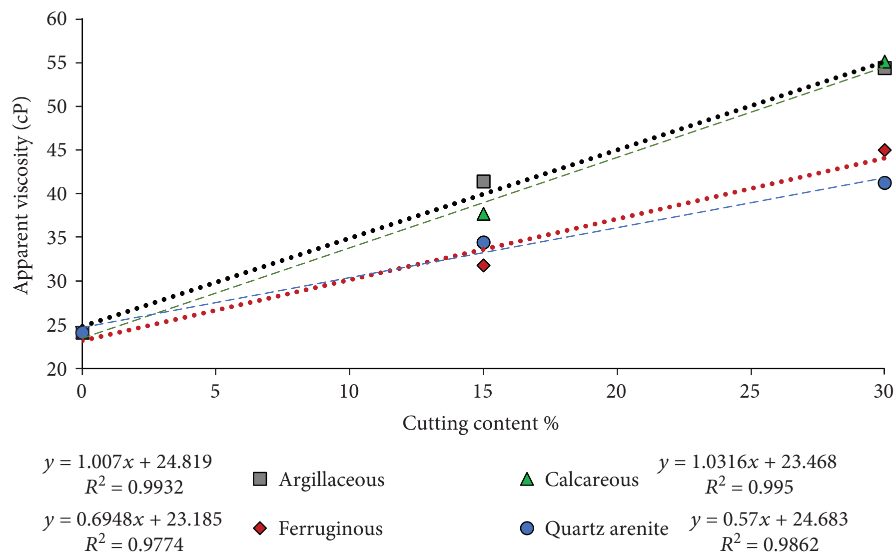

Figure 5: Drilling fluid apparent viscosity.

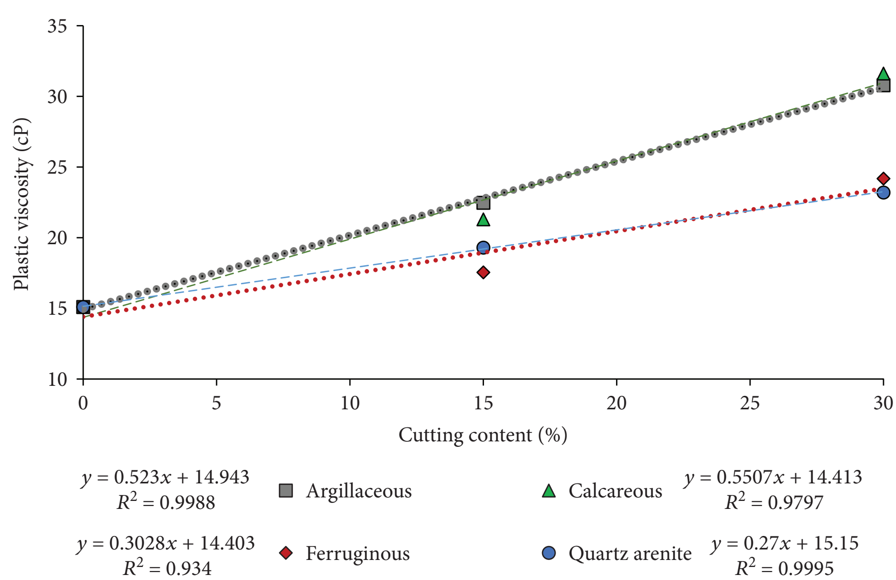

Figure 6: Drilling fluid plastic viscosity.

medium. Therefore, it is not just a matter of reducing the filter cake thickness; emphasis must be placed on providing good sealing properties as well. The high amount of solid invasion was confirmed by taking the weight of the ceramic disc of this sample after removing the filter cake and comparing it with the original weight of the ceramic disc before the filter cake was deposited.

Finally, for the ferruginous sandstone, the results show that there is an improvement in the filter cake permeability but the thickness was too small compared to the other samples. Typically, if the filter cake permeability is low, the filtration rate will be reduced, which will minimize the solid precipitation and invasion. This observation confirmed that the ferric oxide can deposit a filter cake with better characteristics. Several studies were conducted to evaluate the effect of ferric oxide nanoparticles on the sealing properties of filter cake [4, 15, 44–47]. It was proved that ferric oxide particles effectively improve the sealing properties of the filter cake and form a thin, non-erodible filter cake with low permeability and filtrate invasion into the formation. This is attributed to the high positive charge (+39.5 to 45 mV at 78°F) of ferric oxide particles, which indicates a high potential stability in suspension, thus leading to better particle dispersion and filter cake structure [47].

It was found that the drilled cuttings reduced the solubility by 25-30% when compared with the clean fluid. Consequently, the process of filter cake removal in the presence of drilled cuttings becomes more difficult as shown in Table 4. The results of this section confirmed the same observation reported in the previous study [23].

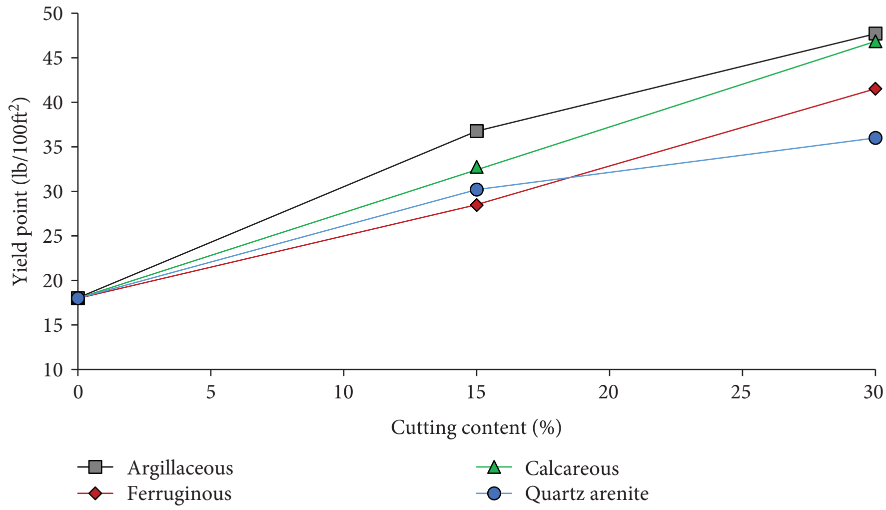

Figure 7: Drilling fluid yield strength.

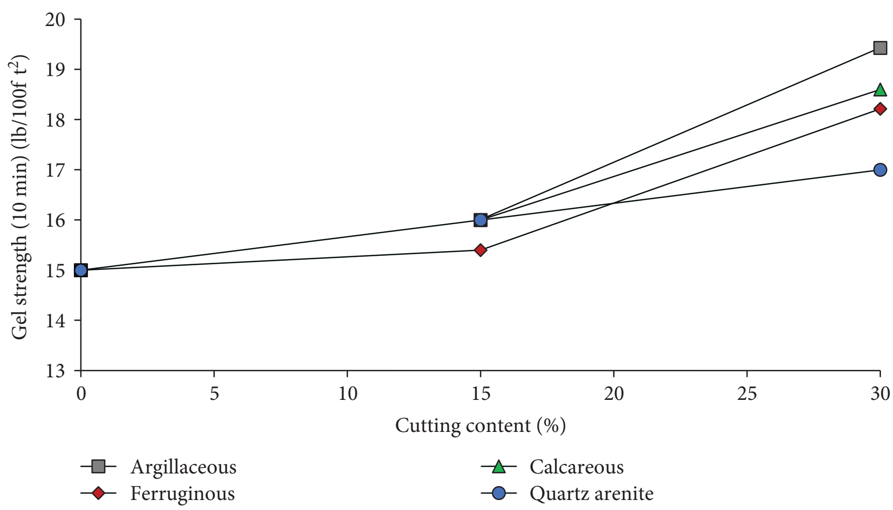

Figure 8: Drilling fluid gel strength (10 min).

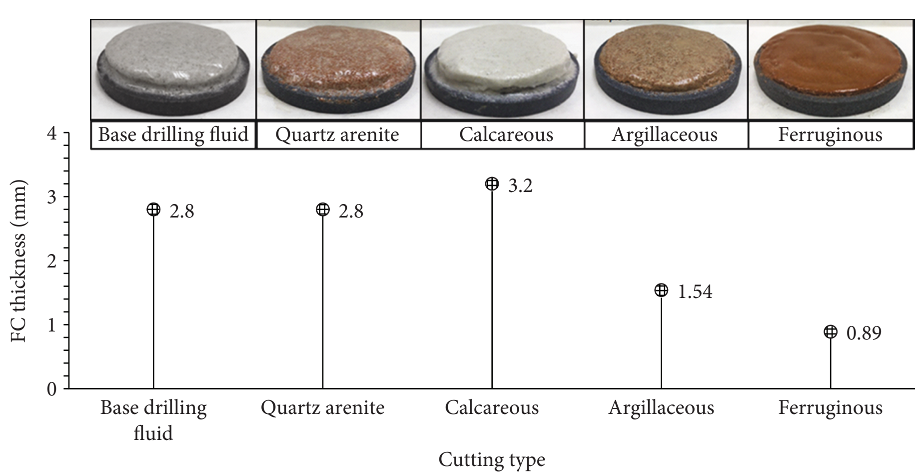

Figure 9: Filter cake thickness of different cutting types.

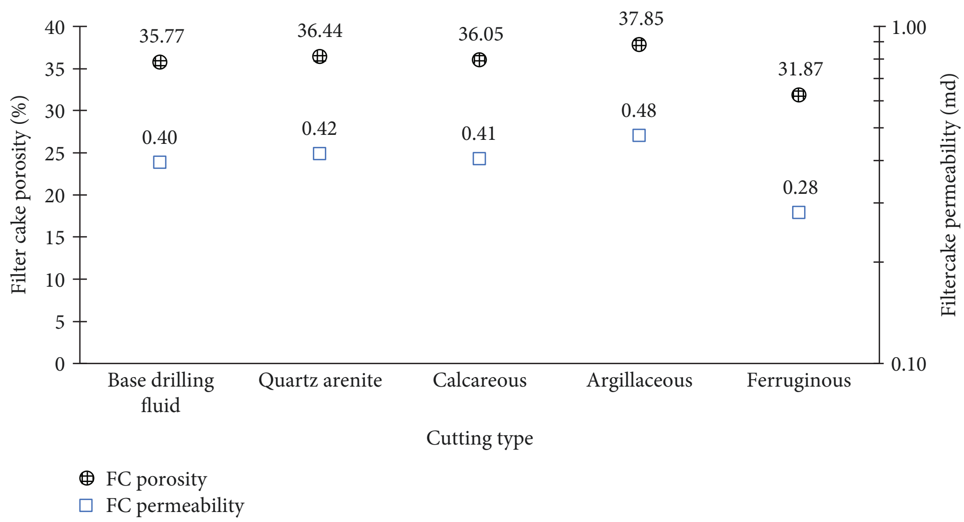

Figure 10: Filter cake porosity and permeability.

Table 4: Solubility for different types of sandstone cuttings.

Experiment no.	Solid description		Total solids weight (gm)	Solvent	Solubility (%)
	Weighting material (calcite)	Cutting particles			
1	1 gm	0 gm	1 gm	GLDA 20 wt.% low pH (pH = 4) at 100°C	92.45
2	0.7 gm	0.3 gm quartz arenite	1 gm		64.60
3	0.7 gm	0.3 gm calcareous	1 gm		68.76
4	0.7 gm	0.3 gm argillaceous	1 gm		66.35
5	0.7 gm	0.3 gm ferruginous	1 gm		65.32

4. Conclusions

This experimental study was conducted to address the effect of drilled cuttings of quartz arenite, calcareous, argillaceous, and ferruginous sandstone concentration on filter cake and drilling fluid properties. This work was conducted using two cutting concentrations (15 and 30 wt.% of the drilling fluid) to investigate the effect of sand-cutting mineralogy on the drilling fluid and filter cake properties. Based on the obtained results, the following conclusions are drawn:

(1) As the quartz arenite, calcareous, argillaceous, and ferruginous sandstone formation cutting contents increased in the drilling fluid, the rheological properties (AV, PV, YP, and gel strength) increased

(2) For cutting concentrations lower than 15%, the results showed that the argillaceous-based drilling fluid viscosity was the highest compared to those of the other drilling fluid types. Ferruginous sandstone drilled cuttings improved the yield point plastic viscosity ratio. YP/PV ratio increased from 1.2 (based fluid) to 1.58

(3) For high cutting concentrations, 30 wt.%, argillaceous and calcareous had the highest drilling fluid viscosity. Ferruginous-based drilling fluid reported the lowest increase in plastic viscosity as compared with other formulations

(4) Calcareous- and arenite-based drilling fluids produced higher filter cake thickness compared to ferruginous- and argillaceous-based drilling fluids

(5) Ferruginous sandstone drilled cuttings produced the ideal filter cake. The based drilling fluid filter cake thickness was reduced by 66% after adding 30% of ferruginous sandstone. In addition, the filter cake permeability was reduced by 25%.

(6) Finally, increasing the argillaceous cutting content in the filter cake increased the permeability of the filter cake and allowed the solid particles of the filter cake to invade the formation more deeply

Data Availability

The data used to support the findings of this paper are included within the article.

Conflicts of Interest

The authors declare that there are no conflicts of interest regarding the publication of this paper.

Acknowledgments

This work was financially supported by the College of Petroleum Engineering & Geosciences (CPG) at King Fahd University of Petroleum and Minerals, Dhahran, Saudi Arabia.

References

[1] J. A. T. Bourgoyne, K. K. Millheim, M. E. Chenevert, and J. F. S. Young, *Applied Drilling Engineering*, Society of Petroleum Engineering, 1991.

[2] M. E. Hossain and A. A. Al-Majed, *Fundamentals of Sustainable Drilling Engineering*, Scrivener, 2015.

[3] J. Cai, S. Gu, F. Wang et al., "Decreasing coalbed methane formation damage using microfoamed drilling fluid stabilized by silica nanoparticles," *Journal of Nanomaterials*, vol. 2016, Article ID 9037532, 11 pages, 2016.

[4] O. Mahmoud, H. A. Nasr-el-Din, Z. Vryzas, and V. Kelessidis, "Effect of ferric oxide nanoparticles on the properties of filter cake formed by calcium bentonite-based drilling muds," *SPE Drilling & Completion*, vol. 33, no. 4, pp. 363–376, 2018.

[5] R. Rafati, S. R. Smith, A. Sharifi Haddad, R. Novara, and H. Hamidi, "Effect of nanoparticles on the modifications of drilling fluids properties: a review of recent advances," *Journal of Petroleum Science and Engineering*, vol. 161, pp. 61–76, 2018.

[6] H. Mao, Z. Qiu, Z. Shen, W. Huang, H. Zhong, and W. Dai, "Novel hydrophobic associated polymer based nano-silica composite with core–shell structure for intelligent drilling fluid under ultra-high temperature and ultra-high pressure," *Progress in Natural Science: Materials International*, vol. 25, no. 1, pp. 90–93, 2015.

[7] D. Pan, C. Vipulanandan, N. Amani, S. A. Reddy, and C. G. Chockalingam, "Effects of nanoclay on the rheological properties and resistivity of synthetic based drilling fluids under high temperature," in *Offshore Technology Conference*, Houston, Texas, USA, May 2018.

[8] M. C. Li, Q. Wu, K. Song, Y. Qing, and Y. Wu, "Cellulose nanoparticles as modifiers for rheology and fluid loss in bentonite water-based fluids," *ACS Applied Materials & Interfaces*, vol. 7, no. 8, pp. 5006–5016, 2015.

[9] H. M. Ahmad, M. S. Kamal, and M. A. Al-Harthi, "Rheological and filtration properties of clay-polymer systems: impact of polymer structure," *Applied Clay Science*, vol. 160, pp. 226–237, 2018.

[10] C. Ezeakacha, S. Salehi, A. Ghalambor, and M. Karimi, "An integrated study of mud plastering effects for reducing filtrate's invasion," in *SPE International Conference and Exhibition on Formation Damage*, Lafayette, Louisiana, USA, February 2016.

[11] C. P. Ezeakacha, S. Salehi, and H. Bi, "How does rock type and lithology affect drilling fluid's filtration and plastering," in *AADE National Technical Conference and Exhibition*, Houston Texas, April 2017.

[12] M. Mahmoud, B. S. Bageri, S. Elkatatny, and S. H. al-Mutairi, "Modeling of filter cake composition in maximum reservoir contact and extended reach horizontal wells in sandstone reservoirs," *Journal of Energy Resources Technology*, vol. 139, no. 3, article 032904, 2017.

[13] J. T. Dewan and M. E. Chenevert, "Mud cake build-up and invasion in low permeability formations: application to permeability determination by measurement while drilling," in *SPWLA 34th Annual Logging Symposium*, Onepetro, 1993.

[14] B. S. Bageri, S. H. Al-Mutairi, and M. A. Mahmoud, "Different techniques for characterizing the filter cake," in *SPE Middle East Unconventional Gas Conference and Exhibition*, Muscat, Oman, January 2013.

[15] S. Salehi, S. A. Madani, and R. Kiran, "Characterization of drilling fluids filtration through integrated laboratory experiments and CFD modeling," *Journal of Natural Gas Science and Engineering*, vol. 29, pp. 462–468, 2016.

[16] J. M. Peden, M. R. Avalos, and K. G. Artur, "The analysis of the dynamic filtration and permeability impairment characteristics of inhibited water based muds," in *SPE Formation Damage Control Symposium*, Lafayette. LA, March 1982.

[17] A. Hartmann, M. Özerler, C. Marx, and H. J. Neumann, "Analysis of mudcake structures formed under simulated borehole conditions," *SPE Drilling Engineering*, vol. 3, no. 4, pp. 395–402, 1988.

[18] R. M. Hodge, B. G. Augustine, R. C. Burton, W. W. Sanders, and D. A. Stomp, "Evaluation and selection of drill-in-fluid candidates to minimize formation damage," *SPE Drilling & Completion*, vol. 12, no. 3, pp. 174–179, 1997.

[19] J. Simpson, "Drilling fluid filtration under stimulated downhole conditions," in *SPE ATME Symposium on Formation Damage Control*, New Orleans, LA, February 1974.

[20] R. Murphy, D. Jamison, T. Hemphill, S. Bell, and C. Albrecht, "Apparatus for measuring the dynamic solids settling rates in drilling fluids," in *SPE Annual Technical Conference and Exhibition*, San Antonio, Texas, U.S.A., September 2006.

[21] X. Qin, H. Lu, Y. Li et al., "Preparation and evaluation of a profile control agent base on waste drilling fluid," *Journal of Chemistry*, vol. 2017, Article ID 3737510, 7 pages, 2017.

[22] M. Mahmoud, B. Ba Geri, K. Abdelgawad et al., "Evaluation of the reaction kinetics of diethylenetriaminepentaacetic acid chelating agent and a converter with barium sulfate (barite) using a rotating disk apparatus," *Energy & Fuels*, vol. 32, no. 9, pp. 9813–9821, 2018.

[23] B. S. Ba geri, M. Mahmoud, S. H. al-Mutairi, and A. Abdulraheem, "Effect of sand content on the filter cake properties and removal during drilling maximum reservoir contact wells in sandstone reservoir," *Journal of Energy Resources Technology*, vol. 138, no. 3, article 032901, 2016.

[24] J. M. Davison, G. Daccord, L. P. Prouvost, and A. Gilmour, "Rig-site monitoring of the drilling fluid solids content and solids-control equipment discharge," *SPE Drilling & Completion*, vol. 14, no. 2, pp. 130–138, 1999.

[25] T. H. Omland, A. Saasen, K. Taugbol et al., "Improved drilling process control through continuous particle and cuttings monitoring," in *SPE Digital Energy Conference and Exhibition*, Houston, Texas, U.S.A, April 2007.

[26] A. Saasen, T. H. Omland, S. Ekrene et al., "Automatic measurement of drilling fluid and drill-cuttings properties," *SPE Drilling & Completion*, vol. 24, no. 4, pp. 611–625, 2009.

[27] E. Pitoni, D. A. Ballard, and R. M. Kelly, "Changes in solids composition of reservoir drill in fluids during drilling and the impact on filter cake properties," in *SPE European Formation Damage Conference*, The Hague, Netherlands, June 1999.

[28] P. Xu, H. Q. Xiong, X. L. Pu, J. Q. Liu, and X. Liu, "Polymer drilling fluid with micron-grade cenosphere for deep coal seam," *Journal of Chemistry*, vol. 2015, Article ID 967653, 9 pages, 2015.

[29] H. Wu, P. Chen, X. Fan et al., "Research on rapid identification and evaluation technology for gas formation during

underbalanced drilling," *Geofluids*, vol. 2017, Article ID 2742637, 8 pages, 2017.

[30] B. S. Bageri, A. Al-Majed, S. H. Al-Mutairi, A. Ul-Hamid, and A. Sultan, "Evaluation of filter cake mineralogy in extended reach and maximum reservoir contact wells in sandstone reservoirs," in *Drilling Conference and Exhibition*, Amsterdam, The Netherlands, March 2013.

[31] L. E. Bartlettt, "Effect of temperature on the flow properties of drilling fluids," in *Annual Fall Meeting of the SPE of AIME*, kuston, Tex, October 1967.

[32] R. Bland, G. Mullen, Y. Gonzalez, F. Harvey, and M. Pless, "HP/HT drilling fluid challenges," in *Asia Pacific Drilling Technology Conference and Exhibition*, Bangkok, Thailand, November 2006.

[33] E. E. Bouse and J. E. Carrasquero, "Drilling mud solids control and waste management," in *SPE Latin America Petroleum Engineering Conference*, Caracas, Venezuela, March 1992.

[34] J. C. Machado and P. F. Castilho, "Solids control and low-solids: important binary to drill deep wells," in *SPE Latin America Petroleum Engineering Conference*, Caracas, Venezuela, March 1992.

[35] G. S. Ormsby, "Drilling fluid solids removal," in *Drilling Practices Manual*, pp. 133–204, Society of Petroleum Engineers, 2016.

[36] B. S. Bageri, S. Elkatatny, M. Mahmoud, and A. A. Majed, "Impact of sand content on filter cake and invert emulsion drilling fluid properties in extended reach horizontal wells," *International Journal of Oil, Gas and Coal Technology*, vol. 19, no. 2, p. 135, 2018.

[37] B. S. Bageri, M. A. Mahmoud, A. S. Sultan, S. H. Al-Mutairi, and A. Abdulraheem, "Effect of the drilled cuttings on filter cake sealing properties and internal invasion depth in MRC wells," in *Oil & Gas Show and Conference*, Mishref, Kuwait, October 2015.

[38] B. S. Bageri, M. A. Mahmoud, S. H. Al-Mutairi, and A. Abdulraheem, "Filter cake porosity and permeability profile along the horizontal well and their impact on filter cake removal," in *International Petroleum Technology Conference*, Doha, Qatar, December 2015.

[39] T. Liang, F. Gu, E. Yao et al., "Formation damage due to drilling and fracturing fluids and its solution for tight naturally fractured sandstone reservoirs," *Geofluids*, vol. 2017, Article ID 9350967, 9 pages, 2017.

[40] F. J. Pettijohn, P. E. Potter, and R. Siever, *Sand and Sandstone*, Springer-Verlag, 1974.

[41] R. L. Folk, "Petrology of sedimentary rocks," 1980.

[42] J. T. Dewan and M. E. Chenevert, "A model for filtration of water-base mud during drilling: determination of mudcake parameters," *Society of Petrophysicists and Well-Log Analysts*, vol. 42, no. 3, pp. 237–250, 2001.

[43] Z. I. Khatib, "Prediction of formation damage due to suspended solids: modeling approach of filter cake buildup in injectors," in *SPE Annual Technical Conference and Exhibition*, New Orleans, Louisiana, September 1994.

[44] M. M. Barry, Y. Jung, J. K. Lee, T. X. Phuoc, and M. K. Chyu, "Fluid filtration and rheological properties of nanoparticle additive and intercalated clay hybrid bentonite drilling fluids," *Journal of Petroleum Science and Engineering*, vol. 127, pp. 338–346, 2015.

[45] O. Mahmoud, H. A. Nasr-El-Din, Z. Vryzas, and V. C. Kelessidis, "Using ferric oxide and silica nanoparticles to develop modified calcium bentonite drilling fluids," *SPE Drilling & Completion*, vol. 33, no. 1, pp. 012–026, 2018.

[46] Z. Vryzas, O. Mahmoud, H. A. Nasr-El-Din, and V. C. Kelessidis, "Development and testing of novel drilling fluids using Fe2O3 and SiO2 nanoparticles for enhanced drilling operations," in *International Petroleum Technology Conference*, Doha, Qatar, December 2015.

[47] O. Mahmoud, H. A. Nasr-El-Din, Z. Vryzas, and V. C. Kelessidis, "Characterization of filter cake generated by nanoparticle-based drilling fluid for HP/HT applications," in *SPE International Conference on Oilfield Chemistry*, Montgomery, Texas, USA, April 2017.

Hindawi
Geofluids
Volume 2019, Article ID 1201958, 21 pages
https://doi.org/10.1155/2019/1201958

Research Article

Modelling of Time-Dependent Wellbore Collapse in Hard Brittle Shale Formation under Underbalanced Drilling Condition

Shanpo Jia,[1,2] Zhiqiang Xiao,[3] Bisheng Wu,[4] Caoxuan Wen,[3] and Lufeng Jia[3]

[1]*Institute of Unconventional Oil & Gas, Northeast Petroleum University, Daqing 163318, China*
[2]*State Key Laboratory of Oil & Gas Reservoir Geology and Exploitation, Southwest Petroleum University, Chengdu 610500, China*
[3]*Research Center of Geomechanics and Geotechnical Engineering, Yangtze University, Jingzhou 434023, China*
[4]*Department of Hydraulic Engineering, Tsinghua University, Beijing 100084, China*

Correspondence should be addressed to Shanpo Jia; jiashanporsm@163.com and Zhiqiang Xiao; xiaozhiqiangxl@163.com

Received 7 December 2018; Revised 14 March 2019; Accepted 19 March 2019; Published 16 April 2019

Academic Editor: Pietro Teatini

In recent years, the lithologic traps in a mid-depth formation are the focus of oil or gas exploration and development for eastern oilfields in China. The Shahejie Formation develops thick hard brittle shale, and the wellbore instability problem is prominent due to obvious hydration effect for long immersion time during drilling. Through the analysis of laboratory tests and field test results of physical and chemical properties and microstructure and mechanical properties of hard brittle shale, the instability mechanism is discussed for the wellbore in the shale formation. To simulate the whole process of progressive collapse of a wellbore in a hard brittle shale formation, a coupled hydraulic-mechanical-chemical (HMC) model is developed and this model is compiled with ABAQUS software as the solver. Then the coupled HMC model is applied to simulate the progressive evolution process of wellbore collapse in a hard brittle shale formation, and the influence of different parameters on the progressive failure of the wellbore is analysed. The results show that the wellbore enlargement rate increases with the drilling fluid immersion time and the influence of different parameters on the wellbore enlargement rate is different. The water absorption diffusion coefficient and the activity of the drilling fluid have the most obvious influence on the expansion of the wellbore, and the sensitivity is strong. The permeability of shale has little effect on the wellbore enlargement rate. The calculated progressive failure process of the wellbore is basically consistent with that of the actual drilling.

1. Introduction

The oil or gas exploration and development of a mid-depth formation have become the focus for eastern oilfields in China. Hard brittle shale in a mid-depth formation, which is affected by the existence of cracks and hydration effects, often causes wellbore instability problem for long immersion time. The wellbore instability in hard brittle shale has become the main bottleneck restricting the drilling speed. From the point of view of reducing drilling costs and accelerating exploration and development for oil or gas, it is of great significance to study the wellbore stability of hard brittle shale in a mid-depth formation.

The Nanpu sag is a continental lacustrine sedimentary basin, which forms a high-quality source of rocks such as semideep lake and deep lake phase shale and oil shale. The main source rock is the lithologic trap of the Shahejie Formation with the depth of more than 4000 m. Several hundred meters of hard brittle shale is developed in the Shahejie Formation, which has high clay mineral content and microcrack development. During the actual drilling process, the hydration effect of hard brittle shale causes the wellbore instability by differential pressure penetration, crack self-water absorption, and long immersion time. Many complicated situations, such as drilling tool resistance and well logging retaining, often occur due to the wellbore collapse and diameter enlargement in a hard brittle shale formation, which seriously affects the drilling efficiency. The original mechanical balance and chemical balance of the formation are broken after the wellbore is drilled. Due to the coupling action of hydraulic gradient and chemical gradient, the disturbed zone of the wellbore is developed and it becomes a changed heterogeneous area with time by the seepage diffusion and the hydration effect of the drilling fluid. This series of effects has led to a very complex process for the wellbore in hard brittle shale. Aiming at the wellbore stability problem of shale, many scholars have carried out a lot of research work and obtained many meaningful research results. In general, they mainly focus on the following aspects: firstly, from the point of view of physical and chemical characteristic analyses of shale, the collapse mechanism of the shale wellbore is studied and discussed [1, 2]; secondly, from the perspective of coupling experiment of the shale wellbore, different experimental schemes are designed to study the collapse mechanism of the shale wellbore [3–6]; thirdly, the collapse mechanism of the shale wellbore is analysed by numerical simulation method and reasonable suggestions are given [7, 8].

Generally speaking, the development of the coupling model for shale wellbore stability can be divided into four stages. The first stage is the application of the thermoelastic analogy method [9, 10], which compares the hydration expansion stress of shale to the thermal expansion stress and the movement of water into shale to the thermal diffusion. The quantitative model established by this method can consider the effect of water content changes on the shale wellbore stability but ignores the nature of the chemical interaction between the shale and the drilling fluid. The second stage is the method of free energy thermodynamics of water molecules [2, 11]. The theory holds that the difference in activity (chemical potential) between drilling fluid and shale drives free water into and out of the shale, changing the pore pressure of the wellbore to affect the effective stress near the wellbore. By appropriate strength criteria of shale, the optimum mud concentration and optimum mud density for maintaining wellbore stability can be determined. The free energy thermodynamics model of water molecules negates the effect of differential pressure on water movement in shale and also negates the effects of ion diffusion and ion exchange on shale hydration and does not consider time effects. The third stage is the nonequilibrium thermodynamic method [12–16]. Nonequilibrium thermodynamic method is a comprehensive method to study the chemomechanical coupling of wellbore stability of shale. However, it is difficult to determine the model parameters, which can only be applied to ideal solution with low mass concentration. The combined effect of fluid pore pressure and rock deformation is not taken into account, and it is conservative to adopt linear elasticity for shale in the coupled model. The fourth stage is the application of total water potential [17–19]. The method holds that the difference in total water potential (the sum of pore pressure and chemical potential) is the root cause of water flow. The total water potential method can consider the comprehensive effect of pore pressure and chemical potential, but many parameters are difficult to determine, and no solution is given.

According to the previous studies, the wellbore instability mechanism is discussed by analysing the physical and chemical properties and microstructure and mechanical properties of hard brittle shale. To depict the evolution law of wellbore failure, a coupling constitutive model was developed considering the actual unloading process, strength weakening, and plastic deformation of shale during drilling. The influence of different parameters on the progressive failure of the wellbore is analysed, and the understanding of wellbore collapse is improved, which can provide a reference for the optimization of drilling fluid to prevent or slow down the wellbore instability for a hard brittle shale formation.

2. Mechanism of Wellbore Collapse in a Hard Brittle Shale Formation

During drilling, the diameter of shale in the Shahejie Formation varies greatly and the problem of wellbore instability is prominent. The lithology, mineral composition, microstructure, and hydration effect of shale need to be tested and studied.

2.1. Formation Mineral Composition. The whole rock minerals and clay minerals of the hard brittle shale are tested by X-ray diffraction method. The composition of the whole rock and the content of clay minerals are shown in Tables 1 and 2.

Clay and quartz are the main minerals in shale of the Shahejie Formation. Feldspar and calcite are also developed in different degrees. Brittle minerals (quartz, feldspar, and calcite) are relatively developed, with quartz content ranging from 6.71% to 39.94%. The clay content is relatively high, ranging from 19.09% to 43.06%. Illite and illite/montmorillonite are the main clay minerals. The relative content of illite is 34.47~56.64%, and the content of illite/montmorillonite is 6.72~39.74%. No montmorillonite is found in the Shahejie Formation.

2.2. Microstructure Structure of Shale. Microstructure analysis of shale can reveal orientation arrangement, cementation structure of clay minerals, and microcrack distribution. The development degree and size of microcracks are important factors for drilling fluid performance optimization. Scanning electron microscope (SEM) is one of the most effective means to observe microstructures in shale. The microstructure of shale and occurrence of clay minerals in the Shahejie Formation are analysed by SEM, which are shown in Figure 1.

From Figure 1, the shale of the Shahejie Formation is highly compacted and well cemented but the microcracks, microholes, and bedding are well developed. From the viewpoint of rock mechanics, the development of microcracks and microholes can destroy the integrity of shale, weaken the mechanical properties, and provide a channel for drilling fluid to enter the formation during drilling. Under the action of pressure difference and capillary force, the drilling fluid invaded the formation along microcracks or microholes. On the one hand, it may induce hydraulic fracturing and aggravate wellbore failure; on the other hand, it also increases the probability and degree of interaction between drilling fluid and clay minerals in a formation, which leads to the decrease of formation rock mechanical strength and the increase of wellbore instability.

Table 1: Mineral composition of shale.

Well	Depth (m)	Percentage of minerals (%)					
		Clay minerals	Quartz	Calcite	Plagioclase	Orthoclase	Dolomite
W-81	4900.01	43.06	39.94	1.71	12.21	0.00	3.08
W-82	4149.86	25.33	6.71	38.98	0.00	12.73	16.25
W-96	3901.10	19.09	36.45	9.07	27.54	6.42	1.44

Table 2: Relative content of clay minerals.

Well	Relative content (%)					Interlayer ratio (%)
	Illite (I)	Montmorillonite (S)	Illite/montmorillonite (I/S)	Kaolinite (K)	Chlorite (C)	
W-81	49.78	0.00	12.63	6.27	31.33	15.00
W-82	56.54	0.00	6.72	0.00	36.74	10.00
W-96	34.47	0.00	39.74	10.62	15.17	25.00

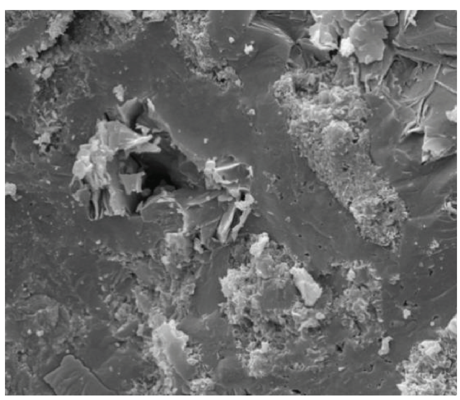

(a) Flaky clay mineral

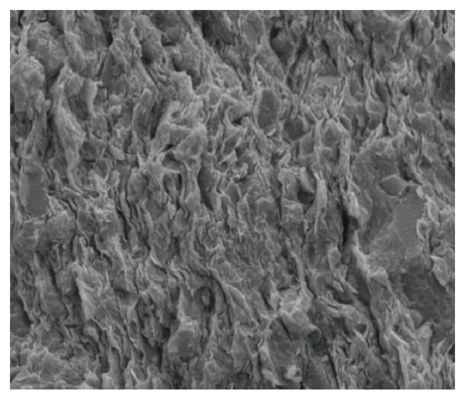

(b) Flaky structure

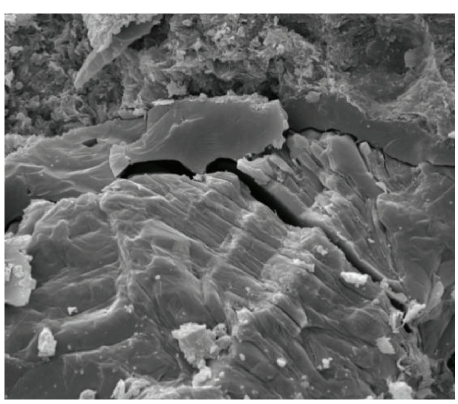

(c) Microcrack

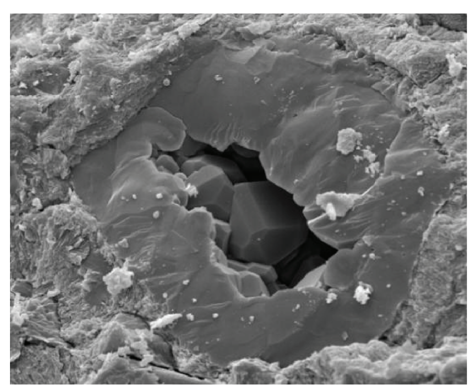

(d) Microhole

Figure 1: SEM images of the shale core in well W-82.

2.3. Influence of Drilling Fluid Action on the Shale Structure. After hydration, clay minerals in shale can expand and produce expansion stress. Microcracks in shale can produce stress concentration at the crack tip by the influence of water or drilling mud.

The drilling mud used in the field is water-based KCl filming drilling fluid. The microstructure changes of shale after fluid action were observed by high-power polarizing microscope, which are shown in Figures 2 and 3. Under the action of clear water and drilling mud, microcracks in shale will initiate, expand, or bifurcate and clear water and drilling mud will invade the interior of shale along microcracks, further aggravating the failure of shale.

2.4. Cation Exchange Capacity. Cation exchange, i.e., cation exchange adsorption, is one of the important characteristics of shale and can be used to predict the potential water sensitivity of a formation. When the clay is dispersed in water, the

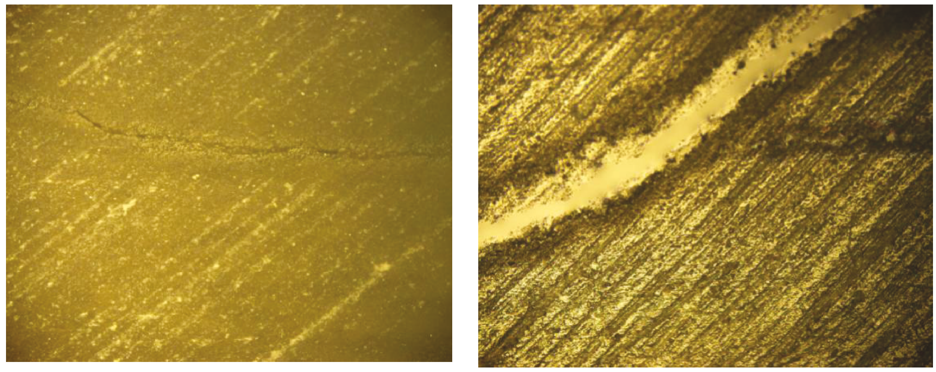

(a) Before invasion (b) 48 h after invasion

Figure 2: Clear water intrusion along microcracks in shale.

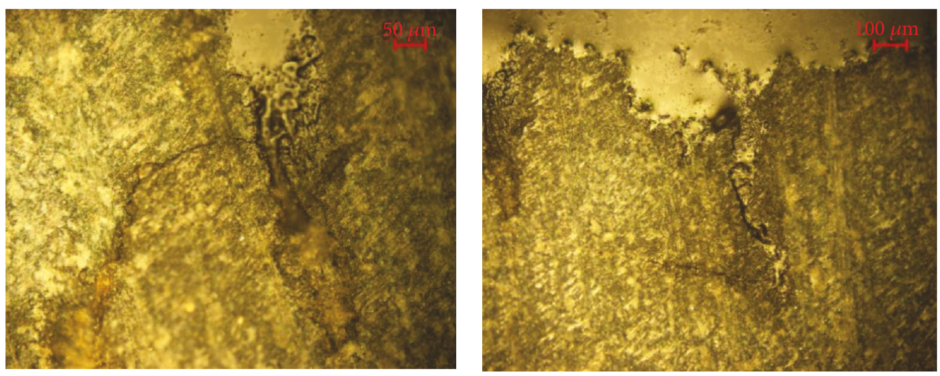

(a) Before invasion (b) 96 h after invasion

Figure 3: Morphological changes of microcracks under the intrusion of drilling fluid.

adsorbed cations will diffuse from the surface of the clay. By measuring the cation exchange capacity (CEC value) of the shale, the hydration, expansion, and dispersion of the shale can be reflected.

The cation exchange capacity of shale samples was measured, and the results show that the range of CEC of the Shahejie Formation was 90~235 mmol/kg with an average of 146.25 mmol/kg. The shale of the Shahejie Formation has a certain hydration ability and is prone to wellbore instability under the action of water-based drilling fluid.

3. Effect of Drilling Fluid on Mechanical Properties of Shale

The mechanical properties of shale are important factors to represent the failure characteristics of the wellbore under external disturbance and drilling fluid, which are directly related to the density of available safe drilling fluid, the performance of drilling fluid, and the manifestations of wellbore accidents.

3.1. Mechanical Properties of Original Shale. To minimize the disturbance of the drilling coring, the rock cores are quickly vacuum sealed and stored in a room with a given temperature and humidity. Considering the water sensitivity of shale, the water drilling method cannot be used for rock sample processing in the laboratory. After the drilling cores are frozen for more than 2 hours, the rock samples can be drilled down by using liquid nitrogen to cool the drill bit. During the rock sample processing, the room is set with a certain humidity and the processing time is also shortened as much as possible for reducing the water evaporation of rock samples. The processing time is controlled within half an hour. The initial water saturation has a significant impact on the shale hydration effect, and the humidity control of the rock sample is set with reference to the initial water content. The initial water saturation is determined according to the following steps: (1) measuring the length and diameter of the rock sample, (2) placing the sample in an oven at 105°C for 48 hours, (3) obtaining the water-containing volume according to the mass difference of the rock sample before and after drying, and (4) calculating the water saturation by dividing the water-containing volume to the pore volume of the rock sample.

The triaxial compression mechanical properties of the original rock were tested from the Shahejie Formation of W-82 well, and the stress-strain curves are shown in Figure 4. The elastic modulus of shale is 18.27~23.59 GPa, the Poisson's ratio is 0.12~0.23, the cohesive force is 24.14 MPa, and the internal friction angle is 21.7°. In addition, the Brazilian splitting experiments were carried out on five samples and the tensile strength of shale is 1.13~6.09 MPa with the average value of 4.41 MPa.

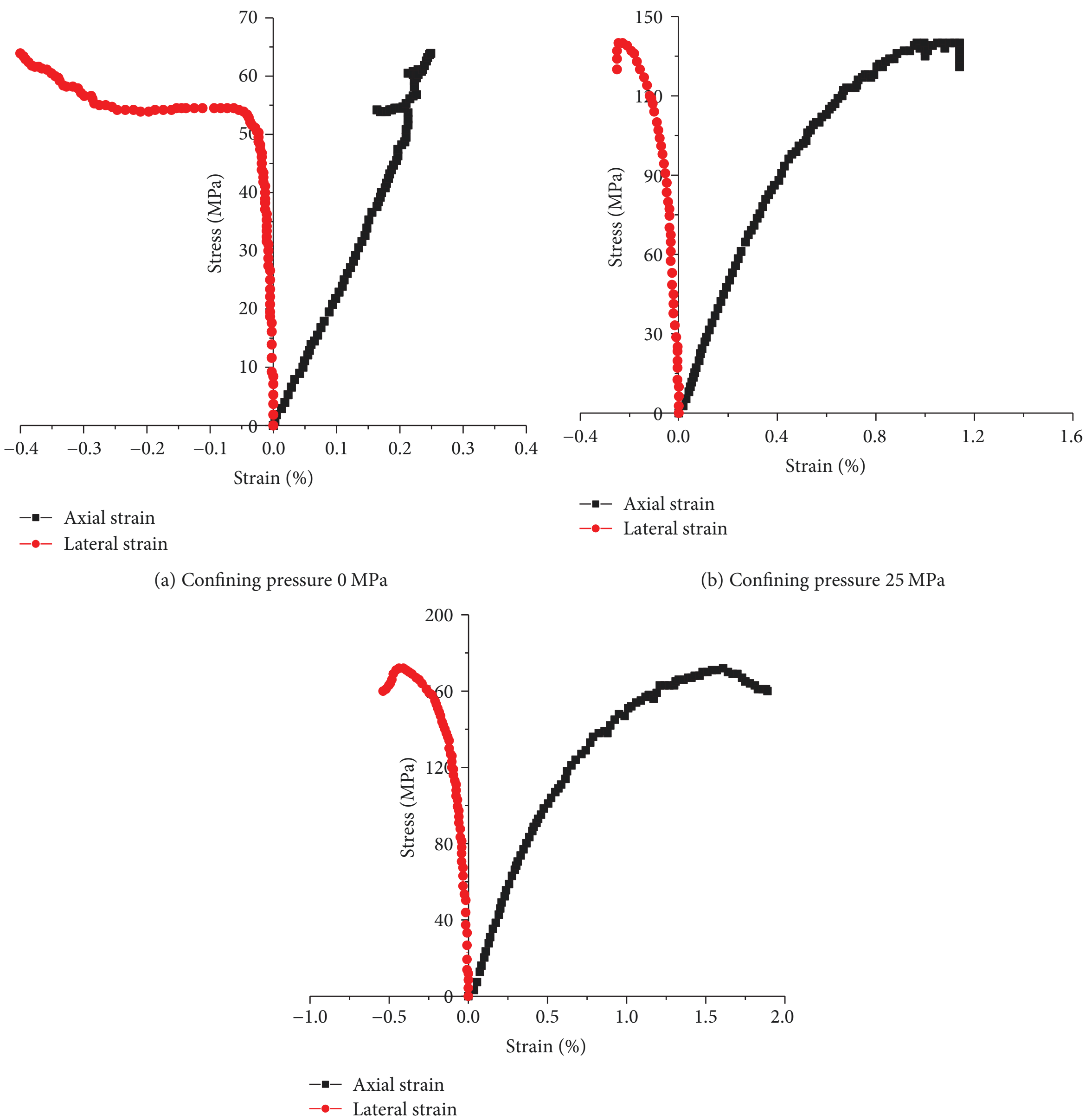

(a) Confining pressure 0 MPa
(b) Confining pressure 25 MPa
(c) Confining pressure 50 MPa

FIGURE 4: Triaxial test results of original rock in the W-82 well (depth 4150 m).

Brittleness is an inherent mechanical property of rock, which is controlled by rock composition, structure, confining pressure, temperature, and other factors. At present, rock mineral composition and elastic parameters are two widely used evaluation indexes for rock brittleness in the petroleum engineering field. Based on the brittleness evaluation of rock mineral components, the brittleness evaluation results of shale of brittle minerals are as follows: the brittleness index of shale in well W-82 is 0.664, that of shale in well W-96 is 0.809, and that of shale in well W-81 is 0.569.

Rickman et al. [20] thought that the larger the Young's modulus and the smaller the Poisson's ratio, the greater the brittleness of shale. The two parameters can be used to characterize the brittleness of shale. According to the results of triaxial compression tests, the brittleness index of core #1 (confining pressure 0 MPa) is 0.424, that of core #2 (confining pressure 25 MPa) is 0.367, and that of core 3# (confining pressure 50 MPa) is 0.326.

Through the analysis of rock mechanical properties, the shale failure mode is mainly brittle under the condition of triaxial compression. The brittle mineral content is higher, the elastic modulus is relatively higher, and Poisson's ratio is relatively low, indicating that the shale in this formation exhibits high brittleness.

3.2. Effect of Drilling Fluid Action on Mechanical Properties of Shale. To evaluate the change of mechanical properties of shale under the action of drilling fluid and provide a basis for the evaluation of drilling fluid to maintain rock strength performance, the mechanical properties of shale have been tested under the action of drilling fluid. The fluid for the immersion tests is water-based KCl filming drilling mud.

Hardness is a parameter reflecting the ability of rock to resist tool invasion and failure. The shape requirement of the rock sample for the indentation hardness test is lower than that of the triaxial compression test and direct shear test, which is convenient for a large number of tests. Due to the difficulty to obtain the drilling cores of shale and the limited samples used for triaxial tests, the influence of drilling fluid on the mechanical properties of shale was tested by the hardness testing method.

The change characteristics of the strength of shale can be described by testing the hardness of shale immersed in drilling fluid at different immersion time. Three groups of shale hardness tests were carried out at the same location under original condition, immersed drilling fluid for 6 hours and 12 hours. The test results are shown in Figure 5. It can be seen that the shale hardness decreases gradually with the increase of immersion time. The reduction of shale hardness under drilling fluid immersion indicates that the influence of drilling fluid on shale strength cannot be neglected.

Due to the shortage of drilling cores, the shale samples of the same layer in the adjacent area were tested. The results show that the integrity of shale samples is destroyed during the immersion process and macrocracks are found. Some samples are broken into fragments, and the degree of hydration is serious. Uniaxial and triaxial compression tests of shale samples immersed in drilling fluid for 0 hour (original rock), 6 hours, and 12 hours were carried out. The test results are shown in Table 3. It can be seen that the mechanical strength of hard brittle shale decreases gradually with immersion time in drilling fluid under the same confining pressure. After 6 hours of drilling fluid immersion, the strength of shale decreased by 16.32% on average and the strength decreased by 23.10% on average after immersion for 12 hours.

From the above analysis of experimental results, the main factors that lead to wellbore instability during the drilling process in hard brittle shale can be summarized as follows:

(1) Shale has high clay mineral content, and the content of illite/montmorillonite mixed layer is well developed. As a mineral between expansive clay and nonexpansive clay, the illite/montmorillonite mixed layer is easy to absorb water and cause nonuniform hydration expansion. The cation exchange tests also prove that the shale is prone to hydration reaction and its structural strength is weakened by the external fluid

(2) Microcracks and microholes in shale of the Shahejie Formation are well developed, which provide a flow channel and hydration space for external fluid, resulting in a decrease of shale strength and an increase for the wellbore failure risk

(3) The brittleness of the Shahejie Formation is relatively strong. Stress release or unloading, wellbore pressure fluctuation, low drilling rate, and long immersion time during the drilling process are more likely to lead to wellbore cracks that provide a channel for drilling fluid and aggravate wellbore instability

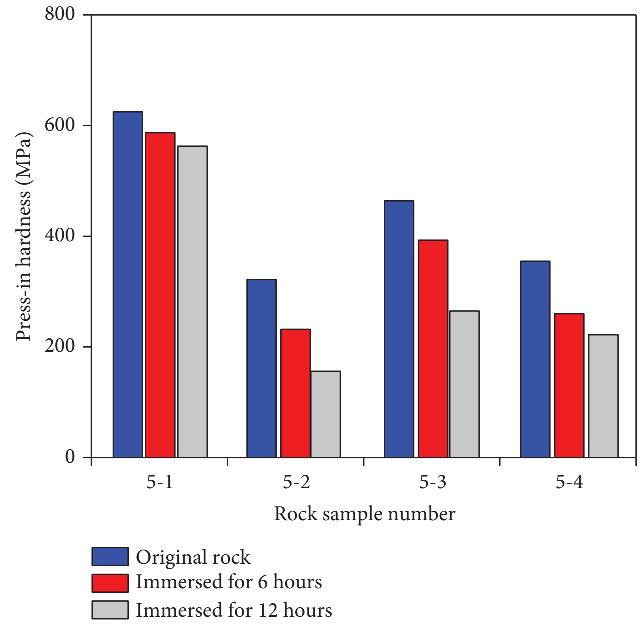

Figure 5: Hardness change with drilling fluid immersion.

For modelling of the time-dependent wellbore failure process in a shale formation, the diffusion and seepage of drilling fluid in the shale formation and its strength weakening behavior should be taken into account [21].

4. Coupled Hydraulic-Mechanical-Chemical (HMC) Model of Shale

According to the governing equation of chemical-poreelastic mechanics and elastic-plastic constitutive relation, a coupled HMC model describing time-dependent wellbore failure of shale is established. It is assumed that plastic deformation mainly affects the mechanical balance of rock.

4.1. Navier Equation for Displacement. According to Biot's theory, the porous media is assumed to consist of an elastic porous solid matrix, in which pore space is saturated by fluids containing many chemicals. Assuming that the chemical potential expansion coefficients of diluent and solute in solution are the same as those of ω_0, the Navier-type equation for displacement is derived by using momentum balance equation:

$$\left(K + \frac{G}{3}\right)\nabla(\nabla \mathbf{u}) + G\nabla^2\mathbf{u} - \alpha\nabla p - \omega_0\left(1 - \frac{\rho_s}{\rho_D}\right)\nabla C = 0, \quad (1)$$

where K and G are bulk modulus and shear moduli, respectively, $\mathbf{u}$ is rock displacement, α is Biot's coefficient, p is pore pressure, C is the solute mass fraction, and ρ_s and ρ_D are the densities of solute and diluent, respectively.

4.2. Pressure Diffusion and Solute Transport in Shale. When drilling fluid enters the shale formation, the chemical potential difference and hydraulic pressure difference between

Table 3: Strength changes of shale under drilling fluid immersion.

Sample	Immersion time (h)	Confining pressure (MPa)	Compressive strength (MPa)	Cohesion (MPa)	Internal friction angle (°)
1	0	0	30.80	9.83	24.89
2		50	153.46		
3	6	0	23.79	7.86	23.09
4		50	138.30		
5	12	0	21.48	7.32	21.42
6		50	129.00		

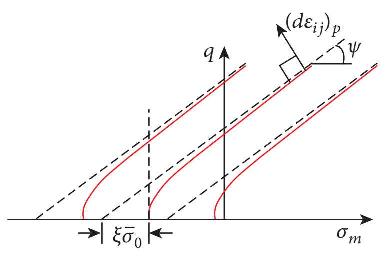

Figure 6: A family of flow potentials in the meridional stress plane.

formation fluid and drilling fluid lead to the redistribution of formation pore pressure. Considering that shale has the semi-membraneous properties in drilling fluid and ignoring the effect of solid deformation on fluid flow, the coupled fluid diffusion equation is given [22, 23]:

$$\frac{k}{\eta C' n}\nabla^2 p + I_m \frac{RT}{V} \ln \frac{1}{C_{\text{shale}}}\frac{\partial C}{\partial t} = \frac{\partial p}{\partial t}, \tag{2}$$

where k is permeability, η is the fluid viscosity, C' is the fluid compressibility, n is the porosity, I_m is membrane efficiency, R is the universal gas constant, T is temperature, V is molar volume, and C_{shale} is the initial mass fraction in shale formation.

The conservation of solutes in rocks produces the following equation for solute transfer:

$$n\dot{C} - D\nabla^2 C = 0, \tag{3}$$

where D is the solute diffusion coefficient.

4.3. Elastoplastic Constitutive Relation. It is assumed that the saturated porous medium exhibits a partial elastic and partially plastic manner after undergoing initial yielding. Therefore, the strain change caused by the stress increment can be divided into elastic and plastic components:

$$d\varepsilon_{ij} = \left(d\varepsilon_{ij}\right)_e + \left(d\varepsilon_{ij}\right)_p. \tag{4}$$

Assuming that the plastic strain increment is proportional to the stress gradient, it can be defined by plastic potential G:

$$\left(d\varepsilon_{ij}\right)_p = d\lambda \frac{\partial G}{\partial \sigma_{ij}}, \tag{5}$$

where $d\lambda$ is proportionality constant and called the plastic multiplier.

To ensure that the plastic flow direction is defined uniquely, the flow potential is chosen as a continuous and smooth function, which is a von Mises circle in the deviatoric stress plane. The potential function asymptotically approaches the linear Drucker-Prager flow potential at high confining pressure stress and intersects the hydrostatic pressure axis at 90°. A family of flow potentials in the meridional stress plane is shown in Figure 6. The plastic potential G is defined as follows:

$$G = \sqrt{\left(\xi\bar{\sigma}_0 \tan\psi\right)^2 + q^2} - \sigma_m \tan\psi, \tag{6}$$

where ξ is the model parameter $\xi = 0.1$, $\bar{\sigma}_0$ is initial yield stress, σ_m is the confining pressure, q is Mises stress, and ψ is the dilation angle of the rock.

The general form of the plastic yield function can be given by

$$F\left(\sigma_{ij}, \kappa'\right) = 0, \tag{7}$$

where κ' is the hardening parameter, which is influenced by the hydration effect.

The Drucker-Pracker yield criterion has been widely used in the problem of wellbore stability in shale formations to describe the elastoplastic behavior of shale [24–28]. In this study, the elastoplastic calculation is performed using the Drucker-Prager criterion. A modified Drucker-Prager yield criterion can be expressed as follows [29]:

$$F = \sqrt{l_0{}^2 + q^2} - \sigma_m \tan\varphi - c, \tag{8}$$

where c is cohesion, φ is the friction angle of the rock, $l_0 = c_0 - \sigma_t$, c_0 is initial cohesion, and σ_t is tensile strength.

4.4. Strength Weakening Model of Shale. Rock strength varies with the water content of shale formation. According to the above test results, the strength can be assumed to be approximately linear attenuation with the water content. The strength weakening model of shale can be defined as [22]

$$\begin{cases} c = c_0 - K_s(w - w_0), \\ \varphi = \varphi_0 - L_s(w - w_0), \end{cases} \tag{9}$$

where c_0 and φ_0 are the cohesion and friction angle, respectively, at the initial water content w_0, K_s is cohesion coefficient, and L_s is friction angle coefficient.

According to mass conservation equation, the diffusion equation of water can be defined as [30]

$$C_f\left(\frac{\partial^2 w}{\partial x^2}+\frac{\partial^2 w}{\partial y^2}\right)=\frac{\partial w}{\partial t}, \tag{10}$$

where C_f is water absorption diffusion coefficient of shale.

4.5. Permeability Evolution of Shale. Assuming that elastic deformation of shale cannot causes damage, plastic deformation and damage occur simultaneously. After yielding failure of shale, the internal pore and fracture in rock gradually germinate and penetrate each other and the permeability of shale increases obviously. In the study of wellbore stability, permeability is often considered as constant in most previous studies. However, in fact, permeability around the wellbore varies during drilling excavation.

According the equation of Kozeny-Carman, the permeability and porosity evolution of shale can be defined as

$$\begin{cases} k=k_0\left[\left(\dfrac{1}{n_0}\right)(1+\varepsilon_v)^{2/3}-\left(\dfrac{1-n_0}{n_0}\right)(1+\varepsilon_v)^{-1/3}\right]^3, \\ n=1-\dfrac{1-n_0}{\varepsilon_v+1}, \end{cases} \tag{11}$$

where k_0 is the initial permeability of shale, n_0 is the initial porosity, and ε_v is the volumetric strain.

4.6. Solution Strategy. Based on the above analysis, the decoupled numerical method is adopted to solve the coupled HMC model of shale. Due to the relative independence of solute transport equation and mass conservation equation, they can be solved first. Then the pressure transfer model and the solid deformation can be solved synergistically. The HMC model of shale involves two calculation modules embedded in ABAQUS software, namely, the rock consolidation module and the mass diffusion module.

Although the HM coupling field and mass diffusion field of rock are different, they essentially contain two basic contents: linearization and time step discretization (or load increment). The calculation of the HM field and diffusion field can be designed separately by two independent systems. By means of data communication, the coupling of parameters at each time step can be realized and the related coefficients can be continuously revised at each time step and the mutual correction is carried out at a series of time steps. Based on the previous research on the THM coupling method [31], using MATLAB as the platform and ABAQUS as the solver, the analysis software for modelling time-dependent wellbore collapse in shale formation is developed. The data storage and communication between different calculation modules are realized by ABQMAIN subroutine, and strength weakening and permeability evolution are realized by USDFLD subroutine.

In multifield coupled analysis, the models for mass diffusion analysis and HM analysis require the same meshes, analysis steps, initial time increment, and time period for data communication. The ABAQUS has the interpolation capability to obtain the nodal quantities at a given time. This coupled problem is solved through a "staggered solution technique" as shown in Figure 7 and as follows:

(1) First, a water content analysis is performed using the mass diffusion module in ABAQUS, where water absorption diffusion coefficient of shale is assumed to be constant. Water content histories are written onto an external file used in step 3

(2) The solute mass fraction analysis is performed through the second mass diffusion module in ABAQUS where the solute diffusion coefficient is assumed to be constant and the porosity is changed with time. In the first cycling analysis, the porosity is assumed to be constant, and in the subsequent analysis, it is read from an external file. Solute mass fraction histories are written onto an external file used in step 3

(3) The water content and solute mass fraction histories are used by the rock consolidation module in ABAQUS, in which the rock strength is performed as a function of water content and permeability evolution is the function of volumetric strain by USDFLD subroutine. The HM model calculates stresses, pore pressure, porosity, etc. as function of time. The porosity histories are written onto an external file used in step 2

(4) The ABQMAIN subroutine reads the files with solute mass fraction, water content, and porosity data and creates new files containing histories of solute mass fraction, water content, and porosity. The porosity histories are used by the solute mass fraction model in subsequent analysis

Steps 2-4 are repeated if the material parameter values are found to be different compared to those of the previous solution.

The USDFLD subroutine is used to redefine the field variable at the material integration point and also to obtain information at the material integration point. Under the conditions of hydration, the mechanical parameters of the rock are affected by the water content and change with the water content. Similarly, the permeability and porosity are influenced by the change of volumetric strain. Here, the water content and volumetric strain can be defined as the field variables, so that the mutual calling between the subroutines and the related module are realized.

5. Application

5.1. Project Overview. The W lithologic trap of Nanpu sag is an important exploration area in the Jidong oilfield in China,

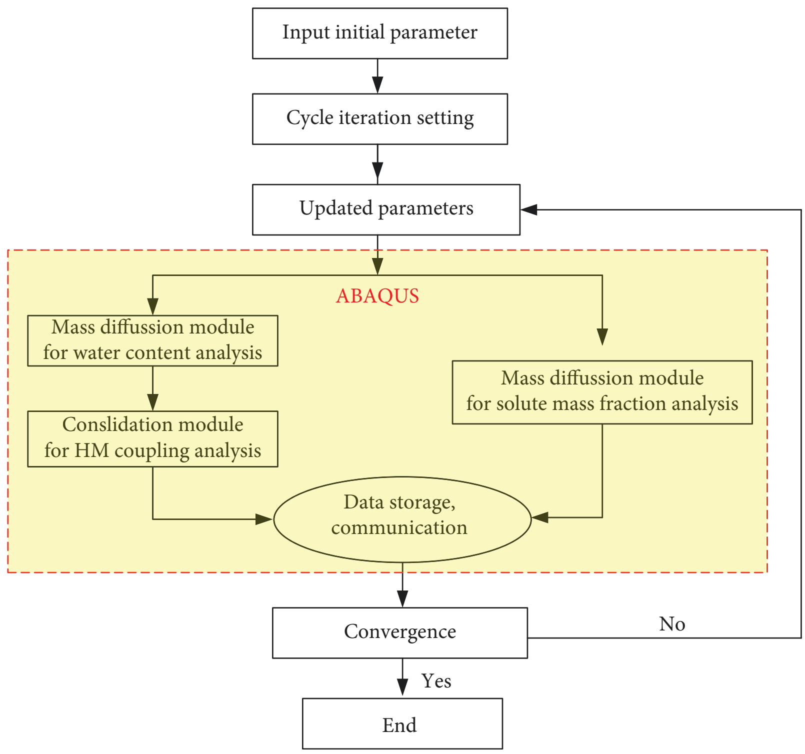

Figure 7: Flowchart of the multifield coupling implementation.

Table 4: Pressure tests of the Shahejie Formation.

Layer	Formation pressure coefficient	Collapse pressure coefficient	Fracture pressure coefficient
Es1	1.31	1.32	1.8
Es2, Es3	1.30	1.33	1.93

which is located in the west of Huanghua Depression in the Bohai Bay Basin. The drilled formations are the Paleogene Shahejie Formation, Dongying Formation, Neogene Guantao Formation, Minghuazhen Formation, and Quaternary Plain Formation from bottom to top. The area, thickness, and closure range of the W trap are 356km^2, 840 m and 1000 m, respectively. The first number of the Shahejie Formation develops a large set of shale as caprock for lithologic reservoirs.

According to the drilling well history, drilling fluid, and well completion data, statistical analysis on drilling complex accidents was done on 20 drilled wells in the W trap. The result shows that the most prominent accident is leakage, followed by borehole wall caving and collapse, and the leakage accident occurs about four times more than the latter. The fracture pressure coefficient in shale target formation is more than 1.8 (Table 4). The maximum equivalent density of drilling fluid used in complex formation is 1.6. Combined with drilling core observation and imaging logs, the fractures are relatively well developed around the wellbore for leakage accidents. Increasing the density of drilling fluid is not ideal for inhibiting wellbore collapse and diameter enlargement. For some wells, the wellbore diameter increases instead when the drilling fluid density increases from 1.23 to 1.39.

The hard brittle shale of the Shahejie Formation has microcracks and some microholes, which provide a channel for drilling fluid to invade. The presence of developed cracks and hydration effect make the leakage problem using the conventional drilling method more serious. Therefore, the implementation of an underbalanced drilling method is an effective way to improve the reservoir protection and prevent drilling fluid leakage. The formation pressure coefficient of the Shahejie Formation is higher than 1.3 (Table 4), and then the liquid-based drilling fluid system is selected for the underbalanced circulation medium. Taking W-82 well as the research object, the dynamic damage law of wellbore under the condition of underbalanced drilling is studied. The total depth of W-82 is 4745 m, and the underbalanced drilling footage is 598.07 m from 4146.93 m to 4745 m in the Shahejie Formation.

5.2. Computational Condition. According to the symmetry of the wellbore, one-quarter of the wellbore is used for modeling analysis, which is shown in Figure 8. To simulate the drilling unloading, the element removing technique is used to deal with the excavated part of the wellbore. The radius of the wellbore is 0.108 m, and the length and width of the calculation model are set as 15 m to reduce the pore pressure influence of the wellbore on the outside of the model. The plane strain quadrilateral element is used to discretize the model, the total number of grids is 1993, and the total number of nodes is 2087. The divided grid is shown in Figure 9.

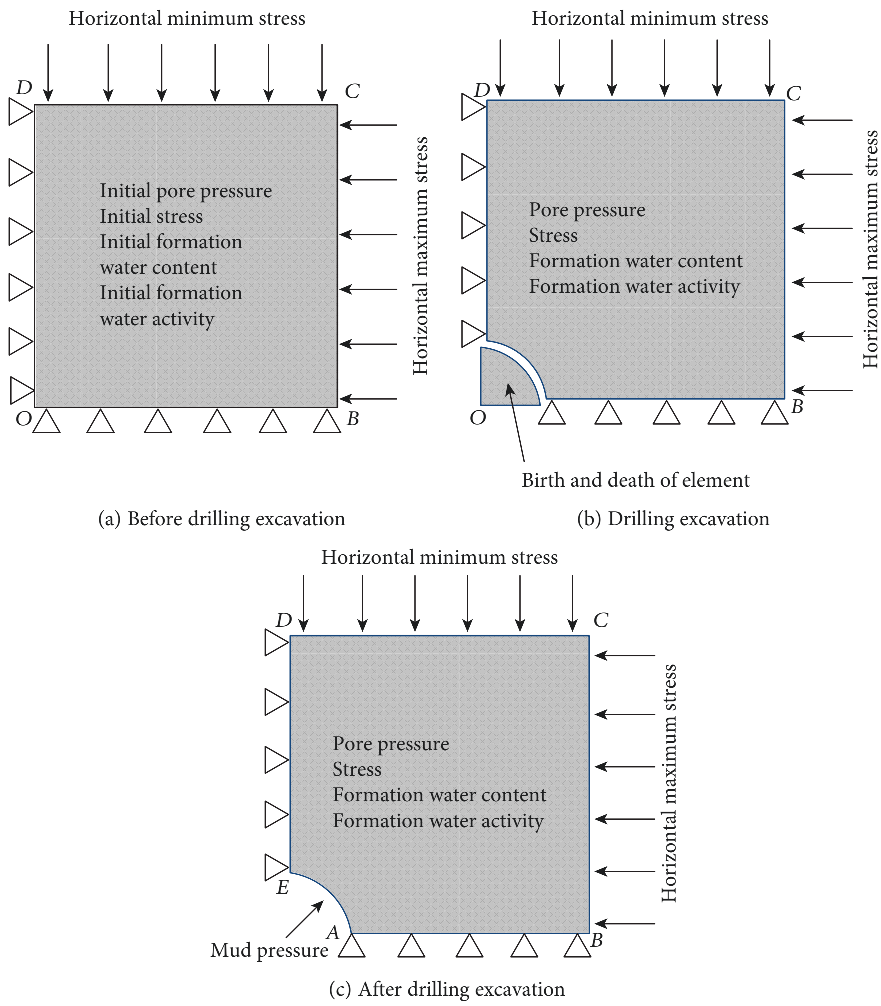

FIGURE 8: Schematic diagram of the calculation model.

Initial pore pressure, initial stress, initial water content, and initial water activity are defined inside the shale formation. For the mechanical boundary conditions, OB and OD are set as normal constraint conditions, the maximum horizontal earth stress is applied on the BC side, and the minimum horizontal earth stress is applied on the CD side. After drilling excavation, the AE side is applied as mud pressure, water content condition, drilling fluid activity condition, and seepage condition.

The analysis steps that simulate the progressive failure process of the wellbore are defined as follows: the first step is in situ stress balance, which is to restore the initial stress field, i.e., the stress state before drilling excavation. By defining the inside stress field and outside boundaries of the model, the initial in situ stress field can meet the requirements of calculation. The second step is the drilling excavation by the technique of element removing. In this step, the shale formation is excavated firstly, and then the wall of the wellbore is applied mud pressure. Due to relatively short drilling excavation, the wall of the wellbore is considered as impermeable. The third step is the seepage and diffusion stage to simulate the seepage and diffusion effect inside and outside the wellbore. In this step, the wall of the wellbore is considered as permeable for a longer period. The strength of the surrounding rock of the wellbore is weakened by hydration effect, and the wellbore failure process is simulated in 53 days.

According to laboratory tests, field data, logs, and related geological data of adjacent areas, the calculation parameters at the depth of 4250 m in the Shahejie Formation are defined as follows: overburden pressure at 91.63 MPa, maximum horizontal principal stress at 81.22 MPa, minimum horizontal principal stress at 68.72 MPa, and formation pressure coefficient at 1.3; elastic modulus of shale at 20.2 GPa, Poisson's ratio at 0.16, cohesion at 24.1 MPa, internal friction angle at 21.7°, equivalent permeability at 1.01 mD, and the porosity at 9%; initial formation water content at 2% and saturated water content at 10%; K_s at 2.71 MPa and L_s at 2.50°; and activity diffusion coefficient at 5×10^{-9} m^2/s and formation water absorption diffusion coefficient at 9.5×10^{-9} m^2/s.

5.3. Progressive Failure Process of the Wellbore. Taking the drilling fluid equivalent density 1.1 as an example, the

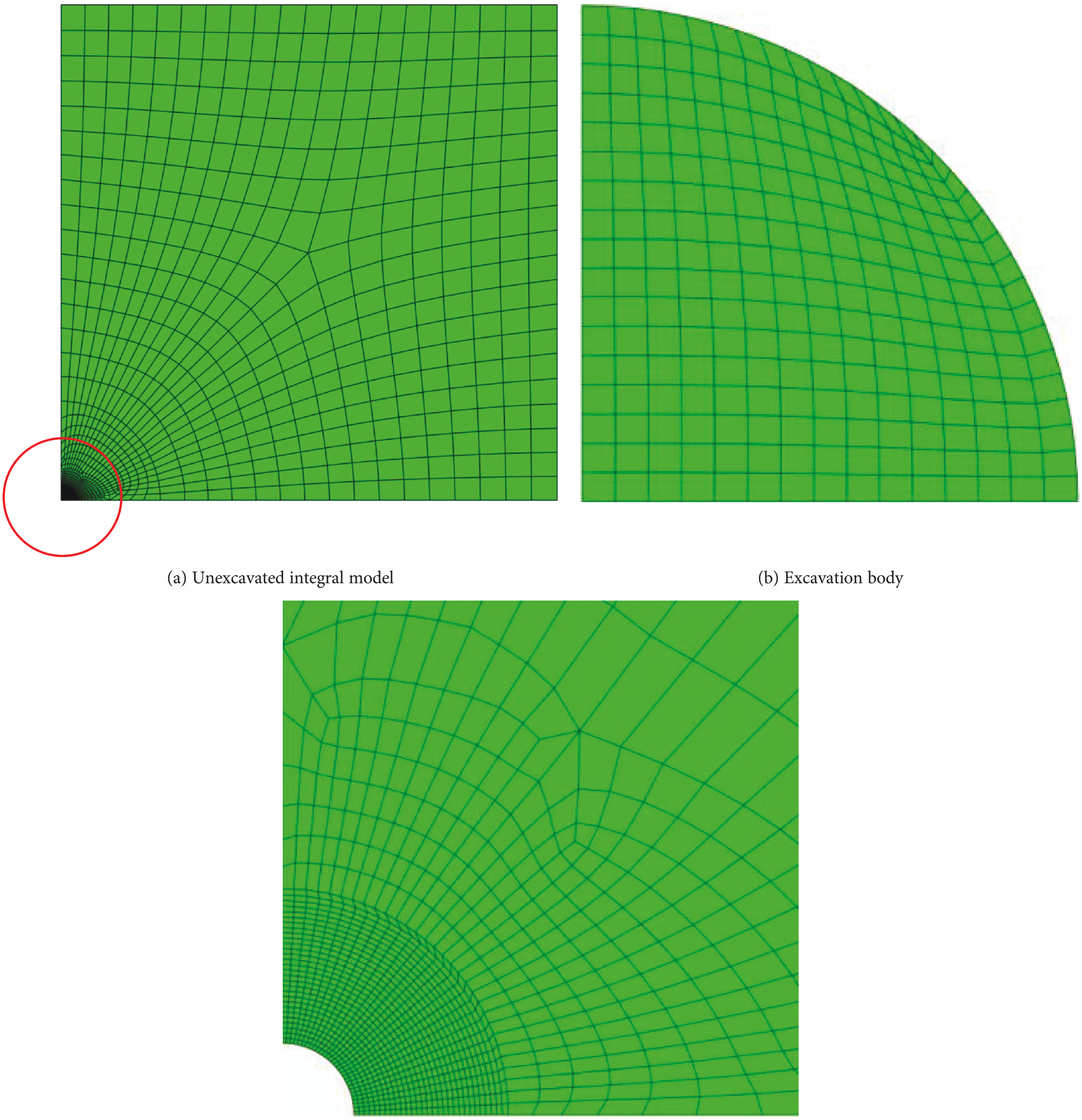

(a) Unexcavated integral model

(b) Excavation body

(c) Wellbore local model after excavation

Figure 9: Meshes of the analysis model.

underbalanced drilling method is used to open the shale formation. The above calculation model is simulated to investigate the progressive collapse and failure process of the wellbore considering the influence of the seepage and hydration diffusion in shale by drilling fluid.

Figure 10 shows the pore pressure distribution after drilling excavation. It can be found that the pore pressure gradually increases with the distance from the wellbore wall and tends to the initial pore pressure value. The change rate of pore pressure decreases gradually with drilling time increasing. The disturbed zone of the seepage field is about 20 times of the wellbore radius after 5 days and 55 times after 53 days of drilling excavation.

Figure 11 presents the distribution of water content after the formation was drilled. The water content gradually decreases with the increase of the distance from the wellbore wall and tends to the minimum value of 2%. In the early stage after the formation was drilled, the water content changes sharply and fluctuates to a certain extent. After that, the change rate of the water content

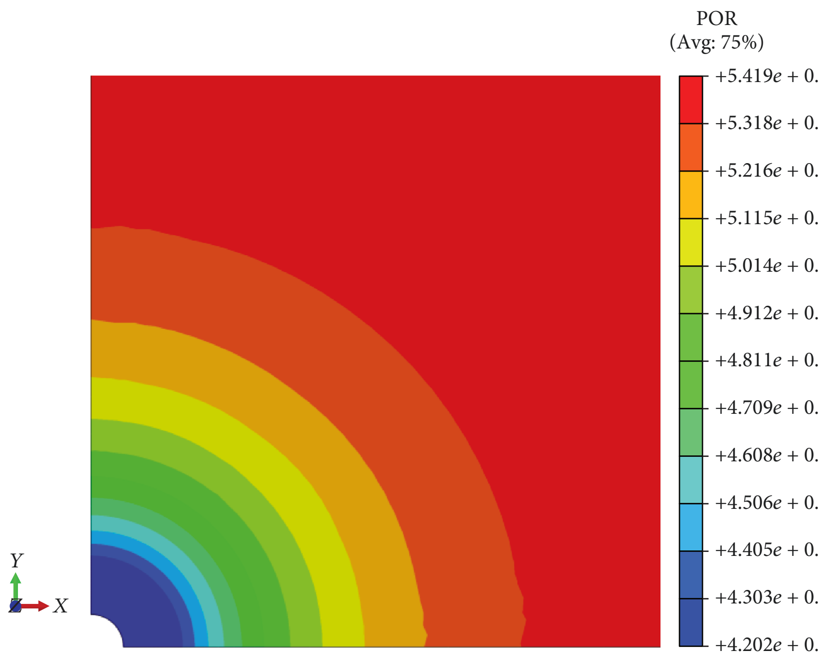

(a) 5 d

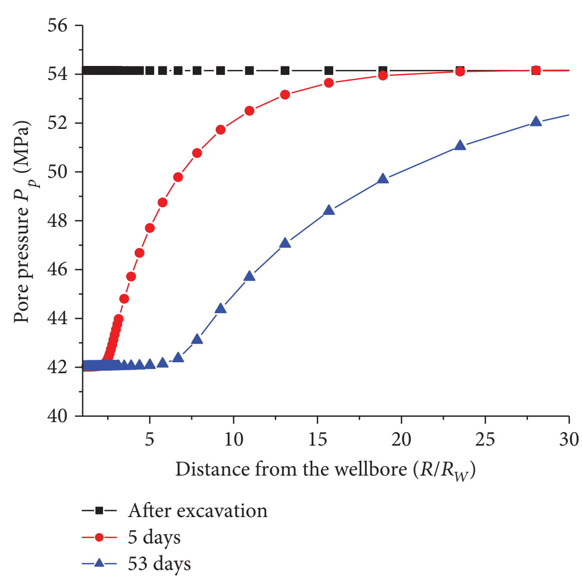

(b) Change along the radial direction

FIGURE 10: Pore pressure distribution of the wellbore after drilling.

decreased with the increase of the immersion time by drilling fluid.

The cohesion and internal friction angle of shale are changed by water content evolution. The distribution and variation laws of cohesion and internal friction angle are similar to that of the water content, which are shown in Figures 12 and 13.

The progressive failure process of the wellbore is shown in Figures 14 and 15. It can be found that the extent and scope of wellbore collapse in the y direction (ED line, shown in Figure 8(c)) are obviously larger than those in the x direction (AB line) and the damaged zone is basically elliptical, which is consistent with the field imaging logs. The collapse scope increases with immersion time. The maximum plastic strain is 0.52% after drilling excavation, while the maximum plastic strain is 0.81% after 5 days of drilling excavation.

For the depth of wellbore collapse (as shown in Figure 16), the damaged zone increased rapidly and then tends to be stable and increases linearly by the influence of hydration effect. Therefore, the hydration effect of shale in the Shahejie Formation is very obvious and the wellbore collapse is a time-dependent progressive failure process.

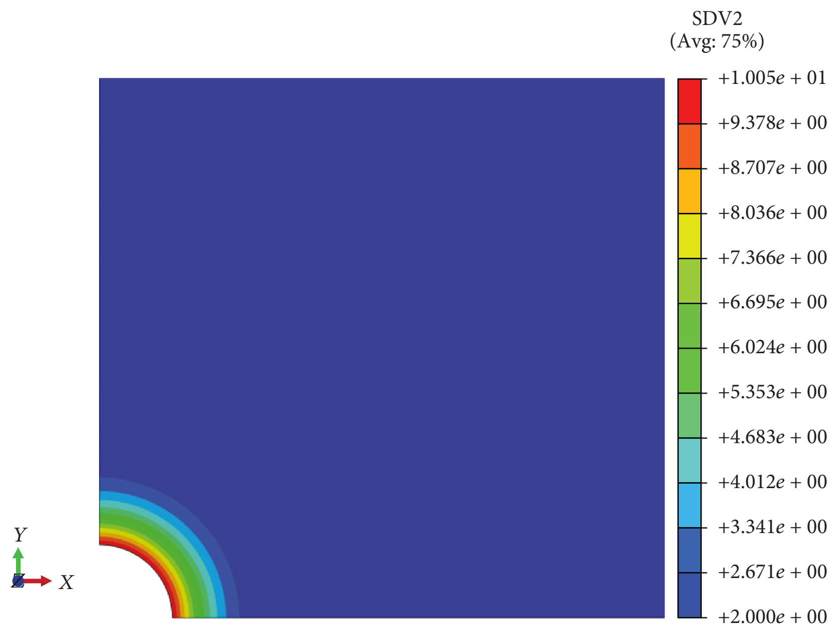

(a) 5 d

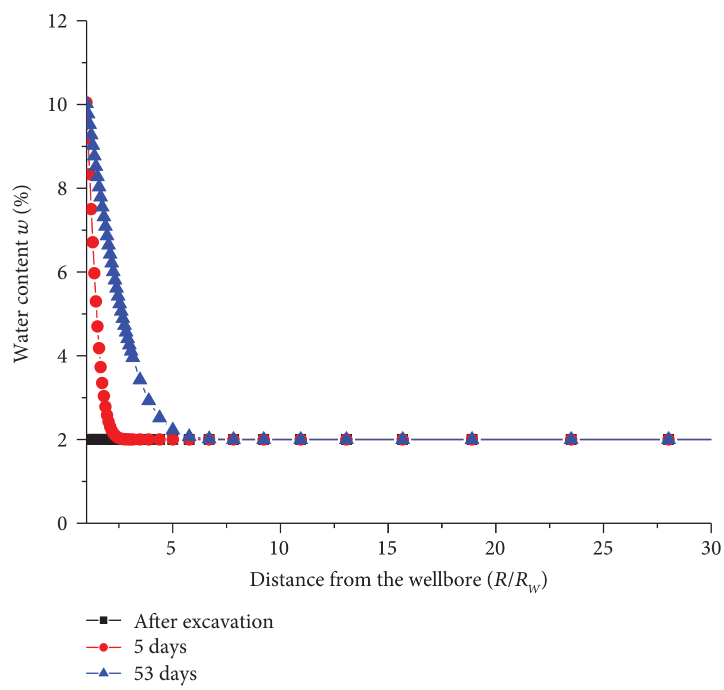

(b) Change along the radial direction

FIGURE 11: Water content distribution of wellbore after drilling.

5.4. Parametric Study. By obtaining the plastic zone range corresponding to AB and ED at different time, and taking its average value as the borehole enlargement value, the ratio of the borehole enlargement value to the outer diameter of the drilling bit is defined as the wellbore enlargement rate. Through numerical analysis, the collapse period chart under different influence parameters can be established for shale formation.

Figure 17 shows the wellbore enlargement rate varying with time under different drilling fluid densities. The wellbore enlargement rate increases with the drilling fluid immersion time and the wellbore enlargement rate decrease with the increase of the drilling fluid density. Taking the drilling fluid density of 1.2 as an example, the wellbore enlargement rate is 18.07% after drilling excavation and 58.22% after 7 days of immersion with an increase of 40%. It can be seen that hydration effect by drilling fluid has a great influence on the progressive collapse of wellbore in shale formation.

Figure 18 presents the variation of the wellbore enlargement rate with time under the influence of water absorption diffusion

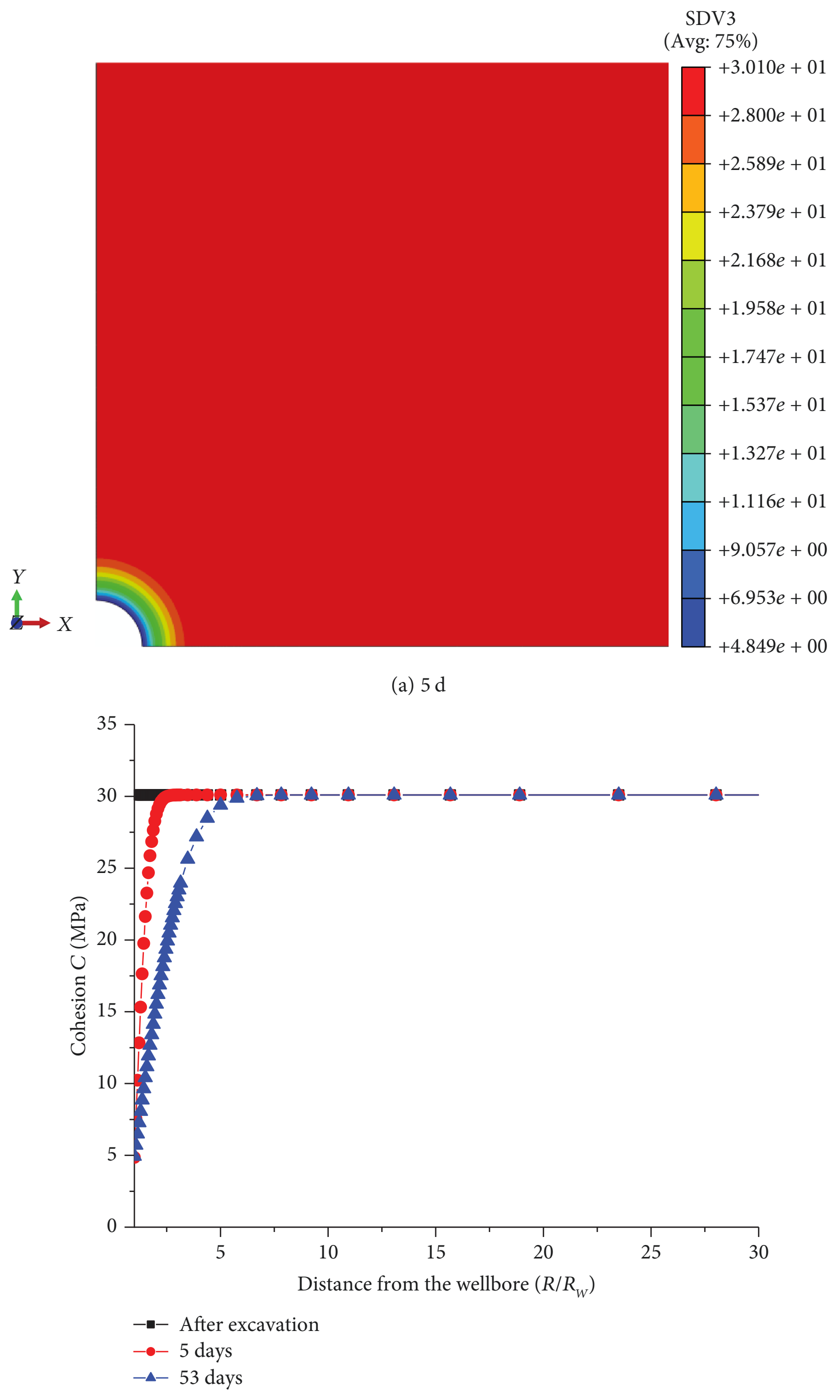

(a) 5 d

(b) Change along the radial direction

Figure 12: Variation of formation cohesion after drilling.

coefficient. When the water absorption diffusion coefficient is 5.0×10^{-10} m^2/s, the wellbore enlargement rate increases from 18.07% to 47.18% in 53 days. The wellbore enlargement rate is 117.16% after 53 days of drilling fluid immersion for the water absorption diffusion coefficient of 1.4×10^{-8} m^2/s. The water absorption diffusion coefficient has a very large influence on the wellbore collapse, and the larger the water absorption diffusion coefficient, the more obvious the collapse. The water absorption diffusion coefficient is a parameter that characterizes the transfer velocity of water in shale formation, which determines the ability of shale to absorb water and affects the hydration effect.

The inflow and outflow of formation water are affected by the drilling fluid activity. The drilling fluid activity affects the activity of formation water, thus affecting the hydration effect of shale. Figure 19 shows the wellbore enlargement rate with time under different drilling fluid activities. The original activity of formation water is 0.7, while the wellbore collapse does not

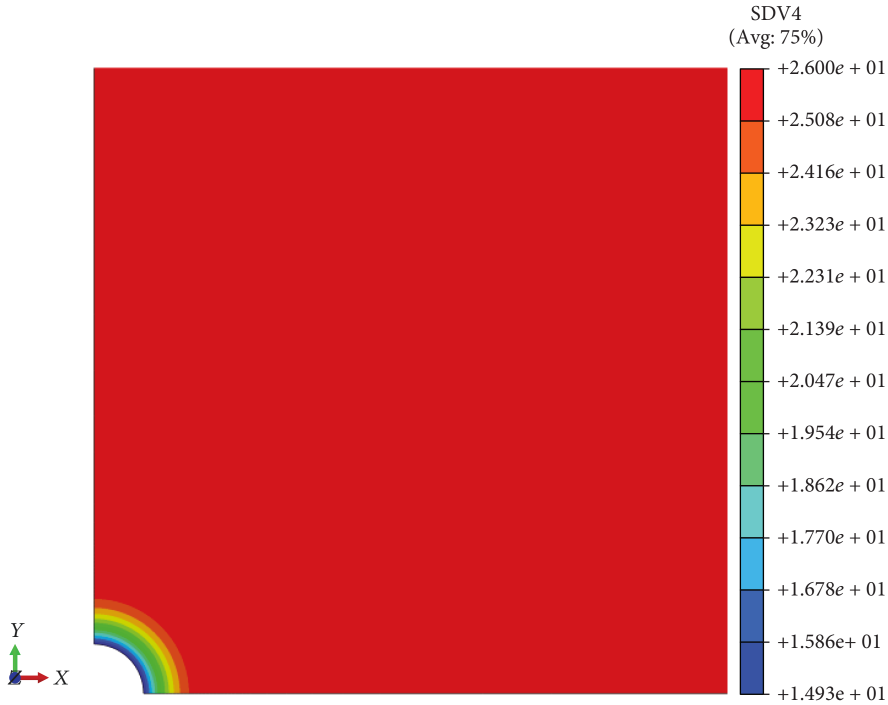

(a) 5 d

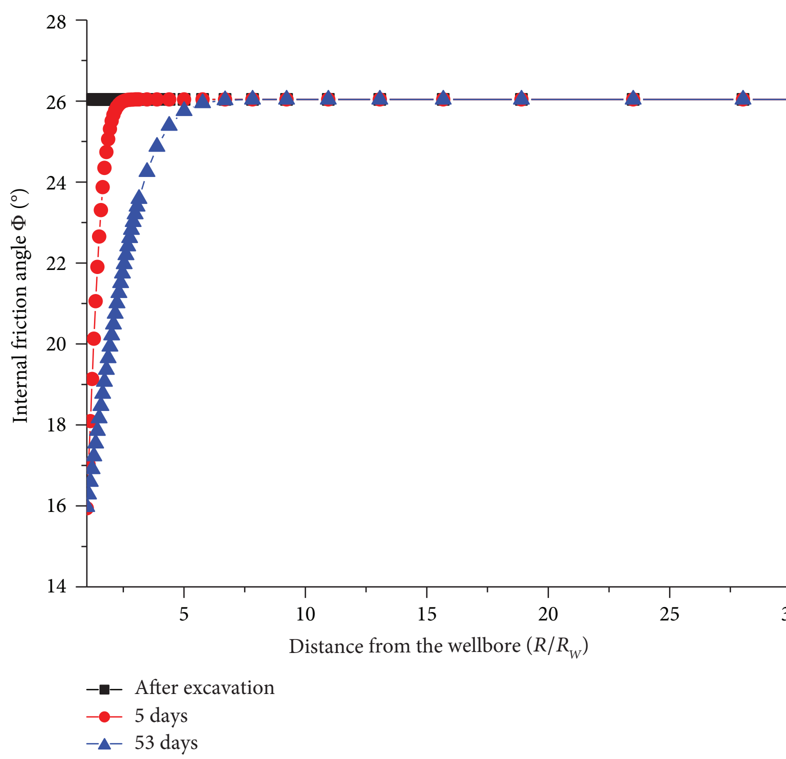

(b) Change along the radial direction

FIGURE 13: Variation of the friction angle of the formation after drilling.

change with time for the drilling fluid activity less than 0.7. When the drilling fluid activity is greater than the original activity of formation water, the drilling fluid erodes into the formation, causing the hydration effect obviously. With the increase of immersion time, the wellbore enlargement rate increases. When the drilling fluid activity is 0.95, the wellbore enlargement rate increases from 18.07% after excavation to 210.96% after 53 days.

Figure 20 shows the wellbore enlargement rate varying with time under different permeabilities of shale. It

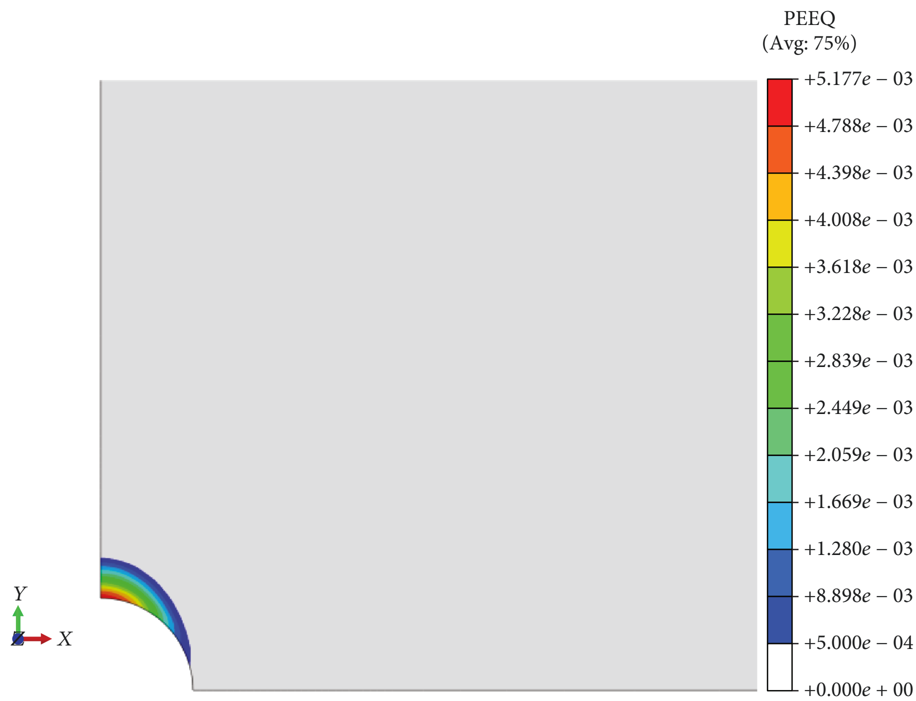

(a) Equivalent plastic strain distribution after excavation

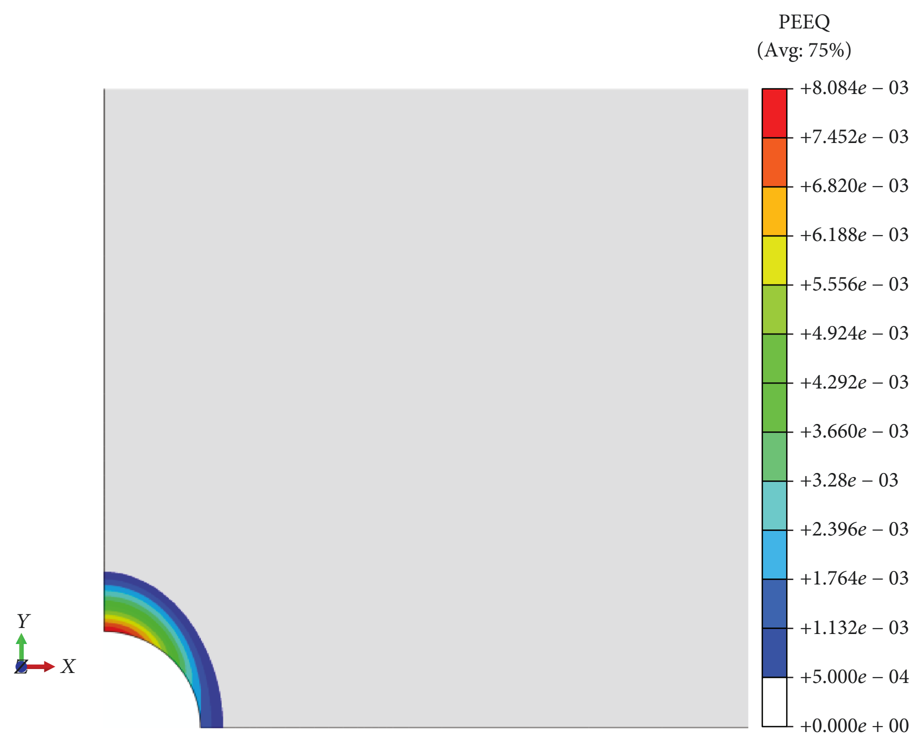

(b) Equivalent plastic strain distribution after 5 days

Figure 14: Progressive failure process of the wellbore with a drilling fluid density of 1.1.

can be seen that the influence of permeability on the wellbore enlargement rate is not obvious. However, the overall trend is that the wellbore enlargement rate at a small permeability is slightly smaller than the wellbore enlargement rate at a large permeability. The permeability of shale affects the ability of water to penetrate, but the effect on the wellbore enlargement rate is relatively weak.

According to the above analysis, the effects of different parameters on the wellbore collapse are different. Under underbalanced drilling conditions, drilling excavation disturbances cause the original crack extension and new

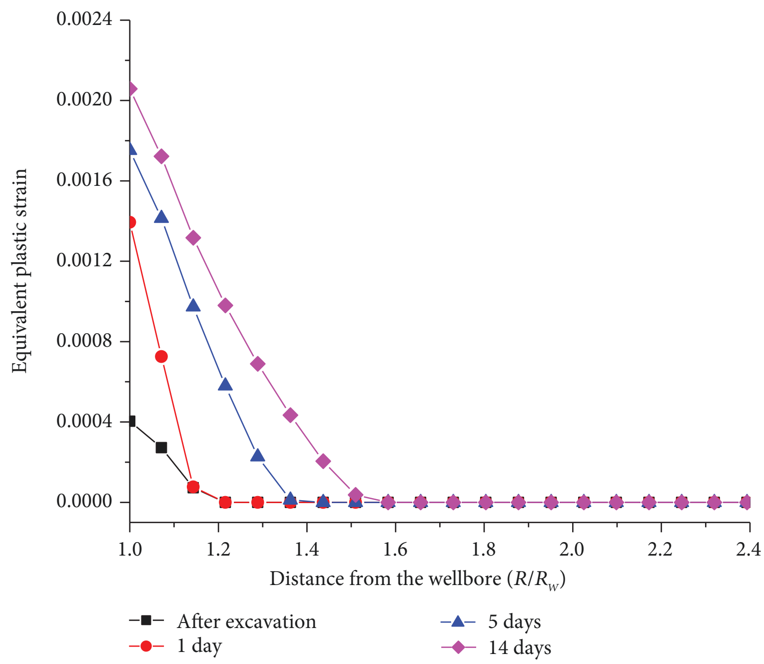

(a) AB line

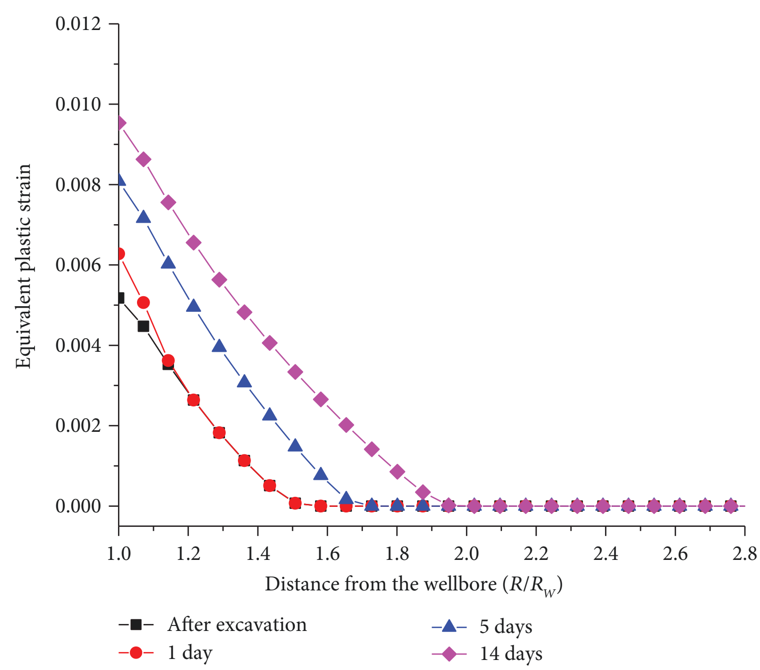

(b) ED line

Figure 15: Equivalent plastic strain along selected lines with a drilling fluid density of 1.1.

microcracks, which causes the shale hydration to expand by the self-water absorption effect of the microcracks. Due to hydration effect, the strength of shale gradually decreases, which is the intrinsic factor that leads to the progressive collapse of the wellbore. For using underbalanced drilling condition in a hard brittle shale formation, the drilling speed should be fast, the strong inhibition of drilling fluid to shale should be strictly controlled, and the circulation time should be minimized.

5.5. Comparison with Field Results. To verify the reliability and accuracy of the coupling model of the wellbore, the numerical results were compared with the field measured data.

In the actual drilling process, the wellbore is allowed to have a certain collapse. There is no drilling accident as long as there is no accumulated rock debris. Generally, the qualified wellbore conditions during drilling are as follows: the average wellbore enlargement rate is not more than 15%, or the maximum wellbore enlargement rate of the oil/gas

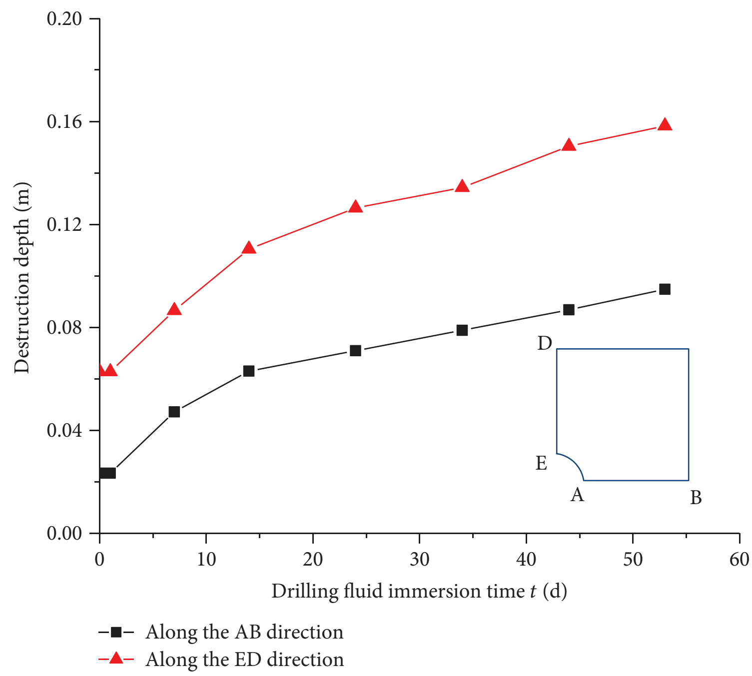

FIGURE 16: Failure depth change of the wellbore when the drilling fluid density is 1.1.

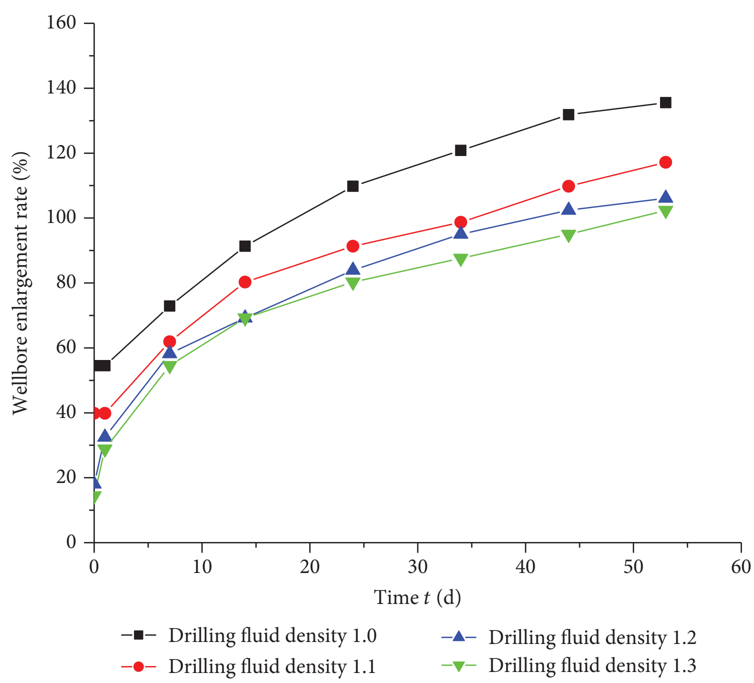

FIGURE 17: Curves of the wellbore enlargement rate with time under different drilling fluid densities.

reservoir is not more than 30% and the maximum wellbore section accounts for less than 30% of the whole reservoir. For the Shahejie Formation, the density of drilling mud is $1.2\,g/cm^3$ used for underbalanced drilling condition. During the drilling process, the wellbore is basically stable, only a few slight wellbore collapses occur, and there are no drilling accidents. The wellbore stability condition satisfies the requirements of underbalanced drilling with an average drilling rate of 1.78 m/h. According to the calculation results shown in Figures 18–20, the calculation value of the wellbore enlargement rate is 18% after drilling excavation, which is consistent with the field results.

During the process of water-based underbalanced drilling, the risk of leakage and reservoir damage by drilling fluid is reduced due to the drilling fluid pressure being lower than the formation pressure. However, the existence of capillary force makes the shale absorb water in a countercurrent mode, especially in the microcracks. As a result, the water absorption

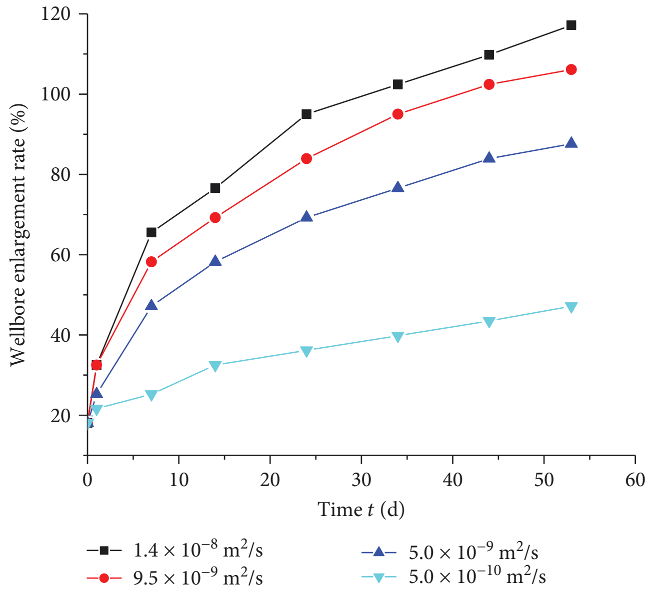

Figure 18: Curve of the wellbore enlargement rate with time under different water absorption and diffusion coefficients.

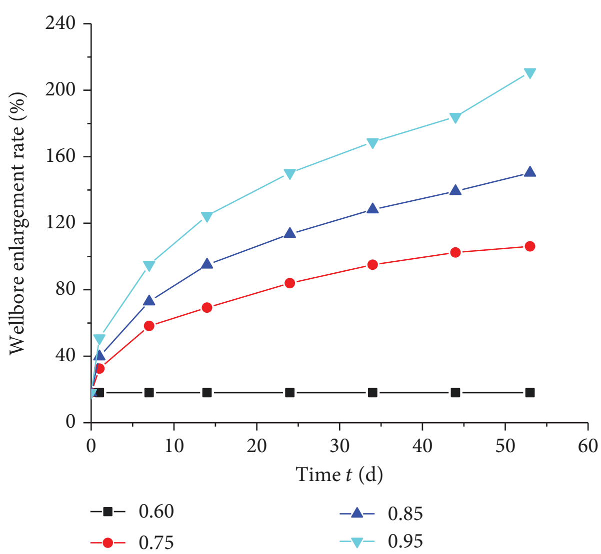

Figure 19: Curve of the wellbore enlargement rate with time under different drilling fluid activities.

causes the shale to be hydrated remarkably. In addition, the wellbore lacks the pressure balance by drilling fluid, which aggravates the wellbore collapse. A large number of falling rock blocks have been returned when pulling the drill string from the hole and starting logging work, and it is difficult to connect the column of the drilling string. Figure 21 shows the well diameter curve of the shale formation in W-82. The wellbore enlargement rate is between 55% and 85% in the depth of 4265 m to 4275 m, and the numerical value of the wellbore enlargement rate is about 84%. Then drill stem testing was carried out, and the wellbore has been immersed by drilling fluid for 53 days from drilling excavation to drilling down through the hole, which causes more rock blocks to be

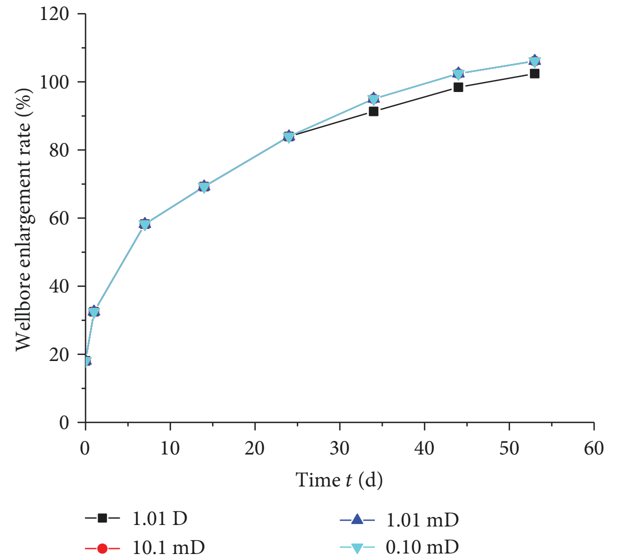

Figure 20: Curve of the wellbore enlargement rate with time under different shale permeabilities.

falling (Figure 22), formation instability, and wellbore collapse. The predicted wellbore enlargement rate in this paper has exceeded 100%, and the wellbore collapse is serious, which basically coincides with the actual drilling. The proposed model in this study can effectively reflect the progressive failure process of the wellbore in shale formation.

6. Conclusions

The microcracks of hard brittle shale in the mid-depth formation are well developed, the content of illite/montmorillonite mineral and illite in the formation is higher, and the shale is easy to be self-water hydration expanded, which is the root cause for wellbore instability during drilling. To simulate the whole process of progressive failure of hard brittle shale, a HMC model is developed, which is compiled with ABAQUS software as the solver.

In the initial stage of underbalanced drilling, there is no instability problem in the wellbore. As the immersion time increases, the wellbore gradually becomes unstable. Due to the influence of hydration, the wellbore enlargement rate increases with the increase of drilling fluid immersion time and different parameters have different effects on the wellbore enlargement rate. Water absorption diffusion coefficient and drilling fluid activity have a great influence on wellbore enlargement, while the permeability of shale on the wellbore enlargement rate is weak. The calculated results are basically consistent with the actual drilling, and the validity of the proposed model is verified.

Whether the drilling fluid can maintain the rock strength of the hard brittle shale well or not largely determines whether the drilling fluid can maintain the wellbore stability of the hard brittle shale formation. As for strong hydration characteristics and developed microcracks of hard brittle shale, the effective solution for the wellbore stabilization technology is to strengthen sealing and improve inhibition

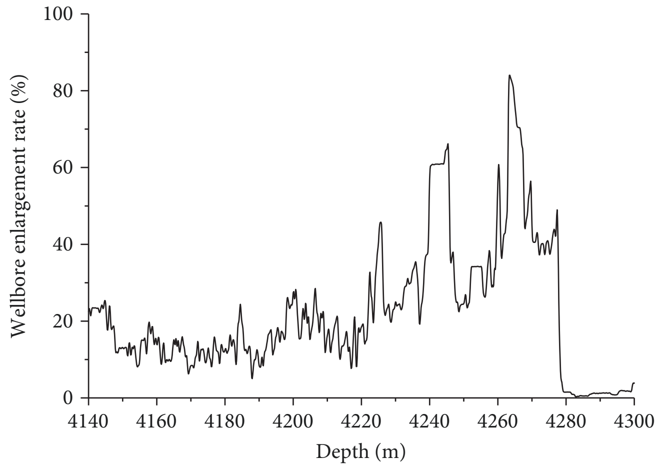

Figure 21: Field results of the enlargement rate of the W-82 well.

Figure 22: Returned rock block in the shale formation of the W-82 well.

ability of drilling fluid, instead of relying on increasing drilling fluid density.

Data Availability

The data used to support the findings of this study are included within the article.

Conflicts of Interest

The authors declare that there are no conflicts of interest regarding the publication of this paper.

Acknowledgments

The authors gratefully acknowledge the support of the Open Research Fund of the State Key Laboratory of the Oil and Gas Reservoir Geology and Exploitation (Grant no. PLN1507).

References

[1] J. Wang, S. Q. Lu, K. L. Zhu et al., "Maintaining wellbore stability in deep shale drilling in Nanpu oilfield," *Offshore Oil*, vol. 32, no. 1, pp. 92–96, 2012.

[2] A. H. Hale, F. K. Mody, and D. P. Salisbury, "Experimental investigation of the influence of chemical potential on wellbore stability," pp. 377–389, 1992.

[3] M. E. Chenevert, "Shale alteration by water adsorption," *Journal of Petroleum Technology*, vol. 22, no. 9, pp. 1141–1148, 1970.

[4] J. P. Simpson and H. L. Dearing, "Downhole simulation cell shows unexpected effects of shale hydration on borehole wall (includes associated papers 19519 and 19885)," *SPE Drilling Engineering*, vol. 4, no. 1, pp. 24–30, 1989.

[5] F. K. Mody and A. T. Uday, "Development of novel membrane efficient water-based drilling fluids through fundamental understanding of osmotic membrane generation in shales," in *SPE Annual Technical Conference and Exhibition*, San Antonio, TX, USA, September 2002.

[6] E. V. Oort, "Manipulation of coupled osmotic flows for stabilization of shales exposed to water-based drilling fluids," in *SPE Annual Technical Conference and Exhibition*, Dallas, TX, USA, October 1995.

[7] T. Huang, X. L. Pu, X. Luo, H. Yu, and S. J. Xu, "Stability analysis of shale wellbore based on fluid-solid coupling theory," *Journal of Oil and Gas Technology*, vol. 36, no. 10, pp. 117–121, 2014.

[8] H. Wen, M. Chen, Y. Jin et al., "Study on stability chemo-mechanical coupling of wellbore in inclined section of hard brittle shale," *Petroleum Exploration and Development*, vol. 41, no. 6, pp. 748–754, 2014.

[9] C. H. Yew and M. E. Chenevert, "Wellbore stress distribution produced by moisture adsorption," *SPE Drilling Engineering*, vol. 5, no. 04, pp. 311–316, 1990.

[10] R. Z. Huang, M. Chen, J. G. Deng, K. P. Wang, and Z. X. Chen, "Study on the coupling of mechanics and chemistry of shale wellbore stability," *Drilling Fluids and Completion Fluids*, vol. 12, no. 3, pp. 15–21, 1995.

[11] F. K. Mody and A. H. Hale, "Borehole-stability model to couple the mechanics and chemistry of drilling-fluid/shale interactions," *Journal of Petroleum Technology*, vol. 45, no. 11, pp. 1093–1101, 1993.

[12] E. V. Oort, A. H. Hale, and F. K. Mody, "Critical parameters in modelling the chemical aspects of wellbore stability in shales and in designing improved water based shale drilling fluids," pp. 171–186, 1996.

[13] F. T. Lomba, M. E. Chenevert, and M. M. Sharma, "The ion-selective membrane behavior of native shales," *Journal of Petroleum Science and Engineering*, vol. 25, no. 1-2, pp. 9–23, 2000.

[14] F. T. Lomba, M. E. Chenevert, and M. M. Sharma, "The role of osmotic effects in fluid flow through shale," *Journal of Petroleum Science and Engineering*, vol. 25, no. 1-2, pp. 25–35, 2000.

[15] M. Yu, G. Chen, and M. E. Chenevert, “Chemical and thermal effects on wellbore stability of shale formations,” in *SPE Annual Technical Conference and Exhibition*, New Orleans, LA, USA, September 2001.

[16] J. G. Zhang and M. E. Chenevert, “Maintaining the stability of deviated and horizontal wells: effects of mechanical, chemical and thermal phenomena on well designs,” in *International Oil & Gas Conference and Exhibition in China*, Beijing, China, December 2006.

[17] P. T. Chee, G. R. Brian, S. S. Rahman, and R. Andika, “Effects of swelling and hydration stress in shale on wellbore stability,” in *SPE Asia Pacific Oil and Gas Conference and Exhibition*, Kuala Lumpur, Malaysia, April 1997.

[18] C. P. Tan, S. S. Rahman, B. G. Richards, and F. K. Mody, “Integrated rock mechanics and drilling fluid design approach to manage shale instability,” in *SPE/ISRM Rock Mechanics in Petroleum Engineering*, Trondheim, Norway, July 1998.

[19] C. Tan, B. Richards, and S. S. Rahman, “Managing physico-chemical wellbore instability in shales with the chemical potential mechanism,” in *SPE Asia Pacific Oil and Gas Conference*, October 1996.

[20] R. Rickman, M. Mullen, E. Petre, B. Grieser, and D. Kundert, “A practical use of shale petrophysics for stimulation design optimization: all shale plays are not clones of the Barnett shale,” in *SPE Annual Technical Conference and Exhibition*, Denver, CO, USA, September 2008.

[21] Y. H. Lu, M. Chen, Y. Jin, X. Q. Teng, W. Wu, and X. Q. Liu, “Experimental study of strength properties of deep shale under drilling fluid immersion,” *Chinese Journal of Rock Mechanics and Engineering*, vol. 31, no. 7, pp. 1399–1405, 2012.

[22] H. Y. Huang, *Numerical Simulation of Time Dependent Wellbore Instability in Shale Formation and Application*, China University of Petroleum, Qingdao, 2016.

[23] S. Yin, B. F. Towler, M. B. Dusseault, and L. Rothenburg, “Fully coupled THMC modeling of wellbore stability with thermal and solute convection considered,” *Transport in Porous Media*, vol. 84, no. 3, pp. 773–798, 2010.

[24] F. Meng, G. F. Fuh, and J. A. Spencer, “Managing geomechanics principles for proper handling of wellbore-stability problems in shale and depletion effects on formations while drilling,” in *SPE Annual Technical Conference and Exhibition*, Florence, Italy, September 2010.

[25] C. Y. Zhou and F. X. Zhu, “An elasto-plastic damage constitutive model with double yield surfaces for saturated soft rock,” *International Journal of Rock Mechanics and Mining Sciences*, vol. 47, no. 3, pp. 385–395, 2010.

[26] Q. Tao and A. Ghassemi, “Poro-thermoelastic borehole stress analysis for determination of the in situ stress and rock strength,” *Geothermics*, vol. 39, no. 3, pp. 250–259, 2010.

[27] T. Hemphill, V. X. Nguyen, Y. Abousleiman, and M. H. Tran, “Changing the safe drilling window with invert emulsion drilling fluids: advanced wellbore stability modeling using experimental results,” in *International Oil and Gas Conference and Exhibition in China*, Beijing, China, June 2010.

[28] A. Zervos, P. Papanastasiou, and J. Cook, “Elastoplastic finite element analysis of inclined wellbores,” in *SPE/ISRM Rock Mechanics in Petroleum Engineering*, Trondheim, Norway, July 1998.

[29] S. P. Jia, W. Z. Chen, J. P. Yang, and P. S. Chen, “An elastoplastic constitutive model based on modified Mohr-Coulomb criterion and its numerical implementation,” *Rock and Soil Mechanics*, vol. 31, no. 7, pp. 2051–2058, 2010.

[30] H. C. Shen and X. Q. Hu, “Research on in-situ stress and wellbore stability of overthrust structural belt and its application,” *Xinjiang Petroleum Geology*, vol. 32, no. 2, pp. 193–196, 2011.

[31] S. P. Jia, C. S. Zou, Y. Z. Wang, X. J. Tan, and X. X. Gan, “Numerical analysis of oil drilling construction process based on thermal-flow-solid coupling model,” *Rock and Soil Mechanics*, vol. 33, no. s2, pp. 321–328, 2012.

Hindawi
Geofluids
Volume 2019, Article ID 2624716, 13 pages
https://doi.org/10.1155/2019/2624716

Research Article

Numerical Simulations of Fracture Propagation in Jointed Shale Reservoirs under CO_2 Fracturing

Qi Zhang ,[1,2] Dan Ma ,[1,2] Jiangfeng Liu ,[2] Jiehao Wang ,[3] Xibing Li ,[1] and Zilong Zhou[1]

[1]*School of Resources and Safety Engineering, Central South University, Changsha, 410083 Hunan, China*
[2]*State Key Laboratory for Geomechanics and Deep Underground Engineering, China University of Mining and Technology, Xuzhou, 221116 Jiangsu, China*
[3]*Department of Energy and Mineral Engineering, EMS Energy Institute and G3 Center, Pennsylvania State University, University Park, PA 16802, USA*

Correspondence should be addressed to Dan Ma; dan.ma@csu.edu.cn

Received 8 November 2018; Revised 5 February 2019; Accepted 5 March 2019; Published 7 April 2019

Guest Editor: Qianbing Zhang

Water-based hydraulic fracturing for the exploitation of shale gas reservoirs may be limited by two main factors: (1) water pollution and chemical pollution after the injection process and (2) permeability decrease due to clay mineral swelling upon contact with the injection water. Besides, shale rock nearly always contains fractures and fissures due to geological processes such as deposition and folding. Based on the above, a damage-based coupled model of rock deformation and gas flow is used to simulate the fracturing process in jointed shale wells with CO_2 fracturing. We validate our model by comparing the simulation results with theoretical solutions. The research results show that the continuous main fractures are formed along the direction of the maximum principal stress, whilst hydraulic fractures tend to propagate along the preexisting joints due to the lower strength of the joints. The main failure type is tensile damage destruction among these specimens. The preexisting joints can aggravate the damage of the numerical specimens; the seepage areas of the layered jointed sample, vertical jointed sample, and orthogonal jointed sample are increased by 32.5%, 29.16%, and 35.05%, respectively, at time $t = 39$ s compared with the intact sample. The preexisting horizontal joints or vertical joints promote the propagation of hydraulic fractures in the horizontal direction or vertical direction but restrain the expansion of hydraulic fractures in the vertical or horizontal direction.

1. Introduction

In recent years, the application of hydraulic fracturing has significantly increased the production of oil and natural gas. It is estimated that hydraulic fracturing has improved recoverable reserves of oil by at least 30% and of natural gas by 90% [1]. In addition, more than 60% of oil and gas wells need to be fractured first, especially for unconventional gas resource deposited in deep underground shale layers with extremely small permeability (usually less than 1 mD) [2, 3]. Hydraulic fracturing may increase permeability of shale by three to five orders of magnitude [4]. Thus, the production of the fractured gas wells increases dramatically. In all, hydraulic fracturing introduced in oil and gas fields has revolutionized gas production around the world [5, 6].

However, the water-based fracturing technology has some limitations and environmental concerns. First, hydraulic fracturing consumes large amounts of water. According to a report [7], the water use for hydraulic fracturing accounts for 9% of total freshwater consumption in Texas. The large consumption of water will restrict the oil and gas reservoir developments in a water-deficient area [8, 9]. Second, due to the large amount of water and chemical reagents used in the hydraulic fracturing, it may cause potential water pollution and chemical pollution if the treatment of flowback fluids with chemical reagents is insufficient [10–12]. Third, for the reservoirs containing clay minerals, the permeability may decrease after water injection, thereby decreasing the production of gas reservoirs [13–15]. The main reason is that, when the hydration minerals meet injection water, clay minerals can swell and result in blockage of seepage channels [16]. All of these disadvantages of hydraulic fracturing promote the study and development of waterless fracturing [17].

Several waterless fracturing technologies have been introduced in oil and gas industries over the past few decades, including oil-based fracturing, N_2 fracturing, and CO_2 fracturing [18]. Oil-based fracturing was first used in Colorado, Texas, and Kansas in late 1940s [19]. Compared with hydraulic fracturing, it could be conducted in frozen areas. However, oil-based fracturing is expensive and may impair the effective permeability of wells [20]. N_2 fracturing and CO_2 fracturing are the two most popular fracturing methods because they are more economical and efficient compared with hydraulic fracturing [21]. According to engineering production data [22], the production of the reservoirs stimulated by CO_2 is 1.9 times as much as the production of those stimulated by N_2. The laboratory experiment results indicate that the gas with lower viscosity, higher diffusivity, and lower surface tension can penetrate into smaller pore space to create more complex fracture networks compared with hydraulic fracturing [23, 24]. In addition, the fracture surface created by gas fracturing has a larger roughness and complexity, resulting in a greater increase in permeability [4].

In addition, shale reservoirs always contain kinds of joints caused by the geological deposition and folding [25–27]. The existing joints have a significant influence on the initiation and propagation of the induced hydraulic fractures [28–30]. The fracture networks of jointed reservoirs may be very complex due to the reopening of the existing joints, the expansion of hydraulic fractures, and the intersection between joints and hydraulic fractures [31]. Nitrogen fracturing experiments were conducted on shale samples vertical and parallel to the bedding plane; the results indicated that a relative complex fracture surface is formed in the shale sample vertical to the bedding plane [32]. He et al. [33] performed hydraulic fracturing on shale with bedding planes; the results showed that the bedding planes in shale formation have a significant influence on the propagation of hydraulic fractures. However, the mechanism of the fracture initiation and propagation in kinds of jointed reservoirs is not well investigated. It is important to learn the distribution of fracture networks for the successful design of stimulation in jointed reservoirs.

To this end, the numerical tools COMSOL and MATLAB are used to simulate the hydraulic fracture propagation driven by injection fluids in several jointed reservoirs. The distribution of fracture networks and the development of horizontal and vertical fracture radii are studied in this work.

2. Governing Equations

In the numerical simulation, CO_2 is injected into the borehole. Then, the rock mass begins to fracture with the increasing injection pressure. The process of CO_2 fracturing involves solid deformation and fluid seepage. In this part, a series of governing equations are set up for solid mechanic field and flow field. Besides, damage equations are introduced to describe the destruction of the calculation elements.

2.1. Rock Deformation and Damage Evolution Equations. In this work, shale rock is assumed as an elastic continuum material, whose constitutive relation satisfies with the physical equation of elasticity. It should be noted that the influence of pore pressure on stress distribution is also considered in the equation. Thus, the modified physical equation can be induced as

$$\sigma_{ij} = 2G\varepsilon_{ij} + 2G\frac{\nu}{1-2\nu}\varepsilon_\nu\delta_{ij} - \alpha p\delta_{ij}, \quad (1)$$

where σ_{ij} is the total stress tensor, ε_{ij} is the total strain tensor, $G = E/2(1+\nu)$ is the shear modulus of rock, E is the elastic modulus of the rock, ν is Poisson's ratio of the rock, $\varepsilon_\nu = \varepsilon_{11} + \varepsilon_{22} + \varepsilon_{33}$ is the volumetric strain, δ_{ij} is the Kronecker delta, α is the Biot coefficient, and p is the pore pressure.

The relationship between strain and displacement is expressed by a geometric equation as follows:

$$\varepsilon_{ij} = \frac{1}{2}\left(u_{i,j} + u_{j,i}\right), \quad (2)$$

where u_i and u_j are the components of displacement in i and j directions, respectively.

Substituting the modified physical equation (1) and the geometric equation (2) into the equilibrium equation, then the modified Navier-type equation is induced as

$$Gu_{i,jj} + \frac{G}{1-2\nu}u_{j,ji} - \alpha p_i + f_i = 0, \quad (3)$$

where f_i is the component of the net body force.

Since the initiation and propagation of hydraulic fractures are studied in this work, a damage model is introduced to characterize the damage condition during the injection process. The damage model is used to determine whether shale damage occurs after every calculation step. For the calculation element, when the stress state meets the maximum tensile stress criterion or the Mohr-Coulomb criterion, the tensile crack or shear crack occurs. It should be noted that the tensile crack is first generated, because the compressive strength is ten times greater than the tensile strength. Equations (4) and (5) are the maximum tensile stress criterion and the Mohr-Coulomb criterion, respectively:

$$F_1 = \sigma_1 - f_{t0} = 0, \quad (4)$$

$$F_2 = -\sigma_3 + \sigma_1\frac{1+\sin\varphi}{1-\sin\varphi} - f_{c0} = 0, \quad (5)$$

where σ_1 and σ_3 are the first and third principle stresses; f_{t0} and f_{c0} are the tensile strength and compressive strength of rock, respectively; and φ is the internal friction angle.

When elements start to be damaged, the elastic modulus reduces correspondingly according to damage theory [34]. The evolution of elastic modulus is defined as

$$E = E_0(1-D),$$
$$k = k_0 \exp(\alpha_k D), \tag{6}$$

where E_0 is the initial elastic modulus of rock and D is the damage variable and is calculated as [35–37]

$$D = \begin{cases} 0, & F_1 < 0, F_2 < 0, \\ 1 - \left|\dfrac{\varepsilon_t}{\varepsilon_1}\right|^2, & F_1 = 0, dF_1 > 0, \\ 1 - \left|\dfrac{\varepsilon_c}{\varepsilon_3}\right|^2, & F_2 = 0, dF_2 > 0, \end{cases} \tag{7}$$

where ε_1 and ε_3 are the first and third principal strains and ε_t and ε_c are the tensile strain and compressive strain, respectively.

2.2. Gas Flow Equation. Gas flow equations are defined to describe the injection gas flow in this part. The gas continuity equation during gas transportation is defined as

$$\frac{\partial m}{\partial t} + \nabla \cdot \left(\rho_g q_g\right) = Q_m, \tag{8}$$

where m is the gas mass per volume of rock, ρ_g is the density of the injection gas, q_g is the seepage velocity of the gas, Q_m is the source origin, and t is the time variable.

On the basis of Darcy's law, the seepage velocity of gas is shown as

$$q_g = -\frac{k}{\mu}\nabla p, \tag{9}$$

where k is the permeability of the rock and μ is the dynamic viscosity coefficient.

Assuming that shale rock is saturated by CO_2 after the injection, the gas content per volume of rock can be defined as $m = \rho_g \phi$, and ϕ is the porosity of the rock. Injected CO_2 gas enters the supercritical state when the pressure exceeds 7.56 MPa at the temperature 76.8 degrees Celsius [38]. When the injection CO_2 is transformed from the gaseous state to the supercritical state, density and viscosity change dramatically under the different pressure. The evolution of density and viscosity of CO_2 varying with pressure is shown in Figure 1. The relationship between density, viscosity, and pressure can be described by interpolating function in the model calculation. Thus, the first item in equation 7 is induced to equation (10) [39] as

$$\frac{\partial m}{\partial t} = \phi\frac{\partial \rho_g}{\partial t} + \rho_g\frac{\partial \phi}{\partial t} = \frac{\partial p}{\partial t}\phi c \rho_g. \tag{10}$$

The density of CO_2 changes rapidly with pressure whilst the porosity of shale changes slightly during hydraulic fracturing. Thus, $\rho_g(\partial\phi/\partial t)$ is ignored since $\rho_g(\partial\phi/\partial t)$ is much smaller than $\phi(\partial\rho_g/\partial t)$, where $c = (1/\rho_g)(\partial\rho_g/\partial p)$ is the

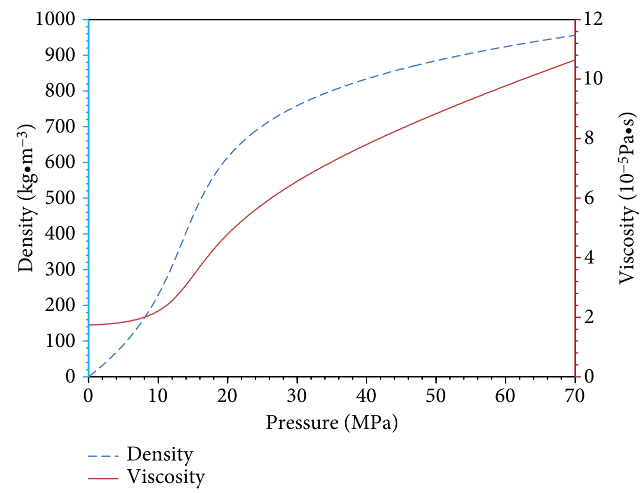

Figure 1: The evolution of density and viscosity of CO_2 with pressure ($T = 76.8^\circ$C).

compressibility coefficient of CO_2 and c can be calculated from Figure 1.

Putting equations (9) and (10) into equation (8), the gas continuity equation can be induced into equation (11) as

$$\frac{\partial p}{\partial t}\phi c \rho_g + \nabla \cdot \left(-\frac{k}{\mu}\rho_g \nabla p\right) = Q_m. \tag{11}$$

Considering the influence of solid mechanics on the evolution of porosity, the dynamic evolution of porosity can be described by [40]

$$\phi = \alpha - (\alpha - \phi_0)\exp\left[\varepsilon_v - \varepsilon_{v0} - \frac{(p - p_0)}{K_s}\right], \tag{12}$$

where ϕ_0 is the initial porosity of shale rock, ε_{v0} is the initial volumetric strain, p_0 is the initial pore pressure, and K_s is the bulk modulus of rock grains.

2.3. Characterization of Rock Heterogeneity. Since rock is heterogeneous material with natural fissures and induced fissures [41], Weibull distribution function is introduced to represent the heterogeneity of shale rock in this part [42]. In this work, parameters, such as elastic modulus and strength, are assumed to conform to the Weibull distribution and produced in MATLAB. Weibull statistical distribution and the probability density function are defined as

$$f(x, \bar{x}, \lambda) = \frac{\lambda}{\bar{x}}\left(\frac{x}{\bar{x}}\right)^{\lambda-1}\exp\left[-\left(\frac{x}{\bar{x}}\right)^{\lambda}\right], \tag{13}$$

where x is the mechanical parameter of rock, $\bar{x}$ is the average value of x, and λ is the coefficient of heterogeneity.

3. Numerical Simulation Setup

3.1. Model Geometry. Before the simulation, the models for gas fracturing, boundary settings, and parameters are introduced in this part. The 2D calculation model here is a 2D

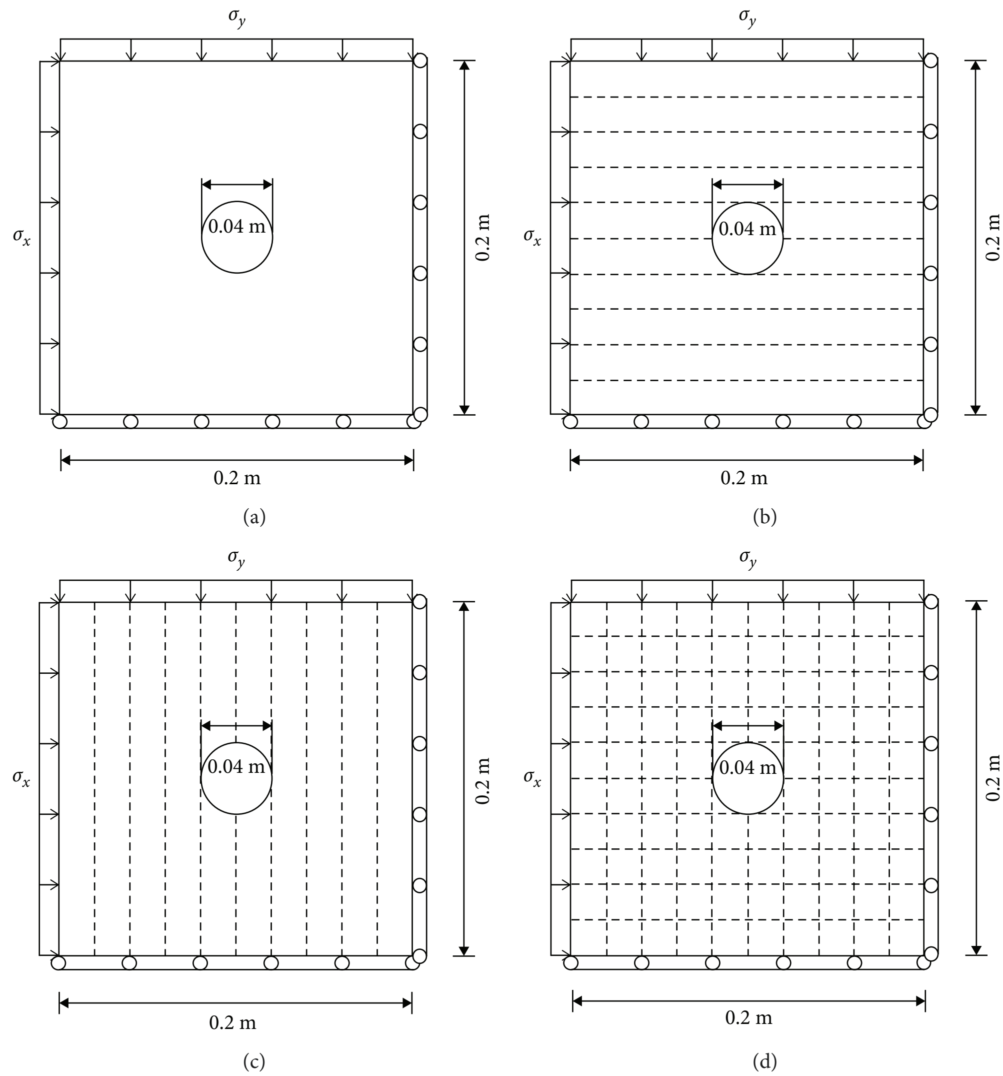

Figure 2: Numerical samples with different kinds of joints: (a) intact sample, (b) sample with layered joints, (c) sample with vertical joints, and (d) sample with orthogonal joints.

Table 1: Mechanical parameters for the simulations.

Mechanical parameters	Rock matrix	Joint	Unit
Elastic modulus	36	18	GPa
Poisson's ratio	0.225	0.25	—
Rock density	2600	2600	kg/m^3
Compressive strength	62	31	MPa
Tensile strength	8.2	4.1	MPa
Initial rock permeability	10^{-18}	1.3×10^{-17}	m^2
Initial rock porosity	0.01	0.015	—
Biot coefficient	0.2	0.3	—
Internal fraction angle	0.117π	0.117π	rad

plane cross-section through a horizontal well, which is a 2D plane square with a length of 0.2 m and a borehole with a diameter of 0.04 m drilled in the center. The distribution of preexisting horizontal joints, vertical joints, and orthogonal joints is showed in Figure 2. The thickness of the joints is 1 mm among these models. For mechanical boundary settings, the load applied on the left boundary is equal to that on the upper boundary, the value is 5 MPa, whilst the right boundary and lower boundary are roller boundaries; these boundary settings are the same for the intact sample, layered jointed sample, vertical jointed sample, and orthogonal jointed sample. The gas is injected from the inner boundary with the injection rate of 0.0106 m^3/s. As for seepage boundaries, there is no flow boundary on the outer boundaries. The parameters for the rock matrix and joints are listed in Table 1; it should be noted that the elastic modulus, tensile strength, and compressive strength of joints are only half of those of the rock matrix.

3.2. Numerical Implementation of the Model. In the front parts, the coupling equations and model geometry are established. Due to the complexity of the coupling relationship between solid deformation and fluid flow, these equations are difficult to be directly calculated. Thus, the finite element method is adopted to solve coupling equations via COMSOL

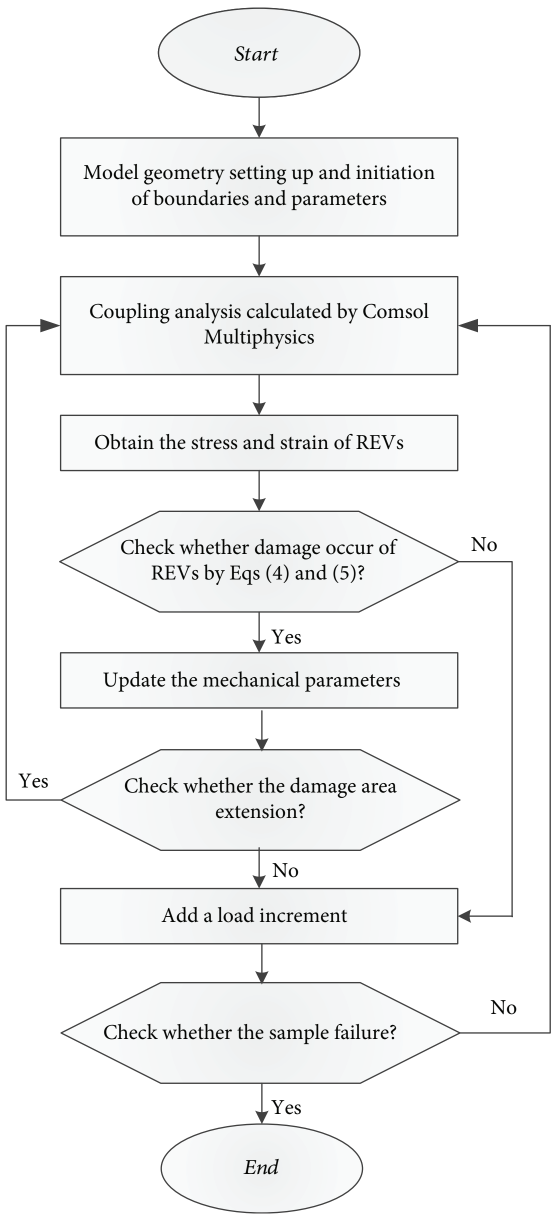

Figure 3: Calculation procedures of the numerical model.

Multiphysics and MATLAB. The distribution of stress and pore pressure is obtained to further discuss the condition of the numerical sample. The flow chart of numerical calculation procedures is showed in Figure 3.

3.3. Model Validation. It is important to validate the effectiveness of the model before it is used to simulate the fracture propagation in the jointed reservoirs. The classical theoretical solution for forecasting the breakdown pressure [43] is shown as

$$p_b = \sigma_t - \sigma_1 + 3\sigma_3 - p_0, \tag{14}$$

where p_b is the breakdown pressure, σ_t is the tensile strength of the rock, σ_1 and σ_3 are the maximum and minimum principal stresses, respectively, and p_0 is the initial pore pressure.

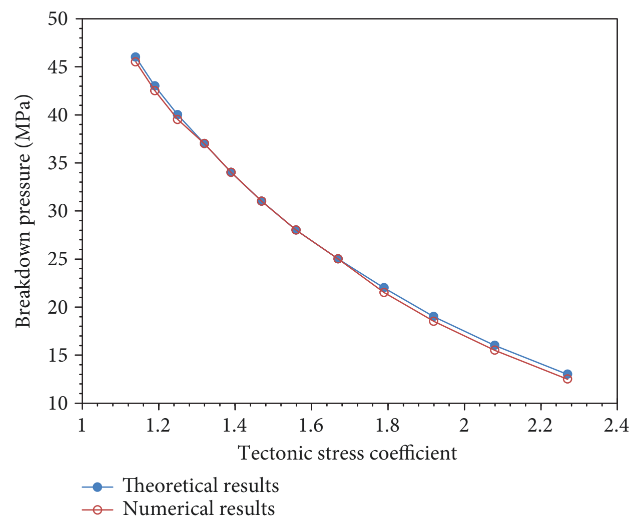

Figure 4: Comparison of the theoretical solution and numerical solution of breakdown pressure under different tectonic stress coefficients.

The numerical specimen used in this part is the same with the intact sample shown in Figure 2(a). In this part, the initial pore pressure is 1 MPa, the average tensile strength and compressive strength of the specimen are 5.9 MPa and 59.4 MPa, respectively, and the average elastic modulus of the numerical specimen is 35.9 GPa. The horizontal stress is fixed at 25 MPa, and the vertical stress is varying from 10 MPa to 25 MPa. A tectonic stress coefficient $\beta(\sigma_x/\sigma_y)$ is defined in this part, and the breakdown pressure versus the tectonic stress coefficient is calculated in this part.

A comparison of the breakdown pressure with different tectonic stress coefficients by the theoretical solution and numerical solution is shown in Figure 4. The results show that the numerical simulation results agree well with results obtained from the theoretical equation, indicating that the proposed model is suitable to simulate the hydraulic fracture propagation under CO_2 fracturing.

4. Results and Discussion

4.1. Fracture Propagation in the Intact Sample. The hydraulic fracture initiation and propagation in an intact sample without joints are shown in Figure 5. To distinguish tensile cracks and shear cracks, the damage in tension is defined as negative whilst that in shear is defined as positive. It can be seen that the fractures first appear around the borehole and propagate gradually to the surrounding rock with the increase of injection gas pressure [44]. Eventually, several main fractures are formed uniformly in the rock sample. As shown in Figure 5, hydraulic fractures are principally formed in the tensile mode in the intact sample during gas fracturing, and the number of damaged elements in the tensile mode accounts for 93.6% of the total number of damaged elements at time $t = 37$ s.

Figure 6 shows the development of the seepage area versus injection time. It should be noted that the cracks (damage area) are generated from the destruction of the elements. The

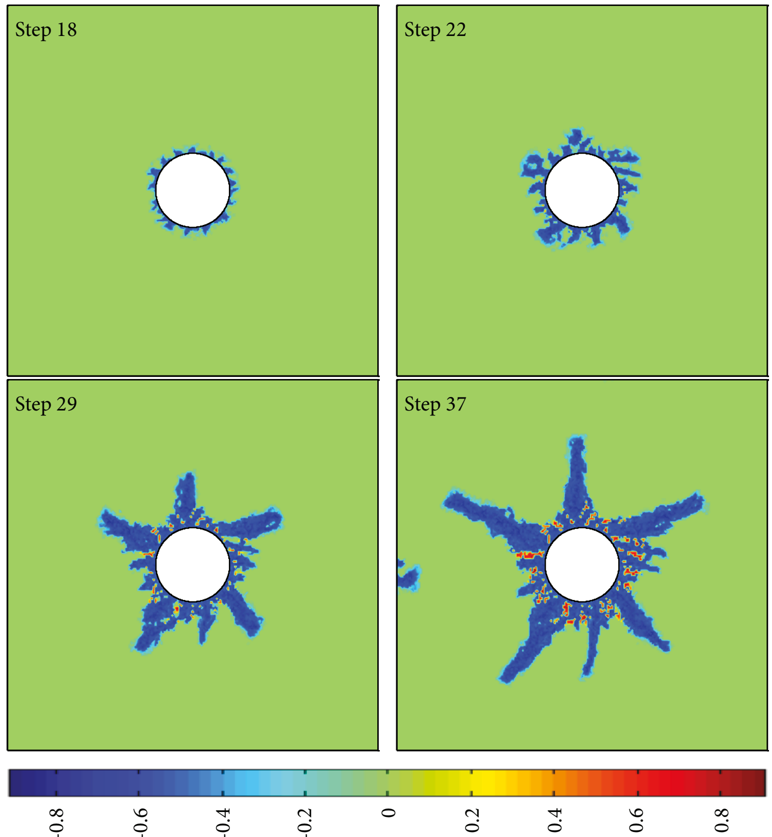

Figure 5: Distribution and evolution of the fracture in the intact sample.

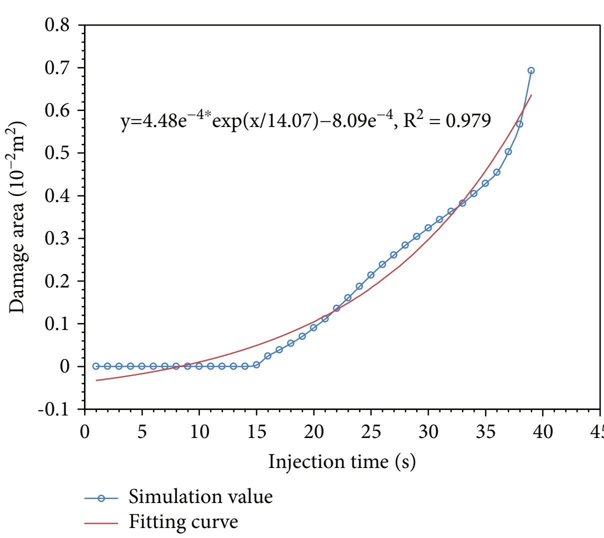

Figure 6: Development of the seepage area versus injection time in the intact sample.

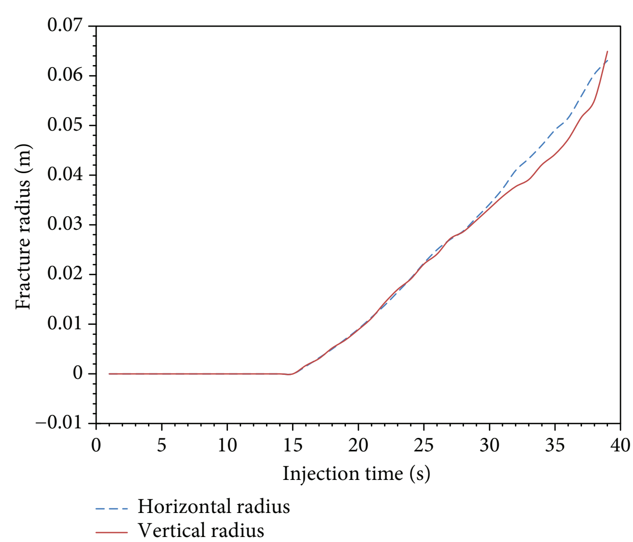

Figure 7: Development of horizontal and vertical fracture radii versus injection time in the intact sample.

seepage area keeps as $0\,\mathrm{m}^2$ due to the low gas pressure from $t = 0$ s to $t = 15$ s. Then, the seepage area increases slowly from $3.27e^{-5}$ m^2 to $3.44e^{-3}$ m^2 from $t = 16$ s to $t = 31$ s with fracture initiation and gradual propagation. Besides, it increases dramatically from $3.44e^{-3}$ m^2 to $6.93e^{-3}$ m^2 from $t = 31$ s to $t = 39$ s, indicating that unstable fracture propagation occurs. The whole process of the evolution of the seepage area can be fitted by an exponential function as shown in Figure 6.

The development of horizontal and vertical fracture radii versus injection time in the intact sample is presented in Figure 7. It can be seen that hydraulic fractures initiate at time $t = 16$ s. As the injection gas pressure in the borehole further increases, the fracture radii in horizontal and vertical

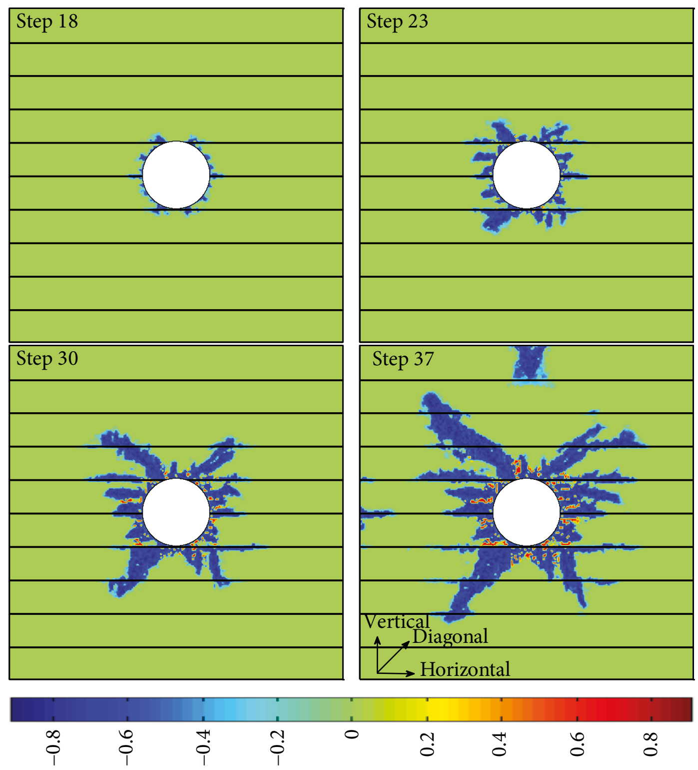

Figure 8: Distribution and evolution of the fracture in the layered jointed sample.

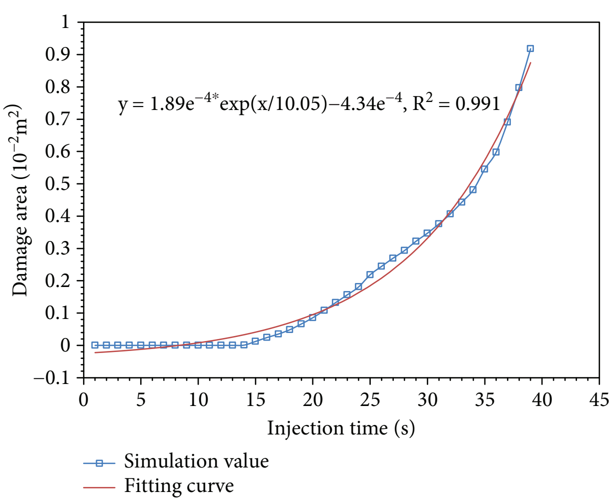

Figure 9: Development of the seepage area versus injection time in the layered jointed sample.

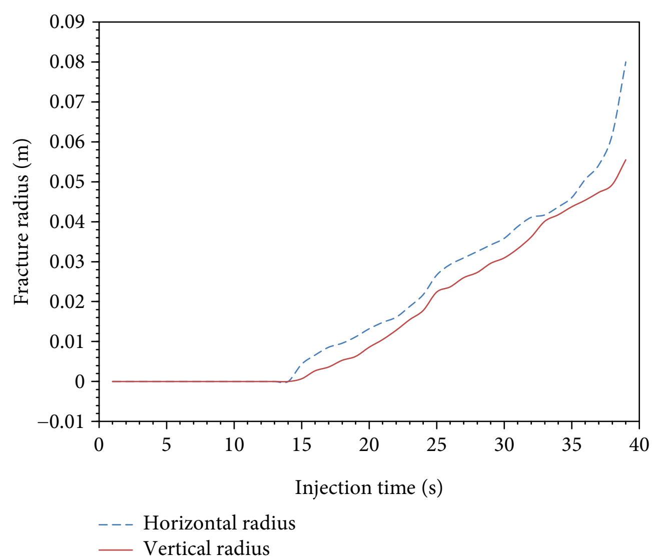

Figure 10: Development of horizontal and vertical fracture radii versus injection time in the layered jointed sample.

directions increase at a similar rate, reaching $6.3e^{-2}$ m and $6.49e^{-2}$ m at time $t = 39$ s, respectively. The slight difference of two curves shown in Figure 7 may result from the heterogeneity of mechanical parameters assigned to the sample.

4.2. Fracture Propagation in the Layered Jointed Sample. In the shale gas wells, the surrounding rock contains kinds of joints and fissures caused by the geological deposition and folding. The existence of these joints and fissures has a significant influence on the propagation of hydraulic fractures. Based on the above, hydraulic fracture propagation in kinds of joint samples will be discussed in the following parts. The fracture propagation in layered jointed samples is researched in this part.

The distribution and evolution of the fracture in the layered jointed sample are presented in Figure 8. At time $t = 15$ s, the sample begins to fracture. Hydraulic fractures first emerge around the drilling hole at time $t = 18$ s due to stress concentration in the inner boundary. With the increase of the injection time, hydraulic fractures propagate to the

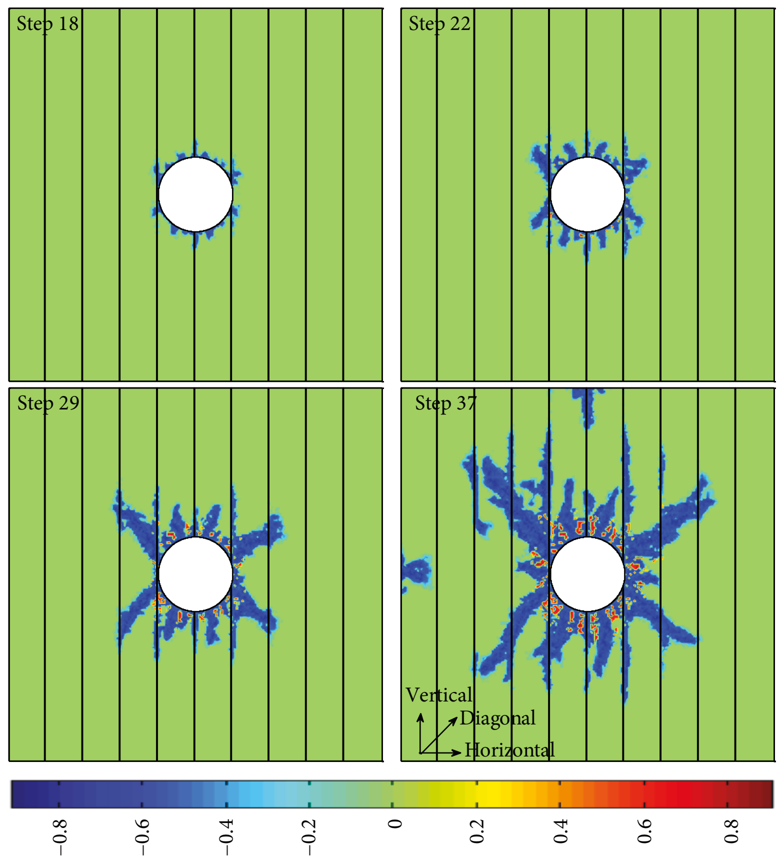

FIGURE 11: Distribution and evolution of the fracture in the vertical jointed sample.

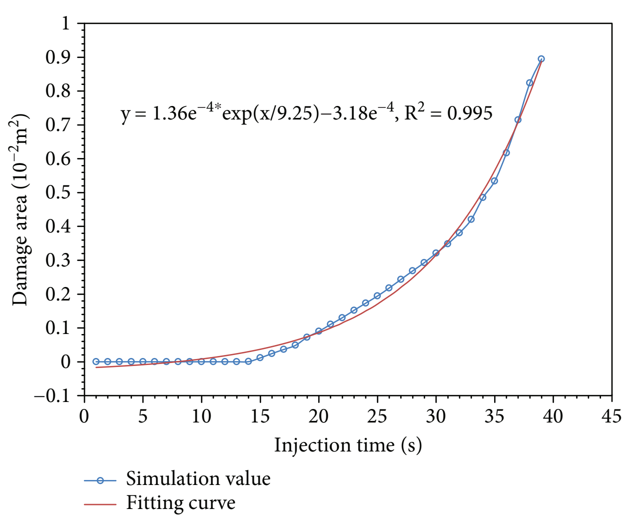

FIGURE 12: Development of the seepage area versus injection time in the vertical jointed sample.

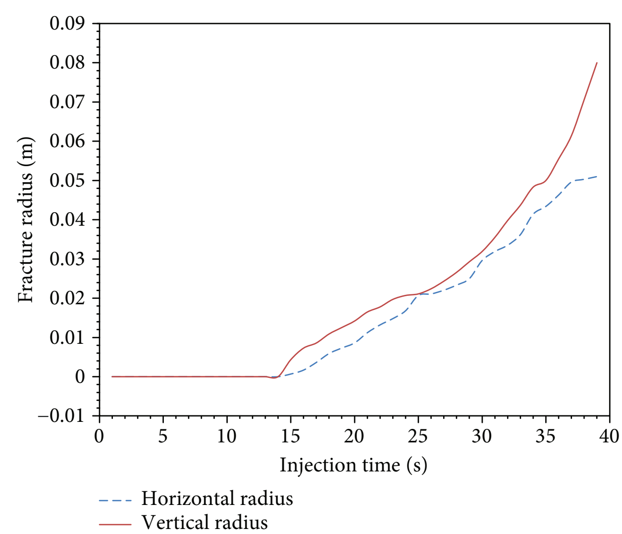

FIGURE 13: Development of horizontal and vertical fracture radii versus injection time in the vertical jointed sample.

surrounding rock. Finally, fractures propagate along the diagonal direction and horizontal direction forming several main fractures, as shown in Figure 8. The distribution of the fracture is different from that in the intact sample. This result from the fracture propagation favors the horizontal preexisting joints along which the least energy is dissipated due to their low strength and elastic modulus.

The seepage area begins to increase from time $t = 14$ s; then, it increases slowly from $7.92e^{-6}$ m^2 to $3.22e^{-3}$ m^2 from time $t = 14$ s to $t = 29$ s due to the low injection gas pressure at the initial stage. With the increase of injection gas pressure, the seepage area increases rapidly from $3.22e^{-3}$ m^2 to $9.18e^{-3}$ m^2 from time $t = 29$ s to $t = 39$ s. The seepage area increases by 32.5% in this case compared with that in the

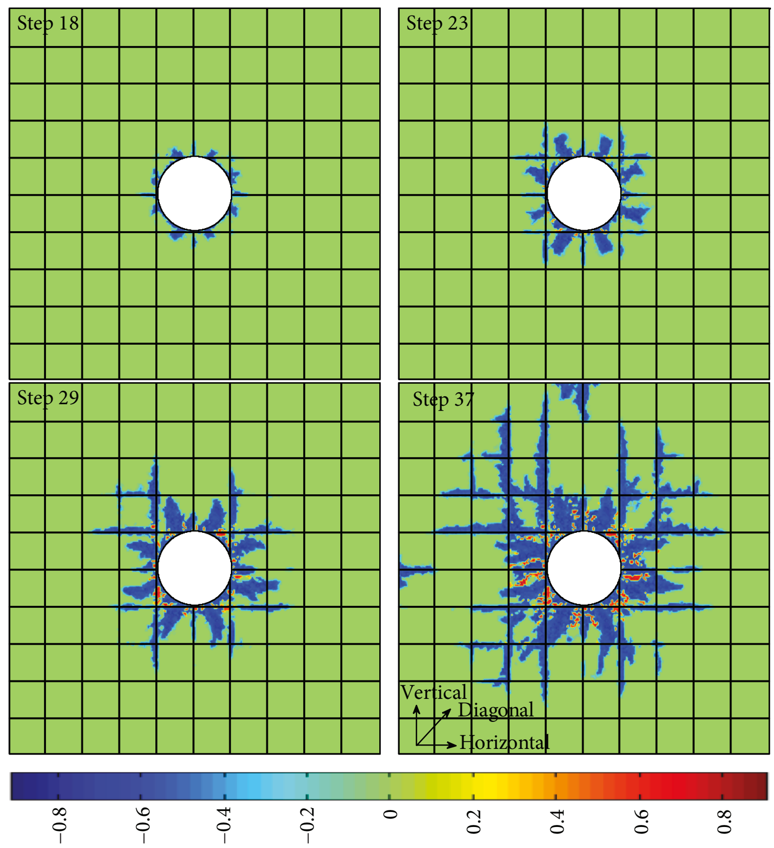

FIGURE 14: Distribution and evolution of the fracture in the orthogonal jointed sample.

intact sample at time $t = 39$ s. An exponential function is used to describe the development of the seepage area (Figure 9).

Figure 10 is the development of horizontal and vertical fracture radii versus injection time in the layered jointed sample. Both the horizontal radius and vertical radius increase with the injection time. It can be seen that the horizontal radius is larger than the vertical radius during the whole fracturing process, due to the low strength of the joint in the horizontal direction. The horizontal radius and vertical radius are $8e^{-2}$ m and $5.55e^{-2}$ m at time $t = 39$ s, respectively. Compared with the intact sample (horizontal radius and vertical radius are $6.3e^{-2}$ m and $6.49e^{-2}$ m, respectively, at time $t = 39$ s), the preexisting joints promote the expansion of cracks in the horizontal direction but restrain the crack expansion in the vertical direction.

4.3. Fracture Propagation in the Vertical Jointed Sample. The distribution and evolution of hydraulic fractures in the vertical jointed sample are presented in Figure 11. It can be seen that fractures are first generated around the borehole due to stress concentration. Then, fractures propagate along the diagonal direction and vertical direction with the increase of injection pressure, probably resulting from the equal load applied on the horizontal and vertical directions, and the preexisting joints in the vertical direction. Eventually, several main fractures are formed along the diagonal and vertical directions. Tensile damage is the main model of destruction, and the number of tensile cracks accounts for 93.9% of the total cracks.

It can be seen from Figure 12 that the seepage area increases slowly from $3.96e^{-6}$ m^2 to $2.18e^{-3}$ m^2 with the injection time varying from $t = 14$ s to $t = 26$ s, owing to only a small amount of crack propagation at the low injection pressure stage. Then, the seepage area increases sharply from $2.18e^{-3}$ m^2 to $8.95e^{-3}$ m^2 with the injection time varying from $t = 26$ s to $t = 39$ s, due to the propagation of several main fractures at the same time in this period. Besides, the development of the seepage area is fitted by an exponential function, as shown in Figure 12.

The development of horizontal and vertical fracture radii versus injection time in the vertical jointed sample is presented in Figure 13. It can be seen from the curve that fractures begin to propagate at time $t = 15$ s. With the increase of injection gas pressure, both the horizontal and vertical radii increase gradually. It should be noted that the vertical radius is greater than the horizontal radius in the whole injection process. The horizontal and vertical radii are $5.1e^{-2}$ m and $8e^{-2}$ m, respectively, at time $t = 39$ s. Compared with the intact sample (horizontal radius and vertical radius are $6.3e^{-2}$ m and $6.49e^{-2}$ m, respectively, at time $t = 39$ s), the preexisting vertical joints promote the expansion of cracks in the vertical direction but restrain the crack expansion in the horizontal direction.

4.4. Fracture Propagation in the Orthogonal Jointed Sample. Orthogonal joints are also common in naturally fractured reservoirs. The distribution and evolution of hydraulic fractures after gas fracturing in the orthogonal jointed sample

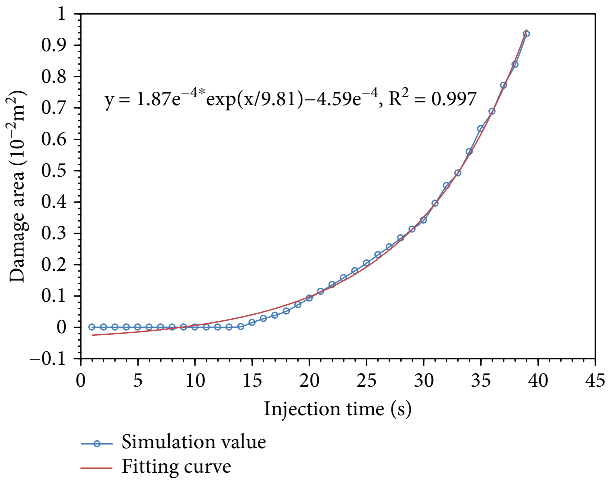

Figure 15: Development of the seepage area versus injection time in the orthogonal jointed sample.

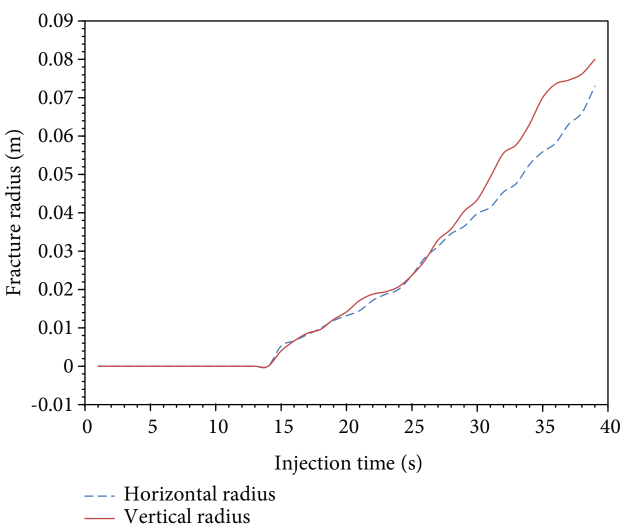

Figure 16: Development of horizontal and vertical fracture radii versus injection time in the orthogonal jointed sample.

are shown in Figure 14. Fractures appear around the borehole at the initial stage (at time $t = 18$ s), and it propagates to surrounding rock along the horizontal and vertical directions at time $t = 29$ s. The preexisting orthogonal joints play a significant role in the propagation direction of the fracture: many generated fractures are extended in the direction of the preexisting natural fractures, as shown in Figure 14. During this period, fractures begin to expand gradually to form continuous cracks; the seepage area increases gradually from $1.98e^{-5}$ m^2 to $3.13e^{-3}$ m^2. The main fractures are connected to form the crush area near the injection hole at time $t = 37$ s. As shown in Figure 15, the seepage area increases dramatically from $3.13e^{-3}$ m^2 to $9.36e^{-3}$ m^2, and a complex fracture network is developed eventually. The seepage area increases 35.05% compared with that of the intact sample at time $t = 39$ s. Tensile damage is the primary damage mode in this situation with 93.02% of the damaged elements being in the tensile mode.

Table 2: Numerical results of the intact sample, layered jointed sample, vertical jointed sample, and orthogonal jointed sample under CO_2 fracturing.

Sample	Damage area (10^{-2} m^2)	Horizontal radius (m)	Vertical radius (m)
Intact	0.693	0.063	0.0649
Layered jointed	0.918	0.08	0.0555
Vertical jointed	0.895	0.051	0.08
Orthogonal jointed	0.936	0.073	0.08

Figure 16 is the development of horizontal and vertical fracture radii with injection time in the orthogonal jointed sample. The fractures begin to propagate into the further surrounding rock at time $t = 15$ s. The horizontal radius and vertical radius are almost identical before time $t = 26$ s; then, the vertical radius becomes greater than the horizontal radius in the following process, which may result from the heterogeneous mechanical parameters used in this model. The horizontal radius and vertical radius are $7.3e^{-2}$ m and $8e^{-2}$ m at time $t = 39$ s, respectively. Compared with the intact sample (the horizontal radius and vertical radius are $6.3e^{-2}$ m and $6.49e^{-2}$ m, respectively, at time $t = 39$ s), the preexisting joints promote the expansion of fractures in the vertical direction.

Based on the numerical simulations conducted on the intact sample, layered jointed sample, vertical jointed sample, and orthogonal jointed sample, the numerical results can be concluded in Table 2. The numerical results indicate that the preexisting horizontal joints or vertical joints promote the propagation of hydraulic fractures in the horizontal direction or vertical direction but restrain the expansion of hydraulic fractures in the vertical or horizontal direction. And the preexisting orthogonal joints promote the propagation of hydraulic fractures both in the horizontal direction and vertical direction. The similar results can also be observed in the research of Wang et al. [28] as shown in Figure 17. In addition, the preexisting joints can aggravate the damage of the numerical specimens; the seepage areas of the layered jointed sample, vertical jointed sample, and orthogonal jointed sample are increased by 32.5%, 29.16%, and 35.05%, respectively, at time $t = 39$ s compared with the intact sample.

5. Conclusions

In this work, a series of numerical simulations are performed on jointed samples under the CO_2-based hydraulic fracturing. A damage model is introduced to describe the initiation and propagation of microcrack in the fracturing process. The mechanical mechanism of the propagation of hydraulic fractures in several kinds of joint reservoirs is researched in this work. The numerical results of the intact sample, layered jointed sample, vertical jointed sample, and orthogonal jointed sample under CO_2 fracturing are shown in Table 2. Based on the results, the following conclusions are obtained.

It is shown that several continuous main fractures are formed uniformly in the intact sample. For the jointed

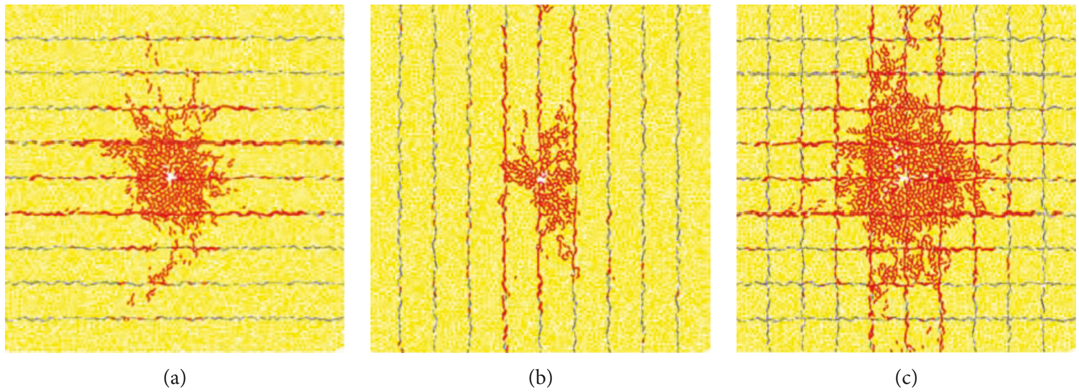

Figure 17: The distribution of hydraulic fractures of jointed samples: (a) layered jointed sample, (b) vertical jointed sample, and (c) orthogonal jointed sample [28].

samples, hydraulic fractures mainly propagate along the preexisting joints due to the lower strength and elastic modulus of joints compared with the rock matrix. Hydraulic fractures intersect with preexisting joints to form complex fracture networks. Besides, tensile damage is the main failure model in these numerical samples.

The variations of the seepage area versus injection time among these conditions are similar. The seepage area increases smoothly at the beginning since hydraulic fractures propagate slowly under low injection pressure, and then, it increases rapidly with the propagation of a large amount of hydraulic fractures to the surrounding rock. The whole process can be described by an exponential function. The seepage areas of the layered jointed sample, vertical jointed sample, and orthogonal jointed sample are increased by 32.5%, 29.16%, and 35.05%, respectively, at time $t = 39$ s compared with the intact sample. For the complexity of the fracture networks, it can be described by the development of horizontal and vertical fracture radii. The preexisting horizontal joints or vertical joints promote the propagation of the fracture in the horizontal direction or vertical direction but restrain the fracture expansion in the vertical or horizontal direction. In addition, the hydraulic fracture propagation is promoted along the preexisting orthogonal joints to form the complex fracture networks.

Data Availability

The numerical simulation data used to support the findings of this study are included within the article.

Conflicts of Interest

The authors declare that they have no conflicts of interest.

Acknowledgments

This work was supported by the National Natural Science Foundation of China (51804339), the China Postdoctoral Science Foundation (2018M640760), and the Innovation-Driven Project of Central South University. The corresponding author would like to thank the financial support by the State Key Laboratory for GeoMechanics and Deep Underground Engineering, China University of Mining and Technology (SKLGDUEK1805). We would like to thank ShiningStar Translation (email: shiningstartrans@foxmail.com) for providing linguistic assistance during the preparation of this manuscript.

References

[1] C. T. Montgomery and M. B. Smith, "Hydraulic fracturing: history of an enduring technology," *Journal of Petroleum Technology*, vol. 62, no. 12, pp. 26–40, 2010.

[2] A. Reinicke, E. Rybacki, S. Stanchits, E. Huenges, and G. Dresen, "Hydraulic fracturing stimulation techniques and formation damage mechanisms—implications from laboratory testing of tight sandstone–proppant systems," *Chemie der Erde-Geochemistry*, vol. 70, pp. 107–117, 2010.

[3] V. Grechka, P. Mazumdar, and S. A. Shapiro, "Predicting permeability and gas production of hydraulically fractured tight sands from microseismic data," *Geophysics*, vol. 75, no. 1, pp. B1–B10, 2010.

[4] Y. Jia, Y. Lu, D. Elsworth, Y. Fang, and J. Tang, "Surface characteristics and permeability enhancement of shale fractures due to water and supercritical carbon dioxide fracturing," *Journal of Petroleum Science and Engineering*, vol. 165, pp. 284–297, 2018.

[5] D. Rahm, "Regulating hydraulic fracturing in shale gas plays: the case of Texas," *Energy Policy*, vol. 39, no. 5, pp. 2974–2981, 2011.

[6] D. Ma, M. Rezania, H. S. Yu, and H. B. Bai, "Variations of hydraulic properties of granular sandstones during water inrush: effect of small particle migration," *Engineering Geology*, vol. 217, pp. 61–70, 2017.

[7] J. P. Nicot and B. R. Scanlon, "Water use for shale-gas production in Texas, US," *Environmental Science & Technology*, vol. 46, no. 6, pp. 3580–3586, 2012.

[8] A. Josifovic, J. J. Roberts, J. Corney, B. Davies, and Z. K. Shipton, "Reducing the environmental impact of hydraulic fracturing through design optimisation of positive displacement pumps," *Energy*, vol. 115, pp. 1216–1233, 2016.

[9] I. Mrdjen and J. Lee, "High volume hydraulic fracturing operations: potential impacts on surface water and human health,"

International Journal of Environmental Health Research, vol. 26, no. 4, pp. 361–380, 2016.

[10] A. Vengosh, R. B. Jackson, N. Warner, T. H. Darrah, and A. Kondash, "A critical review of the risks to water resources from unconventional shale gas development and hydraulic fracturing in the United States," *Environmental Science & Technology*, vol. 48, no. 15, pp. 8334–8348, 2014.

[11] D. Ma, H. Duan, J. Liu, X. Li, and Z. Zhou, "The role of gangue on the mitigation of mining-induced hazards and environmental pollution: an experimental investigation," *Science of the Total Environment*, vol. 664, pp. 436–448, 2019.

[12] D. Ma, X. Cai, Q. Li, and H. Duan, "In-situ and numerical investigation of groundwater inrush hazard from grouted karst collapse pillar in longwall mining," *Water*, vol. 10, no. 9, p. 1187, 2018.

[13] A. Lisjak, B. S. A. Tatone, O. K. Mahabadi et al., "Hybrid finite-discrete element simulation of the EDZ formation and mechanical sealing process around a microtunnel in Opalinus Clay," *Rock Mechanics and Rock Engineering*, vol. 49, no. 5, pp. 1849–1873, 2016.

[14] Z. Zhou, X. Cai, D. Ma et al., "Water saturation effects on dynamic fracture behavior of sandstone," *International Journal of Rock Mechanics and Mining Sciences*, vol. 114, pp. 46–61, 2019.

[15] Z. Zhou, X. Cai, D. Ma, L. Chen, S. Wang, and L. Tan, "Dynamic tensile properties of sandstone subjected to wetting and drying cycles," *Construction and Building Materials*, vol. 182, pp. 215–232, 2018.

[16] J. D. Arthur, B. K. Bohm, B. J. Coughlin, M. A. Layne, and D. Cornue, "Evaluating the environmental implications of hydraulic fracturing in shale gas reservoirs," in *SPE Americas E&P environmental and safety conference*, San Antonio, TX, USA, March 2009.

[17] Q. Zhang, D. Ma, Y. Wu, and F. Meng, "Coupled thermal-gas-mechanical (TGM) model of tight sandstone gas wells," *Journal of Geophysics and Engineering*, vol. 15, no. 4, pp. 1743–1752, 2018.

[18] L. Wang, B. Yao, M. Cha et al., "Waterless fracturing technologies for unconventional reservoirs-opportunities for liquid nitrogen," *Journal of Natural Gas Science and Engineering*, vol. 35, pp. 160–174, 2016.

[19] J. B. Clark, "A hydraulic process for increasing the productivity of wells," *Journal of Petroleum Technology*, vol. 1, no. 01, pp. 1–8, 1949.

[20] C. F. Smith, "Gas well fracturing using gelled non-aqueous fluids," in *Fall Meeting of the Society of Petroleum Engineers of AIME*, Las Vegas, NV, USA, September 1973.

[21] S. Kothare, *Economics and Applicability of Nitrogen for Fracking*, Air Products and Chemicals, Inc, 2012.

[22] A. B. Yost, "Analysis of production response to CO_2/sand fracturing: a case study," in *SPE Eastern Regional Meeting*, Charleston, WV, USA, November 1994.

[23] J. Zhou, G. Liu, Y. Jiang et al., "Supercritical carbon dioxide fracturing in shale and the coupled effects on the permeability of fractured shale: an experimental study," *Journal of Natural Gas Science and Engineering*, vol. 36, pp. 369–377, 2016.

[24] Y. Chen, Y. Nagaya, and T. Ishida, "Observations of fractures induced by hydraulic fracturing in anisotropic granite," *Rock Mechanics and Rock Engineering*, vol. 48, no. 4, pp. 1455–1461, 2015.

[25] X. Zhang, B. Wu, R. G. Jeffrey, L. D. Connell, and G. Zhang, "A pseudo-3D model for hydraulic fracture growth in a layered rock," *International Journal of Solids and Structures*, vol. 115-116, pp. 208–223, 2017.

[26] Q. Zhang, D. Ma, J. Liu, K. Zhang, and Z. Fan, "Numerical studies on the failure process of heterogeneous rock material with preexisting fracture under uniaxial compression," *Advances in Civil Engineering*, vol. 2018, Article ID 9203549, 12 pages, 2018.

[27] D. Ma, H. Duan, X. Cai, Z. Li, Q. Li, and Q. Zhang, "A global optimization-based method for the prediction of water inrush hazard from mining floor," *Water*, vol. 10, no. 11, p. 1618, 2018.

[28] T. Wang, W. Hu, D. Elsworth et al., "The effect of natural fractures on hydraulic fracturing propagation in coal seams," *Journal of Petroleum Science and Engineering*, vol. 150, pp. 180–190, 2017.

[29] J. Wang, D. Elsworth, and M. K. Denison, "Hydraulic fracturing with leakoff in a pressure-sensitive dual porosity medium," *International Journal of Rock Mechanics and Mining Sciences*, vol. 107, pp. 55–68, 2018.

[30] X. Zhang, B. Wu, L. D. Connell, Y. Han, and R. G. Jeffrey, "A model for hydraulic fracture growth across multiple elastic layers," *Journal of Petroleum Science and Engineering*, vol. 167, pp. 918–928, 2018.

[31] A. Riahi and B. Damjanac, "Numerical study of interaction between hydraulic fracture and discrete fracture network," in *Effective and Sustainable Hydraulic Fracturing*, InTech, 2013.

[32] P. Hou, F. Gao, Y. Ju et al., "Experimental investigation on the failure and acoustic emission characteristics of shale, sandstone and coal under gas fracturing," *Journal of Natural Gas Science and Engineering*, vol. 35, pp. 211–223, 2016.

[33] J. He, C. Lin, X. Li, and X. Wan, "Experimental investigation of crack extension patterns in hydraulic fracturing with shale, sandstone and granite cores," *Energies*, vol. 9, no. 12, p. 1018, 2016.

[34] W. C. Zhu and C. A. Tang, "Micromechanical model for simulating the fracture process of rock," *Rock Mechanics and Rock Engineering*, vol. 37, no. 1, pp. 25–56, 2004.

[35] C. H. Wei, W. C. Zhu, Q. L. Yu, T. Xu, and S. Jeon, "Numerical simulation of excavation damaged zone under coupled thermal–mechanical conditions with varying mechanical parameters," *International Journal of Rock Mechanics and Mining Sciences*, vol. 75, pp. 169–181, 2015.

[36] W. C. Zhu, D. Gai, C. H. Wei, and S. G. Li, "High-pressure air blasting experiments on concrete and implications for enhanced coal gas drainage," *Journal of Natural Gas Science and Engineering*, vol. 36, pp. 1253–1263, 2016.

[37] D. Ma, X. Miao, H. Bai et al., "Effect of mining on shear sidewall groundwater inrush hazard caused by seepage instability of the penetrated karst collapse pillar," *Natural Hazards*, vol. 82, no. 1, pp. 73–93, 2016.

[38] WebBook, NIST, "Thermophysical properties of fluid systems," 2016, http://webbook.nist.gov/chemistry/fluid/.

[39] J. Wang, D. Elsworth, Y. Wu, J. Liu, W. Zhu, and Y. Liu, "The influence of fracturing fluids on fracturing processes: a comparison between water, oil and SC-CO2," *Rock Mechanics and Rock Engineering*, vol. 51, no. 1, pp. 299–313, 2018.

[40] T. Xia, F. Zhou, J. Liu, J. Kang, and F. Gao, "A fully coupled hydro-thermo-mechanical model for the spontaneous

combustion of underground coal seams," *Fuel*, vol. 125, pp. 106–115, 2014.

[41] Y. H. Huang, S. Q. Yang, W. L. Tian, J. Zhao, D. Ma, and C. S. Zhang, "Physical and mechanical behavior of granite containing pre-existing holes after high temperature treatment," *Archives of Civil And Mechanical Engineering*, vol. 17, no. 4, pp. 912–925, 2017.

[42] R. P. Covert and G. C. Philip, "An EOQ model for items with Weibull distribution deterioration," *AIIE Transactions*, vol. 5, no. 4, pp. 323–326, 1973.

[43] M. Hubbert and D. Willis, "Mechanics of hydraulic fracturing," *Transactions of Society of Petroleum Engineers of AIME*, vol. 210, pp. 153–168, 1957.

[44] D. Ma, Q. Li, M. R. Hall, and Y. Wu, "Experimental investigation of stress rate and grain size on gas seepage characteristics of granular coal," *Energies*, vol. 10, no. 4, p. 527, 2017.

Hindawi
Geofluids
Volume 2019, Article ID 6053756, 17 pages
https://doi.org/10.1155/2019/6053756

Research Article

A Study on the CO_2-Enhanced Water Recovery Efficiency and Reservoir Pressure Control Strategies

Zhijie Yang[1] **Tianfu Xu**[1] **Fugang Wang**[1] **Yujie Diao**[2] **Xufeng Li**[2] **Xin Ma**[2] **and Hailong Tian**[1]

[1]*Key Laboratory of Groundwater Resources and Environment, Ministry of Education, Jilin University, Changchun, Jilin Province 130021, China*
[2]*Key Laboratory of Carbon Dioxide Geological Storage, Center for Hydrogeology and Environmental Geology Survey, China Geological Survey, Baoding, Hebei Province 071051, China*

Correspondence should be addressed to Fugang Wang; wangfugang@jlu.edu.cn

Received 4 November 2018; Accepted 16 January 2019; Published 14 March 2019

Guest Editor: Bisheng Wu

CO_2 geological storage (CGS) proved to be an effective way to mitigate greenhouse gas emissions, and CO_2-enhanced water recovery (CO_2-EWR) technology may improve the efficiency of CO_2 injection and saline water production with potential economic value as a means of storing CO_2 and supplying cooling water to power plants. Moreover, the continuous injection of CO_2 may cause a sharp increase for pressure in the reservoir system, so it is important to determine reasonable reservoir pressure control strategies to ensure the safety of the CGS project. Based upon the typical formation parameters of the China Geological Survey CO_2-EWR test site in the eastern Junggar Basin, a series of three-dimensional (3D) injection-extraction models with fully coupled wellbores and reservoirs were established to evaluate the effect of the number of production wells and the well spacing on the enhanced efficiency of CO_2 storage and saline production. The optimal key parameters that control reservoir pressure evolution over time are determined. The numerical results show that a smaller spacing between injection and production wells and a larger number of production wells can enhance not only the CO_2 injection capacity but also the saline water production capacity. The effect of the number of production wells on the injection capacity and production capacity is more significant than that of well spacing, and the simulation scenario with 2 production wells, one injection well, and a well spacing of 2 km is more reasonable in the demonstration project of Junggar Basin. CO_2-EWR technology can effectively control the evolution of the reservoir pressure and offset the sharp increase in reservoir pressure caused by CO_2 injection and the sharp decrease of reservoir pressure caused by saline production. The main controlling factors of pressure evolution at a certain spatial point in a reservoir change with time. The monitoring pressure drops at the beginning and is controlled by the extraction of water. Subsequently, the injection of CO_2 plays a dominant role in the increase of reservoir pressure. Overall, the results of analysis provide a guide and reference for the CO_2-EWR site selection, as well as the practical placement of wells.

1. Introduction

CO_2 geological storage (CGS) in deep saline aquifers is a potential technology to lower carbon emissions and thereby mitigate global climate change [1]. It has attracted much attention from the Chinese government and enterprises in recent years, particularly in coal-rich regions [2–5]. Traditional CGS projects may cause a series of problems due to the continuous large-scale injection of CO_2 and the reservoir pressure build-up, such as caprock fracturing, upward CO_2 leakage, fault activation, and induced seismicity, all of which will limit the injection capacity of CO_2 and threaten the safety and security of CGS projects [6–8]. The alternative geoengineering approach of CCUS (Carbon Capture, Utilization, and Storage) technology [9–12] is an attractive and potentially viable way to significantly reduce anthropogenic carbon emissions with the benefit of economically productive activities [13].

CGS combined with enhanced water recovery (CO_2-EWR) technology is proposed to make up for the shortcomings of the traditional CCS technology [14–21]. Compared with traditional deep saline aquifer CGS projects, CO_2-EWR not only can mitigate the excessive build-up of reservoir pressure by a reasonable engineering design of the extraction wells to improve the capability of the injected CO_2 but also produce deep saline water that can be used for industrial or agricultural utilizations after a treatment to effectively alleviate water shortage in arid areas [14, 18].

Davidson et al. [22] suggested that future constraints on CCS deployment are likely to be necessary in areas that have a significant potential demand for deep geologic CO_2 storage and in areas that are already experiencing water stress. To reduce risks associated with the overpressure in the reservoir and to increase the capacity of saline water production and CO_2 storage, Kobos et al. [14] developed a methodology of combining thermal power plants, CO_2 storage in deep saline aquifers and extraction of saline waters. They indicated that injection-induced overpressure particularly in the near-well regions can be relieved by producing water from dedicated water production wells and that the treated saline waters can be used as cooling water for power plants [14, 23], but the adverse consequences are the associated higher costs of the intervention operations [24]. The brine extraction combined with CO_2 injection could effectively reduce the reservoir pressure, and the amount of CO_2 dissolved in the brine will increase significantly due to the extraction of saline water, thereby improving the security of CO_2 storage [25–27].

A series of mathematical/numerical models have been developed to find out the relationship between the reservoir pressure evolution and the process of CO_2 injection or brine extraction. Buscheck et al. [18] introduced active CO_2 reservoir management (ACRM) to prove that brine extraction can reduce pressure build-up and increase storage capacity. The concept of "impact-driven pressure management (IDPM)" suggests that strategic well placement and optimization of extraction may allow for a significant reduction in the saline water production volumes [28]. Li et al. [16] primarily studied the influence of well arrangements and formation parameters on the reservoir pressure evolution by a 3D standard numerical model in the Junggar Basin. Then, the optimizer combining the genetic algorithm and TOUGH2 (GA-TOUGH2) is used to achieve both the maximum efficiency of water production and the maximum capacity of CO_2 storage, taking into account the safety of CGS [19], following the work of Li et al. [16].

Generally, researches about CO_2-EWR are now in the stage of theoretical study, and only one actual project, the Gorgon Project in Australia [29, 30], has been implemented throughout the entire world. How to reasonably optimize the arrangement of the production wells to achieve the trade-off between the safety of CO_2 geological storage and the largest utilization of deep saline water, as well as a strategy of reservoir pressure control, must be studied in an actual CO_2-EWR project. Li et al. [16] and Liu et al. [19] have performed some numerical simulations, whereby the reservoir properties were assumed to be isotropic without considering the heterogeneity in actual conditions, and the range of their models was small with a coarse resolution of each individual grid block. Moreover, the assumption of the closed surrounding boundaries deviates from reality and had a great negative impact on the modeling results.

The impact of the number of production wells and the well spacing on the enhanced efficiency of CO_2 storage and saline production, as well as the key parameters controlling reservoir pressure evolution over time, need to be studied further. Based upon the geological and hydrogeological conditions of the CO_2-EWR test site in the eastern Junggar Basin of China, a series of 3D injection-extraction models with fully coupled wellbores and reservoirs were established to simulate the process of CO_2-EWR over a long period of time. The evolution of the reservoir pressure and the enhanced efficiency of CO_2 storage and saline water production were evaluated. The results of analysis can provide significant information for the actual operation of a CO_2-EWR project.

2. Geology and Reservoir Characterization

The Junggar Basin, located in the northern part of the Xinjiang Uygur Autonomous Region in western China, has the greatest early opportunity for CO_2-EWR or storage of a large volume of carbon emissions in deep saline aquifers with a suitable geology. The water shortage is very serious in the eastern part of the basin, where it is the most enriched area of coal resources in Xinjiang. There are more than sixty coal chemical enterprises in this area, which have exacerbated the crisis of CO_2 emissions and water shortage [31]. The CO_2-EWR test site is situated in the Fukang depression of the Junggar Basin with gentle formations, and the dip angle is approximately five degrees from southwest to northeast.

One deep hole in the site was used for the prefeasibility study of the CO_2-EWR technology. According to the well logging data and drilling data of the existing wells, three reservoir intervals without faults had been perforated between the depths of 1945.5 and 2994 m to carry out CO_2-EWR research. The three perforated intervals are all sandstone aquifers developed in the Cretaceous Donggou Formation and Lian-Sheng Formation, as shown in Figure 1.

The second perforated interval, with a depth of 2241.9-2267.5 m, is employed for the current simulation study based on the pumping tests. The porosity and permeability of the reservoir were determined through the geological investigation and sample analysis (Figure 2), and we assumed that each layer was isotropic.

The variation of porosity and permeability is caused by the periodicity of strata formation sedimentation. The middle part of the strata (high permeability and porosity) and the overlying and underlying layers (low permeability and porosity) form a closed reservoir system where CO_2 can be safely sealed.

3. Simulation Approach

3.1. Simulation Tool. The simulations in the paper were carried out using the well-known multiphase flow solver TOUGH2-MP/ECO2N code [32–35], the parallel version

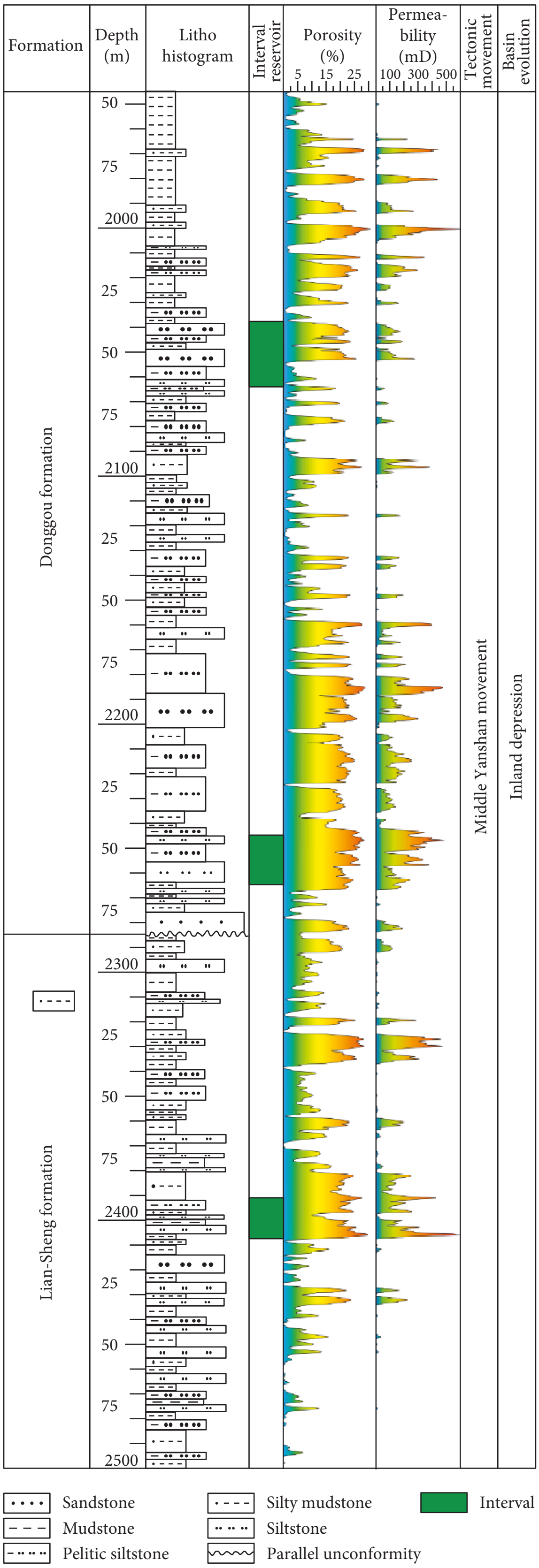

Figure 1: Stratigraphic structure characteristics of the study area (the blue color represents lower porosity and permeability, and the orange color represents higher porosity and permeability).

of a fully coupled wellbore-reservoir simulator [36–38] with the fluid property module "ECO2N," which was designed for applications to CO_2 geologic sequestration in deep saline aquifers.

The model domain was constructed using the preprocessing interface software TOUGHVISUAL [39, 40], which was developed for the pretreatment and postprocessing of TOUGH family codes. The friendly interface software can easily create regular or irregular grids, based on the characterizations of geological conceptual models.

3.2. Simulation Scenarios. The number (n) of production wells and the distance (d) between wells may have various impacts on CO_2 migration and reservoir pressure evolution. We designed several simulation scenarios (Table 1) corresponding to the main concerns of evaluating the impacts of the number of production wells and the well spacing on the enhanced efficiency of CO_2 storage and saline water production, as well as the key parameters controlling reservoir pressure evolution over time.

The arrangements of the number of production wells and well spacing refer to the previous research results [41, 42].

3.3. Grid Subdivision. Based on the actual geological conditions of drilling data and geophysical exploration data, a 3D numerical model of the target strata of the CO_2-EWR test site was constructed (Figure 3). The depths of the top and bottom layers of the real target reservoir were 2241.9 m and 2267.5 m, respectively, with a total thickness of 25.6 m. In order to reduce the influence of lateral boundary on the simulation results, the model domains in the X and Y directions were both 20 km.

In view of the model precision of the evaluation and the calculation capability of the computer, a model mesh with an irregular nonequidistant grid subdivision was adopted on the horizontal plane. Each column of well elements was connected to 32 columns of rock elements surrounding the well. A radially discretized submesh was generated with the number of grid units increasing with the distance to the injection/extraction well. The vertical meshes were strictly divided based on the lithology characteristics of the existing well. A total of 18 geological strata were assigned to the 18 grid layers with an average thickness of approximately 1 m. The entire 3D mesh consisted of 23,949 grid blocks for the base-case model with one injection well and one pumping well, and the distance between wells was 2 km (Figure 3).

Figure 4 shows the different 3D grids for the different simulation scenarios. Figures 4(a) and 4(b) represent the sole CO_2 injection and the sole water production scenarios, respectively. Figures 4(c)–4(e) show the scenarios with one injection well and one pumping well, of which the distances between the two wells were 1 km, 3 km, and 5 km, respectively. As shown in Figures 4(f) and 4(g), there were two or four production wells around one injection well with fixed distance between wells of 2 km. The number of model elements is different due to the arrangement of production wells (Table 1).

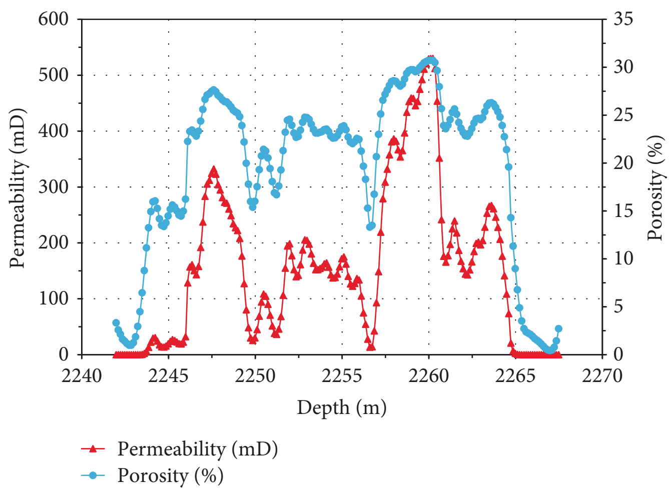

Figure 2: Porosity and permeability of the reservoir formations according to borehole logging data.

Table 1: Detailed information of different simulation scenarios.

Scenarios	Number of injection wells	Number of production wells	Distance d between wells (km)	Number of model elements
Base case	1	1	2	23,949
Case 1	1	0	/	29,721
Case 2	0	1	/	29,721
Case 3	1	1	1	22,905
Case 4	1	1	3	24,273
Case 5	1	1	5	24,813
Case 6	1	2	2	33,837
Case 7	1	4	2	53,577

3.4. Boundary and Initial Conditions. Based on previous numerical works [43, 44], the Dirichlet boundary conditions were preferred for the lateral boundaries (far enough) with a constant pressure and temperature. The upper and bottom boundaries of the reservoir were assumed to be impermeable due to the great thickness and low permeability of the overlying and underlying layers.

The wellbore was treated as an inner boundary (pressure boundary) rather than a flux boundary because it is a more reliable and efficient way to inject CO_2 in the wellhead of the injection well by the pressure boundary [45, 46], and the same was done for the production well. In addition, the injection pressure at the wellhead was specified as 7 MPa for the supercritical condition of CO_2 [47]. The pressure perturbation due to water extraction should not exceed the fracture pressure of the strata [48, 49], so the bottom hole flowing pressure in the production well was fixed at 7.28 MPa, which is 30% of the reservoir hydrostatic pressure.

The reservoir was initially filled with only saline water with a salinity of 4.32% (mass fraction) according to the pumping tests in the existing well. The initial reservoir pressures and temperature were determined with the monitoring data of the well (Table 2). As mentioned above, we treated the wellbore as a pressure boundary, and the injection pressure at the wellhead was also specified as a constant 7 MPa in previous studies, with the CO_2 gas at saturation and zero salinity [46].

4. Results and Discussion

4.1. The Shut-In Time for Different Scenarios. The post-processing cost of the extracted saline water will be very expensive if the content of CO_2 in the production stream is too high, which will greatly increase the production cost of enterprises. Hence, a well shut-in time is proposed when the CO_2 content in the production stream is higher than 10%, and the simulations are terminated [19]. For the base-case CO_2-EWR scenario, the well shut-in time is 3.95 years.

As shown in Figure 5, the time required for CO_2 to migrate from the injection well to the production well varies. With the increase in the well spacing between the production well and injection well, the shut-in time increases gradually, and the shut-in time decreases gradually with the increase in the number of production wells. However, the number of production wells has little effect on the shut-in time compared with the well spacing.

After analyzing the shut-in time of each scenario, the effects of CO_2 injection combined with saline water production on CO_2 spatial migration, CO_2 injection and saline water production capacity, and the evolution of reservoir pressure are analyzed in the following section.

4.2. CO_2 Migration in Reservoirs. When the supercritical CO_2 migrates to the production well and reaches a certain concentration ($Sg = 0.1$), the spatial distribution of CO_2 in the model of CO_2-EWR is obviously different from that of single CO_2 injection, as shown in Figures 6 and 7. Considering the symmetry of the CO_2 spatial distribution, we only analyzed the spatial distribution of CO_2 in the X-Z plane ($Y = 0$ m) near the injection well.

4.2.1. Effect of the Well Spacing on CO_2 Migration. Figures 6(b), 6(d), 6(f), and 6(h) show the distribution of

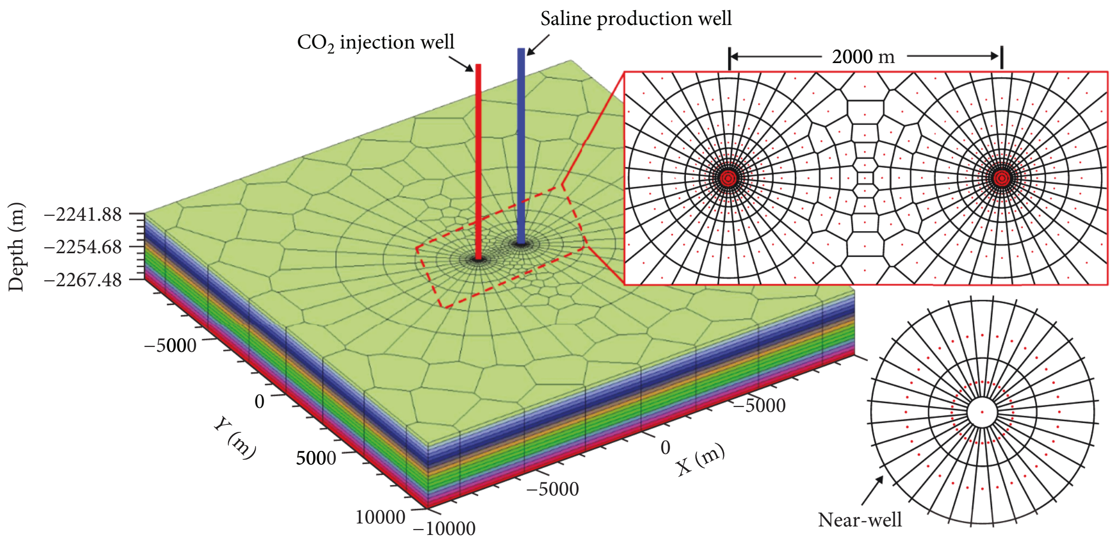

FIGURE 3: The 3D grid of the CO_2-EWR modeling area (base case).

supercritical CO_2 in the CO_2-EWR model at the end of the simulation when the well spacing was 1 km, 2 km, 3 km, and 5 km, respectively, in comparison to the spatial distribution of CO_2 at the same time in the solo CO_2 injection model, as shown in Figures 6(a), 6(c), 6(e), and 6(g). During the injection period, there is a single-phase region of the supercritical CO_2 near the injection well, and the saturation of the supercritical CO_2 decreases gradually with the increasing distance from the injection well in one model. Because of the obvious pore-permeability heterogeneity in the vertical direction, the mudstone layer with relatively low permeability divides CO_2 into several areas vertically, so the spatial distribution of CO_2 is obviously different in the vertical direction. The roof of the reservoir is mudstone with very low permeability, which can effectively prevent CO_2 from migrating to adjacent aquifers, and this improves the safety of CO_2 geological storage.

The placement of production wells makes it easier for CO_2 to migrate towards the wells, resulting in the asymmetric distribution of CO_2 on both sides of the injection well. At the end of the simulation in the CO_2-EWR model, the supercritical CO_2 on the right side of the injection well had already migrated to the production well with a very high saturation (the maximum CO_2 migration distances were 1 km, 2 km, 3 km, and 5 km, respectively). However, the maximum CO_2 migration distances on the left side of the injection well were 584 m, 1230 m, 1896 m, and 2962 m, respectively.

In the solo CO_2 injection model, the spatial distribution of the supercritical CO_2 on both sides of the injection well was symmetrical, and the migration distance was small. Compared with the CO_2-EWR models at the same time, the maximum CO_2 migration distances were 449 m, 1020 m, 1614 m, and 2790 m, respectively, which were not only smaller than the maximum migration distance of the supercritical CO_2 but also smaller than the CO_2 migration distance on the left side of the injection well. The preferential lateral migration of CO_2 was due to the release of reservoir pressure by the saline water production.

4.2.2. Effect of the Number of Production Wells on CO_2 Migration. Figures 7(b), 7(d), and 7(f) show the spatial distribution of supercritical CO_2 in the CO_2-EWR model with 1, 2, and 4 production wells (well spacing of 2 km) at the end of the simulation, in comparison to the spatial distribution of CO_2 at the same time in the solo CO_2 injection model, as shown in Figures 7(a), 7(c), and 7(e).

As shown in Figure 7, the spatial distribution of CO_2 in the CO_2-EWR model with different numbers of production wells was basically similar, the maximum migration distance of CO_2 was 2 km, and CO_2 had migrated to the production wells. In the solo CO_2 injection model, the maximum migration distances of CO_2 were 1020 m, 992 m, and 910 m, respectively, at the same time.

The results of the influence of the well spacing and the number of production wells on CO_2 migration show that the well spacing has a significant effect on the shut-in time, so the maximum migration distance of CO_2 varies greatly. In contrast, the number of production wells has little effect on the shut-in time, so the maximum migration distance of CO_2 has little effect. Compared with traditional CO_2 geological storage technology, the arrangement of production wells can promote the horizontal migration of CO_2, thereby reducing the accumulation of CO_2 concentration and pressure near the injection wells, which can significantly reduce the risk of CO_2 leakage from the reservoir.

4.3. Enhanced Efficiency of the Injection and Production Capacity. In the traditional CCS storage process, the reservoir pressure build-up may limit the injection capacity of CO_2 due to the continuous large-scale injection of CO_2. The placement of saline water production wells at a certain distance from the injection wells can effectively release reservoir pressure and thus may improve the injection efficiency of CO_2. At the same time, CO_2 injection may offset the reservoir pressure reduction caused by solo saline water production, where water is extremely needed and groundwater exploitation is essential. At the same time, this can improve the efficiency

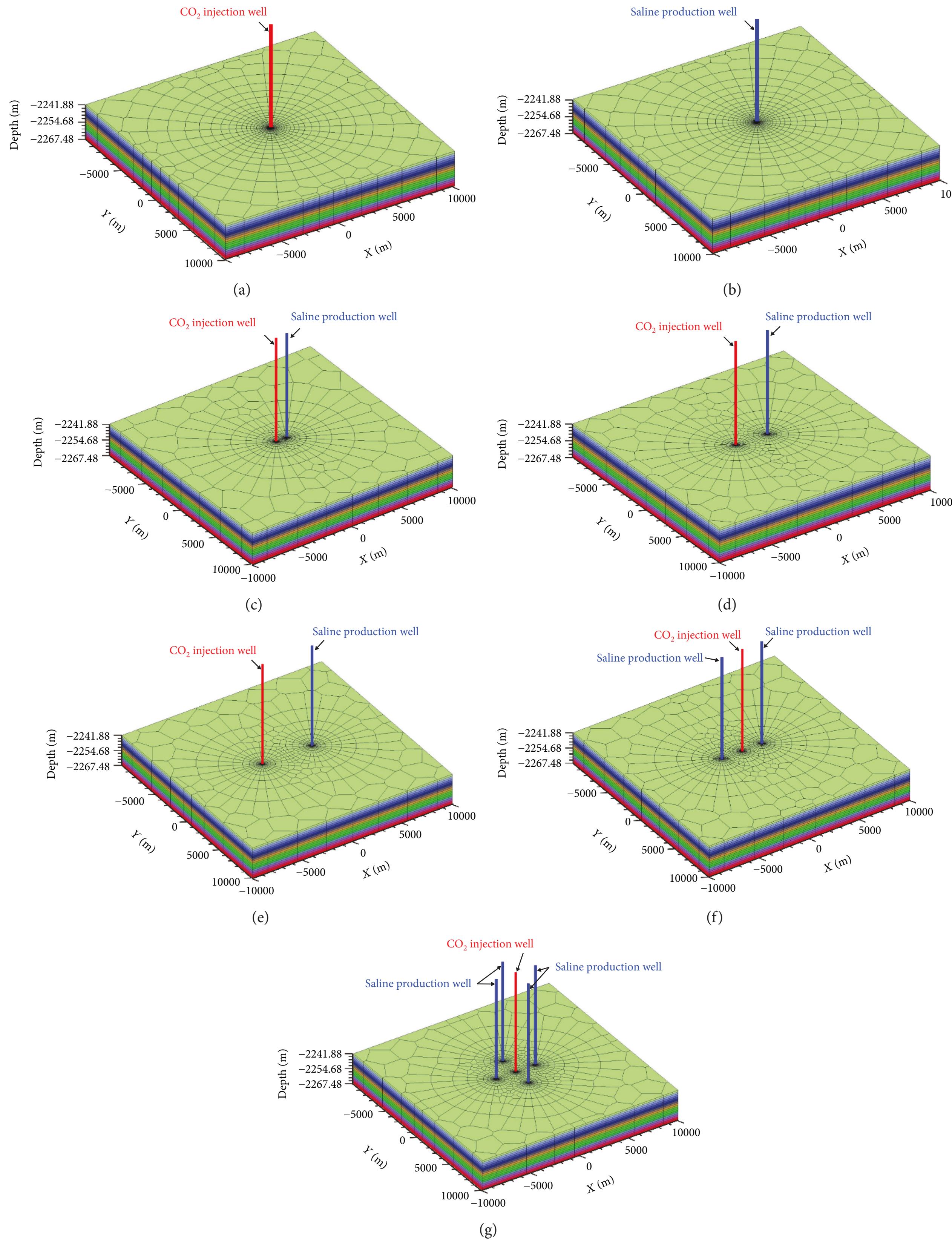

Figure 4: The 3D grid for the simulation scenarios. (a) Sole CO_2 injection. (b) Sole water production. (c) 1 injection well and 1 production well with the well spacing of 1 km. (d) 1 injection well and 1 production well with the well spacing of 3 km. (e) 1 injection well and 1 production well with the well spacing of 5 km. (f) 1 injection well and 2 production wells with the well spacing of 2 km. (g) 1 injection well and 4 production wells with the well spacing of 2 km.

Table 2: Geometric and hydrogeological specifications for the simulation.

Reservoir	
Thickness	25.60 m
Porosity	Figure 2
Permeability	Figure 2
Rock grain density	2650 kg/m^3
Rock specific heat	920 J/kg/°C
Rock thermal conductivity	2.51 W/m/°C
Initial conditions	
Reservoir fluid	Saline water (salinity of 4.32%)
Reservoir temperature	63.00°C
Average reservoir pressure	21.89 MPa
Initial CO_2 saturation	0
Wellbores	
Diameter	0.20 m
Roughness	0.046 mm
Heat conductivity	2.51 W/m/°C
Inclination of wells	Vertical
Injection-production distance	Table 1
Injection pressure (wellhead)	7.00 MPa
Production pressure (downhole)	7.28 MPa

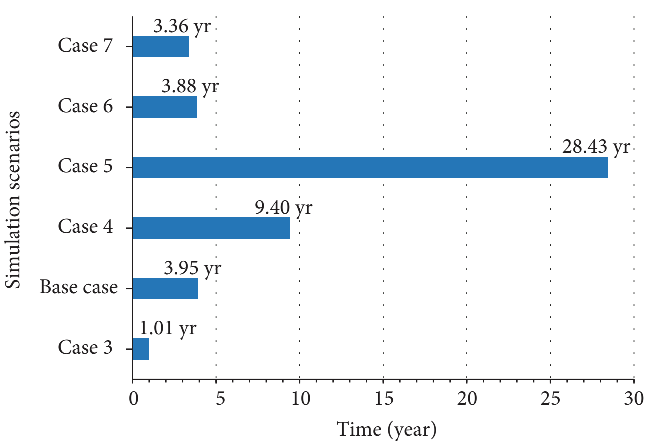

Figure 5: The shut-in time for different CO_2-EWR simulation scenarios (year).

of saline water production, and the produced saline water can be used for local industry and agriculture after treatment.

Then we need to quantitatively evaluate the influence of the well spacing and the number of production wells on the CO_2 injection capacity and saline water production capacity during the process of CO_2-EWR.

4.3.1. Influence of the Placement of the Production Wells on the Injection and Production Capacity. When there is only one production well, the influence of the well spacing on the CO_2 injection capacity and saline water production capacity is shown in Figure 8.

Figures 8(a) and 8(c) show that the injection rate increases rapidly at the beginning of the CO_2 injection period and that the injection rate can be stabilized after a long simulation time. During the simulation period, the injection capacity of CO_2 is linearly related to the time. In the solo CO_2 injection model, the injection rate was 19.52 kg/s, and the amount of injected CO_2 was 2.32 million tons after 4 years. In the CO_2-EWR model with a well spacing of 1 km, the injection rate under the same wellhead pressure was 35.32 kg/s at a time of 1.01 years when the simulation was terminated because the CO_2 content in the production stream was higher than 10%, the injection rate was increased by 101.48% compared with the solo CO_2 injection model at the same time, and the CO_2 injection amount was approximately 1 million tons. When the well spacing was 2 km, the injection rate of CO_2 was 33.90 kg/s, 73.85% higher than the solo injection model, and 3.78 million tons of CO_2 was injected after 3.95 years. When the well spacing was 3 km and 5 km, the injection rate was 28.46 kg/s and 25.51 kg/s and had increased by 45.80% and 30.69% after 4 years, respectively. After 9.4 years and 28.43 years, the CO_2 injection amounts were 8.40 million tons and 24.92 million tons, respectively.

The influence of well spacing on the CO_2 injection rate and amount is significant. The smaller the well spacing, the greater the CO_2 injection rate due to the more obvious influence of the production wells on the reservoir pressure. However, with the increasing well spacing, the longer the simulation period and the larger the cumulative injection amount.

As shown in Figures 8(b) and 8(d), at the early stage of saline production, the production rate will reach a peak, and then, the production rate will continue to decline, finally reaching a stable stage in a short period of time. The effect of the well spacing on the production rate and amount was not obvious. In the solo saline water production model, the stable rate was 53.88 kg/s, and the total amount of produced saline water could be 6.86 million tons in four years. When the well spacing was 1 km in the CO_2-EWR model, the increase for pressure in the reservoir system caused by CO_2 injection will transmit to the production well in a short time. As a result, more saline water is displaced to the production well by the high-pressure CO_2, and the saline water production rate will be higher than others with larger well spacing, so the production rate was 66.29 kg/s at 1.01 years, which is 22.60% higher than that of the solo saline water production model at the same time, and the amount of saline water production was 2.15 million tons. When the well spacing is 2 km, the production rate was 62.39 kg/s, an increase of 15.79% compared with the solo production model, and the production amount increased to 7.60 million tons after 3.95 years. When the well spacing is 3 km and 5 km, the production rate was approximately 56.17 kg/s and 55.09 kg/s after 4 years and had only increased by 4.25% and 2.25%, which is close to the solo saline water production rate at the same time. However, after 9.40 years for the 3 km well spacing and 28.43 years for the 5 km well spacing, the saline water production amounts were approximately 16.69 million tons and 49.57 million tons, respectively.

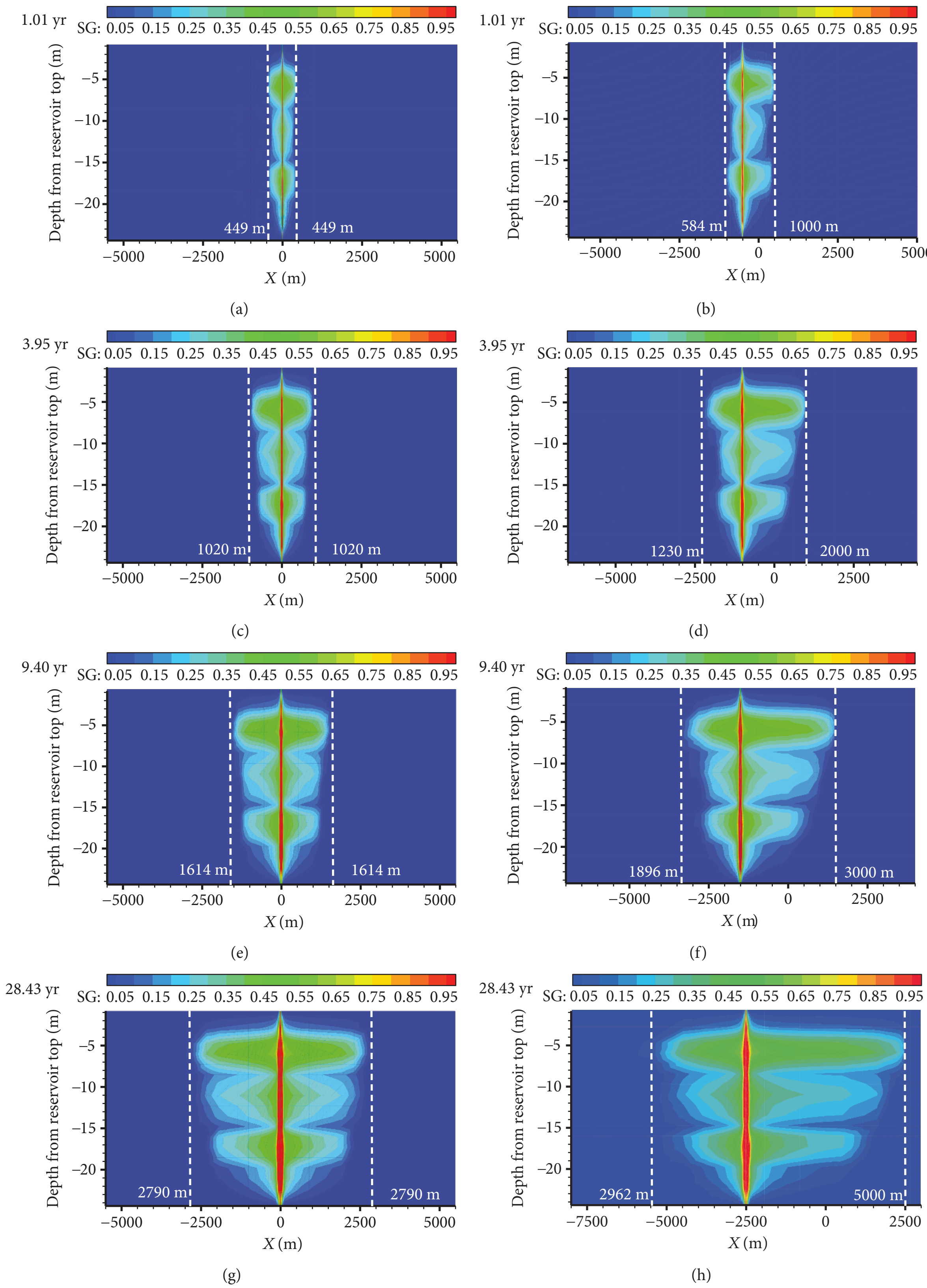

Figure 6: Spatial distribution of the supercritical CO_2 at the end of the simulation in different scenarios (analysis of the well spacing). (a) Sole CO_2 injection at 1.01 years. (b) The well spacing of 1 km at 1.01 years. (c) Sole CO_2 injection at 3.95 years.(d) The well spacing of 2 km at 3.95 years. (e) Sole CO_2 injection at 9.40 years. (f) The well spacing of 3 km at 9.40 years. (g) Sole CO_2 injection at 28.43 years. (h) The well spacing of 5 km at 28.43 years.

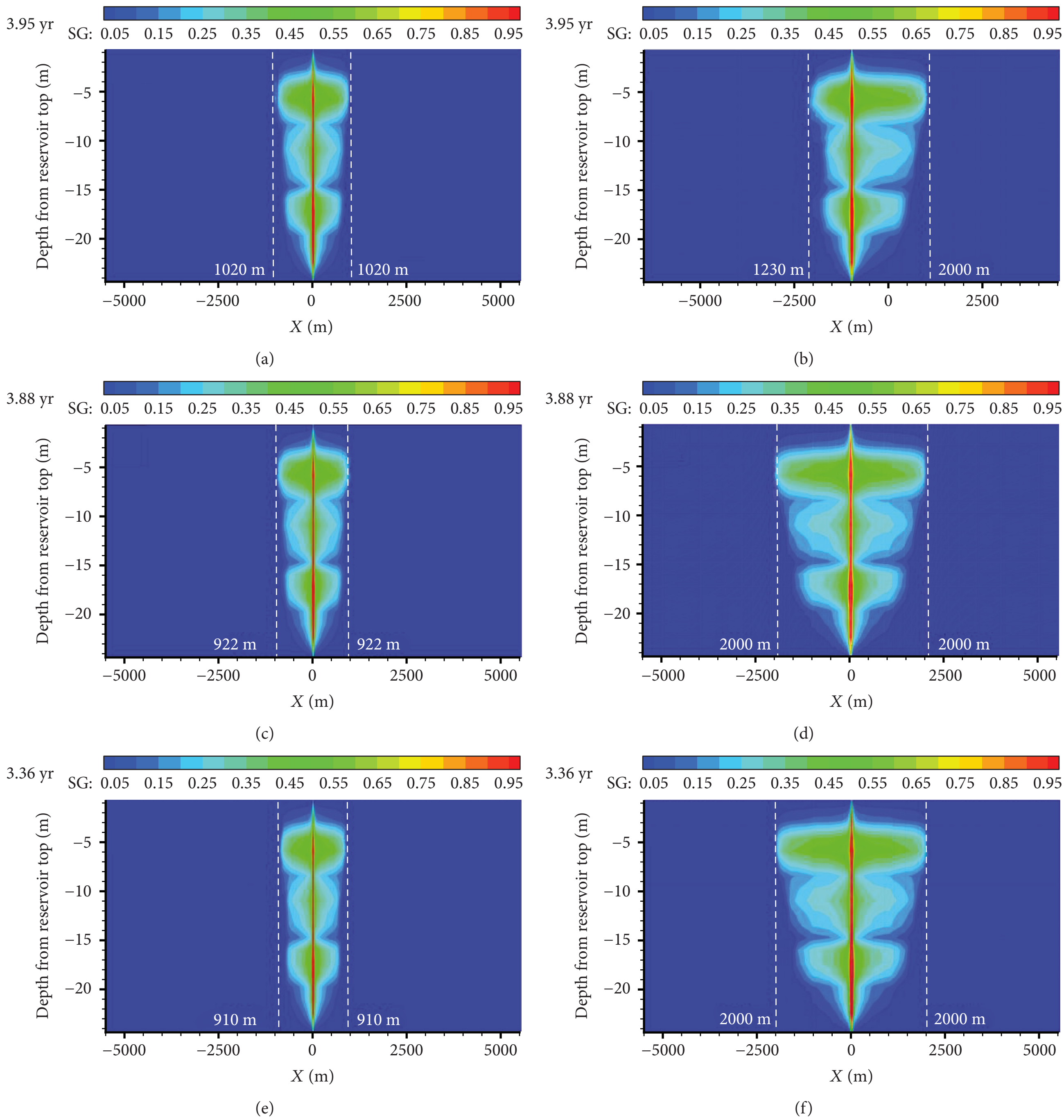

FIGURE 7: Spatial distribution of the supercritical CO_2 at the end of the simulation in different scenarios (analysis of number of the production wells). (a) Sole CO_2 injection at 3.95 years. (b) One production well at 3.95 years. (c) Sole CO_2 injection at 3.88 years. (d) Two production wells at 3.88 years. (e) Sole CO_2 injection at 3.36 years. (f) Four production wells at 3.36 years.

Hence, the effect of well spacing on the enhancement of the saline water production rate is not as significant as that of the CO_2 injection rate during the process of CO_2-EWR. When the well spacing increases to a certain distance (for example, 3 km in this study), the enhancement effect of CO_2-EWR on the rate of saline water production is negligible, but the amount of saline water production increases significantly with increasing well spacing due to the increase in the simulation period.

Figure 9 shows the effect of different numbers of production wells on the CO_2 injection and production capacity when the well spacing was fixed to 2 km.

As shown in Figures 9(a) and 9(c), the number of production wells had a great influence on both the CO_2 injection rate and the injection amount. When there was no production well, the injection rate of CO_2 was only 19.52 kg/s, and the cumulative injection amount was 2.32 million tons after 4 years. When there was one production well, the injection

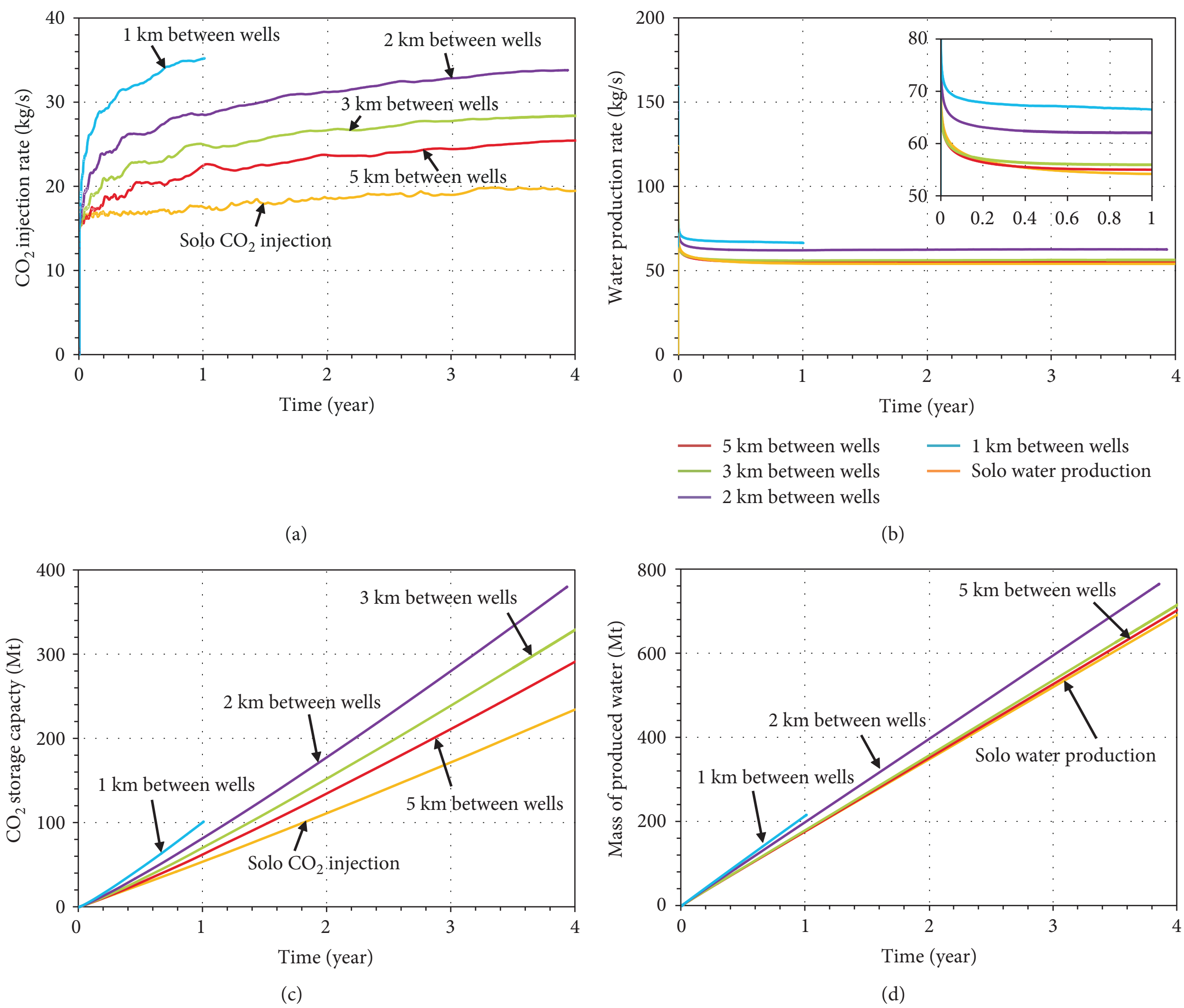

FIGURE 8: The effect of the well spacing on the CO_2 injection and saline water production capacity. (a, b) Injection and production rates. (c, d) Injection and production amounts.

rate of CO_2 was 33.90 kg/s at the end of 3.95 years, which is 73.85% higher than that of the single CO_2 injection model at the same time, and the cumulative injection amount was 3.77 million tons. When there were two production wells, the injection rate was 45.25 kg/s at 3.88 years, which was 1.30 times the solo injection rate with the CO_2 injection amount totaling 4.69 million tons. At the end of 3.36 years in the model with 4 production wells, the injection rate of CO_2 was 65.48 kg/s, an increase of 229.54%, and the total CO_2 injection amount reached 5.95 million tons. The increase in the number of production wells had a positive effect on the efficiency of CO_2 injection.

It can be seen from Figure 9(b) that the rate of saline water production in each well declines rapidly at the beginning of the simulation during the process of CO_2-EWR, but with the passing of simulated time, the rate rises slightly. Because the process of CO_2 injection can lead to an increase in the reservoir pressure, this will offset the pressure decrease caused by saline water extraction near the production wells, and the injected CO_2 can promote the migration of saline water to the production wells, thereby replenishing the saline water in the production area.

When the spacing between the injection and production wells is fixed, the stable production rate of saline water in each production well decreases gradually with the increase in the number of production wells, as shown in Figure 9(b). In the solo production model, the stable production rate was 53.88 kg/s, with a total amount of saline water production of 68.62 million tons after 4 years. The production rate was 62.39 kg/s, an increase of 15.79%, when there was one production well at the time of 3.95 years, and the amount of production was 7.60 million tons. In the model with two production wells, the steady rate in each production well was 55.58 kg/s after 3.88 years, only increasing by 3.16%. The total amount of saline water production in the two wells was 13.59 million tons. When the number of production wells increased to 4, the rate of saline water production in each well was 50.32 kg/s at the end of 3.36 years, which was lower than that of the solo saline water production rate. When the number of production wells increases, the saline

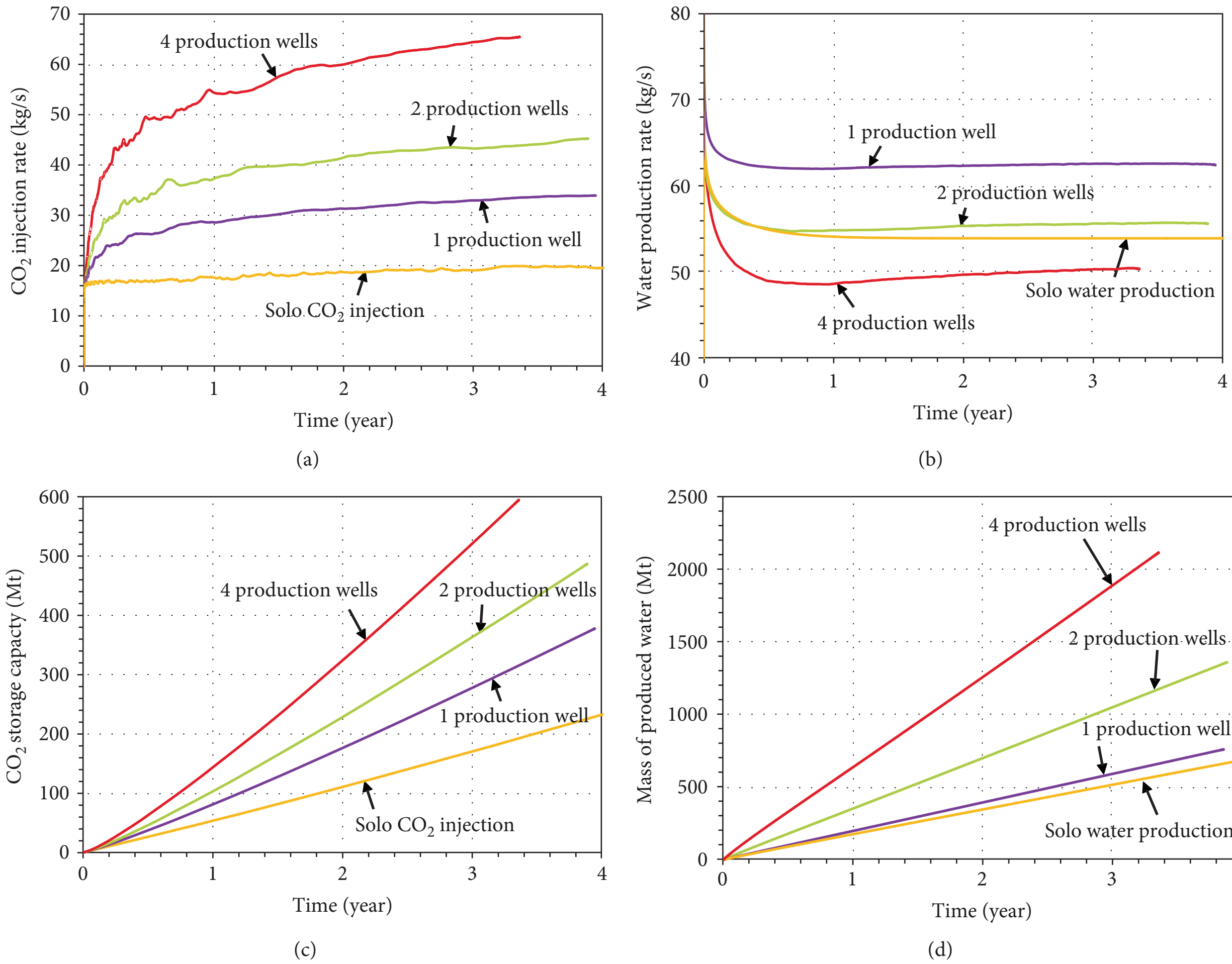

FIGURE 9: The effect of the number of production wells on the CO_2 injection and saline water production capacity. (a, b) Injection and production rates. (c, d) Injection and production amounts.

water in the reservoir is extracted in a short time, and the rate of saline water recharge in the production area cannot meet the demand for short-term extraction. Although the rate of saline water production in each well decreases with the increase in the number of production wells, the total rate of all wells was still very large, and the total amount of saline water production of four wells was 21.14 million tons in 3.36 years (Figure 9(d)).

4.3.2. Optimization Scenario for the CO_2-EWR Project in the Junggar Basin. To optimize the arrangement of production wells, we evaluated the effects of the well spacing and the number of production wells on the annual CO_2 injection amount and annual saline water production amount (Figures 10 and 11). Firstly, the suitable well spacing for the site was applied (Figures 10 and 11), then the preferred number of production wells was determined (Figures 10–12). Finally, we came to the reasonable optimization scenario for the CO_2-EWR project in the Junggar Basin of China.

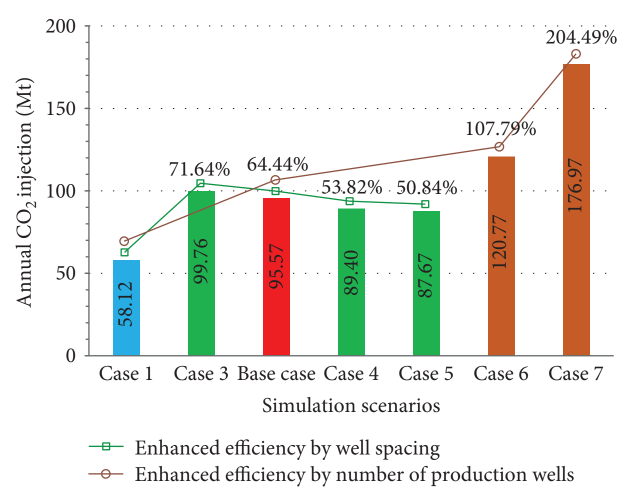

FIGURE 10: Influence of the arrangement of the production wells on the CO_2 injection capacity.

Figure 10 shows the effect of the well spacing and the number of production wells on the annual CO_2 injection amount. In the solo CO_2 injection model and the CO_2-EWR model with one production well with different well spacing, the annual CO_2 injection amount is less than 1 million tons. With the increase in well spacing, the enhancement efficiency

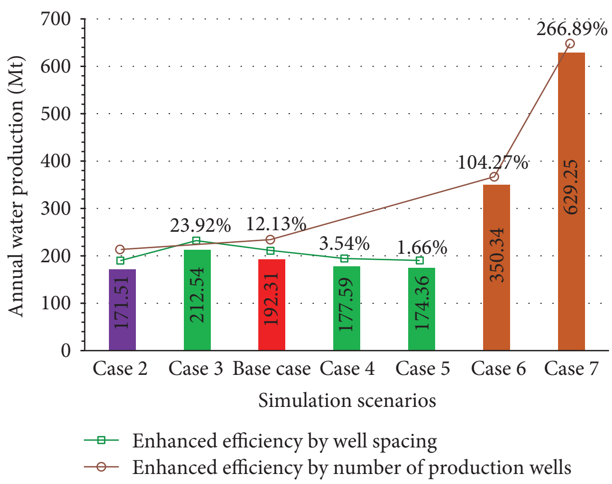

Figure 11: Influence of the placement of the production wells on the saline water production capacity.

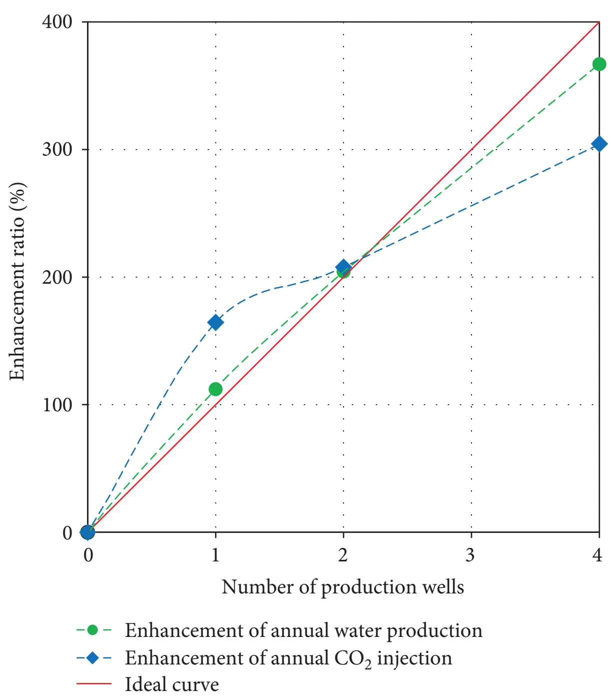

Figure 12: The enhanced efficiency of the number of production wells on the CO_2 injection and saline water production capacity.

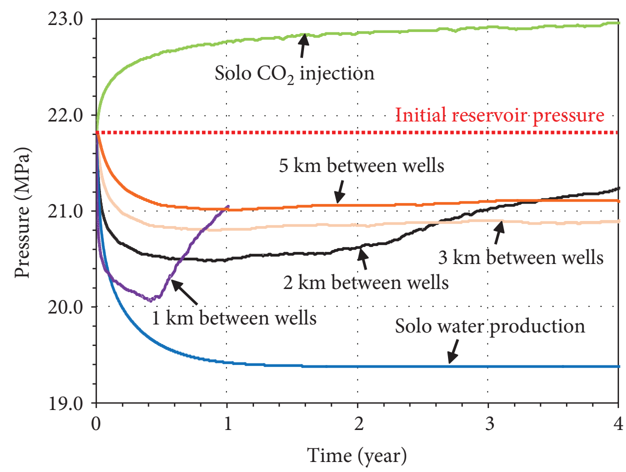

Figure 13: The pressure evolution curve at the monitoring point under different well distance layout conditions.

of CO_2 injection is gradually weakened, and the influence of the well spacing on the CO_2 injection amount is not obvious. When the number of production wells increases to 2 and 4, the annual CO_2 injection amount increases to more than 1 million tons, and the increase in the number of production wells has a significant effect on the enhancement of CO_2 injection capacity.

The influence of the well spacing and the number of production wells on the annual saline water production amount is shown in Figure 11. The well spacing has little effect on the enhancement efficiency of saline water production. When the well spacing is within 2 km, the enhancement efficiency is between 12.13% and 23.92%. The enhancement efficiency of annual saline water production is less than 3.54% when the well spacing is greater than 3 km. The number of production wells has a significant influence on the annual saline water production amount. Although the production rate in a single well decreases with the increase in the number of production wells (Figure 9(b)), the total production amount is still very large due to the large number of production wells. The annual operating time of coal-fired power generating units is approximately 5,500 hours, and the installed water consumption rate is approximately 0.6 $m^3/(s{\cdot}GW)$ in the study area at present [50]. In this study, when there are two production wells, the annual saline water production capacity is 3.03 million tons, which can meet the annual water consumption demand of a thermal power plant with an installed capacity of 300 MW.

The above analyses of the influence of the placement of production wells on the CO_2 injection and saline water production capacity indicate that the CO_2 injection and saline water production capacity decrease with increasing well spacing. Therefore, the smaller well spacing can meet the needs of massive CO_2 injection and salt water production, but the simulation period is too short to generate enough economic benefits when the well spacing is less than 1 km (Figures 8(c) and 8(d)). When the well spacing is greater than 3 km, the enhancement efficiency of CO_2-EWR technology on the CO_2 injection and saline water production is not obvious, so a 2 km well spacing is more suitable for our study area.

As shown in Figures 10 and 11, the effect of the number of production wells on the injection capacity and production capacity is more significant than that of well spacing, but the increase in production wells will correspondingly increase the project cost, so it is necessary to analyze the enhanced efficiency of production wells. From Figure 12, it can be seen that the enhancement efficiency of CO_2 injection and saline water production declines when there are more than two production wells. The enhancement efficiency is higher than the theoretical enhancement efficiency when the number of production wells is one and two. To maximize the enhancement efficiency of CO_2 injection and saline water production

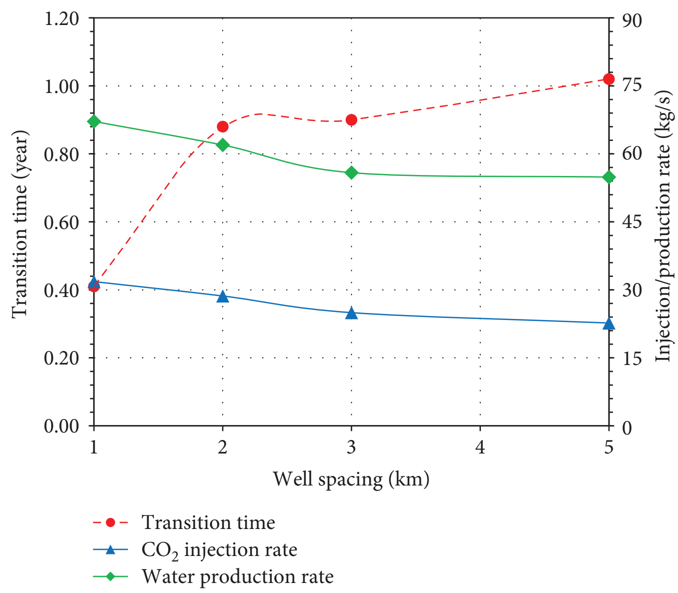

Figure 14: Influence of the well spacing on the transition time point, injection rate, and production rate.

and to obtain the greatest economic benefits, the scenario with two production wells is more reasonable.

In summary, the implementation of CO_2 injection combined with saline water production technology has a great enhancement efficiency for both CO_2 injection and saline water production capacity. CO_2-EWR technology can not only achieve the goal of lowering carbon emissions to mitigate global climate change but also produce enough water resources to meet the local water demand. The actual site simulation of the Junggar Basin shows that the simulation scenarios with 2 production wells with one injection well and a 2 km well spacing are more reasonable.

4.4. Controlling Factors of the Reservoir Pressure Evolution. The pressure in the reservoir is monitored, and the pressure monitoring point is in the middle of the injection well and the production well, $z = -7$ m below the caprock. The initial reservoir pressure of the monitoring point is 21.82 MPa. The analysis of the temporal variation of the pressure and the controlling factors of reservoir pressure evolution at this point for different simulation scenarios can provide guidance for reservoir safety evaluations and reservoir protection strategies for CO_2-EWR project design and operation.

As shown in Figure 13, the reservoir pressure increases rapidly in the solo CO_2 injection model at the early stage. After 1 year, the reservoir pressure increases slowly and finally stabilizes after 3 years. The stable pressure was 22.93 MPa, an increase of 1.11 MPa compared with the initial pressure. At the same time, the reservoir pressure decreased sharply because of the saline water production in the solo water production model, and the reservoir pressure reached a stable state after 2 years with a pressure of 19.38 MPa, a decrease of 2.44 MPa.

In the CO_2-EWR model, the pressure of the monitoring point dropped notably because of the saline water production during the early simulation stage. Then, the pressure rose slowly due to the continuous CO_2 injection. When there is only one production well with a well spacing of 1 km, the reservoir pressure decreased to 20.07 MPa after 0.41 years. As the injection-production well spacing was small, the CO_2 injection affected the monitoring point earlier, and the reservoir pressure rapidly rose to 21.05 MPa at 1.01 years. The evolution of the pressure at the monitoring point was mainly controlled by the water production during the early stage lasting 0.41 years. Then, the pressure increased, and the controlling factors changed to the CO_2 injection process. When the well spacing was 2 km, the pressure at the monitoring point decreased to the lowest value of 20.48 MPa at 0.88 years, then rose slowly to 20.54 MPa after 4 years. When the well spacing was 3 km and 5 km, the reservoir pressure decreased to a stable value of 20.80 MPa and 21.01 MPa, respectively. The pressure in the reservoir was mainly controlled by saline water production during the early stage, and the pressure at the monitoring point decreased rapidly. However, when the well spacing was less than 3 km, the monitoring point was close to the injection well and the CO_2 injection process quickly affected the monitoring point as time passed, resulting in a significant rise in the pressure. Finally, the reservoir pressure could be restored to the initial pressure of the formation.

Figure 14 indicates the influence of the well spacing on the transition time point, injection rate, and production rate; the transition time point indicates the transformation moment of the main controlling factors on the pressure evolution. The transition time point increased gradually with the well spacing, and the CO_2 injection rate and saline water production rate gradually decreased at this time point. When the well spacing was greater than 2 km, the decreasing trend of the injection and production rate was weakened, and the increasing trend of the transition time point was weakened accordingly. The pressure evolution at the monitoring point was controlled by the saline water production before the transition time point

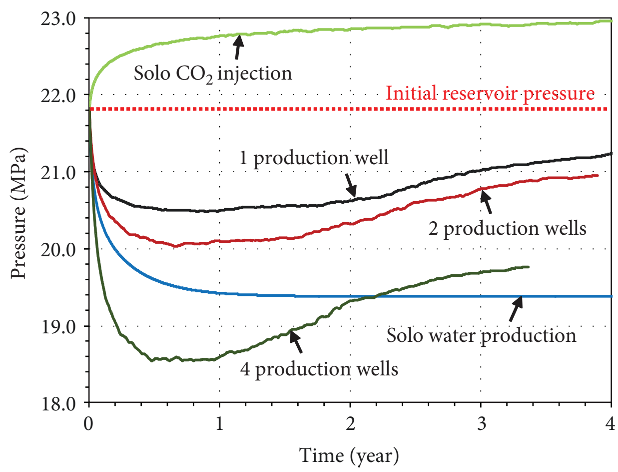

FIGURE 15: The pressure evolution curve at the monitoring point under different numbers of production well conditions.

and then controlled by CO_2 injection. The enhancement efficiency of CO_2 injection and saline water production by the CO_2-EWR technology was weakened (Figure 8) as the distance between the monitoring point to the injection or production well increased with the increase in well spacing, and the increasing trend of the transition time point also slowed down.

Figure 15 shows the temporal variation of the pressure at the monitoring point under different numbers of production well conditions. Although CO_2 injection can raise the reservoir pressure slightly, it still dropped rapidly with the increasing number of production wells as time passed. The pressure at the monitoring point dropped to 18.54 MPa after 0.48 years when there were four production wells in the reservoir, which was 3.28 MPa lower than the initial reservoir pressure, and it did not reach the critical fracture pressure [51]. Then, the pressure rose gradually due to CO_2 injection, and the pressure was restored to 19.76 MPa after 3.36 years, which was still lower than the original hydrostatic pressure of the reservoir; hence, the threat to the mechanical properties and to the security of the reservoir was weakened. When there were one or two production wells, the pressure at the monitoring point decreased slightly, with a maximum decrease of 1.76 MPa. In the later stage, the pressure was mainly controlled by CO_2 injection. Although the initial reservoir pressure could not be restored to the initial pressure, it was significantly improved compared with the scenario of solo water production.

As shown in Figure 16, when the well spacing was fixed to 2 km, the transition time point of the main controlling factors on the monitoring pressure was progressively advanced, and the CO_2 injection rate increased gradually with the number of production wells. At the same time, the water production rate of each well decreased gradually. The transition time point was reduced to 0.48 years when there were four production wells, and the CO_2 injection rate and water production rate were 49.53 kg/s and 48.98 kg/s, respectively. Then, the CO_2 injection rate increased gradually, but the production rate decreased gradually (Figure 9(a)). Therefore, the pressure evolution at the monitoring point was mainly controlled by the CO_2 injection in this stage, so the pressure rose gradually (Figure 15).

To explore the relationship between the main controlling factors of the pressure evolution at the monitoring point and the injection and production rate, we analyzed the temporal variation of the pressure and of the injection and production rate in the base-case model with one production well and one injection well, with a well spacing of 2 km, as shown in Figure 17. At the beginning of the simulation, the rate of saline water production was much higher than the CO_2 injection rate, and the pressure at the monitoring point decreased rapidly. Then, the water production rate decreased as the CO_2 injection rate increased, and the trend of the pressure decrease was weakened. The main controlling factor of the pressure in this stage was the process of saline water production, and the reservoir pressure remained stable for some time. As the simulation continued, the production rate reached a stable level, while the CO_2 injection rate still increased slowly, and the pressure increased gradually. The main controlling factor of the pressure in this stage was CO_2 injection.

The variation tendency of the pressure at the monitoring point is the same in Figure 17 as for the other simulation scenarios during the process of CO_2-EWR. The main controlling factors of the pressure evolution at a certain spatial point in the reservoir change with time. The transition time point is affected by the well spacing, the number of production wells, and the spatial position in the reservoir. When the monitoring point is in the middle of the injection well and the production well as is the case in our model with one production well and one injection well and a well spacing of 2 km, the pressure evolution is mainly controlled by the water production in the first 0.88 years; then, the main controlling factor of the pressure is the process of CO_2 injection.

Moreover, CO_2-EWR technology can effectively control the reservoir pressure and avoid the drastic increase in reservoir pressure caused by traditional CO_2 geological storage and the drastic decrease of reservoir pressure caused by solo saline water extraction. Therefore, it can become an effective CCUS technology.

5. Conclusions

Based upon the geological and hydrogeological conditions of the CO_2-EWR test site in the eastern Junggar Basin, a series of 3D injection-extraction models with fully coupled wellbores and reservoirs were established to evaluate the effect of the number of production wells and the well spacing on the enhanced efficiency of CO_2 storage and saline production, as well as the key parameters controlling the reservoir pressure evolution, and the following conclusions were obtained:

(1) CO_2-EWR technology can promote the horizontal migration of CO_2 during the process of CGS, thereby reducing the accumulation of the CO_2 concentration and pressure near the injection wells, which can

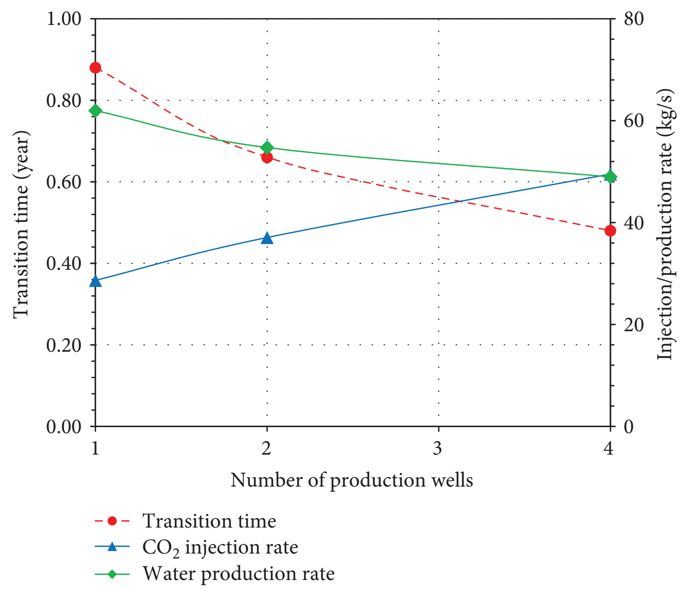

FIGURE 16: Influence of the number of production wells on the transition time point, injection rate, and production rate.

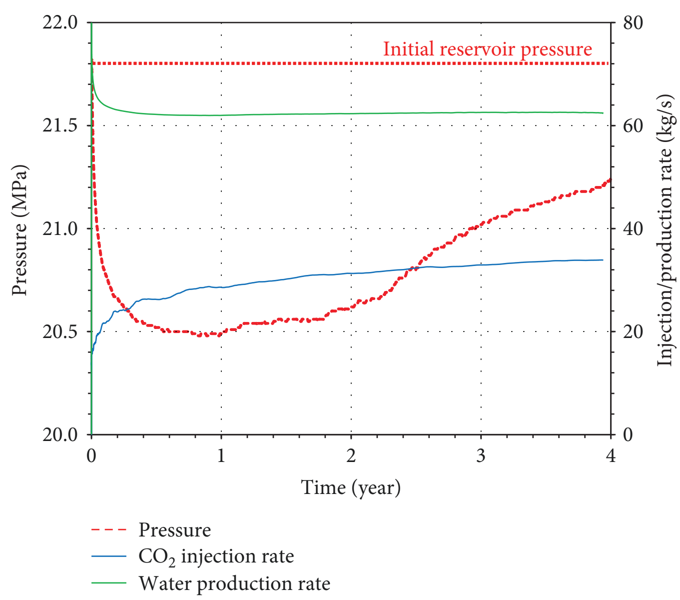

FIGURE 17: Temporal variation of the monitoring pressure and the injection and production rate.

significantly reduce the risk of CO_2 leakage along the injection wellbore

(2) A smaller spacing between the injection and production wells and a larger number of production wells can enhance not only the CO_2 injection capacity but also the saline water production capacity. However, the effect of the number of production wells on the injection and production capacity is more significant than that of the well spacing

(3) The actual site simulation of the Junggar Basin shows that the simulation scenario with 2 production wells, one injection well, and a well spacing of 2 km is the most reasonable, and the annual production capacity can meet the water requirements of a 300 MW thermal power plant

(4) During the CO_2-EWR process, the main controlling factors of the pressure evolution at a certain spatial point in a reservoir change with time. The transition time point is affected by the well spacing, the number of production wells, and the spatial position in the reservoir

(5) CO_2-EWR technology can effectively control the evolution of the reservoir pressure and offset the sharp increase in reservoir pressure caused by CO_2 injection and the sharp decrease of reservoir pressure caused by saline production. It can avoid possible

reservoir damage during the implementation of a CGS project and ensure the reservoir stability and safety of the project

The implementation of a CO_2-EWR project plays an active role in the eastern Junggar Basin, which can not only achieve the goal of lowering carbon emissions to mitigate global climate change but also produce enough water resources to meet the local water demand. The potential of CO_2 injection and saline water production can be significant. The sensitivity analysis of the reservoir parameters and the influence of geochemistry on CO_2 migration and the capacity of CO_2 injection and saline water production need to be studied further.

Data Availability

The data used to support the findings of this study are available from the corresponding author upon request.

Conflicts of Interest

The authors declare that they have no conflicts of interest.

Acknowledgments

This work was jointly supported by the National Key Research and Development Program of China (no. 2016YFB0600804), the Major Project of China National Science and Technology (no. 2016ZX05016-005), the China Geological Survey Project (no. 121201012000150010), the 111 Project (no. B16020), and the National Natural Science Foundation of China (no. 41772247).

References

[1] IPCC, *The Physical Science Basis. Fourth Assessment Report*, Cambridge University Press, Cambridge, UK, 2007.

[2] D. Best and B. Beck, "Status of CCS development in China," *Energy Procedia*, vol. 4, pp. 6141–6147, 2011.

[3] W. Chen and R. Xu, "Clean coal technology development in China," *Energy Policy*, vol. 38, no. 5, pp. 2123–2130, 2010.

[4] The Administrative Center for China's Agenda 21, *Technology Roadmap Study on Carbon Capture, Utilization and Storage in China*, Science Press, Beijing, China, 2012.

[5] X. Zhang, J. L. Fan, and Y. M. Wei, "Technology roadmap study on carbon capture, utilization and storage in China," *Energy Policy*, vol. 59, pp. 536–550, 2013.

[6] X. Lei, S. Ma, W. Chen, C. Pang, J. Zeng, and B. Jiang, "A detailed view of the injection-induced seismicity in a natural gas reservoir in Zigong, southwestern Sichuan Basin, China," *Journal of Geophysical Research: Solid Earth*, vol. 118, no. 8, pp. 4296–4311, 2013.

[7] J. Birkholzer, Q. Zhou, and C. Tsang, "Large-scale impact of CO_2 storage in deep saline aquifers: a sensitivity study on pressure response in stratified systems," *International Journal of Greenhouse Gas Control*, vol. 3, no. 2, pp. 181–194, 2009.

[8] IEAGHG, *Potential Impacts on Groundwater Resources of CO2 Storage*, IEAGHG, Cheltenham, UK, 2011.

[9] F. Quattrocchi, E. Boschi, A. Spena, M. Buttinelli, B. Cantucci, and M. Procesi, "Synergic and conflicting issues in planning underground use to produce energy in densely populated countries, as Italy: geological storage of CO_2, natural gas, geothermics and nuclear waste disposal," *Applied Energy*, vol. 101, pp. 393–412, 2013.

[10] M. M. F. Hasan, E. L. First, F. Boukouvala, and C. A. Floudas, "A multi-scale framework for CO_2 capture, utilization, and sequestration: CCUS and CCU," *Computers & Chemical Engineering*, vol. 81, pp. 2–21, 2015.

[11] D. A. Wood, "Carbon dioxide (CO_2) handling and carbon capture utilization and sequestration (CCUS) research relevant to natural gas: a collection of published research (2009–2015)," *Journal of Natural Gas Science and Engineering*, vol. 25, pp. A1–A9, 2015.

[12] M. Extavour and P. Bunje, "CCUS: utilizing CO_2 to reduce emissions," *Chemical Engineering Progress*, vol. 112, pp. 52–59, 2016.

[13] J. F. D. Tapia, J. Y. Lee, R. E. H. Ooi, D. C. Y. Foo, and R. R. Tan, "Planning and scheduling of CO_2 capture, utilization and storage (CCUS) operations as a strip packing problem," *Process Safety and Environmental Protection*, vol. 104, pp. 358–372, 2016.

[14] P. H. Kobos, M. A. Cappelle, J. L. Krumhansl, T. A. Dewers, A. Mcnemar, and D. J. Borns, "Combining power plant water needs and carbon dioxide storage using saline formations: implications for carbon dioxide and water management policies," *International Journal of Greenhouse Gas Control*, vol. 5, no. 4, pp. 899–910, 2011.

[15] Q. Li, Y. N. Wei, G. Liu et al., "Feasibility of the combination of CO_2 geological storage and saline water development in sedimentary basins of China," *Energy Procedia*, vol. 37, pp. 4511–4517, 2013.

[16] Q. Li, Y. N. Wei, G. Liu, and Q. Lin, "Combination of CO_2 geological storage with deep saline water recovery in western China: insights from numerical analyses," *Applied Energy*, vol. 116, pp. 101–110, 2014.

[17] Q. Li, Y. N. Wei, G. Liu, and H. Shi, "CO_2-EWR: a cleaner solution for coal chemical industry in China," *Journal of Cleaner Production*, vol. 103, pp. 330–337, 2015.

[18] T. A. Buscheck, Y. Sun, M. Chen et al., "Active CO_2 reservoir management for carbon storage: analysis of operational strategies to relieve pressure buildup and improve injectivity," *International Journal of Greenhouse Gas Control*, vol. 6, pp. 230–245, 2012.

[19] D. Liu, R. Agarwal, and Y. Li, "Numerical simulation and optimization of CO_2-enhanced water recovery by employing a genetic algorithm," *Journal of Cleaner Production*, vol. 133, pp. 994–1007, 2016.

[20] W. L. Bourcier, T. J. Wolery, T. Wolfe, C. Haussmann, T. A. Buscheck, and R. D. Aines, "A preliminary cost and engineering estimate for desalinating produced formation water associated with carbon dioxide capture and storage," *International Journal of Greenhouse Gas Control*, vol. 5, no. 5, pp. 1319–1328, 2011.

[21] R. D. Aines, T. J. Wolery, W. L. Bourcier, T. Wolfe, and C. Hausmann, "Fresh water generation from aquifer-pressured carbon storage: feasibility of treating saline formation waters," *Energy Procedia*, vol. 4, pp. 2269–2276, 2011.

[22] C. L. Davidson, J. J. Dooley, and R. T. Dahowski, "Assessing the impacts of future demand for saline groundwater on commercial deployment of CCS in the United States," *Energy Procedia*, vol. 1, no. 1, pp. 1949–1956, 2009.

[23] P. E. S. Bergmo, A. A. Grimstad, and E. Lindeberg, "Simultaneous CO_2 injection and water production to optimise aquifer storage capacity," *International Journal of Greenhouse Gas Control*, vol. 5, no. 3, pp. 555–564, 2011.

[24] T. le Guénan and J. Rohmer, "Corrective measures based on pressure control strategies for CO_2 geological storage in deep aquifers," *International Journal of Greenhouse Gas Control*, vol. 5, no. 3, pp. 571–578, 2011.

[25] B. Court, K. W. Bandilla, M. A. Celia et al., "Initial evaluation of advantageous synergies associated with simultaneous brine production and CO_2 geological sequestration," *International Journal of Greenhouse Gas Control*, vol. 8, pp. 90–100, 2012.

[26] Y. Li, Q. Fang, Y. Ke, J. Dong, G. Yang, and X. Ma, "Effect of high salinity on CO_2 geological storage: a case study of Qianjiang depression in Jianghan basin," *Earth Science*, vol. 37, pp. 283–288, 2012.

[27] T. Kabera and Y. L. Li, "Injecting CO_2 and pumping out saline formation water simultaneously to control pressure build-up while storing CO_2 in deep saline aquifers," *Defect and Diffusion Forum*, vol. 332, pp. 63–75, 2012.

[28] J. T. Birkholzer, A. Cihan, and Q. Zhou, "Impact-driven pressure management via targeted brine extraction—conceptual studies of CO_2 storage in saline formations," *International Journal of Greenhouse Gas Control*, vol. 7, pp. 168–180, 2012.

[29] M. A. Flett, G. J. Beacher, J. Brantjes et al., "Gorgon Project: subsurface evaluation of carbon dioxide disposal under Barrow Island," *Journal of Petroleum Technology*, vol. 61, pp. 71-72, 2008.

[30] M. Flett, J. Brantjes, R. Gurton, J. Mckenna, T. Tankersley, and M. Trupp, "Subsurface development of CO_2 disposal for the Gorgon Project," *Energy Procedia*, vol. 1, no. 1, pp. 3031–3038, 2009.

[31] J. Zhou, X. Zhuang, A. Alastuey, X. Querol, and J. Li, "Geochemistry and mineralogy of coal in the recently explored Zhundong large coal field in the Junggar basin, Xinjiang province, China," *International Journal of Coal Geology*, vol. 82, no. 1-2, pp. 51–67, 2010.

[32] K. Pruess, "Numerical simulation of CO_2 leakage from a geologic disposal reservoir, including transitions from super- to subcritical conditions, and boiling of liquid CO_2," *SPE Journal*, vol. 9, no. 2, pp. 237–248, 2013.

[33] K. Pruess, *ECO2N: A TOUGH2 Fluid Property Module for Mixtures of Water, NaCl, and CO_2*, Lawrence Berkeley National Laboratory. Earth Sciences Division, Berkeley, CA, USA, 2005.

[34] K. Pruess, C. Oldenburg, and G. Moridis, *TOUGH2 User's Guide, Version 2.0. Report LBNL4 43134, Lawrence Berkeley National Laboratory*, Lawrence Berkeley National Laboratory. Earth Sciences Division, Berkeley, CA, USA, 1999.

[35] K. Zhang, Y. Wu, and K. Pruess, *User's Guide for TOUGH2-MP-A Massively Parallel Version of the TOUGH2 Code*, Lawrence Berkeley National The Laboratory Earth Sciences Division, Berkeley, CA, USA, 2008.

[36] L. Pan, C. M. Oldenburg, Y. Wu, and K. Pruess, *T2Well/E-CO2N Version 1.0: Multiphase and Non-Isothermal Model for Coupled Wellbore-Reservoir Flow of Carbon Dioxide and Variable Salinity Water*, Lawrence Berkeley National Laboratory. Earth Sciences Division, Berkeley, CA, USA, 2011.

[37] L. Pan and C. M. Oldenburg, "T2Well—an integrated wellbore–reservoir simulator," *Computers & Geosciences*, vol. 65, pp. 46–55, 2014.

[38] T. Xu, G. Feng, Z. Hou, H. Tian, Y. Shi, and H. Lei, "Wellbore–reservoir coupled simulation to study thermal and fluid processes in a CO_2-based geothermal system: identifying favorable and unfavorable conditions in comparison with water," *Environmental Earth Sciences*, vol. 73, no. 11, pp. 6797–6813, 2015.

[39] Y. Yang, F. Bu, T. Xu, and F. Wang, "The anisotropy effect on CO_2-water two phase fluid migration-improve the TOUGH2 simulator function," *Journal of Northeastern University*, vol. 35, pp. 1211–1216, 2014.

[40] Y. Yang, T. Xu, F. Wang, H. Lei, G. Jing, and G. Yue, "Toughvisual: a user-friendly pre-processing and post-processing graphical interface for TOUGHREACT," in *Proceedings TOUGH Symposium*, pp. 17–19, Berkeley, CA, USA, 2012.

[41] Q. Fang, *CO_2 Geological Storage Combined with Brine Production in High-Salinity and Low-Permeability Aquifers*, China University of Geosciences, Wuhan, China, 2014.

[42] Z. Dai, R. Middleton, H. Viswanathan et al., "An integrated framework for optimizing CO_2 sequestration and enhanced oil recovery," *Environmental Science & Technology Letters*, vol. 1, no. 1, pp. 49–54, 2013.

[43] F. Bu, T. Xu, F. Wang, Z. Yang, and H. Tian, "Influence of highly permeable faults within a low-porosity and low-permeability reservoir on migration and storage of injected CO_2," *Geofluids*, vol. 16, no. 4, 781 pages, 2016.

[44] F. Wang, J. Jing, Y. Yang et al., "Impacts of injection pressure of a dip-angle sloping strata reservoir with low porosity and permeability on CO_2 injection amount," *Greenhouse Gases: Science and Technology*, vol. 7, no. 1, pp. 92–105, 2017.

[45] C. Li, K. Zhang, Y. Wang, C. Guo, and F. Maggi, "Experimental and numerical analysis of reservoir performance for geological CO_2 storage in the Ordos Basin in China," *International Journal of Greenhouse Gas Control*, vol. 45, pp. 216–232, 2016.

[46] Z. Yang, T. Xu, F. Wang, Y. Yang, X. Li, and N. Zhao, "Impact of inner reservoir faults on migration and storage of injected CO_2," *International Journal of Greenhouse Gas Control*, vol. 72, pp. 14–25, 2018.

[47] K. Pruess and J. Garcia, "Multiphase flow dynamics during CO_2 disposal into saline aquifers," *Environmental Geology*, vol. 42, no. 2-3, pp. 282–295, 2002.

[48] J. B. Walsh, "Effect of pore pressure and confining pressure on fracture permeability," *International Journal of Rock Mechanics and Mining Sciences & Geomechanics Abstracts*, vol. 18, no. 5, pp. 429–435, 1981.

[49] G. R. Johnson and W. H. Cook, "Fracture characteristics of three metals subjected to various strains, strain rates, temperatures and pressures," *Engineering Fracture Mechanics*, vol. 21, no. 1, pp. 31–48, 1985.

[50] M. Han, "Analysis and countermeasures on water consumption in thermal power plants," *Industrial Water Treatment*, vol. 30, pp. 4–7, 2010.

[51] M. K. Hubbert, "Mechanics of hydraulic fracturing," *Developments in Petroleum Science*, vol. 210, pp. 369–390, 1972.

Hindawi
Geofluids
Volume 2019, Article ID 1038412, 11 pages
https://doi.org/10.1155/2019/1038412

Research Article

Study of Single Phase Mass Transfer between Matrix and Fracture in Tight Oil Reservoirs

Renyi Cao[1,2] **Zhongyi Xu,**[1,3] **Linsong Cheng,**[1,2] **Yuanyuan Peng,**[4] **Yang Wang,**[1,2] **and Zhuoliang Guo**[1,2]

[1] *State Key Laboratory of Petroleum Resources and Prospecting, China University of Petroleum, Beijing 102249, China*
[2] *College of Petroleum Engineering, China University of Petroleum, Beijing 102249, China*
[3] *SINOPEC Petroleum Exploration and Production Research Institute, Beijing 100083, China*
[4] *Research Institute of Petroleum Exploration and Development, PetroChina, Beijing 100083, China*

Correspondence should be addressed to Renyi Cao; caorenyi@126.com

Received 6 July 2018; Revised 28 October 2018; Accepted 25 November 2018; Published 3 March 2019

Guest Editor: Bisheng Wu

In tight fractured reservoirs, oil in matrices is mainly explored due to mass transfer mechanisms during the pressure depletion process. In the modeling of mass transfer in fractured reservoirs using the dual porosity concept, the shape factor is the most important parameter and should be described accurately. However, the current shape factors are not suited for tight oil reservoir simulation because the characteristics of tight oil reservoirs are not taken into account. In order to solve this problem, a new mass transfer function for tight fractured oil reservoirs is proposed by introducing a new time-related correction factor which could consider not only the existence of the boundary layer in nano-microscale throats in tight porous media but also the heterogeneous pressure distribution in matrix blocks. In addition, special contact relations between matrix and fracture are included. The correction factor presented in this study is verified using the experimental data and numerical simulation results. Data analysis results demonstrate that the lower and slower the pressure propagation velocity, the longer the duration time of unsteady flow compared to conventional reservoirs. Therefore, in the calculation of mass transfer flow in tight oil reservoirs, the unsteady flow between fracture and matrix cannot be ignored.

1. Introduction

At present, the oil production process of tight oil reservoirs is normally applied after the artificial fracturing procedure. During the pressure depletion process, oil in matrix blocks is produced by the mechanism of single phase mass transfer, normally. Similar to the conventional fractured oil reservoir, dual porosity is usually used to represent fractured reservoirs which was firstly proposed by Barenblatt et al. [1]. Barenblatt et al. assumed that the flow from the matrix to the fracture is pseudo-flow; Warren and Root [2] proposed a pseudo-steady analytical radical solution of single phase mass transfer flow in fractured reservoirs and applied the analytical solution in well test analysis. The continuity equation describing the planar flow of a compressible fluid in a fracture is described as follows:

$$\frac{k_{fx}}{\mu}\frac{\partial^2 p_f}{\partial x^2} + \frac{k_{fy}}{\mu}\frac{\partial^2 p_f}{\partial y^2} - \phi_m C_m \frac{\partial p_m}{\partial t} = \phi_f C_f \frac{\partial p_f}{\partial t}. \quad (1)$$

On the assumption that the flow of the matrix follows Darcy's law, the rate expression of mass transfer is described by

$$\phi_m C_m \frac{\partial p_m}{\partial t} = \sigma \frac{k}{\mu}(p_m - p_f). \quad (2)$$

In Eq. (2), σ is the characteristic coefficient of the fractured matrix block and it is usually termed as the shape factor. Different scholars have great differences on the selection of shape factor values. In Warren and Root's model, the shape factor is defined as follows:

$$\sigma = \frac{4n(n+2)}{L^2}. \tag{3}$$

In Eq. (3), $n(n = 1,2,3)$ represents the dimension of the matrix block. For the case of 1, 2, and 3 sets of fractures (1-D, 2-D, and 3-D situations), the values of σ are $12/L^2$, $32/L^2$, $60/L^2$. Kazemi et al. [3] also have proposed the shape factor as follows in Eq. (4):

$$\sigma = 4\left(\frac{1}{{L_x}^2} + \frac{1}{{L_y}^2} + \frac{1}{{L_z}^2}\right). \tag{4}$$

In Eq. (4) L_x, L_y, and L_z are the lengths of the matrix block in the x, y, and z directions, respectively. When $L_x = L_y = L_z = L$, for the situation of 1, 2, and 3 sets of fractures, values of σ in different situations are $4/L^2$, $8/L^2$, and $12/L^2$.

Coats [4] has proposed different expressions of shape factor and compared with the fine grid numerical simulation. Simulation results reported by Bourbiaux shows that Coat's calculation results are more in coincidence with the reference solution, and Kazemi et al.'s results deviate from fine grid results. These mass transfer models mentioned above are proper for the conventional fractured oil reservoir in which the fluid flow in the matrix obeys Darcy's law and the mass transfer between the matrix and the fracture can be assumed as a steady or pseudo-steady flow. Hassanzadeh and Pooladi-Darvish [5] analyzed the effects of fracture boundary conditions on the matrix-fracture transfer shape factor. Hassanzadeh and Pooladi [6] extend their previous analysis and use infinite-acting radial and linear dual-porosity models, where the boundary condition is chosen at the wellbore, as opposed to that at the matrix boundary.

Ranjbar and Hassanzadeh [7] used the matrix–fracture transfer shape factor for modeling the flow of a compressible fluid in dual-porosity media. Ranjbar et al. [8] had investigated the effect of the fracture pressure depletion regime on the shape factor for a single-phase flow of a compressible fluid. In the current study, a model for evaluation of the shape factor is derived using solutions of a nonlinear diffusivity equation subject to different pressure depletion regimes. A combination of the heat integral method, the method of moments, and Duhamel's theorem is used to solve this nonlinear equation. Ranjbar [9] analyzed one-dimensional matrix-fracture transfer in dual porosity systems with variable block size distribution. Ranjbar et al. [10] present a semi-analytical solution for release of a single-phase liquid or gas from cylindrical and spherical matrix blocks with various block size distributions and different pressure depletion regimes in the fracture.

However, at present, there is no mass transfer function for tight oil reservoirs. The main reason is that as for tight oil reservoirs, there are some particular characteristics compared to other reservoirs. These characteristics are due to the following: (1) a large amount of nanoscale or microscale throats present in tight porous media, with a boundary layer effect which leads to nonlinear flow behavior in matrix blocks [11, 12], cannot be neglected; (2) the flow pattern has its own characteristics due to the contact relation between the matrix and the artificial fractures in tight oil reservoirs; (3) due to the low permeability of matrix blocks, the pressure sweep velocity is slow, the distribution of pressure in the matrix block is heterogeneous, and therefore, it is not appropriate to assume that the pressure distribution in the matrix is homogeneous and to use an average pressure at the center of the matrix to represent the pressure in the matrix.

In view of the abovementioned problems, a new mass transfer model is proposed. Firstly, in order to reflect the nonlinear flow behavior in matrix blocks, a model of tight formation permeability is used to replace the permeability in the traditional mass transfer model. Secondly, according to the contact relation between the matrix and the fracture, the new mass transfer model is divided into three categories which is the matrix-planar fracture model (1-D), the matrix--planar/naturally fracture model (2-D), and the matrix-volume fracture model (3-D). Then, based on the assumption of an unsteady flow between matrix blocks and fractures, a time-dependent correction factor is obtained to modify the traditional mass transfer flow model. At last, the proposed model is verified by comparing with experimental data or simulation results.

2. Mathematical Methods

2.1. Permeability Model of Tight Formation. The range of the tight oil formation throat radius distribution ranges from 20 nm to 1.2 μm, and the permeability is at the magnitude of 10^{-1} mD [13]. The existence of the boundary layer cannot be ignored in these nanoscale or microscale throats. The influence of the boundary layer on the throat is shown in Figure 1. The fluid flow in the throat of unconventional oil reservoirs reduces the effective flow due to the presence of the boundary layer. In some extreme cases, when the boundary layer thickness is equal to the original throat radius, the presence of the boundary layer can even cause all fluids in the throat to become immobile. According to Tian et al. [14], the boundary layer thickness can be quantitatively expressed by

$$h = \begin{cases} r0.25763e^{-0.261r}(\nabla P)^{-0.419}\mu, & \nabla P < 1\ \text{MPa/m}, \\ r0.25763e^{-0.261r}\mu, & \nabla P > 1\ \text{MPa/m}. \end{cases} \tag{5}$$

h is the thickness of the boundary layer, in μm, r is the radius of the throat in tight porous media, in μm, μ is viscosity, and ∇p is the pressure gradient, in MPa/m.

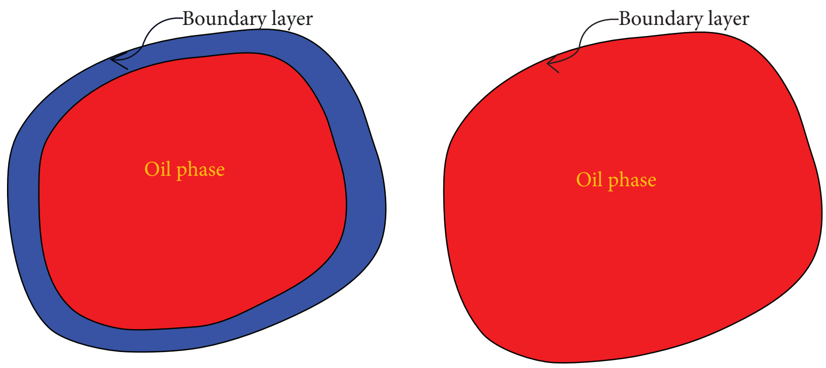

(a) Fluid flow when a boundary exists in the throat (b) Fluid flow when no boundary layer exists

Figure 1: The influence of the boundary layer on the flow of tight throat.

Due to the influence of the boundary layer, the radius of the original throat is larger than the effective flow radius. Therefore, the effective throat radius is used to characterize the flow in micro- or nanoscale throats. The effective throat radius is equal to the original throat radius minus the boundary layer thickness given by

$$r_{\mathrm{eff}} = r_i - h. \tag{6}$$

The matrix core can be equivalent to a microcircular tube capillary bundle model. It is assumed that the model is composed of a circular tube with a continuous radius and that the flow of fluid in the matrix can be obtained according to the Poiseuille equation:

$$Q_{\mathrm{i}} = N\frac{\pi r_{\mathrm{i}}^4 \Delta P}{8\mu\tau L}. \tag{7}$$

For the pore throat distribution of a tight core, the Gauss probability distribution function (Eq. (8)) can be used [15–18]. Figure 2 shows the pore throat radius distribution and the cumulative pore throat distribution curve expressed by the Gauss function. Because of the different distribution of the pore throat in different cores, the pore throat distribution can be changed by changing the mean pore throat value and the standard deviation between pore throat and pore, thus representing the pore throat composition of different cores. For the distribution of pores and throats as normal distribution, the throat distribution can be described by the Gauss function, and the pore throat that cannot be fitted to the normal distribution can be represented by finding other functions.

$$f(r_i) = \frac{1}{\sqrt{2\pi\sigma}}\exp\left(-\frac{(r_i - \nu)}{2\sigma^2}\right)^2. \tag{8}$$

Combining Eq. (7) and Eq. (8), the flow rate when the pores and throat distribution obey the Gauss function can be presented by

$$Q = \frac{\sum_{i=1}^{i=n} \pi N f(r_i) r_i^{\,4} \cdot \Delta P}{8\mu\tau L}. \tag{9}$$

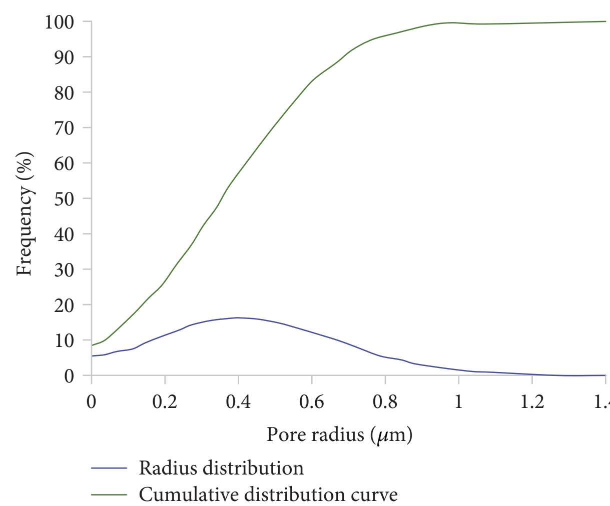

Figure 2: Schematic of Gauss distribution.

Based on Darcy's law, the flow rate of porous media can be expressed as

$$Q = \frac{K_{\mathrm{m}} A \Delta P}{\mu L}. \tag{10}$$

The matrix cross-sectional area can be expressed as

$$A = \frac{\sum_{i=1}^{i=n} \pi N f(r_i) r_i^{\,2}}{\varphi_{\mathrm{m}}}. \tag{11}$$

The flow rate expression is obtained by substituting Eq. (11) into Eq. (10):

$$Q = \frac{K_{\mathrm{m}} \sum_{i=1}^{i=n} \pi N f(r_i) r_i^2 \cdot \Delta P}{\varphi_{\mathrm{m}} \mu L}. \tag{12}$$

Eq. (12) and Eq. (9) are combined to obtain the permeability of the tight oil reservoir:

$$K_{\mathrm{m}} = \frac{\varphi_{\mathrm{m}} \sum_{i=1}^{i=n} \left[\exp\left(-(r_i - \nu)/2\sigma^2\right)^2 r_i^4\right]}{8\tau \sum_{i=1}^{i=n} \left[\exp\left(-(r_i - \nu)/2\sigma^2\right)^2 r_i^2\right]}. \tag{13}$$

Eq. (13) does not consider the effect of the boundary layer. Since the boundary layer effect cannot be neglected in the tight oil reservoir, the thickness of the boundary layer shall be subtracted from the original radius of the throats. Then, the permeability of the tight oil reservoir is obtained as

$$K_{\mathrm{m}}=\begin{cases}\dfrac{\varphi_{\mathrm{m}}\sum_{i=1}^{i=n}\left[\exp\left(-(r_i-\nu)/2\sigma^2\right)^2\left(r_i-r_i\cdot 0.25763e^{-0.261r_i}(\nabla P)^{-0.419}\cdot\mu\right)^4\right]}{8\tau\sum_{i=1}^{i=n}\left[\exp\left(-(r_i-\nu)/2\sigma^2\right)^2\left(r_i-r_i\cdot 0.25763e^{-0.261r_i}(\nabla P)^{-0.419}\cdot\mu\right)^2\right]}, & \nabla P<1\,\mathrm{MPa}\cdot\mathrm{m}^{-1},\\[2ex] \dfrac{\varphi_{\mathrm{m}}\sum_{i=1}^{i=n}\left[\exp\left(-(r_i-\nu)/2\sigma^2\right)^2\left(r_i-r_i\cdot 0.25763e^{-0.261r_i}\cdot\mu\right)^4\right]}{8\tau\sum_{i=1}^{i=n}\left[\exp\left(-(r_i-\nu)/2\sigma^2\right)^2\left(r_i-r_i\cdot 0.25763e^{-0.261r_i}\cdot\mu\right)^2\right]}, & \nabla P>1\,\mathrm{MPa}\cdot\mathrm{m}^{-1}.\end{cases} \quad (14)$$

2.2. Mass Transfer Model. Because of the stress distribution, fracture network complexity, and the difference of fracturing technique, different forms of matrix fracture contact relations are formed in the reservoir after the fracturing procedure. Figure 3(a) shows a matrix-planar fracture contact model in 1-D, Figure 3(b) shows the matrix-planar/-naturally fractured model in 2-D, and Figure 3(c) shows the matrix-complex fracture in 3-D. For a different contact model of matrix and fractures, mass transfer will happen when the original balanced pressure distribution changes. Analytical solutions of the mass transfer rate of different contact relation models are characterized in the following section.

2.2.1. Matrix-Planar Fracture Mass Transfer Model. The contact relation of the matrix and fracture in 1-D is shown in Figure 4. Under the pressure difference, fluid in the matrix flows linearly into the fracture. During the process of linear flow, the pressure in the matrix changes continually. Thus, in the calculation process, pressure change in the matrix should be considered to avoid introduction of a significant error.

The continuity equation of fracture can be expressed as

$$\nabla\cdot\left[\frac{k_{\mathrm{f}}}{\mu B}\nabla p_{\mathrm{f}}\right]=\phi_{\mathrm{f}}c_{\mathrm{t}}\frac{\partial p_{\mathrm{m}}}{\partial t}-q_{\mathrm{m}\to\mathrm{f}}. \quad (15)$$

The continuity equation of the matrix can be expressed as

$$\nabla\cdot\left[\frac{k_{\mathrm{m}}}{\mu B}\nabla p_{\mathrm{m}}\right]=\phi_{\mathrm{m}}c_{\mathrm{t}}\frac{\partial p_{\mathrm{m}}}{\partial t}+q_{\mathrm{m}\to\mathrm{f}}. \quad (16)$$

The mass transfer rate is a function of pressure difference, matrix permeability, and shape of matrix blocks, and it can be expressed as

$$q=\sigma\frac{k_{\mathrm{m}}}{\mu B}\left(P_{\mathrm{m}}-P_{\mathrm{f}}\right). \quad (17)$$

As shown in Figure 5, single phase mass transfer depends on the pressure difference between matrix blocks and fractures. The mass transfer rate can also be expressed by writing Darcy's law between the matrix and the fracture as given by

$$q=\frac{Ak_{\mathrm{m}}}{\mu B}\frac{\left(P_{\mathrm{m}}-P_{\mathrm{f}}\right)}{L}. \quad (18)$$

The flow rate at the interface can be expressed as follows:

$$q=-A_{\mathrm{mf}}\frac{k_{\mathrm{m}}}{\mu B}\frac{\partial P}{\partial x}. \quad (19)$$

Assuming a planar fracture, the area of interface is given by

$$A_{\mathrm{mf}}=2\frac{\phi_{\mathrm{f}}}{w_{\mathrm{f}}}V_{\mathrm{f}}. \quad (20)$$

To calculate the mass transfer rate properly, the following assumptions are made:

(1) The fracture pressure is chosen as the pressure at the interface p_{f} due to the smaller size of the fracture relative to the matrix

(2) The matrix pressure is selected as average pressure $\bar{p}_{\mathrm{m}}$ of the matrix block which is involved in the flow, and the position of average pressure $\bar{p}_{\mathrm{m}}$ is selected at the half width of the matrix that is involved in the flow

(3) When 1-D single phase mass transfer occurred, the position change of the average pressure of the matrix is shown in Figure 5:

Due to the extremely low permeability of the tight matrix block, mass transfer between matrix and fracture is slow. During every step of this process, only part of the matrix block is involved to contribute to the mass transfer (shown in Figure 5). As the mass transfer process proceeds, more and more matrix block regions are involved, and the average pressure point is selected at the center of the involved matrix block which contributes to the mass transfer, so the average pressure point (red point in Figure 5) continually changes its position as the mass transfer process proceeds.

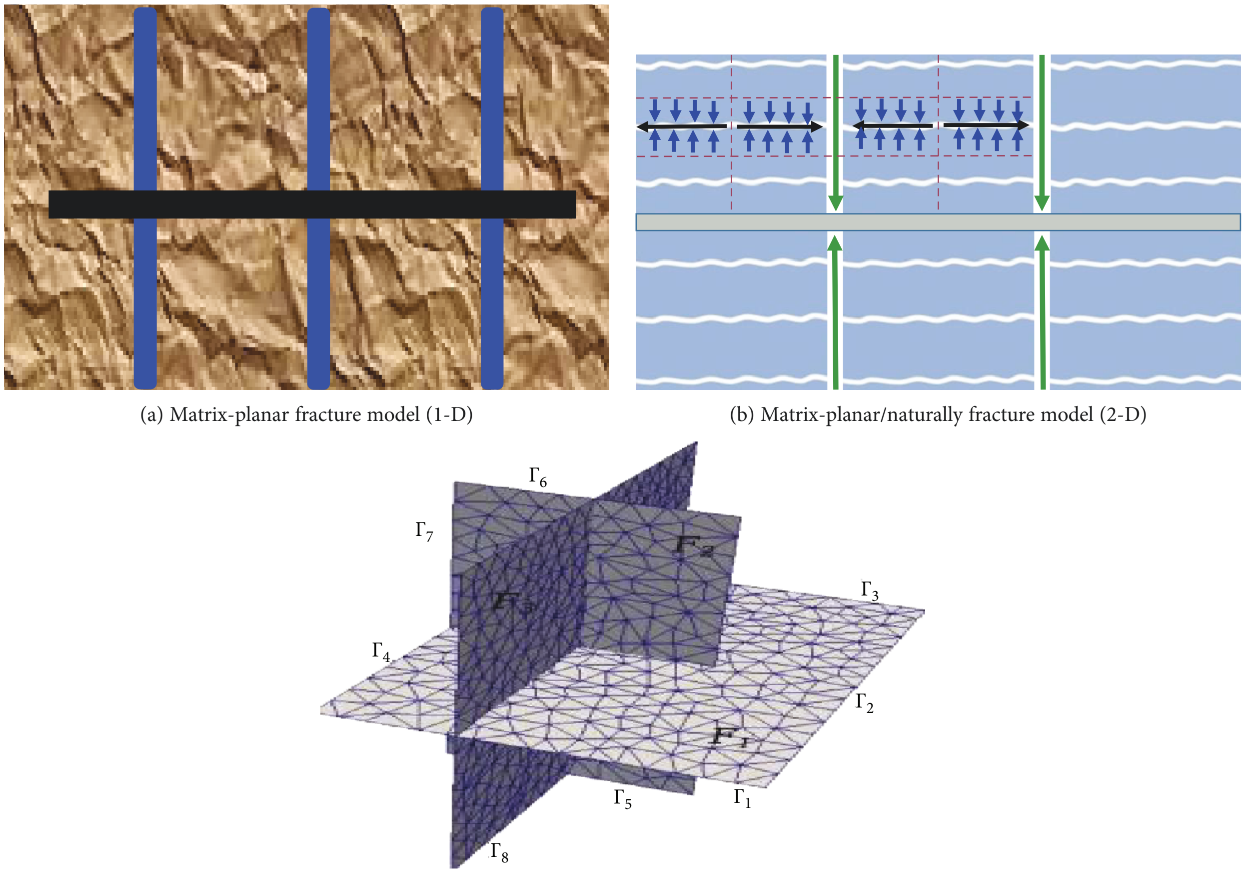

(a) Matrix-planar fracture model (1-D)

(b) Matrix-planar/naturally fracture model (2-D)

(c) Matrix-volume fracture model (3-D)

FIGURE 3: Different contact modes between matrix and fracture.

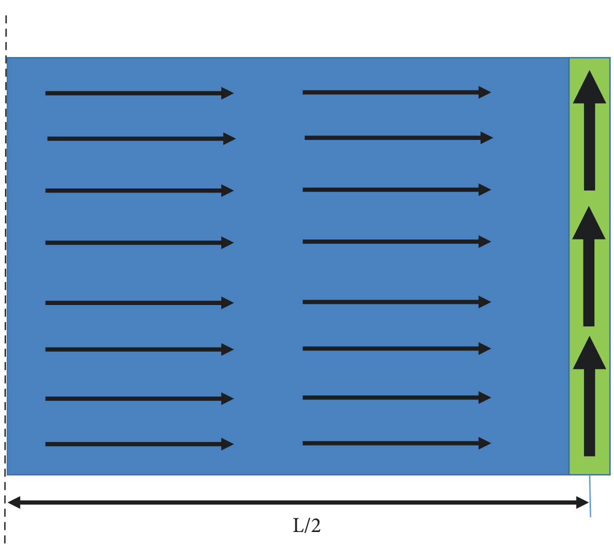

FIGURE 4: The schematic for 1-D mass transfer flow between matrix and fracture.

These assumptions are not consistent with the actual situation, but convenient for calculation. To alleviate this problem, a correction factor C_f is introduced and then the mass transfer rate can be expressed as

$$q = C_f A \frac{k_m}{\mu B} \frac{\left(\bar{P}_m - P_f\right)}{L/2}. \tag{21}$$

For a single phase slightly compressible fluid, the flow in the matrix can be written using

$$\frac{\partial P_m}{\partial t} = \frac{k_m}{\phi_m \mu c_t} \frac{\partial^2 P_m}{\partial x^2}. \tag{22}$$

subject to the initial condition

$$P_m = P_i, \quad -\frac{L}{2} \le x \le \frac{L}{2}, \quad t = 0, \tag{23}$$

and the boundary condition

$$\frac{\partial P_m}{\partial x} = 0, \quad x = 0. \tag{24}$$

$$\begin{aligned} &P_m = P_f, \quad x = -\frac{L}{2}, \quad t > 0, \\ \text{or} \quad &P_m = P_f, \quad x = \frac{L}{2}, \quad t > 0. \end{aligned} \tag{25}$$

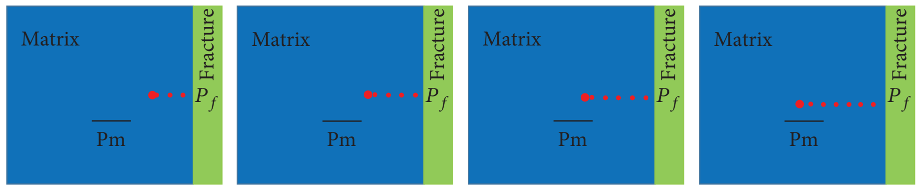

Figure 5: Schematic for the change of matrix average pressure.

If M_t is the cumulative mass transfer from matrix to fracture at time t, then M_∞ represents the total mass transfer when the time approaches to infinity; the ratio of M_t and M_∞ can be given as (Crank, 1995)

$$\frac{M_t}{M_\infty} = 1 - \sum_{j=0}^{\infty} \frac{8}{(2j+1)^2\pi^2} \exp\left[-\frac{(2j+1)^2\pi^2 kt}{\phi\mu c_t L^2}\right], \quad (26)$$

The ratio given by Eq. (26) can also be transformed into the ratio of increment of density:

$$\frac{M_t}{M_\infty} = \frac{\overline{\rho}_m - \rho_i}{\rho_f - \rho_i}. \quad (27)$$

Fluid is assumed as slightly compressible, thus

$$\rho(P) = \rho_i[1 + c(P - P_i)]. \quad (28)$$

Combining Eq. (17)–Eq. (28), an analytical solution is obtained as follows:

$$\frac{\overline{P}_m - P_f}{P_i - P_f} = \sum_{j=0}^{\infty} \frac{8}{(2j+1)^2\pi^2} \exp\left[-\frac{(2j+1)^2\pi^2 k_m t}{\phi_m \mu c_t L^2}\right]. \quad (29)$$

Because the mass transfer rate is equal to the accumulate flow per unit volume of matrix,

$$q = -\phi_m c_t V \frac{\partial \overline{P}_m}{\partial t}. \quad (30)$$

The partial derivative of pressure $\overline{P}_m$ to time t is as follows:

$$\frac{\partial \overline{P}_m}{\partial t} = -(P_i - P_f) \sum_{j=0}^{\infty} \frac{8k_m}{\phi_m \mu c_t L^2} \exp\left[-\frac{(2j+1)^2\pi^2 k_m t}{\phi_m \mu c_t L^2}\right]. \quad (31)$$

Substituting Eq. (31) into Eq. (22),

$$q = L^3 \frac{k_m}{\mu}\frac{8V}{L^2}(P_i - P_f) \sum_{j=0}^{\infty} \exp\left[-\frac{(2j+1)^2\pi^2 k_m t}{\phi_m \mu c_t L^2}\right], \quad (32)$$

$$q = C_f \frac{k_m A_1}{\mu} \frac{\left(\overline{P}_m - P_f\right)}{L/2}. \quad (33)$$

In Eq. (33), $A_1 = 2L^2$, V is the volume of the matrix involved in the mass transfer process and the correction coefficient can be expressed as follows:

$$C_f = \frac{q\mu BL}{2Ak_m\left(\overline{P}_m - P_f\right)}. \quad (34)$$

Substituting Eq. (32) and the pressure difference of the average pressure of the matrix and the pressure of the fracture $(\overline{P}_m - P_f)$ into Eq. (34), the final expression of correction coefficient C_f is obtained as

$$C_f = \frac{\pi^2}{4} \frac{\sum_{j=0}^{\infty} \exp\left[-(2j+1)^2\pi^2 t_D\right]}{\sum_{j=0}^{\infty} (2j+1)^{-2} \exp\left[-(2j+1)^2\pi^2 t_D\right]}, \quad (35)$$

where $t_D = (k_m/\phi_m \mu c_t L^2)t$.

When the value of dimensionless time t_D is large enough, the correction factor converged into the shape factor of the pseudo-steady mass transfer flow:

$$C_f = \frac{\pi^2}{4}. \quad (36)$$

For the correction coefficient C_f of pseudo-steady mass transfer flow, Lim and Aziz use the constant shape factor σ to replace C_f; the mass transfer rate can be expressed as follows:

$$q = \frac{\pi^2}{L^2} V \frac{k_m}{\mu}\left(\overline{P}_m - P_f\right), \quad (37)$$

where $V = LA_0$ is the volume of the matrix and $A = 2A_0$,

$$q = \frac{\pi^2}{4} A \frac{k_m}{\mu} \frac{\left(\overline{P}_m - P_f\right)}{L/2}. \quad (38)$$

The correction coefficient of the pseudo-steady mass transfer coefficient is then

$$C_f = \frac{\pi^2}{4} = 2.47. \quad (39)$$

2.2.2. Matrix-Planar/Naturally Fracture Mass Transfer Model. Figure 6 shows the schematic for the contact between the matrix and hydraulic-natural fractures. Under this circumstance, matrix blocks are surrounded by fractures, and fluid flow from the matrix to fractures is 2-D planar flow. For convenience, the contact relation between matrix and fracture is simplified as shown in Figure 7 and the change of average

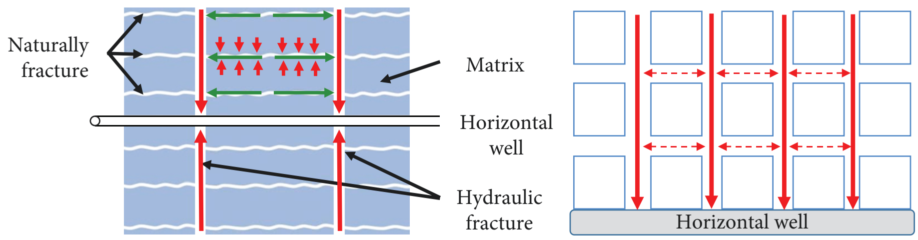

Figure 6: Schematic for contact between matrix and hydraulic-natural fractures.

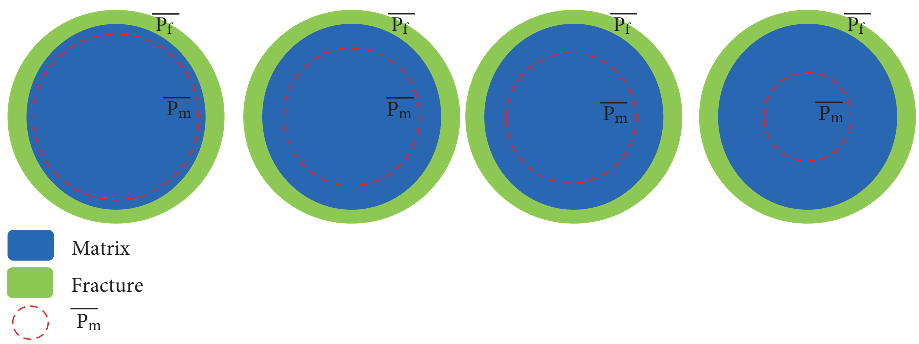

Figure 7: Schematic for the change of average pressure.

pressure in the matrix during the process of mass transfer is also shown in Figure 7, where after the simplification the contact relation becomes a circular contact between matrix and fracture.

Under the assumption of 2-D circular contact relation, the pressure diffusion equation in the matrix block can be written in the following form:

$$\frac{\partial P}{\partial t}=\frac{1}{r}\frac{\partial}{\partial r}\left(\frac{rk_{\mathrm{m}}}{\phi_{\mathrm{m}}\mu c_{\mathrm{t}}}\frac{\partial P}{\partial r}\right). \tag{40}$$

The boundary and initial conditions are

$$\begin{aligned} P_{\mathrm{m}}&=P_{\mathrm{i}}, \quad 0\le r\le R, \quad t=0,\\ P_{\mathrm{m}}&=P_{\mathrm{f}}, \quad r=R, \quad t>0. \end{aligned} \tag{41}$$

Then, for the analytical solution of two-dimensional radical flows, after handing, the pressure difference relation can be written as

$$\frac{\bar{P}_{\mathrm{m}}-P_{\mathrm{f}}}{P_{\mathrm{i}}-P_{\mathrm{f}}}=\sum_{n=1}^{\infty}\frac{4}{\alpha_n{}^2}\exp\left[-\frac{\alpha_n{}^2k_{\mathrm{m}}t}{\phi_{\mathrm{m}}\mu c_{\mathrm{t}}R^2}\right], \tag{42}$$

$$J_0(R\alpha_n)=0 \tag{43}$$

In Eq. (43), J_0 is the Bessel function of the first kind of order zero, and α_n is the root of the Bessel function.

$$\frac{\partial\bar{P}_{\mathrm{m}}}{\partial t}=-(P_{\mathrm{i}}-P_{\mathrm{f}})\sum_{n=1}^{\infty}\frac{4k_{\mathrm{m}}}{\phi_{\mathrm{m}}\mu c_{\mathrm{t}}R^2}\exp\left[-\frac{\alpha_n{}^2k_{\mathrm{m}}t}{\phi_{\mathrm{m}}\mu c_{\mathrm{t}}R^2}\right], \tag{44}$$

$$q=-\phi_{\mathrm{m}}c_{\mathrm{t}}V\frac{\partial\bar{P}_{\mathrm{m}}}{\partial t}. \tag{45}$$

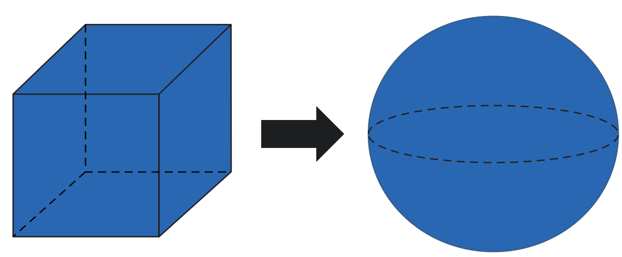

Figure 8: Schematic for contact between matrix and volume fractures.

After substituting Eq. (44) into Eq. (45), the mass transfer rate of Eq. (46) can be obtained as given by

$$q=L^3(P_{\mathrm{i}}-P_{\mathrm{f}})\sum_{n=1}^{\infty}\frac{4k_{\mathrm{m}}}{\mu R^2}\exp\left[-\frac{\alpha_n^2k_{\mathrm{m}}t}{\phi_{\mathrm{m}}\mu c_{\mathrm{t}}}\right]. \tag{46}$$

Figure 7 shows that the position of the average pressure in 2-D situation changes as the mass transfer process keeps proceeding. The theory is the same as in Figure 5.

$$q=C_{\mathrm{f}}\frac{k_{\mathrm{m}}A_2}{\mu}\frac{\left(\overline{P_{\mathrm{m}}}-P_{\mathrm{f}}\right)}{L/2}, \tag{47}$$

$$\begin{aligned} C_{\mathrm{f}}&=\frac{\sum_{n=0}^{\infty}2(P_{\mathrm{i}}-P_{\mathrm{f}})k_{\mathrm{m}}\left(L^4/R^2\right)\exp\left(-\left(\alpha_n^2k_{\mathrm{m}}t/\phi_{\mathrm{m}}\mu c_{\mathrm{t}}\right)\right)}{4L^2(P_{\mathrm{i}}-P_{\mathrm{f}})k_{\mathrm{m}}\sum_{n=0}^{\infty}\left(4/R^2\alpha_n^2\right)\exp\left(-\left(\alpha_n^2k_{\mathrm{m}}t/\phi_{\mathrm{m}}\mu c_{\mathrm{t}}\right)\right)}\\ &=\frac{\sum_{n=0}^{\infty}L^2\exp\left(-t_{\mathrm{D}}\right)}{8\sum_{n=0}^{\infty}1/\alpha_n^2\exp\left(-t_{\mathrm{D}}\right)}. \end{aligned} \tag{48}$$

In Eq. (47), $A_2=4L^2$, $t_{\mathrm{D}}=k_{\mathrm{m}}t/\phi_{\mathrm{m}}\mu c_{\mathrm{t}}$.

Table 1: Reservoir parameters of Yanchang Formation.

Parameter	No. 1	No. 2	No. 3	No. 4	No. 5	No. 6	No. 7	No. 8
Porosity (%)	8.20	6.20	12.70	8.40	6.80	6.00	5.10	12.10
Gas permeability (10^{-3} μm^2)	0.40	0.16	0.12	0.18	0.10	0.10	0.05	0.23
Liquid permeability (10^{-3} μm^2)	0.014	0.006	0.004	0.005	0.003	0.003	0.001	0.01

Table 2: Data of throat distributions of Yanchang Formation.

Throat radius (μm)	No. 1 (%)	No. 2 (%)	No. 3 (%)	No. 4 (%)	No. 5 (%)	No. 6 (%)	No. 7 (%)	No. 8 (%)
0-0.01	38.41	27.42	5.52	52.03	46.86	38.69	66.50	7.31
0.01-0.02	9.12	20.21	12.61	9.70	8.34	15.58	9.04	16.23
0.02-0.05	15.84	17.42	29.65	17.41	11.35	21.59	8.78	17.56
0.05-0.10	12.62	10.43	19.56	10.94	11.21	13.09	5.98	10.25
0.10-0.20	12.17	9.31	15.5	2.95	11.05	4.07	3.09	12.34
0.20-0.30	6.73	8.12	9.51	1.66	5.54	2.11	1.77	11.21
0.30-0.40	2.78	3.84	4.76	0.91	1.64	0.91	0.86	8.65
0.40-0.50	1.11	2.22	1.52	0.57	0.36	0.48	0.42	8.64
0.50-0.60	0.51	1.01	0.78	0.32	0.21	0.25	0.28	4.76
0.60-1.00	0.31	0.37	0.65	0.26	0.14	0.13	0.22	3.05

2.2.3. Matrix-Volume Fracture Mass Transfer Model. Figure 8 shows the schematic of contact between matrix blocks and volume fracture in 3-D. Under this circumstance, matrix blocks are surrounded by fractures, and fluid flow from matrix blocks to fracture can be simplified as spherical flow.

Under the assumption of 3-D contact, the pressure diffusion equation in the matrix block can be written in the following form:

$$\frac{\partial P}{\partial t} = \frac{k_\mathrm{m}}{\phi_\mathrm{m}\mu c_\mathrm{t}}\left(\frac{\partial^2 P}{\partial r^2} + \frac{2}{r}\frac{\partial P}{\partial r}\right). \tag{49}$$

The boundary condition and initial condition are

$$\begin{aligned} P_\mathrm{m} &= P_\mathrm{i}, \quad 0 \le r \le R, \quad t = 0 \\ P_\mathrm{m} &= P_\mathrm{f}, \quad r = R, \quad t > 0. \end{aligned} \tag{50}$$

The analytical solution of the 3-D pressure diffusion equation can be written as follows [19]:

$$\begin{aligned} \frac{\bar{P}_\mathrm{m} - P_\mathrm{f}}{P_\mathrm{i} - P_\mathrm{f}} &= \frac{6}{\pi^2}\sum_{n=1}^{\infty}\frac{1}{n^2}\exp\left[-\frac{n^2\pi^2 k_\mathrm{m} t}{\phi_\mathrm{m}\mu c_\mathrm{t} R^2}\right], \\ \frac{\partial \bar{P}_\mathrm{m}}{\partial t} &= -6\left(P_\mathrm{i} - P_\mathrm{f}\right)\sum_{n=1}^{\infty}\frac{k_\mathrm{m}}{\phi_\mathrm{m}\mu c_t R^2}\exp\left[-\frac{n^2\pi^2 k_\mathrm{m} t}{\phi_\mathrm{m}\mu c_t R^2}\right], \\ q &= -\phi_\mathrm{m} c_\mathrm{t} V\frac{\partial \bar{P}_\mathrm{m}}{\partial t}, \\ q &= 6L^3\left(P_\mathrm{i} - P_\mathrm{f}\right)\sum_{n=1}^{\infty}\frac{k_\mathrm{m}}{\mu R^2}\exp\left[-\frac{n^2\pi^2 k_\mathrm{m} t}{\phi_\mathrm{m}\mu c_\mathrm{t} R^2}\right]. \end{aligned} \tag{51}$$

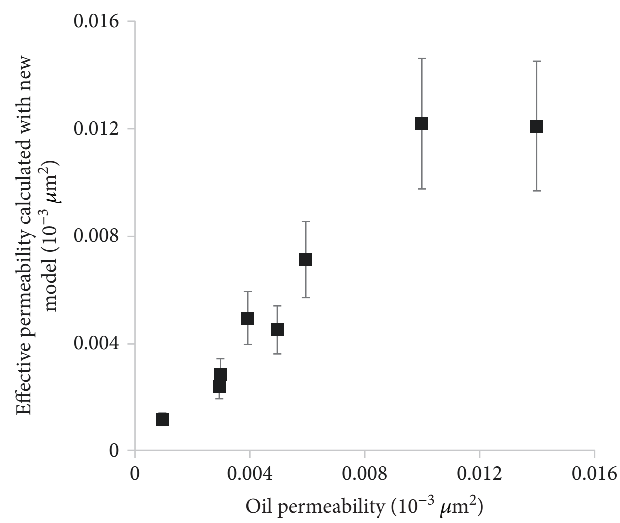

Figure 9: Comparison between experimental data and calculated data from the model.

The correction factor of the mass transfer equation in 3-D is

$$q = C_\mathrm{f}\frac{k_\mathrm{m} A_3}{\mu}\frac{\left(\overline{P_\mathrm{m}} - P_\mathrm{f}\right)}{L/2}. \tag{52}$$

In Eq. (52), $A_3 = 6L^2$.

$$\begin{aligned} C_\mathrm{f} &= \frac{3L^4\sum_{n=0}^{\infty}\left(P_\mathrm{i} - P_\mathrm{f}\right)k_\mathrm{m}/R^2\exp\left(-\left(n^2\pi^2 k_\mathrm{m} t/\phi_\mathrm{m}\mu c_\mathrm{t} R^2\right)\right)}{6k_\mathrm{m}L^2\left(6/\pi^2\right)\sum_{n=0}^{\infty}\left(P_\mathrm{i} - P_\mathrm{f}\right)1/n^2\exp\left(-\left(n^2\pi^2 k_\mathrm{m} t/\phi_\mathrm{m}\mu c_\mathrm{t} R^2\right)\right)} \\ &= \frac{\pi^2 L^2\sum_{n=0}^{\infty}1/R^2\exp\left(-n^2\pi^2 t_\mathrm{D}\right)}{12\sum_{n=0}^{\infty}1/n^2\exp\left(-n^2\pi^2 t_\mathrm{D}\right)}. \end{aligned} \tag{53}$$

Table 3: The main parameters of the model.

Model parameter	Value	Model parameter	Value
Matrix permeability ($10^{-3}\ \mu m^2$)	0.001/0.01/0.1/1	Total compressibility (10^{-4} MPa^{-1})	6.7
Oil viscosity (mPa•s)	1	Half-length of fracture (m)	100
Reservoir thickness (m)	10	Matrix porosity (%)	20
Matrix initial pressure (MPa)	20	Fracture pressure (MPa)	15

Eq. (53) shows the correction factor in the circumstance of 3-D and in Eq. (53) $t_D = k_m t/\phi_m \mu c_t R^2$.

3. Model Validation

3.1. Validation of Tight Oil Permeability Model. For the validation of the tight oil permeability model, the accuracy of the model is verified by comparing with the experimental results obtained by Wang et al. [13, 20]. In his experiment, throat size distribution and core permeability are obtained, respectively, from mercury injection and the core displacement experiment.

Main parameters and throat size distribution used in the core experiment are listed in Tables 1 and 2. Based on the distribution of throat size and some other related reservoir parameters, the effective permeability of the tight oil reservoir can be calculated from the proposed permeability model. A comparison of the calculated and experimental results is shown in Figure 9. The error line gives the difference between the experimental and measured values. The results shown in Figure 9 demonstrate an acceptable agreement between experimental and calculated permeabilities which verifies the tight oil reservoir permeability model.

3.2. Validation of Tight Oil Mass Transfer Model. For the matrix-planar fracture and matrix-planar/naturally fracture model, their corresponding correction factors are compared with the constant shape factor which is previously proposed by Lim and Aziz [21]. The main parameters used in calculation are listed in Table 3, and the change of the mass transfer flow correction factor with time is shown in Figure 10. The results are shown in Figure 11 and demonstrate that the tight oil mass transfer correction factor decreases as time increases and finally tends to a stable value similar to the traditional shape factor [21].

For formation with different permeabilities, the correction factors of mass transfer flow are different (Figure 10). For the tight oil reservoir, since the permeability of the reservoir is low, the pressure propagation is low and the time at which the correction factor reaches steadiness is obviously longer than that of high permeability reservoirs. Therefore, when calculating the mass transfer flow in tight oil reservoirs, the time-related correction factor should be considered. For high-permeability reservoirs, due to high-pressure diffusivity, the time of the correction coefficient reaches steadiness much faster than that of tight oil reservoirs. Therefore, the time-related correction coefficient has great influence on the mass transfer flow in high-permeability reservoirs.

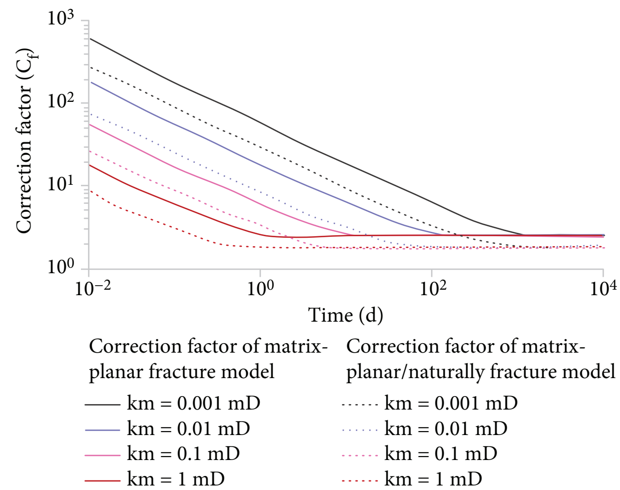

Figure 10: The change of the mass transfer flow correction factor with time.

For the 3-D model, the mass transfer rate and cumulative flow are compared with numerical simulation results; the traditional mass transfer model with a constant shape factor is previously proposed by Lim and Aziz [21]. The main parameters used in calculation are also listed in Table 3, except the permeability of the matrix which is 0.1 mD.

A comparison of the mass transfer rate is shown in Figure 11(a), and the results show the mass transfer rate of the tight oil reservoir which agrees well with numerical simulation results except the very early stage of the mass transfer process. This could be caused by the assumption of radical flow which may not coincide with the real situation at the early stage. Besides, in Figure 11(a) the mass transfer rate with a constant shape factor is obviously lower than the one with the time-related correction factor at the early and middle stages. However, during the late stage, as the time-related correction factor changes, its value gradually approaches to the value of the constant shape factor, then the mass transfer rate with the time-related correction factor turns the same with the mass transfer rate with the constant shape factor. Due to the better fitting of numerical simulation results, the proposed correction factor C_f is proven to be more suitable for the tight oil matrix block. On the other hand, the corresponding cumulative mass transfer is shown in Figure 11(b) and compared with the constant shape factor. The cumulative mass transfer with the time-dependent correction factor is much close to the numerical simulation results due to the higher mass transfer rate at the early and middle stages of the mass transfer process. Overall, even though there is little discrepancy, the result of the new model

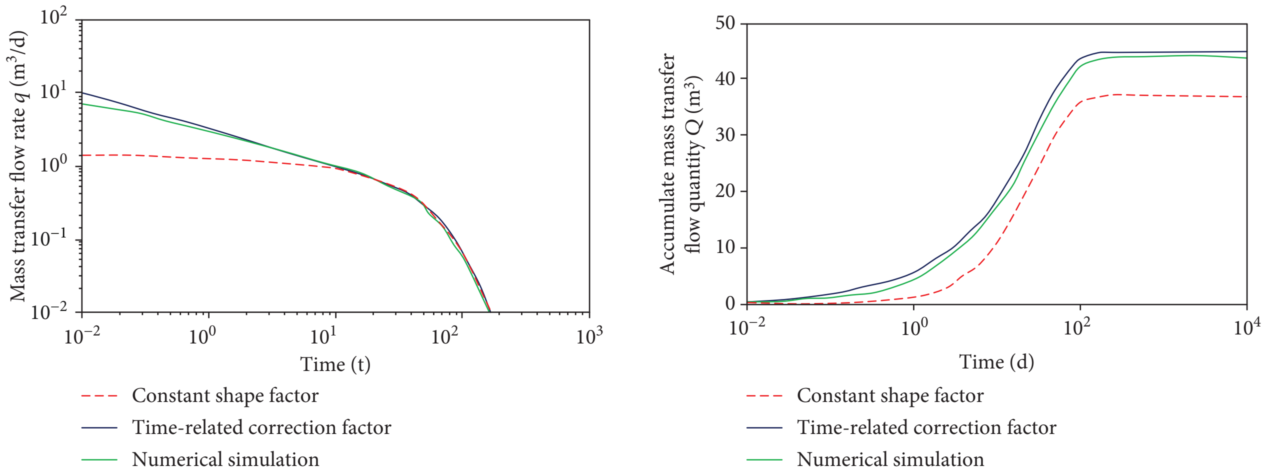

(a) The impact of the correction factor on the mass transfer rate (b) The impact of the correction factor on accumulate mass transfer quantity

FIGURE 11: The impact of the mass transfer flow correction factor to the flow rate.

is much closer to the real situation of the mass transfer in the tight fractured oil reservoir.

4. Conclusion

(1) A tight matrix permeability model is established by considering both the boundary layer and the throat distribution of tight oil reservoirs. A nonlinear flow in the matrix can be described through the new matrix permeability model

(2) Three kinds of models have been proposed to reflect the contact relation of matrix and fracture based on the actual complex fracture network distribution during the fracturing process: matrix-planar fracture (1-D) model, matrix-planar/naturally fracture (2-D) model, and matrix-volume fracture (3-D) model

(3) The correction factor has considered two main characteristics in tight fractured oil reservoirs: the first is the change of pressure distribution in the matrix during the mass transfer process and the second is the existence of the boundary layer in tight porous media. Data analysis results show that despite little discrepancy at the early stage, the newly proposed correction factor made a much more accurate calculation result of the mass transfer rate compared to the traditional mass transfer function with a constant shape factor

(4) For fractured tight oil reservoirs, the pressure propagation velocity in the matrix is low, and the duration time of the unsteady mass transfer flow between matrix fractures is very long, so the unsteady mass transfer flow plays an important role in the exploration of tight oil reservoirs

Nomenclature

H: Thickness of boundary layer, μm
R: Radius of throat, μm
v: Mean pore radius, μm
μ: Oil viscosity, mPa•s
∇p: Pressure drop, MPa/m
r_{eff}: Effective throat radius, μm
r_{i}: Original throat radius, μm
$f(r)$: The micro throat distribution function
N: The total number of microtubes
A: The cross-sectional area of the core, μm^2
φ_{m}: Porosity of matrix, %
φ_{f}: Porosity of fracture, %
Q: Total flow rate of capillary bundle model, cm^3/day
L: Length of capillary bundle model, cm
k_{m}: Matrix permeability of tight oil reservoir, mD
k_{f}: Fracture permeability, mD
p_{f}: Average pressure in fracture, mD
$\bar{p}_{\mathrm{m}}$: Average pressure in matrix block, mD
$q_{\mathrm{m}\rightarrow\mathrm{f}}$: Mass transfer flow rate, cm^3/day
C_{t}: Total compressibility
Q: Mass transfer rate, cm^3/day
V_{f}: Volume of fracture, cm^3
M_{∞}: Total mass transfer quantity when the time approaches to the ultimate time
M_{t}: Accumulate mass transfer quantity t at time t
ρ_{i}: Oil density at initial time, g/cm^3
ρ_{f}: Oil density in fracture at time t, g/cm^3
$\bar{\rho}_{\mathrm{m}}$: Average oil density in matrix, g/cm^3
C_{f}: Correction factor, dimensionless.

Data Availability

The parameters of the model, experimental data, and calculated data used to support the findings of this study are included within the article.

Conflicts of Interest

The authors declare that there is no conflict of interest regarding the publication of this article.

Acknowledgments

The author acknowledge the support of this research provided by the National Natural Science Foundation of China (No. 51674273, U1762210, and 51574258), the Major State Basic Research Development Program (973 Program) (No. 2015CB250900), National Science and Technology Major Project of China (2017ZX05013002-005), and Major Projects of China National Petroleum Corporation (No. 2016B-1303).

References

[1] G. I. Barenblatt, I. P. Zheltov, and I. N. Kochina, "Basic concepts in the theory of seepage of homogeneous liquids in fissured rocks [strata]," *Journal of Applied Mathematics & Mechanics*, vol. 24, no. 5, pp. 1286–1303, 1960.

[2] J. E. Warren and P. J. Root, "The behavior of naturally fractured reservoirs," *Society of Petroleum Engineers Journal*, vol. 3, no. 3, pp. 245–255, 1963.

[3] H. Kazemi, L. S. Merrill, K. L. Porterfield, and P. R. Zeman, "Numerical simulation of water-oil flow in naturally fractured reservoirs," *Society of Petroleum Engineers Journal*, vol. 16, no. 6, pp. 317–326, 1976.

[4] K. H. Coats, "Implicit compositional simulation of single-porosity and dual-porosity reservoirs," in *SPE Symposium on Reservoir Simulation*, Houston, Texas, February 1989.

[5] H. Hassanzadeh and M. Pooladi-Darvish, "Effects of fracture boundary conditions on matrix-fracture transfer shape factor," *Transport in Porous Media*, vol. 64, no. 1, pp. 51–71, 2006.

[6] H. Hassanzadeh and M. Pooladi, "Shape factor in the drawdown solution for well testing of dual-porosity systems," *Advances in Water Resources*, vol. 32, no. 11, pp. 1652–1663, 2009.

[7] E. Ranjbar and H. Hassanzadeh, "Matrix–fracture transfer shape factor for modeling flow of a compressible fluid in dual-porosity media," *Advances in Water Resources*, vol. 34, no. 5, pp. 627–639, 2011.

[8] E. Ranjbar, H. Hassanzadeh, and Z. Chen, "Effect of fracture pressure depletion regimes on the dual-porosity shape factor for flow of compressible fluids in fractured porous media," *Advances in Water Resources*, vol. 34, no. 12, pp. 1681–1693, 2011.

[9] E. Ranjbar, "One-dimensional matrix-fracture transfer in dual porosity systems with variable block size distribution," *Transport in Porous Media*, vol. 95, no. 1, pp. 185–212, 2012.

[10] E. Ranjbar, H. Hassanzadeh, and Z. Chen, "Semianalytical solutions for release of fluids from rock matrix blocks with different shapes, sizes, and depletion regimes," *Water Resources Research*, vol. 49, no. 4, pp. 2174–2196, 2013.

[11] W. C. Li, Y. M. Zhang, and F. Wang, "Application of constant-rate mercury penetration technique to study of pore throat characteristics of tight reservoir: a case study from the Upper Triassic Yanchang Formation in Ordos Basin," *Lithologic Reservoirs*, vol. 24, no. 6, pp. 60–65, 2012.

[12] J. Wu, L. Cheng, C. Li et al., "Experimental study of nonlinear flow in micropores under low pressure gradient," *Transport in Porous Media*, vol. 119, no. 1, pp. 247–265, 2017.

[13] R. F. Wang, P. P. Shen, Z. Q. Song, and H. Yang, "Characteristics of micro-pore throat in ultra-low permeability sandstone reservoir," *Acta Petroiei Sinica*, vol. 30, no. 4, pp. 560–563, 2009.

[14] X. Tian, L. Cheng, and R. Cao, "Characteristics of boundary layer in micro and nano throats of tight sandstone oil reservoirs," *Chinese Journal of Computational Physics*, vol. 33, no. 6, pp. 717–725, 2016.

[15] W. R. Purcell, "Capillary pressures - their measurement using mercury and the calculation of permeability therefrom," *Journal of Petroleum Technology*, vol. 1, no. 2, pp. 39–48, 1949.

[16] P. H. Nelson, "Pore-throat sizes in sandstones, tight sandstones, and shales," *AAPG Bulletin*, vol. 93, no. 3, pp. 329–340, 2009.

[17] W. K. Camp, "Pore-throat sizes in sandstones, tight sandstones, and shales: discussion," *AAPG Bulletin*, vol. 95, no. 8, pp. 1443–1447, 2011.

[18] L. L. Latour, R. L. Kleinberg, P. P. Mitra, and C. H. Sotak, "Pore-size distributions and tortuosity in heterogeneous porous media," *Journal of Magnetic Resonance. Series A*, vol. 112, no. 1, pp. 83–91, 1995.

[19] J. Crank, *The Mathematics of Diffusion*, Oxford University Press, London, 1975.

[20] R. Wang, M. Chen, and W. Sun, "The research of micro-pore structure in super-low permeability sandstone reservoir of the Yanchang Formation in Ordos Basin," *Geological Review*, vol. 54, no. 2, pp. 270–277, 2008.

[21] K. T. Lim and K. Aziz, "Matrix-fracture transfer shape factors for dual-porosity simulators," *Journal of Petroleum Science & Engineering*, vol. 13, no. 3-4, pp. 169–178, 1995.

Hindawi
Geofluids
Volume 2019, Article ID 2438075, 10 pages
https://doi.org/10.1155/2019/2438075

Research Article

A Method to Accurately Determine the Methane Enrichment Zone of a Longwall Coal Mine

Guorui Feng[1], **Ao Zhang**[2], **Shengyong Hu**[2], **Xiangqian Guo**[3,4], **Chao Li**[3,4], **Guocai Hao**[2] **and Zhen Li**[2]

[1]*College of Mining Engineering, Taiyuan University of Technology, Taiyuan 030024, China*
[2]*College of Safety and Emergency Management Engineering, Taiyuan University of Technology, Taiyuan 030024, China*
[3]*Shanxi Jincheng Anthracite Mining Group Co. Ltd., Jincheng 048000, China*
[4]*State Key Laboratory of Coal and CBM Co-Mining, Jincheng 048006, China*

Correspondence should be addressed to Shengyong Hu; hsyztx@163.com

Received 10 September 2018; Revised 16 November 2018; Accepted 29 November 2018; Published 27 February 2019

Guest Editor: Bisheng Wu

Large numbers of gobs are produced as a result of underground longwall mining, and a large amount of these gobs is known to contain methane gas reserves. The efficient drainage of these methane resources is directly dependent on accurately determining the methane enrichment zone (MEZ) in longwall mining gobs. In this study, a method for accurately determining the MEZ within the zone of interconnected fractures, which utilized a surface directional borehole (SDB) technique, was proposed. The SDB was designed and implemented in a longwall gob located in the Sihe Coal Mine in China's Shanxi Province. The trajectory of the SDB constantly varied in the different overlying stratum layers and locations above the gob. The methane flow rate and concentration from the SDB, along with the methane concentration in the upper corner of the longwall face, were monitored and obtained as the longwall face advanced. Then, by analyzing the acquired data of the different horizontal and vertical positions of the SDB, the accurate locations of the MEZ within the zone of interconnected fractures were determined. There were the methane decrease zone (MDZ) and methane shortage zone (MSZ) below and above the MEZ, respectively. The results showed that in the MEZ, both the methane flow rate and concentration displayed slight decreasing trends and maintained high levels as the distance from the roof of the coal seam increased. In the MDZ, a sharp decline was observed in the methane flow rate. However, a relatively high methane concentration had still been maintained. In the MSZ, both the methane flow rate and concentration displayed dramatic fluctuation and relatively low levels. The average methane flow rates in the MEZ were determined to be 1.3 and 1.6 times higher than those in the MDZ and MSZ, respectively.

1. Introduction

Coal is one of the most important global energy sources and contributes to up to 70% of China's primary energy production and consumption [1]. Underground mines account for 90% of the total amount of coal mines in China, and highly gassy mines share 51% of the total [2–4]. As a result, a large amount of methane is released in the longwall gobs of these coal mines and then flows into the longwall faces as the mining processes advance [5]. Methane is a dangerously explosive gas, as well as a clean energy resource [6–8]. The extraction of methane gas from mining gobs not only alleviates the energy shortage issue in China but also serves to prevent the methane purity in the atmosphere of longwall mines from exceeding the recommended safety levels [9–12]. However, methane extraction effects directly rely on the accurate determinations of the MEZ above the longwall gobs in longwall coal mines [2, 13, 14].

As the underground working faces advance, the overlying strata form "three zones" in the vertical direction, which are referred to as the caved zone, fractured zone, and continuous zone [15–20]. Among these three zones, the methane within the gobs is able to flow into the caved zone as well as the lower and middle parts of the fractured zone due to the

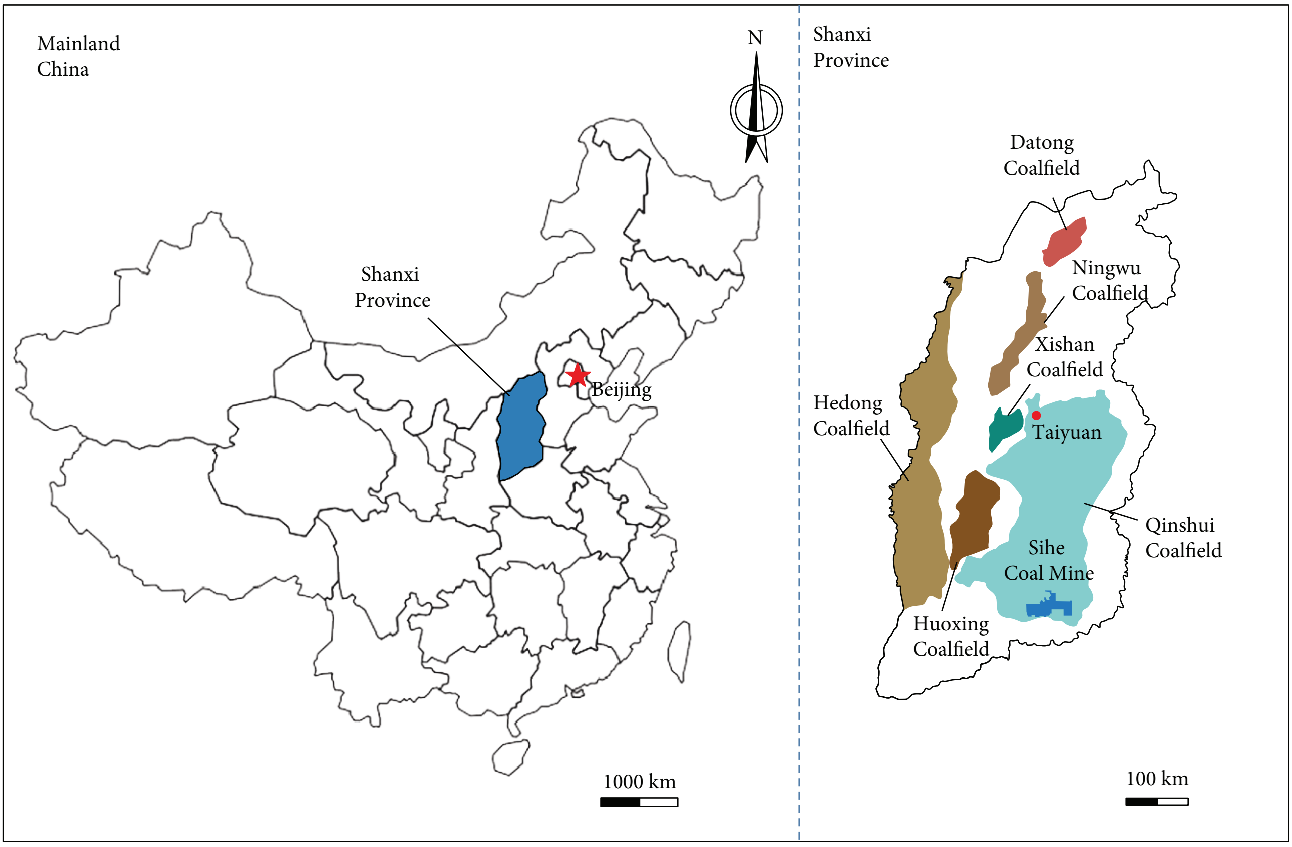

Figure 1: Location of the Sihe Coal Mine.

vertical interconnected fractures within the two zones [19, 21]. Singh and Yadav [22] presented a fractured zone profile induced by coal mining using a viscoelastic model. Das [23] studied the fracture zone divisions of overlying strata by observing and proposing the concept of weighting and caving zone. Qian and Shi [24] proposed the caved zone, the fractured water-inflow zone, and the continuous zone along the vertical direction (from the bottom to the top) in mining gobs. Christopher [25] studied fracture space divisions by dividing the overlying strata into the caving zone, the fracture zone, the dilated zone, and the confined zone. Yuan et al. [26] presented the concept that circular overlying zone existed in a longwall mining panel which could be used for efficient methane extraction. Guo et al. [27] proposed an annular fractured zone for methane drainage by establishing a CFD model based on methane gas drainage conditions. Li et al. [28] studied the distributions of elliptic paraboloid zone using physical simulation experiments and numerical approaches. Gao et al. [29] studied a pear-shaped region around the mining seam using a numerical approach. Qin et al. [30] conducted a research regarding the heights of caved and fractured zones in a longwall panel by employing a CFD numerical method. Qu et al. [31] presented the concepts of the fractured gas-interflow zone, de-stressed gas-desorption zone, and confined gas-adsorption zone based on a conceptual model of overburden rock of a longwall panel. Wang et al. [32, 33] studied the methane flow characteristics of a longwall panel by using building numerical models. Feng et al. [34] studied the methane flow space in abandoned gobs based on physical simulation experiments. However, almost all of these researches related to the MEZ had mainly adopted methods using empire formula, mathematical models, and simulation experiments. The results acquired by these studies contained a variety of assumptions which tended to usually result in some differences from the real field situations. Therefore, in order to achieve more accurate determination results, this study proposed a method which was based on actual MEZ field tests.

In this study, a method which utilized SDB to accurately determine the MEZ within the zone of interconnected fractures was proposed and implemented in the Sihe Coal Mine of China's Shanxi Province. The SDB was designed in a longwall face, and the trajectory of the SDB constantly varied in the different overlying stratum layers and locations above the longwall face. The methane flow rate and concentration from the SDB, as well as the methane concentration in the upper corner of the longwall face, were monitored and obtained as the longwall face advanced. The positions of the MEZ in the zone of interconnected fractures were then accurately determined by analyzing the obtained data.

2. Description of the Studied Coal Mine

The Sihe Coal Mine is located in the southern marginal part of the Qinshui Coalfield in China's Shanxi Province, as shown in Figure 1. It has a length of approximately 23 km

Depth (m)	Thickness (m)	Lithology
274.0	26.0	Sandy mudstone
291.0	17.0	Medium sandstone
311.1	20.1	Sandy mudstone
322.7	11.6	Fine sandstone
323.2	0.5	Siltstone
341.9	18.7	Sandy mudstone
354.3	12.4	Fine sandstone
359.9	5.6	Sandy mudstone
363.7	3.8	Siltstone
365.8	2.1	Sandy mudstone
370.0	4.2	Medium sandstone
371.1	1.1	Fine sandstone
373.6	2.5	Sandy mudstone
375.2	1.6	Medium sandstone
376.0	0.8	Sandy mudstone
385.2	9.2	Medium sandstone
398.2	13.0	Fine sandstone
406.7	8.5	Siltstone
410.1	3.4	Sandy mudstone
416.2	6.1	3# coal seam
427.5	11.3	Sandy mudstone

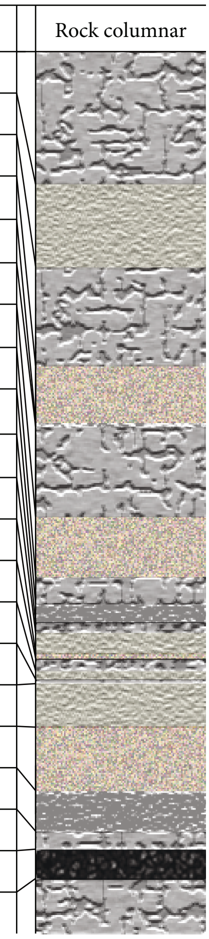

Figure 2: Stratigraphic column of the studied mine.

in a west-to-east direction and width of almost 12 km in a north-to-south direction and covers a total area of approximately 230 km^2. The Sihe Coal Mine is considered to be a gassy coal mine, with a methane content of approximately 13 m^3/t and a pressure rate of approximately 0.29 MPa. The estimated methane resources measure 1.03×10^{10} m^3.

The main minable coal seam in the Sihe Coal Mine is the #3 Coal Seam, which is located in the lower group of the Shanxi Formation. There is approximately 1.5×10^9 t of coal resources stored in the Sihe Coal Mine, and 2.1×10^8 t of that total is minable in the #3 Coal Seam. The average number of dips in the #3 Coal Seam is 5, which are nearly horizontal and considered to be stable within the mining area. The average thickness of the #3 Coal Seam is approximately 6.1 m. The thicknesses of immediate roof and floor areas of the #3 Coal Seam are approximately 3.4 m and 11.3 m, respectively, and consist primarily of sandy mudstone. A typical stratigraphic column from this coal mine is shown in Figure 2.

A current working face is situated in the Sihe Coal Mine, and the layout of this working face is shown in Figure 3. The working face's mining seam was the #3 Coal Seam, and its depth and thickness were about 416.2 m and 6.1 m, respectively. The length of the working face in the direction of the current mining was 1281.5 m, and the incline width was 301.5 m. A longwall mining method had been adopted in the working face, and a "U"-type ventilation system was in place.

3. Method

In the study area, it was observed that as the working face advanced, the corresponding positions of the SDB continuously varied in both the horizontal and vertical directions. As a result, the gob methane within different positions of the overlying strata above the formed gob could be extracted by the SDB. It was found that both the methane flow rate and concentration displayed major variations during the entire SDB drainage period. Therefore, based on these data variations, the zones with different methane flow rates and concentrations could be successfully determined. Then, the locations of the MEZ within the zone of interconnected fractures could be accurately identified by combining the advancing distances and their corresponding trajectory locations within the overlying strata. Moreover, methane drainage effects were found to directly influence the methane concentration of the upper corner of the working face. Therefore, based on its variations during the entire drainage period,

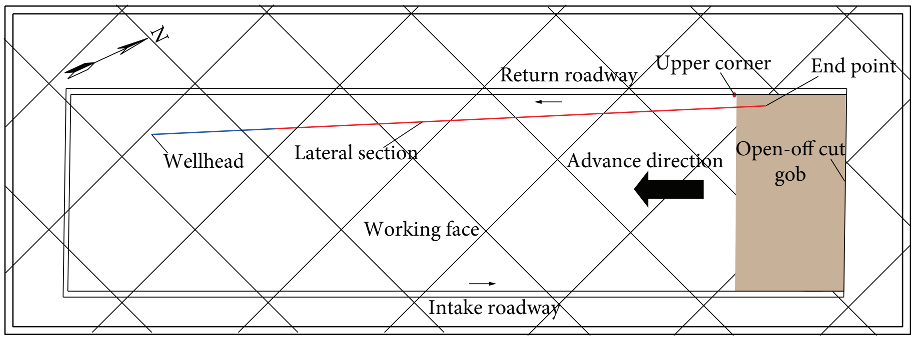

Figure 3: Layout of the working face.

the accuracy of this method could be further verified from another aspect.

In this study, based on the abovementioned principle, an SDB was designed and implemented in the studied working face of the Sihe Coal Mine. The trajectories of the SDB along the mining direction and within the overlying strata of the working face are shown in Figures 3 and 4, respectively. The SDB included a vertical section, build section, and lateral section, and the lateral section was selected as the study part. As shown in Figures 3 and 4, the study part (lateral section) of the SDB was not parallel to the return roadway. However, its horizontal positions were found to have become gradually closer to the return roadway of the working face as the SDB stretched from its starting position to its ending position. Similarly, the vertical positions of the study part were observed to have become gradually farther away from the coal seam as the SDB stretched from its starting position to its ending position. In detail, the distances between the horizontal positions and the return roadway and the distances between the vertical positions and the coal seam varied from 13.5 to 48.7 m and 10.62 to 55.56 m, respectively. As can be seen in Figure 4, the study part was located above the coal seam and was 805 m in length. The distance from the SDB end point to the open-off cut of the working face was approximately 138 m. It was observed that the gas began to flow through the SDB when the working face had advanced past its end point by approximately 390 m.

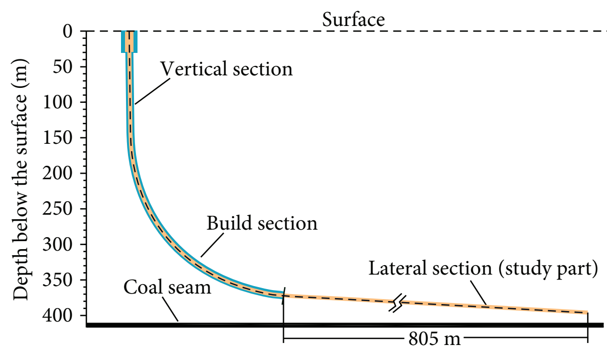

Figure 4: Trajectory of the SDB.

4. Results and Discussion

4.1. Relationship between the Methane Flow Rate and Concentration and the Advancing Distances. Though the fractures within the caved zone and the lower and middle parts of the fractured zone are interconnected, the methane contents and concentrations of different locations within the zone of interconnected fractures are significant as the mining processes. Based on this, the detailed divisions of the zone of interconnected fractures were achieved by capturing the methane flow rates and concentrations through the SDB over the entire drainage period. Also, the methane concentration of the upper corner in the longwall face was monitored continuously at the same time. The detailed variations in the methane flow rate and concentration as the working face advancement distance increased are shown in Figure 5.

Based on the obvious differences of methane flow rate and concentration under different locations in the zone of interconnected fractures, the zone boundaries among the different zones were determined. It can be seen in Figure 5 that both the methane flow rate and concentration displayed the highest levels when the advance distance range was approximately 600 to 810 m. The zone with the highest methane flow rate and concentration was considered as the MEZ. In the MEZ, both the methane flow rate and concentration displayed gradual decreasing trends despite some fluctuation. For example, the methane flow rate and concentration had declined from 1,285 m^3/h to 973 m^3/h and from 85% to 75%, respectively. The average methane flow rate and concentration in the MEZ were determined to be 1135 m^3/h and 75.5%, respectively. In addition, there was a dramatic fall (from 1,174 m^3/h to 476 m^3/h) in the methane flow rate and a slight decrease (from 90% to 72%) in the methane concentration, when the working face advancement distance ranged between approximately 390 and 600 m. In this study, this zone was referred as the methane decrease zone (MDZ) and was located below the MEZ. The average methane flow rate and concentration in the MDZ were determined to be 906 m^3/h and 77%, respectively. Furthermore, low methane flow rates and concentrations were observed when the working face advancement distance range was approximately 810 to 1,046 m. This zone was referred to as the methane shortage zone (MSZ) in this study and was located above the MEZ. In

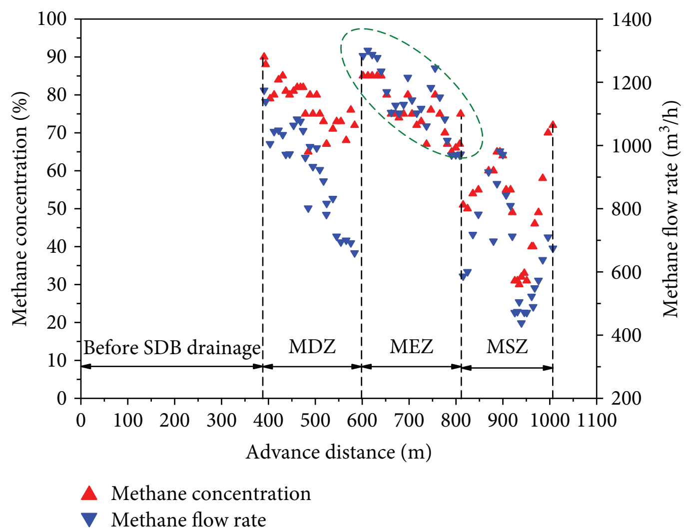

FIGURE 5: Methane flow rate and concentration variations with the increases in the working face advancement distances.

the MSZ, both the methane flow rate and concentration were found to display dramatic fluctuations and averaged only 710 m^3/h and 54.5%, respectively.

The bulking-factor-controlled caving model was widely used to estimate the height of the caved zone [35, 36]. The height of the caved zone (H_c) depends on the mining thickness (M) and bulking factor (k) and can be expressed as

$$H_c = \frac{(1-\lambda)M}{k-1}, \quad (1)$$

where $0 \le \lambda \le 1$ is the sagging coefficient. In the Sihe Coal Mine, the sagging coefficient (λ), bulking factor (k), and mining thickness (M) is 0, 1.20-1.25, and 6.1 m, respectively. Based on equation (1), the height range of the caved zone was calculated to be 24.4 to 30.5 m.

Besides, in accordance with the results of previous related studies [37, 38], the heights of the overburden zones could be expressed and estimated by the following:

$$H_c = \frac{100M}{0.49M + 19.12} \pm 4.71, \quad (2)$$

$$H_f = \frac{100M}{1.19M + 28.57} \pm 4.76, \quad (3)$$

where H_c and H_f represent the heights (m) of the caved zone and the fractured zone, respectively, and M denotes the mining thickness (m). Therefore, based on equation (2) the height range of the caved zone was confirmed to be 22.9 to 32.3 m, which coincides with the result calculated by equation (1). In addition, based on equation (3), the height range of the fractured zone was 60.6 to 83.6 m.

Also, the results of previous related studies [28, 34, 39] had revealed that the methane concentrations in the MEZ could be expressed as

$$C = ae^b, \quad (4)$$

where C represents the methane concentration in the MEZ; a is constant; and b represents the height from the floor.

Equation (4) indicated that the methane concentration in the MEZ had displayed an exponential growth trend with the increases in the vertical height. Furthermore, the MEZ had been located in the top of the fractured zone in previous studies. However, in this study, a gradual decreasing trend of the methane concentration was observed as the vertical height within the MEZ increased (Figure 6), and the MEZ was located below the MSZ and above the MDZ. The determination of the MEZ distribution, as well as the correlation between the methane concentrations and the vertical height, had been achieved using theoretical analysis, simulation experiments, and empirical formula in the previous studies [28, 34, 39]. Also, in the previous studies, the actual conditions had been simplified and the methane enrichment process was not dynamic. Therefore, there was enough time for the methane to rise in the MEZ owing to its low density when compared with the surrounding air under the aforementioned conditions. However, this study found that under the actual conditions in the examined mine, both the working face advancement and the methane drainage processes were continuous, and the fractured zone and MEZ were continuously evolving. It was observed that the methane gas within the gobs potentially did not quickly flow into the top of the fracture in great amounts due to the fact that vertical stress had been recovered and the stratum fractures behind the working face had gradually closed [5, 27, 40]. Instead, most of the methane had flowed into the zone where the stratum fractures were stretched having been induced by the mining activities. Therefore, it was concluded that the MEZ may have been characterized by smaller zone ranges in situ.

The detailed methane concentration variation of the upper corner in the studied working face as the advancement distance of the working face had increased is detailed in Figure 7. As can be seen in the figure, it was evident that

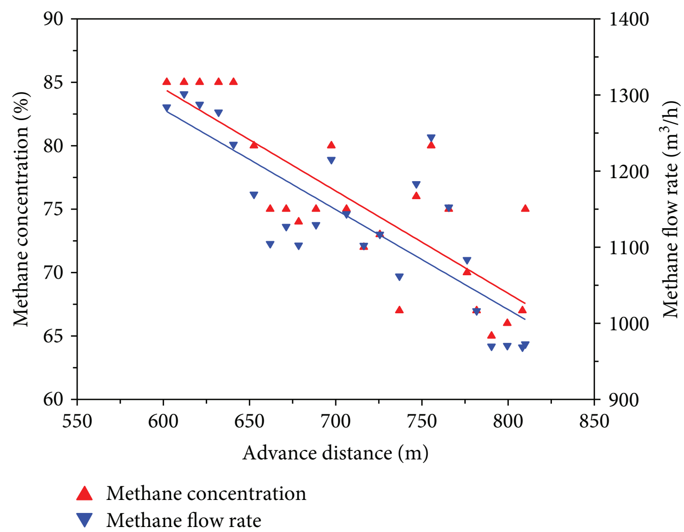

FIGURE 6: Methane flow rate and concentration variations within the MEZ.

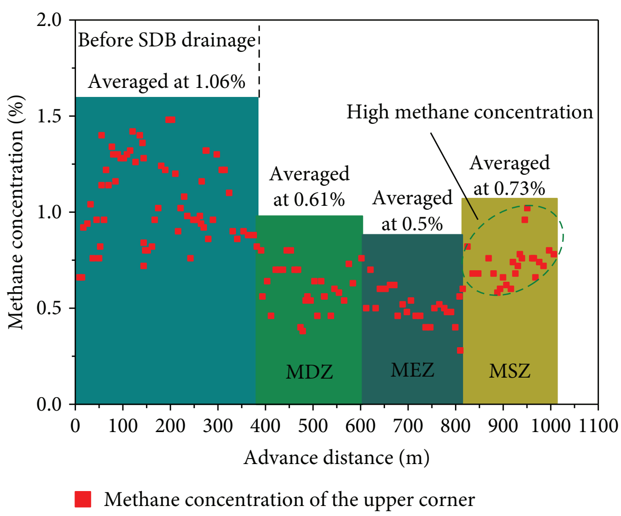

FIGURE 7: Methane concentration variations of the upper corner as the working face advancement distance increased.

the methane concentration in the upper corner was relatively high before the SDB began the drainage process when compared to after the drainage process was in progress. Prior to the SDB beginning the methane gas drainage, the average methane concentration in the upper corner was determined to be 1.06%. In contrast, it was observed to have decreased to 0.60% during the drainage process. The average methane concentrations of the upper corner in the three zones were 0.61%, 0.50%, and 0.73%, respectively, which indicated that methane had been efficiently extracted in the MEZ.

4.2. MEZ Distribution. The location of the MEZ was obtained by analyzing the relationships between the methane flow rate and concentration and the working face advancement distances (Figure 5). Then, based on the obtained results, the location of the MEZ could be accurately determined by combining the advancement distances and their corresponding trajectory locations within the overlying strata. Figure 8 illustrates the correlations between the zone divisions and the zone locations. The horizontal and vertical location ranges in which the three zones corresponded were obtained through combining the results shown in Figure 8 with the mining distances. The horizontal boundaries of the MEZ were determined to range between 42.09 and 54.05 m from the return roadway, and the vertical boundaries ranged from 35.29 to 47.31 m from the roof of the coal seam. Moreover, the horizontal boundaries of the MDZ and MSZ ranged between 31.05 and 42.09 m and 54.05 to 65.27 m from the return roadway, respectively. It was determined in this study that the vertical boundaries of the MDZ and MSZ ranged from 24.94 to 35.29 m and from 47.31 to 75.17 m from the roof of the coal seam, respectively.

The strata located in the central section of the panel tended to be compacted, and the fractures at the edges of the incline direction which were maintained after the development of the overburden rocks were relatively stable in the areas where the mining activities had been implemented. The circle-shape zone near the corners of the panel where the vertical fractures were well-developed and maintained was referred to as the "abscission circle" [30, 41], as detailed in Figure 9.

Figure 8 illustrates the locations of the three zones above the gob, and Figure 10 shows the schematics of the three zone divisions in the incline profile above the gob. As can be seen in Figures 8 and 10, the horizontal location of the MEZ was within the abscission circle. However, its vertical location was in the lower part of the fractured zone (rock blocks). In the MEZ, fractures were well-developed and produced considerable gas migration channels which ensured the highest methane extraction effects. The horizontal location of the MDZ was near the return roadway and was also located within the abscission circle. Its vertical location was situated on the borders of the caved and fractured zones. There was found to be an abrupt drop in

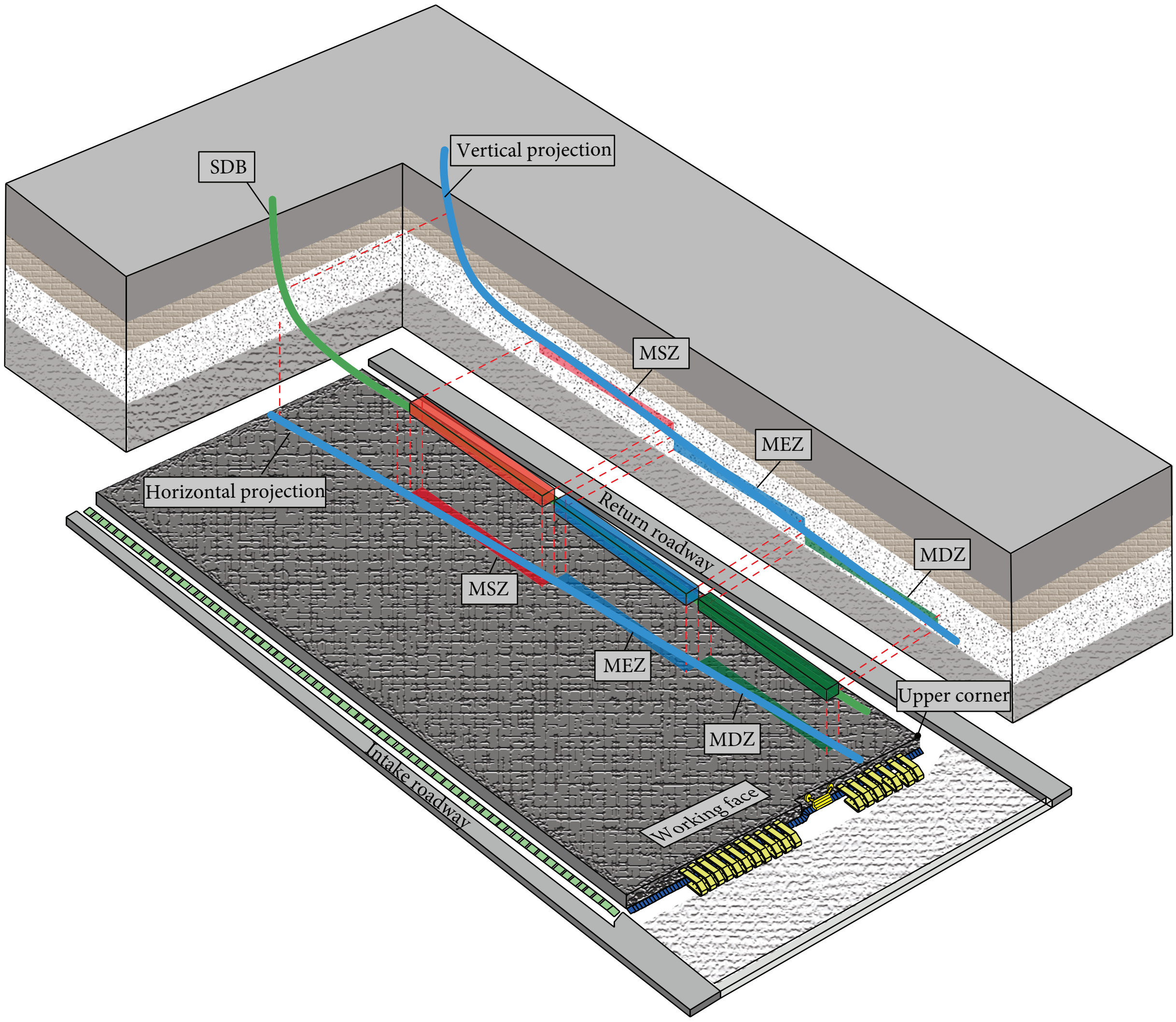

Figure 8: Space locations of the MDZ, MEZ, and MSZ.

permeability on the borders of the two zones [21], which caused the methane flow rate to dramatically decline in the MDZ. The MSZ was located in the compacted area in the horizontal direction, and the middle part of the fractured zone (through-going vertical fractures) in the vertical direction. The methane gas flow was therefore reduced in the MSZ due to the poorly developed vertical fractures in this zone. As a result, the methane flow rate and purity were found to be low in the MSZ. Among the three zones, the highest methane flow rate and purity were observed in the MEZ. It was concluded that improved methane drainage effects could be achieved when the lateral section of the SDB, or a high-level suction tunnel, was arranged in the MEZ.

5. Conclusions

A method for determining the methane enrichment zone (MEZ) within the zone of interconnected fractures of a longwall coal mine was proposed and implemented. In the proposed method, an SDB was designed and implemented in a longwall face located in the Sihe Coal Mine of China's Shanxi Province. The trajectory of the SDB varied constantly in the different overlying stratum layers and locations above the mine gob. The data regarding the methane flow rate and concentration obtained from the SDB and the methane concentrations in the upper corner as the longwall face advanced were monitored and obtained simultaneously.

The MEZ had been accurately determined in the examined mine. In the MEZ, both the methane flow rate and concentration were found to be the highest despite falling slightly as the active mining face distance increased. It was observed that two zones existed below and above the MEZ, which were referred to as the methane decrease zone (MDZ) and the methane shortage zone (MSZ), respectively. Within the MDZ, both the methane flow rate and concentration displayed gradual decreasing trends as the distance of the mining face advancement increased. Within the MSZ, the methane flow rate and concentration were determined to be lowest among the three zones and also had displayed dramatic fluctuation.

Among the three zones, the highest methane flow rate and purity were identified to be found in the MEZ. The methane concentration in the upper corner was found to

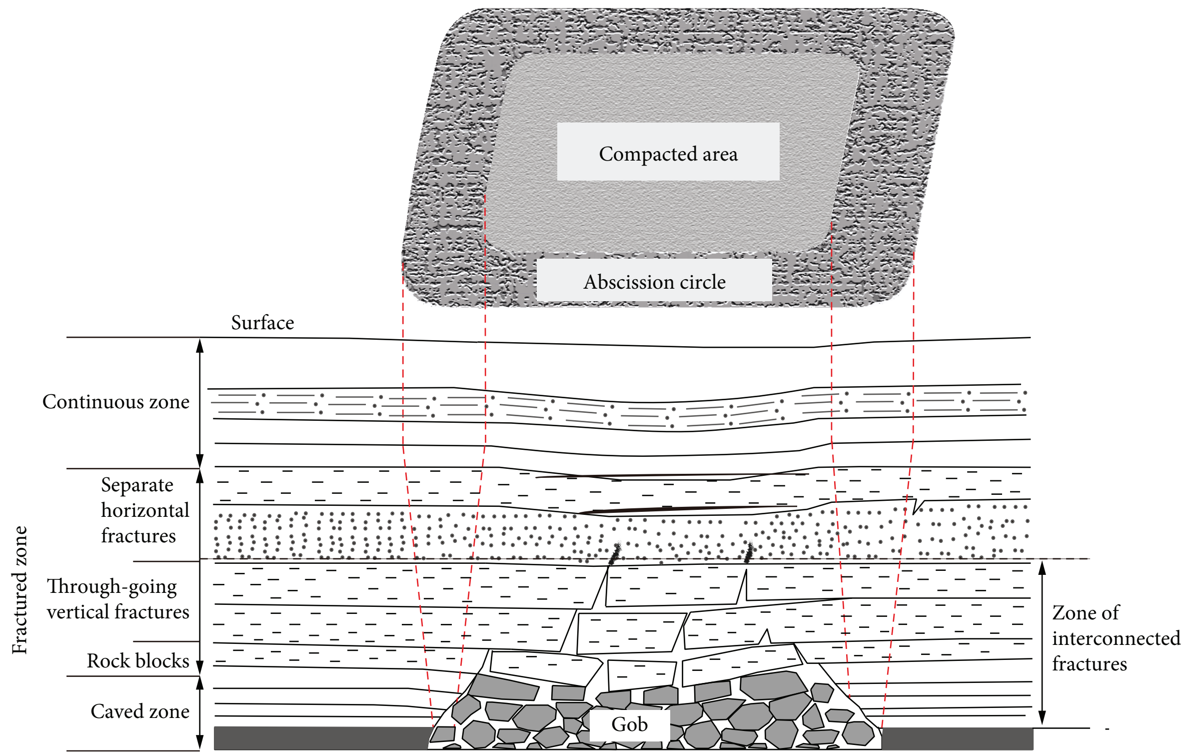

FIGURE 9: Schematic diagram of the "three zones" [19, 41] and "abscission circle" [30, 42].

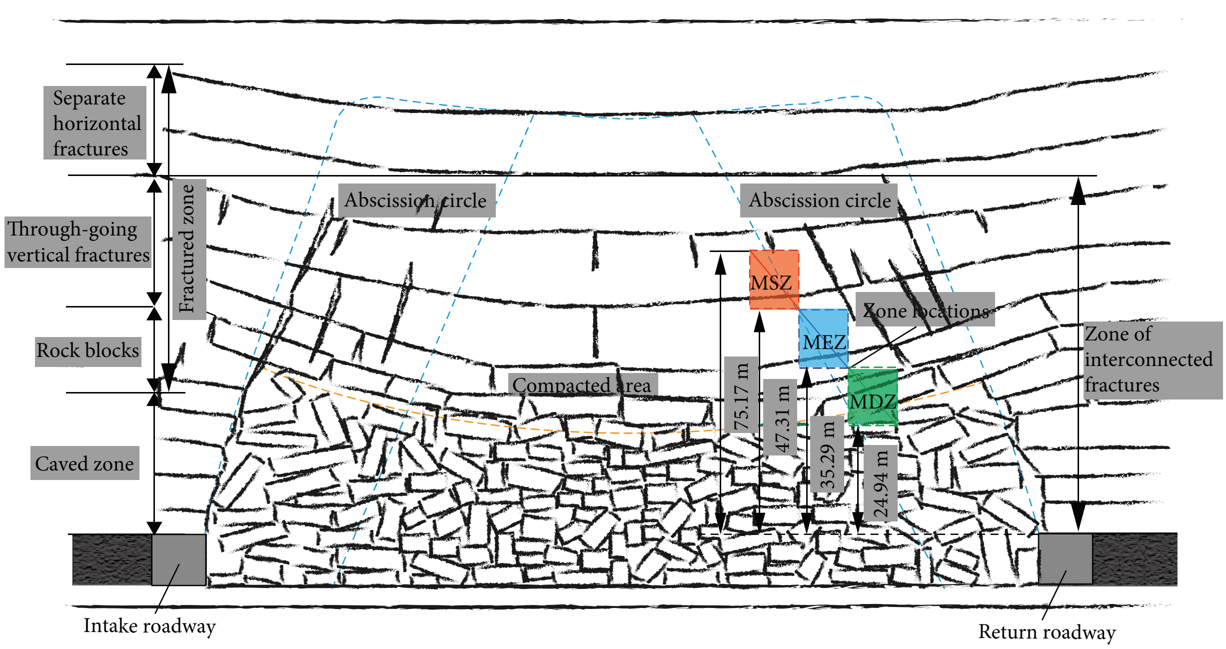

FIGURE 10: Schematics of the zone divisions in the incline profile of the longwall face.

be lower, where a lower methane flow rate and purity were identified. However, the methane concentration in the upper corner was higher in the two other zones. More effective methane drainage was achieved when the lateral section of the SDB, or a high-level suction tunnel, was arranged in the MEZ.

Data Availability

Some data used to support the findings of this study are included within the article. Other data used to support the findings of this study are available from the corresponding author upon request.

Conflicts of Interest

The authors declare that they have no conflicts of interest.

Acknowledgments

This research was supported by the National Natural Science Foundation of China (51504160, 51574172) and the Joint Funds of the National Natural Science Foundation of China (U1710258, U1710121). This work was also supported by the Program for the Outstanding Innovative Teams of Higher Learning Institutions of Shanxi and the Training Program of First-Class Discipline for Young Academic Backbone of Taiyuan University of Technology.

References

[1] J. C. Wang, S. L. Yang, Y. Li, L. K. Wei, and H. H. Liu, "Caving mechanisms of loose top-coal in longwall top-coal caving mining method," *International Journal of Rock Mechanics and Mining Sciences*, vol. 71, pp. 160–170, 2014.

[2] G. R. Feng, S. Y. Hu, Z. Li et al., "Distribution of methane enrichment zone in abandoned coal mine and methane drainage by surface vertical boreholes: a case study from China," *Journal of Natural Gas Science and Engineering*, vol. 34, pp. 767–778, 2016.

[3] K. Jin, Y. P. Cheng, W. Wang, H. B. Liu, Z. D. Liu, and H. Zhang, "Evaluation of the remote lower protective seam mining for coal mine gas control: a typical case study from the Zhuxianzhuang Coal Mine, Huaibei Coalfield, China," *Journal of Natural Gas Science and Engineering*, vol. 33, pp. 44–55, 2016.

[4] Z. Aitao and W. Kai, "A new gas extraction technique for high-gas multi-seam mining: a case study in Yangquan Coalfield, China," *Environment and Earth Science*, vol. 77, no. 4, p. 150, 2018.

[5] C. Zhang, S. H. Tu, Q. S. Bai, G. Y. Yang, and L. Zhang, "Evaluating pressure-relief mining performances based on surface gas venthole extraction data in longwall coal mines," *Journal of Natural Gas Science and Engineering*, vol. 24, pp. 431–440, 2015.

[6] C. Ö. Karacan, F. A. Ruiz, M. Cotè, and S. Phipps, "Coal mine methane: a review of capture and utilization practices with benefits to mining safety and to greenhouse gas reduction," *International Journal of Coal Geology*, vol. 86, no. 2-3, pp. 121–156, 2011.

[7] V. Palchik, "Time-dependent methane emission from vertical prospecting boreholes drilled to abandoned mine workings at a shallow depth," *International Journal of Rock Mechanics and Mining Sciences*, vol. 72, pp. 1–7, 2014.

[8] Y. K. Liu, S. H. Shao, X. X. Wang, L. P. Chang, G. L. Cui, and F. B. Zhou, "Gas flow analysis for the impact of gob gas ventholes on coalbed methane drainage from a longwall gob," *Journal of Natural Gas Science and Engineering*, vol. 36, pp. 1312–1325, 2016.

[9] F. B. Zhou, T. Q. Xia, X. X. Wang, Y. F. Zhang, Y. N. Sun, and J. S. Liu, "Recent developments in coal mine methane extraction and utilization in China: a review," *Journal of Natural Gas Science and Engineering*, vol. 31, pp. 437–458, 2016.

[10] N. Szlązak, D. Obracaj, and J. Swolkień, "Methane drainage from roof strata using an overlying drainage gallery," *International Journal of Coal Geology*, vol. 136, pp. 99–115, 2014.

[11] N. Guanhua, X. Hongchao, L. Zhao, Z. Lingxun, and N. Yunyun, "Improving the permeability of coal seam with pulsating hydraulic fracturing technique: a case study in Changping coal mine, China," *Process Safety and Environmental Protection*, vol. 117, pp. 565–572, 2018.

[12] G. H. Ni, Z. Li, and H. C. Xie, "The mechanism and relief method of the coal seam water blocking effect (WBE) based on the surfactants," *Powder Technology*, vol. 323, pp. 60–68, 2018.

[13] L. Ying-ke, Z. Fu-bao, L. Lang, L. Chun, and H. Shen-yong, "An experimental and numerical investigation on the deformation of overlying coal seams above double-seam extraction for controlling coal mine methane emissions," *International Journal of Coal Geology*, vol. 87, no. 2, pp. 139–149, 2011.

[14] C. Ö. Karacan, "Analysis of gob gas venthole production performances for strata gas control in longwall mining," *International Journal of Rock Mechanics and Mining Sciences*, vol. 79, pp. 9–18, 2015.

[15] I. A. Turchaninov, M. A. Iofis, and E. V. Kasparian, *Principles of Rock Mechanics*, Nedra, Leningrad, Russia, 1977.

[16] H. Kratzsch, *Mining Subsidence Engineering*, Springer, Berlin, Germany, 1983.

[17] S. Peng, *Coal Mine Ground Control*, Wiley, New York, NY, USA, 2nd edition, 1986.

[18] B. N. Whittaker and D. J. Reddish, *Subsidence: Occurrence, Prediction and Control*, Elsevier, Barking, 1989.

[19] V. Palchik, "Formation of fractured zones in overburden due to longwall mining," *Environmental Geology*, vol. 44, no. 1, pp. 28–38, 2003.

[20] S. F. Wang, X. B. Li, and D. M. Wang, "Void fraction distribution in overburden disturbed by longwall mining of coal," *Environment and Earth Science*, vol. 75, no. 2, p. 151, 2016.

[21] S. X. Sang, H. J. Xu, L. C. Fang, G. J. Li, and H. Z. Huang, "Stress relief coalbed methane drainage by surface vertical wells in China," *International Journal of Coal Geology*, vol. 82, no. 3-4, pp. 196–203, 2010.

[22] R. P. Singh and R. N. Yadav, "Prediction of subsidence due to coal mining in Raniganj coalfield, West Bengal, India," *Engineering Geology*, vol. 39, no. 1-2, pp. 103–111, 1995.

[23] S. K. Das, "Observations and classification of roof strata behaviour over longwall coal mining panels in India," *International Journal of Rock Mechanics and Mining Sciences*, vol. 37, no. 4, pp. 585–597, 2000.

[24] M. G. Qian and P. W. Shi, *Control of Mine Ground Pressure and Strata*, China University of Mining and Technology Press, Xuzhou, China, 2003.

[25] M. Christopher, "Multiple-seam mining in the United States: background," in *Proceedings of the New Technology for Ground Control in Multiple-Seam Mining, U.S. Department of Health and Human Services, Centers for Disease Control and Prevention, National Institute for Occupational Safety and Health, Pittsburgh Research Laboratory*, pp. 3–14, Pittsburgh, PA, USA, 2007.

[26] L. Yuan, H. Guo, B. T. Shen, Q. D. Qu, and J. H. Xue, "Circular overlying zone at longwall panel for efficient methane capture of multiple coal seams with low permeability," *Journal of China Coal Society*, vol. 36, no. 3, pp. 357–365, 2011.

[27] H. Guo, L. Yuan, B. T. Shen, Q. D. Qu, and J. H. Xue, "Mining-induced strata stress changes, fractures and gas flow

dynamics in multi-seam longwall mining," *International Journal of Rock Mechanics and Mining Sciences*, vol. 54, pp. 129–139, 2012.

[28] S. G. Li, H. F. Lin, P. X. Zhao, P. Xiao, and H. Y. Pan, "Dynamic evolution of mining fissure elliptic paraboloid zone and extraction coal and gas," *Journal of China Coal Society*, vol. 39, no. 8, pp. 1455–1462, 2014.

[29] F. Q. Gao, D. Stead, and J. Coggan, "Evaluation of coal longwall caving characteristics using an innovative UDEC Trigon approach," *Computers and Geotechnics*, vol. 55, pp. 448–460, 2014.

[30] Z. Y. Qin, L. Yuan, H. Guo, and Q. D. Qu, "Investigation of longwall goaf gas flows and borehole drainage performance by CFD simulation," *International Journal of Coal Geology*, vol. 150-151, pp. 51–63, 2015.

[31] Q. D. Qu, J. L. Xu, R. L. Wu, W. Qin, and G. Z. Hu, "Three-zone characterisation of coupled strata and gas behaviour in multi-seam mining," *International Journal of Rock Mechanics and Mining Sciences*, vol. 78, pp. 91–98, 2015.

[32] Z. W. Wang, T. Ren, and Y. P. Cheng, "Numerical investigations of methane flow characteristics on a longwall face part I: methane emission and base model results," *Journal of Natural Gas Science and Engineering*, vol. 43, pp. 242–253, 2017.

[33] Z. W. Wang, T. Ren, and Y. P. Cheng, "Numerical investigations of methane flow characteristics on a longwall face part II: parametric studies," *Journal of Natural Gas Science and Engineering*, vol. 43, pp. 254–267, 2017.

[34] G. R. Feng, A. Zhang, S. Y. Hu et al., "A methodology for determining the methane flow space in abandoned mine gobs and its application in methane drainage," *Fuel*, vol. 227, pp. 208–217, 2018.

[35] F. G. Bell, *Engineering in Rock Masses*, Elsevier, Amsterdam, Netherlands, 2013.

[36] V. Palchik, "Bulking factors and extents of caved zones in weathered overburden of shallow abandoned underground workings," *International Journal of Rock Mechanics and Mining Sciences*, vol. 79, pp. 227–240, 2015.

[37] J. P. Du and L. Q. Wang, *Special Coal Mining Method*, China University of Mining and Technology Press, Xuzhou, China, 2003.

[38] Y. C. Xu, J. C. Li, and S. Q. Liu, "Calculation formula of "two-zone" height of overlying strata and its adaptability analysis," *Coal Mining Technology*, vol. 16, no. 2, pp. 4–8, 2011.

[39] S. Y. Hu, Z. Li, G. R. Feng et al., "Changes on methane concentration after CO_2 injection in a longwall gob: a case study," *Journal of Natural Gas Science and Engineering*, vol. 29, pp. 550–558, 2016.

[40] H. T. Liu, N. J. Ma, J. Li, W. W. Zhang, and S. P. Zhang, "Evolution and distribution characteristics of roof shallow fissure channel," *Journal of China Coal Society*, vol. 37, no. 9, pp. 1451–1455, 2012.

[41] V. Palchik, "Localization of mining-induced horizontal fractures along rock layer interfaces in overburden: field measurements and prediction," *Environmental Geology*, vol. 48, no. 1, pp. 68–80, 2005.

[42] M. G. Qian and J. L. Xu, "Study on ozone characteristics of mining-induced fracture distribution in overlying strata," *Journal of China Coal Society*, vol. 5, pp. 466–469, 1998.

Hindawi
Geofluids
Volume 2019, Article ID 1756856, 9 pages
https://doi.org/10.1155/2019/1756856

Research Article

Analytical Solution for the Steady-State Karst Water Inflow into a Tunnel

Han-song Xie, Chong Jiang, Jia-li He, and Hai-xia Han

School of Resources and Safety Engineering, Central South University, Changsha, 410083 Hunan, China

Correspondence should be addressed to Chong Jiang; jiang4107@sohu.com

Received 30 November 2018; Revised 29 December 2018; Accepted 13 January 2019; Published 25 February 2019

Guest Editor: Bisheng Wu

An analytical solution for the karst water inflow into a lined tunnel in an infinite plane is derived based on conformal mapping. The new solution considers the center distance between the tunnel and the cavern, the radii of the tunnel and the cavern, and the property of the lining, such as the permeability coefficient as well as the lining radius. Numerical models are established and calculated using the finite difference software FLAC3D to compare with the analytical solution of inversion transformation, and a good agreement is found. Then, the parameters of effect are discussed in detail. The results indicate that the karst water inflow shows a curve relationship as the radius of tunnel increase and increases as the lining becomes thinner or the permeability coefficient of the lining increases. Moreover, the pressure head decreases as the tunnel radius and the center distance between the tunnel and the cavern increase.

1. Introduction

Karst water inflow is a key issue affecting the construction and operating phases of drained tunnels [1]. Moreover, some researchers have determined that most tunnels eventually act as drains [2, 3]. Therefore, analytical and numerical methods are the most commonly used methods to calculate the karst water inflow and pressure head of tunnels accurately.

Early researchers deduced analytical solutions for the water ingress into deeply buried tunnels. Lei [4] acquired an analytical solution for the steady flow into a deeply buried tunnel based on the image method. Conformal mapping could be used to investigate different boundary conditions along the tunnel circumference [5–9]. Ying et al. [10] derived an analytical solution for the groundwater ingress into a lined tunnel in a semi-infinite aquifer using the conformal mapping technique. In recent literature, Zhang [11] deduced an analytical solution for the seepage field of a parallel double-hole tunnel in a semi-infinite plane based on the seepage mechanics and image method. Some researchers used the theory of hydraulics and complex functions to solve the analytical solution for the groundwater inflow of surrounding rocks and lining structures [12–15]. Huang et al. [16] validated these analytical solutions with the software FLAC3D. An analytical solution was given by Jiang et al. [17–19] regarding the seepage field in a water-filled karst tunnel based on the inversion of a complex function and groundwater hydraulics theory. The rate and potential distribution of the confined flow of ground water through an opening were obtained by Chisyaki [20] in connection with the permeability of rock masses, the thickness of covered ground, the location of impermeable bedrock, and other parameters. The analytical solution for the nonlinear consolidation of soft soil around a shield tunnel with idealized sealing linings was presented by Cao et al. [21]. An analytical solution for confined flow into a tunnel during progressive drilling was deduced by Perrochet [22, 23]. Arjnoi et al. [24] solved the effect of drainage on pore water pressure distributions and lining stresses in drained tunnels.

However, most of the aforementioned literature have studied high hydraulic pressure tunnels or high hydraulic parallel tunnels in infinite plane. There are few analytical solutions for the karst water inflow and pressure head in karst tunnels. In this paper, a new analytical solution is derived for the steady-state karst water inflow into a circular tunnel with focus on the boundary condition of a pressure head of zero

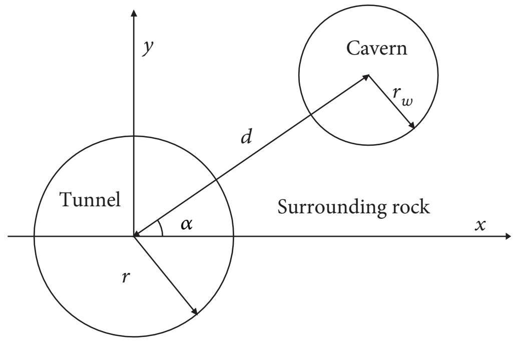

FIGURE 1: Schematic diagram of the karst tunnel in an infinite plane.

along the tunnel circumference based on conformal mapping. A numerical simulation is conducted to verify the solution. A parameter analysis, including the lining permeability and radius, the tunnel and cavern radii, and the center distance between the tunnel and the cavern, is discussed.

2. Definition of the Problem

2.1. Basic Assumptions. The simplified Naqiu Karst Tunnel [25–28] model takes the tunnel center as the origin, the horizontal direction as the x-axis, and the vertical direction as the y-axis to establish the coordinate system as shown in Figure 1. The expression of conformal mapping of a complex variable function is deduced by transforming elevation difference into angle α in the x-y coordinate system, and then the expression of karst water seepage flow is solved. α is the angle between the x-axis and the line connecting the cave center to the tunnel center. The tunnel and the cavern with radii denoted as r and r_w, respectively, are buried in an infinite aquifer. Here, d is defined as the center distance between the tunnel and the cavern. The pressure head in the cavern is H_w, and the horizontal line across the tunnel center is chosen as the elevation reference datum. The pressure head in the tunnel is H_t. The coordinates of A, B, C, D, E, and F are set as $(-r, 0)$, $(0, r)$, $(r, 0)$, (x_1, y_1), (x_3, y_3), and (x_2, y_2), respectively, in Figure 2(a).

Additionally, the basic assumptions of this paper are as follows:

(1) The surrounding rock of the tunnel is homogeneous with isotropic permeability [6]

(2) The aquifer and karst water are incompressible. The flow is in a steady state and is governed by Darcy's law [4]

(3) The pore pressure is constant on the same circumference, the water-filling hole is equal to the pressure head, and the cavern is full of water [10, 17]

2.2. Governing Equation. According to Darcy's law and mass conservation as well as the aforementioned assumptions, the steady-state karst water flow around the tunnel is described by the following Laplace equation [29]:

$$\frac{\partial^2 \phi}{\partial x^2} + \frac{\partial^2 \phi}{\partial y^2} = 0, \tag{1}$$

where ϕ is the total head, equal to the sum of pressure and elevation heads, as shown below:

$$\phi = \frac{P}{\gamma_w} + y, \tag{2}$$

where P is the water pressure and γ_w is the unit weight of water.

2.3. Boundary Conditions. Two boundary conditions along the tunnel and the cavern circumference are needed to solve equation (1). The boundary condition along the cavern circumference can be expressed as

$$\phi_{(y_1=0)} = H_{\mathrm{w}}. \tag{3}$$

In the case of constant total head, the boundary condition along the cavern circumference can be expressed as

$$\phi_{((x-(x_1+x_2)/2)+(y-y_1)=r_w{}^2)} = H_{\mathrm{t}}. \tag{4}$$

3. Analytical Solution

3.1. The Solution for the Karst Water Inflow. The method of conformal mapping can facilitate the derivation of the pressure head and the karst inflow in this study. As shown in Figure 2, the tunnel and the cavern circumference in the z-plane can be mapped as two circles in the w-plane with radii R_0 and R_1, respectively, based on the complex mapping function in equation (5) [30, 31]. The points A, B, C, D, E, and F are mapped in the w-plane to obtain corresponding points A$'$, B$'$, C$'$, D$'$, E$'$, and F$'$ by conformal mapping method in Figure 2(b).

$$R_0 = \frac{1 - A}{1 + A}, \tag{5}$$

where R_0 is the radius of tunnel mapping circle in the w-plane. $A = ((x_1 + iy_1 - r)/(x_1 + iy_1 + r)) \cdot ((x_2 + iy_2 + r)/(x_2 + iy_2 - r))$, and r is the tunnel radius.

It is assumed that both y_1 and y_2 are equal to zero without loss of generality for simplicity. Thus, equation (5) can be expressed as

$$R_0 = \frac{x_2 x_1 - r^2 - \sqrt{\left(x_1^2 - r^2\right)\left(x_2^2 - r^2\right)}}{(x_2 - x_1) r}, \quad 0 < R_0 < 1. \tag{6}$$

Expression of w in the w-plane when $y_1 = 0$ and $y_2 = 0$ is as follows:

$$w = R_0 \frac{(z - r)(x_2 + r)(1 - R_0) + (z + r)(x_1 - r)(1 + R_0)}{(z + r)(x_1 - r)(1 + R_0) - (z - r)(x_2 + r)(1 - R_0)}, \tag{7}$$

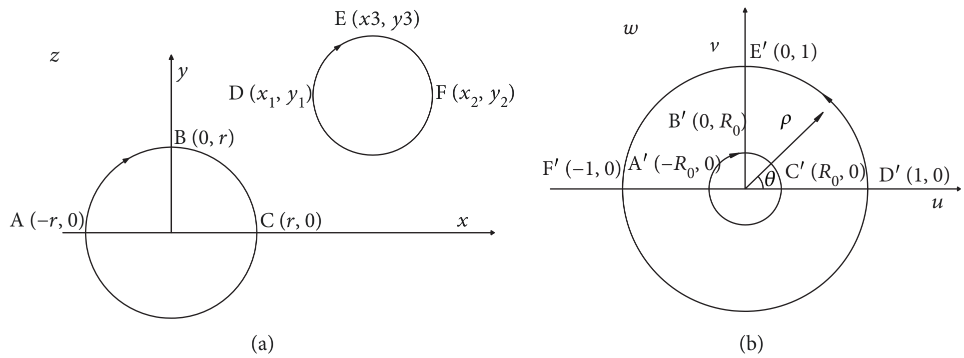

Figure 2: Conformal mapping.

where $z = x + iy$, which is the complex variable function of z in the z-plane. $w = u + iv = f(z)$, which is the complex variable function of w in the w-plane.

Then, equation (1) can be rewritten in terms of coordinate u-v:

$$\frac{\partial^2 \phi}{\partial u^2} + \frac{\partial^2 \phi}{\partial v^2} = 0. \tag{8}$$

By considering the boundary conditions, the solution for total head on a circle with radius ρ in the w-plane can be obtained as

$$\phi = C_1 + C_2 \ln \rho + \sum_{n=1}^{\infty} (C_3 \rho^n + C_4 \rho^{-n}) \cos n\theta, \tag{9}$$

where C_1, C_2, C_3, and C_4 are determined by the boundary conditions along the tunnel and the cavern circumference. n is the natural number in the series, and θ is the angle between ρ and the u-axis in the w-plane. ρ is a radius variable between the tunnel and karst cave mapping circle in the w-plane, and $R_0 \le \rho \le 1$.

The constant C_1 can be expressed by considering the boundary condition along the cavern circumference with $\rho = 1$ in the w-plane while the constant C_2 can be obtained by considering the boundary conditions along the tunnel and the cavern circumference with $\rho = R_0$ in the w-plane.

$$\begin{aligned}
\phi(\rho = 1) &= C_1 + \sum_{n=1}^{\infty} (C_3 + C_4) \cos n\theta \\
&= H_w \rightarrow C_1 = H_w, \quad C_3 = -C_4 = 0, \\
\phi(\rho = R_0) &= C_1 + C_2 \ln R_0 + \sum_{n=1}^{\infty} (C_3 {R_0}^n + C_4 {R_0}^{-n}) \cos n\theta \\
&= H_\mathrm{t} \rightarrow C_2 = \frac{H_\mathrm{t} - H_\mathrm{w}}{\ln R_0}, \quad C_3 = 0.
\end{aligned} \tag{10}$$

Thus,

$$\phi = H_t + \frac{H_t - H_w}{\ln R_0} \ln \rho, \tag{11}$$

where H_t is the pressure head of the tunnel.

The solution for the karst water inflow, which is the volume of water per unit tunnel length, into a drained circular tunnel can be obtained for the constant total head as

$$Q = k \int_0^{2\pi} \frac{\partial \phi}{\partial \rho} \rho d\rho = 2\pi k \frac{H_t - H_w}{\ln R_0}, \tag{12}$$

where Q is the karst water inflow; k is the permeability coefficients of the surrounding rock.

$y_1 = 0$ and $y_2 = 0$; thus, $x_1 = d\text{-}r_w$, $x_2 = d + r_w$, and $x_1 \text{-} x_2 = \text{-}2r_w$; equations (6) and (12) can be rewritten as equations (13) and (14), respectively:

$$R_0 = \frac{d^2 - r_w^2 - r^2 - \sqrt{\left((d + r_w)^2 - r^2\right)\left((d - r_w)^2 - r^2\right)}}{2rr_w}, \tag{13}$$

$$Q = 2\pi k \frac{H_t - H_w}{\ln \left(\left(d^2 - r_w^2 - r^2 - \sqrt{\left((d + r_w)^2 - r^2\right)\left((d - r_w)^2 - r^2\right)}\right)/2rr_w\right)}. \tag{14}$$

The expression of w_2 with α in the w-plane is as follows:

$$w_2 = \frac{w_1 - rA_1}{w_1 A_1 - r}, \tag{15}$$

where $w_1 = -e^{i\alpha} z$ and $A_1 = (d^2 + r^2 - r_w^2 + \sqrt{r^4 + (d^2 - r_w^2)^2 - 2(d^2 + r_w^2)})/2dr$.

3.2. The Solution for the Pressure Head of the Lining Structure. The pressure head along the lining and grouting circumference cannot be solved by the complex function, but it can be solved by using the groundwater seepage mechanics and the theory of infinite aquifer shaft [12]. The

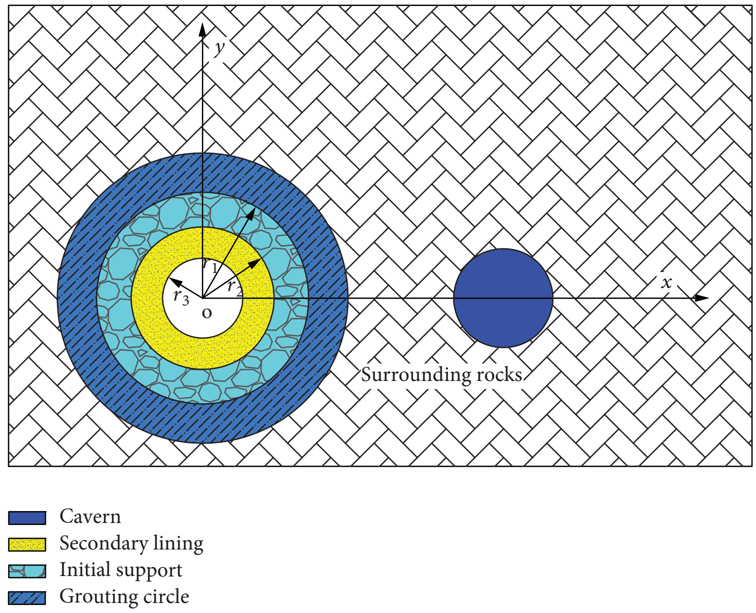

FIGURE 3: The relationships between each lining structure.

pressure head of relationships between the initial support, the secondary lining, and the grouting circle are expressed as equations (16), (17), and (18) and shown in Figure 3:

$$H_t - H_1 = \frac{Q}{2\pi k_1} \ln \frac{r}{r_1}, \quad (16)$$

$$H_1 - H_2 = \frac{Q}{2\pi k_2} \ln \frac{r_1}{r_2}, \quad (17)$$

$$H_2 - H_3 = \frac{Q}{2\pi k_3} \ln \frac{r_2}{r_3}, \quad (18)$$

where H_1, H_2, and H_3 are the pressure head along the joints of the grouting circle and initial support circumference, the initial support and the secondary lining circumference, and the secondary lining inner circumference, respectively; r_1, r_2, and r_3 are the radii of the grouting circle, initial support, and internal of secondary lining, respectively; and k_1, k_2, and k_3 are the permeability coefficients of the grouting circle, initial support, and secondary lining, respectively.

According to different phases of construction such as tunnel excavation and grouting, different distributions of pressure head can be obtained. When the grouting circle, initial support, and two linings are completed, the karst water inflow in the tunnel is

$$Q = \frac{2\pi(H_w - H_3)}{(1/k_2)\ln(r_1/r_2) + (1/k_1)\ln(r/r_1) + (1/k_3)\ln(r_2/r_3) - (1/k)\ln(R_0)}. \quad (19)$$

The pressure head of the circumference of the initial support and secondary lining joint is as follows:

$$H_2 = H_3 + \frac{H_w - H_3}{k_3 A} \ln \frac{r_2}{r_3}. \quad (20)$$

The pressure head of the circumference of the grouting circle and initial support joint is as follows:

$$H_1 = H_3 + \frac{H_w - H_3}{k_3 A} \ln \frac{r_2}{r_3} + \frac{H_w - H_3}{k_2 A} \ln \frac{r_1}{r_2}, \quad (21)$$

where $A = (1/k_2)\ln(r_1/r_2) + (1/k_1)\ln(r/r_1) + (1/k_3)\ln(r_2/r_3) - (1/k)\ln R_0$.

When the tunnel grouting and initial support are completed, the karst water inflow in the tunnel is

$$Q = \frac{2\pi(H_w - H_2)}{(1/k_2)\ln(r_1/r_2) + (1/k_1)\ln(r/r_1) - (1/k)\ln R_0}. \quad (22)$$

The pressure head of the circumference of the grouting circle and initial support joint is as follows:

$$H_1 = H_2 + \frac{(H_w - H_2)\ln(r_1/r_2)}{\ln(r_1/r_2) + (k_2/k_1)\ln(r/r_1) - (k_2/k)\ln R_0}. \quad (23)$$

4. Verification and Discussion

Analytical solutions for the karst water inflow and the pressure head are deduced, and thus, it is necessary to verify them. In the following section, the numerical solution simulated by the finite difference software FLAC3D and the theoretical solution deduced by Jiang et al. [17] are compared with the theoretical solution obtained by the conformal mapping method used in this paper.

4.1. Numerical Verification. The main calculation conditions are shown in Table 1, and the model of 100×100 m is established with FLAC3D. According to the difference of d, the model is divided into 6 groups, each of which sets up 20

Table 1: Characteristic data for verification.

Characteristic	Value
The pressure head of the cavern H_w	54 m
The radius of the tunnel r	7.25 m
The radius of the cavern r_w	4 m
The radius of the grouting circle r_1	2.25 m
The initial support radius r_2	2 m
Permeability coefficient of surrounding rocks k	1.5×10^{-6} cm·s^{-1}
Permeability coefficient of grouting circle k_1	10^{-7} cm·s^{-1}
Permeability coefficient of initial support k_2	10^{-8} cm·s^{-1}

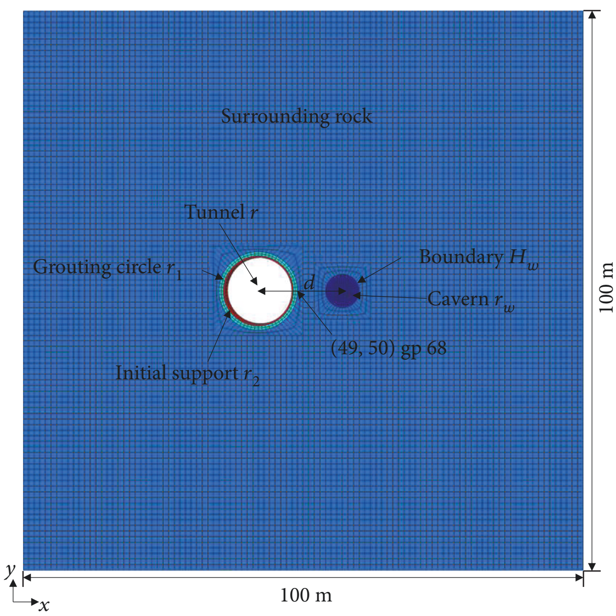

Figure 4: Finite element model of the circular karst tunnel.

models according to the difference of r and r_w. Then, the pore water pressure of the tunnel considering gravity and without considering gravity are obtained, respectively. When $d = 15$ m, the karst tunnel model consists of 33456 elements, as shown in Figure 4.

During the numerical simulation, the pore water pressure was measured at 4 points at the top, bottom, and both sides of the tunnel after excavation, initial support, and grouting, respectively. For example, the coordinates of the monitoring point on the right side of tunnel is (49, 50) and the node number is 68 in Figure 4. The pore water pressure considering gravity is 473662 Pa when the tunnel is stable, while the pore water pressure without considering gravity is 468681 Pa. The values of corresponding points can be obtained in the contour of pore water pressure, as shown in Figures 5 and 6.

4.2. Theoretical Comparison. According to different phases of construction such as tunnel excavation and grouting, different distributions of pressure head can be obtained based on the inversion of complex functions [17]. When tunnel

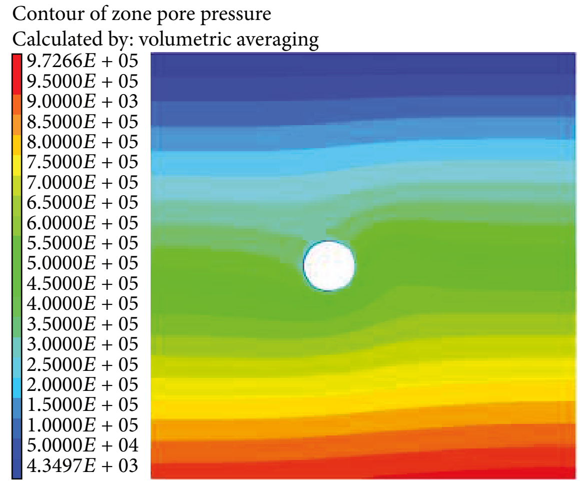

Figure 5: Contour of pore water pressure considering gravity for $d = 15$, $r = 7$, and $r_w = 4$.

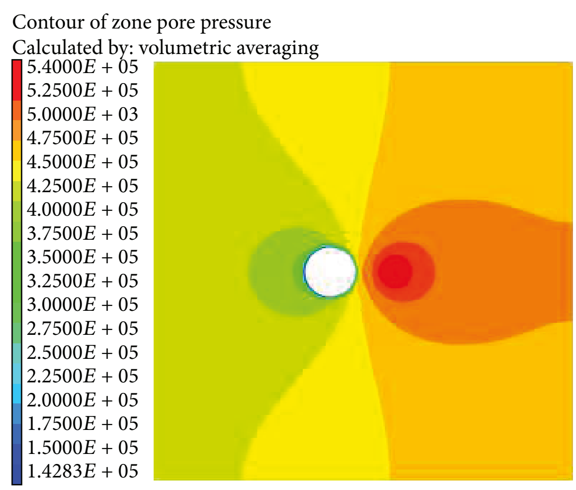

Figure 6: Contour of pore water pressure without considering gravity for $d = 15$, $r = 7$, and $r_w = 4$.

grouting and initial support are completed, the karst water inflow in the tunnel is

$$Q = \frac{2\pi (H_w - H_2)}{(1/k_2)\ln (r_1/r_2) + (1/k_1)\ln (r/r_1) + (1/k)\ln \left((d^2 - r^2)/rr_w \right)}. \tag{24}$$

The pressure head of the grouting circle and initial support joint is as follows:

$$H_1 = H_2 + \frac{(H_w - H_2)\ln (r_1/r_2)}{\ln (r_1/r_2) + (k_2/k_1)\ln (r/r_1) + (k_2/k)\ln \left((d^2 - r^2)/rr_w \right)}. \tag{25}$$

The solution of conformal mapping, the solution of inversion transformation, and the numerical solution are compared under the conditions of Table 1, as shown in Figure 7. It was found from the comparison of numerical solution and theoretical solution that when the grouting ring

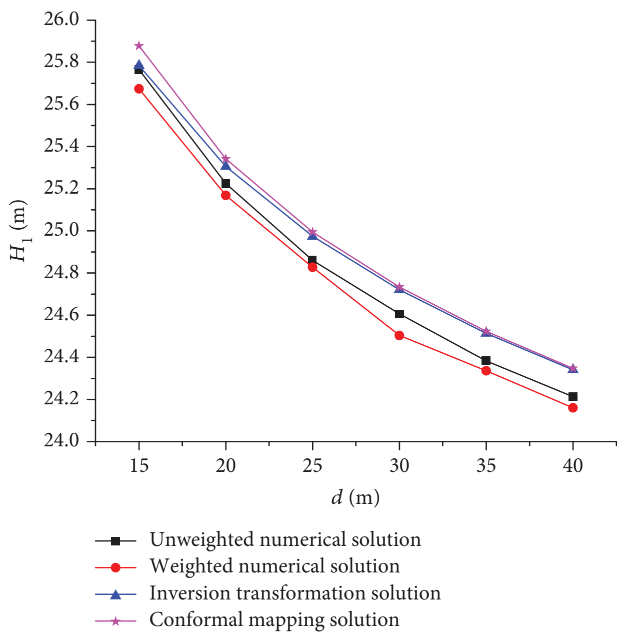

Figure 7: Comparison of numerical solution and theoretical solution for $r = 7.25$ and $r_w = 4$.

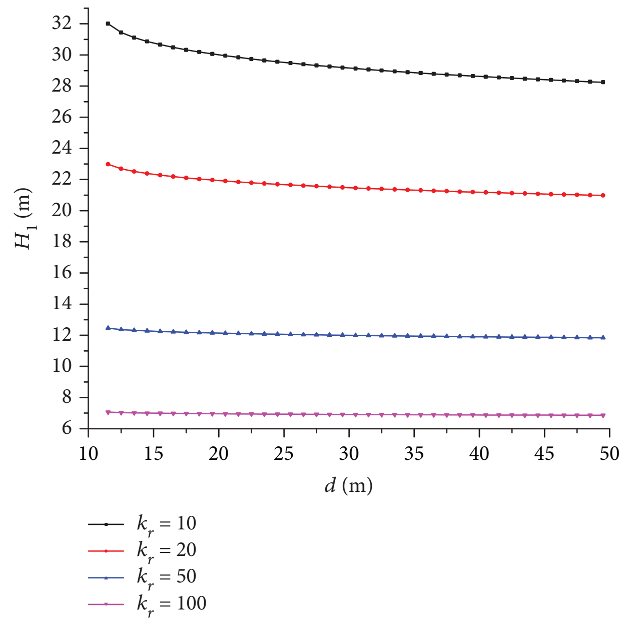

Figure 8: Relationship between the head pressure and distance.

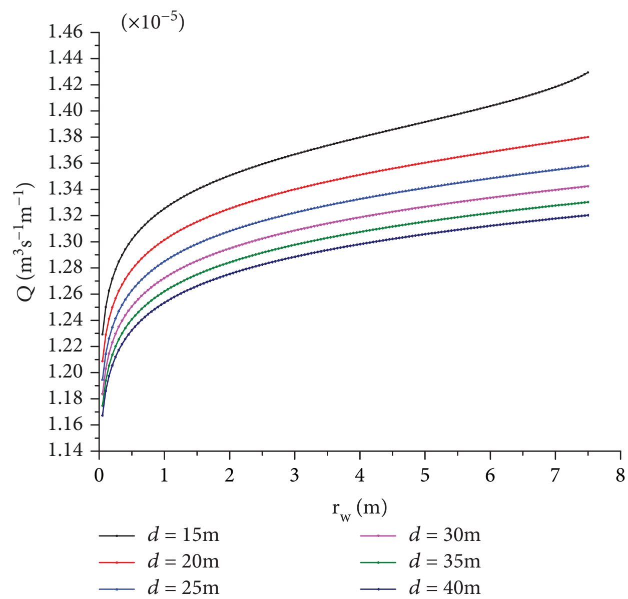

Figure 9: Relationship between the karst water flow and cavern radius.

and the initial support are completed and the secondary lining is not yet completed, H_1 decreases with the increase of d. When $d = 15$ m, H_1 for the theoretical solution, inversion transformation solution, numerical solution considering gravity, and numerical solution without considering gravity are 25.78 m, 25.88 m, 25.67 m, and 25.77 m, respectively. Therefore, the analytical method in this paper is suitable for solving the distribution of seepage field in karst tunnels. In general, a good agreement between the two methods and simulations could be obtained from the comparison.

5. Discussion

The equations (13)–(23) indicate that the parameters affecting karst water inflow into the tunnel include the pressure head of cavern, H_w; the center distance between the tunnel and the cavern, d; the radii of the cavern, grouting circle and initial support, r_w, r_1, and r_2, respectively; and the permeability coefficients of surrounding rocks, grouting circle, and initial support, k, k_1, and k_2, respectively.

5.1. The Effect of Center Distance and Cavern Radius. In this part, the center distance between the tunnel and the cavern d varies from 11.5 to 49.5 m, while the other parameters remain the same as those listed in Table 1. Figure 8 indicates that H_1 gradually decreases as d increases. Moreover, in the case of $k_r = k/k_1 = 10$, pressure head decreases 3.76 m from $d = 11.5$ m to $d = 49.5$ m and the values are 2 m, 0.61 m, and 0.2 m, respectively, in the case of $k_r = 20$, 50, and 100. The slope becomes smaller as d increases, which means the influence of d on H_1 gradually decreases and tends to be stable. This demonstrates that the effect of center distance between the tunnel and the cavern on the pressure head of the grouting circle is obvious when the distance is short.

Figure 9 illustrates the relationship between karst water inflow and cavern radius with different d. With the increase of r_w, the karst water inflow gradually increases and the change rate gradually decreases to a stable state. This means the effect of the cavern radius on the tunnel water inflow is obvious when the radius is increasing, and thus, the block effect of the lining should not be ignored in terms of water ingress estimate.

5.2. The Effect of the Grouting Circle. Figure 10 illustrates the relationship between pressure head and tunnel radius with

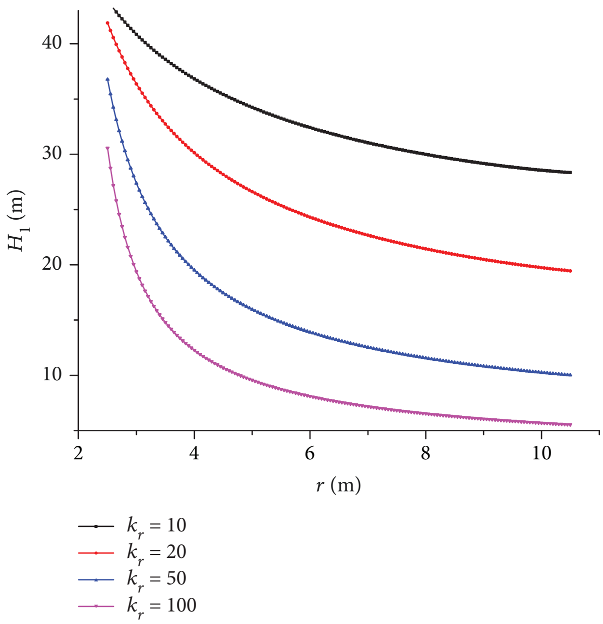

FIGURE 10: Relationship between the pressure head and tunnel radius.

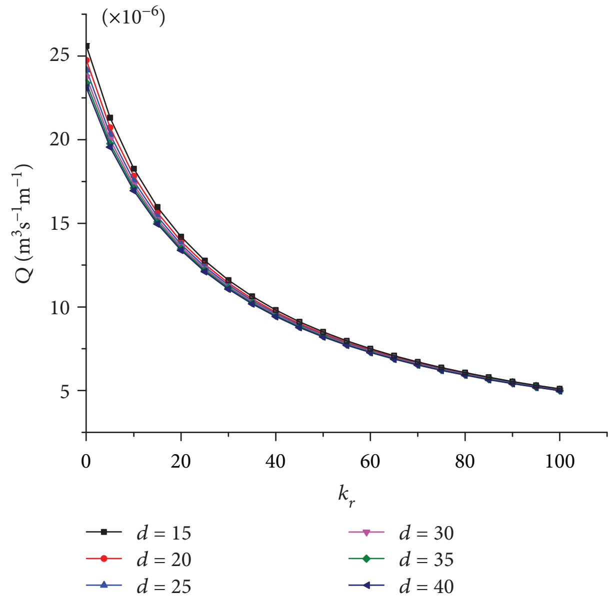

FIGURE 11: Relationship between the karst water inflow and permeability coefficient of the grouting circle.

different d. As r increases, H_1 gradually decreases. Moreover, in the case of $k_r = 10$, the pressure head decreases by 7.08 m from $r = 2.5$ m to $r = 4$ m accounting for 45.5% of the total reduction which is 15.56 m from $r = 2.5$ m to $r = 10.5$ m. And when $r = 10.5$ m, the reductions of the pressure head are 22.43 m, 26.76 m, and 25.03 m, respectively, in the case of $k_r = 20$, 50, and 100. When $r = 4$ m, the reductions of the pressure head are 11.74 m, 17.27 m, and 18.29 m accounting for 52.3%, 64.5%, and 73.1% of the total reduction, respectively. When $r > 4$ m, the reduction rate of H_1 decreases linearly and gradually slows down. When $r < 4$ m, the reduction rate of H_1 is faster than that of $r > 4$ m. Figure 11 illustrates the relationship between the karst water inflow and permeability coefficient of the grouting circle. With the increase of k_r, the karst water inflow gradually decreases and tends to be stable. In addition, the curves for different d in Figure 11 gradually overlap, which means the influence of d on Q is gradually reduced.

5.3. The Effect of Initial Support. Figure 12 illustrates the relationship between the pressure head and radius of the grouting circle for different d. Increasing r_1 means increasing the thickness of the initial support and reducing the thickness of the grouting circle. With the increase of r_1, H_1 gradually increases, and the curves for different d in Figure 12 almost coincide, indicating that d has little influence on H_1 when r_1 remains unchanged.

As shown in Figure 13, Q increases with increase of k_2. Moreover, in the case of $kr = 10$, the karst water inflow increases by 27.6×10^{-6} m^2 s^{-1} from $k_2 = 2.5 \times 10^{-9}$ ms^{-1} to $k_2 = 10^{-7}$ ms^{-1} and increases by 16.243×10^{-6} m^2 s^{-1} from $k_2 = 2.5 \times 10^{-9}$ ms^{-1} to $k_2 = 2 \times 10^{-8}$ ms^{-1}, accounting for 58.85% of the total growth. When the other conditions are kept the same, the change of the initial support permeability

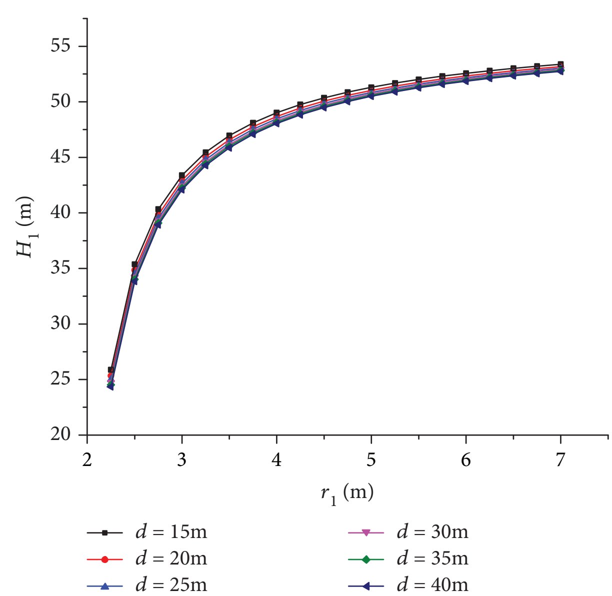

FIGURE 12: Relationship between the pressure head and radius of the grouting circle.

coefficient has an impact on karst water flow at 10^{-8} magnitude, while it has a greater impact at 10^{-9} magnitude with a higher cost. On the other hand, for a sealed tunnel, once the waterproof facilities failed, the karst water inflow would increase dramatically.

6. Conclusion

This paper derived analytical solutions for the steady-state karst water inflow and verified the new solution with

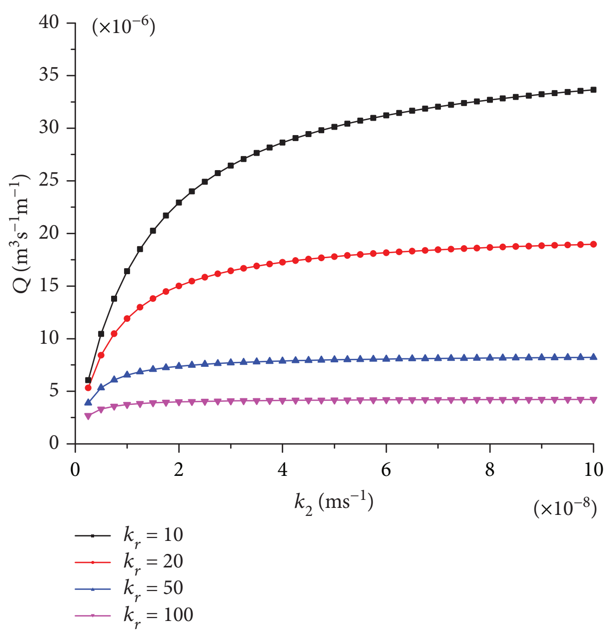

Figure 13: Relationship between the karst water flow and permeability coefficient of the grouting circle.

numerical simulation and analytical solution. The conclusions from this study are summarized as follows:

(1) The expression of karst water seepage flow in the karst tunnel is derived by conformal mapping method and then verified with numerical simulation via the software FLAC3D and analytical solution obtained from the method of inversion transformation

(2) The karst water inflow shows a curve relationship as the tunnel radius increase and increases as the lining becomes thinner or the permeability coefficient of the lining increases. For a sealed tunnel, once the waterproof facilities failed, the karst water inflow would increase dramatically. During construction, we should pay attention to the safety range of the initial support thickness

(3) When the other parameters remain unchanged, H_1 decreases and becomes stable as d increases. When $r > 4$ m, the reduction rate of H_1 decreases linearly and gradually slows down. When $r < 4$ m, the reduction rate of H_1 is faster than that of $r > 4$ m. When $r = 4$ m, the decrease of H_1 with the increase of k_r gradually increases. With the increase of r_1, H_1 gradually increases, and the curves for different d almost coincide, indicating that d has little influence on H_1 when r_1 remains unchanged

(4) The model assumed in this paper has some limitations. There is no surface water on the ground, so the inflow and pressure head of the surface water are not taken into account in the simplified model. Therefore, the inflow and pressure head models of seepage field under the interaction of the surface water and karst water are required for further research

Data Availability

The data used to support the findings of this study are available from the corresponding author upon request.

Conflicts of Interest

The authors declare that there are no conflicts of interest regarding the publication of this paper.

Acknowledgments

This work is supported by the National Natural Science Foundation of China (Grant Nos. 51678570 and 51478479) and Hunan Transport Technology Project (Grant No. 201524).

References

[1] Y. Zhao, F. Wang, C. Li, Y. Cao, and H. Tian, "Study of the corrosion characteristics of tunnel fissures in a karst area in Southwest China," *Geofluids*, vol. 2018, 19 pages, 2018.

[2] J. H. Atkinson and R. J. Mair, "Loads on leaking and watertight tunnel linings, sewers and buried pipes due to groundwater," *Géotechnique*, vol. 33, no. 3, pp. 341–344, 1983.

[3] J. Wongsaroj, K. Soga, and R. J. Mair, "Modelling of long-term ground response to tunnelling under St James's Park, London," *Geotechnique*, vol. 57, no. 1, pp. 75–90, 2007.

[4] S. Lei, "An analytical solution for steady flow into a Ttonnel," *Groundwater*, vol. 37, no. 1, pp. 23–26, 1999.

[5] K. H. Park, A. Owatsiriwong, and J. G. Lee, "Analytical solution for steady-state groundwater inflow into a drained circular tunnel in a semi-infinite aquifer: a revisit," *Tunnelling and Underground Space Technology*, vol. 23, no. 2, pp. 206–209, 2008.

[6] J. G. Wu, *A Coupled Fluid-Mechanical Study on Seepage Field of Tunnels with High Hydraulic Pressure*, Beijing Jiaotong University, 2006.

[7] M. El Tani, "Water inflow into tunnels," in *Proceedings of the Word Tunnel Congress ITA-AITES*, pp. 61–70, Oslo, 1999, Balkema.

[8] C. Butscher, "Steady-state groundwater inflow into a circular tunnel," *Tunnelling and Underground Space Technology*, vol. 32, no. 6, pp. 158–167, 2012.

[9] H. Zhu, J. Shen, F. Zhang et al., "DEM-CFD modeling of proppant pillar deformation and stability during the fracturing fluid flowback," *Geofluids*, vol. 2018, Article ID 3535817, 18 pages, 2018.

[10] H. W. Ying, C. W. Zhu, H. W. Shen, and X. N. Gong, "Semi-analytical solution for groundwater ingress into lined tunnel," *Tunnelling and Underground Space Technology*, vol. 76, pp. 43–47, 2018.

[11] B. Q. Zhang, "Analytical solution for seepage field of twin-parallel tunnel in semi-infinite plane," *Journal of The China Railway Society*, vol. 39, no. 1, pp. 125–131, 2017.

[12] C. W. Du, M. S. Wang, and Z. S. Tan, "Analytic solution for seepage field of subsea tunnel and its application," *Chinese*

Journal of Rock Mechanics and Engineering, vol. 30, no. s2, pp. 3567–3573, 2011.

[13] L. Tong, K. H. Xie, M. M. Lu, and K. Wang, "Analytical study of seepage flow into a lined tunnel in a semi-infinite aquifer," *Rock and Soil Mechanics*, vol. 32, no. 1, pp. 304–308, 2011.

[14] F. Zhang, Y. Fang, D. Elsworth, C. Wang, and X. Yang, "Evolution of friction and permeability in a propped fracture under shear," *Geofluids*, vol. 2017, Article ID 2063747, 13 pages, 2017.

[15] B. Wu, T. Ma, G. Feng, Z. Chen, and X. Zhang, "An approximate solution for predicting the heat extraction and preventing heat loss from a closed-loop geothermal reservoir," *Geofluids*, vol. 2017, Article ID 2041072, 17 pages, 2017.

[16] F. M. Huang, Z. S. Tan, M. S. Wang, and X. Wang, "Analytical solution for water inflow into an underwater tunnel and its application," *Engineering Sciences*, vol. 11, no. 7, pp. 3 568–3 573, 2009.

[17] C. Jiang, H. S. Xie, J. L. He, W. Y. Wu, and Z. C. Zhang, "Analytical solution of seepage field in karst tunnel," *Advances in Civil Engineering*, vol. 2018, Article ID 9215472, 9 pages, 2018.

[18] C. Jiang, Y. Li, L. Liu, and H. Lin, "Nonlinear analysis of flexible pile near undrained clay slope under lateral loading," *Advances in Civil Engineering*, vol. 2018, Article ID 6817362, 13 pages, 2018.

[19] C. Jiang, L. Lin, C. Li, T. B. Li, and J. He, "The undrained vertical and horizontal bearing capacity of internal skirted foundation in clay," *European Journal of Environmental and Civil Engineering*, pp. 1–18, 2018.

[20] T. Chisyaki, "A study on confined flow of ground water through a tunnel," *Groundwater*, vol. 22, no. 2, pp. 162–167, 2010.

[21] Y. Cao, J. Jiang, K. H. Xie, and W. M. Huang, "Analytical solutions for nonlinear consolidation of soft soil around a shield tunnel with idealized sealing linings," *Computers and Geotechnics*, vol. 61, pp. 144–152, 2014.

[22] P. Perrochet, "Confined flow into a tunnel during progressive drilling: an analytical solution," *Ground Water*, vol. 43, no. 6, pp. 943–946, 2005.

[23] P. Perrochet, "A simple solution to tunnel or well discharge under constant drawdown," *Hydrogeology Journal*, vol. 13, no. 5-6, pp. 886–888, 2005.

[24] P. Arjnoi, J. H. Jeong, C. Y. Kim, and K. H. Park, "Effect of drainage conditions on porewater pressure distributions and lining stresses in drained tunnels," *Tunnelling and Underground Space Technology*, vol. 24, no. 4, pp. 376–389, 2009.

[25] H. W. Chen and C. Sha, "Stability analysis of surrounding rock and treatment structures in superlarge karst cave of Naqiu tunnel," *Advances in Civil Engineering*, vol. 2018, Article ID 4842308, 14 pages, 2018.

[26] C. Jiang, J. L. He, L. Liu, and B. W. Sun, "Effect of loading direction and slope on laterally loaded pile in sloping ground," *Advances in Civil Engineering*, vol. 2018, Article ID 7569578, 12 pages, 2018.

[27] H. Lin, H. Wang, X. Fan, P. Cao, and K. Zhou, "Particle size distribution effects on deformation properties of graded aggregate base under cyclic loading," *European Journal of Environmental and Civil Engineering*, pp. 1–18, 2017.

[28] X. Fan, H. Lin, H. Lai, R. Cao, and J. Liu, "Numerical analysis of the compressive and shear failure behavior of rock containing multi-intermittent joints," *Comptes Rendus Mécanique*, vol. 347, no. 1, pp. 33–48, 2019.

[29] M. Y. Zhang, S. R. Jing, and G. J. Li, *Higher Engineering Fluid Dynamics*, Higher Education Press, 2012.

[30] A. Verruijt, *Complex Variable Solutions of Elastic Tunneling Problems*, Rapport COB 96-04, 1996.

[31] A. Verruijt and J. R. Booker, "Complex variable analysis of Mindlin's tunnel problem," in *Development of Theoretical Geomechanics*, pp. 3–22, Balkema, Sydney, 2000.

Hindawi
Geofluids
Volume 2019, Article ID 5067345, 13 pages
https://doi.org/10.1155/2019/5067345

Research Article

Comprehensive Research of Scaling Prediction for Gas Reservoir Fluid considering Phase State

Heng Zheng and Chunsheng Pu

School of Petroleum Engineering, China University of Petroleum (East China), Qingdao, Shandong, China

Correspondence should be addressed to Chunsheng Pu; chshpu_tx@126.com

Received 16 August 2018; Revised 3 December 2018; Accepted 12 December 2018; Published 11 February 2019

Guest Editor: Bisheng Wu

During the exploitation of a gas reservoir containing water, the scaling problem is usually affecting the gas production in gas wells. Although the scale formation that occurs during oil field development is quite different from the aforementioned gas field, the phase behavior plays a pivotal role in the formation of inorganic scale in gas field development. It is a well-known fact that there is no device that can directly measure the extent of scaling formation in a high-temperature and high-pressure reservoir. At the same time, the commonly applied scaling prediction method does not account for the fluid phase state. In this work, the scaling condition and alteration in controlling parameters in an actual gas reservoir were studied by self-developed high-temperature and high-pressure formation fluid equipments. From thermodynamics, a new scaling prediction model for the multiphase equilibrium of gas reservoir fluid is proposed that considers gas, liquid hydrocarbon, formation water, and inorganic salt scale. For the complexity of the direct solution for a phase equilibrium system with a chemical reaction, a simplified method for calculating the phase change and chemical equilibrium in a multiphase equilibrium system with chemical reactions is proposed based on the conservation of materials and the unification of the physical properties of components. The results show that the predicted value of the model was consistent with the experimental results. The new scaling prediction model considered the influence of the phase state which can accurately predict the change of the fluid phase state and the amount of inorganic salt scaling of actual gas reservoir fluids under the condition of multiphase equilibrium. Moreover, the average deviation of the prediction results is about 3%. The predicted scaling amount of the model without considering the effect of phase change is significantly lower than that of the experimental results. More specifically, the average deviation is around 30%. With the decrease of gas reservoir pressure, formation water evaporation intensifies under the influence of the oil and gas phase state, which leads to the increase of the formation water ion concentration when the influence of the fluid phase change is not considered. Then, the prediction of the inorganic salt scaling will be significantly lower.

1. Introduction

In the exploration of gas reservoirs containing water, a scaling problem is usually created which severely affects the production of gas wells [1, 2]. Due to the change of production conditions, such as the chemical reactions in the electrolyte solution and phase changing between oil, gas, and water [3, 4], the scaling formation of gas reservoir fluid is very complicated. Not only will the scaling conditions of inorganic salts themselves change with the change of temperature and pressure but also the dissolution, precipitation, and evaporation of oil and gas components will severely affect the scaling trend of inorganic salts. The current scaling prediction method includes the saturation index method, thermodynamic solubility method, saturation coefficient method, and sulfate compound scaling prediction method. Based on the principle of a chemical equilibrium of solution, these methods only consider the change of solubility of acidic gas with a chemical reaction and do not consider the comprehensive effect of phase change on fluid scaling. Therefore, they cannot truly reflect the process of inorganic salt scaling of gas reservoir fluids.

The alteration in temperature and pressure is not the only factor governing the scaling, but the dissolution and

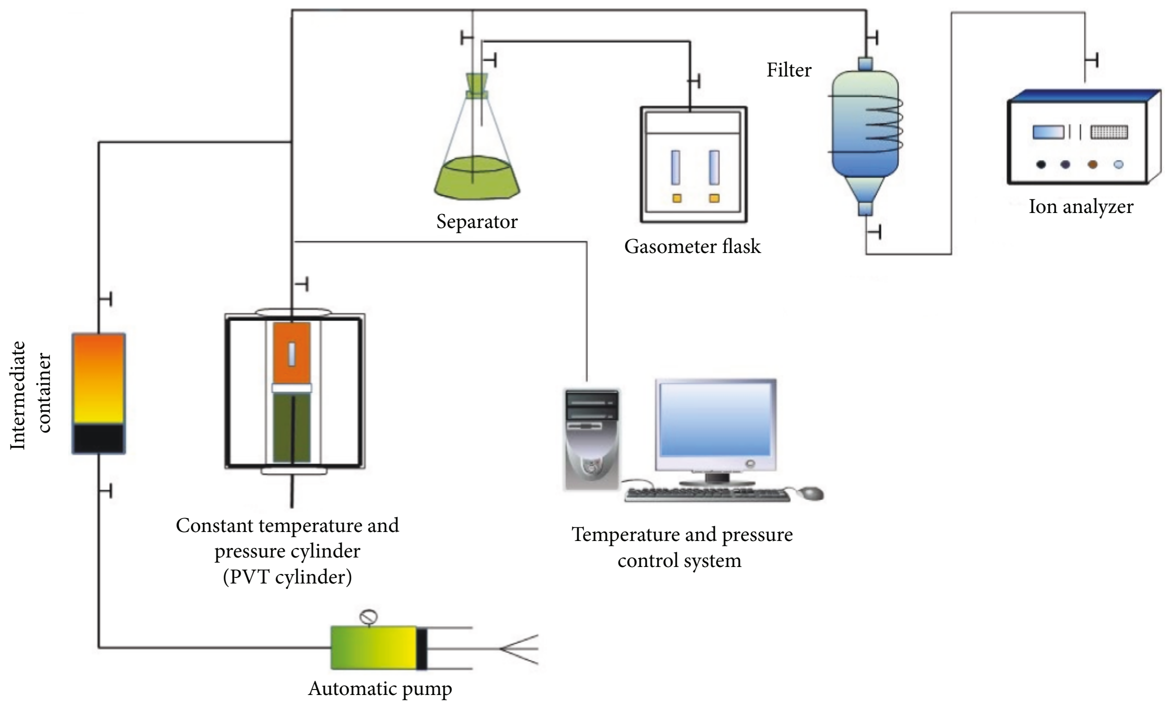

Figure 1: Scaling test device under the high temperature and pressure.

precipitation of oil and gas components and the evaporation of water can also severely influence the inorganic scale formation. Due to the involvement of mass transfer and energy conversation (Peyghambarzadeh et al. [5]), there are many factors, such as temperature [6–8], pressure (Fu et al. [9]), and water composition [10], that affect the scaling in a gas reservoir. Under this complex scenario, it is a challenge to accurately predict the extent of scaling. The most common scaling prediction techniques are the saturation index method, thermodynamic solubility method, and sulfate solubility product constant method [11–13]. Therefore, it is a challenge to predict scaling accurately. Among these methods, Ryznar and Langelier [14, 15] predicted the scaling of carbonate by the calculating saturation index. Zhang et al. [16, 17] predicted the scaling of carbonate by the thermodynamic solubility method. Bourland predicted [18] the scaling tendency by calculating the sulfate solubility product constant. In these prediction models, the influence of temperature and pressure and the composition of the formation water on scaling were taken into consideration, but the phase changes were ignored in the models; thus, they cannot truly reflect the process of the inorganic salt scaling in the gas reservoir fluid. At the same time, it was difficult to measure the amount of formation fluid scaling under a high-temperature and high-pressure condition because the experimental equipment has not yet been developed. It was necessary to establish a model which takes the phase change into account to predict the scaling under a high-temperature and high-pressure condition.

In this research, a set of experimental devices which has taken the phase change of oil, gas, and water into account was developed to understand the scaling law of the fluid in the actual gas reservoir. Based on thermodynamics, a multiphase equilibrium scaling prediction model of gas (natural gas)-liquid (hydrocarbon)-liquid (formation water)-solid (inorganic salt) was proposed that takes into account the change of fluid phase state and the reaction of inorganic salt scaling, and the fluid phase state transformation and scaling law of the actual gas reservoir were investigated.

2. Experiment Description

2.1. Experimental Equipment and Samples. In this research, a set of experimental devices was developed that was able to simultaneously test the phase change of fluid in gas reservoirs under high-temperature and high-pressure conditions and the amount of formation water ion and scaling. The schematic diagram of the device is shown in Figure 1. The whole system included a liquid supply system, sampling unit, PVT constant temperature and pressure system, separator, fluid property detection system, formation water ion analyzer, and temperature and pressure collection control system. The maximum working pressure of the system was up to 70 MPa, and the temperature range was from -50 to 200°C. The main equipment was a PVT analyzer, conventional formation water ion analyzer, and relevant physical property testing devices produced by the Canadian DBR Company. The pressure and temperature measurement accuracy of the device were 0.01 MPa and 0.1°C, respectively. The PID control system was used to adjust the temperature and pressure during the whole experimental process. The temperature control system used the electric heating system to carry out heating and temperature control on the PVT test room. 8 heating rods were used to heat the PVT test chamber to

Table 1: Composition of BS8 formation water.

Ion	Content (mg/l)	Ion	Content (mg/l)
Na^+	2.208×10^3	Cl^-	2.753×10^3
K^+	279.7	SO_4^{2-}	269.0
Ca^{2+}	113.5	HCO_3^-	463.6
Mg^{2+}	9.024	NO_3^-	145.5
Sr^{2+}	17.83	Total	6.256×10^3
pH	6.8 (dimensionless)		

ensure uniform heating. In the heating process, when the temperature of the test room reached the set temperature of the experiment, the control system would turn off the power; when the temperature of the test room dropped by 0.1°C, the electric heating system would reconnect the power supply and reheat the test room. The pressure of the PVT test chamber was controlled by piston movement. In the experiment, the electric motor under the piston would drive the piston up and down, so as to realize the change of the volume of the PVT test room and the pressure of the PVT test room. When the pressure of the PVT test room was higher than the experimental setting value, the electric motor would pull the piston down and increase the volume of the PVT test room, thus reducing the pressure of the test room. When the pressure reached the experimental set point, the control system would turn off the power. When the pressure of the PVT test room was lower than the set value of the experiment, the electric motor would pull the piston upward and compress the volume of the PVT test room, thus increasing the pressure of the test room.

The gas, oil, and water samples obtained from the BS8 well in the Qianmiqiao gas reservoir were used in the experiment. The sample composition was shown in Tables 1–3. The initial formation pressure of the well was 43.57 MPa, the current formation pressure was 11.5 Mpa, the formation temperature was 171.4°C, the production water and gas ratio was $4.33\,m^3/10^4\,m^3$, and the gas-oil ratio was $11{,}507\,m^3/m^3$.

2.2. Experimental Procedures. In the experiment, the formation fluid was first compounded according to the production data and pumped to the intermediate container by an automatic pump. Then, the fluid was heated and pressurized under constant temperature and pressure in a cylinder to restore the formation conditions. It was then held for 24 hours to ensure that the phase changes of the oil, gas, and water in the formation fluid and the scaling reaction proceeded sufficiently and achieved equilibrium. The volume of natural gas saturated with water at the top of the PVT cylinder and the volume of formation water that the gas dissolved were then obtained. Finally, the condensate gas of a small amount of saturated water at the upper part of the PVT tube was discharged, and the natural gas and the saturated water content were flashed to the standard condition and measured. The PVT cylinder was set for half an hour; then, the formation water of natural gas dissolved in the lower part was discharged and measured. The ion detection analyzer was used to measure the concentration of each ion in the formation water. According to the change of ionic concentration and formation water physical property before and after the experiment, the scaling amount of the formation fluid was determined.

2.3. Experimental Data Analysis. Beginning from the initial formation conditions, the high-temperature and high-pressure phase analysis and scaling test of the BS8 well fluid were carried out under five pressure and three temperature conditions, respectively. The results of the experiment are shown in Figures 2–5. It is indicated in Figure 2 that the content of dissolved gas in formation water (GWR) increased as the pressure increased under the same temperature. When the pressure is raised from 5 MPa to 20 MPa, the content of dissolved gas ascended dramatically. When the pressure was over 20 MPa, the rise gradually slowed down. Under the same pressure, the content of dissolved gas went up with the increase of temperature. When the pressure was 5 MPa, the content difference of dissolved gas was smaller under the three different temperatures. When the pressure increased to 20 MPa, an obvious difference appeared. When the pressure went up to 45 MPa, the content difference of dissolved gas enlarged continuously. However, the content of saturated water in natural gas (WGR) decreased when the pressure increased under the same temperature. As demonstrated in Figure 2, the WGR increased with the rise of the temperature under the same pressure. With the increase of pressure, the content difference of saturated water between different temperatures in natural gas gradually decreased. From the WGR curve, the WGR curve experienced a dramatic decrease from 5 MPa to 12 MPa, and a huge content difference appeared when the pressure was 5 MPa. When the pressure was 20 MPa, the WGR became stable, and the content difference decreased greatly compared when the pressure was 5 MPa. The curves of formation water salinity and concentration of each ion measured under the standard condition (Figure 3) indicated that with the decrease of experimental pressure, the salinity of the formation water increased obviously. The main reason was that the bubble pressure of the formation was about 11 MPa when the temperature was 171.4°C. With the drop of pressure, the water was vaporized which caused the volume reduction of formation water. The ions such as Na^+, K^+, Mg^{2+}, Cl^-, and NO^{3-} also showed the same trend. The experimental data showed that these ions had the same concentration change ratio. At high pressure, the changing of the ion content such as Ca^{2+}, HCO^{3-}, and Sr^{2+} was similar to Na^+, but it decreased suddenly and had a trend of decreasing with decreasing pressure when the pressure decreased further. The content of SO_4^{2-} increased with the decrease of pressure. The experimental results demonstrated that some ions participated in the scaling reaction under certain conditions, and inorganic salt scales were formed in the formation fluid.

Under the experimental condition, the ions such as Na^+ and K^+ were not involved in the scaling reaction, and the concentration change was mainly due to the change of water physical properties caused by high temperature and high pressure. Taking the concentration of Na^+ as a standard,

Table 2: Composition of BS8 natural gas.

Ion	CO_2	N_2	C_1	C_2	C_3	IC_4	NC_4	IC_5	NC_5	C_6
Percentage (%)	8.73	0.56	80.22	6.75	2.14	0.57	0.55	0.27	0.19	0.02

Table 3: Composition of BS8 condensate oil.

Ion	CO_2	N_2	C_1	C_2	C_3	IC_4	NC_4	IC_5	NC_5	C_6	C_{7+}
Percentage (%)	0.77	0.07	5.12	2.52	1.88	3.84	2.6	5.82	4.22	13.58	59.58

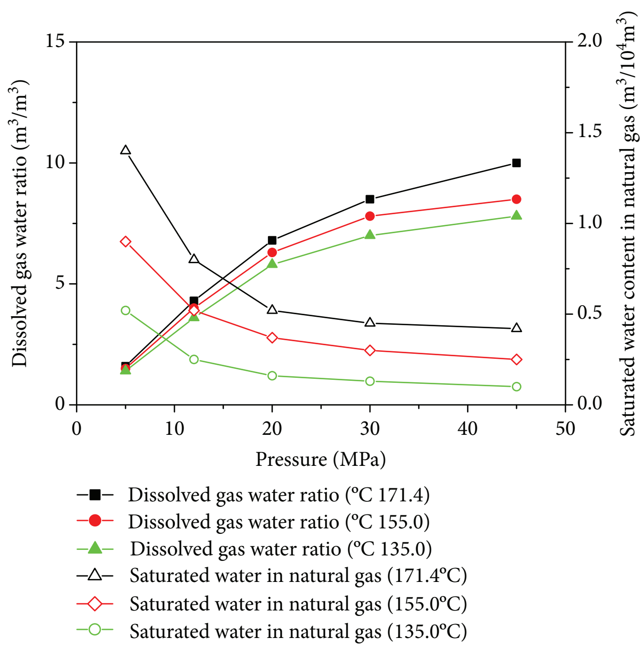

Figure 2: Gas and water dissolved content change curves of BS8 formation fluid.

the change of scale ions in formation water before and after the experiment can be calculated by the test data as follows:

$$C = \frac{C(\mathrm{Na}^+)}{C_i(\mathrm{Na}^+)} \times C_0 - C_n, \tag{1}$$

where C is the change of the molar concentration of the scale ions; $C(\mathrm{Na}^+)$ is the current molar concentration of sodium ions; $C_i(\mathrm{Na}^+)$ is the initial sodium ion molar concentration; C_0 is the initial scale ion molar concentration; and C_n is the current scale ion molar concentration.

According to the change of ion concentration, the type of scaling and the amount of scaling of the inorganic salt in the formation fluid under the standard condition were determined. The amount of scaling under the experimental conditions was also obtained according to the change of the volume coefficient and density of the formation water. As shown in Figure 4, two kinds of inorganic scales, $CaCO_3$ and $SrSO_4$, were generated in the formation water of BS8 in the experimental condition, while the amount of scales was zero under the initial formation pressure. When the pressure was lower than 20 MPa, the $CaCO_3$ scale occurred. When the pressure was lower than 30 MPa, the $SrSO_4$ scale appeared.

At present, as the formation pressure was 11.5 MPa and the formation temperature was 117.4°C, more $CaCO_3$ scales and a small amount of $SrSO_4$ scales appeared in the formation fluid. In addition, the amount of fouling increased with the decrease of experimental pressure and increased with the rise of temperature.

In order to study the influence of fluid phase change on the scaling of inorganic salts, scaling tests were carried out under the same conditions using BS8 degassed formation water. As indicated in Figure 5, it can be concluded that the inorganic scale was generated in the whole experiment. Although the amount of inorganic salt scale in degassed formation water also increased with the decrease of pressure and increased with the rise of the temperature, the change trend was not obvious compared with the formation fluid. This was mainly because the oil and gas components in the actual fluid were more easily dissolved in the formation water under the conditions of high temperature and high pressure. The dissolution of the acid gas CO_2 promoted the reaction of $CaCO_3$ to be dissolved, which led to the low scale of the inorganic salt scaling in the formation fluid. However, with the decrease of pressure, the solubility of the gas components in water decreased, while the evaporation of water into natural gas obviously increased.

3. Scaling Prediction Model

3.1. Model Description. The inorganic salt scaling in a gas reservoir was a complex multiphase system consisting of natural gas, liquid hydrocarbons, formation water, and various solid inorganic salt scales with chemical reactions. Under equilibrium conditions, the system should meet the conditions of material conservation and thermodynamic equilibrium. The system consists of N components and P phases, and the chemical reaction balance and phase equilibrium existed simultaneously and follow the law of element conservation:

$$\sum_{i=1}^{N} \sum_{j=1}^{p} n_{ij}\omega_{ik} = b_k. \tag{2}$$

Only the phase equilibrium exists, and the total molar conservation of the components is observed.

$$\sum_{j=1}^{p} n_{ij} = n_i^{\mathrm{total}}. \tag{3}$$

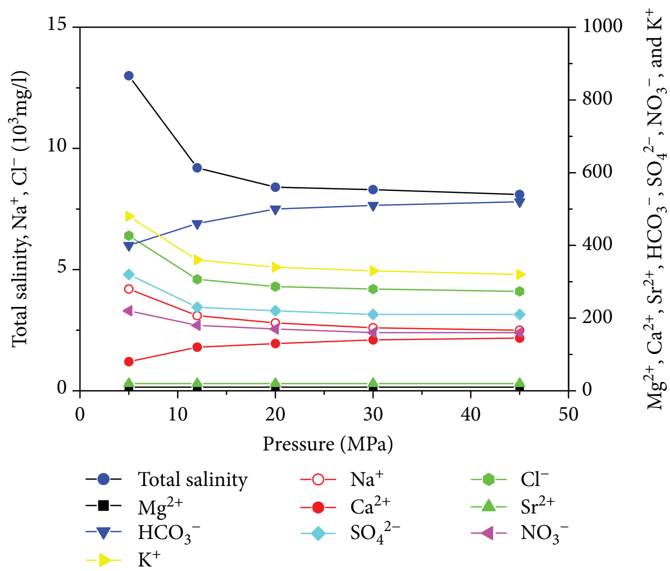

FIGURE 3: BS8 reservoir water's salinity and ion content change curves with pressure (171.4°C).

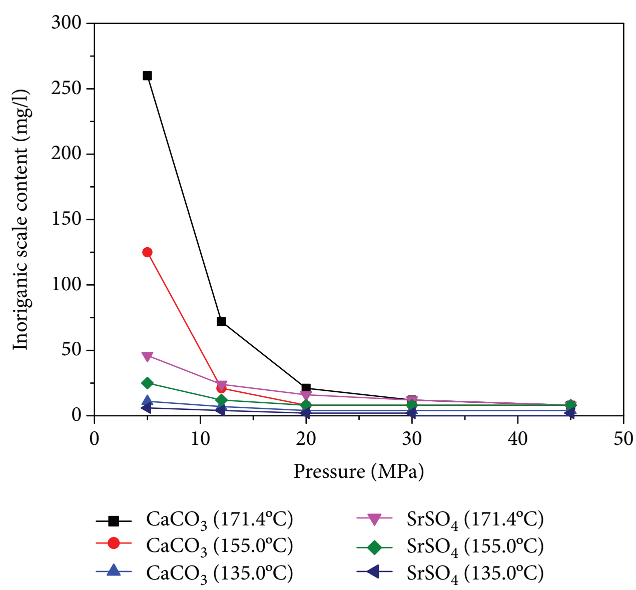

FIGURE 4: Scaling quantity curve of BS8 formation fluid.

For the electrolyte solution with ions, the charge conservation condition should also be satisfied.

$$\sum_{i=1}^{N} n_{iw} Z_i = 0. \tag{4}$$

For a given temperature and pressure, the system should meet the minimum thermodynamic equilibrium condition of Gibbs free energy.

$$\min G(n) = \sum_{i=1}^{N} \sum_{j=1}^{p} n_{ij} \mu_{ij}, \tag{5}$$

where n_{ij} is the number of moles of component i in phase j, ω_{ik} is the mole number of the element k in component i; b_k is the total mole number of the element k; Z_i is the number of charges in component i in the solution; n_{iw} is the number of moles of i in the formation water electrolyte solution; and μ_{ij} is the chemical energy of component i in phase j.

3.2. Model Analysis. The entire gas reservoir multiphase system with inorganic salt scaling was divided into two interactive processes: the first process is the natural gas and liquid hydrocarbon phase change between formation water electrolyte solutions and the other process is the chemical reaction of each ion and inorganic salt in formation water. Further analysis was made on the representation method of the composition of the multiphase system and the calculation method of the thermodynamic equilibrium of the two processes.

3.2.1. Composition Representation Method. In order to clearly express the composition of the phases in the system, the material representation method of phase equilibrium was adopted. Under certain equilibrium conditions,

$$\begin{gathered} V + L + W + \sum_{j=1}^{nm} M_j = 1, \\ V y_i + L x_i + W w_i + \sum_{j=1}^{nm} M_j m_i = z_i, \end{gathered} \tag{6}$$

where V, L, W, and M_j are the molar components of natural gas, liquid hydrocarbon, electrolyte solution, and each solid inorganic scaling, respectively; y_i, x_i, w_i, and m_i are the molar compositions of component i in gas phase, liquid hydrocarbon, aqueous phase, and solid inorganic salt, respectively; and z_i is the molar composition of the components in the total system under a certain condition.

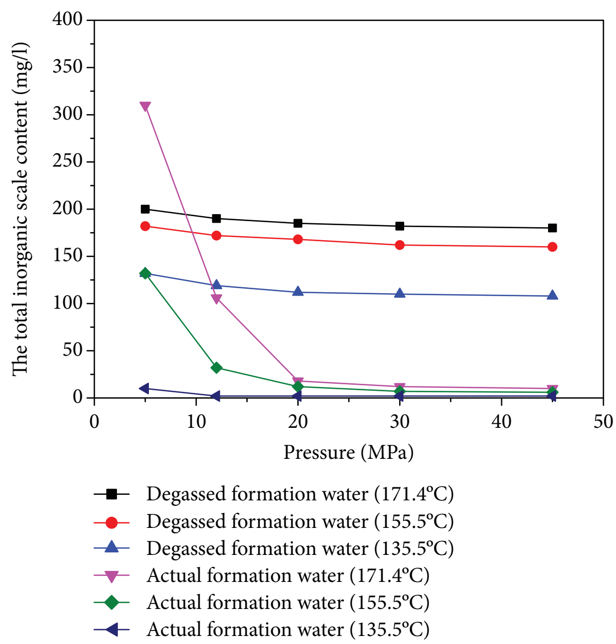

FIGURE 5: Contrast curves of the scaling amount of BS8's degassed formation water and the actual formation fluid.

Unlike the conventional phase equilibrium problem, the molar composition of the components in a multiphase system may change continuously due to the chemical reaction. Under different conditions, the total number of moles of the system and the molar composition of each component are shown as follows:

$$F_{\text{total}} = F_{\text{total}}^{\text{initial}} + \Delta F,$$
$$z_i = \frac{n_{i\text{total}}}{F_{\text{total}}} = \frac{n_{i\text{total}}^{\text{initial}} + \Delta n_i}{F_{\text{total}}^{\text{initial}} + \Delta F} = \frac{F_{\text{total}}^{\text{initial}} \cdot z_i^{\text{initial}} + \Delta n_i}{F_{\text{total}}^{\text{initial}} + \Delta F}, \quad (7)$$

where F_{total} and $F_{\text{total}}^{\text{initial}}$ are the total number of moles of all components of the system at given equilibrium conditions and initial conditions; ΔF is the amount of change in the total moles caused by the chemical reaction; $n_{i\text{total}}$ and $n_{i\text{total}}^{\text{initial}}$ are the initial number of moles of component i at the given equilibrium conditions; Δn_i is the amount of change in the number of moles of component i; and z_i and z_i^{initial} are the molar compositions of component i in a given system under given equilibrium conditions and initial conditions.

3.2.2. Phase Equilibrium. The fugacity of each component in each phase should be equal when the equilibrium of gas, liquid, and liquid was achieved:

$$f_i^V = f_i^L = f_i^W, \quad (8)$$

where

$$f_i^V = x_i \phi_i^V P,$$
$$f_i^L = y_i \phi_i^L P, \quad (9)$$
$$f_i^W = w_i r_i f_i^0.$$

In the formula, f_i^V, f_i^L, and f_i^W are the fugacities of component i in the gas phase, liquid hydrocarbon phase, and water phase, respectively; ϕ_i^V and ϕ_i^L are the fugacity coefficients of components in the gas phase and liquid hydrocarbon phase; f_i^0 is the standard fugacity of pure component i; and r_i is the activity coefficient of component i in the electrolyte solution. Among them, PR state equations can be used to calculate the related thermodynamic parameters of components in gas phase and liquid hydrocarbons; the Pitzer method is used to solve the activity coefficients and standard fugacity of components in formation water.

3.2.3. Chemical Equilibrium in Electrolyte Solution. According to the Gibbs free energy minimum principle and the calculation method of the chemical potential of the solution components, the equilibrium condition in the chemical reaction is as follows:

$$\prod_{i=1}^{N_{re}} (r_i C_i)^{\upsilon_i} = K_{sp}, \quad (10)$$

where υ_i is the stoichiometric number of component i in the chemical reaction; C_i is the concentration of component i in the solution; moles/l; and K_{sp} is the reaction equilibrium constant.

$$Ca^{2+} + SO_4^{2-} \rightleftarrows CaSO_4\downarrow \quad (11)$$

$$Ba^{2+} + SO_4^{2-} \rightleftarrows BaSO_4\downarrow \quad (12)$$

$$Sr^{2+} + SO_4^{2-} \rightleftarrows SrSO_4\downarrow \quad (13)$$

$$Ca^{2+} + 2HCO_3^{-} \rightleftarrows CaCO_3\downarrow + H_2O + CO_2 \quad (14)$$

In the field practice, the Oddo-Tomson Saturation Index was commonly used to obtain the equilibrium conditions for inorganic salt scaling:

$$I_s = \lg\left(C_{A^{n+}}^{\upsilon_A} \cdot C_{B^{m-}}^{\upsilon_B}\right) - \lg K'_{sp}(P, T, S_i) = 0,$$
$$-\lg K'_{sp} = a + bT + cT^2 + dp - eS_i^{1/2} + fS_i - gS_i^{1/2}T, \quad (15)$$

where A^{n+} and B^{m-} are the positive and negative ions in the inorganic reaction; K'_{sp} is a quasiequilibrium constant taking into the activity coefficient; I_S is the saturation index of the inorganic salt; T is the temperature in °F; P is the pressure in psi; S_i is the solution's ion intensity in moles/l; and $a\sim g$ is a regression coefficient for various salts.

The condition of scaling was judged by the saturation index of the inorganic salt (I_S) of each inorganic salt in the solution. When the $I_S < 0$, the solution is undersaturated and no scale appeared in the solution; when the $I_S = 0$, the solution is in a state of saturation but no scaling; when $I_S > 0$, the solution is in a supersaturated state and the scale appeared in the solution.

According to the balance of materials and the equilibrium conditions, the scaling prediction method considering multiphase equilibria in electrolyte solution was deduced. Under equilibrium conditions, the relationship between the amount of inorganic salt scale and solution ion concentration is as follows:

$$\left(C^0_{SO_4^{2-}} - M_{CaSO_4} - M_{BaSO_4} - M_{SrSO_4}\right) \cdot \left(C^0_{Ca^{2+}} - M_{CaCO_3} - M_{CaSO_4}\right) = K'_{SPCaSO_4}, \quad (16)$$

$$\left(C^0_{SO_4^{2-}} - M_{CaSO_4} - M_{BaSO_4} - M_{SrSO_4}\right) \cdot \left(C^0_{Sr^{2+}} - M_{SrSO_4}\right) = K'_{SPSrSO_4}, \quad (17)$$

$$\left(C^0_{SO_4^{2-}} - M_{CaSO_4} - M_{BaSO_4} - M_{SrSO_4}\right) \cdot \left(C^0_{Ba^{2+}} - M_{BaSO_4}\right) = K'_{SPBaSO_4}, \quad (18)$$

$$\frac{\left(C^{sp}_{HCO_3^-}\right)^2 \cdot \left(C^0_{Ca^{2+}} - M_{CaCO_3} - M_{CaSO_4}\right)}{P \cdot y_{CO_2} \cdot f_{gCO_2}} = K'_{SPCaCO_3}, \quad (19)$$

$$\begin{aligned} C^{sp}_{HCO_3^-} + C^{sp}_{CO_3^{2-}} + C^{sp}_{CO_2} + M_{CaCO_3} &= C^{sp}_{HCO_3^-} \\ &+ \frac{\left(C^{sp}_{HCO_3^-}\right)^2 \cdot K_H \cdot K_2}{K_1 \cdot p \cdot y_{CO_2} \cdot f_{CO_2}} \\ &+ \frac{p \cdot y_{CO_2} \cdot f_{CO_2}}{K_H} + M_{CaCO_3} = \text{const}, \end{aligned} \quad (20)$$

where M is the amount of scale in each inorganic salt solution in moles/l; C^{sp} represents the concentration of the components under equilibrium conditions in moles/l; C^0 is the initial concentration of the components in moles/l; K_H is Henry's constant of CO_2 dissolution; K_1 and K_2 are the primary and secondary ionization constants of carbonic acid; const represents the total initial concentration of CO_3^{2-}, HCO_3^-, and CO_2 in the solution in moles/l; and y_{CO_2} and f_{CO_2} are the molar contents and fugacity of CO_2 in the gas phase, respectively. For its formula or equation of state calculation, this paper uses the PR equation of state for calculation.

3.3. Model Solution. In this research, the entire gas reservoir multiphase system with inorganic salt scaling was divided into two interactive processes: the first process is the natural gas and liquid hydrocarbon phase change between formation water electrolyte solutions and the other process is the chemical reaction of each ion and inorganic salt in formation water. Except for the H_2O and CO_2, the other components have only undergone one change process. The problem can be simplified greatly if the phase equilibrium state equation and the chemical reaction calculation method are adopted on the basis of the conservation of material. Meanwhile, the ratio of gas and water in a gas reservoir was very large, and the molar content of ionic components in the whole system was relatively small. The change of the electrolyte solution concentration caused by the phase state change between gas, oil, and water has a greater influence on the scaling of inorganic salt, while the physical property change caused by inorganic salt scaling on the gas, liquid, and liquid phase states is relatively weaker. Therefore, the phase equilibrium of gas, liquid, and liquid in the entire multiphase system is solved firstly, then the chemical equilibrium in the formation water is calculated under the condition of phase equilibrium. Finally, the final condition based on the conservation of materials and the unity of physical properties is determined. The specific solution steps are as follows (Figure 6):

Step 1. We input the pressure (P), temperature (T), and the initial composition $z_i{}^0$. Assuming that there is no scaling in the formation water, the Michelsen discriminant method is used to determine the three-phase stability of gas, liquid, and liquid. The PR equation is used for flash calculation to determine the molar composition for each of phases V^0, L^0, W^0, the composition of the compositions $y_i{}^0$, $x_i{}^0$, $w_i{}^0$, and the corresponding thermodynamic parameters.

Step 2. The composition of formation water determined by flash calculation is used to predict the tendency of inorganic salt scaling. If $I_s \le 0$, it means that there is no scaling in the fluid under the current condition. The calculation result of Step 1 can describe the composition of the entire multiphase equilibrium system, and no further calculation is required. If $I_s > 0$, the solution is in the state of supersaturation. The following calculations need to be continued to determine the equilibrium scale of inorganic salts.

Step 3. If the formation water is not in the chemical equilibrium state, the initial scale of each inorganic salt and the composition of formation water are calculated by equations (11)–(16). If the scale of an inorganic salt accounts for the molar content of the aqueous solution of the formation, the molar content of the inorganic scale in the entire multiphase system is as follows:

$$M'_j = W^0 X_{M_j}. \quad (21)$$

Step 4. After eliminating the inorganic salt scale, the three-phase flash evaporation was used to determine the molar content (V', L', and W') of each phase in the new gas, liquid, liquid three-phase fluid, composition (y'_i, x'_i, and w'_i), and corresponding thermodynamic parameters.

Step 5. We combine the mole content of each phase in the gas, liquid, and liquid three-phase fluid calculated by Step 4 with the inorganic salt scales calculated in Step 3 to preliminarily determine the gas, liquid, liquid,

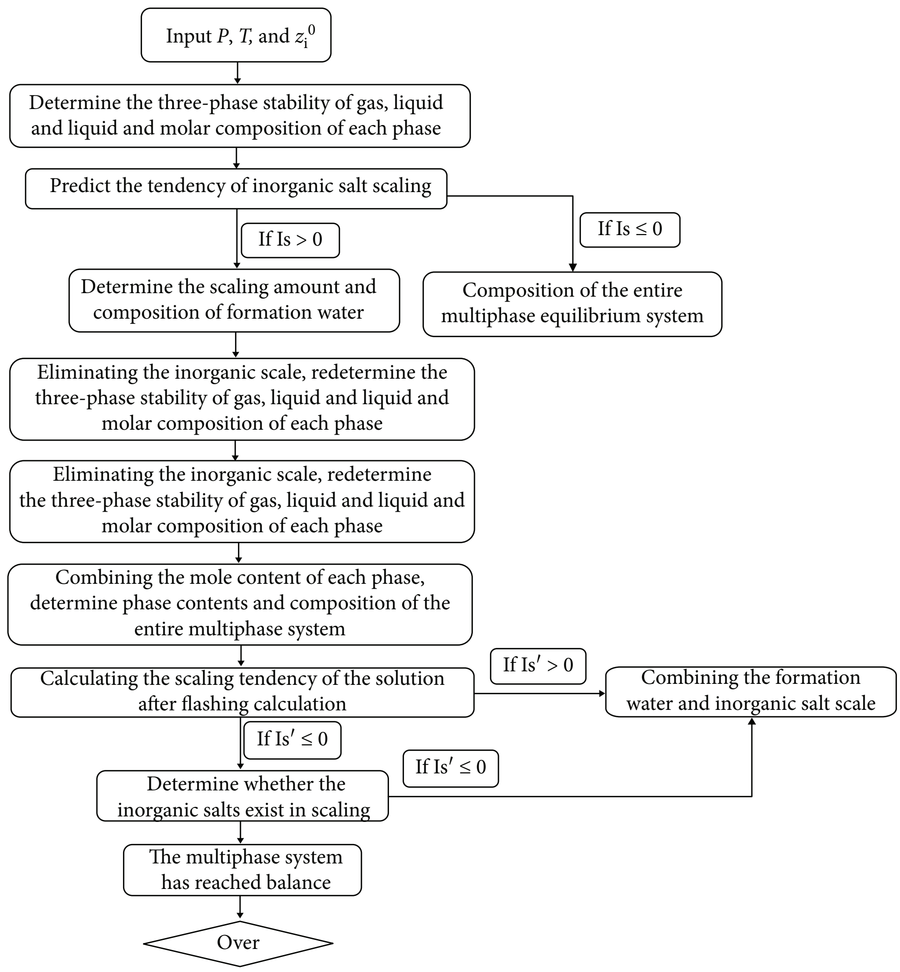

Figure 6: Flow chart of gas-liquid-liquid-solid multiphase equilibrium scale prediction.

and solid phase contents and the composition of the entire multiphase system:

$$
\begin{aligned}
V'' &= V'\left(1-\sum_{j=1}^{nm} M'_j\right),\\
L'' &= L'\left(1-\sum_{j=1}^{nm} M'_j\right),\\
W'' &= W'\left(1-\sum_{j=1}^{nm} M'_j\right),\\
M''_j &= M'_j,\\
z''_i &= V'\left(1-\sum_{j=1}^{nm} M'_j\right)y'_i + L'\left(1-\sum_{j=1}^{nm} M'_j\right)x'_i\\
&\quad + W'\left(1-\sum_{j=1}^{nm} M'_j\right)w'_i + \sum_{j=1}^{nm} M'_j m_{ij} = V''y'_i\\
&\quad + L''x'_i + W''w'_i + \sum_{j=1}^{nm} M''_j m_{ij}.
\end{aligned}
\tag{22}
$$

Table 4: Composition of injection water.

Ion	Content (mg/l)	Ion	Content (mg/l)
Na^+	13400	Cl^-	19840
K^+	310	SO_4^{2-}	2470
Ca^{2+}	620	HCO_3^-	132
Mg^{2+}	15.42	NO_3^-	754
Sr^{2+}	0		

Step 6. We calculate the scaling tendency of the solution after flashing calculation in Step 4. If the I_s of the existing inorganic salt that has been scaled reached $I_s = 0$ and the I_s of the inorganic salt that has not been scaled reached $I_s \leq 0$, then the formation water was in a chemical equilibrium state and the entire gas-liquid-liquid-solid system has reached equilibrium, and the calculation results from Step 4 was the balanced composition of the multiphase system under the current conditions and it is not necessary to continue calculation. If $I_s > 0$, it means that the formation water was still in a state of supersaturation and the amount of scaling needs to be recalculated.

Table 5: Comparative analysis of scale amount in electrolyte solution.

Mass fraction (%)	Scale amount (mg/l) Experimental results	Prediction results under phase equilibrium	Prediction results without phase equilibrium	Error (%) Model without phase equilibrium	Model with phase equilibrium
0	0.00	0.00	0.00	0.00	0.00
10	360.02	370.24	370.54	2.70	2.70
20	330.54	320.21	340.74	3.00	3.00
30	260.17	250.54	250.35	3.80	3.80
40	210.32	220.87	210.21	4.70	0.00
50	160.28	140.03	150.32	12.50	6.20
60	130.14	110.58	120.33	15.30	7.60
70	100.70	80.31	90.91	20.00	10.00
80	70.21	60.68	75.35	14.20	7.10
90	40.36	50.25	45.23	25.00	12.50
100	0.00	0.00	0.00	0.00	0.00

Table 6: Comparative analysis of the predicted scale amount of BS8 reservoir fluid and the experiment data.

Temperature (°C)	Pressure (MPa)	Scale amount (mg/l)			Error (%)	
		Experimental results	Prediction results under phase equilibrium	Prediction results without phase equilibrium	Model with phase equilibrium	Model without phase equilibrium
171.4	43.57	1.36	1.42	0.85	4.44	67.27
	30	8.98	8.83	7.90	1.69	10.38
	20	14.52	13.89	12.71	4.35	8.12
	11.5	88.59	90.18	70.49	1.79	22.23
	5	281.67	292.98	216.10	4.01	27.29
155	30	1.24	1.22	0.38	1.62	67.31
	20	6.70	6.72	5.67	0.18	15.63
	11.5	12.36	11.65	9.91	5.73	14.07
	5	144.32	141.93	95.39	1.66	32.24
135	5	8.13	7.71	2.36	5.25	65.74

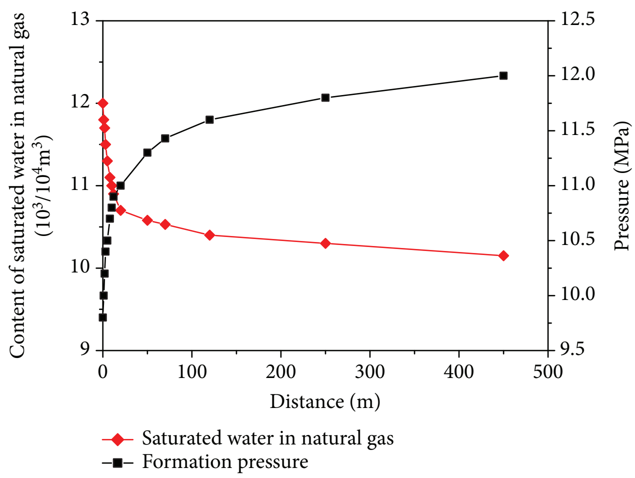

Figure 7: Saturated water content distribution curve of BS8 formation gas.

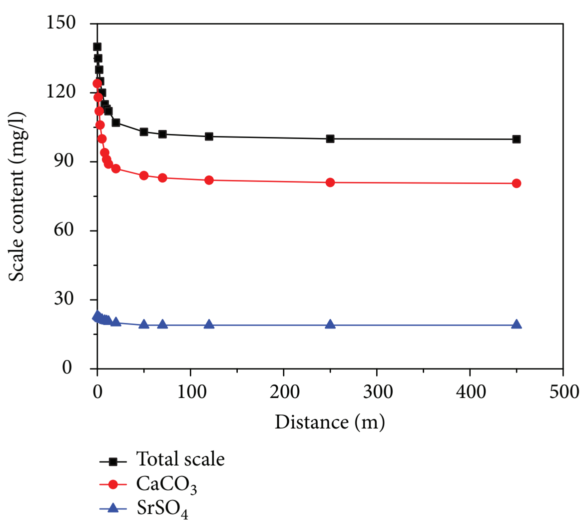

Figure 8: Balanced scaling amount in BS8 formation water.

If $I_s < 0$, the amount of inorganic salt that is calculated in Step 3 is too high and needs to be recalculated.

Step 7. We combine the formation water that was still in a nonchemical equilibrium state with the inorganic salt scale. Then, the formation water that was still in a nonchemical equilibrium state is combined with the inorganic salt scale. Steps 3-6 are then repeated to have the chemical balance of the formation fluid calculation, and the multiphase flash calculation of gas, liquid, and liquid until the total system is balanced.

4. Validation and Application

4.1. Model Validation. The prediction of inorganic salt scaling in an electrolyte solution is an important part of the Multiphase Equilibrium Prediction model. The accuracy of this part is of great significance to the comprehensive prediction of formation fluid. Based on the data of formation water and injected water in the Qianmiqiao reservoir, the scaling of formation water and injected water mixtures is predicted by using the model established above. Afterwards, the model outcomes were compared with the experimental data and the predicted values of the Oddo-Tomson model, respectively. In the simulation, the pressure and temperature were 10 MPa and 171.4°C, respectively, and the composition of formation water is shown in Table 1. Besides this, the composition of injection water is shown in Table 4.

By comparing the experimental value of electrolyte solution scaling, the predicted value was calculated by applying the Oddo-Tomson model as shown in Table 5. It can be concluded that the predicted values of the Oddo-Tomson model and the established model were close to the experimental value with an error of 9.2% and 3.2%, respectively. The Oddo-Tomson saturation index was a common method to predict the scale amount in an electrolyte solution. However, the new model had a higher accuracy in predicting electrolyte scaling, which indicated that it was feasible to predict inorganic salt scaling in an electrolyte solution by using this model in the Multiphase Equilibrium scaling prediction.

The proposed model for predicting multiphase equilibrium fouling and the prediction model of formation water scaling based on the Oddo-Tomson saturation index were applied to predict the scale of the fluid in the BS8 well fluid under experimental conditions, and the predicted results were compared with the experimental result to verify the reliability of the proposed model. From the results (Table 6), it is demonstrated that the predictive value of scale in the proposed multiphase equilibrium scaling model was close to the experimental results, with an average deviation of 3.5%. In comparison, the prediction results of the model based on the Oddo-Tomson saturation index was significantly lower than the experimental values, and the average error was 30%. The reliability of the proposed model was verified. The advantage of the proposed model was that the phase change of the reservoir fluid can be described accurately, which was necessary to predict the amount of scaling in a gas reservoir. In comparison, the model based on the Oddo-Tomson saturation index ignored the influence of phase change on scaling. In the simulation, the compositions of formation water, natural gas, and condensate oil are shown in Tables 1–3. When the temperature was 171.4°C, the scale amount under 5 different pressure values (43.57 MPa, 30 MPa, 20 MPa, 11.5 MPa, and 5 MPa) was predicted. When the temperature was 155°C, the scale amount under 4 different pressure values (30 MPa, 20 MPa, 11.5 MPa, and 5 MPa) was predicted. When the temperature was 135°C, the scale amount under 5 MPa was predicted.

4.2. Application. The multiphase equilibrium scaling model was used to predict the inorganic salt scaling and fluid phase changes in the BS8 wellbore and formation. At present, the wellhead pressure was 3 MPa and the temperature was 60°C. The other production data were described above. The prediction results are shown in Figures 7–10. As demonstrated in Figure 7, it could be seen that the pressure of BS8

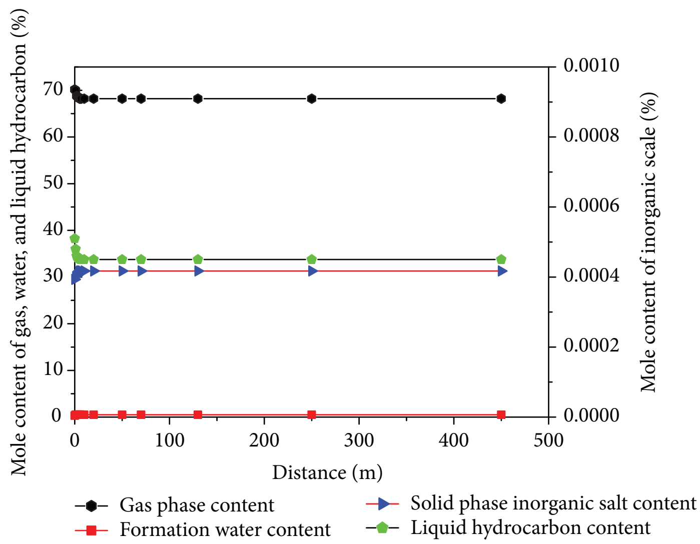

Figure 9: Phase distribution of BS8 fluid in formation.

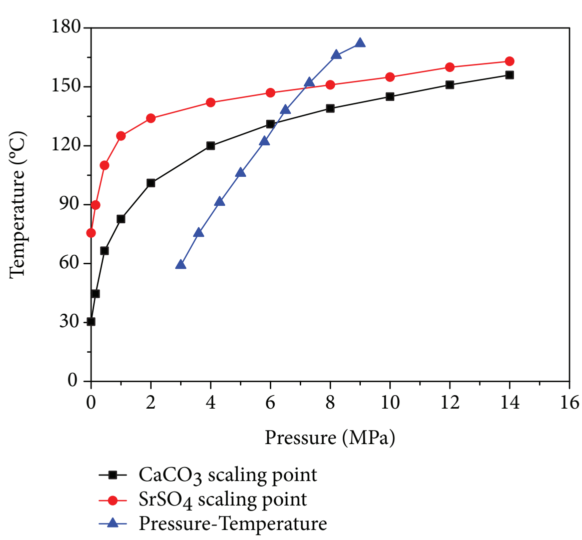

Figure 10: Scaling points of BS8 formation fluid.

decreased continuously from the near-wellbore area, and the pressure reduction caused the formation water to evaporate into the natural gas. The closer to the wellbore, the higher the saturated water content of the natural gas was. According to the prediction, the saturated water content at the bottom of the well reached 12%. As indicated in Figure 8, much $CaCO_3$ and a little of $SrSO_4$ scale were generated in the current formation under equilibrium conditions. With the decrease of the formation pressure, the amount of scale increased from the formation to the near-wellbore area, and the total inorganic salt scale at the bottom of the well reached 133.8 mg/l. As indicated in Figure 9, the molar content of the gas phase and inorganic salt in the formation fluid increased with the decrease of pressure, and the molar content of free formation water continuously decreased. From the prediction of the scaling pressure and temperature curve of the inorganic salt in the BS8 formation fluid (Figure 10), it indicated that the temperature of the $SrSO_4$ scaling point was lower than that of $CaCO_3$ at the same pressure. When the temperature and pressure curves were above the scaling point, the corresponding inorganic salt scale would be generated in the fluid. Currently, the $SrSO_4$ scale was formed at the depth of 2700 m in the BS8 well, while the $CaCO_3$ scale was produced at a well depth of about 3000 m. With the decrease of the wellbore temperature, the amount of inorganic salt from the bottom to the wellhead continuously decreased.

5. Conclusion

(1) A set of experimental devices for testing the amount of inorganic salt scales in formation fluids under high-temperature and high-pressure conditions was developed. The high-temperature and high-pressure phase analysis and scaling test of the actual gas reservoir fluid in the BS8 well were carried out by the devices. The experimental results demonstrated that with the decrease of formation pressure, the dissolved gas volume of formation water decreased, while the saturated water content in natural gas increased. In addition, two kinds of $CaCO_3$ scale and $SrSO_4$ scale were generated in the gas reservoir fluid under experimental conditions. The amount of fouling increased with the decrease of pressure and increased with the increase of temperature. The change of scaling with the pressure and temperature in the actual gas reservoir is more obvious than the degassing formation water

(2) A new model for predicting the scale of inorganic salts in gas-liquid-liquid-solid multiphase equilibria is established. According to the composition characteristics of gas reservoir fluid, the chemical equilibrium calculation of the inorganic salt scaling under

the condition of gas, liquid, and liquid equilibrium is put forward. The method can simplify the complicated problem of directly solving the phase equilibrium system of a chemical reaction

(3) The new multiphase equilibrium scaling model was proposed which can accurately predict the amount of inorganic salt scale in the actual gas reservoir fluid. The prediction results were close to the experimental data with an average deviation of 3%. In comparison, the prediction results of models that did not consider phase changes were significantly lower than the experimental data, and the average deviation was about 30%. To accurately predict the amount of scaling in gas reservoir fluids, it is necessary to consider the changes in the phase state of the fluid

(4) Through the prediction of the scaling in the BS8 well, much $CaCO_3$ and a little of $SrSO_4$ scale were generated in the current formation under equilibrium conditions. With the decrease of the formation pressure, the amount of scale increased from the formation to the near-wellbore area, and the total inorganic salt scale at the bottom of the well reached 133.8 mg/l

Abbreviation

PVT: Pressure, volume, and temperature relationship.

Data Availability

The data for the paper can be accessed through the following link: https://www.dropbox.com/s/eo9n49ss8pqssyl/data.xlsx?dl=0.

Conflicts of Interest

The authors declare that they have no conflicts of interest.

Acknowledgments

The authors express their appreciation to the National Science and Technology Major Project (No. 2009ZX05009), a project of the China Natural Science Foundation (50774091), for financially supporting this work. The authors also express their appreciation to the support from the China Postdoctoral Science Foundation (2018M631765). At the same time, we would like to thank Nasir Khan for his help in the process of writing the manuscript and Wang Yong and Jianshe Feng for the samples they provided during the experiment.

References

[1] G. Jing, S. Tang, X. Li, and H. Wang, "The analysis of scaling mechanism for water-injection pipe columns in the Daqing Oilfield," *Arabian Journal of Chemistry*, vol. 10, pp. S1235–S1239, 2017.

[2] S. Muryanto, A. P. Bayuseno, H. Ma'mun, M. Usamah, and J. Jotho, "Calcium carbonate scale formation in pipes: effect of flow rates, temperature, and malic acid as additives on the mass and morphology of the scale," *Procedia Chemistry*, vol. 9, pp. 69–76, 2014.

[3] M. Salman, H. Qabazard, and M. Moshfeghian, "Water scaling case studies in a Kuwaiti oil field," *Journal of Petroleum Science and Engineering*, vol. 55, no. 1-2, pp. 48–55, 2007.

[4] N. Wang, D. Z. Chen, and L. S. Zou, "Influence of non-thermal plasma pre-treatment on the scaling characteristics of viscous oil wastewater during evaporation," *Applied Thermal Engineering*, vol. 75, pp. 779–788, 2015.

[5] S. M. Peyghambarzadeh, A. Vatani, and M. Jamialahmadi, "Application of asymptotic model for the prediction of fouling rate of calcium sulfate under subcooled flow boiling," *Applied Thermal Engineering*, vol. 39, pp. 105–113, 2012.

[6] S. M. Alsadaie and I. M. Mujtaba, "Dynamic modelling of heat exchanger fouling in multistage flash (MSF) desalination," *Desalination*, vol. 409, pp. 47–65, 2017.

[7] I. Babuška, R. S. Silva, and J. Actor, "Break-off model for $CaCO_3$ fouling in heat exchangers," *International Journal of Heat and Mass Transfer*, vol. 116, pp. 104–114, 2018.

[8] C. S. Bandi, R. Uppaluri, and A. Kumar, "Global optimization of MSF seawater desalination processes," *Desalination*, vol. 394, pp. 30–43, 2016.

[9] Y. Fu, W. van Berk, and H.-M. Schulz, "Temporal and spatial development of scale formation: one-dimensional hydrogeochemical transport modeling," *Journal of Petroleum Science and Engineering*, vol. 112, pp. 273–283, 2013.

[10] N. Andritsos and A. J. Karabelas, "The influence of particulates on $CaCO_3$ scale formation," *Journal of Heat Transfer*, vol. 121, no. 1, pp. 225–227, 1999.

[11] M. Haghshenasfard, G. H. Yeoh, M. Dahari, and K. Hooman, "On numerical study of calcium sulphate fouling under sub-cooled flow boiling conditions," *Applied Thermal Engineering*, vol. 81, pp. 18–27, 2015.

[12] A. R. Konak, "A new model for surface reaction-controlled growth of crystals from solution," *Chemical Engineering Science*, vol. 29, no. 7, pp. 1537–1543, 1974.

[13] G.-M. Zhang, G.-Q. Li, W. Li, Z. Zhang, X.-l. Leng, and M.-c. Tian, "Particulate fouling and composite fouling assessment in corrugated plate heat exchangers," *International Journal of Heat and Mass Transfer*, vol. 60, pp. 263–273, 2013.

[14] M. Amiri, J. Moghadasi, M. Jamialahmadi, and M. P. Shahri, "Prediction of the amount of calcium carbonate scale formation in Iranian oilfields at different pressures," *Energy Sources, Part A: Recovery, Utilization, and Environmental Effects*, vol. 35, no. 13, pp. 1197–1209, 2013.

[15] J. W. Ryznar and W. F. Langelier, "A new index for determining amount of calcium carbonate scale formed by a water," *Journal American Water Works Association*, vol. 36, no. 4, pp. 472–483, 1944.

[16] W. N. Al Nasser and F. H. Al Salhi, "Scaling and aggregation kinetics determination of calcium carbonate using inline technique," *Chemical Engineering Science*, vol. 86, pp. 70–77, 2013.

[17] Y. Zhang, H. Shaw, R. Farquhar, and R. Dawe, "The kinetics of carbonate scaling—application for the prediction of downhole carbonate scaling," *Journal of Petroleum Science and Engineering*, vol. 29, no. 2, pp. 85–95, 2001.

[18] J. Bourland, *Le syndrome de prader-labhart-willi: à propos de quatre observations, dont trois d'une même fratrie*, Journal of Neuroradiology, 2018.

Hindawi
Geofluids
Volume 2019, Article ID 4125363, 14 pages
https://doi.org/10.1155/2019/4125363

Research Article

Wear Mechanism of Abrasive Gas Jet Erosion on a Rock and the Effect of Abrasive Hardness on It

Yong Liu,[1,2] Huidong Zhang,[1,2] Pathegama Gamage Ranjith,[3] Jianping Wei,[1,2] and Xiaotian Liu[4]

[1]*State Key Laboratory Cultivation Base for Gas Geology and Gas Control, Henan Polytechnic University, Jiaozuo, 454000 Henan, China*
[2]*The Collaborative Innovation Center of Coal Safety Production of Henan Province, Jiaozuo, 454000 Henan, China*
[3]*Deep Earth Energy Laboratory, Department of Civil Engineering, Monash University, Building 60, Melbourne, Victoria 3800, Australia*
[4]*Safety Technology Training Institute, Henan Polytechnic University, Jiaozuo, 454000 Henan, China*

Correspondence should be addressed to Yong Liu; yoonliu@126.com

Received 22 September 2018; Revised 24 November 2018; Accepted 17 December 2018; Published 7 February 2019

Guest Editor: Andrew Bunger

The existing erosion models of abrasive gas jet tend to neglect the effects of the rebounding abrasive. To address this shortcoming, abrasive wear tests were conducted on limestone by using an abrasive gas jet containing different types of particles and with different standoff distances. The results indicate that erosion pits have the shape of an inverted cone and a hemispherical bottom. An annular platform above the hemispherical bottom connects the bottom with the side of the pit. The primary cause of the peculiar pit shape is the flow field geometry of the gas jet with its entrained particles. There is an annular region between the axis and boundary of the abrasive gas jet, and it contains no abrasive. Particles swirling around the axis form a hemispherical bottom. After rebounding, the abrasive with the highest velocity enlarges the diameters of both the hemispherical bottom and erosion pit and induces the formation of an annular platform. The surface features of different areas of the erosion pit are characterized using a scanning electron microscope (SEM). It can be concluded that the failure modes for different locations are different. The failure is caused by an impact stress wave of the incident abrasive at the bottom. Plastic deformation is the primary failure mode induced by rebounding particles at the sides of the hemispherical bottom. The plastic deformation induced by the incident abrasive and fatigue failure induced by the rebounding abrasive are the primary failure modes on the annular platform. Fatigue failure induced by rebounding particles is the primary mode at the sides of the erosion pits. The rock failure mechanism that occurs for particles with different hardness is the same, but the rock damaged by the hard abrasive has a rougher surface.

1. Introduction

Abrasive gas jets are widely used in surface treatment engineering such as in drilling and lacquer and rust removal from metals and ceramics [1–3]. In recent years, they have been introduced in unconventional oil and gas production [4–6]. In particular, the abrasive gas jet can assist in drilling coalbed methane, can avoid problems that often occur in water jet-assisted drilling such as borehole collapse, and have broad application prospects [7, 8]. An important theoretical basis for the application of an abrasive gas jet is the clarification of its erosive wear mechanism on a rock. The existing abrasive-impact rock-breaking mechanisms are classified into two categories. In one type of mechanism, the focus is primarily on crack propagation on the surface and inside of the rock induced by the abrasive impacting the rock [9–12]. The concept of this rock failure mechanism is that when the abrasive impacts a rock, a stress concentration occurs on its contact surface, which leads to cracks on the rock surface. A part of the load propagates into the rock in the form of a stress wave and is superimposed on the crack surface of the rock, thus resulting in shear failure of the rock. The other

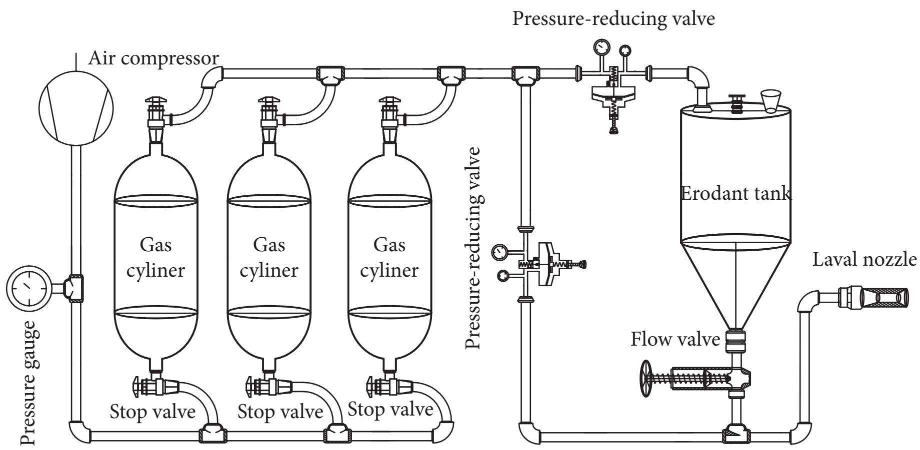

Figure 1: Schematic of connections in the high-pressure gas jet erosion system.

mechanism focuses on erosive wear. Analyzing the erosion morphology of a rock surface requires an understanding of the erosion wear mechanism of the abrasive. Intergranular brittle fracture and plastic flow are the two main mechanisms of material failure due to abrasive impact. Intergranular fracture is dominant during vertical impacts. However, both mechanisms play an equally important role in the case of a small-incident-angle impact [13–15]. Momber compared and analyzed the erosion wear characteristics of four types of rocks: porphyric rhyolite, Portuguese granite, Jurassic limestone, and argillaceous schist. He concluded that the surfaces of porphyric rhyolite and Portuguese granite showed lateral fractures. Lateral fractures, pileup, and lip formation were exhibited on the surfaces of Jurassic limestone and argillaceous schist. Plastic deformation was found to play a major role in schist erosion. Moreover, the rock-erosion wear formula considering plastic deformation and lateral cracking was established [16–20]. Regardless of the mechanism used for analyzing rock failure, it is necessary to first clarify and define the impact force of the abrasive. Numerous factors affect the impact force of an abrasive, such as the jet incidence pressure, erodent mass flow, and standoff distance. These three factors determine the velocity of an abrasive when it impacts a rock. However, in addition to the abrasive speed, the erosion wear of a rock is also related to the abrasive characteristics, such as its size, hardness, and shape. Therefore, it is difficult to describe the erosion wear mechanism of a rock using formulas. The existing erosion wear formulas only consider the primary erosion and neglect the effect of secondary erosion induced by rebounding particles. An abrasive impacts a rock surface and breaks into smaller abrasives, which rebound under the reacting force. These rebound abrasives can cut the rock effectively. Brown et al. believed that the effect of secondary erosion should not be neglected in high-angle erosion [21].

Deng et al. showed that there is a significant reduction in the specific erosion rate for high particle concentrations. This reduction was considered to be a result of the shielding effect induced by rebounding particles during particle impacts [22]. Macchini et al. also believed that the cause of shielding is the increased likelihood of interparticulate collisions, i.e., the high collision probability between incoming and rebounding particles that reduces the frequency and the severity of particle impacts on the target surface [23]. The results of the study of Nguyen et al. also show that the change in erosion rates with the particle mass flow has been attributed to rebounding particles interfering with incident particles, resulting in a lower erosion rate [24]. In addition to the shielding effect, the collision frequency of particles when moving inside the system is another critical factor. It is believed that a strong interaction often happens at a higher impinging angle as well as at a higher particle mass flow or higher impinging velocity [25, 26]. A strong particle-particle interaction can cause a reduction in energy transfer to the surface, which, in turn, leads to a reduction in the erosion rate. Both the shielding effect and particle-particle interaction cause energy and velocity loss in the particle-surface collision [27]. Erosive gas jet-assisted drilling is mostly perpendicular erosion. Therefore, the effects of secondary erosion and rebound abrasive on the velocity of the incident abrasive and rock erosion cannot be ignored.

In this work, to clarify and define the erosion wear mechanism of a rock induced by abrasive gas jet, the erosion wear characteristics of the rock were analyzed by experiments along with the effect of the abrasive type. The failure characteristic of the rock surface eroded by abrasive gas jet was examined via a scanning electron microscope (SEM).

2. Erosion Experiment

2.1. Experimental System. A high-pressure experimental abrasive gas jet system is used for the experiment. It consists of a high-pressure air compressor, high-pressure gas cylinder, digital pressure gauge, pressure control valve, gate valve, abrasive tank, and operation box. The high-pressure air compressor has a maximum pressure of 40 MPa and maximum air intake of 2 m^3/min, whereas the high-pressure gas cylinder has a maximum allowable pressure of 40 MPa. The system devices are connected as shown in Figure 1. The nozzle used is a Laval nozzle, whose structural parameters are displayed in Figure 2. Before the experiment, high-pressure gas is stored in the high-pressure gas cylinder and the outlet pressure is adjusted with the pressure-regulating valve. The inlet pressure ranges between 0 and 40 MPa, whereas

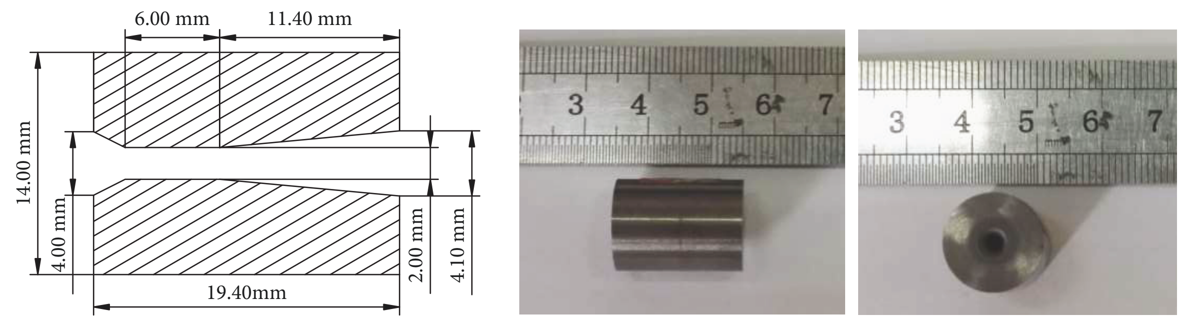

Figure 2: Nozzle structure parameters.

Table 1: Experimental parameters.

Pressure (MPa)	Abrasive	Abrasive mesh	Abrasive mass flow (g/s)	Standoff distance (mm)
15	Quartz sand/garnet/brown aluminum oxide/silicon carbide	80	16	100
15	Quartz sand/garnet/brown aluminum oxide/silicon carbide	80	16	120
15	Quartz sand/garnet/brown aluminum oxide/silicon carbide	80	16	150
15	Quartz sand/garnet/brown aluminum oxide/silicon carbide	80	16	200

the outlet pressure ranges between 0 and 25 MPa. The pressure-regulating valve, which has an adjustable outlet pressure accuracy of 0.1 MPa, can accurately control the jet pressure, thereby ensuring a constant jet pressure during the experiment to meet the experimental requirements. The high-pressure gate valve is installed below the abrasive tank to precisely control the mass flow rate of the abrasive. This gate is suitable for controlling the flow of the solid particles under high-pressure conditions. Before the experiment, the gate valve scale for the mass flows of the different abrasive is determined by calibration.

2.2. Experimental Parameters. Because numerous factors affect the erosion effect, e.g., the abrasive diameter, abrasive shape, and abrasive hardness [28–31], the experimental parameters of the abrasive and gas jet should be determined along with the engineering characteristics and technological status of erosive gas jet-assisted drilling. At present, widely used abrasives include quartz sand, garnet, brown corundum, and silicon carbide. From the perspective of hardness, brown corundum (Mohs hardness: 9) and silicon carbide (Mohs hardness: 9.5) have a better erosion effect than garnet (Mohs hardness: 8) and quartz sand (Mohs hardness: 7) but they have a greater negative effect on the service life of the nozzle [32–34]. An abrasive has an optimal particle size such that as the particle size increases, the erosion volume and depth first increase and then decrease [35, 36]. The maximum pressure of the existing high-pressure air compressor is up to 90 MPa, but its air inflow is low. Assisted drilling requires a high air inflow to remove the rock fragments well. An effective approach to achieve a high air inflow is decreasing the pressure of the air compressor. In the research results of Liu et al. and Wen et al. [7, 37, 38], the critical pressure for limestone breakage by abrasive gas jet was 15 MPa, which was set as the outlet pressure of the air compressor. The optimal abrasive size and mass flow were 80 meshes and 16 g/s, respectively, when the gas pressure was 15 MPa. In addition to the jet and abrasive parameters, the standoff distance is an important factor affecting the erosion of the rock. The standoff distance essentially governs the impact velocity of the abrasive and thereby affects rock erosion. An abrasive is mainly accelerated in the nozzle and potential core of a free jet. The velocity of an abrasive increases continually in the potential core of the free jet section of a gas jet until a force, such as the drag force, virtual mass force, and pressure gradient force, cannot make the abrasive accelerate further. The standoff distance determines the acceleration length of the abrasive. At the optimal standoff distance, the abrasive can accelerate to the maximum velocity. Typically, if the standoff distance is optimal, the efficiency of rock breakage is the highest. However, this is impossible in engineering applications. The standoff distance depends on the length of the potential core; however, its length is not greater than the length of the potential core. In addition, the length of the potential core increases with the increase in the gas jet pressure. Therefore, it can be understood that the standoff distance indirectly depends on the gas pressure. The present research shows that the abrasive velocity reaches the maximum at a standoff distance of 100 mm when the jet pressure is 15 MPa and the mass flow of the abrasive is 16 g/s. However, it is difficult to maintain the standoff distance optimally and invariantly during operation. Consequently, the erosion wear characteristics of the rock need to be analyzed at different standoff distances. The experimental parameters are listed in Table 1.

2.3. Experimental Phenomena. Because many researchers have performed numerous interesting and relevant studies on the effect of the abrasive and gas jet parameters on the erosion wear depth and volume, these parameters are not analyzed in this study. This paper focuses on the failure models of a rock eroded by abrasive gas jets and the mechanisms of

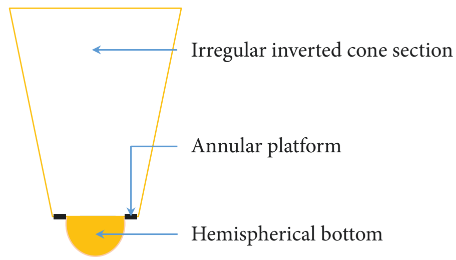

Figure 3: Schematic of the erosion pit.

the different failure models of the rock. The erosion characteristic of the rock sample reveals the occurrence of an interesting phenomenon in the erosion pits of the selected four types of abrasive at any standoff distance. Taking as an example a rock sample eroded by garnet abrasive to introduce this phenomenon shows that, generally, the erosion pit has an irregular conical shape. However, the shape of the bottom of the erosion pit is completely different from that obtained with a water jet or other jets. The bottom of the erosion pit is hemispherical. There is an annular platform above the hemispherical bottom that connects the bottom and side of the erosion pit, as shown in Figure 3. Figure 4 presents the shape of the erosion pit at different standoff distances.

The shape of the erosion pit is basically the same at different standoff distances. The upper part of the erosion pit has an inverted conical shape. An annular platform and a hemispherical bottom are located below the inverted conical shape. When the standoff distance is short, the diameter of the mouth of the erosion pit is short and the erosion pit is deep. With the increase in the standoff distance, the diameter of the mouth of the erosion pit increases and the depth decreases. When the standoff distance is 100 mm, the diameter of the mouth is 34.5 mm and the erosion depth is 34.34 mm. When the standoff distance is increased to 200 mm, the diameter of the mouth is 55.8 mm and the erosion depth is 25.4 mm. The width of the annular platform increases with the standoff distance. The width of the annular platform at the four standoff distances is 1.36 mm, 5.24 mm, 8.78 mm, and 10.5 mm, respectively. The depth of the hemispherical bottom is 6 mm, 7 mm, 8 mm, and 6.2 mm, respectively, and the erosion is the deepest at the standoff distance of 150 mm.

2.4. Analysis of Experimental Phenomenon. The distinct shape of the erosion pit of an abrasive gas jet is induced by the combination of the erosion of an incident abrasive and its rebound abrasive. If a rebound abrasive does not erode a rock surface, the shape of the erosion pit will be consistent with the sectional shape of the gas jet, as shown in Figure 5(a). After the erosion of a rock, the impact energy divides the abrasive into smaller pieces, which causes them to rebound with high velocity. A rebound abrasive continually erodes the wall of the erosion pit, increasing the pit's diameter, as shown in Figure 5(b). Therefore, the shape of the erosion pit depends on the gas jet shape and rebound abrasive. To clarify and define the effect of the gas jet and rebound abrasive on the shape of the erosion pit, the flow field structure of the gas jet and characteristics of the motion of the abrasive were numerically simulated in Fluent.

2.4.1. Numerical Simulation Model. The numerical simulation geometric model as designed based on the erosion parameters, such as the erosion pit parameters and nozzle parameter, and at a standoff distance of 100 mm is depicted in Figure 6. A structured grid is used for mesh division and the mesh number is 23160 based on the mesh sensitivity analysis. The inlet and outlet boundaries are the pressure inlet and outlet, respectively, and the wall surface is a nonslip wall. The inlet pressure is the same with the experiment pressure. The boundary condition of the erosion pit is a reflection wall. The discrete-phase reflection coefficient is used to represent the change in momentum after particle impact, which is calculated by a polynomial in terms of impacting angle. All the inlet temperatures are 300 K and outlet pressures are 0.1 MPa; the garnet abrasive is 3500 kg/m^3 and its diameter is 180 μm. The initial velocity of the abrasive depends on the gas jet velocity. The gas and solid phases are calculated based on a continuous-phase model and a discrete-phase model (DPM), respectively. After the gas phase becomes convergent and stable, the DPM starts to calculate the parameters of the abrasive, such as the velocity and spatial location.

In this study, for the gas phase, the RNG $k-\varepsilon$ turbulence model can simulate, among other properties, the high-Reynolds number flow of the jets. The gas is assumed to be an ideal gas. The governing equations for the RNG $k-\varepsilon$ turbulence model are [39]

$$\begin{aligned}\frac{\partial(\rho k)}{\partial t}+\frac{\partial(\rho k u_i)}{\partial x_i}&=\frac{\partial}{\partial x_j}\left(\alpha_k\mu_{\text{eff}}\frac{\partial k}{\partial x_j}\right)+G_k+G_b\\&\quad-\rho\varepsilon-Y_M+S_k,\\\frac{\partial(\rho\varepsilon)}{\partial t}+\frac{\partial(\rho\varepsilon u_i)}{\partial x_i}&=\frac{\partial}{\partial x_j}\left(\alpha_\varepsilon\mu_{\text{eff}}\frac{\partial\varepsilon}{\partial x_j}\right)+C_{1\varepsilon}\frac{\varepsilon}{k}\left(G_k+C_{3\varepsilon}G_b\right)\\&\quad-C_{2\varepsilon}\rho\frac{\varepsilon^2}{k}-R_\varepsilon+S_\varepsilon,\end{aligned}\tag{1}$$

where

$$\begin{aligned}\mu_{\text{eff}}&=\mu+\mu_t,\\\mu_t&=\rho C_\mu\frac{k^2}{\varepsilon},\\G_b&=\varphi g_i\frac{\mu_t}{\text{Pr}_t}\frac{\partial T}{\partial x_i},\\G_k&=-\rho\overline{u_i'u_j'}\frac{\partial u_j}{\partial x_i},\\Y_M&=2\rho\varepsilon\frac{k}{a^2},\\R_\varepsilon&=\frac{C_\mu\rho\eta^3\left(1-(\eta/\eta_0)\right)}{1+\beta\eta^3}\frac{\varepsilon^2}{k},\\\eta&=\frac{Sk}{\varepsilon}.\end{aligned}\tag{2}$$

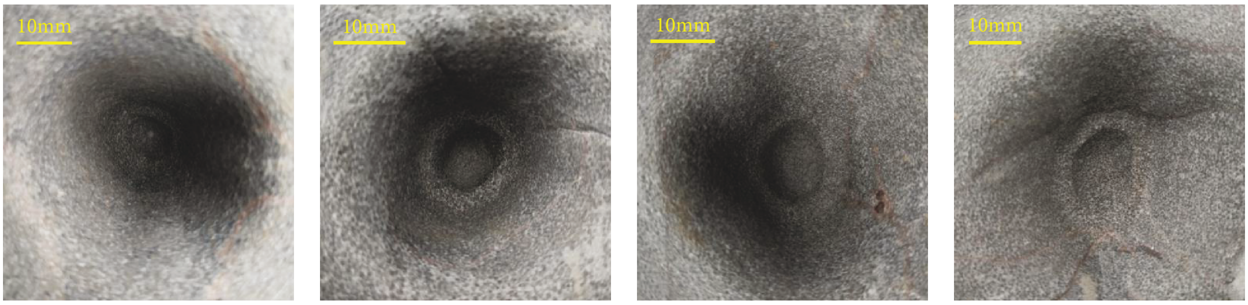

(a) 100 mm (b) 120 mm (c) 150 mm (d) 200 mm

Figure 4: Features of the erosion pit at various standoff distances.

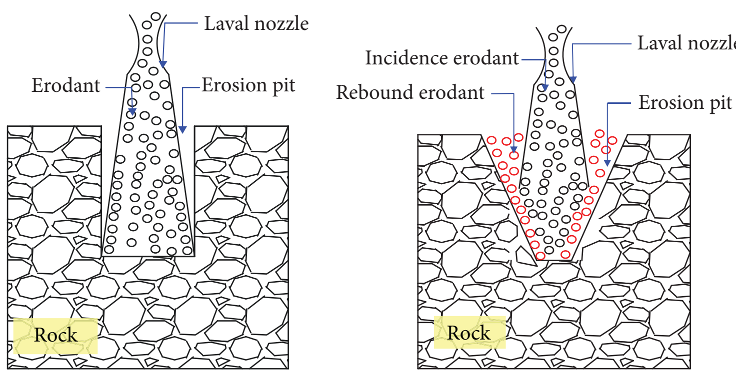

(a) (b)

Figure 5: Schematic of the erosion pit feature: (a) is a hypothetical erosion pit feature without considering the rebound abrasive and (b) is a real erosion pit feature considering the reflection abrasive.

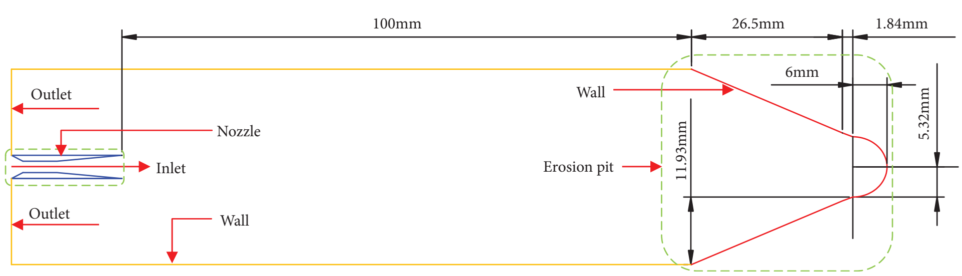

Figure 6: Numerical simulation geometric model.

ρ is density; k is turbulent kinetic energy; ε is the dissipation rate of k; t is time; x_i are the Cartesian coordinates; u_i and u_j are velocity components along i and j, which are subscripts of tensors instead of tensors; μ is gas viscosity; μ_t is eddy viscosity; G_k is the generation term of the turbulent kinetic energy k resulting from the mean velocity gradient; G_b is the generation term of the turbulent kinetic energy owing to buoyancy; Y_M is the contribution of the fluctuating dilatation in compressible turbulence to the overall dissipation rate; α_k and α_ε are the reciprocals of the effective Prandtl numbers for turbulent kinetic energy and dissipation rate, respectively; Pr_t is the turbulence Prandtl number; $C_{1\varepsilon}$, $C_{2\varepsilon}$, and $C_{3\varepsilon}$ are empirical constants; g_i is the component of gravitational acceleration in the i direction; φ is the thermal expansion coefficient; and a is the acoustic velocity, S is the modulus of the mean rate-of-strain tensor, C_μ and η_0 are both constants, and S_k and S_ε are user-defined source terms.

The DPM is introduced in the solid-fluid flow to simplify the simulation of the motion in the particle phase. The DPM can be used to calculate the trajectories of a portion of the particles in the discrete phase; nevertheless, a simulation of the particle motion with a universal application value can be performed. The motion of the coal particles is defined by the Lagrangian multiphase flow model. The pressure and drag forces on the particles are calculated in a Lagrangian framework. The velocity distribution of the particles can be evaluated by the force balance on the particle. The governing equation is as follows [40–42]:

$$m_p \frac{d\vec{u}_p}{dt} = \vec{F}_D + \vec{F}_G + \vec{F}_B + \vec{F}_L + \vec{F}_{\mathrm{VM}} + \vec{F}_B + \vec{F}_P, \quad (3)$$

where m_p is the particle mass, $\vec{u}_p$ is particle velocity, $\vec{F}_D$ is drag force vector, $\vec{F}_G$ is gravity force vector, $\vec{F}_B$ is Magus buoyancy force vector, $\vec{F}_L$ is lift force vector, $\vec{F}_{\mathrm{VM}}$ is virtual mass force vector, and $\vec{F}_P$ is pressure gradient force vector.

$$F_D = \frac{3\mu_m C_D \mathrm{Re}_p}{4d_p^2 \rho_p}\left(\vec{u}_f - \vec{u}_p\right), \tag{4}$$

where u_f is the velocity of the fluid, ρ_p is the density of the particle, d_p is the diameter of the particle, μ_m is dynamic viscosity, C_D is the drag coefficient, and Re_p is the relative Reynolds number.

$$\vec{F}_G + \vec{F}_B = \frac{\left(\rho_p - \rho\right)}{\rho_p} g \cdot \vec{e}, \tag{5}$$

where $\vec{e}$ is a unit vector.

$$\vec{F}_{\mathrm{VM}} = C_{\mathrm{VM}} \frac{\rho}{\rho_p}\frac{d}{dt}\left(\vec{u}_f - \vec{u}_p\right), \tag{6}$$

where C_{VM} is the virtual mass coefficient.

$$\vec{F}_L = C_L \frac{\rho}{\rho_p}\left(\vec{u}_f - \vec{u}_p\right) \times \nabla \times \vec{u}, \tag{7}$$

where C_L is the lift coefficient.

$$\vec{F}_B = \frac{3}{2} d_p^2 \sqrt{\pi \rho \mu_m} \int_{t_0}^{t} \frac{(d/d\tau)\left(\vec{u}_f - \vec{u}_p\right)}{\sqrt{t-\tau}} d\tau, \tag{8}$$

where τ is the time variable.

$$\vec{F}_P = -V_p \nabla P, \tag{9}$$

where V_p is the particle volume.

The solid-phase angular momentum equation is

$$I\frac{d\vec{\omega}}{dt} = \vec{T}, \tag{10}$$

where I is the moment of inertia, $\vec{\omega}$ is particle angular velocity, and $\vec{T}$ is torque.

2.4.2. Analysis of Numerical Simulation Results. When the gas flows through the nozzle, the static pressure decreases gradually, which leads to the increasing of gas velocity. Because the gas velocity is less than the velocity of sound at the entrance of the nozzle, the gas accelerates in the convergent section of the nozzle. When the gas flows into the throat section, the gas accelerates in the first 1 mm. Then the acceleration is inapparent in the middle section of the throat, because the static pressure is barely changed and velocity is approximately equal to sound velocity, as shown in Figures 7(a) and 7(c). When a gas jet is ejected from a nozzle, the jet pressure decreases and the velocity increases. The gas jet compresses the surrounding air to form an expansion wave. When the static pressure of the gas jet is equal to the boundary pressure, the expansion wave reflects and superposes to form a compression wave. The expansion and compression waves alternately develop forward to form a free jet section, as shown in Figures 7(b) and 7(d). The pressure and density of the expansion and compression waves are not uniformly distributed, which induces the uneven distribution of the abrasive in the gas jet. The abrasive velocity at the axis of the jet reaches the maximum value of 290 m/s, which is higher than the velocity at the boundary of the gas jet. However, abrasives with high velocity are obviously fewer at the boundary. The primary interesting feature of the flow field structure of the abrasive gas jets is the presence of an annular region without an abrasive between the axis and boundary, as shown in Figure 8(a). When the abrasive gas jets reach the rock surface, the jet radius R_{j} is smaller than the radius R_{p} of the mouth of the erosion pit. Therefore, this verifies that the rebound abrasive mainly results in an increase in the diameter of the erosion pit. As presented in Figure 8(b), the rebound abrasive collides with the incident abrasive after impacting the rock, which reduces the velocity of the incident abrasive. In addition, with the increase in the number of rebound abrasives, the velocity of the incident abrasive continuously decreases, as shown in Figure 8(c).

The rebound of an abrasive significantly affects the shape of the erosion pit and distribution of the abrasive velocity. Therefore, the effect of the rebound abrasive cannot be ignored in the analysis of the erosion pit shape. When an abrasive exactly reaches the rock surface, in the absence of the effect of the rebound abrasive, the abrasive velocity at the axis of the jet is high. The abrasive applies an impact force on the rock surface, which is transmitted into the rock in the form of stress waves, including longitudinal, transverse, and Rayleigh waves. The longitudinal and transverse waves propagate in the rock, whereas the Rayleigh wave propagates on the rock surface. The longitudinal wave propagates within the solid in a compression-tension manner, which will generate a radial tensile stress when the wave front rapidly expands forward [11]. However, the abrasive motion in the transverse wave is perpendicular to the propagation direction, which can generate a shear stress and circumferential tensile stress in the rock [43]. The Rayleigh surface wave, with vertical and horizontal components, will accordingly induce tensile and shear stresses. The tensile and shear stresses generated by the abrasive impact may account for the initiation and extension of the cracks in the rock. Moreover, the interference and reflection of the different waves will result in the reinforcement of the stress wave, which is conducive to the generation of cracks [44].

When more abrasives simultaneously impact the rock surface, the cracks formed by the impact of each abrasive intersect with each other, which leads to rock damage.

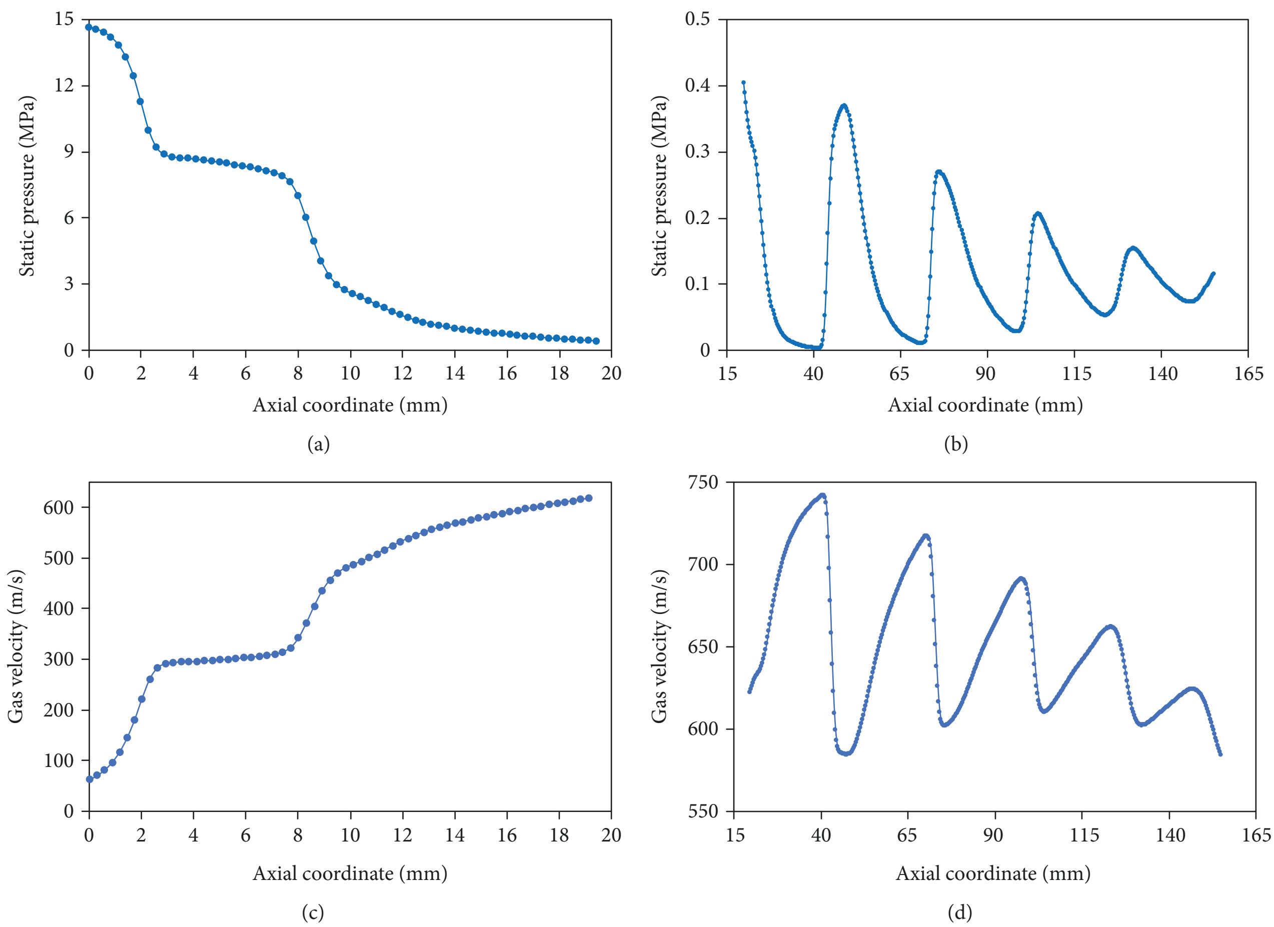

Figure 7: The static pressure and velocity of the gas jet.

Because the stress wave propagates in the rock in the form of spherical waves [45], the initial shape of the erosion pit rock surface is sphere like. After impacting the rock, the abrasive begins to rebound because of the reactive force. The abrasive is vertically incident, and the rebound angle is large. However, under the obstruction of an incident abrasive, the rebound abrasive moves along the bottom surface of the erosion pit (Figure 9(a)), secondarily erodes the surface of the erosion pit, and increases the diameter of the hemispherical bottom. With the increase in the number of rebound abrasives and depth of the erosion pit, the rebound abrasive not only erodes the side of the hemispherical bottom but also moves along the side of the erosion pit, eroding it and increasing its diameter (Figure 9(b)). Because of the presence of the annular region in the abrasive gas jets without an abrasive, the rebound abrasive tends to move toward the annular region (Figure 9(c)). The rebound abrasive in the annular region erodes the side of the erosion pit and promotes the formation of the annular platform, which connects the erosion pits between the bottom and side. Moreover, the volume and diameter of the erosion pit continuously increase. With the increase in the rebound abrasive and erosion time, the former affects the velocity of the incident abrasive more significantly. Only a small part of the incident abrasive can maintain a high velocity, continuously form cracks in the rock, and increase the diameter of the hemispherical bottom. The rebound abrasive not only affects the velocity of the incident abrasive but also leads to the randomized direction of the abrasive velocity at the bottom of the erosion pit. Only a part of the high-velocity abrasive can continue to be perpendicular to the direction of incidence and erode the erosion pit. This implies that although the rebound abrasive plays an important role in increasing the volume and diameter of the erosion pit, they have an adverse effect on the increase in the depth of the erosion pit.

The incident and rebound abrasives jointly affect rock erosion. The incident abrasive of the jet axis can form a spherical stress wave, which leads to the formation of a hemispherical bottom at the base of the erosion pit. The rebound abrasive increases the diameter of the hemispherical bottom and form an annular platform by combining the effect of the annular region of the abrasive gas jets. The annular platform connects the hemispherical bottom and side of the erosion pit; however, there is a clear boundary. The rebound abrasive that moves along the wall of the erosion pit increases its diameter.

The flow field structure of the abrasive gas jets, and the characteristics of the abrasive movement are the main reasons for the characteristics of the erosion pit. In the erosion process, some regions are eroded by the combination of the

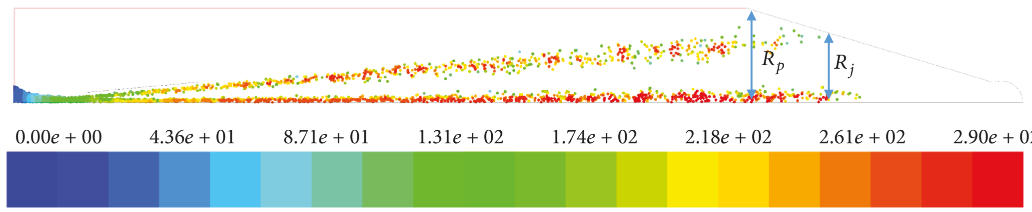

(a) The abrasive just reaches the rock surface

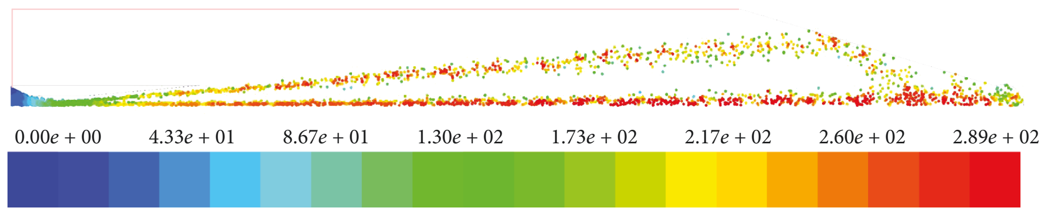

(b) The abrasive at the axis begins to rebound after eroding the rock

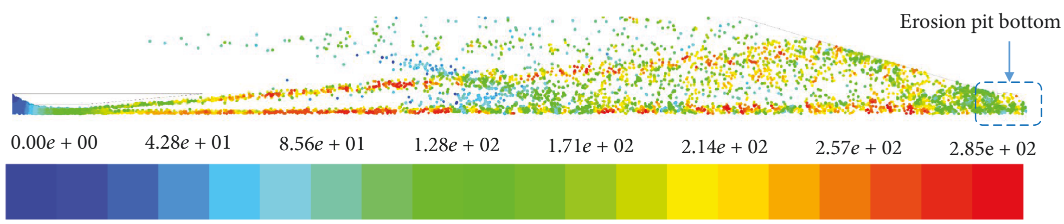

(c) The complete process of the formation of the erosion pit

Figure 8: Flow field structure and velocity distribution of the abrasive gas jets during erosion of the rock.

incident and rebound abrasives, whereas other regions are eroded separately by an incident abrasive or rebound abrasive. There is no strict distinction between an incident abrasive and a rebound abrasive for abrasive erosion, and some studies have even neglected the role of the rebound abrasive. From the above analysis, it can be seen that rebound abrasives play an important role in rock erosion. Therefore, it is necessary to analyze the erosion mechanism of the rebound abrasive.

3. Rock Erosion Mechanism

3.1. Erosion Mechanism. To clarify and define the erosion mechanism of the abrasive gas jets, the erosive rock was scanned by a SEM manufactured by the Field Electron and Ion Company. The model is FEI quanta 250FEGG, with a resolution of 2.5 nm and voltage of 10 kV. Considering as an example the rock eroded by a garnet abrasive, the base and side of the hemispherical bottom, annular platform, and erosion pit side were scanned based on the different erosion regions of the incident and rebound abrasives, respectively (Figure 10).

The result of the SEM of the limestone eroded by garnet is displayed in Figure 10. As shown in Figures 11(a)–11(d), the failure characteristics of the rocks are different in various parts of the erosion pit. Fractures (denoted as "F") and lip formation (denoted as "P") occur on the surface at the base of the hemispherical bottom, as shown in Figure 11(a) and the part marked with "△" in Figure 11(b). The fractures, which are distributed irregularly, partly connect to a larger fracture that transmits through the rock surface. The area of the rock surface without a fracture appears clearly as a discontinuous lip formation. Thus, the area without the fracture or lip formation of the rock surface is the original surface that is not eroded by the abrasive. In addition, there is no residual abrasive at the base of the hemispherical bottom. The results of the SEM and numerical simulation of the abrasive motion characteristics can reveal the mechanism of rock erosion by abrasive gas jets. It is known from the results of the previous section that only a part of the high-velocity abrasive impacts the rock surface because of the shield effect of the rebound abrasive. The impact force of a high-speed abrasive can cause a brittle rupture of the rock, inducing a fracture on the surface and inside the rock [46]. The fractures formed by the adjacent abrasive connect to each other to form through the fracture, which strips one part of the rock mass from the surface and forms rock fragments. The impact force of a low-velocity abrasive is too small to cause a brittle fracture but is sufficiently large to press the abrasive into the rock surface and induce plastic flow of the rock. This leads to the formation of pits and flanges, namely, lip formation. When the second abrasive presses into the pit and surrounding flanges, the plastic flow will occur again. Such repeated plastic deformation and work hardening finally cause the rock to gradually harden and drop off brittlely [20]. The number of fractures is obviously larger than that of lip formations, and there is no residual abrasive at the base. It can be identified that the rock mass is peeled off after the fractures are being transmitted through the rock. Therefore, the stress wave formed by the impact force is the main reason for the rock failure at the base of the hemispherical bottom.

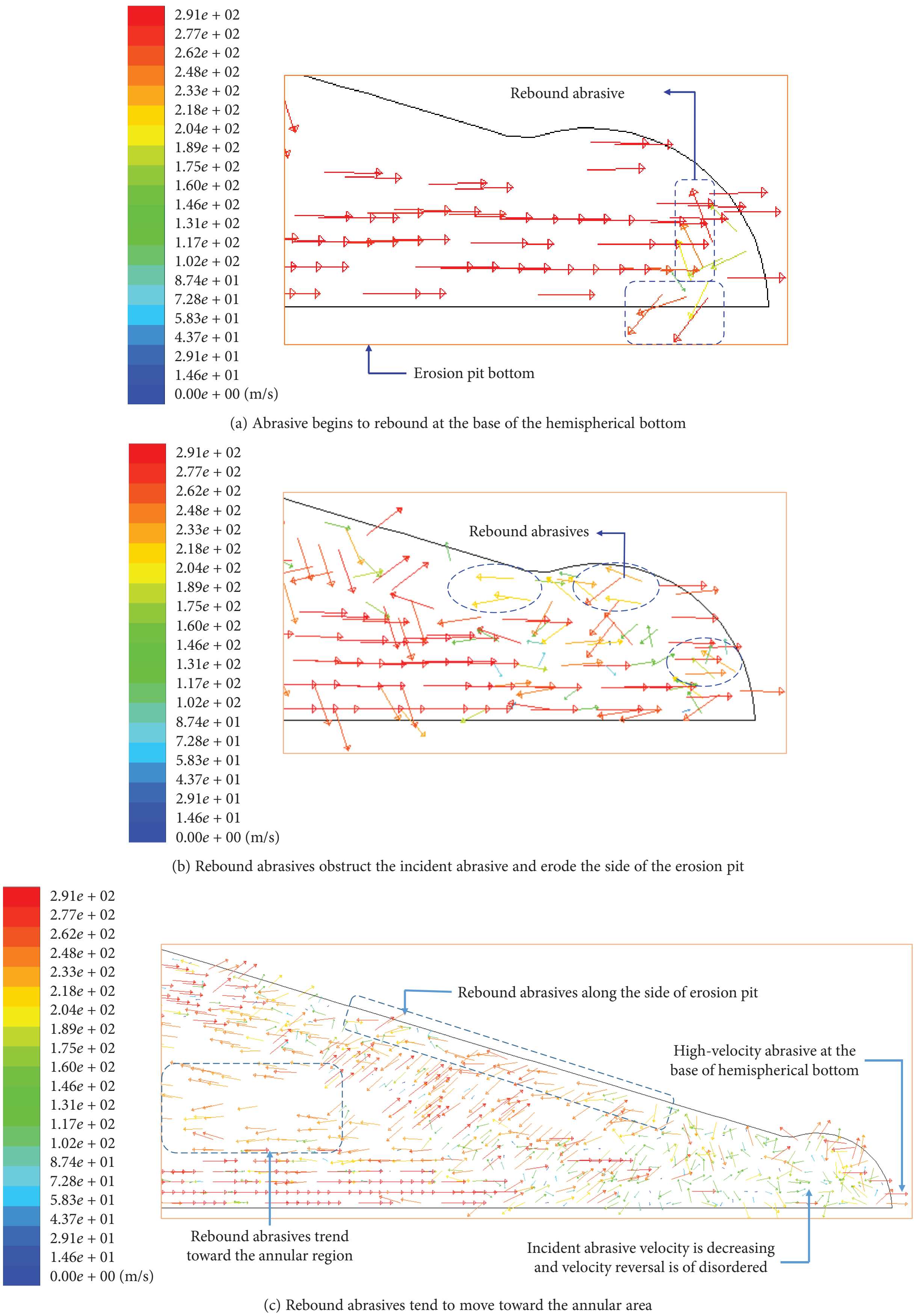

Figure 9: Abrasive distribution and motion direction of the abrasive during rock erosion by the abrasive gas jets.

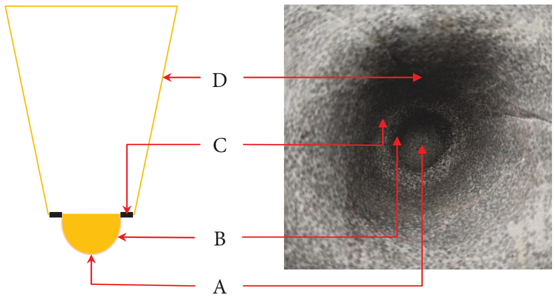

Figure 10: Position of scanning electron microscope. (A) Base of the hemispherical bottom. (B) The side of the hemispherical bottom. (C) Annular platform of the erosion pit. (D) The side of the erosion pit.

The failure characteristics of the side of the hemispherical bottom are obviously different from those at the base (in Figure 11(b), the triangle mark section is the base of the hemispherical bottom). From the comparison, it can be found that the failure of the side of the hemispherical bottom is mainly characterized by lip formation and there is a residual abrasive (marked with "○" in Figure 11(b)). The results of the numerical simulation exhibit that the side of the hemispherical bottom is mainly eroded by the rebound abrasive. The diameter of the rebound abrasive decreases because of the breakage of the incident abrasive after impact with the rock. The velocity of the rebound abrasive decreases because of the blockage of the incident abrasive. Therefore, the impact force of the abrasive applied on the side of the hemispherical bottom cannot lead to brittle rupture of the rock; it instead causes plastic deformation. The angle of embedding of the residual abrasive shows that the impact angle of the abrasive is large, similar to the result of Figures 9(b) and 9(c). Therefore, the rebound abrasive only leads to lip formation on the side of the hemispherical bottom.

Figure 11(c) is the SEM image of the annular platform of the erosion pit; the area marked with "□" is the boundary between the annular platform (upper section) and the side of the hemispherical bottom (lower section). The failure characteristics of the annular platform are similar to those of the side of the hemispherical bottom. Lip formation is the main failure characteristic of the annular platform, i.e., the rock of the annular platform fails primarily with the characteristic of plastic deformation. In addition, there are lateral cracking (denoted as "L") and residual abrasives but the residual abrasives are embedded at a shallow depth. According to the results of the numerical simulation, the rebound abrasive purely and simply erodes the annular platform. The failure mechanism of the rock is different owing to the different erosion angles of the rebound abrasive. When the erosion angle of the abrasive is large, the abrasive can produce lip formation on the rock surface. When the erosion angle of the abrasive is small (almost parallel to the rock surface), the abrasive will roll easily on the rock surface and will not effectively erode the wear rock. However, some abrasive can erode the rock and form flake-like lateral cracking when their angle is between those abrasives that can cause lip formation and rolling. When the abrasive moves to the annular platform, the velocity is lower than that at the hemispherical bottom. The normal stress of the impact force of the abrasive is lower than the yield limit of the rock, which cannot cause plastic deformation of the rock. However, the impact frequency of the abrasive is higher, which is equivalent to applying cyclic stress on the rock. If a rock only undergoes elastic deformation, there would be no damage but the rock surface will be hardened [47]. When the cyclic stress is further applied, a hardened slip plastic deformation layer and crack appear on the rock surface and the crack is parallel to the movement direction of the abrasive. This is consistent with the delamination theory proposed by Suh et al. [48].

The velocity of the rebound abrasive continuously decreases with its upward motion. Instead of plastic deformation, flake-like lateral cracks are formed on the rock surface (as shown in Figure 11(d)). The main failure form of the side of the erosion pit is fatigue damage caused by the cyclic stress of the rebound abrasive, which is consistent with the research results of Momber [19, 20] and Verhoef [49]. However, they failed to specify whether the erosion was of the incident or rebound abrasive.

From the above analysis, it can be concluded that the incident and rebound abrasives jointly erode the rock. However, they erode different parts separately and their erosion mechanisms are also different. At the base of the hemispherical bottom, the impact stress wave of the incident abrasive causes the expansion and connection of the fracture on the rock surface and inside the rock, which leads to rock failure. At the side of the hemispherical bottom, plastic deformation is the main failure characteristic and is induced by the rebound abrasive with a large impact angle. At the annular platform, in addition to the rock failure caused by the plastic deformation induced by the incident abrasive erosion, there is also fatigue failure caused by the rebound abrasive with a low impact angle. At the side of the erosion pit, fatigue failure is the main characteristic, which is induced by the rebound abrasive.

3.2. Influence of Abrasive Hardness on Erosion Failure. The other eroded rock samples were scanned by the SEM with the same method, and the scanning results are shown in Figure 12. Figures 12(a) and 12(b) are the quartz sand-eroded images of the side and bottom, respectively, of the erosion pit. Figures 12(c) and 12(d) are brown aluminum oxide-eroded images of the side and bottom, respectively, of the erosion pit. Figures 12(e) and 12(f) are the silicon carbide-eroded images of the side and bottom, respectively, of the erosion pit. By comparing and analyzing the erosion images of the side and bottom of the erosion pit, it can be concluded that lateral cracking is the main failure of the side of the type of erosion pits but the roughness of the surface is different. The surfaces eroded by brown corundum and silicon carbide are obviously rougher than those eroded by quartz sand. The roughness of the rock surface eroded by silicon carbide is greater than that by brown corundum. There is an intergranular fracture due to fatigue stress on the sides of the erosion pits eroded by the brown corundum and silicon carbide, and the fracture surface is smooth. This indicates that the erosion wear mechanism of the side of

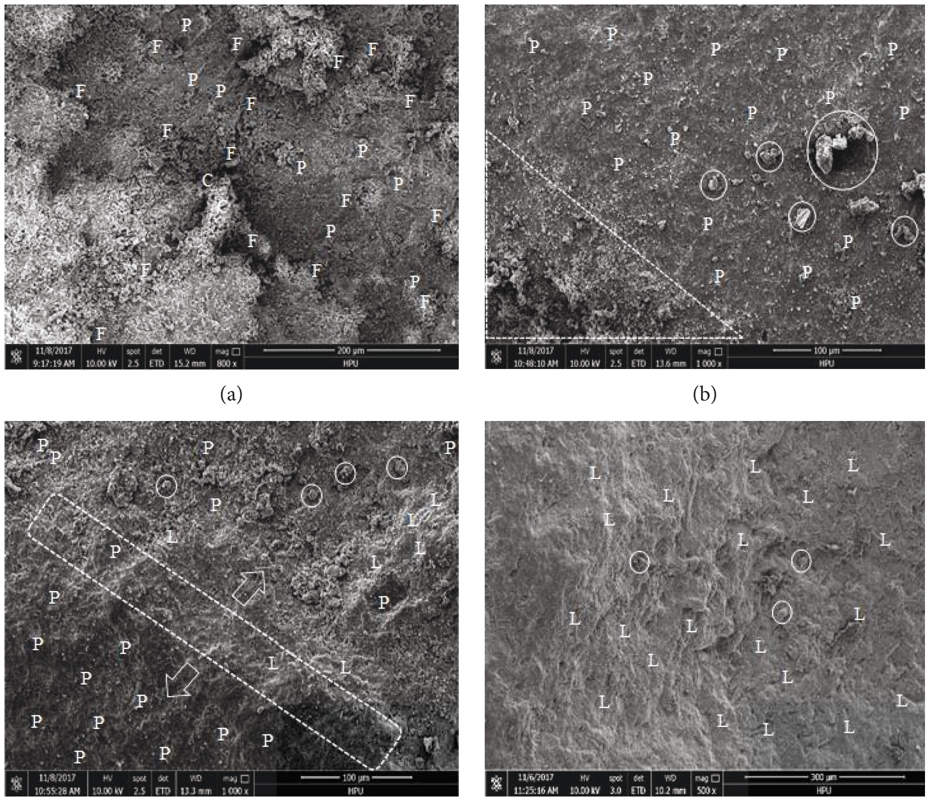

(a) (b) (c) (d)

Figure 11: SEM images of the eroded limestone section.

the erosion pit is not related to the abrasive hardness but is only relevant to the direction of the force of the abrasive. The wear mechanism of the side of the erosion pit is the fatigue failure caused by the shear force of the rebound abrasive with a low incidence angle. The abrasive with a higher hardness is more difficult to destroy, and the energy dissipation on the new surface of the abrasive is small. Therefore, the energy conversion rate of a harder abrasive is higher. Thus, when the energy of the incident abrasive is the same, the force of the harder abrasive on the rock is greater, resulting in a larger range of elastic deformation of the rock. When fatigue failure occurs, the diameter of the peeling rock is larger, leaving a rough erosion surface.

The rock failure at the base of the hemispherical bottom of the three erosion pits is the same as that of the erosion pit eroded by garnet, and the fracture is the main failure characteristic. In addition, lip formation occurs due to the plastic deformation on the rock surface. As is the difference in the side of the erosion pit, the rock surfaces of the base of the hemispherical bottom eroded by brown corundum and silicon carbide have greater roughness. The incident and rebound abrasives jointly erode the rock of the base of the hemispherical bottom. In addition, the impact velocity and impact angle are both large, which leads to the formation of a fracture on the surface and inside the rock. The hard abrasive has a higher rebound velocity. The influence area and fragment size of the peeling rock are larger. Therefore, the rock surface is rougher.

From the comparative analysis, it can be concluded that the abrasive hardness has no effect on the erosion wear mechanism of the abrasive but it can affect the roughness of the rock surface. Therefore, under the same incident condition, the abrasive with higher hardness has a greater damage range and erosion depth. This also demonstrates that a hard abrasive has a high erosion efficiency.

4. Conclusions

In this work, rebound particles of the abrasive gas jet are verified to play an important role in the formation of erosion pits. It induces an irregular inverted cone-shaped erosion pit, whereas the bottom of the erosion pit is hemispherical. Besides the rebound particles, the flow field of the gas jet is another primary factor that leads to the formation of an erosion pit. The annular region without an abrasive between the axis and boundary of the jet affects the flow direction of rebound particles, which leads to the formation of an annular platform lying above the hemispherical bottom and under the side of the erosion pit. The erosion wear mechanism of the rock is different in different areas of erosion, because of the involvement of the rebound particles. At the base of the hemispherical bottom, the impact stress wave of the incident abrasive causes rock failure. The rebound abrasive is barely involved in this area. As more and more rebound particles participate in rock erosion, the mechanism of rock erosion is from plastic deformation to fatigue failure. Such as at the

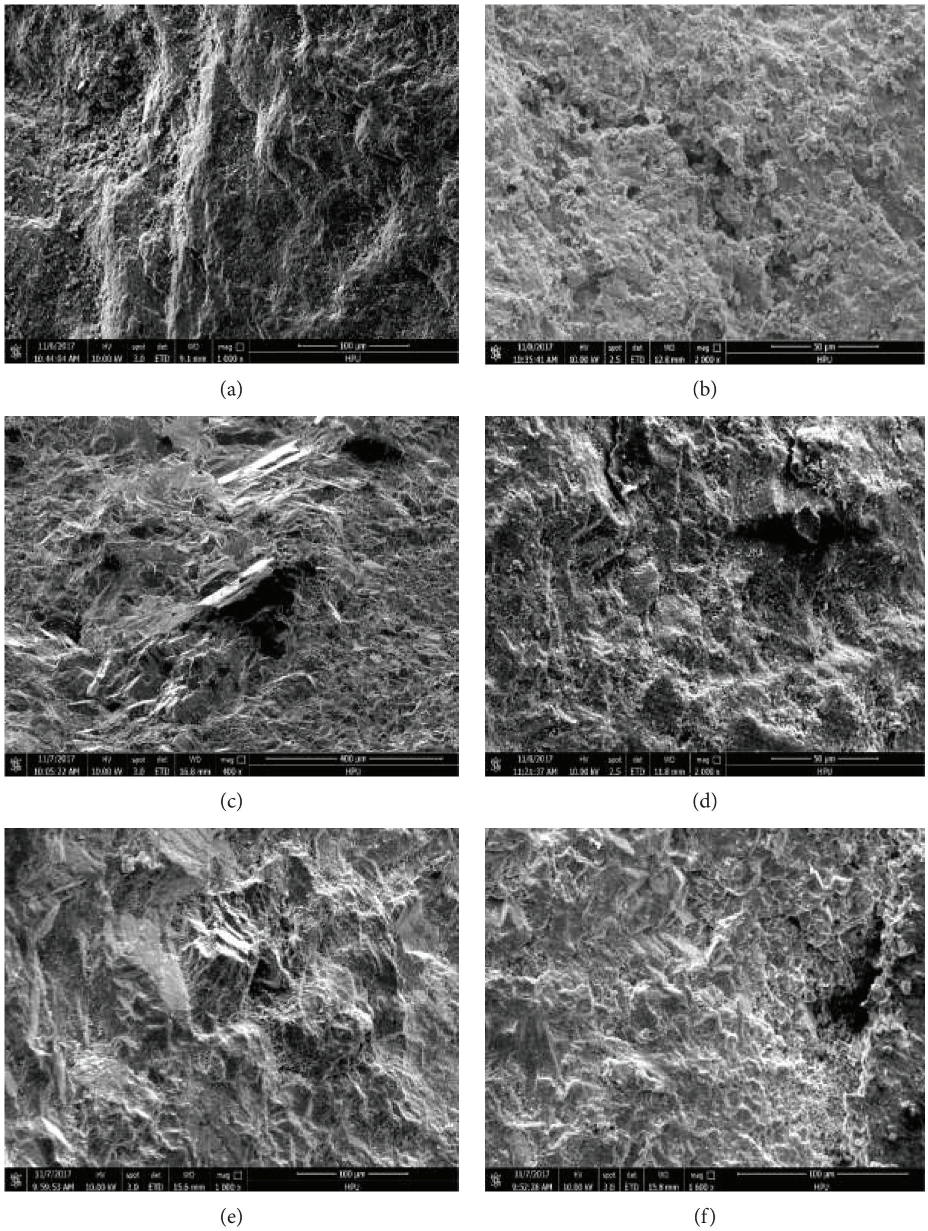

(a) (b) (c) (d) (e) (f)

Figure 12: SEM images of the side and bottom of the erosion pit.

annular platform, the rock failure is caused by plastic deformation and fatigue failure also occurs; at the side of the erosion pit, the fatigue failure is the main characteristic. Abrasive hardness has no effect on the erosion wear mechanism of the rock. However, hard abrasives are more destructive and can induce a greater erosion depth and rougher surface.

Data Availability

The data of the paper refers to numerical simulation and experiment. Their calculation method and results are listed in the paper. That is to say, the data used to support the findings of this study are included within the article. We hope that it can give everyone an evidence to judge the conclusion of the paper.

Conflicts of Interest

The authors declare that they have no conflicts of interest.

Acknowledgments

This paper was jointly funded by the National Science Foundation of China (51704096, 51604092), the National Key Research and Development Program of China (2017YFC0804207), the Program for Innovative Research Team in University (IRT_16R22), the Science Research Funds for the Universities of Henan Province (J2018-4), and the Scientific Research Foundation of State Key Laboratory Cultivation Base for Gas Geology and Gas Control (WS2017A02).

References

[1] J. M. Fan, C. Y. Wang, and J. Wang, "Modelling the erosion rate in micro abrasive air jet machining of glasses," *Wear*, vol. 266, no. 9-10, pp. 968–974, 2009.

[2] H. Nouraei, A. Wodoslawsky, M. Papini, and J. K. Spelt, "Characteristics of abrasive slurry jet micro-machining: a comparison with abrasive air jet micro-machining," *Journal of Materials Processing Technology*, vol. 213, no. 10, pp. 1711–1724, 2013.

[3] J. Wang, A. Moridi, and P. Mathew, "Micro-grooving on quartz crystals by an abrasive air jet," *Proceedings of the Institution of Mechanical Engineers Part C-Journal of Mechanical Engineering Science*, vol. 225, no. 9, pp. 2161–2173, 2011.

[4] H. Z. Wang, G. S. Li, Z. G. He, Z. H. Shen, M. Wang, and Y. W. Wang, "Mechanism study on rock breaking with supercritical carbon dioxide jet," *Atomization and Sprays*, vol. 27, no. 5, pp. 383–394, 2017.

[5] H. Z. Wang, G. S. Li, Z. H. Shen et al., "Experiment on rock breaking with supercritical carbon dioxide jet," *Journal of Petroleum Science and Engineering*, vol. 127, pp. 305–310, 2015.

[6] H. Z. Wang, M. Wang, B. Yang, Q. Lu, Y. Zheng, and H. Q. Zhao, "Numerical study of supercritical CO2 and proppant transport in different geometrical fractures," *Greenhouse Gases: Science and Technology*, vol. 8, no. 5, pp. 898–910, 2018.

[7] Y. Liu, B. C. Liang, and X. T. Liu, "Experimental and numerical optimization of coal breakage performance parameters through abrasive gas jet," *International Journal of Heat and Technology*, vol. 35, no. 4, pp. 747–754, 2017.

[8] Z. Wen, B. Liang, and X. Liu, "Experimental study on influence of abrasive characteristics on coal breaking by abrasive gas jet," *Zhongguo Anquan Shengchan Kexue Jishu*, vol. 103, 2017.

[9] Y. Liu, J. Wei, and T. Ren, "Analysis of the stress wave effect during rock breakage by pulsating jets," *Rock Mechanics and Rock Engineering*, vol. 49, no. 2, pp. 503–514, 2016.

[10] Y. Liu, J. Wei, T. Ren, and Z. Lu, "Experimental study of flow field structure of interrupted pulsed water jet and breakage of hard rock," *International Journal of Rock Mechanics and Mining Sciences*, vol. 78, pp. 253–261, 2015.

[11] Y. Lu, F. Huang, X. Liu, and X. Ao, "On the failure pattern of sandstone impacted by high-velocity water jet," *International Journal of Impact Engineering*, vol. 76, pp. 67–74, 2015.

[12] M. Mieszala, P. L. Torrubia, D. A. Axinte et al., "Erosion mechanisms during abrasive waterjet machining: model microstructures and single particle experiments," *Journal of Materials Processing Technology*, vol. 247, pp. 92–102, 2017.

[13] V. Hadavi, C. E. Moreno, and M. Papini, "Numerical and experimental analysis of particle fracture during solid particle erosion, part I: modeling and experimental verification," *Wear*, vol. 356-357, pp. 135–145, 2016.

[14] V. Hadavi, C. E. Moreno, and M. Papini, "Numerical and experimental analysis of particle fracture during solid particle erosion, part II: effect of incident angle, velocity and abrasive size," *Wear*, vol. 356-357, pp. 146–157, 2016.

[15] A. Limpichaipanit and R. I. Todd, "The relationship between microstructure, fracture and abrasive wear in Al2O3/SiC nanocomposites and microcomposites containing 5 and 10% SiC," *Journal of the European Ceramic Society*, vol. 29, no. 13, pp. 2841–2848, 2009.

[16] A. Momber, "Bruchbilder in Kalknatronglas nach Kontaktbeanspruchung mit hohen Andruckkräften," *Forschung im Ingenieurwesen*, vol. 75, no. 3, pp. 165–182, 2011.

[17] A. Momber, "Fracture features in soda-lime glass after testing with a spherical indenter," *Journal of Materials Science*, vol. 46, no. 13, pp. 4494–4508, 2011.

[18] A. W. Momber, "Wear of rocks by water flow," *International Journal of Rock Mechanics and Mining Sciences*, vol. 41, no. 1, pp. 51–68, 2004.

[19] A. W. Momber, "A probabilistic model for the erosion of cement-based composites due to very high-speed hydro-abrasive flow," *Wear*, vol. 368-369, pp. 39–44, 2016.

[20] A. W. Momber, "A refined model for solid particle rock erosion," *Rock Mechanics and Rock Engineering*, vol. 49, no. 2, pp. 467–475, 2016.

[21] R. Brown, S. Kosco, and E. J. Jun, "The effect of particle shape and size on erosion ofaluminum alloy 1100 at 90° impact angles," *Wear*, vol. 88, no. 2, pp. 181–193, 1983.

[22] T. Deng, A. R. Chaudhry, M. Patel, I. Hutchings, and M. S. A. Bradley, "Effect of particle concentration on erosion rate of mild steel bends in a pneumatic conveyor," *Wear*, vol. 258, no. 1-4, pp. 480–487, 2005.

[23] R. Macchini, M. S. A. Bradley, and T. Deng, "Influence of particle size, density, particle concentration on bend erosive wear in pneumatic conveyors," *Wear*, vol. 303, no. 1-2, pp. 21–29, 2013.

[24] V. B. Nguyen, Q. B. Nguyen, C. Y. H. Lim, Y. W. Zhang, and B. C. Khoo, "Effect of air-borne particle– particle interaction on materials erosion," *Wear*, vol. 322-323, pp. 17–31, 2015.

[25] Q. B. Nguyen, V. B. Nguyen, C. Y. H. Lim et al., "Effect of impact angle and testing time on erosion of stainless steel at higher velocities," *Wear*, vol. 321, pp. 87–93, 2014.

[26] K. Sugiyama, K. Harada, and S. Hattori, "Influence of impact angle of solid particles on erosion by slurry jet," *Wear*, vol. 265, no. 5-6, pp. 713–720, 2008.

[27] G. P. Tilly, "A two stage mechanism of ductile erosion," *Wear*, vol. 23, no. 1, pp. 87–96, 1973.

[28] G. Fowler, I. R. Pashby, and P. H. Shipway, "The effect of particle hardness and shape when abrasive water jet milling titanium alloy Ti6Al4V," *Wear*, vol. 266, no. 7-8, pp. 613–620, 2009.

[29] Z. Mazur, R. Campos-Amezcua, and A. Campos-Amezcua, "Shape modification of an axial flow turbine nozzle to reduce erosion," *International Journal of Numerical Methods for Heat & Fluid Flow*, vol. 19, no. 2, pp. 242–258, 2009.

[30] G. A. Petasyuk, "System and criterial method of the identification and quantitative estimation of the geometrical shape of the abrasive powder grain projection," *Powder Technology*, vol. 264, pp. 78–85, 2014.

[31] C. G. Telfer, M. M. Stack, and B. D. Jana, "Particle concentration and size effects on the erosion-corrosion of pure metals in aqueous slurries," *Tribology International*, vol. 53, pp. 35–44, 2012.

[32] J. X. Deng, "Erosion wear of boron carbide ceramic nozzles by abrasive air-jets," *Materials Science and Engineering: A*, vol. 408, no. 1-2, pp. 227–233, 2005.

[33] J. X. Deng, L. L. Liu, J. H. Liu, X. F. Yang, and M. W. Ding, "Erosion wear behavior and failure mechanisms of ceramic nozzles," *Rare Metal Materials and Engineering*, vol. 34, pp. 223–226, 2005.

[34] Y. H. Feng, J. X. Deng, and Z. L. Ding, "Erosion wear of ceramic sandblasting nozzles," *Rare Metal Materials and Engineering*, vol. 31, pp. 178–181, 2002.

[35] I. Konyashin and B. Ries, "Wear damage of cemented carbides with different combinations of WC mean grain size and co content. Part II: laboratory performance tests on rock cutting and drilling," *International Journal of Refractory Metals & Hard Materials*, vol. 45, pp. 230–237, 2014.

[36] C. Trevisiol, A. Jourani, and S. Bouvier, "Effect of hardness, microstructure, normal load and abrasive size on friction and on wear behaviour of 35NCD16 steel," *Wear*, vol. 388-389, pp. 101–111, 2017.

[37] Y. Liu, J. Zhang, T. Zhang, and H. D. Zhang, "Optimal nozzle structure for an abrasive gas jet for rock breakage," *Geofluids*, vol. 2018, Article ID 9457178, 14 pages, 2018.

[38] Z. H. Wen, Y. Liu, X. T. Liu, and B. C. Liang, "Experimental research into the effects of abrasive characteristics on abrasive gas jet coal-breaking performance," *International Journal of Heat and Technology*, vol. 35, no. 1, pp. 32–36, 2017.

[39] N. Koutsourakis, J. G. Bartzis, and N. C. Markatos, "Evaluation of Reynolds stress, k-ε and RNG k-ε turbulence models in street canyon flows using various experimental datasets," *Environmental Fluid Mechanics*, vol. 12, no. 4, pp. 379–403, 2012.

[40] Z. Amiri and S. Movahedirad, "Bubble-induced particle mixing in a 2-D gas-solid fluidized bed with different bed aspect ratios: a CFD-DPM study," *Powder Technology*, vol. 320, pp. 637–645, 2017.

[41] H. Ling, F. Li, L. Zhang, and A. Conejo, "Investigation on the effect of nozzle number on the recirculation rate and mixing time in the RH process using VOF + DPM model," *Metallurgical and Materials Transactions B*, vol. 47, no. 3, pp. 1950–1961, 2016.

[42] H. Wang, W. Nie, W. Cheng, Q. Liu, and H. Jin, "Effects of air volume ratio parameters on air curtain dust suppression in a rock tunnel's fully-mechanized working face," *Advanced Powder Technology*, vol. 29, no. 2, pp. 230–244, 2018.

[43] Y. Liu, T. Zhang, and X. T. Liu, "Analysis of the stress wave effect during coal breakage by a high-pressure abrasive air jet," *Advances in Mechanical Engineering*, vol. 10, no. 6, 2018.

[44] Y. Z. Xue, H. Si, and Q. T. Hu, "The propagation of stress waves in rock impacted by a pulsed water jet," *Powder Technology*, vol. 320, pp. 179–190, 2017.

[45] I. Belyatinskaya, V. Fel'Dman, V. Milyavsky, T. Borodina, and A. Belyakov, "Transformations of rock-forming minerals under stepwise shockwave compression of quartz-feldspar--biotite-garnet schist from the Southern Urals," *Moscow University Geology Bulletin*, vol. 67, no. 1, pp. 30–42, 2012.

[46] M. Petrica, E. Badisch, and T. Peinsitt, "Abrasive wear mechanisms and their relation to rock properties," *Wear*, vol. 308, no. 1-2, pp. 86–94, 2013.

[47] Y. Ju, H. J. Wang, Y. M. Yang, Q. A. Hu, and R. D. Peng, "Numerical simulation of mechanisms of deformation, failure and energy dissipation in porous rock media subjected to wave stresses," *Science China-Technological Sciences*, vol. 53, no. 4, pp. 1098–1113, 2010.

[48] M. S. Suh, T. Hinoki, and A. Kohyama, "Erosive wear mechanism of new SiC/SiC composites by solid particles," *Tribology Letters*, vol. 41, no. 3, pp. 503–513, 2011.

[49] P. N. W. Verhoef, "Sandblast testing of rock," *International Journal of Rock Mechanics and Mining Sciences & Geomechanics Abstracts*, vol. 24, no. 3, pp. 185–192, 1987.

Hindawi
Geofluids
Volume 2018, Article ID 4653937, 10 pages
https://doi.org/10.1155/2018/4653937

Research Article

Creep Strain and Permeability Evolution in Cracked Granite Subjected to Triaxial Stress and Reactive Flow

Fan Zhang,[1,2] Jianjian Zhao,[1] Dawei Hu,[2] Qian Sheng,[2] and Jianfu Shao[1,3]

[1]*School of Civil Engineering, Architecture and Environment, Hubei University of Technology, Wuhan, China*
[2]*State Key Laboratory of Geomechanics and Geotechnical Engineering, Institute of Rock and Soil Mechanics, Chinese Academy of Sciences, Wuhan, China*
[3]*Laboratory of Mechanics of Lille, University of Lille, Villeneuve-d'Ascq, France*

Correspondence should be addressed to Dawei Hu; dwhu@whrsm.ac.cn

Received 25 June 2018; Accepted 20 September 2018; Published 10 December 2018

Guest Editor: Fengshou Zhang

Fluid flow and fluid-rock interaction mainly take place in fracture network, consequently resulting in deformation and permeability variation of rock and deterioration of the wellbore performance. Mechanical-reactive flow coupling creep tests are performed on cracked granite under various confining pressures and acid and alkaline solution flows. The testing results show that the confining pressure and solution pH significantly influence the creep deformation, creep strain rate, and permeability. A primary creep stage and secondary creep stage are observed in all creep tests in this study; notably, the sample under a confining pressure of 10 MPa and acid solution injection undergoes creep failure for over 2700 hours. The acid solution has a more obvious influence on the creep behavior than that of the alkaline solution. With an increase in confining pressure, the total creep strain and creep strain rate in the samples gradually decrease during the injection of either solution. The permeability of the samples injected with either solution gradually deceases during the testing process, and this deceasing rate increases with the confining pressure. The scanning electron microscopy observations on the crack surfaces after the creep tests show that the surfaces of the fractures injected with the acid solution are smooth due to the dissolution of the matrix, while those injected with the alkaline solution include voids due to the dissolution of quartz. These experimental results could improve the understanding of the long-term transport and mechanical behaviors of wellbore.

1. Introduction

Rock reservoir in subsurface energy resources is under triaxial stress condition, and hydraulic fracking is used to generate fluid transport path for the production of hydrocarbon and geothermal energy [1]. Recent studies suggest that some additives or supercritical CO_2 could be used in enhanced geothermal systems to improve energy extraction [1, 2]. The reactive ions in the fluid could cause fluid-rock interaction in rock materials [3–5]. In the long-term service period of wellbore, the rock formation is required to not only have enough bearing capacity in the early stage but also, and more importantly, meet the long-term deformation limitation as its performance deteriorates due to the coupling effect of triaxial stress and fluid-rock interaction. Previous studies [2, 6] indicated that the fluid-rock interactions have a strong influence on the physical and mechanical properties (e.g., elastic modulus, strength, and permeability) of the rock. Under long-term conditions, the application of stress may aggravate the influences chemical erosion [5, 7–10]. This phenomenon may cause the excessive rock deformation, result in instability of wellbore wall, and decrease the production. Therefore, it is highly needed to investigate the coupling effect of triaxial stress and fluid-rock interaction.

Some scholars carried out experimental studies on the triaxial mechanical behavior of granite after chemical erosion [11–14]. The effects of chemical solutions with different pH values on the strength and deformation of granite were discussed, and the corrosion mechanism of granite by chemical solution was also analyzed. Zhang et al. [15] carried out a triaxial compression test of granite treated by heating and rapid cooling. The experimental result showed that the granite

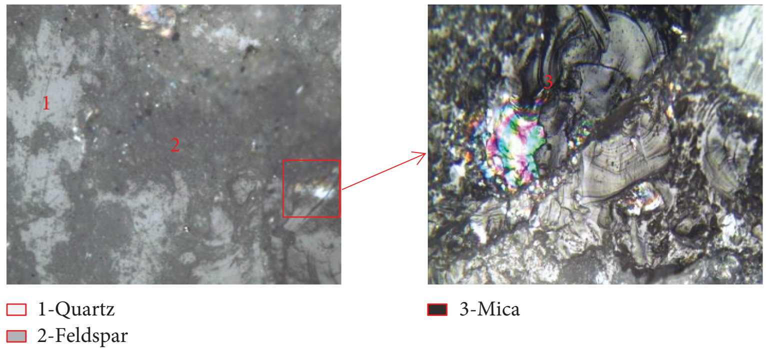

Figure 1: Microscopic structure of the mineral compositions.

strength tended to decrease with the increase in treatment temperature. Chen et al., Polak et al., and Wang et al. [16–18] carried out experimental studies on the effect of mechanical-hydraulic-chemical coupling on permeability and revealed the evolution of permeability with testing time. A considerable research effort has been made to investigate the effect of chemical corrosion and mechanical loading on other porous materials [11, 12, 14, 19–23] The coupling conditions, e.g., stress level, solution pH, and rock mineral compositions, have a great impact on the mechanical and transport properties of rocks. Several constitutive models were proposed to describe the mechanical response and transport evolutions of a cement-based material subjected to mechanical-reactive flow coupling [24]. Mechanical damage induced by applied stress and chemical damage induced by chemical erosion were defined independently. The evolutions of the creep rate and chemical deterioration of materials were analyzed.

The previous investigations mainly studied porous materials, e.g., sandstone, cement, and chalk. However, the host rocks of extracting subsurface energy resources (e.g., enhanced geothermal systems, conventional and unconventional gas, and oil) have low porosities, and their permeability under intact conditions is also low. Therefore, fluid transportation and fluid-rock interaction mainly take place in cracks within the host rocks. The long-term mechanical-reactive flow coupling behavior of cracked rock is clearly different from that of porous rock and thus critical to study.

Granite materials are now widely used in many engineering applications due to their high mechanical strength and low permeability. Studying the creep properties of granite under mechanical-chemical coupling is of great significance for long-term work in many projects. In this paper, the long-term mechanical behavior of granite with preformed fractures in acid-alkaline environment is studied, and the influence of alkaline solution and acid solution on the physical and mechanical behavior of granite are analyzed. This paper is organized as follows. In Section 2, the physical parameters of granite and uniaxial/triaxial compression strength are tested. In Section 3, the creep test of granite with preformed fractures with injecting alkaline and acid solution into the samples during creep test, respectively, is presented. At the same time, the change of permeability of granite with preformed cracks in long-term creep test is monitored to prove the influence of chemical solutions. Finally, the effects of confining pressure, the type of the solution, creep strain rate, and permeability are analyzed. The microstructure of fracture surfaces of the granite samples after creep test is also observed.

2. Test Preparations

The material used in this study is granite from an underground tunnel excavation, and all the samples are drilled from one large block without any observable joints. The density of the samples in their natural condition is 2.61 g/cm^3. X-ray diffraction tests show that the main mineral compositions are quartz (30%), soda feldspar (21.05%), potash feldspar (45.19%), and mica (23.05%). At the microscopic level, quartz grains are scattered in a matrix of soda feldspar, potash feldspar, and mica, which act to cement the larger grains (see Figure 1). The diameter and height of the samples are 37 and 74 mm, respectively.

The intact granite samples have very low permeability, and it is difficult to achieved steady seepage in the samples. Moreover, interactions between rock and reactive solutions mainly occur in excavation damage zones, where cracks are generated in the surrounding rocks after excavation due to stress redistribution (Pepe et al., 2017). Given that tension and shear failure are the two common rock damage mechanisms observed in surrounding rocks, the samples are first subjected to triaxial compressive stress until failure, and different confining pressures, e.g., 0, 5, and 10 MPa, are applied to create different crack patterns (see Figure 2). The typical stress-strain curves of the triaxial compression tests are shown in Figure 3. The samples undergo brittle failure under the confining pressure magnitudes applied in this study. Additionally, under low confining pressure (e.g., 0 MPa), the sample failure is marked by a distinctive peak stress due to the coalescence of tensile cracks, ultimately splitting the sample. Under higher confining pressures (e.g., 5 and 10 MPa), this distinctive peak stress becomes less pronounced. The failure of the sample transitions from tensile cracking to shear cracking. A similar phenomenon has been observed in sandstone [25] and granite [8].

A thermal-hydrological-mechanical-reactive flow coupling testing system is used to perform creep tests with acid and alkaline solution injection, and the sketch diagram of this testing system is presented in Figure 4. The whole testing system is placed into a large oven to perform the tests at

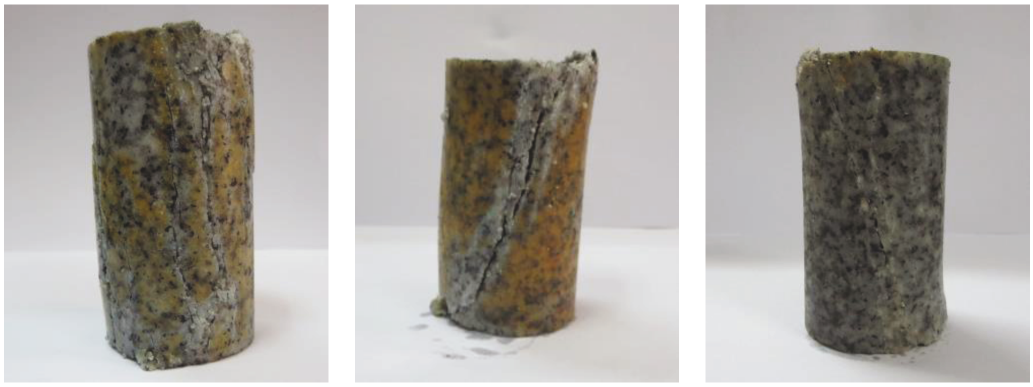

Pc = 0 MPa

(a)

Pc = 5 MPa

(b)

Pc = 10 MPa

(c)

FIGURE 2: Crack patterns after failure.

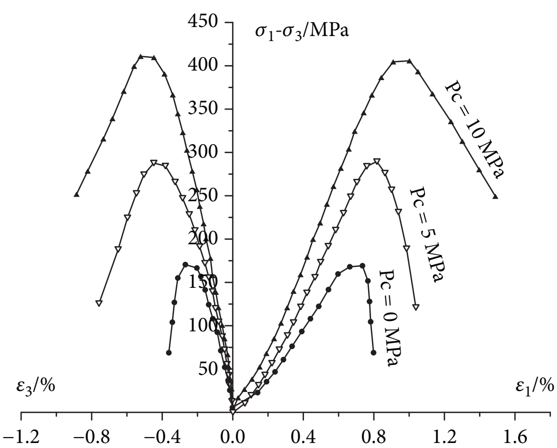

FIGURE 3: Typical stress-strain curves of the triaxial compression tests.

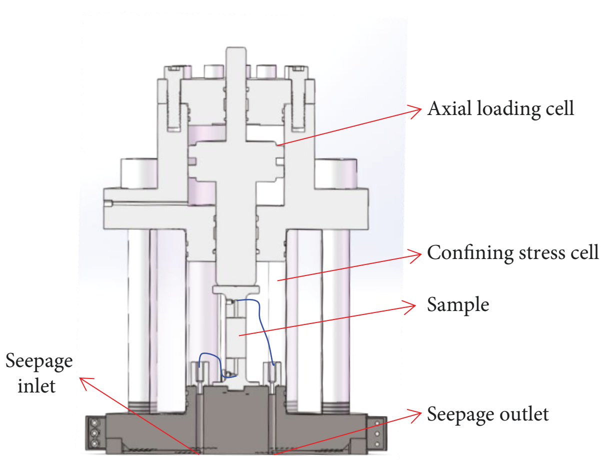

FIGURE 4: Schematic of triaxial compression apparatus.

a predetermined temperature. The testing room is also equipped with an air conditioner and is held at a constant temperature of 20 ± 2°C. Consequently, the temperature conditions during the tests can be controlled to a precision of ±0.2°C.

Throughout this paper, the rock mechanics sign convention is used; compressive stresses and strains are positive. Furthermore, a fixed coordinate frame is used for the cylinder sample, and the cylinder axis is parallel to the x_1 axis. σ_i and ε_i $(i = 1, 2, 3)$ denote the three principal stresses and strains in this frame, while p is the interstitial pressure.

After the triaxial compression tests are completed, the cracked samples are directly used in the subsequent creep tests. The same magnitude of confining pressure is applied to the cracked samples after triaxial compression at confining pressures of 5 and 10 MPa, whereas a confining pressure of 2 MPa is applied to the cracked samples after triaxial compression at a confining pressure of 0 MPa; this low confining pressure can avoid seepage flow between the sample and jacket. The axial stress is reloaded to the predetermined levels, which correspond to 70% of the residual strength of the cracked samples under confining pressures of 2, 5, and 10 MPa. Detailed information about the stress path of the studied samples is presented in Table 1.

Two kinds of solutions with different pH values, namely, a H_2SO_4 solution with pH = 2 and a NaOH solution with pH = 12, are injected into the cracked samples. The pressure at the inlet is 1 MPa, and the pressure at the outlet is identical to atmosphere pressure; a pressure gradient is thus achieved to induce seepage through the samples. A metering pump with a precision of 0.01 MPa is used to apply the pressure gradient and record the seepage volume during the tests.

3. Test Results

3.1. Creep Strain Curves. Six creep tests are performed on the cracked samples; 3 levels of confining pressure and 2 solutions, with pH = 2 and pH = 12, are studied. The variations in creep strain with time are presented in Figure 5.

The creep curves of the fractured granite under mechanical-reactive flow coupling conditions show obvious creep characteristics. In the initial creep stages, the strain clearly increases with time. After a certain period, the rate of increase in the strain decreases, and the sample enters the stable stage. All the samples in this study undergo a primary creep stage and secondary creep stage, whereas sample

Table 1: Detailed information of the samples used in the triaxial compression tests and creep tests.

Sample no.	Triaxial compression test	Creep test			
	Confining pressure (MPa)	Confining pressure (MPa)	Deviatoric stress (MPa)	Seepage pressure (MPa)	Injected solution
1	0	2	34.52	1	pH = 2
2	0	2	34.52	1	pH = 12
3	5	5	48.35	1	pH = 2
4	5	5	48.35	1	pH = 12
5	10	10	63.62	1	pH = 2
6	10	10	63.62	1	pH = 12

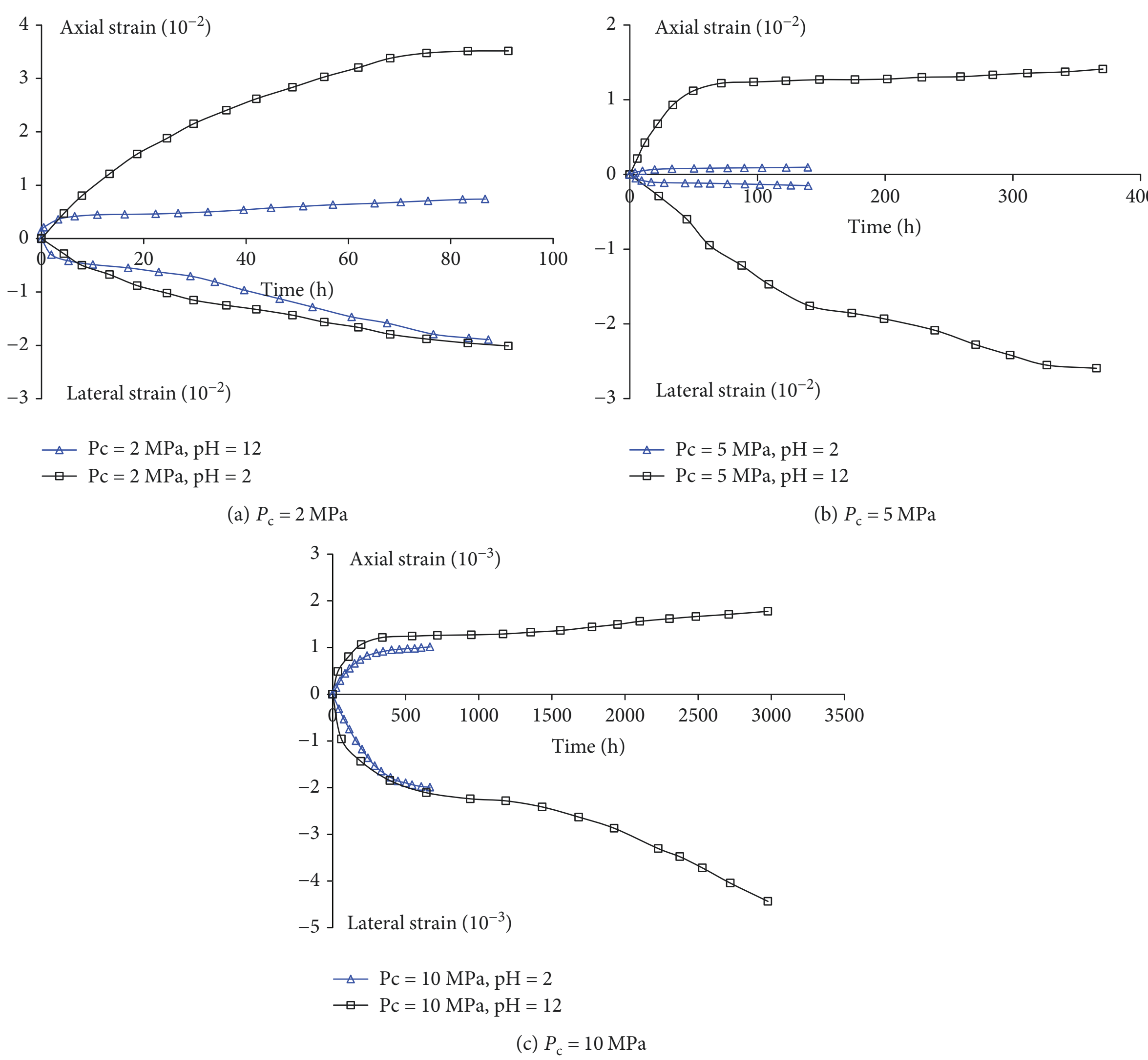

(a) $P_c = 2$ MPa

(b) $P_c = 5$ MPa

(c) $P_c = 10$ MPa

Figure 5: Creep strain evolutions of the cracked samples under different confining pressures and reactive solution injection.

no. 6 (confining pressure of 10 MPa with acid solution injection, Figure 5(c)) undergoes a tertiary creep stage before ultimately losing its strength.

Compared with the alkaline solution, the acid solution induces a more obvious effect on the creep behavior. Under all confining pressures, the creep strains of the samples injected with the acid solution are greater than those injected with the alkaline solution. Moreover, the time to a stable creep strain during the injection of an acid solution is greater than that of an alkaline solution, and this phenomenon becomes more significant when the confining pressure increases. The differences in creep behavior between the samples injected with acid and alkaline solutions are attributed to the different mechanisms of the solution-mineral reactions;

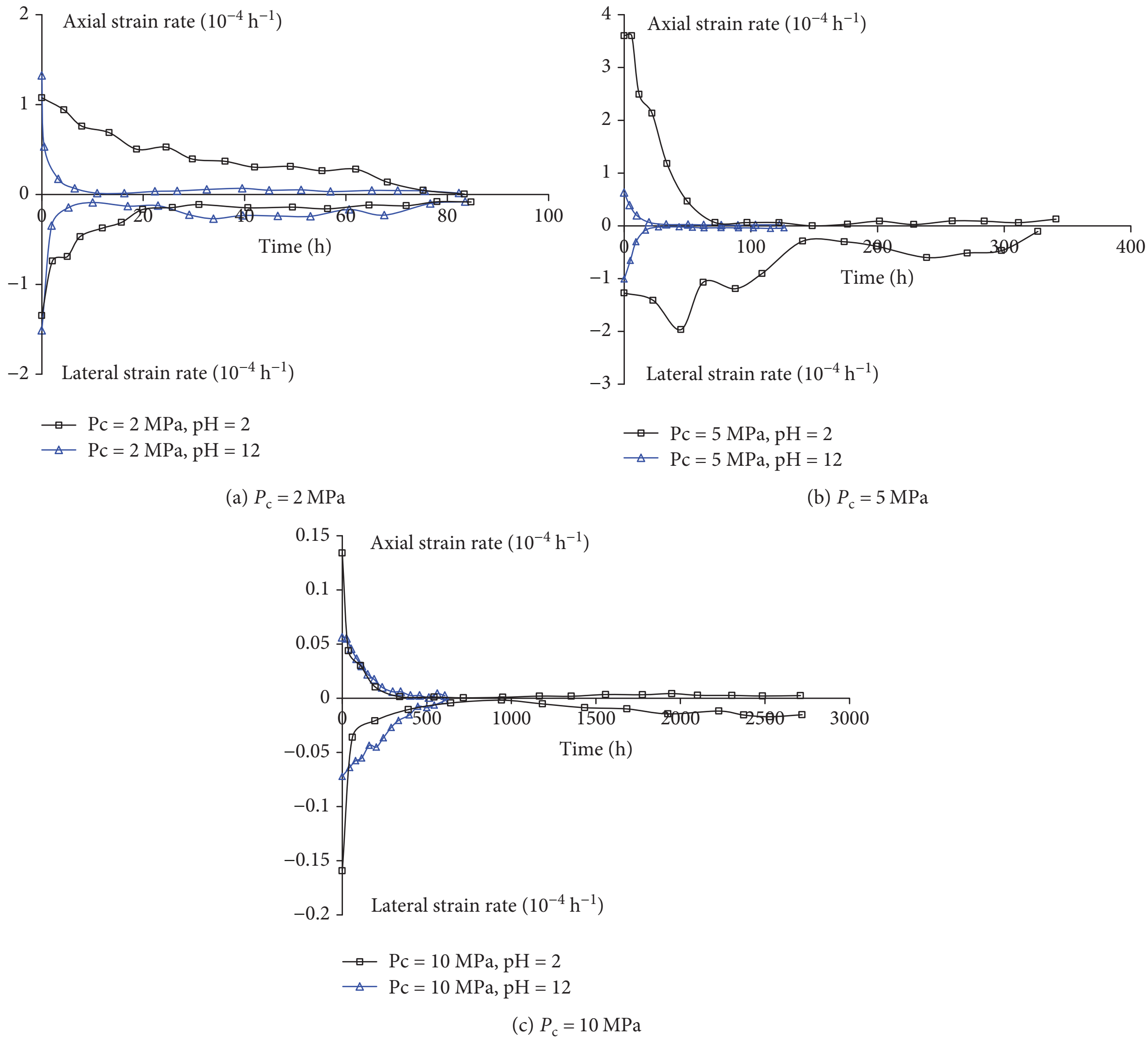

(a) $P_c = 2$ MPa

(b) $P_c = 5$ MPa

(c) $P_c = 10$ MPa

FIGURE 6: Creep strain rate evolutions of the cracked samples under different confining pressures and reactive solution injection.

these mechanisms will be explained in the following sections. Similar results have been observed in artificially fractured granite [26, 27]. The results have been shown that the feldspar and biotite are relative more sensitively reacted with the acid solution than the quartz, and the acidizing solutions change the mechanical properties of rocks. Luo et al. [26] stated that the degree of rough of crack surface decreases after 600 h chemical reaction, and the original rough crack surface gradually becomes smooth due to the chemical reaction of granite in chemical reagents. On the other hand, the degree of corrosion of granite under acidic conditions is higher than that under alkaline conditions; thus, the fracture surface in the acidic environment is strongly corroded, while the fracture surface in the alkaline environment is relatively rough.

The confining pressure also has a significant effect on the creep behavior. With an increase in confining pressure, the creep strains during injection of either the acid or alkaline solution gradually decrease, and the total creep strain under a confining pressure of 10 MPa is one order of magnitude less than that under a confining pressure of 2 or 5 MPa. This phenomenon could be explained by the limitation of deformation due to confining pressure. Similar results were shown in considering the hydrological-mechanical coupling in fractured rocks [28–30].

3.2. Creep Strain Rate. To further analyze the effect of confining pressure and solution pH on the creep behavior, the creep strain rates are calculated and presented in Figure 6. The creep rate is calculated from the following relation:

$$\dot{\varepsilon}_t = \frac{\varepsilon_{t+1} - \varepsilon_t}{\Delta t}, \tag{1}$$

where $\dot{\varepsilon}_t$ represents the creep rate at creep time t. ε_{t+1} and ε_t represent the creep strains corresponding to time $t + 1$ and time t, respectively. Δt is the time interval between time t and $t + 1$.

As mentioned above, the injection of the acid solution has a more significant effect on the creep behavior than

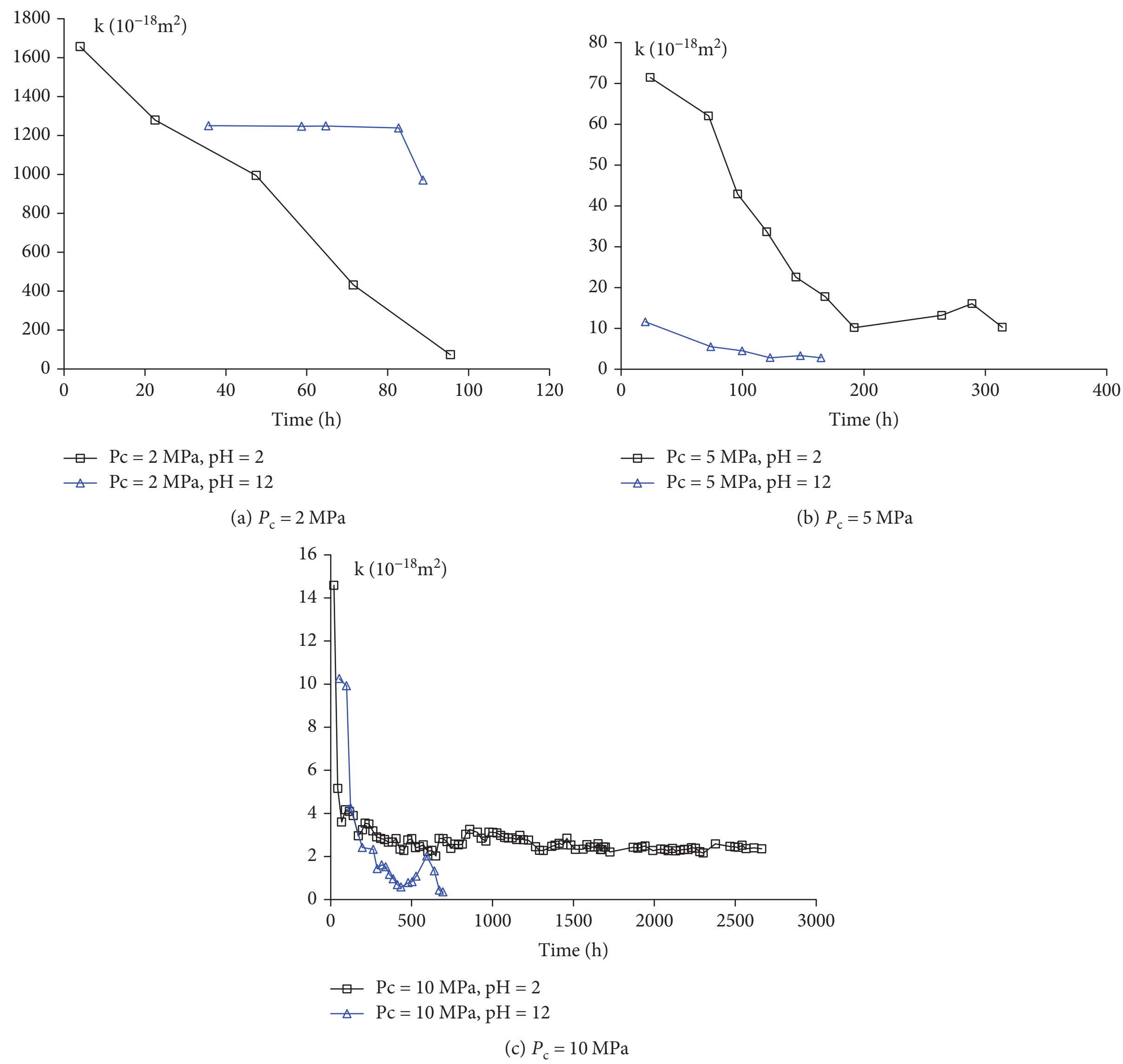

(a) $P_c = 2$ MPa

(b) $P_c = 5$ MPa

(c) $P_c = 10$ MPa

Figure 7: Permeability evolutions of the cracked samples under different confining pressures and reactive solution injection.

that of the alkaline solution. The curves of creep strain rate in Figure 6 confirm these results. The creep strain rates in both the axial and lateral directions with injection of the acid solution are greater and take a longer time to reach stability than those of the alkaline solution. Notably, the creep strain rate in the lateral direction under a confining pressure of 10 MPa and acid solution injection is significantly greater than that in the axial direction during the tertiary creep stage. Therefore, the sample undergoes volumetric dilation during the creep failure stage, and this volumetric dilation is attributed to the shear deformation of the compressive shear fractures (see Figure 2).

3.3. Permeability Tests. The permeability of the samples during the mechanical-reactive flow coupling tests is measured regularly at a predetermined time interval. Given the correlation between permeability and fracture aperture, the permeability evolutions could be used to evaluate the fracture aperture and transport properties of the cracked samples. The steady-state method is applied in this study, and the permeability of a sample can be calculated by using Darcy's law by measuring the flow rate of the seepage fluid.

$$k\left(\mathrm{m}^2\right) = \frac{Q\mu L}{\Delta p A}, \tag{2}$$

where k is the intrinsic permeability (m^2); Q is the injection flow rate ($\mathrm{m}^3 \cdot \mathrm{s}^{-1}$); μ denotes the dynamic fluid viscosity coefficient; L and A are the length and cross section of the sample, respectively; and Δp is the pressure difference between the inlet and outlet of the seepage and it is equal to 1 MPa.

In Figure 7, the initial permeability of the cracked samples during the initial creep stage is highly dependent on the confining pressure. The permeability under a confining pressure of 2 MPa is two orders of magnitude greater than that under a confining pressure of 10 MPa. Consequently, the permeability of all the samples decreases as time increases and stabilizes under high confining pressures. The rate of decrease in the permeability of the samples injected with the acid solution is slightly greater than that of samples injected with the alkaline solution. Therefore, confining pressure has a greater effect on the permeability evolution than the effect of injecting a reactive solution. Similar results showed that the fracture aperture and permeability basically decrease with time under various external confinements (stresses) and solution transport for different rocks [17, 31, 32]. According to previous hydrological-mechanical-chemical coupling models [28, 30], the decrease in permeability is directly attributed to the aperture decrease caused by pressure solution.

4. Discussions

The results above indicate that the creep strain and permeability of the cracked samples depend on the confining pressure and the reactive solutions. The rock-solution reaction during the creep tests is discussed in the following subsection.

4.1. Rock-Solution Reaction. The abovementioned X-ray diffraction tests show that soda feldspar, potash feldspar, and mica account for 70% of the total mineral content of the samples, and quartz accounts for the remaining 30%. Under the studied acidic condition (pH = 2), the former three minerals undergo dissolution to some degree due to the acid ions [33], while quartz is nearly inactive. The reaction process can be described as follows:

$$NaAlSi_3O_8 + 4H^+ + 4H_2O = Al^{3+} + 3H_4SiO_4 + Na^+ \quad (3)$$

$$KAlSi_3O_8 + 4H^+ + 4H_2O = Al^{3+} + 3H_4SiO_4 + K^+ \quad (4)$$

$$KAl_3SiO_{10}(OH)_2 + 10H^+ = 3Al^{3+} + 3SiO_2 + K^+ + 6H_2O \quad (5)$$

However, under the studied alkaline condition (pH = 12), the quartz undergoes slight dissolution due to the alkaline ions, while the former three minerals are nearly inactive. The reaction between the quartz and alkaline ions is described as follows:

$$SiO_2 + 2NaOH = Na_2SiO_3 + H_2O \quad (6)$$

Previous studies (Lehner, 1990; Wolery, 1992) indicated that the reaction rate in (3–5) is significantly greater than that in (6); therefore, the injection of the acid solution has a greater influence on the creep behavior than that of the alkaline solution.

4.2. Fracture Surface Observations. Scanning electron microscopy (SEM) is applied to observe the fracture surface morphology of the cracked samples after the creep tests. A sheet of 1 cm^2 was taken at different positions on the fracture surface of each sample. And SEM test was performed after progress of conductive coating, and three sheets were taken for each sample. And the SEM images are shown in Figure 8. At each confining pressure, the fracture surfaces injected with acid solution are smooth, while those injected with alkaline solution are rough and include voids. According to the microscopic structure of the mineral composition, shown in Figure 1, the soda feldspar, potash feldspar, and mica grains form a rock matrix and encapsulate the quartz grains. When the acid solution comes into contact with the fracture surfaces, the rock matrix undergoes dissolution, and the dissolved ions are transported in the seepage flow. Consequently, the quartz grains debond from the fracture surface and are transported in the seepage flow once the surrounding matrix has dissolved. Therefore, the fracture surfaces in contact with the acid solution are smooth. However, when the alkaline solution comes into contact with the fracture surfaces, the quartz grains dissolve, while the surrounding matrix is nearly unaffected. Therefore, voids on the fracture surface are caused by the dissolution of quartz grains.

In addition, it can be seen from the creep curve that the sample in the acid environment under a confining pressure of 10 MPa reaches creep failure over 2700 hours. This time is much larger than the other several conditions, for example, lower confining pressure and alkaline environment. It is apparent that the rupture surface is rough after the uniaxial/triaxial compression test. Therefore, the specimen still has the ability to withstand a certain load. Since the acidic solution is highly corrosive to the fracture surface, the fracture surface is gradually smoothed. However, the fracture surface in the alkaline solution is rough. Under the action of the creep load, the fracture surface easily leads to the piercement of the test sleeve of the wrapped sample and consequently causes the end of the test. Therefore, the creep time of the sample in an acidic environment is larger than that in an alkaline environment.

5. Conclusions

Triaxial creep tests were performed on cracked samples injected with reactive solutions. Three different confining pressures, namely, 2, 5, and 10 MPa, and a corresponding residual strength of 70% were applied during the tests. Additionally, two solutions with different pH values, namely, a H_2SO_4 solution with pH = 2 and a NaOH solution with pH = 12, were injected into the cracked samples during the tests. And at the same time conduct the permeability test. It can be found that the permeability of the fractured granite in the acidic solution is greater than the permeability of the fractured granite in the alkaline solution. Finally, a SEM experiment was performed on the fracture surface and can get the following conclusions:

(1) The failure mode of granite samples changes from brittle failure to ductile failure with the increase of confining pressure in the triaxial compression test. And the residual strength after the peak gradually increases with the increase of confining pressure as well

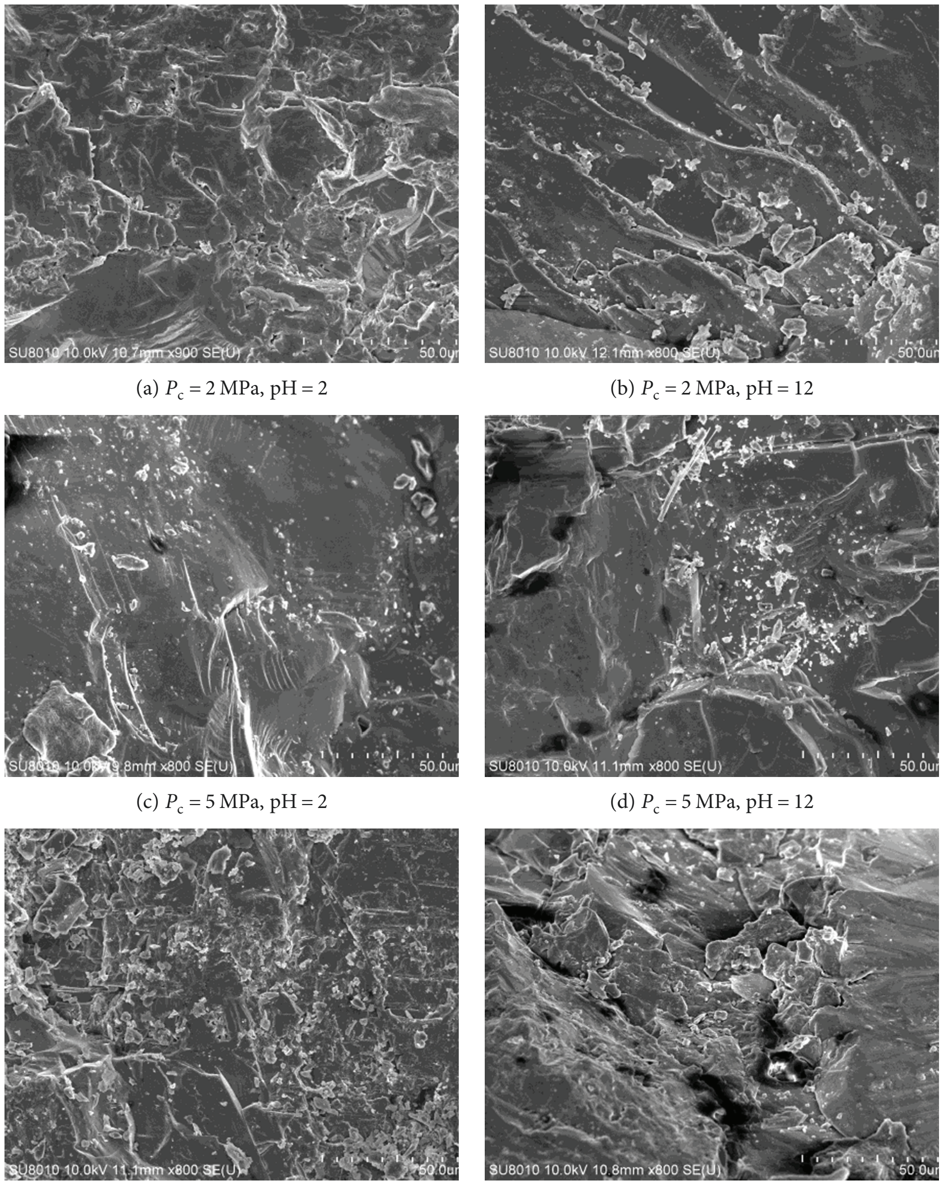

(a) $P_c = 2$ MPa, pH = 2 (b) $P_c = 2$ MPa, pH = 12

(c) $P_c = 5$ MPa, pH = 2 (d) $P_c = 5$ MPa, pH = 12

(e) $P_c = 10$ MPa, pH = 2 (f) $P_c = 10$ MPa, pH = 12

Figure 8: Photographs of the microstructures at the fracture surfaces of the samples after the creep tests.

(2) The degree of corrosion of granite in alkaline environment is worse than that in acid environment

(3) Confining pressure has a significant effect on the long-term stability of granite

The study of long-term mechanical properties of granite requires more time rather than the short-term mechanical study. Therefore, the research on the creep properties of multifield coupled of granite is still rare in the world at present, especially considering the long-term performance research under the thermal-hydrological-mechanical-chemical (THMC) coupling processes. So, the next work will focus on the long-term mechanical properties of granite under multiphysics coupling conditions.

Symbols

P_c: Confining pressure
x_1: Axis direction of pressure chamber
σ_i: Principal stresses in this frame ($i = 1, 2, 3$)
ε_i: Principal strains in this frame ($i = 1, 2, 3$)
p: Interstitial pressure
t: Creep time
$\dot{\varepsilon}_t$: Creep rate at creep time t
ε_t: Creep strains corresponding to time t
ε_{t+1}: Creep strains corresponding to time $t + 1$
Δt: Time interval between time t and $t + 1$
k: Intrinsic permeability
Q: Injection flow rate

μ: Dynamic fluid viscosity coefficient
L: Length of the samples
A: Cross section of the samples
Δp: Pressure difference between the inlet and outlet of the seepage channel.

Data Availability

The experimental data used to support the findings of this study are included within the article.

Conflicts of Interest

The authors declare that they have no conflicts of interest.

Acknowledgments

Financial support from the National Sciences Foundation of China (nos. 51479193 and 51779252) and the "100 Talent Program" of the Chinese Academy of Sciences is gratefully acknowledged.

References

[1] E.-S. Salama, M. B. Kurade, R. A. I. Abou-Shanab et al., "Recent progress in microalgal biomass production coupled with wastewater treatment for biofuel generation," *Renewable and Sustainable Energy Reviews*, vol. 79, pp. 1189–1211, 2017.

[2] Y. Pan, T. Tian, C. O. Park et al., "Survival of tissue-resident memory T cells requires exogenous lipid uptake and metabolism.," *Nature*, vol. 543, no. 7644, pp. 252–256, 2017.

[3] H. Milsch, A. Seibt, and E. Spangenberg, "Long-term petrophysical investigations on geothermal reservoir rocks at simulated in situ conditions," *Transport in Porous Media*, vol. 77, no. 1, pp. 59–78, 2009.

[4] J. Taron, D. Elsworth, and K.-B. Min, "Numerical simulation of thermal-hydrologic-mechanical-chemical processes in deformable, fractured porous media," *International Journal of Rock Mechanics and Mining Sciences*, vol. 46, no. 5, pp. 842–854, 2009.

[5] H. Zhou, D. Hu, F. Zhang, J. Shao, and X. Feng, "Laboratory investigations of the hydro-mechanical–chemical coupling behaviour of sandstone in CO_2 storage in aquifers," *Rock Mechanics and Rock Engineering*, vol. 49, no. 2, pp. 417–426, 2016.

[6] Q. Wei, F. Xiong, S. Tan et al., "Porous one-dimensional nanomaterials: design, fabrication and applications in electrochemical energy storage," *Advanced Materials*, vol. 29, no. 20, article 1602300, 2017.

[7] X. Chen, S. F. Thornton, and J. Small, "Influence of hyperalkaline pH leachate on mineral and porosity evolution in the chemically disturbed zone developed in the near-field host rock for a nuclear waste repository," *Transport in Porous Media*, vol. 107, no. 2, pp. 1–17, 2015.

[8] D. Hu, H. Zhou, J. Shao, and F. Zhang, "4- Stress-induced permeability evolutions and erosion damage of porous rocks," in *Porous Rock Fracture Mechanics*, pp. 63–92, Woodhead Publishing, 2017.

[9] V. R. Sandeep, A. Chaudhuri, and S. Kelkar, "Permeability and flow field evolution due to dissolution of calcite in a 3-D porous rock under geothermal gradient and through-flow," *Transport in Porous Media*, vol. 112, no. 1, pp. 39–52, 2016.

[10] C. Zhao, B. E. Hobbs, A. Ord, P. Hornby, and S. Peng, "Effect of reactive surface areas associated with different particle shapes on chemical-dissolution front instability in fluid-saturated porous rocks," *Transport in Porous Media*, vol. 73, no. 1, pp. 75–94, 2008.

[11] A. Fakhimi and B. Hemami, "Rock uniaxial compression test and axial splitting," *Procedia Engineering*, vol. 191, Supplement C, pp. 623–630, 2017.

[12] M. G. Karfakis and M. Akram, "Effects of chemical solutions on rock fracturing," *International Journal of Rock Mechanics and Mining Sciences & Geomechanics Abstracts*, vol. 30, no. 7, pp. 1253–1259, 1993.

[13] S. Miao, M. Cai, Q. Guo, P. Wang, and M. Liang, "Damage effects and mechanisms in granite treated with acidic chemical solutions," *International Journal of Rock Mechanics and Mining Sciences*, vol. 88, Supplement C, pp. 77–86, 2016.

[14] G. M. Ren, H. Wu, Q. Fang, J. Z. Liu, and Z. M. Gong, "Triaxial compressive behavior of UHPCC and applications in the projectile impact analyses," *Construction and Building Materials*, vol. 113, Supplement C, pp. 1–14, 2016.

[15] F. Zhang, J. Zhao, D. Hu, F. Skoczylas, and J. Shao, "Laboratory investigation on physical and mechanical properties of granite after heating and water-cooling treatment," *Rock Mechanics and Rock Engineering*, vol. 51, no. 3, pp. 677–694, 2018.

[16] W. Chen, J. Liu, F. Brue et al., "Water retention and gas relative permeability of two industrial concretes," *Cement and Concrete Research*, vol. 42, no. 7, pp. 1001–1013, 2012.

[17] A. Polak, D. Elsworth, J. Liu, and A. S. Grader, "Spontaneous switching of permeability changes in a limestone fracture with net dissolution," *Water Resources Research*, vol. 40, no. 3, 2004.

[18] H. Wang, W. Xu, J. Shao, and F. Skoczylas, "The gas permeability properties of low-permeability rock in the process of triaxial compression test," *Materials Letters*, vol. 116, Supplement C, pp. 386–388, 2014.

[19] F. Agostini, Z. Lafhaj, F. Skoczylas, and H. Loodsveldt, "Experimental study of accelerated leaching on hollow cylinders of mortar," *Cement and Concrete Research*, vol. 37, no. 1, pp. 71–78, 2007.

[20] X.-T. Feng, W. Ding, and D. Zhang, "Multi-crack interaction in limestone subject to stress and flow of chemical solutions," *International Journal of Rock Mechanics and Mining Sciences*, vol. 46, no. 1, pp. 159–171, 2009.

[21] F. H. Heukamp, F. J. Ulm, and J. T. Germaine, "Mechanical properties of calcium-leached cement pastes: triaxial stress states and the influence of the pore pressures," *Cement and Concrete Research*, vol. 31, no. 5, pp. 767–774, 2001.

[22] D. Kuhl, F. Bangert, and G. Meschke, "An extension of damage theory to coupled chemo-mechanical processes," in *European Congress on Computational Methods in Applied Sciences and Engineering (ECCOMAS 2000)*, CD-RoM, Barcelona, Spain, 2000.

[23] S. Y. Xie, J. F. Shao, and N. Burlion, "Experimental study of mechanical behaviour of cement paste under compressive stress and chemical degradation," *Cement and Concrete Research*, vol. 38, no. 12, pp. 1416–1423, 2008.

[24] D. Hu, H. Zhou, F. Zhang, and J. Shao, "Modeling of short- and long-term chemomechanical coupling behavior of

cement-based materials," *Journal of Engineering Mechanics*, vol. 140, no. 1, pp. 206–218, 2014.

[25] D. W. Hu, H. Zhou, F. Zhang, and J. F. Shao, "Evolution of poroelastic properties and permeability in damaged sandstone," *International Journal of Rock Mechanics and Mining Sciences*, vol. 47, no. 6, pp. 962–973, 2010.

[26] J. Luo, Y. Zhu, Q. Guo et al., "Chemical stimulation on the hydraulic properties of artificially fractured granite for enhanced geothermal system," *Energy*, vol. 142, pp. 754–764, 2018.

[27] E. Mohtarami, A. Baghbanan, M. Eftekhari, and H. Hashemolhosseini, "Investigating of chemical effects on rock fracturing using extended finite element method," *Theoretical and Applied Fracture Mechanics*, vol. 89, pp. 110–126, 2017.

[28] K.-B. Min, J. Rutqvist, C.-F. Tsang, and L. Jing, "Stress-dependent permeability of fractured rock masses: a numerical study," *International Journal of Rock Mechanics and Mining Sciences*, vol. 41, no. 7, pp. 1191–1210, 2004.

[29] J. Taron and D. Elsworth, "Thermal–hydrologic–mechanical–chemical processes in the evolution of engineered geothermal reservoirs," *International Journal of Rock Mechanics and Mining Sciences*, vol. 46, no. 5, pp. 855–864, 2009.

[30] Z. Zhao, L. Liu, I. Neretnieks, and L. Jing, "Solute transport in a single fracture with time-dependent aperture due to chemically medicated changes," *International Journal of Rock Mechanics and Mining Sciences*, vol. 66, pp. 69–75, 2014.

[31] W. B. Durham, W. L. Bourcier, and E. A. Burton, "Direct observation of reactive flow in a single fracture," *Water Resources Research*, vol. 37, no. 1, pp. 1–12, 2001.

[32] I. Yurtdas, S. Y. Xie, N. Burlion, J. F. Shao, J. Saint-Marc, and A. Garnier, "Deformation and permeability evolution of petroleum cement paste subjected to chemical degradation under temperature," *Transport in Porous Media*, vol. 86, no. 3, pp. 719–736, 2011.

[33] Y. Jiang, W. Y. Yang, and L. Ma, "Aperture evolution of single fracture in granite under triaxial compressive stress and chemical solution seepage," *Chinese Journal of Rock Mechanics and Engineering*, vol. 31, no. 9, pp. 1869–1878, 2012.